~~CONFIDENTIAL~~

THE PHYSICS OF PRESSURIZED WATER REACTORS

VOLUME 2, BOOK 2, NAVAL REACTORS PHYSICS HANDBOOK

VOLUME EDITOR
S. KRASIK

Manager, Central Physics and Mathematics
Westinghouse Electric Corporation
Bettis Plant, Pittsburgh, Pennsylvania

NAVAL REACTORS BRANCH, DIVISION OF REACTOR DEVELOPMENT
UNITED STATES ATOMIC ENERGY COMMISSION

NAVAL NUCLEAR PROPULSION INFORMATION REVIEW / DECLASSIFICATION REVIEW

1ST REVIEW – DATE: 3/8/2022
AUTHORITY: ☒ DC ☐ DD
NAME: S T Bell
Stephen T. Bell, Chief Physicist, NR

2ND REVIEW – DATE: 3/8/2022
AUTHORITY: DD
NAME: Laura J Nanko
Laura J. Nanko, Classification Officer, NRLFO

DETERMINATION [CIRCLE NUMBER(S)]
1. CLASSIFICATION RETAINED
② CLASSIFICATION CHANGED TO: UNCLASSIFIED
③ CONTAINS NO NNPI
4. COORDINATE WITH:
5. DECLASSIFIED
6. CLASSIFIED INFO BRACKETED
⑦ OTHER (SPECIFY): Classified Information Redacted

~~CONFIDENTIAL~~

Chapter 9

DESCRIPTION OF CRITICAL ASSEMBLIES

THE DANGER COEFFICIENT TEST FACILITY

by J. R. Brown

9.1 INTRODUCTION

[redacted] The reactor uses U^{235} (enrichment greater than 90 per cent) in the form of uranyl-nitrate in water. The reactor has also been used to obtain experimental data on criticality.

9.2 DESCRIPTION OF REACTOR AND SOLUTION SYSTEM

(a) Reactor Tank Assembly. A two-level steel platform (Fig. 9.1) supports the reactor. The platform's lower level supports the reactor tank assembly while the top level supports the control rod drives, the neutron source housing and drive, the liquid level measuring device, and other equipment. Reflector water is stored in the tank in the foreground while wash water is stored in the two tanks shown in the background to the left.

A cross section of the reactor tank (1/8-inch-thick stainless steel) and the concentric reflector tank is shown in Fig. 9.2. The bottom reflector is a solid Lucite cylinder (34-inch diameter, 10-inch height). The reactor solution enters the core by flowing around the bottom reflector (no reflector provided above reactor core).

In temperature coefficient experiments, the reactor is indirectly heated by the reflector water (electrical immersion heaters, capacity 45-kilowatts, are provided in the reflector).

(b) Solution Storage and Handling System. The hydrogen to U^{235} atomic ratios needed for the desired range of critical heights vary from approximately 1600 to 1800. The 250 gallons of solution needed for the core are stored in 22 stainless steel tanks (5-inch diameter, 11-foot height). The tanks are placed in a line (on 16-inch centers) along the wall of a storage vault (Fig. 9.3), separated by piers of magnesium oxychloride cement, and wrapped in a 0.020-inch-thick cadmium sheet to provide safe storage for any concentrated solution. Drip pans and leak alarms guard against loss of solution. A platform, several feet above the vault floor, permits easy access to the valves. A separate system of five storage tanks is provided for solution awaiting reconcentration.

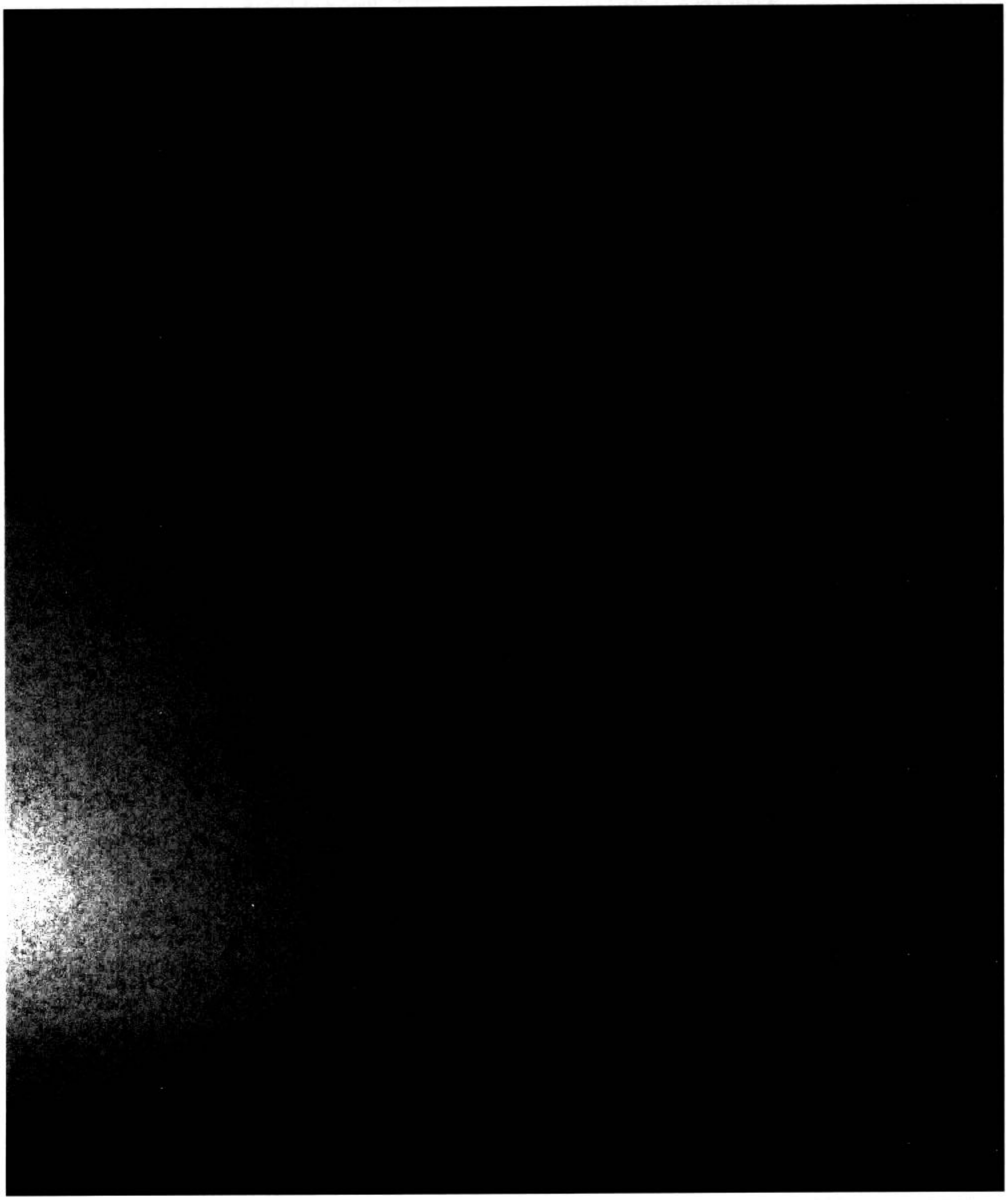

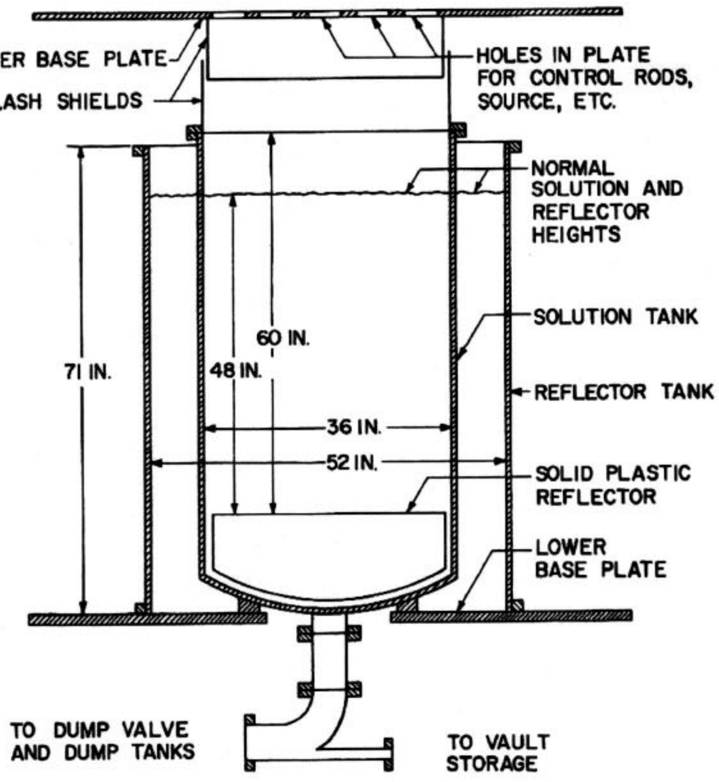

Fig. 9. 2 - Reactor Tank Assembly.

The solution is handled by an air system, shown schematically in Fig. 9.4. Solution is transferred to the reactor by applying 10 psi air pressure to the storage tanks. The solution is returned to storage by applying a vacuum of 15-inches mercury to the vent line. The solution level in each tank is observed by means of an indicator of the air-purge differential-pressure type; solution level can be read to 0.1 inch. The air pressure for the system is obtained from a 100 psi air compressor. A pressure-regulating valve reduces the pressure to 10 psi. The air from the compressor is filtered through a ceramic screen and activated charcoal. All air lines after the filters are stainless steel pipe or tubing.

The solution system is shown schematically in Fig. 9.5. Type 347 stainless steel pipe is used throughout, polished where feasible on the inside to a No. 4 finish, pickled and passivated to ensure maximum resistance to corrosion. Most of the joints are flanged, with fluorothene gaskets, to facilitate assembly and cleaning. All the valves in the solution lines are a diaphragm type, with fluorothene diaphragms and type 347 stainless steel bodies. The mixing tank is used to make up solution, to change concentration, and (as a transfer tank) to force solution by air pressure to various parts of the system. This tank is safe for any solution concentration.

(c) Control and Safety System. The DCTF has three control rods, with the drives located on the top base plate. Two act as safety rods; the third, as a safety and regulating rod. Each rod consists of a hollow cadmium cylinder, 3 inches in diameter, clad with two concentric pieces of stainless steel tubing. The rod drive consists of a rack and pinion unit connected through a magnetic clutch to a variable speed motor. An automobile-type shock

Fig. 9.3 - Vault Storage System for DCTF Solution.

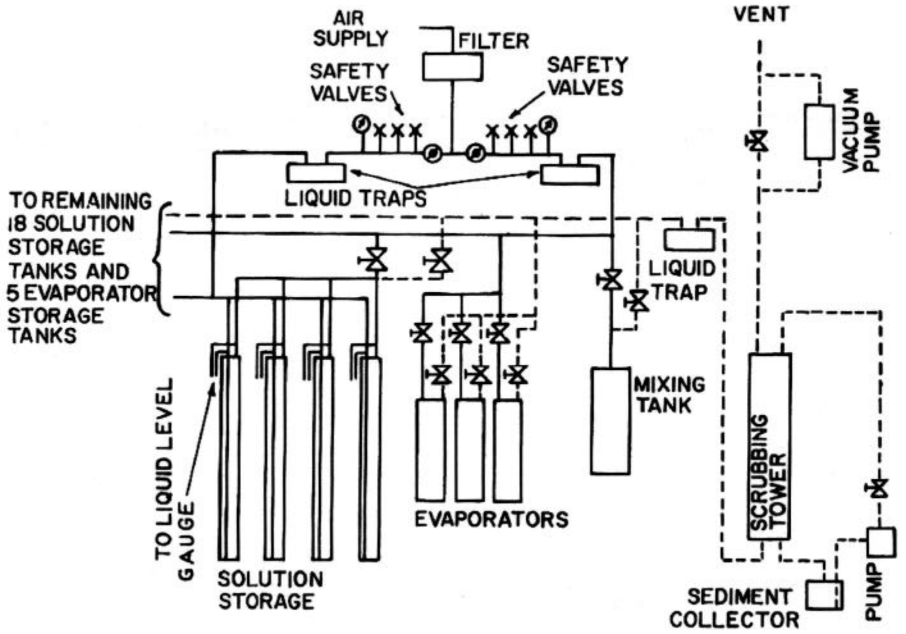

Note that the air supply line, after passing through the filter, splits: The right line supplies pressure for moving solution; the left line supplies pressure for the liquid level indicators. The loop at the right, which includes the sediment collector, pump, and scrubbing tower, circulates Na_2CO_3 solution to collect any air-borne uranium salt particles or solution droplets.

Fig. 9.4 - DCTF Air System for Solution Handling.

absorber is provided to cushion a rod drop. Control rod position is indicated by two selsyns geared to the pinion shaft. The maximum rod speed is 24 inches per minute; the control rods are fully inserted about 0.7 second after a scram.

An additional safety measure is provided by dumping 10 per cent of the reactor solution. The dump valve is an air-operated (air to close, spring open) 4-inch diaphragm valve. The dump tank is made up of two 5-inch-diameter pipes, 10 feet long, 30 inches between centers, and connected at the valve by a Y-section of 3-inch pipe. The tank is sloped to facilitate draining and is vented back through the splash shield into the reactor tank.

The polonium-beryllium neutron source is lowered into the solution on a nylon string wound on a motor-driven drum. In its uppermost position, the neutron source is enclosed by a cadmium-covered paraffin cylinder. An interlock prevents solution from being introduced into the reactor, or control rods from being raised, unless the source is inserted in the reactor. This interlock is automatically overridden when a significant neutron flux is being measured on the instruments.

(d) Solution Height Indication. The height of the reactor solution is determined by a pointed stainless-steel bob on a stainless-steel wire attached to a motor-driven drum. An electronic circuit reverses the motor each time the bob makes or breaks contact with the surface of the liquid. The drum is accurately machined so that the selsyn indicates directly in inches. The indicator can be read to 0.01 inch and oscillates in a range of 0.04 inch.

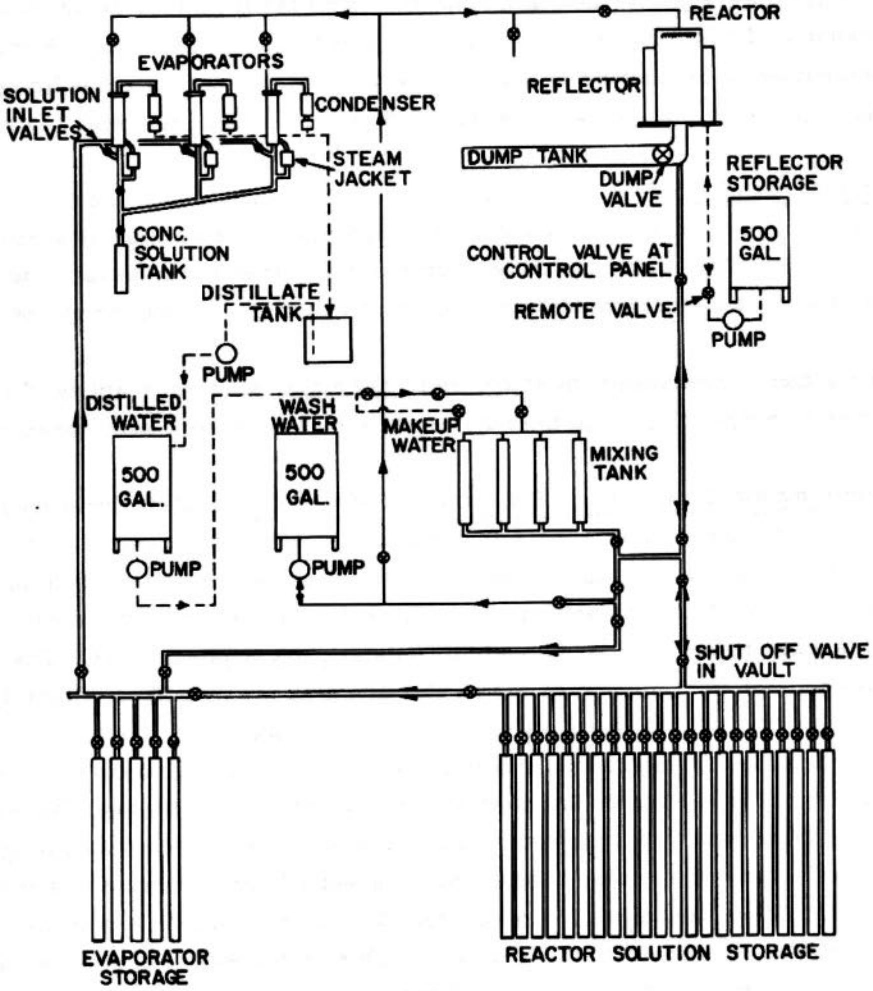

Fig. 9.5 - DCTF Solution Piping System.

(e) Temperature Measurements. Six thermistors, four in the solution and two in the reflector, are lowered into the reactor to measure temperature coefficients. They are positioned to give a good representation of the temperature distribution both axially and radially. During measurements, the thermistor readings are chart-recorded in sequence by a motor-driven, cycling selector switch. From calibration data, the error in a given thermistor reading was estimated to be ±0.020 C°. In any given experiment, the temperature variation throughout the core was found to be less than ±0.1 C°.

9.3 EXPERIMENTAL PROCEDURES

The procedures used with critical experiments have been described in Chap. 8. For the most part, these techniques were used with the DCTF. The few differences are associated with the fact that the DCTF is not a solid fuel reactor.

(a) Determination of Solution Concentration. The initial concentration of the DCTF solution was established by separate gravimetric chemical analyses of six individual samples.

Their average was taken as the initial concentration. At each subsequent stage of experimentation, that is, after each dilution, the concentration was calculated from a knowledge of the quantity of distilled water (or fuel) added and the previous concentration. In addition, gravimetric analyses were performed in conjunction with the inventory accountings. In general, the calculated and measured concentrations differed by less than 0.5 per cent.

The concentration of impurities in the solution was determined by periodic spectrographic analyses. The impurities contributed less than 0.5 per cent to the thermal neutron capture rate.

(b) Determination of Critical Solution Height. The exact height of the reactor for criticality was determined by taking a series of measurements of the reactor at slightly supercritical heights. The period of the reactor was measured at the several heights and the critical height determined by extrapolating a curve of reactivity versus height back to zero reactivity.

From the method of measurement of the critical height, another quantity of interest could be inferred directly. This was the rate of change of reactivity with reactor height $\partial\rho/\partial h$.

(c) Determining the Temperature Coefficient of Reactivity. Aside from technical interest, the temperature coefficient of reactivity was required in order to correct data for temperature drifts during a given day, as well as for changing temperature conditions from day to day.

To measure the temperature coefficient for the reflected reactor, the solution and reflector heights were adjusted until the reactor was slightly supercritical. The reactor was then allowed to stabilize in temperature. The stability was monitored periodically by the thermistor readings and by the constancy of the reactor period.

Next the temperature of the reflector water was raised approximately 15 C° by the use of immersion heaters. The heating of the core solution by conduction through the tank walls was observed with the thermistors and plotted as a function of time. After the heating power was turned off, the reflector and the core temperatures gradually equilibrated at a temperature approximately 8 C° above the initial temperature. Thereafter, the reflector and reactor cooled at a rate of approximately 0.1 C° per hour. During the warming process the reactor became subcritical because of the magnitude of the negative temperature coefficient. To compensate for this, some solution was added to the reactor.

At the higher temperatures, after equilibrium was reached, period measurements were repeated as the reactor and reflector temperature slowly fell. For each of these period measurements, the associated reactivity and temperature T_2 were used together with the initial temperature and reactivity to compute separate values of the temperature coefficient of reactivity. The average of these was then taken as the experimental coefficient. The reactivity gain due to the addition of solution was, of course, taken into account in the computation.

(d) Analysis of Errors in Data. As already noted, the temperature coefficient of reactivity was used to correct for daily temperature drifts. The data taken were related to a single temperature by observing the solution temperature as a function of time during a day's operation. By application of the measured temperature coefficient of reactivity, the reactivity could be referred to a given temperature base, usually 20°C.

The least count of the system insofar as reactivity measurements are concerned is estimated to be 0.05×10^{-4}. Because of temperature gradients, a given critical reactor is not determined to this precision. On typical curves of reactivity versus reactor height, the standard deviation of the experimental points from the curve is about 1×10^{-4} in reactivity. The standard deviation of the slope curve, i. e. $\partial\rho/\partial h$, is estimated to be about 4 per cent. The error in any given critical height determination is believed to be ±0.02 inch.

9.4 CRITICALITY RESULTS

A number of determinations of the criticality of the DCTF were made with no control rods present in the reactor. Some experiments were performed with both the bottom axial reflector and radial water reflector. Others were performed without the radial reflector but with the bottom axial reflector. All measurements quoted for axial height were measured from the top of the solid axial reflector.

Figure 9.6 gives the critical solution height as a function of the hydrogen to uranium-235 atomic ratio. The data with and without a radial reflector are presented on this curve. Figure 9.7 shows $\partial\rho/\partial h$ as a function of the critical height of the reactor. The values obtained are independent of the radial reflector.

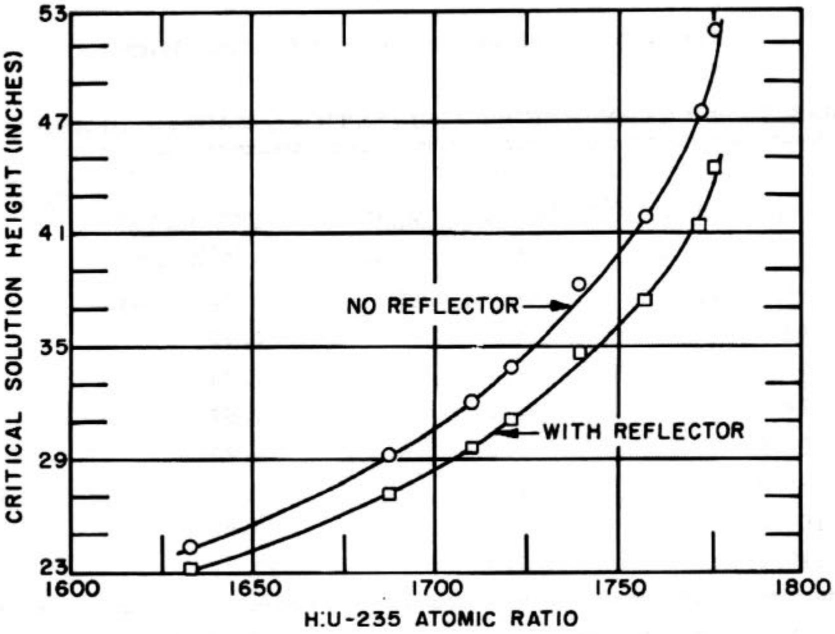

Fig. 9.6 - Critical Solution Height versus Hydrogen to Uranium-235 Atomic Ratio.

The critical mass of uranium-235 has been calculated for each critical condition from the critical solution height and the hydrogen to uranium-235 ratio. The tabulated results for the reflected and the unreflected cores are shown in Table 9.1. For these calculations, the solution density was assigned the constant value of 1.015 grams per cm^3, although it is slightly dependent on concentration.

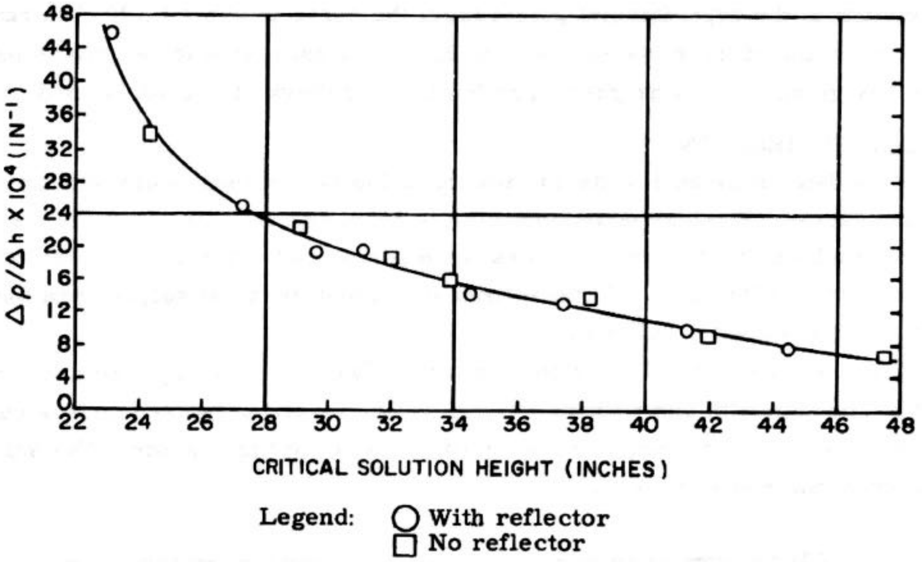

Fig. 9.7 - $\delta\rho/\delta h$ versus Critical Solution Height.

Table 9.1 - SOLUTION HEIGHT AND CRITICAL MASS OF URANIUM-235

$H:U^{235}$ Atomic Ratio	Critical Solution Height (cm)		Critical Mass (kg U-235)	
	With Radial Reflector	Without Radial Reflector	With Radial Reflector	Without Radial Reflector
1633 ± 2	58.7 ± 0.05	61.7 ± 0.05	5.91 ± 0.04	6.21 ± 0.04
1688	69.2	74.2	6.75	7.24
1710	75.2	81.5	7.24	7.85
1721	79.1	86.1	7.57	8.24
1739	86.6	95.3	8.20	9.03
1757	95.5	106.7	8.95	10.00
1773	106.2	120.9	9.87	11.24
1776	110.0	127.0	10.21	11.78

From the data in Figs. 9.6 and 9.7 the reactivity worth of the radial reflector may be calculated. Its value is $46.4 \pm 2.7 \times 10^{-4}$ in reactivity and is apparently independent of solution height.

9.5 TEMPERATURE COEFFICIENT OF REACTIVITY

The temperature coefficient of reactivity was measured for several cases. All except one were measured for the clean reactor condition. The one exception was the case with the central control rod partially inserted. The results are given in Table 9.2. The reactivities were obtained from measured periods using the Hughes data in the inhour equation with no correction for the effectiveness of the delayed neutrons.

Table 9.2 - TEMPERATURE COEFFICIENT OF REACTIVITY

Core Condition	$H:U^{235}$ Atomic Ratio	Temperature Range of Measurement (°C)	$\Delta\rho/\Delta T \times 10^4$
With Radial Reflector	1688	17.8 - 24.8	-1.39
With Radial Reflector	1757	16.1 - 26.0	-1.59
With Radial Reflector	1773	20.3 - 26.5	-1.83
Without Radial Reflector	1710	19.4 - 26.1	-1.53
Without Radial Reflector	1773	19.8 - 27.3	-1.57
With Radial Reflector and Central Rod Partially Inserted (10.7 to 12.4 inches from bottom of core)	1710	21.5 - 28.1	-1.83

9.6 CONTROL ROD STUDIES

DCTF measurements were also made on cores in which one or more control rods were inserted. On measurements made with partially inserted control rods, a constant solution height of 47.0 inches was used. The rod was adjusted to make the reactor critical, and the rod worth was then measured. These two quantities, the critical rod height and the reactivity worth per inch of rod travel $\delta\rho/\delta z$, are plotted in Figs. 9.8 and 9.9, respectively.

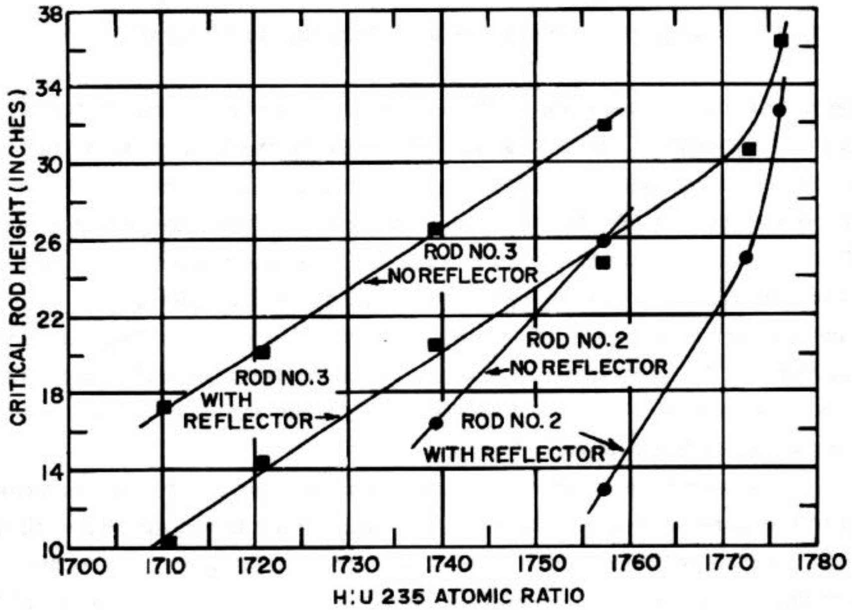

Solution height at 47.00 inches.
Rod No. 2 is 9 inches from the central axis of the core.
Rod No. 3 is on the central axis of the core.

Fig. 9.8 - Critical Rod Height versus Hydrogen to Uranium-235 Atomic Ratio.

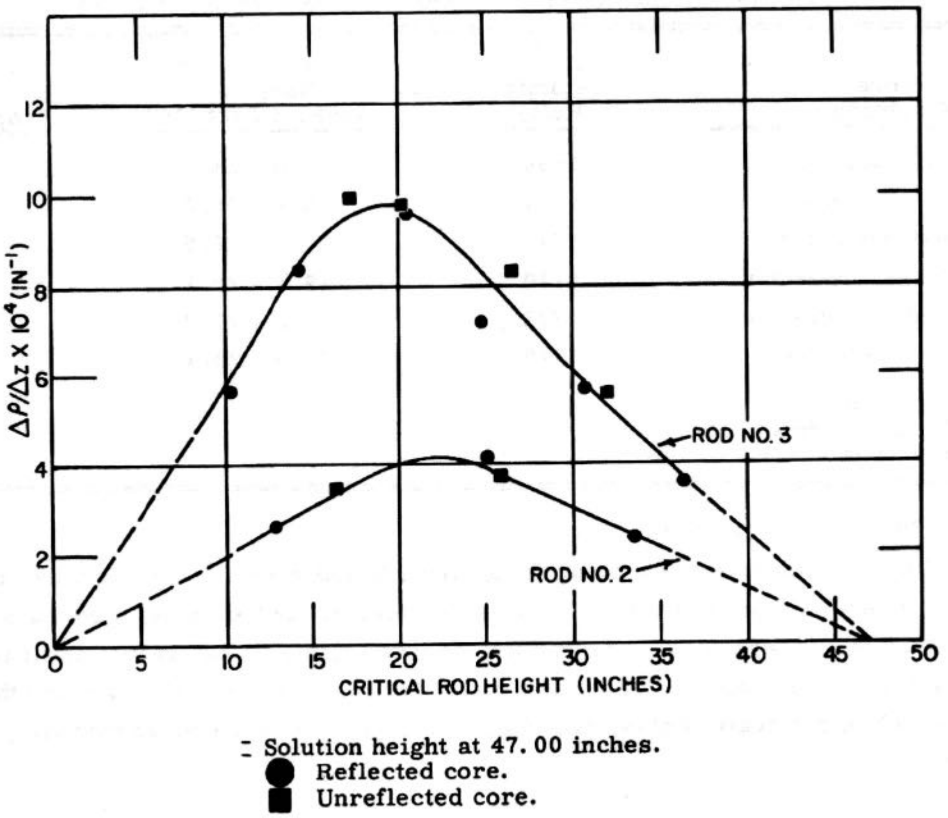

Fig. 9. 9 - $\delta\rho/\delta z$ versus Critical Rod Height.

It may be noted that the maxima of the curves in Fig. 9. 9 do not occur at the mid-core height. A qualitative explanation is that the presence of the bottom axial reflector and the absence of a top reflector cause a shift in the flux peak towards the lower portion of the curve. Furthermore, the presence of a rod also causes a shift in the flux peak towards the bottom of the core. The fact that this shift is more apparent with the central rod indicates that the presence of the rod has an influence on the position of the flux peak.

Data were also taken for cases in which the control rods were fully inserted. These data are plotted in Fig. 9. 10. Measurements were made for both the reflected and unreflected cores for a rod at 0 inches, 9 inches, and 14 inches from the axis of the core. One point was taken with the two outer rods down.

The value of the worth per inch of solution as a function of critical solution height is shown in Fig. 9. 11 for the case with a rod down. This curve may be compared with the similar curve of Fig. 9. 7 for the case with no control rod. The comparison shows that the values of $\delta\rho/\delta h$ for corresponding critical height are nearly identical over the entire range of heights plotted. The scatter in the data presented in Fig. 9. 11 limits the accuracy of comparison.

The total reactivity worth of each control rod may be found by two methods: One, by integrating the differential worth given in Fig. 9. 9. The other, by using the solution height values for the rod in and the rod out, and the measured values of $\partial\rho/\partial h$. The methods give rod worths which are in reasonable agreement. The results are:

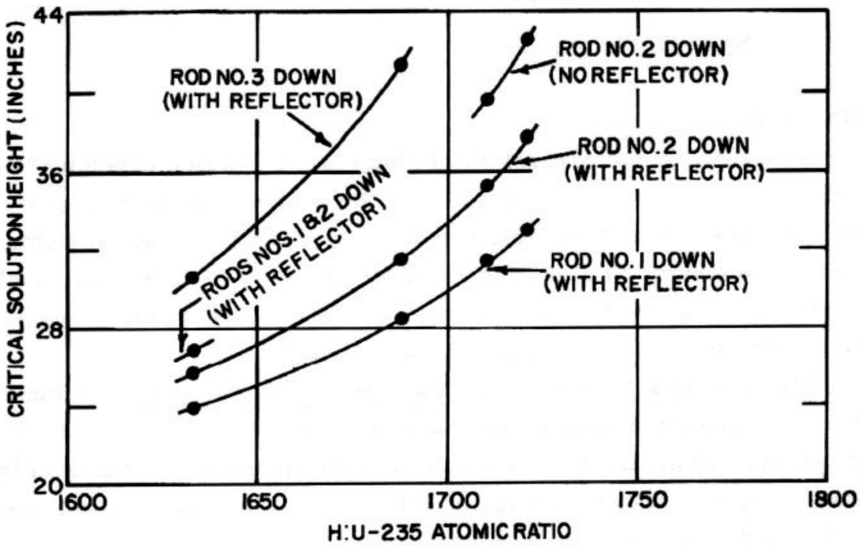

Rod No. 1 is 14 inches from the central axis of the core.
Rod No. 2 is 9 inches from the central axis of the core.
Rod No. 3 is on the central axis of the core.

Fig. 9.10 - Critical Solution Height with Various Control Rods Fully Inserted versus Hydrogen to Uranium-235 Atomic Ratio.

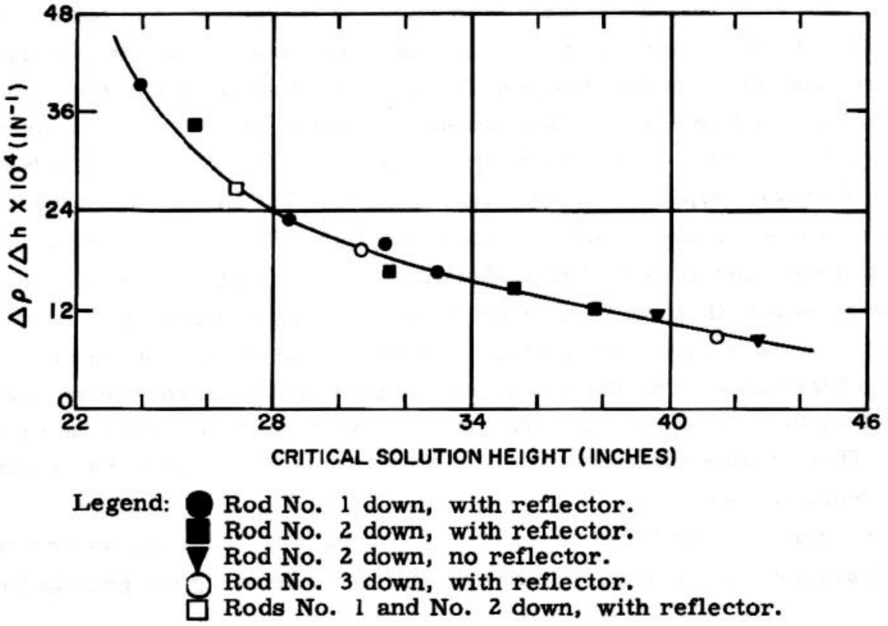

Legend:
● Rod No. 1 down, with reflector.
■ Rod No. 2 down, with reflector.
▼ Rod No. 2 down, no reflector.
○ Rod No. 3 down, with reflector.
□ Rods No. 1 and No. 2 down, with reflector.

Fig. 9.11 - $\delta\rho/\delta h$ versus Critical Solution Height for Various Control Rod Configurations.

Rod No. 1 is worth 0.28 (± 0.05) per cent;

Rod No. 2 is worth 0.87 (± 0.10) per cent;

Rod No. 3 is worth 2.15 (± 0.20) per cent;

The relative rod worths are given reasonably well by a J_0^2 weighting function.

THE TRX FACILITY

by J. R. Brown

9.7 INTRODUCTION

The TRX is a facility for the experimental study of the reactor physics of high uranium-content water-moderated assemblies. The aim of the program is to determine, through measurements on critical assemblies, the effect of fuel diameter, fuel enrichment, water-to-metal ratio, and fuel material on reactor parameters such as critical size, buckling, temperature coefficient, age to thermal, thermal utilization, resonance escape probability, fast fission factor, and other special quantities of interest.

The letters TRX are an abbreviation for Two-Region Experiment. Originally, it had been planned to provide an annular tank about the experimental lattice which could be filled with an enriched uranyl-nitrate solution. The aim was to make up any deficiencies in the lattice reactivity. Because of operational problems, this plan was not adopted and essentially all of the studies on the TRX have been single-region lattices.

9.8 DESCRIPTION OF THE TRX ASSEMBLY

The TRX assemblies use uranium metal or uranium dioxide fuel rods 48 inches long, and clad with aluminum. Extensions are provided at each end to assist in mounting the rods in a lattice plate. A typical TRX core is made up of a hexagonal lattice of such rods suspended from a lattice plate. The lattice plate is drilled with holes located to give the desired water-to-metal ratio. An aluminum guide plate is provided at the bottom, and two 1/4-inch-thick plastic guide plates are provided in the core region. The upper plate may be aluminum or steel depending upon the strength required. Figure 9.12 shows a loaded lattice plate ready to mount in the reactor tank. Figure 9.13 shows the lattice mounted in the reactor tank. The cylindrical objects above the lattice are weights mounted on the control rod cables.

Figure 9.14 shows a typical uranium metal fuel rod. The metal fuel in the TRX has been used in two diameters, namely 0.387 inch and 0.600 inch. The oxide material has been used in the same diameters but at two different densities. The uranium metal is in the form of long rods; the oxide fuel is in the form of sintered pellets approximately 0.5 inch high.

Four control rods are used in the TRX. Figure 9.15 shows a cross section of one of the control rod arrangements. The shape is chosen to permit the control rod to enter the lattice without disturbing the lattice spacing. With the rods withdrawn the lattice is a uniform hexagonal array. This permits the properties of the reactor to be analyzed with a minimum of geometrical complications.

The other features of the TRX assembly (the mechanical mounting, water system, electronic control system, and instrumentation system) are built along the general lines described in Chap. 8.

The TRX is mounted on a two-level elevated platform with the dump tank below the reactor tank. Water is pumped into the bottom of the reactor tank, and a dump valve is provided to empty the reactor tank quickly.

The reactor tank is a single, large cylindrical vessel with provision to support the lattice plate inside. When filled, the radial reflector thickness is greater than 8 inches. The bottom reflector consists of 8 inches of aluminum fuel rod ends and water. The top reflector

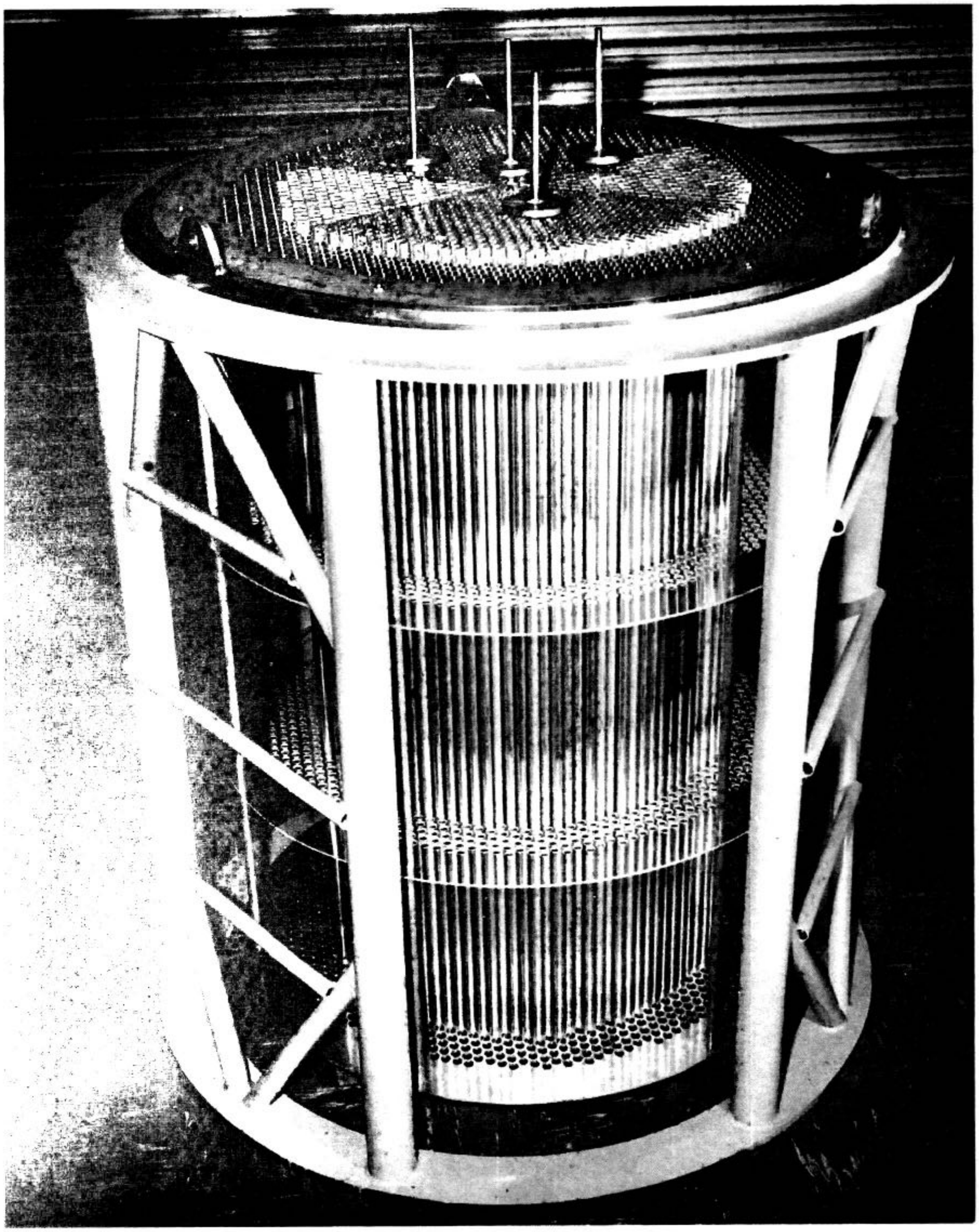

Fig. 9.12 - A TRX Core Before Insertion in the Reactor Tank.

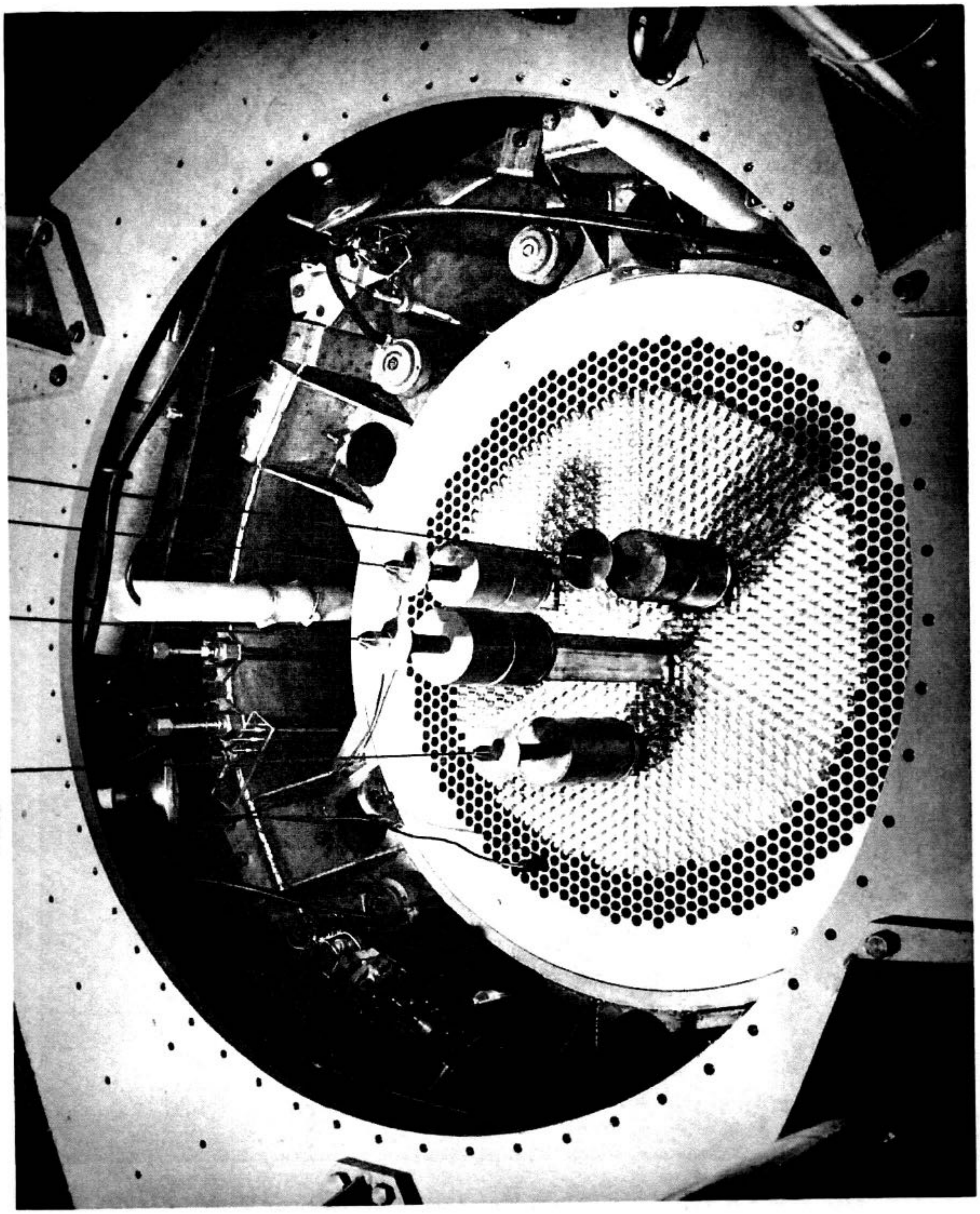

Fig. 9.13 - The Top of a TRX Core in the Reactor Tank.

consists of 6-1/2 inches of aluminum fuel rod ends and water, and 1-1/2 inches of steel or aluminum lattice plate.

As noted above there is no mechanical separation between the fuel region and the reflector region. For temperature coefficient studies the water can be heated electrically by immersion heaters located in the reflector region of the reactor tank. Uniformity of temperature is maintained by thermostatic control of the heaters. The water temperature is not generally heated above 50°C because of the high humidity which develops in the reactor room.

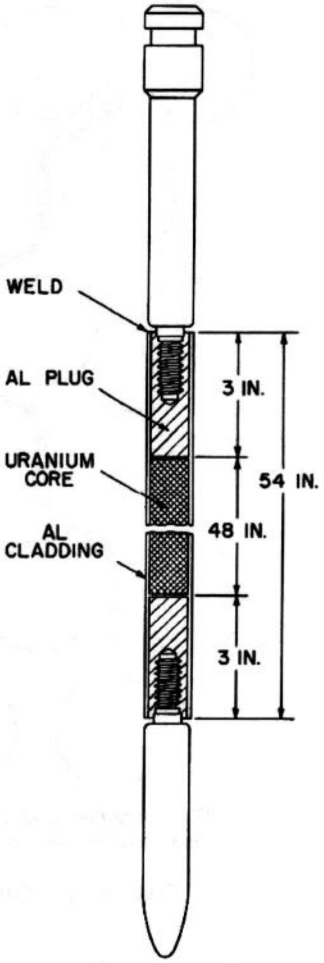

Diameter of fuel, 0.600 ± 0.002 inch
ID of aluminum cladding, 0.610 inch
OD of aluminum cladding, 0.666 ± 0.002 inch

Fig. 9.14 - Fuel Rod.

9.9 MEASUREMENT OF CRITICAL RADIUS

The critical number of fuel rods for a given lattice arrangement is determined by building up an array of fuel rods in a hexagonal pattern, maintaining nearly circular cylindrical radial boundary until criticality is reached. The boundary cannot be an exact circular cylinder because of the hexagonal spacing, but the approximation is quite reasonable for the radii involved in the TRX lattices. To approximate a circular cylinder, the peripheral fuel rods are placed in the vacant lattice positions at the shortest distance from the center. Any other distribution of these rods (keeping the total the same) would place fuel farther from the center and reduce the core reactivity. The best approximation to a circular cylinder thus gives the largest reactivity for a given number of fuel rods. It has been shown experimentally that a hexagonal boundary requires a larger number of fuel rods for criticality than does a circular boundary. For the larger radii encountered in the UO_2 lattices, the number of fuel rods required for criticality is quite insensitive to the position of the fuel around the periphery.

The equivalent radius of the critical assembly is obtained from the area of the unit cell associated with each fuel rod (obtained from the known lattice spacing), multiplying this by the total number of fuel rods, and determining the radius of the circle having the same area.

9.10 MEASUREMENT OF BUCKLING AND REFLECTOR SAVINGS

The geometrical buckling (B_g^2) of the critical core is determined from radial and axial flux plots. These plots give the shape of the fundamental mode, which is $J_o(B_r r)$ radially and $\cos(B_z z)$ axially.

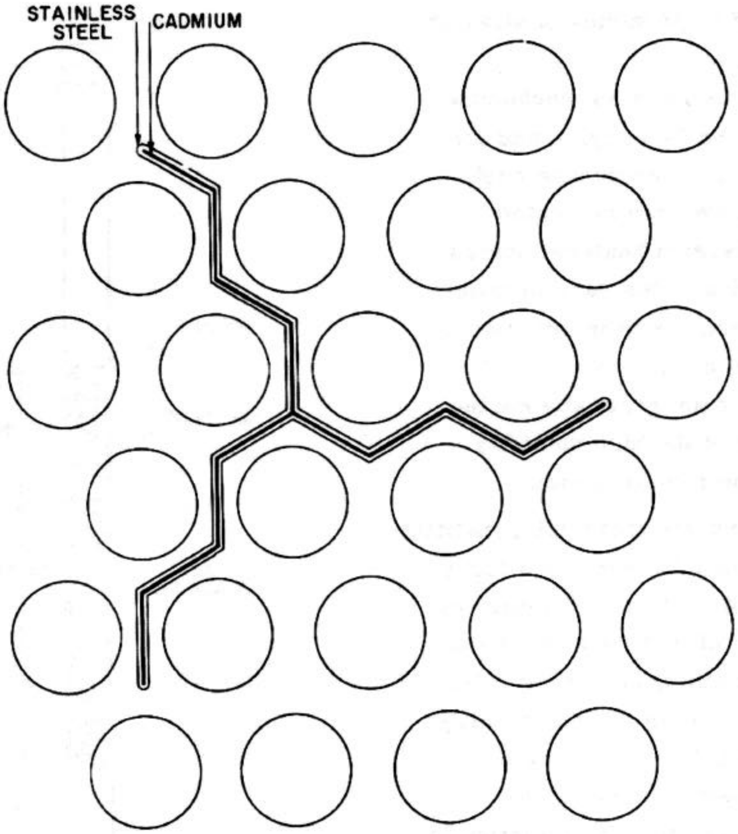

The control rod is cadmium, clad with stainless steel.
The lattice spacing is not disturbed.

Fig. 9.15 - Cross Section of TRX Control Rods.

The flux is determined from the activation of uranium foils placed inside fuel rods, or from the activation of the fuel rod itself. In either method, fission product gamma-rays are counted by using a scintillation counter biased to count gammas above about 400 kev. For fuel rod counting, a 1-inch-high collimator is used. It has been shown that the shape of the detector window does not distort the axial cosine distribution when a fuel rod is scanned for an axial flux plot. Different materials may be used for the foils placed within fuel rods, so that plots of different neutron energy spectra can be obtained. By using foils of nearly pure uranium-238 (having about 5 ppm uranium-235) in two lattices, a plot of the neutron spectrum above 1 Mev has been obtained.

The foil or fuel rod counting rates, as a function of position, are fitted by least squares to the appropriate function. The point, or points, at which the function extrapolates to zero gives the value of the effective radius or height of the equivalent bare core. In general, points from the center of the lattice to about two-thirds of the distance to the lattice boundary are used to make the least squares fit. Points nearer the boundary may be perturbed by the reflector. The effective radius, R_{eff}, and the effective height, H_{eff}, of the equivalent bare core when combined with the geometrical radius, R_g, and the geometrical height, H_g, give the radial and axial reflector savings, λ_R and λ_H, respectively.

$$\lambda_R = R_{eff} - R_g \; ;$$

$$\lambda_H = H_{eff} - H_g \; .$$

Data obtained on the TRX for critical size and critical buckling are summarized in Chap. 12.

9.11 MEASUREMENT OF THE TEMPERATURE COEFFICIENT OF REACTIVITY

The temperature coefficient of reactivity of the TRX has been measured over the range 20°C to 50°C by the techniques described in Chap. 8. The results are shown in Figs. 9.16 through 9.19. Because of statistical errors in the reactivity determination, the error on each point is $\pm 0.05 \times 10^{-4}$. The standard inhour expression given in Chap. 8 was used to convert the measured period to reactivity. A delayed neutron fraction of 0.00755 for fission of U^{235} was used.

It will be recalled that the reactivity difference between two equilibrium temperatures divided by the temperature difference is the temperature coefficient assigned to the average of the two temperatures. This is the correct temperature to assign to the coefficient if the second derivative of the temperature coefficient is zero. Figures 9.16 through 9.19 show that within the errors assigned to the data the second derivative is zero.

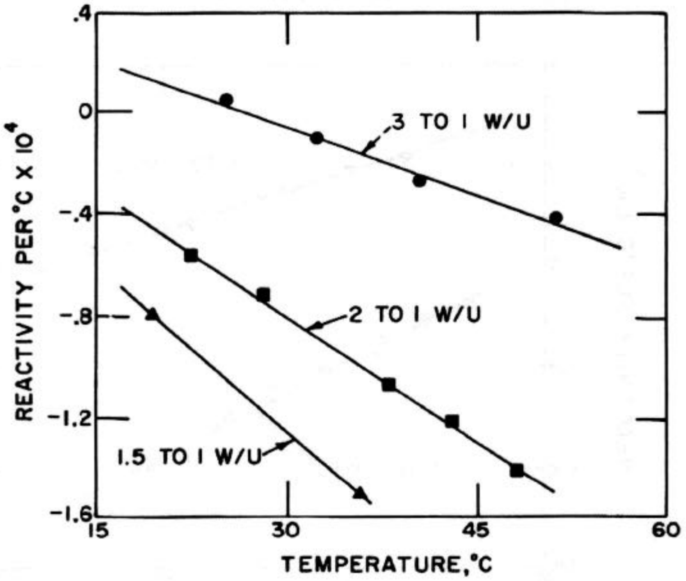

Fuel rods are 0.600-inch diameter metal, containing 1.3% uranium-235.

Fig. 9.16 - TRX Temperature Coefficient.

It can be seen that the first derivative of the temperature coefficient is negative in all cases, as is also the temperature coefficient itself, except for cases involving two lattices; and then only at room temperature.

A notational convention is used on these figures, and elsewhere, in connection with TRX work which requires some explanation. As an example, the nominal water-to-uranium volume

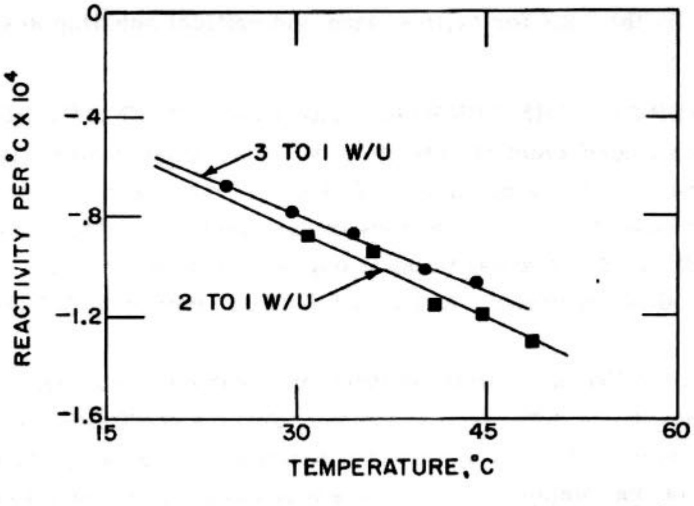

Fuel rods are 0.387-inch diameter metal, containing 1.3% uranium-235.

Fig. 9.17 - TRX Temperature Coefficient.

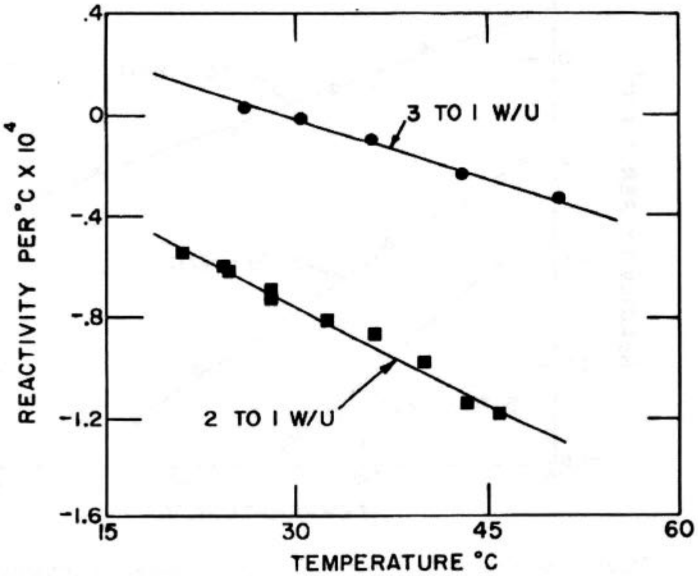

Fuel rods are 0.600-inch diameter metal, containing 1.15% uranium-235.

Fig. 9.18 - TRX Temperature Coefficient.

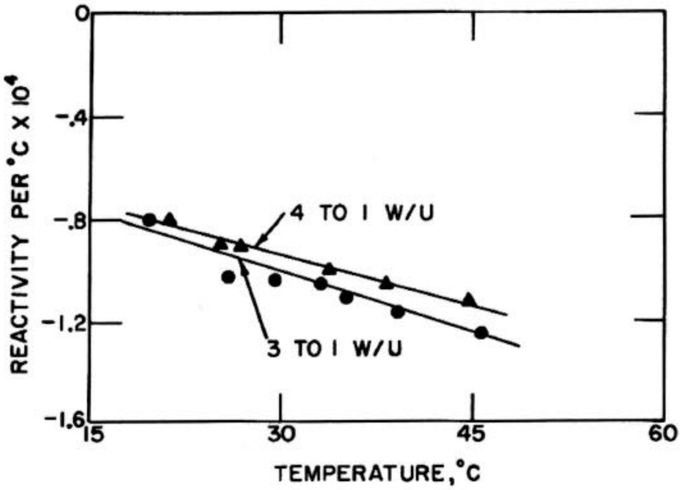

Fuel rods are 0.600-inch diameter oxide; the uranium is enriched to 1.3% uranium-235.

Fig. 9.19 - TRX Temperature Coefficient.

ratio is referred to as 3 to 1 (W/U). The actual ratio, which is close to the nominal, is obtained from the actual spacing of the fuel rods. This is determined by the placement of the holes in the lattice support plates. In referring to a water-to-uranium volume ratio for UO_2 lattices, the volume used for the uranium is that which it would occupy if the uranium content of the UO_2 were metal. Therefore, the ratio of hydrogen atoms to uranium atoms (N_H/N_U) is the same for any two lattices that have the same W/U volume ratio (N_H/N_U = 1.396 W/U).

[redacted]

Pages 443 - 464 have been redacted in their entirety.

[redacted]

THE SUBMARINE FLEET REACTOR FLEXIBLE ASSEMBLY

by G. F. Mechlin

9.18 DESCRIPTION OF FACILITY

The Submarine Fleet Reactor Flexible Assembly (SFR-FA) is an experimental zero power reactor facility for critical experimentation on the comparatively small, light water moderated, highly enriched reactors used for submarine propulsion service. Flexibility of core geometry and loading and a high degree of safety were the paramount objectives of the design. It was expected that, with only minor modifications, a set of modular fuel bundles would allow the construction of cores of varying heights, diameters, loadings, metal-to-water ratios, and numbers and sizes of control rods, which could follow the evolution of an actual reactor design in considerable detail.

[redacted]

The design of the SFR-FA draws heavily on the experience gained on the ZPR-I critical assembly. Three years of operation (January, 1954, to January, 1957) have demonstrated that the SFR-FA is able to provide experimental information on a satisfactory time schedule for a reactor project.

Two identical reactor tanks are provided to allow two greatly different assemblies to co-exist. Such an arrangement provides substantially more flexibility than would be provided by a single tank and at a cost well below that of two isolated and independent facilities. Two of the assemblies on which work has been done are shown in Figs. 9.42 and 9.43. The first is a slab reactor experiment for basic studies; the second is a mock-up reactor experiment. Figure 9.42 shows many of the physical features of the facility. A modular fuel bundle is shown being withdrawn from the core. This is made up of metal strips and plastic fuel tapes to give the metal-to-water ratio of interest. The strips are held in place with book-binding screws and plastic spacers. [redacted]

Figure 9.42 also shows the grid structure used for locating the upper end of the fuel bundles. This upper grid structure consists of extruded aluminum crosses clipped together to form a grid with 2-inch spacings between grid members. Each individual cross can be removed or modified to provide room for control rods or other special elements. The lower ends of the fuel bundles are located by pins on the bundles fitting into holes in the base plate.

Figure 9.44 is a view of the upper two levels of the assembly stand, showing the reactor tank which contains the slab reactor experiment. The lower level which can be seen in the photograph is a working level that provides convenient access to the reactor core. The upper level contains the control rod drive units. In this case, only two drives are connected to safety rods. Each rod is driven independently by a rack and pinion gear assembly. This gear assembly is clamped to bars extending across the top opening which permits the locating of the control rods in any reasonable pattern in the reactor. [redacted]

In addition to the two levels seen in Fig. 9.44, a lower platform on the assembly stand supports the reactor tanks and provides room for instrumentation. The plumbing auxiliaries are at floor level. They provide water-handling facilities to allow heating and circulation of moderator in temperature coefficient experiments, and for storage and transfer of fresh and mildly contaminated moderator.

[redacted]

Fig. 9.42 - Slab Reactor Assembly.

[redacted]

Fig. 9.43 - Mock-up Reactor Assembly.

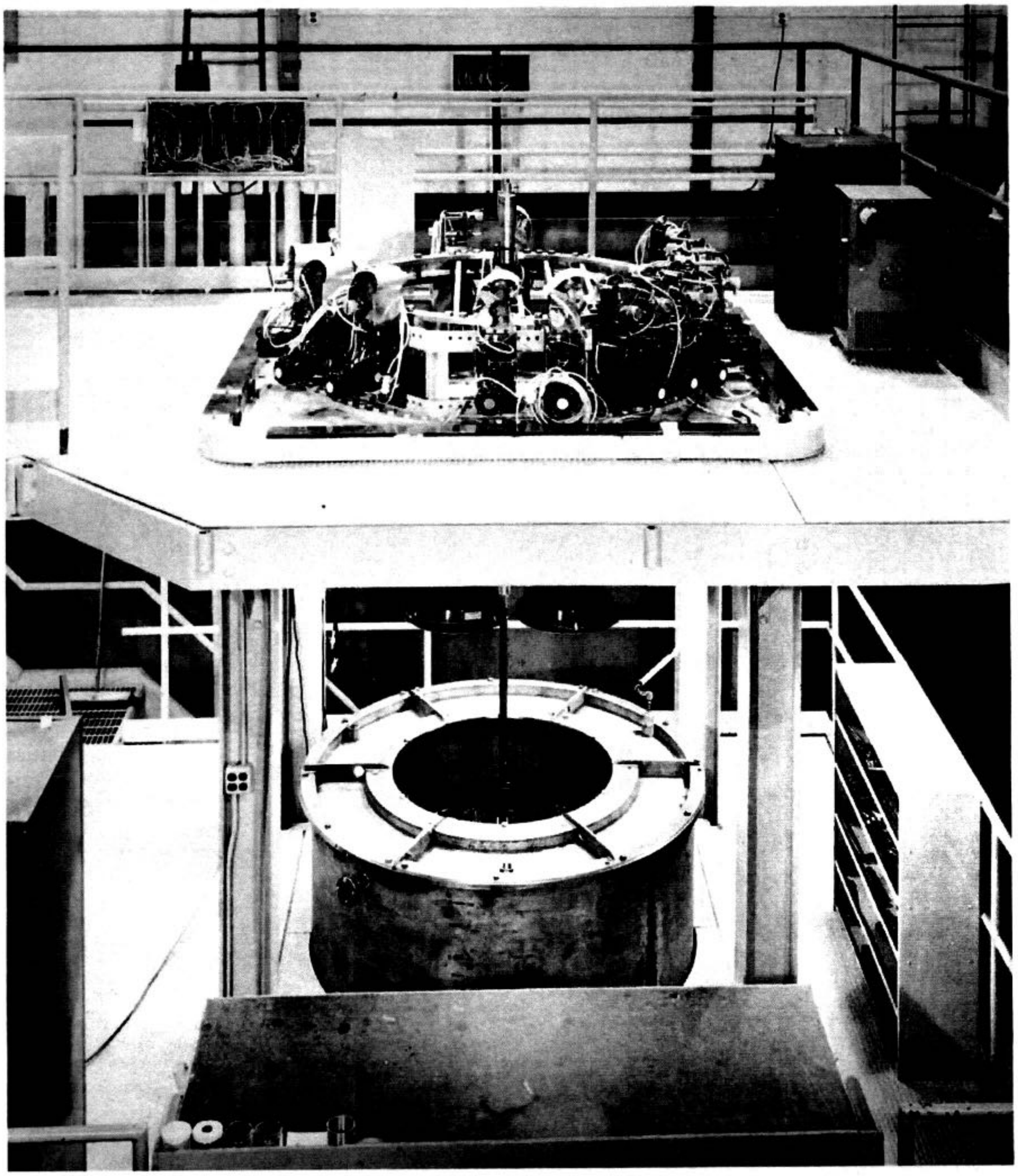

Fig. 9.44 - A Portion of the SFR-FA Assembly Stand.

Fig. 9.45 - Rod Drives for Mock-up Critical Assembly.

[redacted]

Fig. 9.46 - Mock-up of a Section of the SFR Pressure Vessel and Radiation Shield.

[redacted] All rod positions are read on dual selsyn receivers, one for coarse positioning and the other for fine positioning. The control console contains separate control panels and control instrumentation for each reactor tank. The instrumentation and safety interlocks are shared by the two assemblies.

The safety and operating instrumentation includes two compensated boron-lined ionization chambers and two photomultiplier-scintillation crystal detectors. The data-taking instrumentation is entirely independent of the operating instrumentation, and includes three fission counters and a compensated boron-lined ionization chamber. The radiation detectors are placed in thimbles which penetrate the reactor tank walls. The instruments are kept at suitable signal levels by the proper adjustment of these thimbles with respect to the core.

9.19 SLAB REACTOR EXPERIMENTS

The experiments performed on the SFR-FA were of two classes: Simple slab reactor experiments and mock-up experiments. The slab reactor experiments were intended to develop information on the basic properties of the reactor; the mock-up experiments were intended primarily to verify the adequacy of the reactor design.

The slab reactor experiments comprised studies of criticality, flux maps, and temperature coefficient studies. The criticality studies are discussed in considerable detail in Chaps. 13 and 14. It is sufficient to note at this point that a number of studies were completed in which the slab size, metal-to-water ratio, and fuel loading were varied. The construction of the reactor permitted simple geometry reactors to be set up which had a high degree of homogeneity. Furthermore, the control rods were equipped with fueled extensions, so that when the rods were withdrawn a highly uniform slab critical resulted.

[redacted]

Figures 9.47 and 9.48 show thermal and fast neutron flux plots, respectively, obtained for this slab. They represent the neutron flux distributions across the 6-inch dimension of the slab near the center of the other dimensions and extending into the water reflector on each side. Points on the graphs were obtained by counting beta radiations from irradiated wires (1/32-inch diameter; 3/8-inch long) which were an alloy of 14 per cent manganese, 2 per cent molybdenum, and 84 per cent iron. These wires were mounted at suitable positions in plastic wands which were inserted between fuel bundles in the reactor. The fast flux was obtained using the manganese alloy wires covered with about 0.020-inch wall thickness of cadmium tubing. The fast flux has been subtracted from the bare manganese wire curves to give the thermal flux below cadmium cut-off. The small peaks in the thermal flux inside the core occur at 1-inch intervals. These are the moduli of the fuel elements which make up the curve. At each intersection of four fuel elements, there is about a 0.3-square-inch area of zirconium and water containing no fuel. Thus, the flux-plotting methods show the inhomogeneities introduced by the fuel elements themselves.

Temperature coefficient studies were also carried out on the slab reactors. As an example, the results of the study are given for the same 6-inch slab for which the flux data

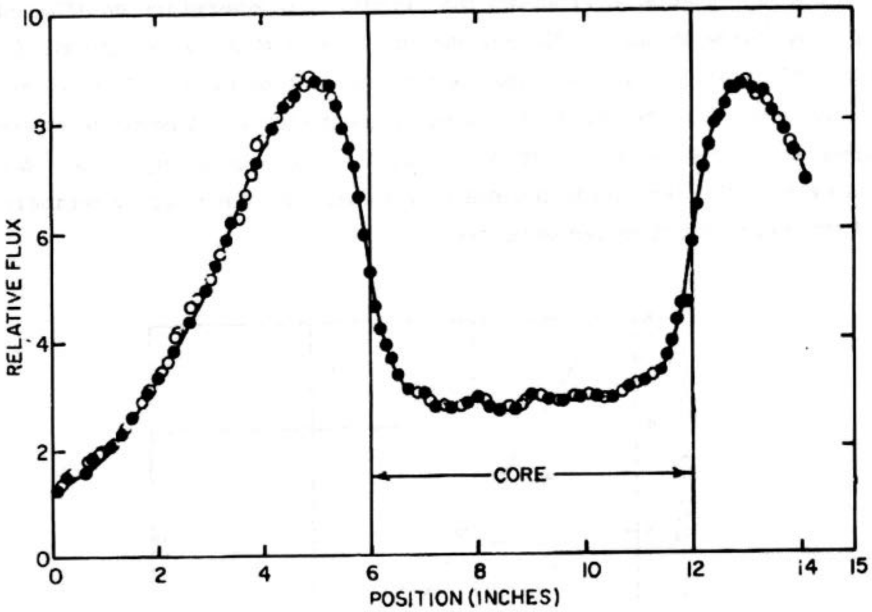

Core size, 6 x 30 x 42 inches; U^{235} loading, 7.95 kilograms; zirconium-to-water ratio, 1.0.

Two symbols are used on the plot only as an aid to separating the experimental points; all points shown represent similar type data.

Fig. 9.47 - Flux Map: Slow Neutron Flux Across Small Dimension of Slab Reactor.

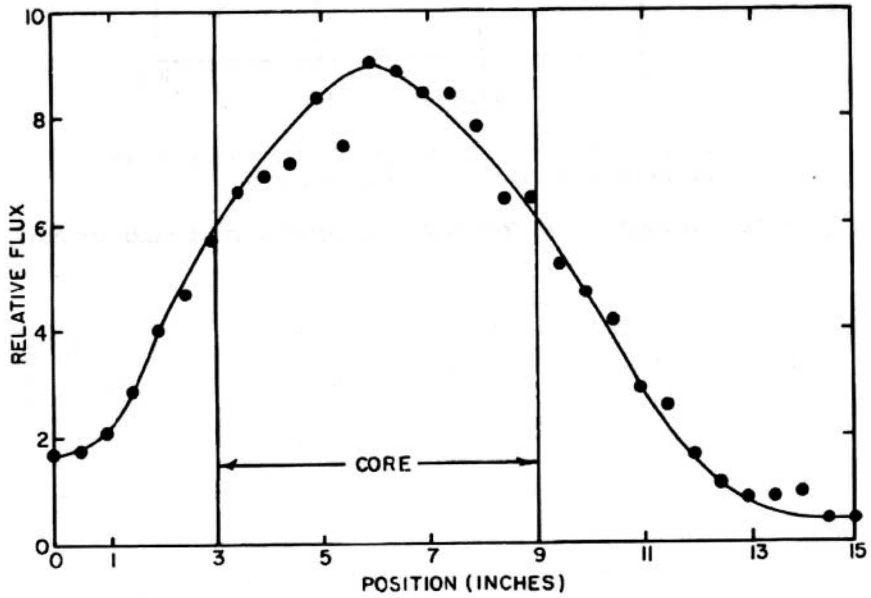

Core size, 6 x 30 x 42 inches; U^{235} loading, 7.95 kilograms; zirconium-to-water ratio, 1.0.

Fig. 9.48 - Flux Map: Fast Neutron Flux Across Small Dimension of Slab Reactor.

were reported above. Figure 9.49 shows the results of temperature coefficient measurements. Because of the low value of the coefficient and the presence of some instabilities, the values have a considerable scatter. A least square straight line has been fitted to the experimental points. It is observed that the temperature coefficient starts out positive at room temperature and appears to cross over to a negative value at approximately 95°F. Measurements were made using a calibrated rod to maintain criticality as the reactor temperature was raised over successive steps in temperature.

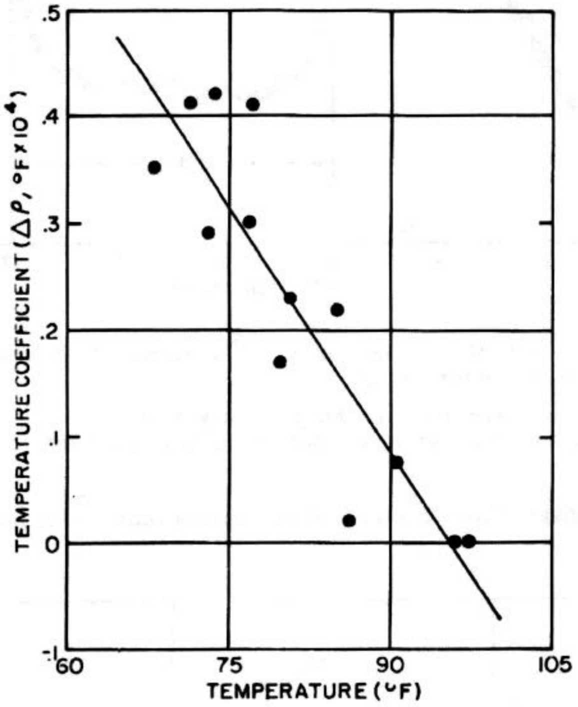

Core size, 6 x 30 x 42 inches; U^{235} loading, 7.95 kilograms; zirconium-to-water ratio, 1.0.

Fig. 9.49 - Temperature Coefficient of Reactivity of Slab Reactor.

9.20 SFR-FA MOCK-UP EXPERIMENTS

[redacted]

(a) Core Criticality and Rod Worth.

[redacted]

[redacted]

[redacted]

Fig. 9.50 - U235 Loading versus Control Rod Bank Height for Criticality.

[redacted]

(b) Temperature Coefficients of Reactivity.

[redacted]

(c) Flux Plots.

[redacted]

[redacted]

Fig. 9.52 - Center Rod Worth versus Rod Position for Several Fuel Loadings.

[redacted]

Fig. 9.53 - Temperature Coefficient of Reactivity for SFR Mock-up Critical Assembly.

[redacted]

(d) Source and Shielding Experiments. In addition to the experimental results which directly concern the reactor core parameters and have been discussed above, the SFR-FA mock-up has been used to obtain experimental information which is applicable to some design problems external to the core. Two of these problems will be discussed: First, the location of one or more neutron sources near the reactor core to simplify engineering designs and at the same time give adequate sensitivity for the start-up control instrumentation; second, the radiation shielding in the thermal shields and, particularly, in the vicinity of the core barrel.

[redacted]

[redacted]

Fig. 9.54 - Mock-up Reactor Cross Section Showing Flux Mapping Locations.

[redacted]

[redacted]

Fig. 9.55 - Axial Flux Plots in the SFR-FA Mock-up Assembly.

[redacted]

[redacted]

Table 9.10 - SOURCE EXPERIMENT COUNTING RATES

Source Position (see Fig. 9.57)	Count Rate counts per second
A	51
B	203
C	10
D	16

[redacted]

[redacted]

Fig. 9.58 - Gamma Intensity in SFR Shield.

THE SUBMARINE ADVANCED REACTOR - PRELIMINARY PILE ASSEMBLY

by J. S. King

9.21 INTRODUCTION

The Submarine Advanced Reactor - Preliminary Pile Assembly (SAR-PPA) was the first critical assembly for the study of water-moderated reactors at KAPL. The program was a brief (3-month) study of early S3G* design concepts. [redacted]

9.22 DESCRIPTION OF THE REACTOR

[redacted]

---

* S3G is the present designation of the reactor project formerly known as SAR (Submarine Advanced Reactor).

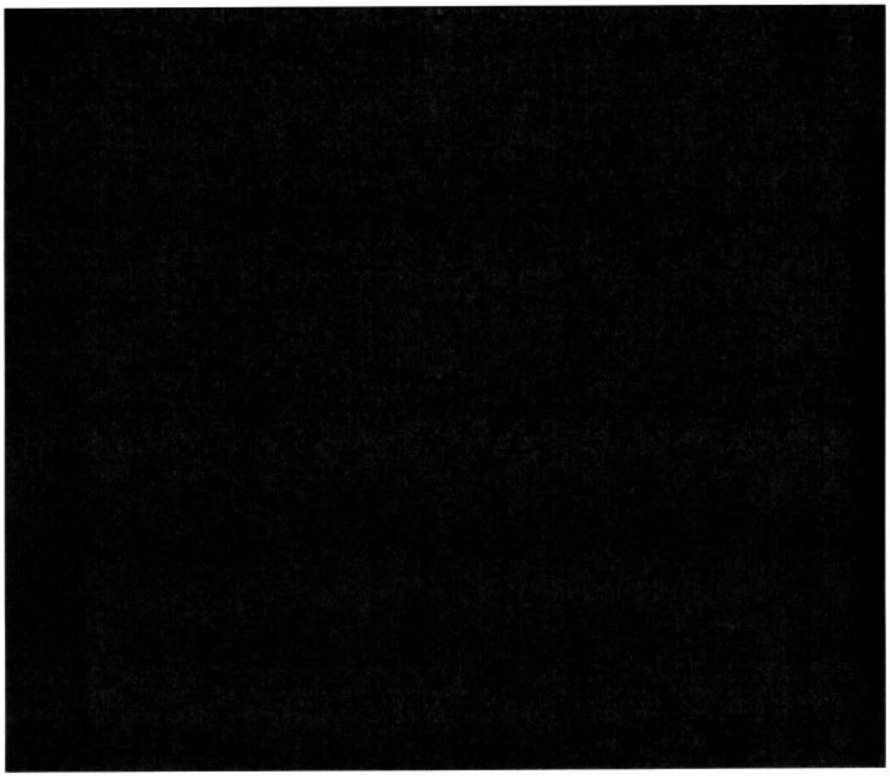

Fig. 9.59 - SAR-PPA Mock-up Geometry.

[redacted]

Table 9.11 - REACTIVITY COEFFICIENTS OF POLYETHYLENE AND WATER (1/4-INCH DIAMETER AXIAL RODS)

[redacted]

9.23 EXPERIMENTAL RESULTS

(a) Reflector Control Range. [redacted]

(b) Comparison of Reflector Materials. [redacted]

Table 9.12 - REACTIVITY CHANGES FOR CHANGES IN REFLECTOR COMPOSITION

[redacted]

[redacted]

Fig. 9.60 - SAR-PPA Control Cylinder Calibration.

[redacted]

(c) Comparison of Stainless Steel with Zirconium as a Core Structural Metal.

[redacted]

[redacted]

Fig. 9.61 - SAR-PPA Radial Power Distributions for Beryllium and Zirconium Reflectors.

[redacted]

(d) Temperature Coefficients.

[redacted]

Table 9.13 - TEMPERATURE COEFFICIENTS AND TEMPERATURE DEFECTS FOR THE SAR-PPA

[redacted]

[redacted]

THE ADVANCED TEST REACTOR

by R. G. Luce

9.24 DESCRIPTION OF THE FACILITY

The Advanced Test Reactor (ATR) was designed as the flexible critical experiment for the S3G program. As such, the principal emphasis in the design was placed upon flexibility. Flexibility was desired in size, fuel loading, core material, metal-to-water ratio and reflector composition.

An over-all view of the ATR is shown in Fig. 9.62. A brief description of the components of the assembly is given below.

(a) Core and Dump Tank, Valves, and Heat Exchanger. The tank is partitioned at floor level into a lower dump tank and an upper core tank. The latter is in several removable sections so that various height cores can be accommodated with operating ease. There are ports in the sides of the tank to receive neutron current chambers and proportional counters.

A slow pump and a fast pump raise the water from the lower into the upper tank. A stand pipe is provided so that the latter pump is effective for only a partial filling of the core tank. There are four fast-acting valves between the lower and upper tank, as well as four air vents on the sides of the lower tank. When the reactor is scrammed, the vents allow the air to escape. Approximately 10 seconds after a reactor scram all water has dropped into the dump tank.

A system to raise the core water temperature to 200°F is available. Water in the core is pumped through a water-to-water heat exchanger in which plant steam heats the secondary water.

(b) Control Safety Mechanisms. In general, cadmium poison safety and control rods have been used on the assembly. The functions of safety rods and control rods are separated to permit a greater flexibility in experimentation. Thus in a design mock-up, the actual rods can be manually positioned and operation controlled by the control rods. [redacted] A polonium-beryllium source, which can be remotely removed from the core into a shielded can, is also provided.

(c) Loading Device. A loading device is available to move samples in and out of the core while the reactor is critical. Its positioning is accurate to 2 mils and can be read from the control panel.

(d) Fuel Material. [redacted]

Pages 488 - 505 have been redacted in their entirety.

[redacted]

THE FLEXIBLE PLASTIC REACTOR

by S. W. Kitchen

9.28 DESCRIPTION OF THE FACILITY

The objective in the design of the Flexible Plastic Reactor (FPR) was to provide a highly flexible and accessible critical assembly adaptable to rapid changes in geometry and composition. At the same time it was necessary to retain reproducibility and reliability of reactor measurements. It appeared that this objective might be met best by the use of polyethylene and void to simulate water. Since this avoided the need for a container, a degree of access was permitted which was not feasible in a water-moderated assembly.

The details of the FPR which was constructed at KAPL, are given below.

(a) Bed Mechanisms. The two assembly halves are mounted on 5 x 5-foot boiler plate tables. The tables are mounted on two heavy-duty tracks, one flat and the other V-shaped, with the stationary table anchored in place at one end of the tracks. The movable table rides on four wheels, and is driven by a constant speed motor through a screw-jack linkage. This linkage insures an automatic slow-down in rate of closure as the halves approach each other. A photograph of the linkage is shown in Fig. 9.78,

(b) Matrix Construction. The matrix construction for each half consists of a 4.5 x 4.5-foot array of individual aluminum tubes clamped within a steel retaining frame. The tubes are 2 feet long, 0.025 inch wall, 67S aluminum drawn to provide a 1.0 x 1.0-inch square outside cross section. If necessary, certain layers can be brazed together to form, in effect, hollow beams. Such beams can support the matrix above local regions where it may be experimentally desirable to create voids larger than the standard 0.95 x 0.95-inch module. A photograph of the array is shown in Fig. 9.79.

Except for the areas reserved for control rod and safety rod insertion, the core material is loaded in the form of stacked strips cut to the appropriate length. The construction of a core slug is shown in Fig. 9.80.

(c) Control and Safety Mechanisms. Six steel-clad cadmium poison safety rods are used for fast safety shutdown of the reactor. An additional four rods are used to provide shim control. The drive mechanisms are mounted horizontally on the movable bridge structure in the rear of each core half. A view of the mechanisms attached to the fixed half of the core is shown in Fig. 9.81. The motors and control rod position indicators are mounted on top of the

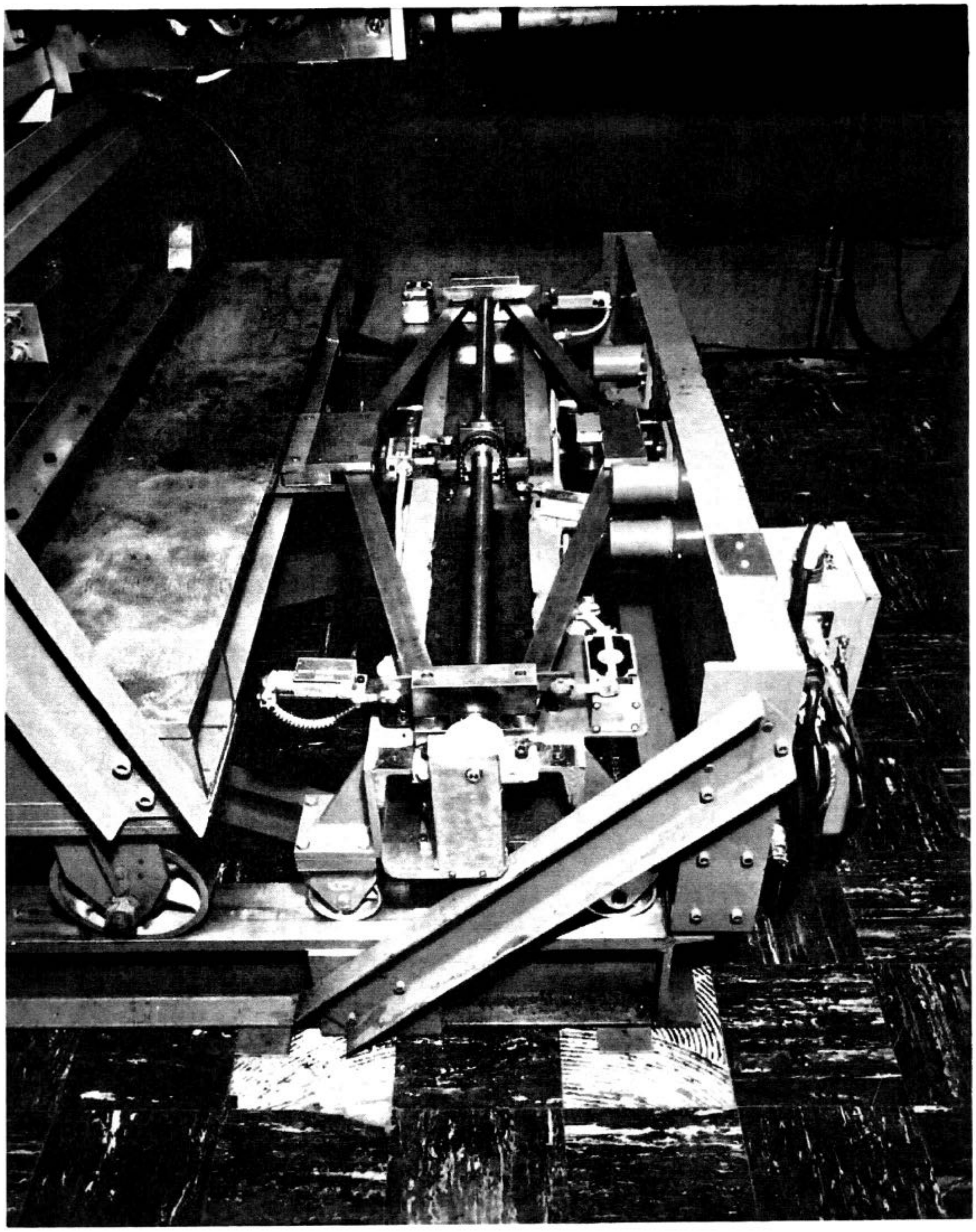

Fig. 9.78 - FPR Table Drive.

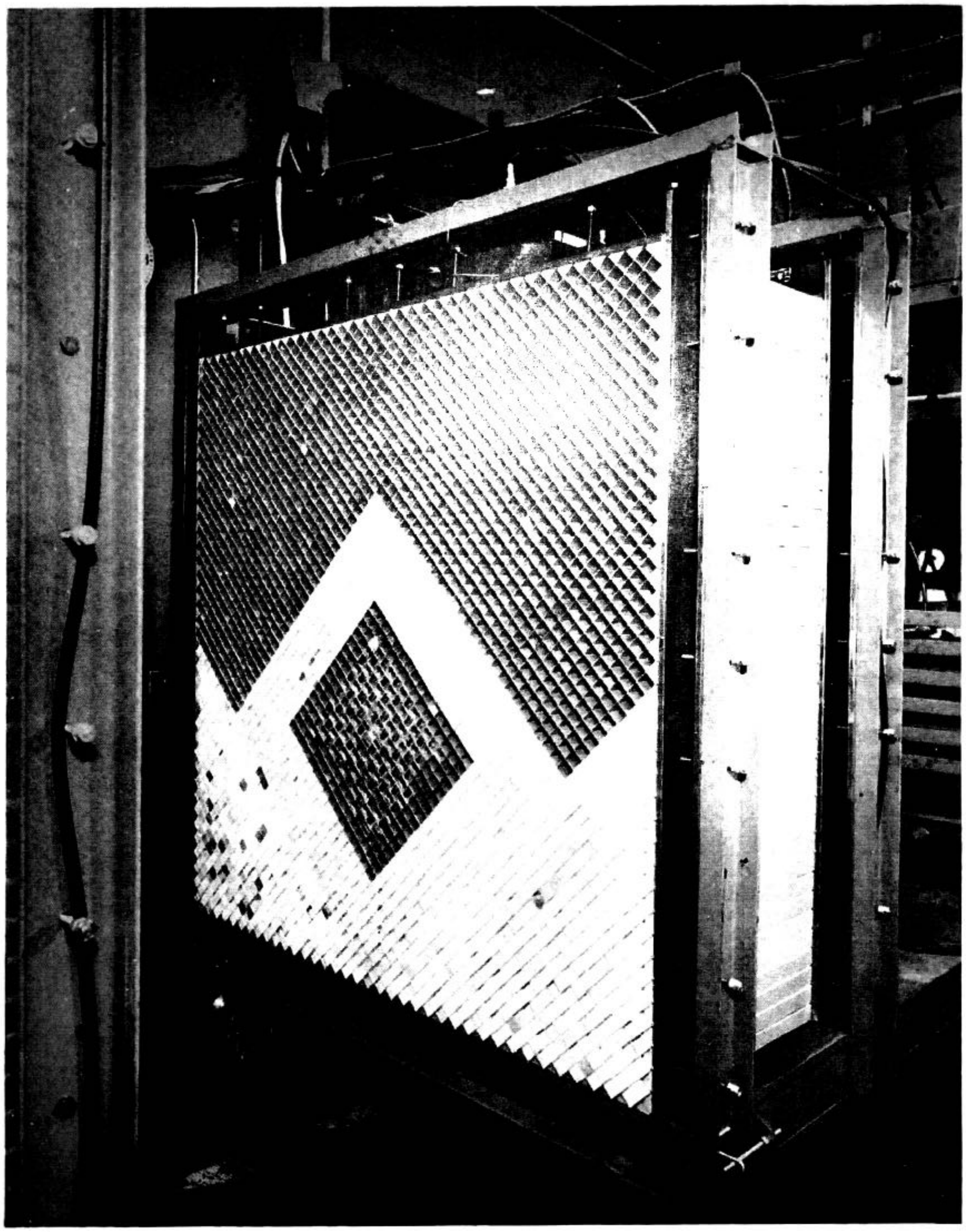

This view shows the array of aluminum tubes clamped to the movable table. The core slugs and reflector materials are stacked in the aluminum tubes.

Fig. 9.79 - FPR Core Assembly.

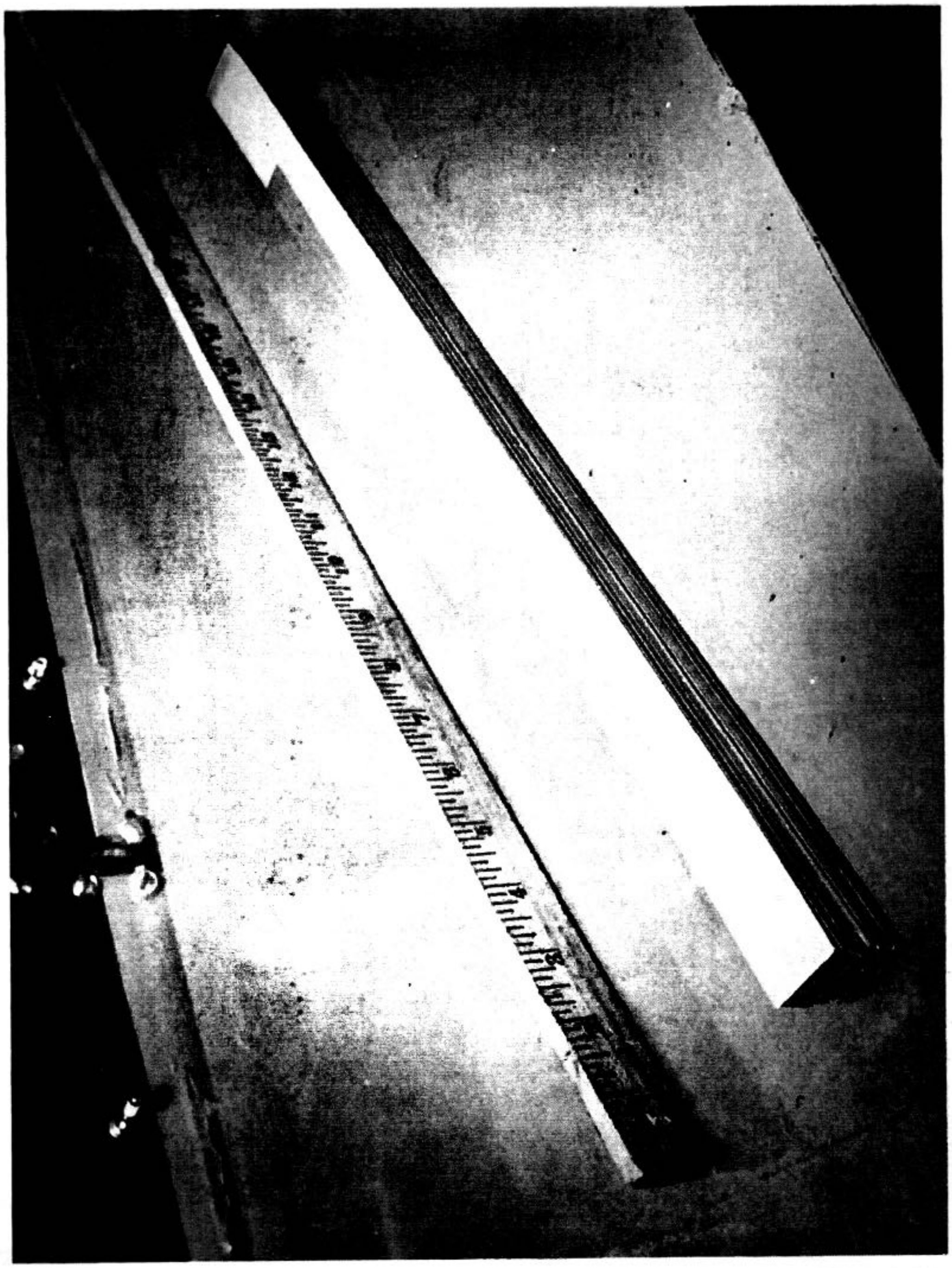

Fig. 9.80 - FPR Core Slug.

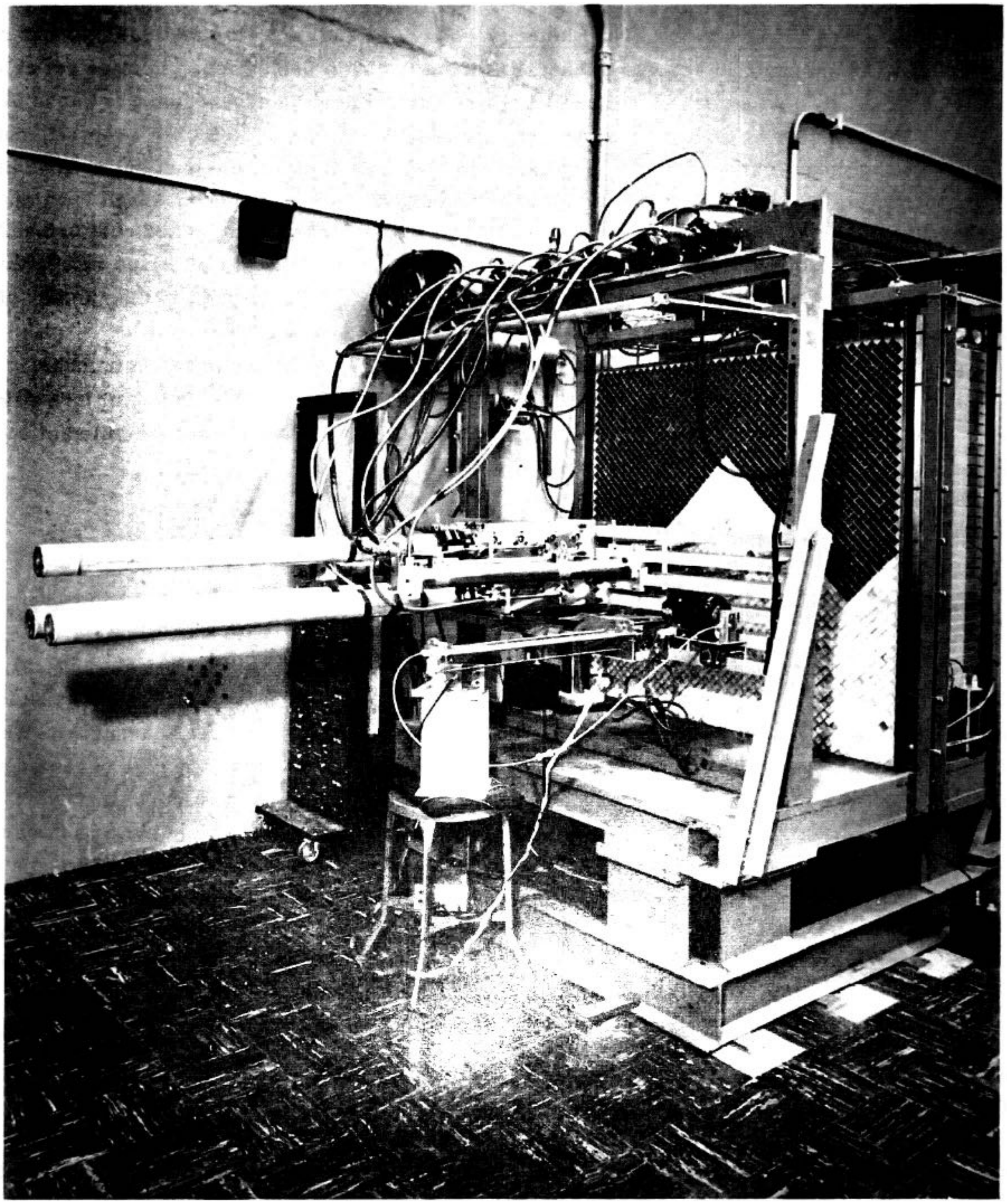

Fig. 9.81 - FPR Control and Safety Rod Mechanisms.

bridge. The mount is adjustable to permit easy relocation of any rod. The safety rods are cocked against a compressed spring by a friction drive operating through a magnetic clutch. When tripped, the rods are driven to the mid-plane in 175 milliseconds with an initial acceleration of 5g.

(d) Core Materials and Fuel Elements. All core and reflector materials are in strip form of a standard width in various thicknesses from 0.020 to 0.100 inch. All side reflector materials are cut to a 24-inch length. All present core materials except fuel are cut to 14, 16, or 18-inch lengths to permit changing the core length from 28 to 36 inches over-all, but still having only one length of material (other than fuel) per slug for any particular core size. To minimize the fuel inventory on hand, the fuel strips are cut to 12, 4 and 2 inch lengths. These strips are 0.002-inch uranium metal, 93 per cent enriched, and coated with 0.5-mil fluorine plastic as a protection against progressive oxidation. The use of strips rather than disks permits both arbitrary location of longitudinal voids and a reduction in the number of individual core elements.

(e) Instrumentation. The instruments used in the FPR are similar in number, function, and character to those used with the ATR critical assemblies. A useful innovation is the addition of six channels of neutron pulse counting which are equipped for automatic timing and print-out and which recycle automatically.

A view of the control console is shown in Fig. 9.82.

THE PRESSURIZED WATER REACTOR FLEXIBLE ASSEMBLY

by R. T. Bayard and W. H. Hartley

The Pressurized Water Reactor Flexible Assembly (PWR-FA) is the flexible critical facility for the PWR Project. It has been used to investigate the behavior of cores consisting of seeds of highly enriched uranium flanked by reflecting blankets of natural uranium. While the PWR-FA was primarily intended as a mock-up type of critical facility, a very considerable portion of the effort has been devoted to slab-type reactors built with the same seed and blanket units constructed for the mock-up experiments. The slab-type experiments have the principal advantage of requiring less material. This permits experimental modifications to proceed faster. In some respects, the analysis is simpler than the mock-up analysis.

The PWR-FA design is very similar to the SFR-FA critical facility described previously in this chapter. For this reason, the description will be limited to those features that differ.

9.29 DESCRIPTION OF THE FACILITY

The reactor vessel is a cylindrical stainless steel tank 9 feet in diameter and 10-feet high. Inside the tank, fuel elements are positioned at their top and bottom ends by removable grids. The lower grid sits on a 3-inch steel base plate which supports the core.

Water is pumped into the tank at a rate determined by an orifice diameter to insure a low rate of reactivity insertion. The water is circulated through the tank by eight pumps and four stirrers, and the temperature is controlled by the flow of cold water and steam in jackets surrounding the tank.

The control rods are driven vertically through the core by a rack and pinion arrangement connected to the drive motor through a magnetic clutch. The rods are raised from the core against the action of gravity and are scrammed by releasing the magnetic clutch. Dual selsyn indicators (coarse and fine) indicate the height of the control rods to ± 0.02 inch.

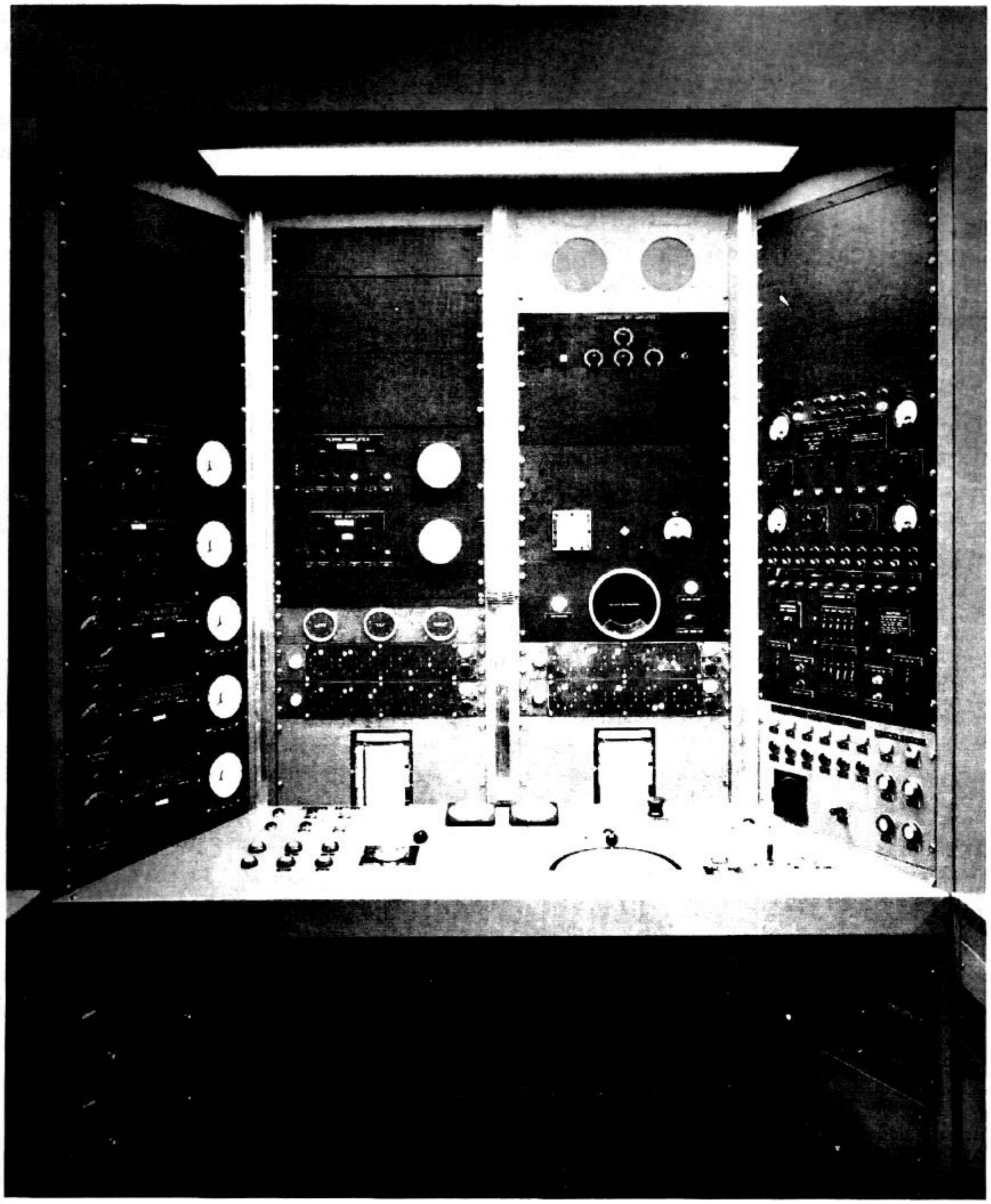

Fig. 9.82 - FPR Control Console.

The safety instrumentation to monitor the core behavior consists of two photomultiplier circuits connected to relay contact level scram circuits, and two boron-lined compensated ionization chambers connected to period scram and level scram circuits. The output of one of these ion chambers is displayed on a logarithmic recorder. In addition to the four scram circuits, there are four ionization chambers with logarithmic amplifiers, and two with linear amplifiers in thimbles piercing the wall of the reactor tank. A five curie polonium-beryllium source is used to provide a detectable flux level during start-up.

Eight fission counters placed about the core in various positions are connected through pulse amplifiers to scaling circuits. These eight circuits serve as the source of experimental data.

For the differential water height type of measurement, special facilities are required to measure the change in moderator level. Since the total moderator level change in the measurement at some heights is of the order of 0.2 inch, it is necessary to measure the changes in moderator level precisely. To do this, a remotely operated selsyn-driven micrometer head was mounted on the end of a control rod drive mechanism. Contact between the water surface and a 0.008-inch diameter tungsten wire mounted on the micrometer is indicated by an ohmmeter connected between the wire and the tank wall. Selsyn indicators on the control rod drive mechanism and on the micrometer drive give the water height. This method measures differential changes in water level which are consistent to 0.001 inch. Absolute values of height, as contrasted with differential heights, are known to 0.02 inch, i.e., the precision of the control rod indication.

9.30 DESCRIPTION OF THE FUEL ELEMENTS AND REACTORS

(a) Seed Elements. The enriched fuel in the seed units of the cores was contained in two forms: One was an alloy of uranium in zirconium; the other was a mixture of U_3O_8 and polyethylene extruded into tape form. The fuel tape was 1.61 inches wide and approximately 0.029 inch thick. When cemented to a bar of Zircaloy with a rubber base cement, the tape formed a fuel bar. A seed sub-unit, called a bundle, was constructed by joining several fuel bars with aluminum pins and rivets, and enclosing them in a square box of Zircaloy plates. A diagram of a typical seed bundle of tape fuel is shown in Fig. 9.83. In the course of the experimentation a number of different types of seed units were used. These are identified by letter (N, P, Q, etc.).

The metal alloy seed unit (designated by the letter L) was made from fuel bars which were an alloy of 6.33 w/o uranium (highly enriched) in zirconium. The bars were 2.25-inches wide and 0.055-inch thick. A combination of ten of these bars and six Zircaloy bars, enclosed on four sides by Zircaloy plates, constituted a seed bundle. A diagram of such a bundle is shown in Fig. 9.84. The black circles shown in the figure represent Zircaloy wires. These serve as spacers between the bars.

Other seed bundles were constructed to obtain somewhat different metal-to-water ratios or slightly different fuel loadings in the seed. Figure 9.85 shows a diagram of a P-type seed bundle and Fig. 9.86 shows a diagram of a Q-type seed bundle. Since the properties of these seed bundles differed only slightly, critical experimentation to determine the reactivity effects of various changes in the seed such as metal-to-water ratio, fuel loading, etc. was possible.

Four seed bundles, arranged as shown in Fig. 9.87, constituted a unit called a cluster. The cluster was arranged to provide a rod channel for a cruciform-shaped control rod.

11 CENTER BARS TO HAVE TAPE
1 OF 11 CENTER BARS TO HAVE TAPE ON BOTH SIDES
NO TAPE ON OUTSIDE BARS

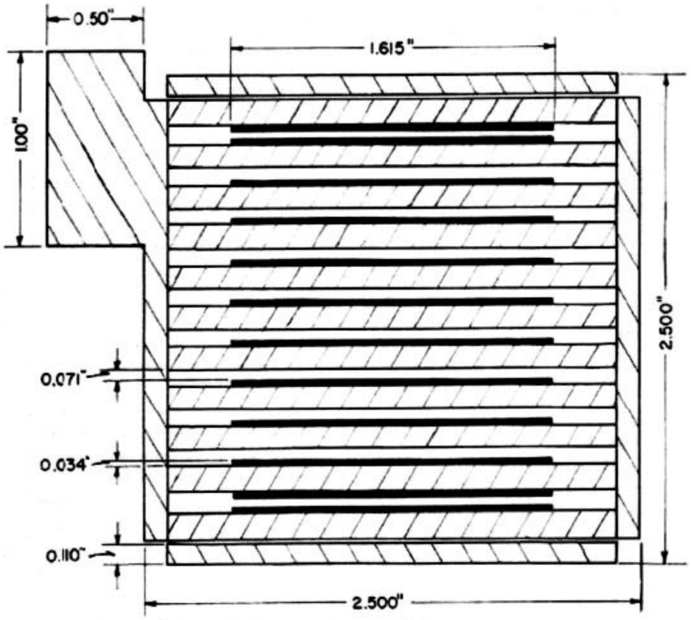

UO₂ FLEX ASSEMBLY SEED BUNDLE -N

Fig. 9.83 - Diagram of an N-Type Seed Bundle.

10 ALLOY FUEL BARS

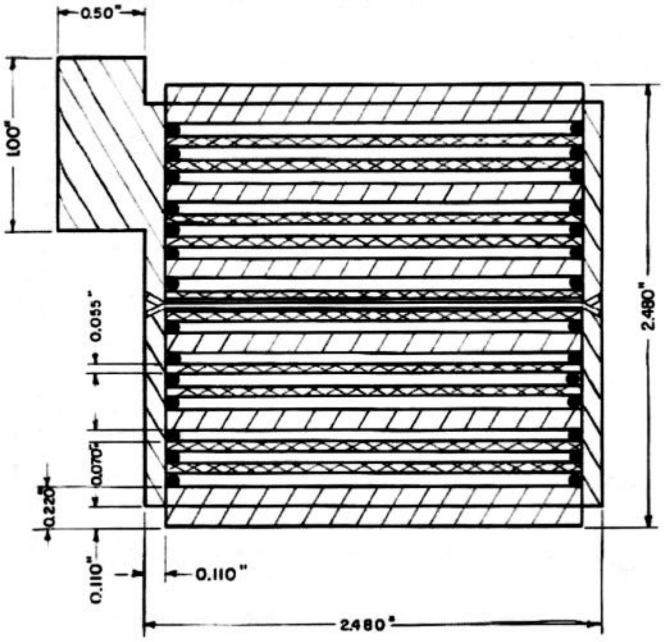

SEED BUNDLE - L

Fig. 9.84 - Diagram of an L-Type Seed Bundle.

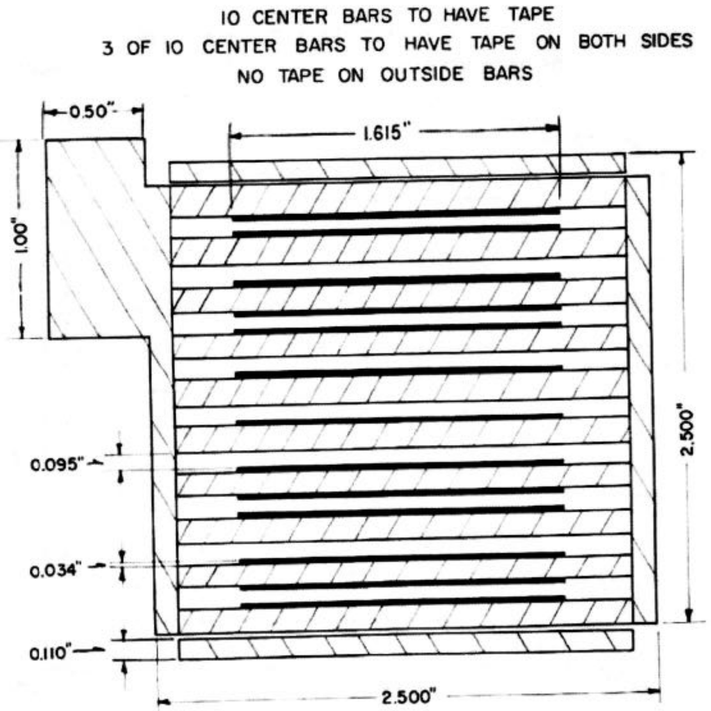

10 CENTER BARS TO HAVE TAPE
3 OF 10 CENTER BARS TO HAVE TAPE ON BOTH SIDES
NO TAPE ON OUTSIDE BARS

UO_2 FLEX ASSEMBLY SEED BUNDLE - P

Fig. 9.85 - Diagram of P-Type Seed Bundle.

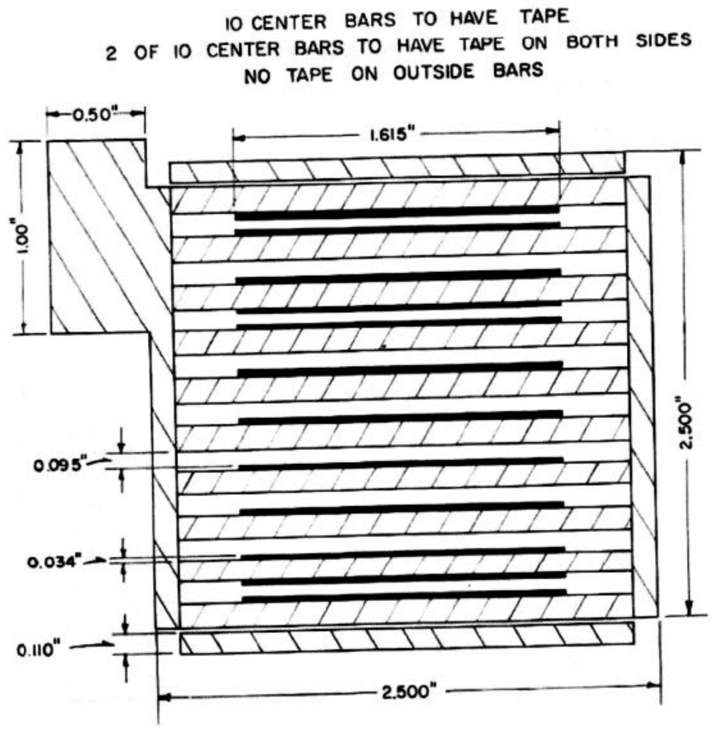

10 CENTER BARS TO HAVE TAPE
2 OF 10 CENTER BARS TO HAVE TAPE ON BOTH SIDES
NO TAPE ON OUTSIDE BARS

UO_2 FLEX ASSEMBLY SEED BUNDLE - Q

Fig. 9.86 - Diagram of Q-Type Seed Bundle.

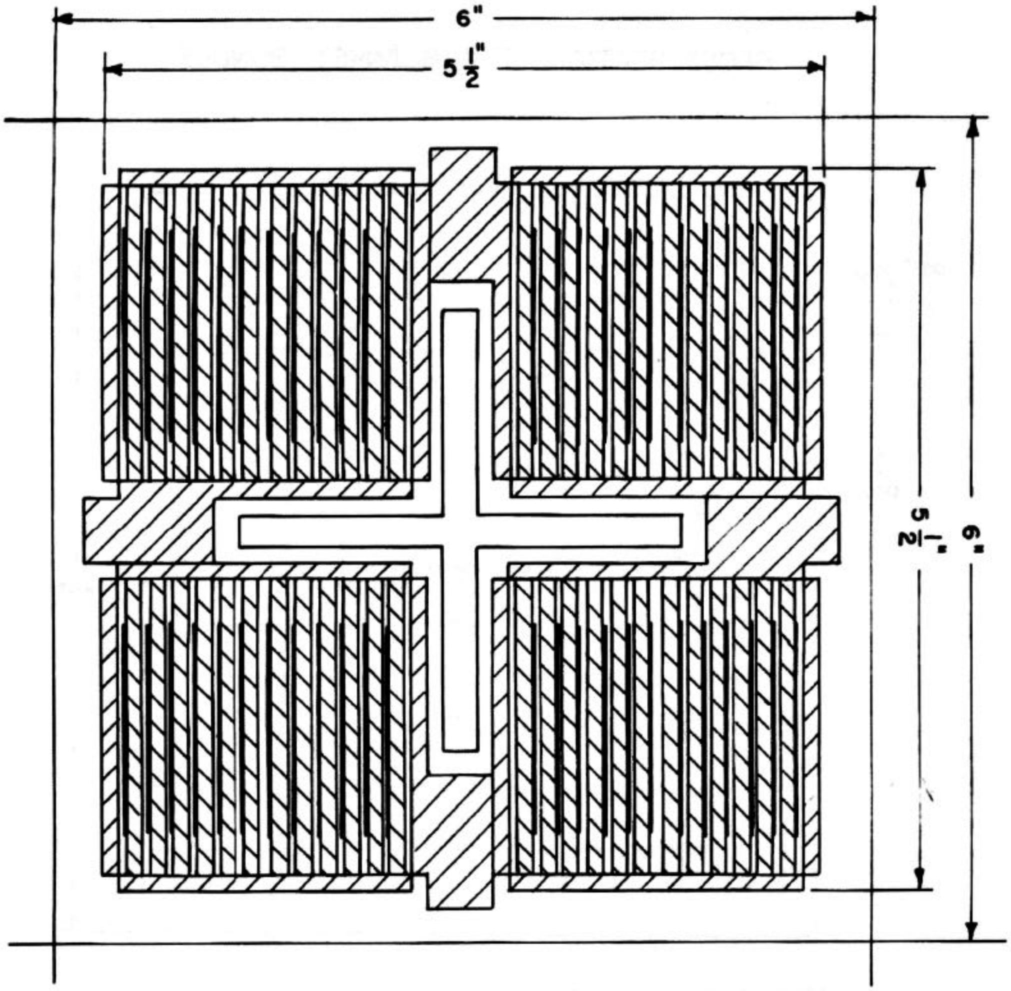

Fig. 9.87 - Diagram of a Seed Cluster (1).

(b) Blanket Elements. The fuel in the blanket region of the slabs was natural uranium dioxide. The UO_2 was compacted, sintered, and ground into right circular cylinders of 0.357 inch diameter by 0.356 inch length. Twenty-six of these pellets comprised a unit fuel length (9.284 inches). Seven fuel units, separated by 1.062-inch-long slugs of Zircaloy, comprised a fuel tube. These units were placed in tubes of aluminum of 0.398-inch outer diameter and 0.362-inch inner diameter, and the ends of the tubes were capped and welded. A square array of 121 of these tubes, spaced by aluminum grids and confined by Zircaloy side plates, was referred to as a blanket bundle. The six aluminum spacer grids were co-planar with the slugs of Zircaloy which separate the unit fuel lengths. The spacer grids and slugs of zirconium were designed to represent the PWR design blanket element which consisted of short lengths (approximately 10 inches) of oxide tube bundles. A blanket bundle is shown in Fig. 9.88

(c) Control Rods. The reactivity of the cores was controlled by a set of cruciform control rods made of an alloy of 30 w/o cadmium-70 w/o silver with a span of 3-3/8 inches. One control rod was provided in each seed cluster.

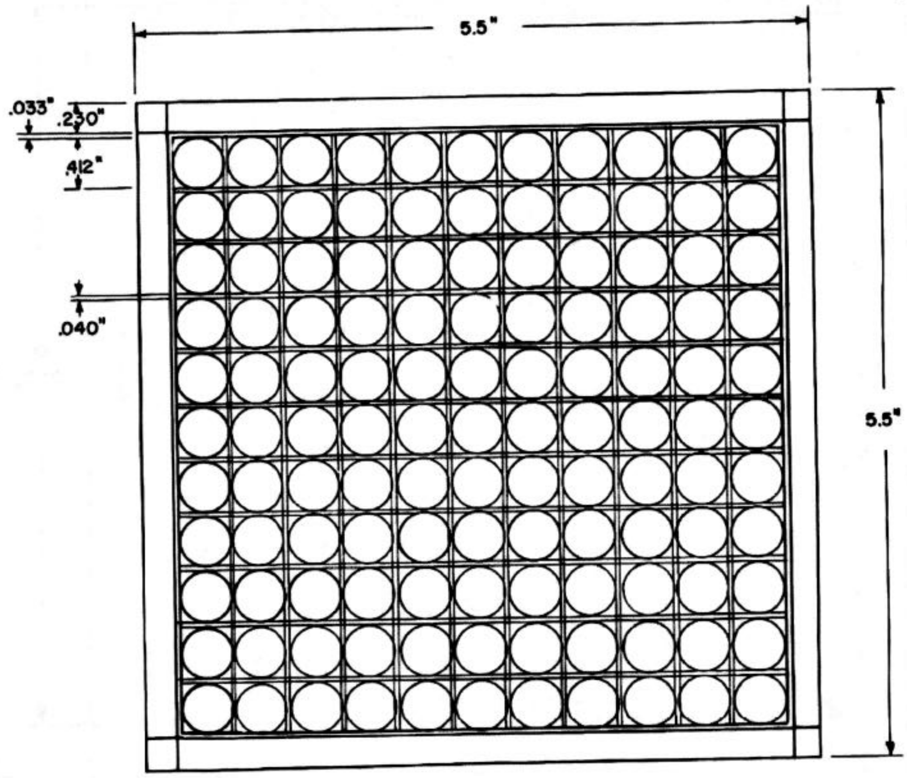

CROSS SECTION OF A BLANKET BUNDLE

DIAMETER OF TUBE = 0.398"

Fig. 9.88 - Cross Section of a Blanket Bundle.

(d) Reactor Arrangements. As noted previously the critical experiments were generally performed on slab arrays or full-scale mock-ups. A slab array was constructed by placing several seed clusters in a row as shown in Fig. 9.89. The fuel material in the seeds was arranged so that all fuel bars were oriented parallel to the face of the slab. Blanket was added to the slab reactors by placing blanket bundles in rows next to the seed sides. In the slab reactor experiments a shorthand notation was used to indicate the number of rows of blanket bundles. A slab which was reflected by one row of blanket on each side of the seed was designated 1 x 1; one which contained two rows on each side was designated 2 x 2, etc.

For the full-scale mock-up studies a seed cluster contained one each of the four types of seed bundles (L, N, P, Q). This assured the greatest homogeneity of the mock-up with the available material. Figure 9.90 shows the arrangement of the seed units for a mock-up critical.

Control rods were provided for each seed cluster in both the slab and mock-up type experiments.

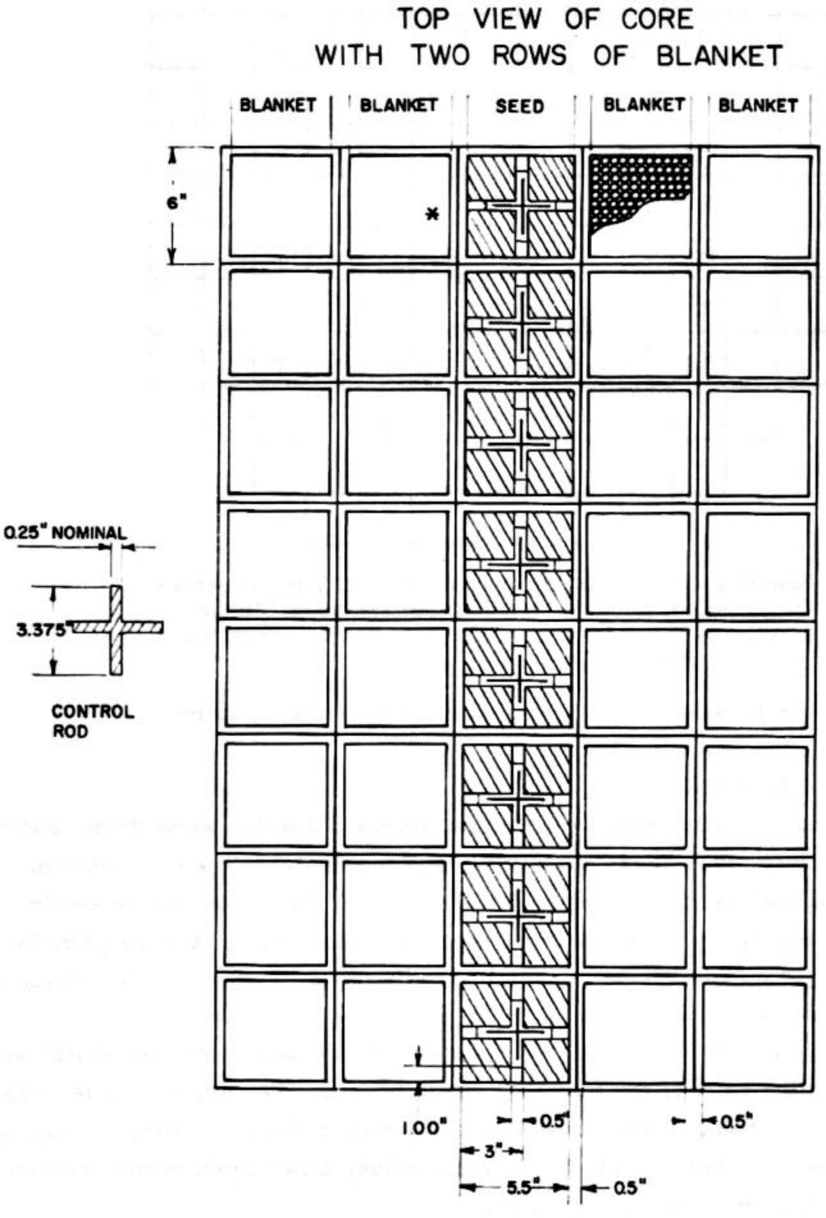

Fig. 9.89 - Top View of a Slab Assembly.

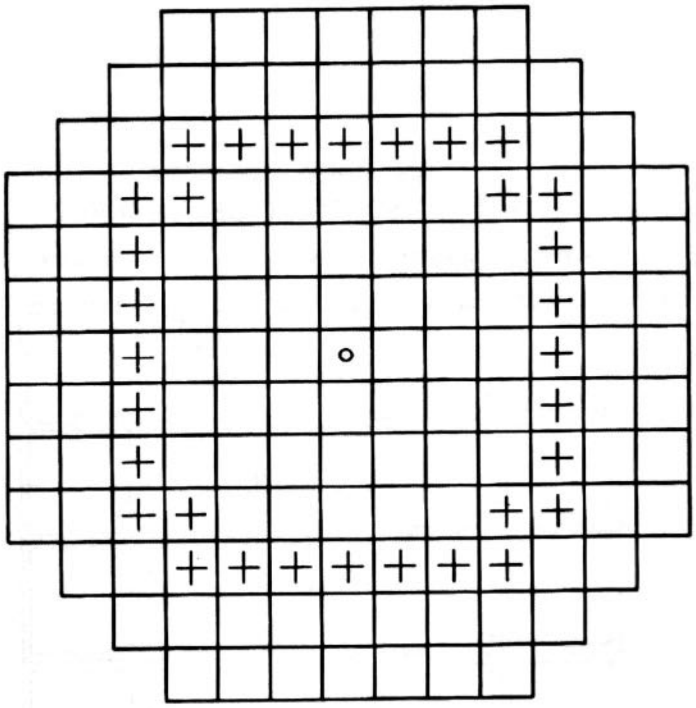

Squares containing crosses represent seed clusters with control rods. All other squares are blanket bundles. The circle at the core center shows the location of the start-up source.

Fig. 9.90 - Top View of the PWR Mock-up Core.

9.31 TYPES OF MEASUREMENTS

The three principal measurements carried out on the PWR-FA were those leading to values of the shutdown reactivity, the excess reactivity, and the neutron flux distribution. In addition, conversion ratio measurements were made in the blanket. These are discussed in Chap. 11.

(a) Excess Reactivity. The excess reactivity measurements were principally the differential water height measurements described in Chap. 8, Sec. 19. In carrying out this particular measurement several experimental details were important.

First, the tips of the bank of control rods were held just above the moderator surface. This was important in the case of the tape fuel seeds because the data were analyzed on the assumption that the fuel region above the water surface contributed nothing to the reactivity. Since the plastic in the tape did provide some moderation, this region would contribute to the reactivity unless the control rods were present.

The second point was the manner of taking the data. The moderator level, together with the control rod bank, was lowered in steps. At each position the reactor period was measured. The reactivity was computed from the measured period through the inhour equation, and a straight line was fitted to the reactivity versus height plot by a least squares analysis. The slope of the line was the moderator worth and the intercept at zero reactivity, the critical height.

(b) Shutdown Reactivity Measurements. Most of the schemes discussed in Chap. 8 were tried for the shutdown reactivity measurement. The method on which the greatest reliance was placed was the negative buckling method described in Chap. 8, Sec. 20. This procedure appeared to give the most consistent and reliable results.

(c) Flux Maps. Both local and general flux maps were taken on the PWR-FA. The techniques used were generally the foil (wire) techniques discussed in Chap. 10.

9.32 SUMMARY AND ANALYSIS OF EXPERIMENTAL DATA

(a) Excess Reactivity Measurement. The results of the differential water worth measurements on the various slabs and on the mock-up are tabulated below. Table 9.25 summarizes the results of the moderator worth measurements on the four slab experiments with the seeds designated as L, N, P, and Q. Table 9.26 summarizes the results of the moderator worth measurements on the full-scale mock-up in which each seed cluster contained one each of L, N, P, and Q subassemblies. In the full-scale mock-up studies the reactor was made critical at various heights by inserting various patterns of control rods completely into the core.

Table 9.25 - MEASURED MODERATOR WORTH VALUES ($\delta p/\delta z$)

Seed L		Seed N	
h (inches)	$\delta p/\delta z$ (in^{-1})	h (inches)	$\delta p/\delta z$ (in^{-1})
18.09	87.40×10^{-4}	20.36	61.66×10^{-4}
19.69	77.68	22.97	52.38
25.48	41.33	32.18	23.17
29.27	30.59	42.26	11.64
		42.62	11.75

Seed P		Seed Q	
h (inches)	$\delta p/\delta z$ (in^{-1})	h (inches)	$\delta p/\delta z$ (in^{-1})
18.04	84.58×10^{-4}	19.05	76.26×10^{-4}
25.60	39.24	21.10	61.28
42.61	11.14	28.24	32.38
		34.75	19.17
		35.41	17.46
		44.80	9.78
		51.94	6.13

Table 9.26 - MEASURED MODERATOR WORTH VALUES - MOCK-UP

Water Height (inches)	$\partial\rho/\partial z$ ($\times 10^4$ in^{-1})
13.42	154.0 ± 1.6
15.46	117.5 ± 1.7
17.19	91.8 ± 4.8
24.52	42.0 ± 0.9

(b) Partial Water Height Experiments. The results for the partial water height experiments are tabulated below in Table 9.27. These are given for the four slab experiments and for the full-scale mock-up. The slab experiments are eight clusters in length, and are symmetrically flanked by one or two rows of blanket clusters. The table also includes the experimental value of the excess reactivity. This is tabulated in three columns. Unadjusted refers to the simple inhour equation without correction using Hughes' original data. The inhour equation was adjusted as discussed in Chap. 8, Sec. 23, to take into account fast fission in U^{238} and the reduced energy of delayed neutrons. These columns are marked adjusted and the subheadings, Hughes and Keepin, refer respectively to the delayed-neutron data used in the two cases.

Table 9.27 - MEASURED CRITICAL HEIGHTS AND EXPERIMENTAL REACTIVITY VALUES

Seed Type	Blanket Configuration	Critical Height (inches)		Excess Reactivity (%) Adjusted	
			Unadjusted	Hughes	Keepin
L	1 x 1	19.60	8.9	10.3	9.6
	2 x 2	17.95	10.3	11.9	11.1
N	1 x 1	22.76	6.7	7.8	7.2
	2 x 2	20.18	8.2	9.5	8.9
P	2 x 2	17.91	9.9	11.5	10.7
Q	1 x 1	18.89	9.1	10.6	9.8
Mock-up	Mock-up	13.42	15.1	17.5	16.3

(c) Shutdown Measurement. The negative buckling in the rodded region of the mock-up core was measured by the method given in Chap. 8. The value obtained for the negative buckling factor was $B_z^2 = -10.9 \pm 0.15 \times 10^{-4}$ cm^{-2}. This value yields a shutdown reactivity of -8.0 ± 0.1 per cent.

(d) Analysis of Excess Reactivity Data. In addition to the reactivity and criticality data, the basic information needed to analyze the reactor experiments is the exact core geometry and the inventory of the core material. The inventory is obtained by weighing, analyzing chemically and physically, and measuring the volume of the structural and fuel materials in the core. The non-water volume in the seed region is determined by measuring the volume of a total seed bundle.

The reactor experiments are analyzed by the same few-group diffusion model as is used in the reactor design. The techniques for obtaining the group parameters, as they apply to the PWR design, are discussed in Chap. 4. Fast constants are obtained from the MUFT calculation (Appendix E). Thermal group constants are obtained by flux weighting the cross sections, where this technique is applicable and averaging over the SOFOCATE spectrum.

Two calculations are necessary to determine the excess reactivity: One, using the critical buckling as input data; the other, using the full height buckling. The ratio of the two eigenvalues is the k_{eff} of the core with no control rods. The results of the calculations for the reactor experiments analyzed are given in Table 9.28.

The third column of the table gives the buckling used in the calculation. This buckling is $(B_y^2 + B_z^2)$ in the slab cases, B_z^2 in the mock-up case. B_y^2 was obtained by assuming that the length of an equivalent bare slab was given by the physical length of the slab (47.5 inches) plus 6 inches total reflector savings. (The value of 6 inches represents an average value obtained from several flux traverses.) B_z^2 for the critical case was obtained from the measured critical height plus 6.5 inches total reflector savings. The same reflector savings was used to compute the vertical buckling for the full-size reactor.

The excess reactivity values given in the fifth column of Table 9.28 were calculated from the expression

$$\rho = \frac{\frac{\lambda_H}{\lambda_c} - 1}{\frac{\lambda_H}{\lambda_c}}$$

where λ_H and λ_c are eigenvalues for the full height and critical reactors, respectively. The experimental values of Table 9.27 are repeated in Table 9.28 for comparison.

Table 9.28 - CALCULATED AND EXPERIMENTAL REACTIVITY VALUES

				Excess Reactivity %		
					Experimental Values (Adjusted)	
Seed Type	Blanket Configuration	$B_y^2 + B_z^2$ (10^4 cm^{-2})	λ	Calculated Values	Hughes	Keepin
L	1 x 1	27.68	1.0142			
	1 x 1	7.73	1.1178	9.27	10.3	9.6
	2 x 2	30.74	1.0123			
	2 x 2	7.73	1.1338	10.71	11.9	11.1
N	1 x 1	23.09	1.0200			
	1 x 1	7.73	1.1001	7.28	7.8	7.2
	2 x 2	26.69	1.0166			
	2 x 2	7.73	1.1168	8.97	9.5	8.9
P	2 x 2	30.84	1.0126			
	2 x 2	7.73	1.1321	10.55	11.5	10.7
Q	1 x 1	25.73	1.0181			
	1 x 1	7.73	1.1095	8.24	8.9	8.3
	2 x 2	28.94	1.0161			
	2 x 2	7.73	1.1255	9.72	10.6	9.8
Mock-up	Mock-up	40.56	1.0060			
		2.51	1.2117	17.0	17.5	16.3

Chapter 10

TECHNIQUES OF FLUX MAPPING

THE FLUX PLOTTING OF LOW POWER REACTORS

by K. E. Relf

10.1 INTRODUCTION

Plots of relative flux in a reactor can be made with miniature fission counters,[1, 2] combination activation and film techniques,[3] and straight foil-activation methods.[4-8] The method applicable to a particular reactor depends upon the information wanted, the spatial resolution required, and the space available in the reactor for placing sensing devices.

Designs of miniature fission counters are described in the references cited. The construction is straightforward, but facilities for assembling, evacuating, filling, and testing are required. Miniature counters are most useful for obtaining data on gross features of a core because of their limited spatial resolution.

The foil-activation techniques require counting facilities and an environment comparatively free of background sources and power line noise. Foils (or wires) are useful for measuring flux distributions where great detail and fine spatial resolution are of interest.

The film techniques require a well-equipped darkroom and one or more microscopes. Because this method is very slow, both the accuracy and the number of points that can be obtained in a given length of time are limited.

The discussion in this chapter is devoted to flux plotting by foil activation. This appears to be the most useful method for making flux distribution measurements with water reactors. Recent advances in automatic counting equipment and data-handling apparatus have made it possible to take and process large amounts of data in a reasonably short time. Foil activation, therefore, offers the reactor physicist a technique with both precision and speed.

10.2 THEORY OF THE FOIL-ACTIVATION TECHNIQUE

The total flux at a point is measured by exposing a suitable material to the neutron flux at a point in the reactor for a length of time t_e. The foil is removed and transferred to a suitable counter, and the activity is counted for a time t_c. After being corrected for background, the count rate is reduced to the value it would have had at the end of exposure if the time of exposure had been sufficient to carry the activation to saturation.

An expression may be derived for the relationship between the flux at the position at which the foil is irradiated and the total count obtained from the foil. Let $\varphi(E)$ be the neutron flux at the foil in the energy interval dE at E. For the particular nuclide being used, let its cross section for activation by neutron capture to the state being counted be $\sigma(E)$ at the energy E. By definition, the total neutron flux Φ in the energy range from E_1 to E_2 is

$$\Phi \equiv \int_{E_1}^{E_2} \varphi(E)\, dE \qquad \text{Eq. (10.1)}$$

and the average activation cross section $\bar{\bar{\sigma}}$ in the energy range from E_1 to E_2 is

$$\bar{\bar{\sigma}}\,\Phi \equiv \int_{E_1}^{E_2} \sigma(E)\, \varphi(E)\, dE \qquad \text{Eq. (10.2)}$$

Let M be the atomic mass number of the nuclide and m the total mass of the nuclide in the foil. Then if A is Avagadro's number, the total number of nuclides of this specie in the foil is $\frac{mA}{M}$, and the total number of active nuclides R_o formed per unit time in the foil during the irradiation is

$$R_o = \frac{mA}{M}\,\bar{\bar{\sigma}}\,\Phi$$

If the decay constant of the activated nuclide is λ, and if Q is the total number of active nuclides present, the rate of decay of the active nuclides is just λQ. During the irradiation period the rate of change of Q is given by the equation

$$\frac{dQ}{dt} = R_o - \lambda Q \qquad \text{Eq. (10.3)}$$

If the initial concentration of active nuclides is zero and the time of irradiation exposure is t_e, the number of active nuclides in the foil at the end of the exposure is

$$Q = \frac{R_o}{\lambda}\,[1 - \exp(-\lambda t_e)] \qquad \text{Eq. (10.4)}$$

The saturation activity is R_o/λ.

If the foil is removed from the flux, the number of active nuclides decays exponentially. The number present at a time t following the exposure is

$$Q = \frac{R_o}{\lambda}\{1 - \exp(-\lambda t_e)\}\{\exp(-\lambda t)\} \qquad \text{Eq. (10.5)}$$

The number of disintegrations in the foil per unit time is λQ and the counting rate is proportional to λQ. If C is the total number of counts accumulated by a counting system, $\frac{dC}{dt}$ is the counting rate.

$$\frac{dC}{dt} = \epsilon\lambda Q = \epsilon R_o\{1 - \exp(-\lambda t_e)\}\{\exp(-\lambda t)\} \qquad \text{Eq. (10.6)}$$

The factor ϵ is the efficiency of the counting system and its value depends on the nature of the radiation from the foil, the counting geometry, and the efficiency of the radiation detector.

If the time between the end of the exposure and the beginning of the count is designated as t_w and the total counting time as t_c, the total count C can be calculated. From this the total flux Φ in the energy range E_1 to E_2 may be calculated,

$$\bar{\Phi} = \frac{M\lambda C}{\epsilon m A \bar{\sigma}} \{1 - \exp(-\lambda t_e)\}^{-1}\{1 - \exp(-\lambda t_c)\}^{-1}\{\exp(\lambda t_w)\} \qquad \text{Eq. (10.7)}$$

The separate values of the fluxes of thermal and of epithermal neutrons are usually required in reactor measurements; for example, in the application of two group diffusion theory. The most common experimental method of separating the two fluxes utilizes foils exposed first bare and subsequently with cadmium covers. This divides the flux into a component below and one above the cadmium cutoff energy. Cutoff, denoted as E_{CD}, is defined as the energy at which the activation of a cadmium-covered foil is identical to that which would be produced if the foil were covered by a material completely black to neutrons below the cutoff energy and completely transparent to neutrons above the cutoff. Its precise value depends upon the cadmium-cover thickness and the neutron energy spectrum in the reactor, as well as the absorption cross section and thickness of the foil. It can be estimated by numerical evaluation of certain integrals provided the flux spectrum is known. In lieu of a known energy distribution, the assumption can be made that the thermal neutrons have a Maxwellian distribution and the epithermal neutrons a 1/E distribution. An experimental method for evaluating the cadmium cutoff energy for a given foil thickness and neutron energy spectrum is described by Kunstadter.[7]

The cadmium ratio of a foil is the ratio of its activity when exposed at a point in a reactor without a cadmium cover to its activity when exposed with a cover. Let $\bar{\sigma}_{TH}$ represent the average activation cross section of the foil over the thermal flux spectrum and Φ_{TH} be the total thermal flux. Let $\bar{\Phi}_{EP}$ be the total epithermal flux (assumed to be 1/E) and $\bar{\sigma}_{EP}$ be the average activation cross section of the foil averaged over the epithermal flux. In terms of the definitions, Eqs. (10.1) and (10.2), $E_1 = 0$ and $E_2 = E_{CD}$ for the thermal flux while $E_1 = E_{CD}$ and $E_2 = \infty$ for the epithermal flux. Thus

$$\bar{\Phi}_{TH} = \int_0^{E_{CD}} \varphi(E)\, dE \qquad \text{Eq. (10.8a)}$$

$$\bar{\sigma}_{TH}\,\bar{\Phi}_{TH} = \int_0^{E_{CD}} \sigma(E)\,\varphi(E)\, dE \qquad \text{Eq. (10.8b)}$$

$$\bar{\Phi}_{EP} = \int_{E_{CD}}^{\infty} \frac{dE}{E} \qquad \text{Eq. (10.9a)}$$

$$\bar{\bar{\sigma}}_{EP}\,\bar{\Phi}_{EP} = \int_{E_{CD}}^{\infty} \frac{\sigma(E)\, dE}{E} \qquad \text{Eq. (10.9b)}$$

By definition the cadmium ratio R_c is then:

$$R_c = \frac{\text{Bare foil activity}}{\text{Cadmium covered foil activity}} = \frac{\bar{\bar{\sigma}}_{TH}\,\Phi_{TH} + \bar{\bar{\sigma}}_{EP}\,\Phi_{EP}}{\bar{\sigma}_{EP}\,\bar{\Phi}_{EP}} \qquad \text{Eq. (10.10)}$$

and

$$R_c - 1 = \frac{\bar{\sigma}_{TH}\,\Phi_{TH}}{\bar{\bar{\sigma}}_{EP}\,\bar{\Phi}_{EP}} \qquad \text{Eq. (10.11)}$$

For precise work with certain types of foils, correction factors may be required. One of these is associated with the absorption of epithermal neutrons by the cadmium cover. This correction is particularly important with indium foils. The correction may be determined experimentally by measuring the epithermal activation as a function of cadmium cover thickness and extrapolating to zero thickness. This is shown in Fig. 10.1. The ordinate is the activity due to epithermal neutrons; experimentally it is the activity of the cadmium covered foils. The correction factor F_{CD} is defined as follows:

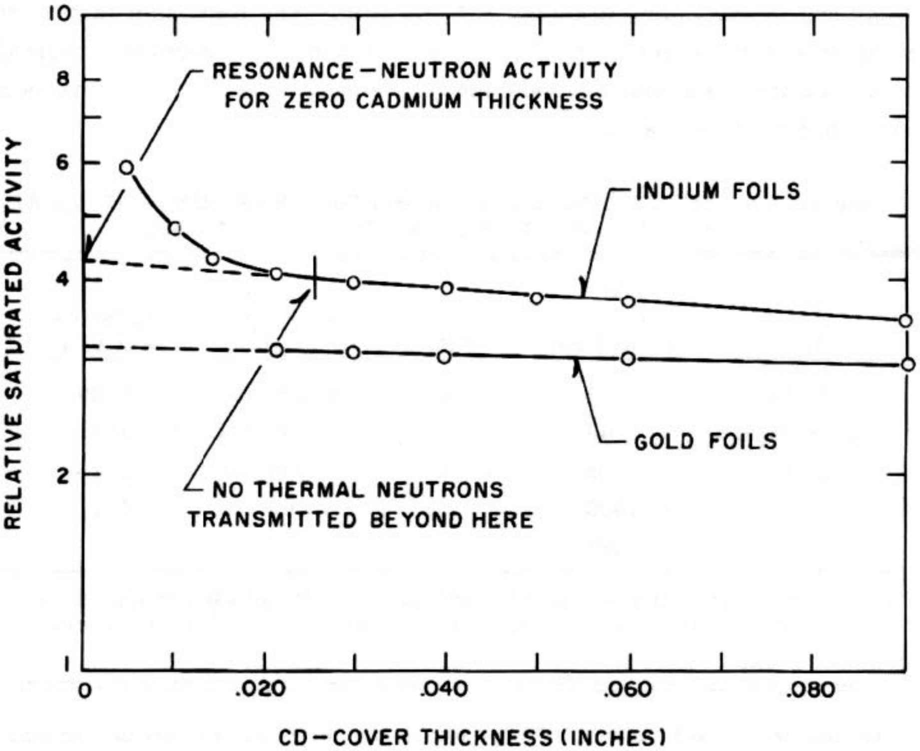

Fig. 10.1 - Relative Saturated Activity versus Cadmium Thickness.[11]

$$F_{CD} \equiv \frac{\text{Relative saturated activity extrapolated to zero cadmium thickness}}{\text{Relative saturated activity at cadmium thickness used}} \qquad \text{Eq. (10.12)}$$

With very thin cadmium covers some of the thermal neutrons leak through the cover. This is shown in the indium curve of Fig. 10.1. If these covers are used, a correction may be made for this effect. For reactor flux measurements in pressurized ratio reactors this effect is generally unimportant and the correction is not made.

Based on the preceding discussion, the method of measuring the thermal and epicadmium neutron flux at a point in a reactor is to expose a bare foil and determine its total activity A_B^T; expose a cadmium-covered foil and determine its total activity A_{CD}^T; compute the epicadmium activity A_B^{EP}. By the definition of Eq. (10.12):

$$A_B^{EP} = A_{CD}^T F_{CD} \qquad \text{Eq. (10.13)}$$

Next, the thermal flux is computed:

$$A_B^{TH} = A_B^T - A_B^{EP} = A_B^T - A_{CD}^T F_{CD} \qquad \text{Eq. (10.14)}$$

In these equations the leakage of thermal neutrons through the cover is neglected.

10.3 ACTIVATION MATERIALS

Foil materials most suitable for the detection of slow neutrons in low power reactors are manganese, indium, dysprosium, uranium-235 and gold. The important factors to consider in choosing a suitable activation material are its half life and decay scheme, thermal neutron activation cross section, availability, and ease of handling. Table 10.1 contains pertinent data for materials most often used.

Table 10.1 - ACTIVATION MATERIALS FOR MEASURING THERMAL NEUTRON FLUX IN LOW POWER REACTORS

Foil Material	$T_{1/2}$	σ_{th} (barns) (0.025 ev)	$\frac{\bar{\sigma}_{EP}}{\bar{\sigma}_{TH}}$	Specific Activity* (dps/gram)	Relative Activity	First Resonance (ev)
Mn^{55}	2.59 hrs	13.2	0.81	1,300,000	1.00	345
Au^{197}	2.66 days	98	14.35	130,000	0.1	4.8
In^{115}	54.05 min	145	12.1	16,000,000	1.23	1.44
Dy^{164}	139.2	< 1000		56,000,000	4.31	1.65
U^{235}**		687				

* The number of disintegrations per second per gram of irradiated material immediately after irradiation for 1 hour in a thermal neutron flux of 4×10^7 n/cm^2-sec.

** See discussion in text.

Manganese has been used extensively for obtaining thermal flux plots because it has a very convenient half life (2.6 hours), a cross section such that extremely thin or thick foils need not be used, is readily available, and offers no problem in handling. One convenient way to use manganese is in the form of 1/32-inch diameter wires cut to suitable lengths. The wire composition is 84 per cent iron, 2 per cent molybdenum, and 14 per cent manganese. Cadmium ratios are obtained by using special cadmium tubing. A chemical analysis of twenty 1-inch samples of this wire indicated the manganese content to be uniform within a standard error of 0.3 per cent. The fact that the half life was 2.6 hours indicates that no activities from the iron, molybdenum, or contaminants were present.

In a light water moderated reactor, depending on the ratio of slowing down to thermal cross section, manganese exhibits a cadmium ratio of about 10. This may be compared to a value around 15 for U^{235}. A cadmium ratio of 10 means that 90 per cent of the manganese activation is caused by thermal neutrons. Thus if rapid, approximate values of the thermal flux distribution are needed, manganese may be used without taking cadmium ratios. A disadvantage of the high cadmium ratio is the low count rate encountered with the covered foils.

A convenient way to use manganese wire is to mount pieces in plastic wands which are inserted in the reactor. The wire, which is obtained in either 4- or 8-foot lengths, is cut into 1/2- or 1-inch pieces, weighed, and taped with Mylar tape into slots milled in Plexiglass wands. Two typical types of wands have been used: One has slots milled on 0.1-inch centers lengthwise along the wand so that 10 flux points per inch are obtained; the other has slots parallel to the long dimension of the wand, spaced 1/2 inch apart. The former have been used for horizontal plotting; the latter for vertical plotting.

Indium yields both the thermal and epithermal neutron distributions because it has an appreciable thermal neutron activation cross section (145 barns at 0.025 ev) as well as an extremely high resonance cross section (26,400 barns at 1.44 ev). Consequently, indium is an excellent material to use in obtaining relative flux plots. The half life of 54 minutes is within the range of convenient working values. Indium metal is available in a variety of thicknesses, all of which can be handled if reasonable caution is observed. A convenient way to use indium is in an alloy with aluminum (90 per cent aluminum, 10 per cent indium).

The counting rate as a function of foil thickness for an indium foil activated by thermal neutrons is illustrated in Fig. 10.2.[8] From this curve it can be seen that foils of 100 mg/cm^2 thickness yield the highest count rate in water and that the count rate is a slowly varying function of foil thickness. The counting rate produced by capture of indium resonance energy neutrons shows an even flatter maximum around 100 to 150 milligrams per square centimeter.[8]

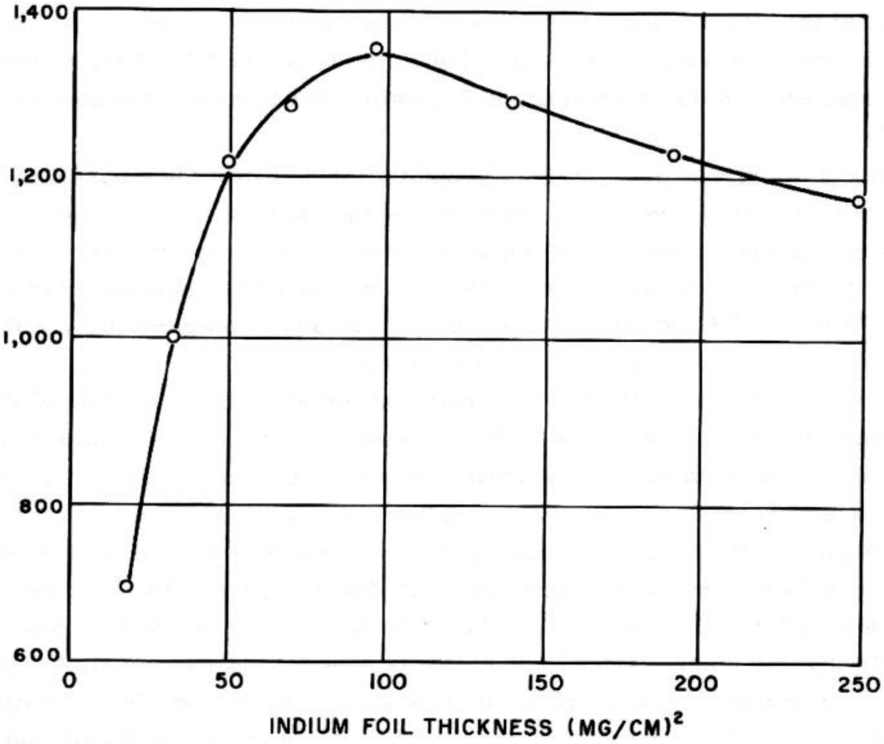

Fig. 10.2 - Variation of Counting Rate Due to Thermal Neutron Capture with Thickness of Indium Foil (Foils 2.5 cm in Diameter).[8]

Indium has one disadvantage in that it possesses an isomer with a 4.5-hour half life produced by fast neutrons (as well as in other ways). The decay from this isomeric state produces a 0.38 Mev gamma ray. This can be discriminated against by a sufficiently high discriminator setting or by using a β-sensitive counter. A minimum irradiation time reduces still further the relative proportion of the 4.5-hour activity.

Indium yields typical cadmium ratios of around three in a light water moderated reactor; so high count rates are obtainable from cadmium-covered foils. On the other hand, because of the low cadmium-ratio, it is necessary to obtain cadmium differences in order to obtain a thermal flux plot.

Uranium is a valuable foil material particularly for special applications. Uranium foils require somewhat more care with procedures than other types of foils but can be used to yield accurate and reproducible results. In reactors fueled with U^{235}, foils of this material can be used to obtain the fission distribution directly if the foils are distributed properly in the fueled zone.

Foils of uranium have been prepared from punchings of UO_2 dispersed in a plastic and from uranium-aluminum alloys. Frequently the foils are prepared directly from the fuel used in the reactor. In certain cases the fuel rods themselves can be counted (see Chap. 9, Sec. 10).

If fission distributions are taken with fueled foils, cadmium ratios are unnecessary unless it is desired to separate thermal and epithermal fissions. Highly depleted foils of U^{238} have been used to obtain the distribution of neutrons above the U^{238} fission threshold (see Chap. 9, Sec. 10).

The use of uranium foils requires special measures for decay correction. Usually a monitor channel is sufficient for this purpose. Experience with uranium foils indicated that a decay curve for each individual count channel must be obtained if the fission-product gamma radiation is counted. On the other hand, if β-counting can be used, this special procedure is not required.

The residual activity of uranium foils prohibits their re-use for a period of 4 to 10 days, the cooling time depending upon the permissible background count rate. The task of making several sets of uniform (or calibrated) foils can be time consuming but once prepared they can be used many times. Irradiation tests of several foils on a foil wheel have been used to demonstrate the uniformity of the uranium concentration. In other cases weighing with a precision balance, as with other foil materials, has been adequate.

Dysprosium is very convenient for thermal flux measurements because of its high cross section and convenient half life (Table 10.1). Its specific activity is 4.3 times that of manganese and 3.5 times that of indium. Dysprosium should be especially useful for extending flux measurements well beyond the core into the reflector. Dysprosium foils have been prepared by mixing the oxide with plastic and forming sheets. The foils are punched from the sheets. Foils of this type have been used to make intracell flux plots (see Chap. 11, Sec. 4).

Gold is a possible activation material for thermal flux measurements, but it does not offer the sensitivity that the other materials do since its specific activity is only 0.1 times that of manganese. It possesses a simple decay scheme and, in pure form, has no extraneous activities. At flux levels of 10^{12} a significant amount of gold-199 can be produced, but at low fluxes only gold-198 activity is formed.

In summary, each foil material possesses one or more advantages over another so that it is usually possible to choose the material best suited to a specific need. Manganese is readily available, easy to work with, has a medium sensitivity to thermal neutrons, and can be used without obtaining cadmium ratios. Indium is easily obtained, moderately easy to handle, has a higher sensitivity to thermal neutrons, and yields both thermal and epithermal neutron distributions; cadmium ratios must be obtained. Uranium is the only material that can give the power distribution directly. While uranium of various enrichments is not difficult to obtain, foils must be made and special procedures used for decay-correction and normalization.

10.4 COUNTING EQUIPMENT AND TECHNIQUES

In this section a few remarks will be made concerning the selection of equipment for a particular counting laboratory.[12] In addition certain precautions taken to assure proper operation of the equipment will be reviewed briefly. Later sections of this chapter discuss special automatic flux counting and data processing systems used in other counting laboratories.

Geiger tubes should not be considered for a counting laboratory because of the effects of spurious counts, long and variable dead-times, aging, and low efficiency for gamma counting. The complex nature of spurious counts causes the ratio of spurious-to-valid counts to depend on count rate, length of discharge, immediate past counting history, tube age, and overvoltage.

Only proportional and scintillation counters have been considered satisfactory. Greatest versatility and maximum speed were offered by the use of scintillation equipment. Alpha, beta, and gamma crystals are interchangeable within 1 or 2 minutes, and crystal types and sizes are available for very specific needs.

The difficulties with scintillation equipment are afterpulsing, fatigue, and pulse-height variation with count rate. The nature of these phenomena is such that no correction is made for them; instead, phototubes that do not exhibit these features must be specially selected. The RCA 6342 and the DuMont 6292 have been found satisfactory when used primarily for integral counting at rates usually less than 100,000 cpm. A new tube, the RCA 6655, is now available with a cesium-antimony cathode and special connections for the shield which may eliminate the troubles exhibited by past phototubes.

In choosing electronic equipment the principal aim was to eliminate corrections and minimize errors. The resolving times of both the amplifiers and scalers were chosen so that no corrections were necessary for scaling losses and so that minimum pile-up occurred in the amplifiers. A line-noise monitor was built to detect noise originating in the power lines, and all equipment was operated from line-voltage regulators.

In operating the counting laboratory a routine preventive maintenance schedule was followed. Before each run, a statistical purity check[13] on the over-all operation of the equipment is made; this has been a very reliable trouble-indicator. The check consists of recording 50 print-outs (counts) of a cobalt-60 source, computing the average value of these 50, and determining if more than two or three (actually 5 per cent of 50 is 2.5) of the 50 lie outside two standard deviations. The standard deviation is derived from the set of 50 counts. Should more than two fall outside these limits, the channel is suspect until an explanation has been found.

Proper operation of the equipment during the course of a run is indicated by the constancy of the count of a long-lived standard and the constancy of the background. Every 20 to 30 minutes two counts of the standard are recorded and compared with the upper and lower limits obtained during the statistical purity check made at the beginning of the run. Only 5 out of 100 counts should exceed the upper and lower limits. Should a count exceed these limits, judgment based on experience must be exercised by the individual in deciding whether the departure is large enough to stop counting. The constancy of the background count serves as a check not only on channel operation but also on the counting environment. A total, for instance, of 1000 background counts should be accumulated at the beginning of the run, and the background count rate and the 95 per cent confidence limits computed from these. Every 20 to 30 minutes two background counts should be recorded and compared with the upper and lower limits. Serious deviations should be investigated. Careless placement of the samples to be counted or the long-lived standard can introduce large and variable background count rates.

Certain automatic features are desirable in a modern counting facility: Scalers with an automatic print-out of the count, automatic sample changers, and a precise, adjustable interval timer. Further automation, such as the punching of IBM cards and date, time, and sample number print-out, is useful.

10.5 ANALYSIS OF ERRORS

One is usually interested only in determining experimentally the relative flux distributions in reactors, not the absolute value of the flux. If therefore, in a given run, the total count from a foil located at a point is corrected for the duration of the count, for the waiting time prior to the count, for the mass of the foil and for the counting efficiency (if different counting arrays are used) of the apparatus, one may derive by Eq. (10.7) a value for the flux at this point relative to the values for the flux at all other points at which foils were activated.

The precision of relative flux values is also dependent upon the precision with which the independent variable, i.e. the position of the foil in the reactor, is obtained. Steep flux gradients exist in some regions of water moderated reactors. These must be located by prior knowledge or by exploratory measurements, and specific techniques for foil insertion and location must be developed to meet the need.

Except for the problem of producing the large quantity of data required, the principal problem in flux mapping is estimating the errors in the procedure and determining means for controlling these errors. Equation (10.7) gives the flux at a point in the lattice as a function of a number of parameters. This equation may be written symbolically in the form

$$\phi = F(\lambda, C, \epsilon, m, \sigma, \frac{M}{A}, t_e, t_w, t_c) \qquad \text{Eq. (10.15)}$$

There is an error associated with our knowledge of each of these parameters. The magnitude of the error and the manner in which they affect the relative flux values determine the precision with which the flux map may be made.

Suppose that each of the errors considered is relatively small and that the error in each parameter is independent of the error in every other parameter. Then the total error in the flux may be written in terms of the partial errors as follows.*

$$s_\phi^2 = \left(\frac{\partial F}{\partial \lambda}\right)^2 s_\lambda^2 + \left(\frac{\partial F}{\partial C}\right)^2 s_c^2 + \dots + \left(\frac{\partial F}{\partial t_c}\right)^2 s_{t_c}^2 \qquad \text{Eq. (10.16)}$$

The letter s has been used to designate the standard deviations.

Before proceeding to apply Eq. (10.16) to Eq. (10.7) one further point should be noted. Basic interest is centered upon the errors in the relative fluxes. Not all of the parameters in Eq. (10.7) are independent in evaluating the errors in the relative flux. For example, the atomic mass of the isotope used for activation is the same number at each point and does not affect the relative flux values; this is also true of the cross section. Insofar as the decay constant of the activated isotope is concerned, this is also true where it enters Eq. (10.7) as a

---

* See Reference 14, p. 161.

factor since it affects all relative fluxes in the same way. It is not true, however, in the exponential terms where the times may be different for different foils.

The fractional standard deviation of the flux may be written as

$$\left(\frac{s_\phi}{\Phi}\right)^2 = \left(\frac{s_C}{C}\right)^2 + \left(\frac{s_\epsilon}{\epsilon}\right)^2 + \left(\frac{s_m}{m}\right)^2 + (\lambda s_{t_w})^2 + \left\{\lambda s_{t_c}\left[\exp(\lambda t_c) - 1\right]^{-1}\right\}^2 + \left\{\lambda s_{t_e}\left[\exp(\lambda t_e) - 1\right]^{-1}\right\}^2 + S_\lambda^2\left\{t_w - t_e[\exp(\lambda t_e) - 1]^{-1} - t_c[\exp(\lambda t_c) - 1]^{-1} + \frac{1}{\lambda}\right\}^2 \quad \text{Eq. (10.17)}$$

Since the errors at different points are now taken to be independent, the relative error in the ratio of the flux at one point to the flux at any other point is given by the relation

$$\frac{s_{\phi 1/\phi 2}}{\Phi 1/\Phi 2} = \left\{\left[\frac{s_{\phi 1}}{\phi 1}\right]^2 + \left[\frac{s_{\phi 2}}{\phi 2}\right]^2\right\}^{1/2} \quad \text{Eq. (10.18)}$$

If $s_{\phi 1/\phi 2}$ is assumed to be the same for all points in the reactor (this is not necessarily so because of different count rates from foils in different parts of the reactor), the relative error of the flux ratio is

$$\frac{s_{\phi 1/\phi 2}}{\Phi 1/\Phi 2} = \left\{2\left[\frac{s_\phi}{\phi}\right]^2\right\}^{1/2} = \sqrt{2}\,\frac{s_\phi}{\phi} \quad \text{Eq. (10.19)}$$

The next step is to estimate the size of each of the terms in Eq. (10.17). The exactness with which foils of the desired size, shape, and nuclide mass can be made determines the value of $(s_m/m)^2$. The choice of foil material determines s_λ since no attempt is made to improve the precision to which the half life is known. After exposure, each foil is removed from the reactor and counted on a nuclear-particle detector for a time interval t_c at a time t_w measured from the time of reactor shutdown. The wait time t_w can be reckoned from any zero time, but all foils in every run must be referred to the same zero time. The preciseness with which t_c and t_w are measured determines the values of the terms s_{t_w} and s_{t_c}. The count obtained from each foil yields a value for $(s_C/C)^2$.

The uniformity with which foils can be placed under the counting head and the degree of stability of the amplifiers and power supplies set the limiting value attainable for $(s_\epsilon/\epsilon)^2$, ϵ being the entire overall efficiency of the counting channel.

The standard deviations of each quantity is difficult to determine precisely, but the order of magnitude of each one can be estimated by performing simple experiments or by making certain assumptions, using available data, and calculating a value. The major assumption made is that the distribution of measurements is normal. Moderate departures from a normal distribution do not appreciably alter values obtained from statistical tables. When several measurements are available (but still not many, e.g., 10), tests can be made to find out if they depart seriously from a normal distribution. The theory of the statistics of small samples indicates that the confidence limits are different from those that apply to an infinite number of samples. For example, for an infinite number of observations, 95 per cent will lie within

$\overline{x} \pm 1.96\, s_x$; for only two observations, 95 per cent will lie within $\overline{x} \pm 12.71\, s_x$; for three, 95 per cent will lie within $\overline{x} \pm 4.30\, s_x$.

The specific methods employed to estimate the pertinent relative errors will now be discussed in greater detail. The estimate is based upon the use of manganese wires.

The efficiency factor ϵ is divided into two components: The change in efficiency caused by power supply drift, amplifier-gain variations, and discriminator drift; the apparent change in efficiency that occurs if a sample is slightly misplaced in a holder or if the holder is not properly seated in its slot. The magnitude of either change is not determined explicitly; rather a series of counts is taken (e. g. 20 to 50), and if the deviations from the mean are only those expected from statistical variations, it is stated that the relative error s_ϵ/ϵ is zero. The count rates are such that the statistical fluctuations expected are no more than 1/2 per cent (40, 000 counts). When changes in efficiency caused by drifts in the characteristics of the equipment are sought, 10 to 50 one-minute counts of a long-lived standard are accumulated before the beginning of the counting period, and two 1-minute counts are recorded every 20 to 25 minutes. In this way shifts in equipment characteristics are quickly detected during the run. The other factor, sample misplacement, is not a function of time but a function of the physical characteristics of the foil (or wire) and the holder. This is determined beforehand by counting and dumping the same foil several times (20 or so) in succession. A statistical table of values may be consulted to answer the question of whether any value recorded differs significantly from the mean value. This factor can be made smaller than the counting statistics and, therefore, taken to be zero.

The relative error s_m/m depends upon how uniformly the atoms of the isotope being activated are distributed throughout the wire or foil. A chemical analysis of 20 samples of manganese wire indicated a relative standard error of 0.3 per cent. With the uniformity of the manganese distribution in the wire established, all other wires can be weighed to a comparable accuracy. Foils can be calibrated with the aid of a rotating foil wheel.

The relative error in the count rate can be estimated as follows assuming constant background.

Let R_b = background counting rate

R_t = counting rate of the sample plus background

R_s = sample counting rate = $R_t - R_b$

Define

$$r = \frac{R_t}{R_b}$$

Then if N_b = total number of background counts and

N_t = total number of sample plus background counts,

the standard deviation in the sample count rate is

$$S_C = \frac{R_s}{\sqrt{N_t}}\left(\frac{r}{r-1}\right) \qquad \text{Eq. (10.20)}$$

This relation is good (95 per cent confidence limit) for $2 \leq r < 20$ if $N_b/N_t \geq 1$ (number of background counts equals number of samples plus background counts). The high-level approximation, $S_C = R_s/\sqrt{N_t}$, can be used if $r \geq 15$ and $N_b/N_t \geq 1.4$. Relative errors of 0.5 per cent are not difficult to attain except with foils at the edges of the core and beyond.

The standard error in t_w, the elapsed time between reactor shutdown and the counting of a given foil, is difficult to determine and is not important (except when uranium foils are used) if normalizing wires or foils are used. It depends only upon how well the clocks in the counting room are synchronized to the clock in the reactor control room. Five seconds is a reasonable estimate for s_{t_w}.

The standard error in the value of the half life is estimated by accepting the stated error of one of the experimental measurements. On this basis, the standard error s_λ is 2.1×10^{-7} seconds^{-1} for manganese-56.

These estimates of the standard errors and relative errors, the average value of each quantity, and the contribution of each term to the total error appear in Table 10.2. When these are substituted into Eqs. (10.17) and (10.19), the value of $s_{\phi 1/\phi 2}/\Phi 1/\Phi 2$ is 0.584 per cent. The statistical error in the counting rate is the greatest contributor to the final error. This presumes great care on the part of the operators to limit the error in ϵ.

Table 10.2 - NUMERICAL VALUES USED TO ESTIMATE THE RELATIVE ERROR s_ϕ/ϕ FOR MANGANESE WIRES

s_ϵ/ϵ	0.000
s_m/m	0.003
s_C/C	0.005
s_{t_w}	5 seconds
s_{t_c}	1/60 second
s_{t_e}	Normalization makes this error negligible.
t_e	6×10^3 seconds
t_c	50 seconds
t_w	different for each sample counted
s_λ	2.1×10^{-7} seconds^{-1}
λ	7.43×10^{-5} seconds^{-1}

The error in normalization among channels and different runs requires separate consideration. Normalization among channels of different sensitivity is accomplished by counting the same samples (usually 30) on each channel and accumulating the order of 10^6 counts per channel. Normalization among runs is accomplished by placing the same wires (foils) in the same place in the reactor during each run. The ratio of the sums of the corrected counts (background, decay, weight) between any two runs then corrects for both power level and irradiation time. (It is these same wires or foils that are counted on each channel and serve as channel normalization factors.) It is of no consequence that, in practice, the factors for channel normalization and power level irradiation time normalization cannot be separated by the method just outlined. What is wanted is the over-all normalization factor. If 10^6 counts are accumulated, $(s_C/C)^2 = 10^{-6}$ and approximately 0.45 per cent error in the normalization factor could be expected. Combining this error with the error of 0.58 per cent yields the relative error of relative flux values among runs.

$$\frac{s_{\phi 1/\phi 2}}{\Phi 1/\Phi 2} = 0.73 \text{ per cent.}$$

The approximations and assumptions made may raise the question of how much confidence can be placed in the value of the error finally computed. This can be determined experimentally by placing two sets of foils in the same positions in the reactor during each run and using one set for normalization, the other for a check on reproducibility of results. If perfect reproducibility were achieved, the point-by-point ratio of the fluxes (count rates) would be unity.

For a set of twelve runs utilizing three channels (giving 36 ratios) the average ratio was found to be 0.9940 ± 0.00451, a relative error of 0.42 per cent. In each run 30 foils were used for normalization and 30 foils were used to check on reproducibility.

Figures 10.3 through 10.6 illustrate data obtained by the techniques discussed. [redacted]

[redacted]

AUTOMATIC NEUTRON FLUX PLOTTING

by Edith B. Fehr

The preceding discussion analyzes in detail the basic problems of flux plotting by the use of foils. This section describes an automatic counting system which was designed to carry out flux measurements efficiently, and to furnish the results in a form suitable for automatic data processing.[18] The equipment and methods described here are the result of a cooperative effort by many members of the Knolls Atomic Power Laboratory Physics Sections.

10.6 EQUIPMENT

The equipment consists of four components: (a) A sample changer; (b) a digital converter that records and converts the counting information into a signal suitable for an IBM card punch (Berkeley Type 5701 Counter Converter); (c) an IBM Summary Punch (Type 514 or 523) with associated equipment for coding the counting information; (d) a timer that controls counting cycles and scanner movement. These components, shown in a block diagram (Fig. 10.7), are described below.

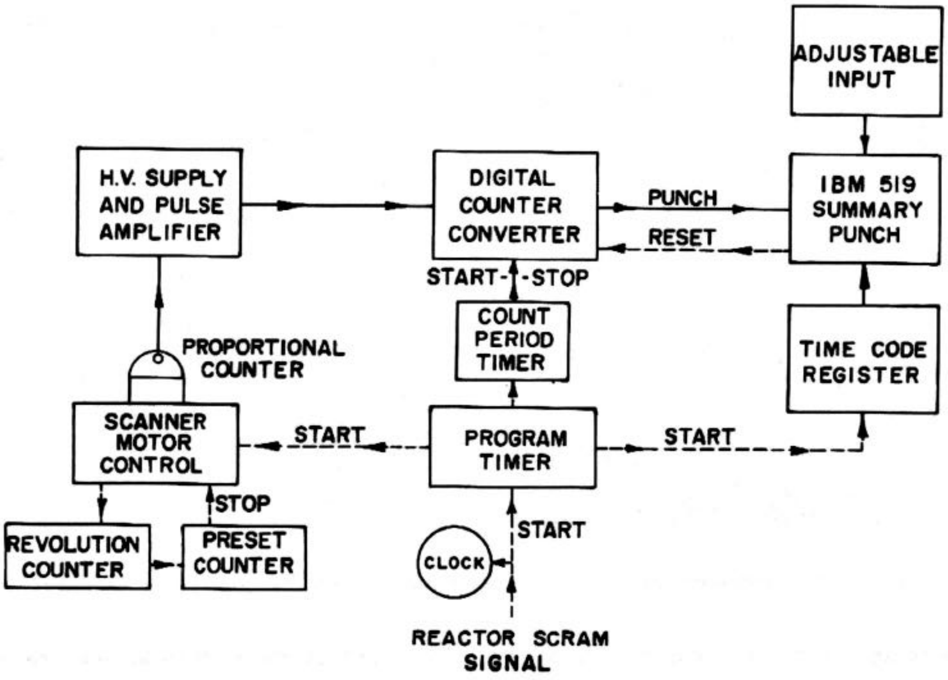

Solid lines represent information channels.
Broken lines represent operational signals.

Fig. 10.7 - Automatic Counting System for Reactor Flux Plotting.

(a) Sample Changer. The sample changer is designed to measure efficiently the activity of materials which have been activated by neutron fluxes in critical assemblies. The changer consists of a scanner that moves a specially designed proportional counter across the sample. [redacted] In order to avoid excessive length of the scanner bed or bending, the sample is held stationary and the counting head moved. [redacted] The principle of construction of the scanner bed and drive mechanism can be seen in Fig. 10.8. The counter assembly is mounted on a carriage which rides on two V-groove ball bearings. The bed and carriage are machined to close tolerances in order to maintain accurate distance between the counter window and the sample.

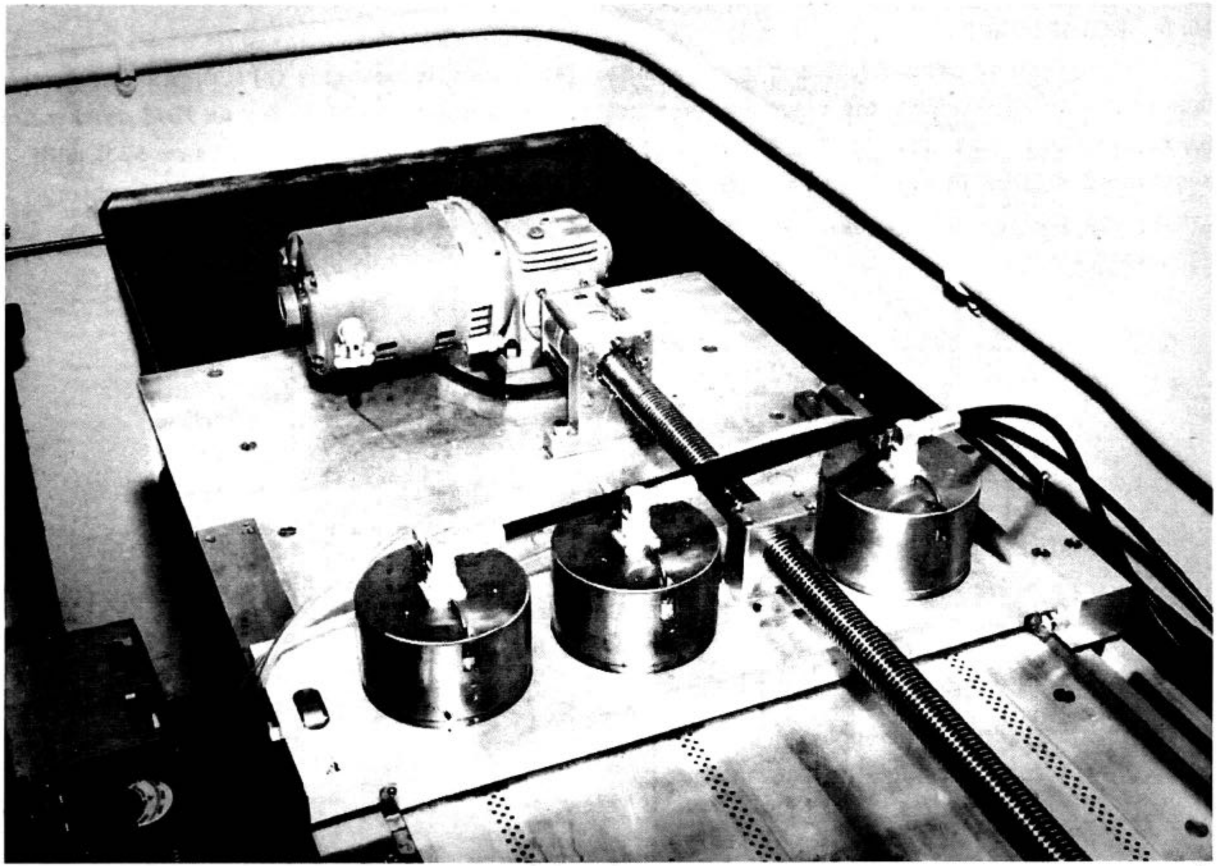

Fig. 10.8 - Scanner Bed, Drive Mechanism, and Proportional Counter.

The carriage is moved by a driving screw. The revolutions of this screw are counted by a digital transducer, an oscillator keyed by a toothed disk on the driving shaft. A detailed description of this system will be found in Reference 15.

The square-wave oscillator signal envelope is differentiated, and a count pulse is derived for both the rise and the fall of the oscillator signal. The counting pulses are fed to a preset counter which, in turn, controls the motor drive. When the preset number of counts is reached, the motor is stopped. Each count corresponds to a travel of 0.010 inch. The counter can be moved in any multiple of this minimum motion. In operation, the motor drive is started by a signal at the end of the counting time. The carriage then moves until the signal from the preset counter stops it at the chosen distance. It remains stationary during the subsequent counting period and moves again at the end of count signal.

Since positioning errors are cumulative, overshoot of the motor drive must be strictly avoided. In our model, no error could be detected after several hundred consecutive steps. For completely automatic operation, there are two limit switches which can be set at any point along the bed to provide continuous back and forth scanning by reversing the motor drive, or to stop the system at the end of one scan.

The proportional counter has to be well shielded and collimated to ensure that the counts at any point of an activated strip or wire represent a true measure of the relative radioactivity at that position. It must not see other portions of the strip. For this reason, β-counting was chosen. Other requirements for the counter are good stability over long time periods and low counting losses, so that good counting statistics are quickly obtained without need for corrections. Finally, since movement of the counter rather than the sample was desired (for reasons of space saving and flexibility in the scanner), there was a premium on small size and low weight of the counter-shield assembly.

By using the lead shield as both body and ground electrode of the counter, the amount of lead and the size of the counter assembly was reduced to a minimum. Figure 10.9 shows a flow-type proportional counter developed on this principle. A hemispherical shell of 7/8-inch radius was pressed into a cylindrical lead block of 6-inch diameter and 3-inch height. Openings for gas inlet and outlet and for the high voltage electrode were then drilled. The high voltage electrode consists of a 1/2-inch-diameter loop of 0.001-inch-diameter tungsten wire which is mounted through a press-fit Teflon insulator.

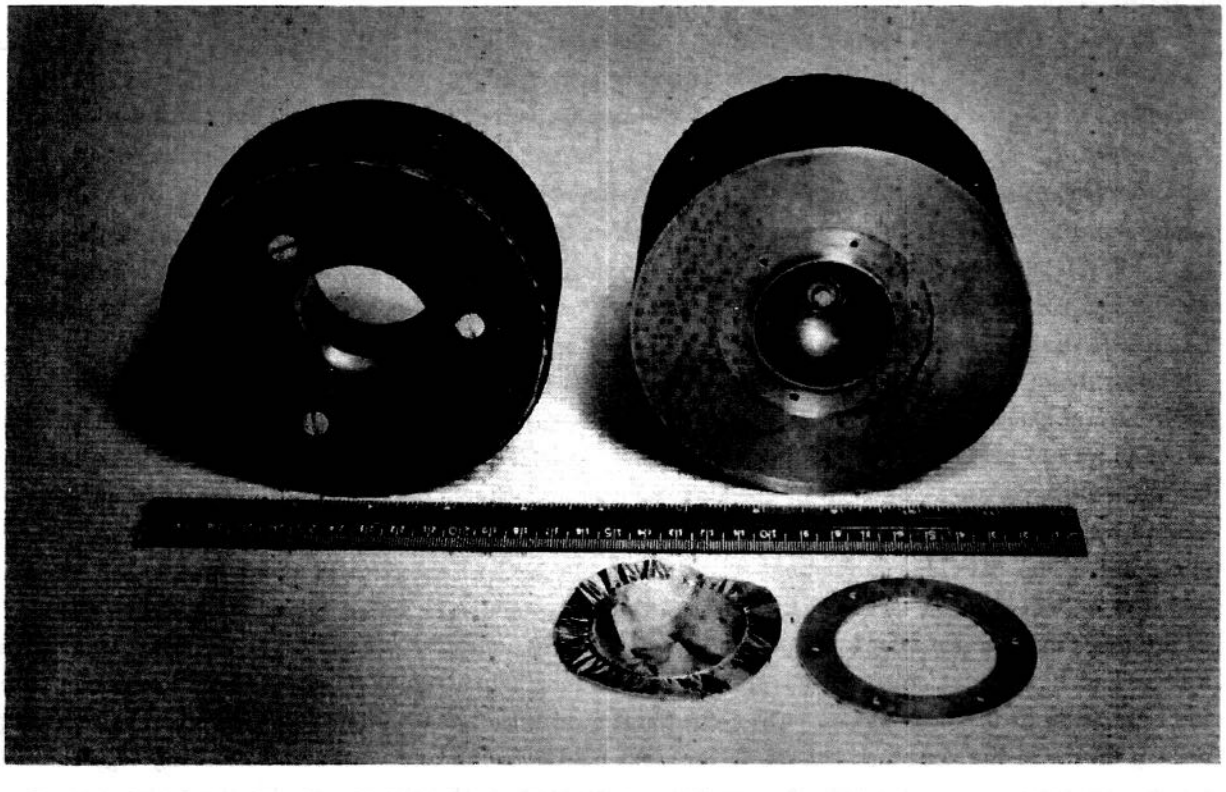

Fig. 10.9 - Flow Type Proportional Counter.

An aluminum window of 0.0005-inch thickness is mounted over the shell opening. Since the counting gas (methane) is introduced under slight pressure, vacuum tightness of the various seals is not necessary. This counter had a plateau length of 400 volts with a slope of 1 per cent per 100 volts.

The counter is mounted over a lead collimating block having a 6-inch diameter and a 2-inch height. A central hole in the collimating block permits the insertion of interchangeable lead blocks with apertures of varying sizes and shapes.

(b) IBM Summary Punch Associated Equipment. As an addition to the plugboard of the IBM Summary Punch, there is an adjustable input board consisting of five 10-position switches. It is used to put identifying numbers on each IBM card. The switches can be connected to any desired column of the IBM card on the plugboard of the summary punch. At present, they occupy the first five columns.

The first decade on the index board is used for a sample identification code. It is left at zero for all cycles which are not to be processed in the IBM-650, such as standard counts, monitor foil counts, or counts occurring during sample changing. An appropriate number (e. g., 1) is selected during the first valid count on the first sample and left until the last valid count for a scan. A new number is selected for the return scan or for the first valid count on the second sample. This code is used, for example, for numerical integration of all ordinates with the same code. The IBM-650 program will also number consecutively all cards having the same code in column 1. This information is used as the abscissa for automatic curve plotting. The remaining four decades are presently used for consecutive numbering of all counting runs.

Another addition to the plugboard is a time code register. This is a three-decade sequence counter consisting of three 10-position stepping switches (C. P. Clare Co. Model 31811). The output is connected on the IBM Summary Punch plugboard to any desired column of the card. At present, it occupies columns 7, 8, and 9. The time code register is started from the reactor scram signal through the cam timer (see Fig. 10.7). It then advances by one unit for each counting cycle. This information is used in the IBM-650 for decay correction of data.

(c) Timer. The timing system consists of a Microflex Clock Timer with auxiliary relays and a 6-Position Cam Timer (Industrial Timer Co. Model MC-4). Figure 10.10 shows an outline diagram of the circuits involved.

The timer controls the following functions. The start of counting period is given by the first cam of the multiple cam timer (the length of the total cycle can be varied between 40 seconds and 10 minutes by using interchangeable cams). The length of counting time is set on the Microflex Clock Timer. For the start of scanner carriage movement, the signal is generated by an auxiliary relay at the end of the counting period from the Microflex Timer. The end point of the carriage movement is controlled by the preset counter described in (a) above, and this preset counter is reset by a signal from the auxiliary relay of the Microflex Timer at the beginning of the count period. The second cam, which is offset from the first cam, gives a signal to the digital counter converter to print out. This signal is given about 1 second before the beginning of the next cycle. Thus the display of the digital counter can be observed visually during the time the carriage moves to the next position. In cases where a printing digital system is used in parallel with the counter converters, a third cam, analogous to the second cam, is used.

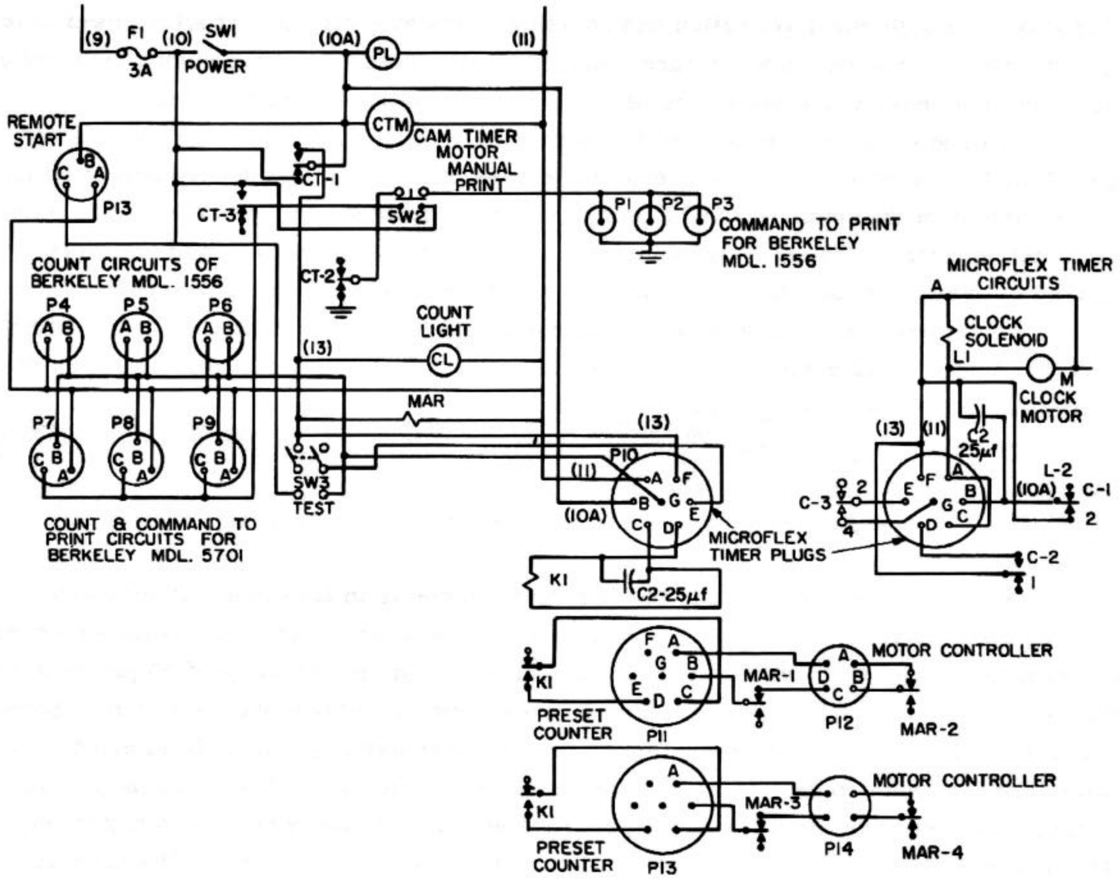

Fig. 10.10 - Schematic Diagram of Program Controller for Automatic Scanner.

Since the decay correction for uranium strips is made from an empirical table, it is necessary to standardize on a counting cycle. Forty seconds was chosen, because this cycle gives adequate counting statistics at reasonable reactor power levels. The counting interval must be shorter than the counting cycle to permit movement of the carriage. For instance, at a drive speed of 5 seconds per inch of travel and a distance of 2 inches between points to be counted, one must allow 10 seconds for travel and 1 second for pickup of the relay, an allowance giving a count interval of 40 - 11 = 29 seconds to be set on the Microflex Timer.

The timing cycle is started at reactor scram time directly from the reactor control room. This starts the time code register.

10.7 EXPERIMENTAL PROCEDURES

Samples in the form of long strips or wires, individual foils, or discs can be handled by the scanner. The preferred type of activation foil is enriched uranium in the form of thin strips identical with the reactor fuel. A special set of such strips with low background is reserved for activation experiments.

The use of uranium strips has the following advantages: There is no disturbance of flux since the activation sample simply replaces reactor fuel; results are obtained directly in terms of fissions occurring without corrections such as those for differences in cross sections or self-shielding effects in reactor fuel; the high cross section permits the obtaining of good counting statistics with short activation and counting times at a very low reactor power level during activation. This condition, in turn, minimizes personnel exposure during removal of samples from the reactor and makes the use of remote handling equipment unnecessary.

A disadvantage of using uranium foil for activation experiments is the complex decay scheme of the fission products, which requires the use of an empirical decay correction factor. The large number of different beta and gamma activities of the mixed fission products puts special requirements on the counting equipment, and a rigid standardization of exposure time is required to obtain reproducible results. The standard irradiation time chosen is 30 minutes, and decay corrections are made to a zero time corresponding to 20 minutes after the end of irradiation. Under these conditions, the decay has been found to be very reproducible. The correction curve obtained for aluminum-clad enriched uranium on the equipment described above is shown in Fig. 10.11. [redacted] The strips are checked by irradiation on a wheel, and correction factors are applied when required.

Manganese strips are used mainly for flux measurements in locations not normally occupied by fuel, such as water gaps. In this case the low cross section of manganese permits use of reasonably thick foils without creating a flux disturbance. An alloy of 80 per cent manganese and 20 per cent copper can be obtained in the form of uniform sheets of 2-mil thickness with good mechanical properties and adequate corrosion resistance. With 30 minutes irradiation time, the 5-minute copper-66 activity becomes negligible after 20 minutes decay, and the low energy radiation from the 12.8-hour copper-64 activity can be reduced to a negligible amount by covering the foil during counting with an aluminum absorber 50 milligrams per square centimeter thick. Thin foils of approximately 3/4-inch width are preferred to wires because they give much better counting statistics for equal resolution.

10.8 DATA REDUCTION

The first field of ten columns of the IBM card is reserved for coding information, such as run and sample number and time and position code information. The remaining seven fields of ten columns each are available for use with up to seven counting channels. Where necessary, corrections for background, sample weight, counting geometry, reactor power level, and activation time are put on program master cards, which precede the input deck. The corrections for decay of uranium are made from the empirical decay curve. This is loaded in the form of a table into the IBM-650 memory drum as part of the program deck. Exponential decay corrections are made from the formula [see Eq. (10.6)]

$$A_o = A_c[1 - \exp(-\lambda t_e)]^{-1} \{\exp[-\lambda(t_w + t_c/2)]\}^{-1} \qquad \text{Eq. (10.21)}$$

where

A_o = count rate at the end of saturation activation

A_c = count rate (counts/minute minus background)

λ = constant of exponential decay

t_e = activation time

$t_w + t_c/2$ = elapsed time from the end of activation to the middle of counting time.

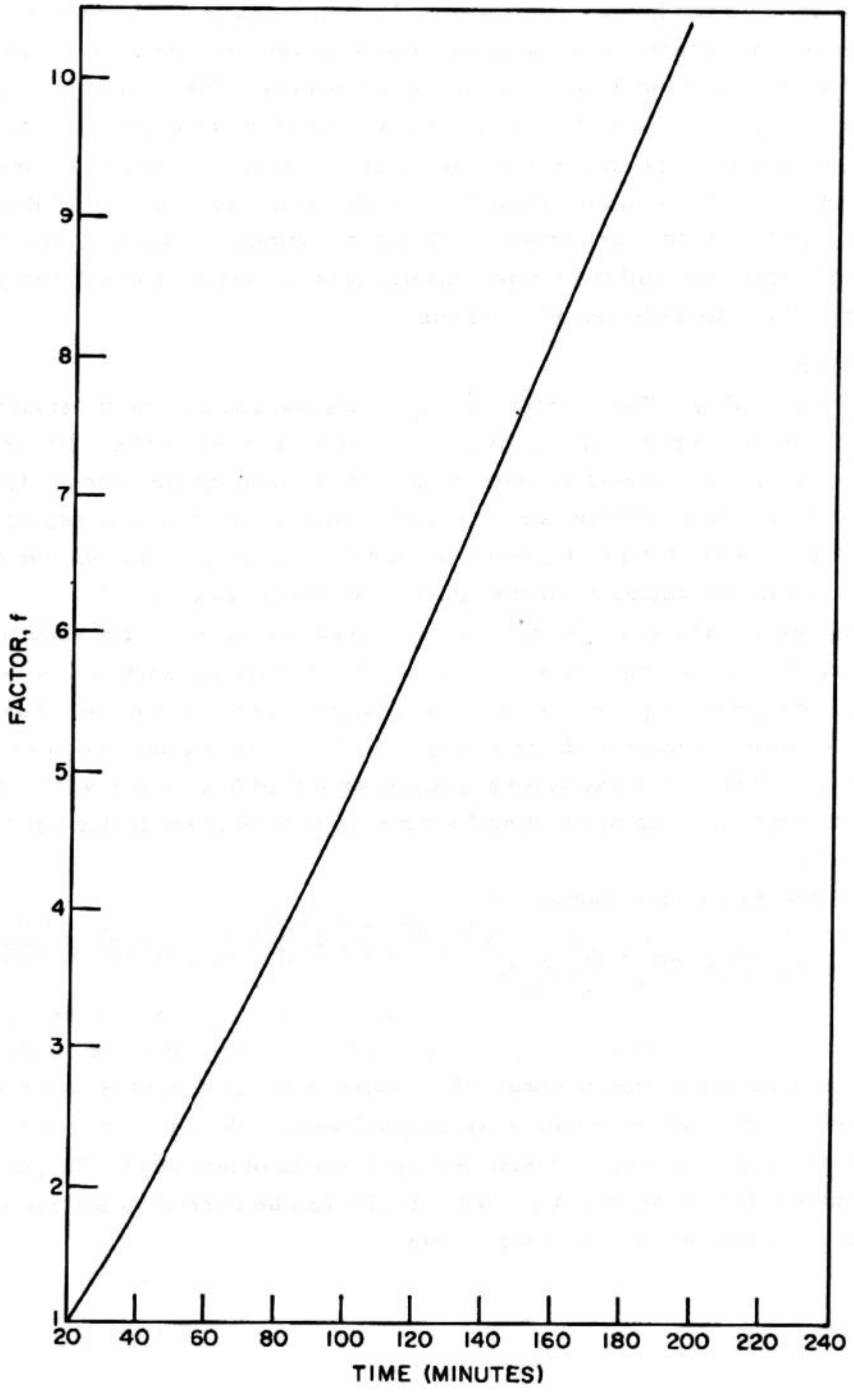

Fig. 10.11 - **Correction Factor for Enriched Uranium Fission Product Decay.**

Counter geometry and foil area or weight correction are added to this formula when absolute results are required.

The output information from the IBM-650 can be listed on the Tabulator for manual plotting or analysis of data, plotted automatically by using one of the standard available curve plotters, or used as input for further calculations.[17] A frequently used program involves numerical integration of the area under a curve, required for calculation of average reactor power and also for calculation of fuel or coolant temperatures. Other calculations involve point or area normalization of sets of curves and many reactor calculations based on flux distributions, such as fission product accumulation or fuel burnout. Standard deviation of a set of source counts can be calculated directly from the counts recorded on IBM cards; this is used regularly to check counter performance. The great simplification of these calculations and the consequent rapid availability of experimental data for analysis constitute perhaps the major advantage of the automatic counting system.

10.9 PERFORMANCE

(a) Reproducibility. The counters are quite stable, and counts of permanent sources remain within the limits of errors of counting statistics over many weeks. Repeat counts of the same activated strips are generally reproduced within counting statistics. The reproducibility of activations involving different strips in different reactor runs depends on the uniformity of the strips, the steepness of the flux gradients, and the accuracy of placing the strips in the reactor and maintaining the geometry of the reactor (widths of water gaps).

(b) Resolution. The scanner was specially designed to represent accurately the changes in neutron flux occurring over short distances with steep gradients. A detailed discussion of the factors governing scanner resolution is given in Reference 16. The resolution obtainable in the present scanner is shown in Fig. 10.12. A rectangular aperture of 0.075-inch width was moved in 0.050-inch steps across manganese foil of 0.275-inch width which had been activated in a uniform flux. The width at half maximum is 0.282 inch instead of the theoretical value of 0.275 inch.

Figure 10.13 presents typical results obtained by using a thin uranium strip as activation foil and scanning with a 1/8-inch aperture. [redacted]

(c) Capacity. When uranium is counted, the use of a 40-second counting cycle permits taking 90 points per hour on each counting channel. The relatively short half-life of fission products limits the counting period to about 3 to 4 hours from the end of irradiation, when the activity has fallen to less than one-tenth of its original value. With time allowed for sample changing, the three-channel scanner enables one operator to obtain 600 to 800 points per reactor run, or about 1500 points per day. The results can be corrected and plotted within 1 or 2 hours after the completion of measurements.

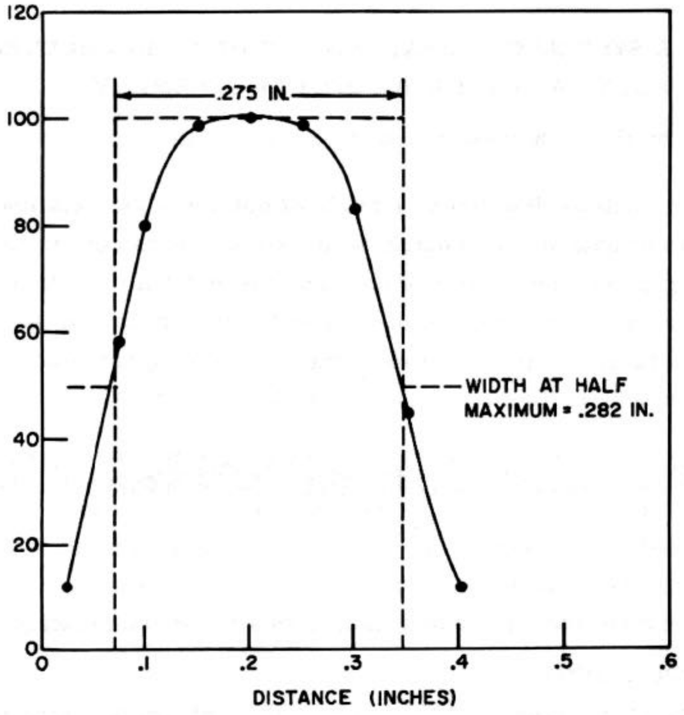

The solid line represents measured activity.
The broken line represents the sample activity.

Fig. 10.12 - Scanner Resolution and Flux Distribution across a 0.275-inch Manganese Foil using a 0.075-inch aperture.

[redacted]

A SYSTEM OF OBTAINING AND REDUCING NEUTRON FLUX DATA FROM A CRITICAL ASSEMBLY

by H. A. Morewitz and R. F. Valentine

The preceding discussions described methods of obtaining the relative neutron flux distribution from experimental data which required approximations to correct for sample decay, or a medium-scale digital computer to calculate the correction. The method described below provides the decay correction without the use of auxiliary computation and presents the data in usable form as it is taken. This is accomplished by varying the time interval over which the individual foils are counted in such a manner as to correct for decay. The time interval is established by counting a monitor foil. [redacted] It is used in conjunction with automatic sample changers in order to count a large number of samples at frequent intervals. With this scheme approximately 1500 precision-cut wires may be activated and counted in one day. The over-all system appears to be more stable and accurate than many that have a small sample capacity.

10.10 COUNTING EQUIPMENT

The unique feature of the system is the method of count timing which provides automatic correction for radioactive decay of the sample. A block diagram of the counting system employed is shown in Fig. 10.14.

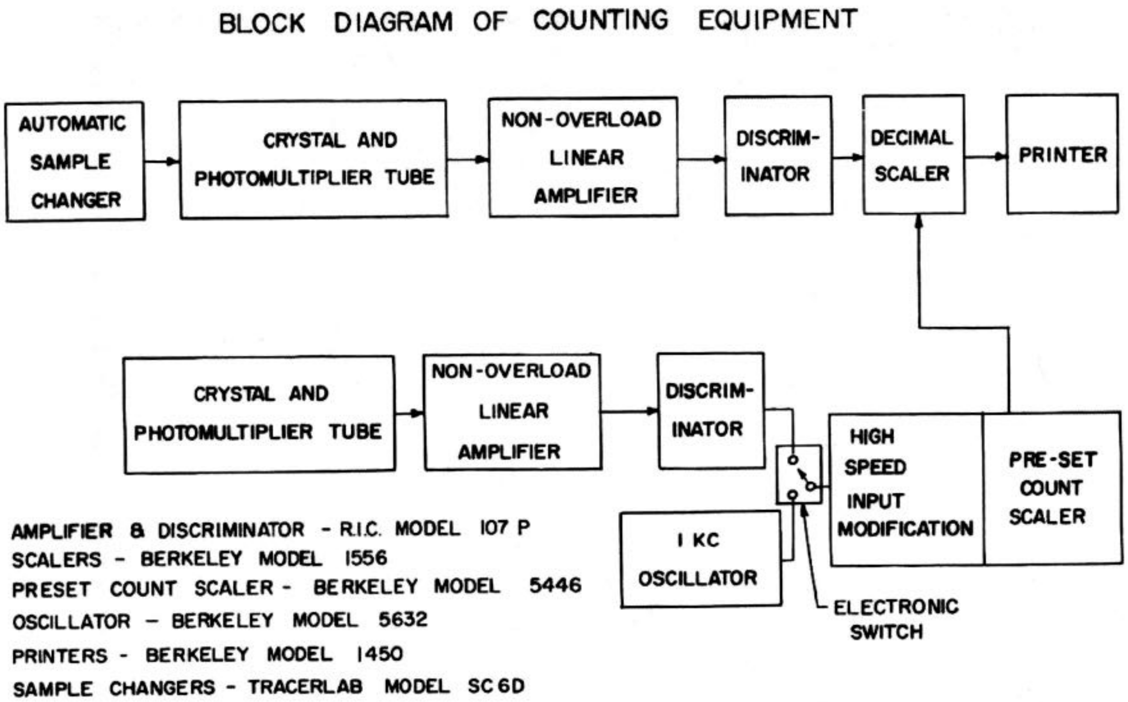

AMPLIFIER & DISCRIMINATOR - R.I.C. MODEL 107 P
SCALERS - BERKELEY MODEL 1556
PRESET COUNT SCALER - BERKELEY MODEL 5446
OSCILLATOR - BERKELEY MODEL 5632
PRINTERS - BERKELEY MODEL 1450
SAMPLE CHANGERS - TRACERLAB MODEL SC 6D

Fig. 10.14 - Block Diagram of Automatic Data Reduction System.

The activity of the sample is measured by counting beta particles with a one-half millimete thick stilbene crystal mounted on a photomultiplier tube. This signal is amplified by a non-overload linear amplifier which feeds a decimal scaler, the accumulated counts of which are printed on a paper tape. The duration of the counting interval in this signal channel is controlled by a gate from a preset count scaler.

The preset count scaler receives its pulses alternately from two sources. The pulses which determine the counting interval are derived from a timing channel consisting of a detector and amplifier identical to those of the signal channel. The dead time which is required for changing samples, etc., is set by feeding the timing scaler from a 1-kc crystal-controlled oscillator. At the end of each signal period, the timing scaler is electronically switched to this oscillator. The counting interval is determined by using a standard sample of foil material, activated simultaneously with the foils of interest. It is placed in front of the timing channel detector, and left undisturbed during the counting run. As the standard decays, the time necessary to achieve the preset count (100, 000 counts is a typical value) will increase exponentially at the rate determined by the half-life of the activated material. Therefore, the counting interval of the signal channel increases in the proper manner to compensate for the decay of the signal foil. One timer circuit can control more than one signal channel.

This method of timing provides several advantages: (1) The data, having been directly corrected, can be presented immediately without any processing time; (2) for a given wire the statistics of counting are independent of the time when the wire is counted during the counting run (in the more conventional type of counting, in which a fixed counting time is employed, a given wire will have poorer statistics as counting progresses); (3) the decay of mixed exponentials such as exists in fission products is compensated as readily as single exponential decay.

10.11 FEATURES OF SYSTEM WHICH MINIMIZE ERRORS

The non-overload amplifiers are used as stretcher-limiters. For this mode of operation the amplifiers are set so that essentially all beta pulses received from the photomultiplier are expanded to uniform pulse height. The limiting action is provided by overdriving the latter stages of the amplifier, which, because of their non-overload characteristics, provide essentially constant-width pulses. This results in long plateaus of counting rate versus discriminator setting, amplifier gain, and photomultiplier voltage. Typical plateau curves are shown in Figs. 10.15 and 10.16. Operation of the amplifiers in this manner has resulted in long-term stability (greater than six months).

To use this system, alloy wires of manganese-iron, indium-aluminum, gold-aluminum, and uranium-zirconium have been drawn to 30-mils diameter. The variation in length of the half-inch wire segments has been reduced to less than one part in a thousand by the simultaneous surface grinding of approximately 3000 wires clamped in a magnetic chuck. This results in a high yield of wires that are within ± 0.5 per cent of a mean value by weight. Wires may be stacked end to end in polyethylene spaghetti tubing for insertion in small diameter slots or in through tubes provided in the critical assemblies. Because there is essentially no length variation in the individual wires, the relative position of each wire is known to a high degree of accuracy.

A commercially available sample changer has been modified to obtain highly reproducible positioning of the wire samples. The induced activity obtained by irradiation of the wires in this critical facility is sufficiently high to make background count insignificant in the

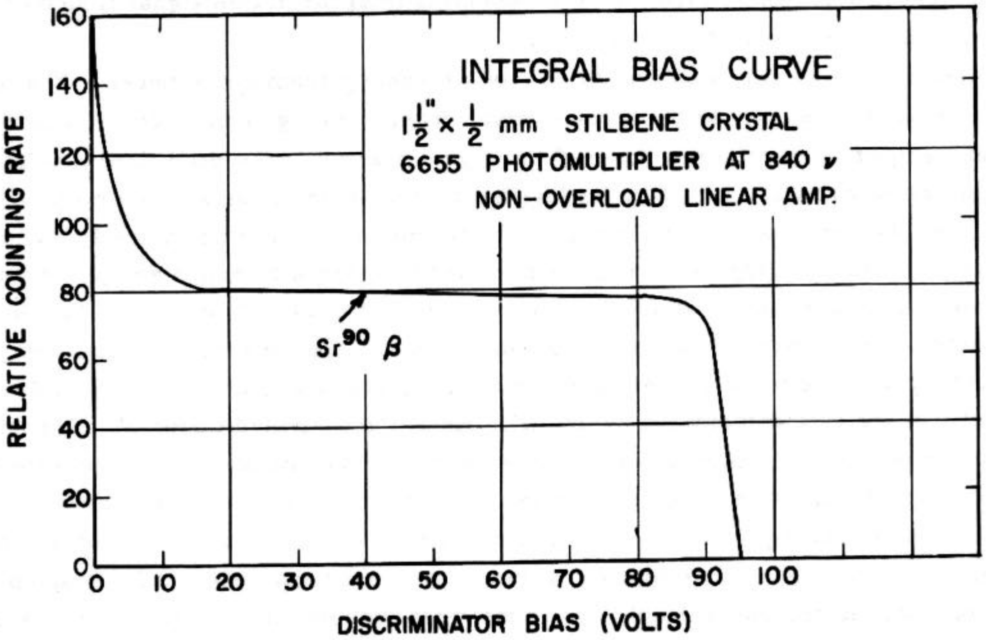

Fig. 10.15 - Plateau Curve for Bias Voltage.

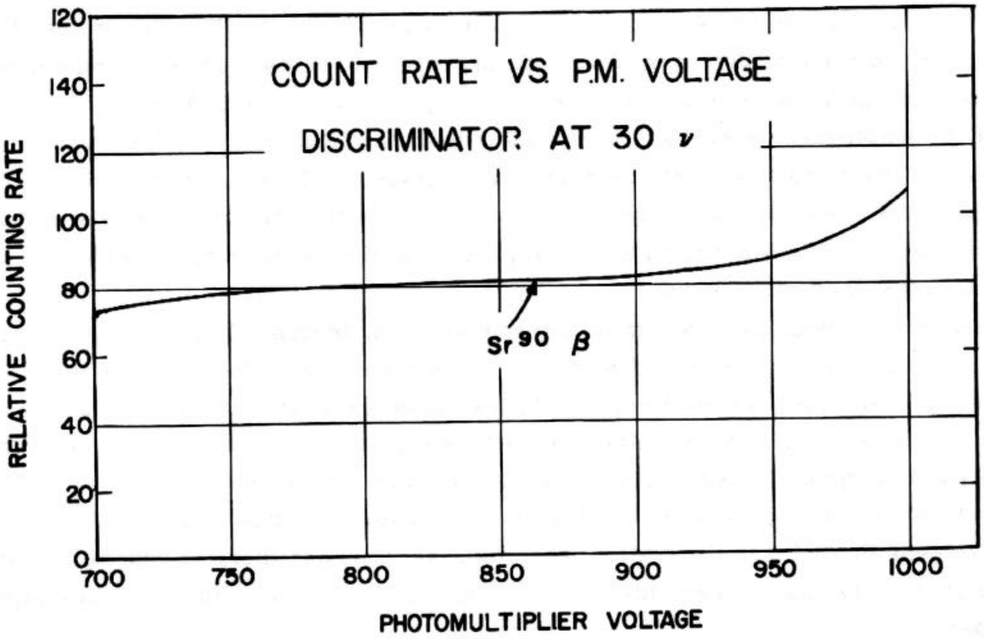

Fig. 10.16 - Plateau Curve for Photomultiplier Voltage.

experimental count. In the event that background counting rates are high, they may be automatically subtracted. Further modifications to the sample changer permit a large number of samples to be stacked on the changer. Injection molded plastic sample holders have been manufactured so that no significant difference between sample holders exists to contribute errors in counts when a large number of these holders is used.

10.12 ERROR ANALYSIS

The inherent counting errors due to the statistical nature of the decay process and the background counts may be determined by standard procedures. Experimental errors due to differences in wire weights, in wire composition, wire holders, wire positioning and electronic changes are equally important but they are more difficult to establish. These errors have been experimentally determined by counting, in the normal fashion, several hundred wires which have been exposed to the same integrated neutron flux. The total error represented by the standard deviation of this large number of counts has been divided into three groups:

1. The error resulting from the statistical nature of the decay processes (standard deviation due to this cause is denoted s_C);
2. The error due to statistical nature of the background counts (standard deviation due to this cause is denoted s_B);
3. All other errors which are proportional to the magnitude of the count (standard deviation due to the lumped experimental errors is denoted s_{Ex}).

Since these errors are independent the total error is equal to the vectorial sum of these three types of errors. Thus,

$$s_{total}^2 = s_C^2 + s_B^2 + s_{Ex}^2$$

The error due to statistical decay is given by

$$s_C = \sqrt{N_s}\sqrt{1 + \frac{N_s}{M}} \qquad \text{Eq. (10.22)}$$

where N_s = the total experimental count minus the background count, and
M = the preset count in the timing channel.

The added contribution to the uncertainty over Eq. (10.20) is due to the fact that the time of count is uncertain due to the statistics in M. The standard deviation of the background count is given by a similar expression in which N_s is replaced by N_b the background count. Subtraction of the statistical and background error from the total observed standard deviation yields the experimental error introduced by the counting procedures. This has been estimated to be approximately 0.8 per cent. The absolute magnitude of this error is dependent on the type of wires being counted. For convenience the experimental error has been combined with statistical and background errors into the family of curves shown in Fig. 10.17. The experimental error used in preparing this curve was $s_{Ex} = 0.0077\ N_s$ where N_s is the sample count (total count minus background). The effect of various background counting rates are shown parametrically.

10.13 APPLICATION OF ERROR ANALYSIS

The counting errors which have been determined experimentally may be used to improve the results obtained from analysis of the flux plot data. An example of such use occurs in the fitting of a cosine function to an experimental axial flux distribution such as that shown in the

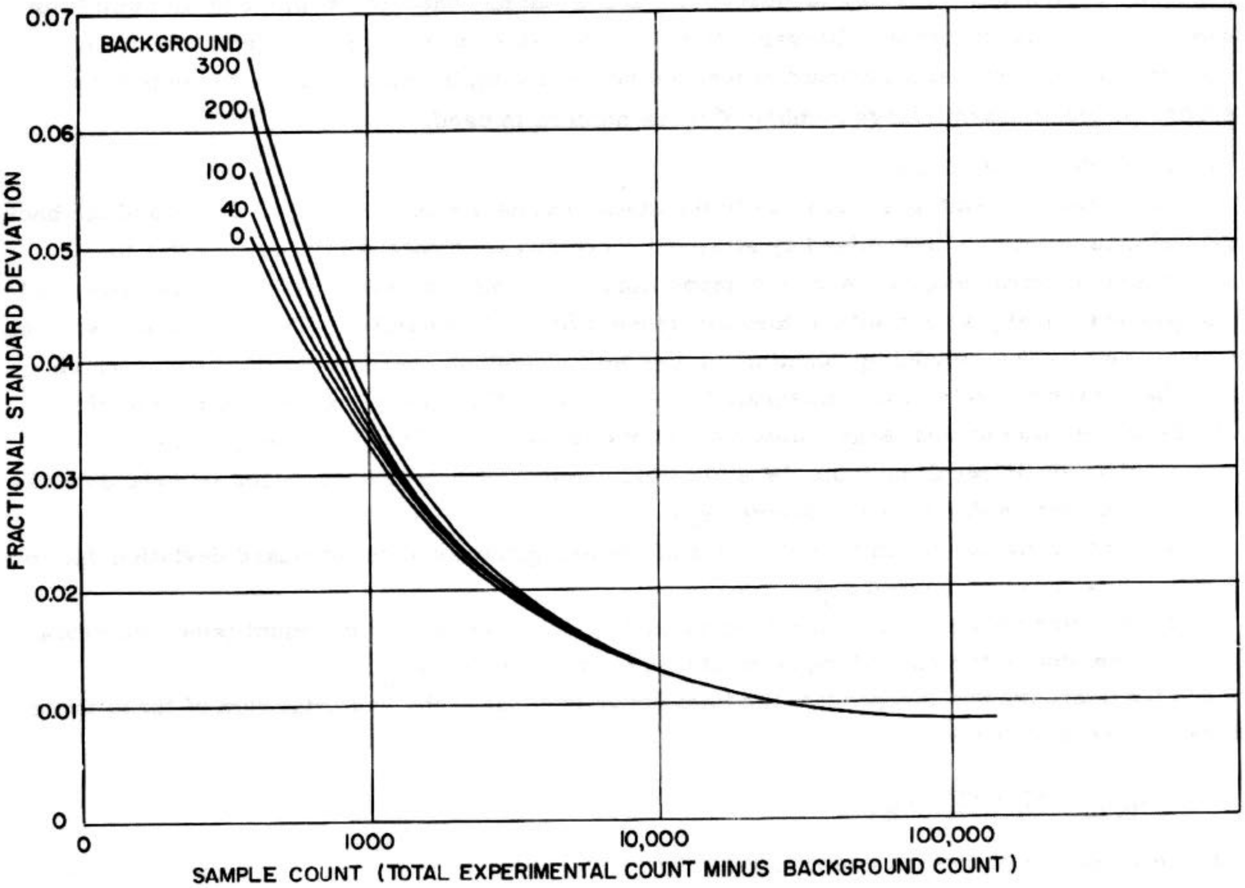

Fig. 10.17 - Fractional Standard Deviation of Count versus Count.

upper curve of Fig. 10.18. A computer code has been developed for fitting a cosine function to experimental data.[19] This code can be used either to minimize the quantity $\Sigma(y_i - y)^2$ in which all points have equal weights, or to minimize the quantity

$$\Sigma \frac{(y_i - y)^2}{\Delta y}$$

in which Δy represents the counting error for each point as determined above. When used in the latter fashion, the weighting provided by the assigned error of the individual points reduces the influence of the absolute residuals (which are highest near the peak of the cosine distribution). If the proper parameters have been obtained by the least squares analysis, division of the individual y_i values by the determined function evaluated at these respective points will yield a quantity which is a horizontal line when plotted as a function of x. In this type of representation, if the value of B in the expression $y = \cos B(c-x)$ has been determined incorrectly, the line will be concave upward or downward, depending upon whether B is too large or too small. If the value of c is determined incorrectly, the line will not be horizontal. The second curve in Fig. 10.18 is a plot of this function using the parameters determined without benefit of point weighting. The lower curve is a plot in which the parameters have been determined in a weighted least squares analysis. It can be seen that the two cases differ. The weighted least squares analysis provides a better fit to the data as shown by the fact that the lower curve is a better horizontal line.

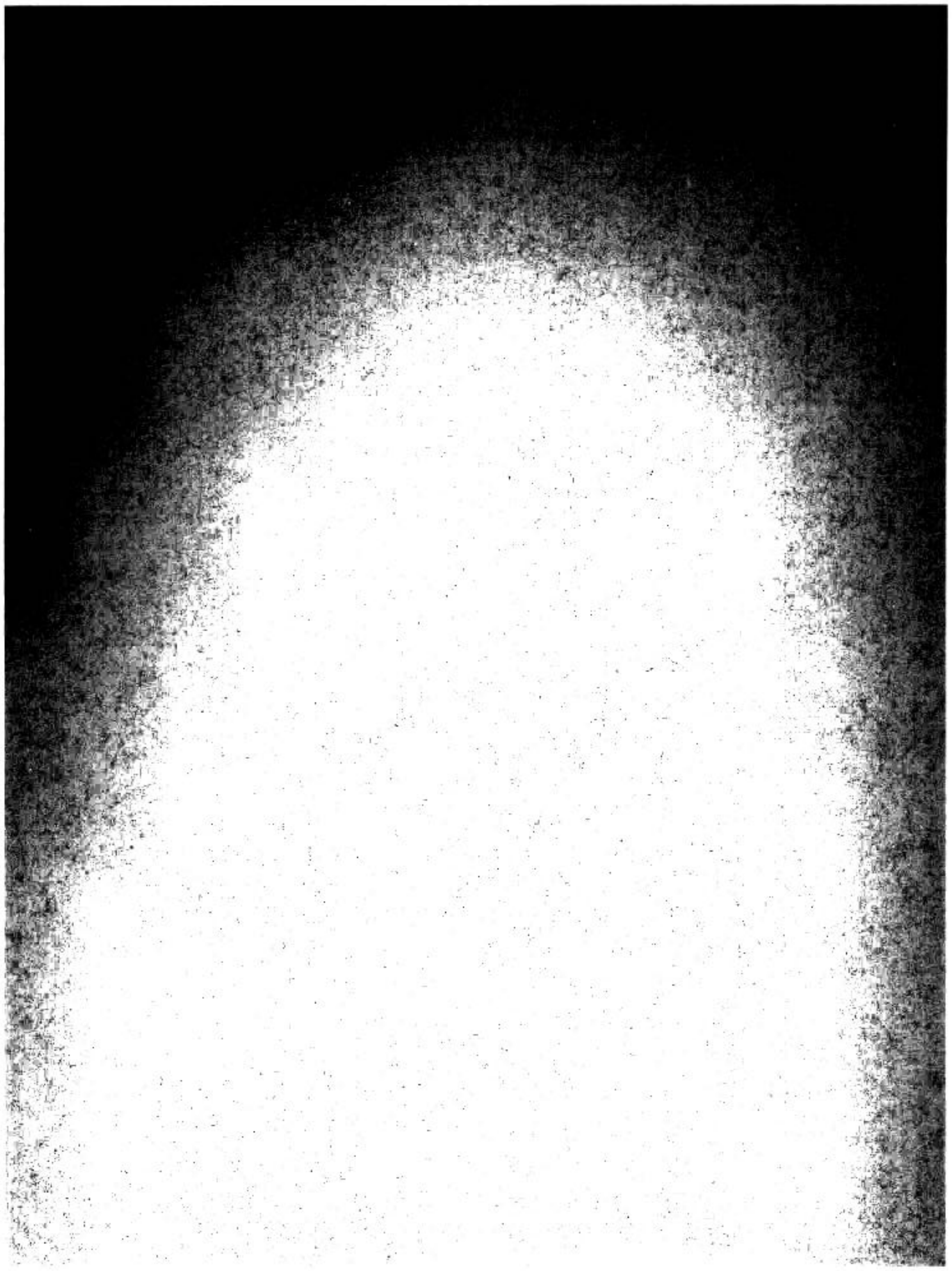

REFERENCES

1. Bruno B. Rossi and Hans H. Staub, Ionization Chambers and Counters, 1st ed., pp. 206-208, McGraw-Hill Book Company, Inc., New York, 1949.
2. E. O. Kiger and G. F. O'Neill, Remotely Movable Small Ion Chamber for Determining Reactor Flux Distribution, Report ANL-4989, February 1953.
3. Dwight S. Young, Neutron Distribution Measurements at Pajarito by Means of Photographic Emulsions, Report LA-1487, May 15, 1952.
4. W. C. Redman and F. A. Smith, Measurement of Detailed Flux Distribution Patterns in Low-Power Reactors, pp. 38-45, Report ANL-4950, December 15, 1952.
5. F. H. Martens et al., Experiments on Zero Power Reactor (ZPR-I), Part III, Report ANL-5199, March 1954.
6. G. O. Bright and F. Schroeder, Neutron Flux Distributions in the Materials Testing Reactor, Part I, Report IDO-16047, February 16, 1953.
7. John W. Kunstadter, A Correction to Be Applied to the Activity of Neutron-Activated Cadmium-Covered Indium Foils, Phys. Rev., 78:484 (1950).
8. W. C. Tittle, Slow-Neutron Detection by Foils, Nucleonics, 8:6 (1951); Nucleonics pp. 60-67, 9:1 (1951).
9. Donald J. Hughes, Pile Neutron Research, Addison-Wesley Publishing Company, Inc., Cambridge, Mass., 1953.
10. M. Blau, I. W. Ruderman, and J. Czeckowski, Photographic Methods of Measuring Slow Neutron Intensities, Rev. Sci. Instrum., pp. 233-236, 21 (1950).
11. David H. Martin, Correction Factors for Cd-Covered Foil Measurements, Nucleonics, 13, No. 3, pp. 52-53 (1955).
12. Kenneth E. Relf, Counting Thousands of Samples in 12 Hours - Automatically, Nucleonics, 15:4, April 1957.
13. Oswald Reidel, Statistical Purity in Nuclear Counting, Nucleonics, pp. 64-67, 12:6 (1954).
14. C. G. Paradine and B. H. P. Rivett, Statistics for Technologists, D. Van Nostrand Company, Inc., New York, 1953.
15. R. S. Stone and E. J. Wade, A Reversible Digital Transducer and Counter, Report KAPL-1247, December 15, 1954.
16. R. T. Frost, An Automatic Neutron Flux Scanner, Report KAPL-1117, March 1, 1954.
    R. T. Frost and E. B. Fehr, Automatic Neutron Flux Scanner, Nucleonics 14:3, March 1956.
17. W. B. Leng and A. L. Dodson, Use of IBM - 650 in Reduction of Foil Counting Data - Memo KAPL-M-WBL-1, April 16, 1957.
18. E. B. Fehr, Automatic Neutron Flux Plotting - Memo KAPL-M-EBF-7, February 26, 1957.
19. Betty L. Anderson and Thomas J. Lawton, Cofit - A Least Squares Cosine Fitting Program for the IBM-704, Report WAPD-TM-26, October 1956.

Chapter 11

TECHNIQUES OF PARAMETER MEASUREMENT IN HIGH URANIUM CONTENT REACTORS

11.1 INTRODUCTION

This chapter gives the methods used in the measurement of some of the more important parameters associated with high uranium content reactors. These include thermal utilization, resonance escape probability, fast fission factor, conversion ratio and the radial distribution of plutonium formation in fuel rods. The experimental techniques were developed as part of the TRX lattice program. The TRX reactor itself is described in Chap. 9. It was noted there that the program on the properties of slightly enriched uranium-water lattices was a cooperative program with Brookhaven National Laboratory. Many of the techniques developed in the program were the result of joint discussions between laboratories and, as a result, the techniques in use at the various laboratories are quite similar. Those described in this chapter are the techniques which have been in use at Bettis; they differ only in slight detail, however, from those used by Brookhaven.

MEASUREMENTS OF THERMAL UTILIZATION, RESONANCE ESCAPE PROBABILITY AND FAST FISSION FACTOR

by D. Klein and G. G. Smith

11.2 THERMAL UTILIZATION - THEORY OF THE MEASUREMENT

The thermal utilization is defined as the number of thermal neutrons absorbed in the fuel per thermal neutron absorbed in the reactor. Referring to the description of the TRX in Chap. 9, the lattice consists of rods of uranium metal or uranium oxide, clad in aluminum tubing and arranged in a triangular lattice pattern. Of the nuclei present in the lattice, the thermal capture of the oxygen may be neglected. The expression for f, the thermal utilization, is then:

$$f = \left\{ 1 + \frac{V_W \, N_H \, \bar{\sigma}_H \, \bar{\Phi}_W + V_{Al} \, N_{Al} \, \bar{\sigma}_{Al} \, \bar{\Phi}_{Al}}{V_U \left[N_{25} \, \bar{\sigma}_{25} + N_{28} \, \bar{\sigma}_{28} \;\; \bar{\Phi}_U \right]} \right\}^{-1} \qquad \text{Eq. (11.1)}$$

In this equation V refers to the volume of a particular material and N to its number density. The subscripts H, 25, 28, and Al refer to hydrogen, U^{235}, U^{238}, and aluminum, respectively. The cross sections indicated in Eq. (11.1) are to be averaged over the neutron spectrum present, i.e.,

$$\bar{\sigma}_{25} = \frac{\int_0^{E_{Cd}} \sigma_{25}(E)\, \phi_U(E)\, dE}{\int_0^{E_{Cd}} \phi_U(E)\, dE} \qquad \text{Eq. (11.2)}$$

where $\phi_U(E)$ is the neutron flux in the uranium in the energy interval dE at energy E. The average neutron flux is given by the equation

$$\bar{\phi}_U = \frac{1}{V_U} \int_{V_U} dV_U \int_0^{E_{Cd}} \phi_U(E)\, dE \qquad \text{Eq. (11.3)}$$

where the spatial integration is carried over the fueled volume of a unit lattice cell. Similar definitions apply to the other fluxes and cross sections. There are two features to be noted in these definitions. First, it is presumed that within each of the media present, the spatial dependence of the neutron flux is separable from the energy dependence, i.e., there is a single neutron energy distribution for the fuel and another for the moderator. Second, the upper limit of the thermal spectrum is taken to be the cadmium cut-off energy. This separates the resonance region from the thermal region (about 0.5 ev for 0.020-inch cadmium).

Two techniques were developed for the thermal utilization measurement. These are referred to as the differential and integral methods. In the differential technique a series of small foils are used to make a thermal flux plot along the radius of the rod extending out into the water. The thermal utilization is calculated from appropriate fits to these data. In the integral method two sector foils containing U^{235} are exposed, one within the fuel and the other in the moderating water. The thermal utilization is deduced from the relative activities of these two foils.

Figure 11.1 illustrates the two methods. Cross sections of four fuel rods arranged in a triangular lattice array are shown on this figure. In the upper portion of this figure the cross-hatched area shows the location of the U^{235} sector foils which are activated to make the integral measurement. In the lower portion of the figure the small circles show a typical arrangement of foils for taking the flux plots in the fuel and moderator during differential measurement. The details of these techniques will be discussed in the following two sections.

The integral technique has largely displaced the differential measurement for obtaining values for thermal utilization because of the simplicity of the method. The differential measurement is valuable, however, since it does provide some detailed data. Results obtained by the two techniques agree well within the uncertainty of the measurements.

11.3 THERMAL UTILIZATION - INTEGRAL MEASUREMENT

(a) Principle of Measurement. Speaking qualitatively, the principle of the integral measurement is as follows: Referring to the upper half of Fig. 11.1, half a unit lattice cell is represented by the area of an equilateral triangle with vertices at the centers of three adjacent fuel rods. The one-half unit lattice cell can be divided into the six congruent triangular areas shown.

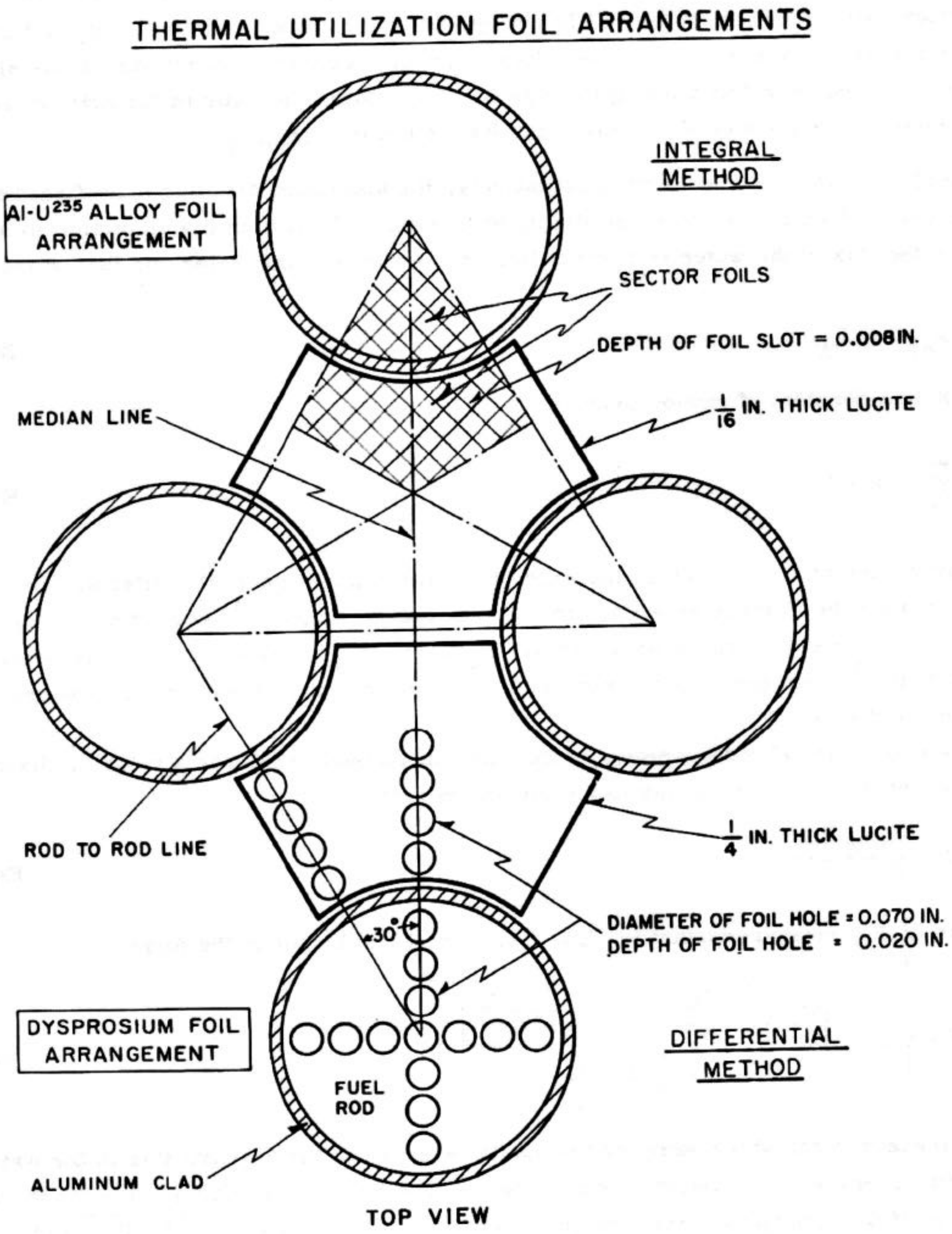

Fig. 11.1 - Integral and Differential Techniques for Thermal Utilization Measurement.

Assuming that the over-all thermal neutron flux is constant in this region, identical neutron fluxes pass through each of these six triangular areas. The fission product activity of a foil placed in one of these triangular areas is proportional to the average neutron flux passing through the area, and therefore proportional to the average neutron flux passing through the unit lattice cell. Further, if the foil is cut into two parts, one in the fuel rod, and one in the water moderator, each part will have a fission product activity proportional to the spatial average of the neutron flux passing through it. Therefore, the ratio of the activity of the foil in the water to the activity of the foil in the fuel is equal to $(\bar{\Phi}_W/\bar{\Phi}_U)$.

To discuss the measurement quantitatively, the aluminum cladding must first be taken into account. This is treated most simply by assuming the flux in the aluminum to be proportional to the flux in the water and that it lies between that in the water and that in the uranium. Thus

$$\bar{\Phi}_{Al} = K\,\bar{\Phi}_W \qquad \text{Eq. (11.4)}$$

where K is a constant of proportionality

$$\frac{\bar{\Phi}_U}{\bar{\Phi}_W} < K < 1\,. \qquad \text{Eq. (11.5)}$$

Now the neutron spectrum in the water moderator is, in general, different from that in the fuel. Defining the average cross section for activation of the U^{235} according to Eqs. (11.2) and (11.3) will result in two average values $\bar{\sigma}_{25W}$ and $\bar{\sigma}_{25U}$. The first of these is the cross section of U^{235} averaged over the spectrum in the water, the second is that averaged over the spectrum in the fuel.

The experimental measurement in the integral method results in a ratio A, the relative activation of the foil in the water to the foil in the fuel.

$$A = \frac{\bar{\bar{\sigma}}_{25W}\,\bar{\Phi}_W}{\bar{\bar{\sigma}}_{25U}\,\bar{\Phi}_U} \qquad \text{Eq. (11.6)}$$

In terms of this measured quantity, Eq. (11.1) for f can be put in the form

$$f = \left\{ 1 + A\,\frac{\left[\dfrac{V_W N_H \bar{\sigma}_H}{V_U N_{25} \bar{\sigma}_{25W}} + \dfrac{K\,V_{Al} N_{Al} \bar{\sigma}_{Al}}{V_U N_{25} \bar{\sigma}_{25W}}\right]}{1 + \dfrac{N_{28}\bar{\sigma}_{28U}}{N_{25}\bar{\sigma}_{25U}}} \right\}^{-1} \qquad \text{Eq. (11.7)}$$

Thus a measurement which samples the spatial average of the thermal flux in the water and the spatial average of the thermal flux in the fuel can be used to infer a value for the thermal utilization if the appropriate average cross sections for hydrogen, U^{235}, U^{238} and aluminum are known. In the application of this method, the cross sections are taken as the average values for a Maxwellian neutron distribution at 0.025 ev.

The expression for thermal utilization in Eq. (11.7) consists of cross section ratios in the same medium, with the exception of the aluminum term, which is small compared to the preceding term in the bracket. Consequently, the proper thermal neutron spectrum for averaging the cross sections is of secondary importance. In fact, if U^{235} behaved as a

1/v absorber, the measurement of thermal utilization would be independent of the thermal spectrum. The error in the measurement due to neutron distributions other than that assumed is discussed later in this section.

As the thermal flux in the aluminum is not measured directly, its contribution to the thermal utilization must be estimated. This is done by assuming the constant K has the value $\frac{1}{2}(1 + 1/A)$. Intracell flux plots obtained from the differential technique support this assumption. Measurements of the activation ratio A in a wide series of measurements gave values less than 1.30. Thus the maximum possible error in K is less than 15 per cent. In the same series of measurements the aluminum term contributed less than 3 per cent to f. Therefore, the maximum possible error in f due to a maximum possible error in K is less than 0.4 per cent.

(b) Method of Measurement. The foils used are uranium-aluminum alloy 0.005 inch thick. The uranium is enriched to over 90 per cent U^{235} and alloyed at 10 weight per cent with 2S aluminum. These choices make the U^{235} atomic density in the foil approximately the same as that in the fuel rods. The shape and location of the foils in the rod is shown in the upper part of Fig. 11.1 by the cross-hatched area. This area represents a repeating section of a unit cell of the lattice. Thus, the ratio of the activity of the foil in the moderator to the activity of the foil in the fuel does represent the ratio of the thermal fluxes in the two regions.

The uranium-aluminum foils are irradiated in the center of the TRX where the radial flux gradient is essentially zero. The foils in the fuel are positioned between two fuel pieces in a split fuel rod. The foils in the water are held in a 1/16-inch Lucite foil holder taped to the fuel rod directly opposite the foil in the fuel. The locations of these are shown in Fig. 11.2 by the sketch on the right. The ratio of foil A activation to foil B activation yields the activation ratio required to apply Eq. (11.7).

Generally speaking, correction for the epicadmium fission in the foils is not important. If desired, this correction to the activation ratio can be obtained from foils C, D, and E of Fig. 11.2. The ratio of the activity of foil D to foil C gives the cadmium ratio for the fuel foil B. The ratio of the activity of foil A to that of foil E gives the cadmium ratio for foil A. The cadmium thickness used to obtain the cadmium ratios is 0.020 inch, corresponding to a cut-off energy of 0.5 ev.

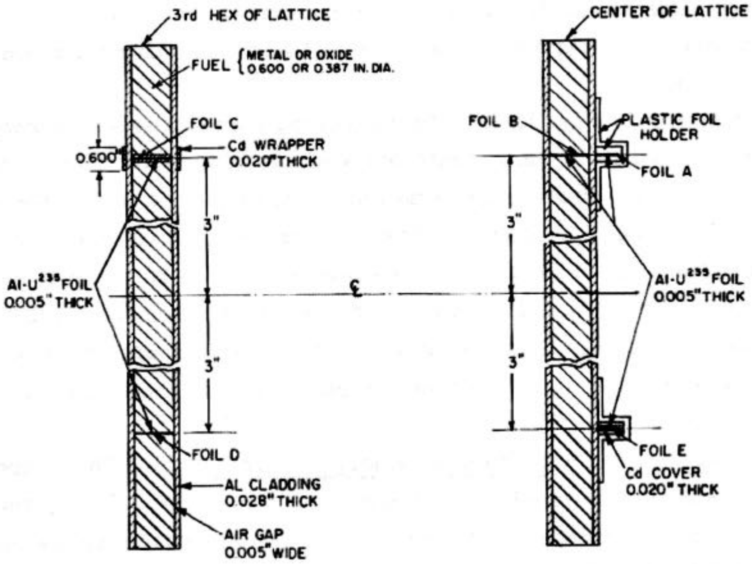

Fig. 11.2 - Thermal Utilization Foil Arrangement (Integral Method).

The activation of the foils is determined by measurement of the fission product γ-radiation using scintillation counter techniques. The equipment consists of the following components: A sodium-iodide crystal 1-3/4 inches in diameter by 2-inches thick mounted on an RCA 5819 photomultiplier tube, a regulated high voltage power supply, a pre-amplifier, a linear amplifier, and a scaler. The foils are calibrated initially by counting the γ-radiation of the natural U^{235} activity above 90 kev. The relative natural activities of the foils are proportional to the relative amounts of uranium-235 in the foils (the attentuation of the 90 kev γ-radiation through 0.005 inch of aluminum is negligible). After the irradiation, fission product γ-rays with energies greater than 400 kev are counted. The 400 kev cut-off is chosen because there is little γ-ray activity of higher energy that does not originate from fission product decay. Since the activities decay as a function of time, the foils are counted alternately, every other minute, for about an hour. The decay curves are plotted to obtain the ratio of activities at any time after irradiation. Air and natural background corrections are made when necessary.

(c) Experimental Investigation of Errors. Several possible sources of error in this measurement were investigated experimentally. In one case a check was made to investigate the shadowing effect of the moderator foil on the foil in the fuel. To make this test two fuel foils were irradiated in symmetric positions. One of the two foils was shadowed by a moderator foil; the other was not. The ratio of the activity of the two fuel foils was found to be 1.00 ± 0.01. This result indicates that there was no shadowing effect.

In another check a series of measurements was also made with foils 0.0025 inch thick to investigate the effects of foil perturbation on the measured flux ratios. The results obtained with this series of foils were consistent with those obtained with 0.005 inch thick foils within the statistical uncertainties of the measurement.

In the course of the development of these techniques, one source of error was discovered which could result in an error of the order of one per cent in the thermal utilization. This error can arise from the piece used to support the foil in the water. In early experiments both aluminum and Lucite foil holders were used. To determine whether this resulted in a difference in the thermal utilization it was decided to measure $(\bar{\phi}_W/\bar{\phi}_U)$ in a lattice using three different thicknesses of Lucite and three different thicknesses of aluminum. In each case, the foil holder cover was identical in dimensions with the foil holder, except for the 0.008 inch deep foil slot which was cut in the foil holder. Both Lucite and aluminum assemblies were suspended by Lucite rods.

The results are shown in Fig. 11.3. The measured flux ratios are plotted as a function of foil holder thickness. Each point represents the average of at least three runs; the spreads are the standard deviations. The straight lines are least squares fits to the experimental points, ignoring the differences in standard deviation from point to point. Within the error limits of the measurement, the two lines extrapolate to a common value at zero thickness.

The data show that, first, $(\bar{\phi}_W/\bar{\phi}_U)$ has a small positive slope for Lucite holders, and second, $(\bar{\phi}_W/\bar{\phi}_U)$ has a relatively large negative slope for aluminum holders. Thus, the use of thick aluminum holders, and the consequent displacement of moderator by aluminum, can lead to significant errors.

(d) Errors Associated with Neutron Energy Distribution. There are two possibilities of errors associated with the thermal neutron energy distribution. First, there is the possibility that some of the foil activation is due to fissioning by neutrons above the cadmium cut-off. This error can be corrected experimentally by taking the cadmium ratio measurements mentioned previously.

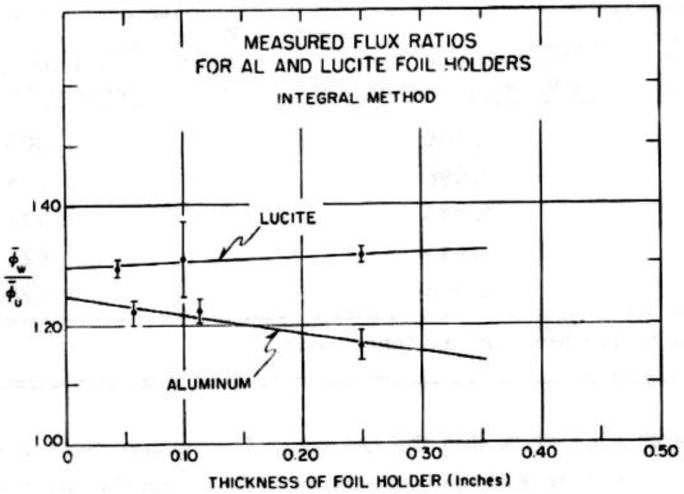

Fig. 11. 3 - Errors Associated with Lucite and Aluminum Foil Holders.

The other source of error is associated with the assumption that the energy distribution in both the fuel and the water is Maxwellian at a temperature of 0.025 ev. This assumption is, of course, not correct. It was noted previously, however, that such an assumption results in an error only because the cross section of U^{235} is not 1/v in its behavior. In the following discussion the magnitude of the error associated with the assumption will be estimated.

If Eq. (11. 7) is written in the form

$$f = \left\{ 1 + A\,G \right\}^{-1} \qquad \text{Eq. (11. 8)}$$

and for purposes of estimating errors the aluminum capture is neglected,

$$G = \frac{V_W N_H \bar{\sigma}_H}{V_U N_{25} \bar{\sigma}_{25W}} \left[1 + \frac{N_{28} \bar{\sigma}_{28U}}{N_{25} \bar{\sigma}_{25U}} \right]^{-1} \qquad \text{Eq. (11. 9)}$$

The changes in G will be examined under various assumptions. From Eq. (11. 8), if Δf is an error in f resulting from an error ΔG in G,

$$\left| \frac{\Delta f}{f} \right| = (1 - f) \frac{\Delta G}{G} \qquad \text{Eq. (11. 10)}$$

so that for the values of f greater than 0.8, the fractional error in f is less than one-fifth the fractional error in G.

The value of G was computed for two sets of conditions assuming the neutron distribution in both the water and fuel to be Maxwellian. In the first, the temperature of the neutrons in the water was assumed to be fixed at 293°K while the temperature of the neutrons in the fuel was assumed to range from room temperature (293°K) up to 700°K. The value of G, normalized to its value with the temperature in both water and fuel at 293°K, was calculated. These are given in the center column of Table 11. 1. In the second calculation the value of G was determined with the temperature of the neutrons in the water and in the fuel equal and ranging from 293°K to 700°K. The values, normalized to that at 293°K, are tabulated in the third column of Table 11. 1.

Table 11.1 - EFFECT OF NEUTRON TEMPERATURE ON VALUE OF G

Temperature of Neutrons in Fuel (°K)	Ratio of G Values	
	Neutrons in Water at Room Temperature	Neutrons in both Water and Fuel at Elevated Temperatures
293	1.000	1.000
400	0.996	1.016
500	0.993	1.022
600	0.993	1.024
700	0.993	1.020

NOTE: Calculated for 1.3% enriched rods.

The results in Table 11.1 show that the change in G in either case is small. Since the neutron temperature in the rods will undoubtedly be higher than the neutron temperature in the water, the change in G will be of the magnitude given in the center columns of Table 11.1 and is negligible.

11.4 THERMAL UTILIZATION - DIFFERENTIAL MEASUREMENT

(a) Method of Measurement. The detector used for this method is dysprosium. Dysprosium has a cross section which is approximately 1/v in the thermal range with a value of over 1000 barns in the thermal range and about 100 barns at 1 ev. Cadmium ratio measurements on dysprosium were taken in the TRX moderator and a value of 35 ± 1 was obtained.

The dysprosium foils were made as follows: Dysprosium oxide powder was mixed at 50 weight per cent with polyethylene powder and the mixture formed into a 0.015-inch disc in a metallurgical hot press. The foils, 0.065 inch in diameter, were punched from the large foil. They averaged 800 micrograms per foil. The foils were calibrated by exposure to a uniform flux. They were placed on a milled hole on the outer edge of an aluminum plate, three inches in diameter. The plate holding 48 foils was placed in the reflector of the TRX. Uniform activating flux was obtained by rotating the plate using a long shaft and a 1-rpm motor.

The foils were positioned in the fuel by machining a thin disc of the fuel rod to a thickness of 1/8 inch. This disc had depressions milled into its face to hold the foils. The locations of the foils are shown in Fig. 11.1. The fuel disc holding the foils was located at the center of a specially constructed fuel rod in order to carry out the irradiation. The foils in the water were held in a piece of 1/4-inch-thick Lucite with depressions milled in the surface. The locations of the foils in the water are also shown in Fig. 11.1. It should be noted that the foils are arranged along two radii, one along the line joining the centers of adjacent rods, the other at 30 degrees to this line. The Lucite foil holder was suspended adjacent to the in-the-rod foils by means of a Lucite rod.

After irradiation, the Dy^{165} β-rays were counted in end-window Geiger counters. Each foil was counted in each of four counters to minimize errors due to geometry and to take account of counter efficiency. The data from the counters were corrected for decay, counter dead-time losses, and foil calibration. The resulting normalized averages were plotted as a function of radial distance from the center of the fuel rod. Figure 11.4 is a plot showing typical data for a metal fuel rod 0.600 inch in diameter.

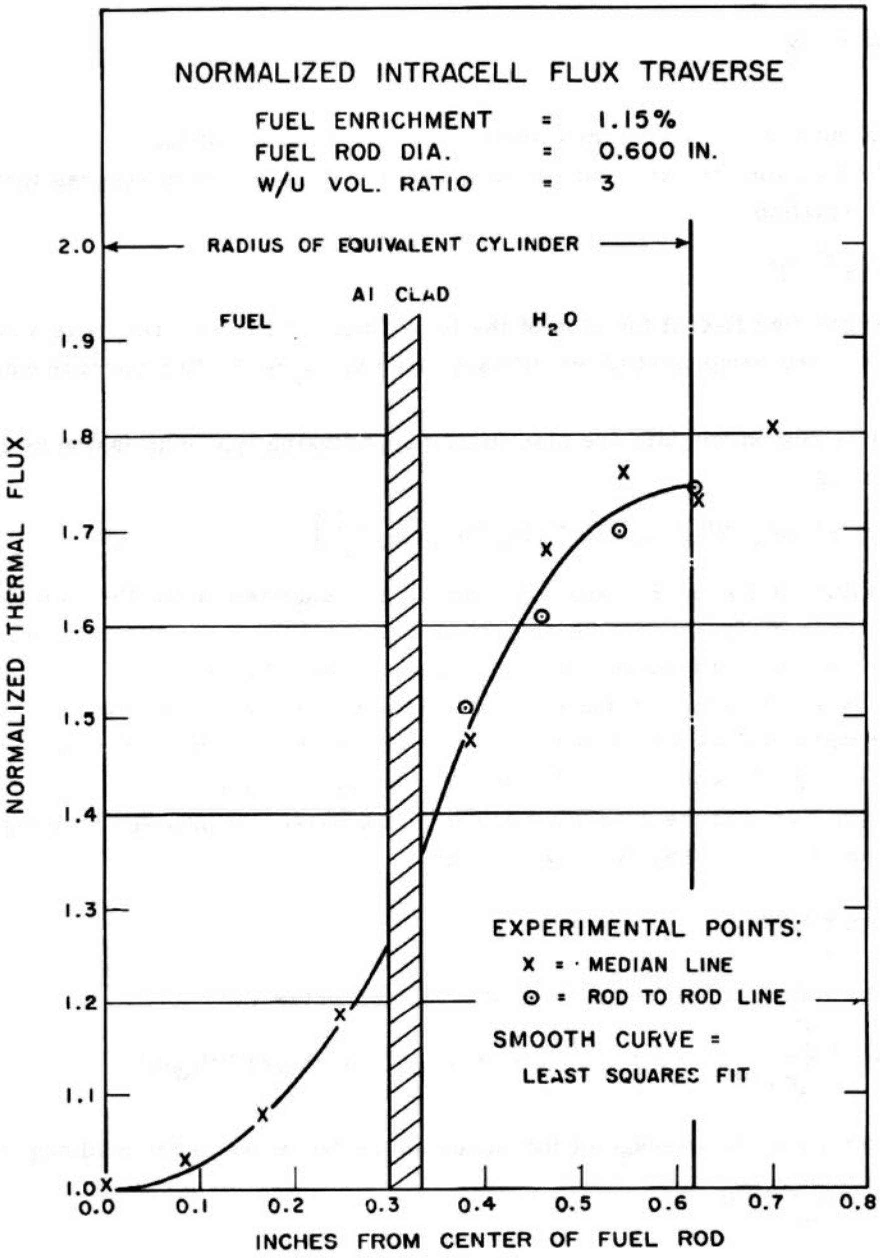

Fig. 11.4 - Flux Plot for Differential Thermal Utilization Measurement.

(b) Method of Fitting Data. The first step in treatment of the data is the conversion of the hexagonal unit cell of the lattice to a cylindrical cell having the same relative water and uranium volumes. If R is the radius of the equivalent cylindrical cell, r_U the radius of the fuel in the rod, and (a) the radius of the outside of the aluminum cladding, R is given by the equation

$$\frac{(R^2 - a^2)}{r_U^{\;2}} = \frac{W}{U} \qquad \text{Eq. (11.11)}$$

where W/U is the water-to-uranium volume ratio of the actual lattice.

Within the fuel rod the experimental flux data are fitted by least-squares technique to a diffusion type equation

$$\phi_i = A\, I_o\, (k\, r_i) \qquad \text{Eq. (11.12)}$$

where I_o is a modified Bessel function of the first kind. In Eq. (11.12), A is a normalizing constant and k is the reciprocal of the diffusion length. ϕ_i is the flux corresponding to the radius r_i.

In the water region the data are also fitted to a diffusion type expression by least squares. The expression is

$$\phi_j = S - B\left[I_1(k_W R) K_o(k_W r_j) + K_1(k_W R)\, I_o\, (k_W r_j)\right] \qquad \text{Eq. (11.13)}$$

In this expression the I's and K's are modified Bessel functions of the first and second kind, respectively. R is the cell radius as defined by Eq. (11.11), ϕ_j is the flux value at the radius r_j, and k_W is the reciprocal of the diffusion length in the water (taken to be 0.41 cm^{-1}). S is the source term and B is an arbitrary constant to be determined. In fitting the experimental data the fit is made to the average of the rod-to-rod and the median line data. The solid curve plotted in Fig. 11.4 is a fit of the data carried out as described.

The average fluxes in the uranium fuel and in the water are obtained by integration of Eqs. (11.12) and (11.13). Thus for the fuel rod

$$\bar{\phi}_{rod} = \frac{2}{kr_U} I_1(kr_U) \qquad \text{Eq. (11.14)}$$

where r_U is the radius of the fuel in the rod. For the water

$$\bar{\phi}_W = S - B\left\{\frac{2a}{k_W(R^2 - a^2)}\right\}\left\{I_1\; k_W(R)\; K_1(k_W a) - K_1(k_W R)\; I_1(k_W a)\right\} \qquad \text{Eq. (11.15)}$$

and for the aluminum, the average of the fluxes on the two sides of the cladding is taken

$$\bar{\phi}_{Al} = \frac{\phi_i(r_U) + \phi_j(a)}{2} \qquad \text{Eq. (11.16)}$$

Equations (11.14), (11.15), and (11.16) give the flux averages to be used in Eq. (11.1). The average cross sections are, as before, taken to be Maxwellian averages at room temperature. Thus all the quantities necessary to calculate the thermal utilization are known.

(c) Summary. As noted previously, in those lattices in which both the differential and integral methods were used the results for the flux ratios in the water to fuel agreed well. Thus either method could be used to obtain satisfactory data. The integral method, however, has largely displaced the differential method for the following reasons:

1. The integral method can be used for lattices with small water-to-uranium volume ratios and for lattices of small diameter rods, where a point-by-point flux plot with dysprosium foils would be impractical.
2. The foil activities obtained in the integral technique are directly related to the average thermal fluxes in the fuel and moderator. Therefore, the data reduction in the integral method is simpler than that in the differential technique.
3. The dysprosium foils used in the differential method are small and relatively fragile. They may chip at any time, changing their Dy_2O_3 content and therefore must be calibrated each time they are used. In contrast to this, the integral method utilizes relatively large metal alloy foils which are not fragile. They need to be calibrated only once, while still virgin, to obtain the relative number of uranium atoms in a pair of foils.

In assigning errors to thermal utilization measurements the uncertainties are determined by combining the following standard deviations:

1. A 2 per cent uncertainty in the cross section values.
2. An estimated 2 per cent uncertainty in the measured flux ratio $(\bar{\phi}_W/\bar{\phi}_U)$, including the uncertainty in the foil calibration. In the most recent measurements the uncertainty in f is estimated to be about ± 0.005 for a value of f around 0.8.

11.5 RESONANCE ESCAPE PROBABILITY - THEORY OF MEASUREMENT

The resonance escape probability in U^{238} will be defined in the following way:

$$p^{28} = \frac{(q)_c}{(q)_c + \Sigma_{ar}^{28}\,\phi_r} \; . \qquad \text{Eq. (11.17)}$$

where p^{28} is the resonance escape probability in U^{238}, $(q)_c$ is the density of neutrons slowing down past the cadmium cut-off energy ϵ_{Cd} per second, and $\Sigma_{ar}^{28}\,\phi_r$ is the epicadmium radiative capture in U^{238}.

$$\Sigma_{ar}^{28}\,\phi_r = \int_{\epsilon_{Cd}}^{\infty} \Sigma_a^{28}(E)\phi(E)dE \qquad \text{Eq. (11.18)}$$

Now the density of neutrons slowing down past the cadmium cut-off energy is equal to the density of neutrons captured in the thermal group, if thermal leakage is neglected. Of the density of neutrons captured in the thermal group the fraction $f(q)_c$ is the rate of capture in fuel. If R is defined to be the ratio of radiative capture in U^{238} in the thermal region to the total thermal capture in fuel, by definition

$$R = \frac{N_{28}\bar{\sigma}_{a28}}{N_{28}\bar{\sigma}_{a28} + N_{25}\bar{\sigma}_{a25}} \qquad \text{Eq. (11.19)}$$

where the $\bar{\sigma}$'s represent averages of the absorption cross section over the thermal flux spectrum in the fuel rod and the N's represent number density.

The rate of thermal capture in U^{238} is then $f\,R(q)_c$.

Now, ρ is defined to be the ratio of radiative capture in U^{238} above the cadmium cut-off energy to the radiative capture in U^{238} below the cadmium cut-off energy. This ratio is equal to the ratio of rates of capture, i.e.,

$$\rho = \frac{\Sigma_{ar}^{28} \phi_r}{f\, R(q)_c} \qquad \text{Eq. (11.20)}$$

Substitution of Eq. (11.20) into Eq. (11.17) gives the result

$$\frac{1 - p^{28}}{p^{28}} = \rho f R \qquad \text{Eq. (11.21)}$$

To determine p^{28}, the quantity ρ is measured. The thermal utilization is measured by the techniques discussed previously. The quantity R is determined by taking Maxwellian averages of the cross sections at room temperature.

The choice of definition for p^{28} was made for the following reason: The conventional definition requires the determination of the number of neutrons escaping radiative capture in U^{238} in slowing down to the thermal group per neutron entering the resonance region. Such a definition requires a knowledge of the competition between U^{238} absorption and other absorptions, such as in U^{235}, as well as a correction for the leakage of resonance energy neutrons. It should also be noted that this definition for p^{28} includes the capture by U^{238} in the energy region between U^{238} resonances as well as that in the resonances themselves. In other words, the so-called smooth 1/v epicadmium radiative capture in U^{238} is lumped into the resonance capture.

11.6 RESONANCE ESCAPE PROBABILITY - MEASUREMENT TECHNIQUE

The determination of the resonance escape probability reduces to a measurement of ρ, the ratio of epicadmium to subcadmium radiative captures in U^{238}. Two methods have been used to measure this quantity.

(a) Depleted Foil Method. Radiative capture in U^{238} leads to the following reaction:

$$U^{238}(n,\gamma)\, U^{239} \xrightarrow[23 \text{ min.}]{\beta^-,\ \gamma} Np^{239} \xrightarrow[56.3 \text{ hr.}]{\beta^-,\ \gamma} Pu^{239}$$

In the de-excitation of the excited states of Pu^{239} to the ground state by internal conversion, a 103 kev X-ray is produced. The intensity of this X-ray is proportional to the U^{238} radiative capture.

The determination of ρ is made in the following manner. Two highly depleted uranium foils (5 ppm U^{235}), one cadmium covered and the other bare, are exposed in flux-symmetric positions in a fuel rod. The 103 kev activities are measured with a NaI scintillation spectrometer and compared at the same time after shutdown. A typical loading scheme is illustrated in Fig. 11.5.

The spectrometer consists of a NaI(Tl) crystal 1/2 inch thick and 1-3/4 inches in diameter, mounted on an RCA 5819 photomultiplier; a linear amplifier, and a twenty-channel pulse height analyzer. The activities of the two irradiated foils and one unirradiated foil (used for natural background corrections) are scanned for at least one half-life (56.3 hours). By subtracting the activity of the background foil from the activities of the two irradiated foils, ρ is determined from the following relationship:

$$\rho = \frac{(Np^{239} \text{ activity of cadmium-covered foil})}{(Np^{239} \text{ activity of bare foil}) - (Np^{239} \text{ activity of cadmium-covered foil})}$$

A plot of typical experimental data is shown in Fig. 11.6.

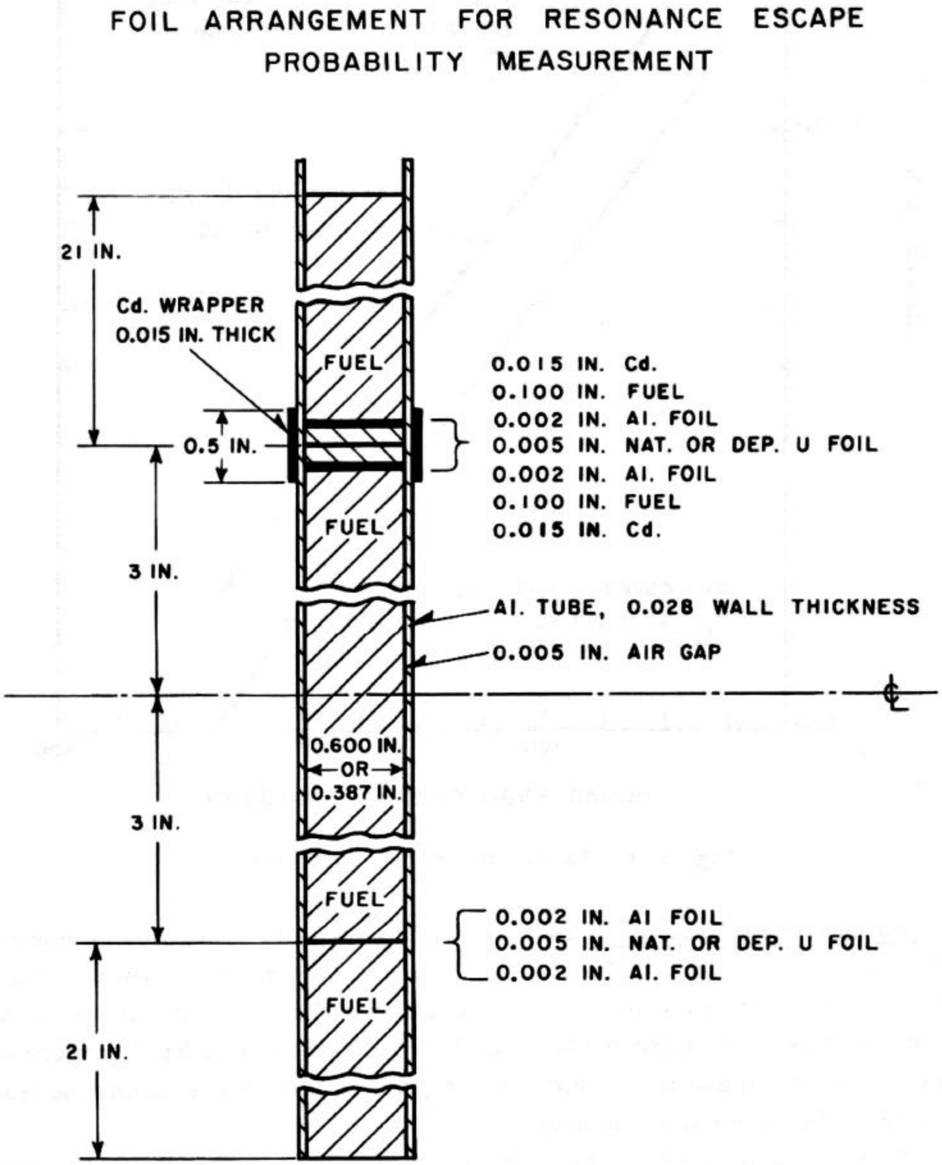

Fig. 11. 5 - Irradiation Package for Resonance Escape Probability Measurement.

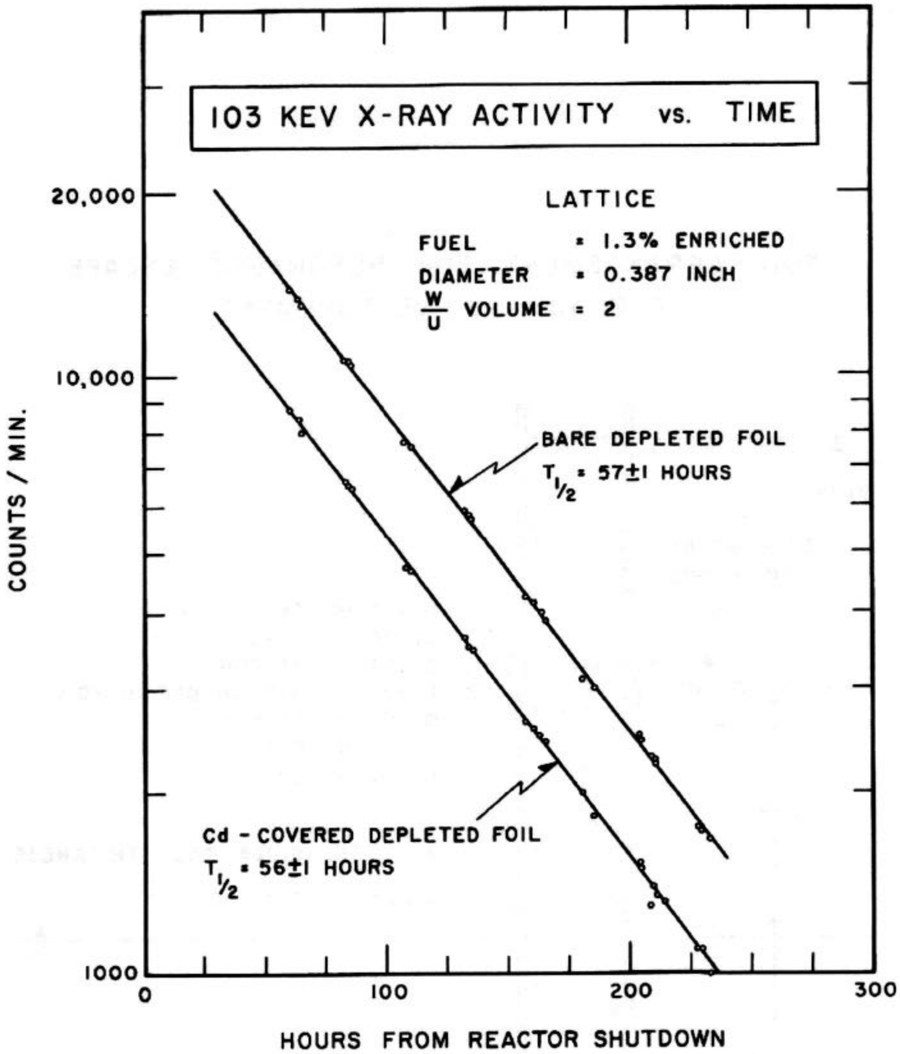

Fig. 11. 6 - Depleted Foil Decay Curves.

(b) Radiochemical Separation Technique. The quantity ρ can also be measured by using a radiochemical separation technique. In this technique natural uranium foils are used since depleted foils are not required. After irradiation in the arrangement shown in Fig. 11. 5, each of the foils is dissolved in hydrochloric acid. Equal amounts of Np^{237} tracer are added to each of the two solutions and the neptunium is separated from the uranium and fission product contamination by radiochemical techniques.

The Np^{239} decay rates of the two solutions are determined by β counting the decay of Np^{239} to Pu^{239} with an end-window Geiger counter. To eliminate counts due to α particles, a 0. 001-inch aluminum foil is placed over the window of the counter.

To obtain the desired ratio of Np^{239} activity in the bare foil (N_b) to that in the cadmium-covered foil (N_{Cd}) corrections are necessary for the original foil weight, the yield of Np from the separation and the amounts of tracer Np^{237} added to the solutions.

If the observed β counting rates of the separated material from the two solutions is designated as N'_b and N'_{Cd} for the bare and cadmium foils, respectively, the corrected ratio is given by Eq. (11. 22).

$$\left[\frac{N_b}{N_{Cd}}\right] = \left[\frac{N'_b}{N'_{Cd}}\right]\left[\frac{W_{Cd}}{W_b}\right]\left[\frac{\alpha_{Cd}}{\alpha_b}\right]\left[\frac{T_b}{T_{Cd}}\right] \qquad \text{Eq. (11.22)}$$

W_{Cd} and W_b are the weights of the original two foils. The ratio of the yields of neptunium from the chemical solution is given by

$$\left[\frac{\alpha_{Cd}}{\alpha_b}\right].$$

This ratio is determined by α counting the Np^{237} tracer activity (it is assumed that the yield of Np^{239} is proportional to the yield of Np^{237}). This α-activity must be corrected for the ratio

$$\left[\frac{T_b}{T_{Cd}}\right]$$

which is the ratio of the amounts of Np^{237} added to the original solutions unless special care is used to make this ratio unity. By careful pipetting, a ratio of 1.000 ± 0.0005 has been achieved.

The weights W of the original foils are determined by weighing with a microbalance. To assure a uniform deposit with uniform α absorption, the separated neptunium is electroplated onto a platinum foil one inch in diameter and 0.005 inch thick. This foil is used for both the α and β counting. The α-activity is determined by using a proportional flow counter with a continuous flow of gas with composition 90 per cent argon + 10 per cent methane. The β-counting is performed as described previously. The T's are determined by standard volumetric chemical techniques.

To assure that each separation and its associated counting are properly performed, two bare and two cadmium-covered foils are irradiated simultaneously. After normalization by Eq. (11.22), the ratio of the activities of the two bare foils as well as the ratio of the activities of the two cadmium-covered activities should be unity.

In comparing measurements which have been made, the results of the radiochemical separation technique and the foil technique have agreed well within their experimental errors. Generally speaking, the foil technique is preferred where applicable and if the necessary electronic equipment is available. The radiochemical technique has served to establish the foil technique, however, and has been useful in making a number of auxiliary experiments.

(c) Experimental Investigation of Errors. In the experimental technique for foil irradiation shown in Fig. 11.5, several auxiliary materials are included in the foil packages. These have been found necessary by experimental studies. The 0.002-inch aluminum foil on each side of the foil undergoing irradiation is necessary to prevent contamination of the foil by fission products from the adjacent fuel material.

In the cadmium-covered package, a fuel wafer 0.100 inch thick is included in the package. If this were not done, the relatively thick cadmium would permit streaming of resonance energy neutrons from the moderator on to the surface of the foil. The magnitude of this effect has been measured. The results are presented in Table 11.2. The last row of data on this table corresponds to the 0.100-inch fuel spacers normally used in the measurement. The data indicate that only a very small spacer thickness is required to stop the streaming of resonance neutrons. It should be noted that the spacers must be of the same composition as the fuel, so that the absorption and scattering characteristics of the fuel are matched.

Table 11. 2 - ρ VERSUS FUEL SPACER THICKNESS

Thickness (U^{238} atoms/cm^2 x 10^{-20})	Cadmium Ratio (Relative Value)
0	1. 00 ± 0. 04
6. 1	1. 13 ± 0. 02
30. 5	1. 19 ± 0. 02
61. 0	1. 20 ± 0. 02
122. 0	1. 20 ± 0. 02

In the foil technique, the use of depleted material was found to be necessary because of the errors introduced by radiation accompanying the decay of U^{235} fission products. After considerable effort to correct for this contamination, it was found necessary to resort to depleted foils. The chemical separation technique, of course, permits the use of natural uranium foils.

The effect on the magnitude of ρ of suppression of fissions by thermal neutrons within the cadmium box has also been determined. The resonance activities of two foils, one surrounded by a cadmium sleeve 0.6 inch high and the other foil surrounded by a cadmium sleeve 0. 1 inch high, were compared. The ratio of the foil activities was 1. 015 ± 0. 02. The effect, if it exists, is within the uncertainty of the experiment.

Experiments have been performed to estimate the effect of the cadmium thickness on the measurement of ρ. If U^{238} exhibited only resonance structure, which was well above the cadmium cut-off energy, there would be no cadmium thickness effect. There is, however, 1/v absorption in U^{238}. As the thickness of the cadmium increases, it becomes more opaque to higher energy neutrons. A series of measurements has been made at several cadmium thicknesses to determine the extent of this effect. The results from these experiments yielded a change in p^{28} of 0. 7 ± 0. 4 per cent for a change in the cut-off energy from 0. 38 ev to 0. 50 ev (0. 010 inch of cadmium to 0. 020 inch of cadmium).

A check has also been made on the use of depleted metal foils in the determination of ρ in oxide lattices. Two low density oxide pellets 0. 100 inch thick, one bare and the other cadmium covered, were chemically separated after irradiation. The value of ρ obtained by using oxide pellets was consistent, within the experimental uncertainty, with the value obtained using metal foils. This experiment confirms the belief that the thin metal foils sample the resonance flux without perturbing it.

The estimates of the uncertainty in p^{28} are the result of a combination of a 3 per cent uncertainty in ρ, a 0. 5 per cent uncertainty in the thermal utilization and a 2 per cent uncertainty in the cross-section values comprising R. In the most recent measurements the uncertainty in p^{28} is approximately ± 0. 005 for a value of p^{28} around 0. 8.

11. 7 FAST FISSION IN URANIUM-238 - THEORY OF THE MEASUREMENT

The energy threshold for fission by neutrons in U^{238} is approximately 700 kev. Since a substantial fraction of the neutrons emitted in fission of U^{235} and U^{238} have energies above this threshold, such neutrons can cause fission in U^{238} before they become degraded in energy. Several quantities can be defined which are measures of this effect. One of the least ambiguous is the quantity δ^{28} defined as the ratio of fissions in U^{238} to those in U^{235}. By definition

$$\delta^{28} = \frac{N_F^{28} \int_0^\infty \sigma_f^{28}(E)\ \phi(E)dE}{N_F^{25} \int_0^\infty \sigma_f^{25}(E)\ \phi(E)dE} \qquad \text{Eq. (11.23)}$$

In this equation N_F^{28} is the number density of U^{238} atoms in the fuel, N_F^{25} is the number density of U^{235} atoms, $\sigma_f^{28}(E)$ is the fission cross section of U^{238} as a function of energy, $\sigma_f^{25}(E)$ is the fission cross section of U^{235} as a function of energy and $\phi(E)$ is the neutron flux in the interval dE at energy E.

To determine δ^{28} experimentally, two foils are exposed to the neutron flux in the reactor. One is a partially depleted foil having number densities of U^{238} and U^{235}, N_D^{28} and N_D^{25} respectively. Another foil is slightly enriched and has the number densities N_E^{28} and N_E^{25} for the U^{238} and U^{235}, respectively. The two foils are exposed and the fission product activity measured as a function of time after exposure. The fission product activity of U^{238} will decay at a different rate in general from that of U^{235} fission products. Let $\mu^{28}(t)$ and $\mu^{25}(t)$ be proportional to the measured activity of U^{238} and U^{235} fission products at a time (t) after fission. Define P(t) as the ratio of these functions.

$$P(t) = \frac{\mu^{25}(t)}{\mu^{28}(t)} \qquad \text{Eq. (11.24)}$$

The experimental quantity which is measured is $\gamma(t)$, the ratio of the activity of one foil, say the depleted foil, to the other, i. e., the enriched foil, as a function of time after exposure. For equal weights of the two foils

$$\gamma(t) = \frac{\mu^{28}(t)\ N_D^{28} \int_0^\infty \sigma_f^{28}(E)\,\phi(E)dE + \mu^{25}(t)\ N_D^{25} \int_0^\infty \sigma_f^{25}(E)\ \phi(E)dE}{\mu^{28}(t)\ N_E^{28} \int_0^\infty \sigma_f^{28}(E)\,\phi(E)dE + \mu^{25}(t)\ N_E^{25} \int_0^\infty \sigma_f^{25}(E)\ \phi(E)dE} \qquad \text{Eq. (11.25)}$$

Equations (11.23), (11.24), and (11.25) can be combined to give for δ^{28}

$$\delta^{28} = P(t)\,\frac{\left[\gamma(t) - N_D^{25}/N_E^{25}\right]}{\left[N_D^{28}/N_E^{28} - \gamma(t)\right]}\left(\frac{N_E^{25}}{N_E^{28}}\right)\left(\frac{N_F^{28}}{N_F^{25}}\right) \qquad \text{Eq. (11.26)}$$

If the enriched foil has the same enrichment as the fuel, the last factors in Eq. (11.26) cancel. Equation (11.26) states that δ^{28} can be measured by determining the relative fission product activities in two foils of different U^{235} content; however, the quantity P(t), the relative activity of the U^{235} and U^{238} fission products being measured, must be known as a function of time after shutdown.

It may be of interest to note that the fast fission factor ϵ may be determined from δ^{28}. Thus

$$\epsilon - 1 = \frac{\nu^{28} - 1}{\nu^{25}}\delta^{28} \qquad \text{Eq. (11.27)}$$

where ν^{28} and ν^{25} are the number of neutrons emitted per fission of U^{238} and U^{235}, respectively. This definition of ϵ differs from a more customary one in which the numerator of

Eq. (11.27) is ($\nu^{28} - 1 - \alpha^{28}$) where α^{28} is the ratio of capture to fission cross section for U^{238} averaged over the energy interval of interest. The definition of Eq. (11.27) is given here because when used with the definition of p^{28} given previously, Eq. (11.17) the correct four-factor value for k_∞ is obtained.

11.8 FAST FISSION IN URANIUM-238 - METHOD OF MEASUREMENT

(a) Foil Measurements. The quantity $\gamma(t)$ is measured by placing a 0.005-inch uranium foil, depleted in U^{235}, and a similar foil, enriched in U^{235}, together in a fuel rod in the center of the lattice. The arrangement of the foils is shown in Fig. 11.7. The foils are protected against fission product contamination from the fuel rod by 0.001-inch aluminum foils.

After irradiation the foils are removed and the resultant fission product activity is counted on a NaI scintillation counter biased to reject pulses below 1.2 Mev. This bias is chosen to eliminate those γ-rays caused by bremsstrahlung of the U^{239} β-rays, which have a maximum energy of 1.2 Mev. The reason for this will be discussed later in connection with experimental problems.

(b) Measurement of P(t). Before describing the method of determining P(t) it would be well to recall what is needed. What is required is a constant of proportionality as a function of time between the measured gamma activity of the foil and the total number of fissions which had taken place in the foil originally. The constant of proportionality is required for both the depleted and enriched foil. The constant of proportionality may be wrong by a factor provided the constants for both foils have the same error since it is only the ratio that is required.

The determination of P(t) provided some formidable experimental difficulties. Their resolution was in the form of a fairly complicated double-chamber fission counter. The design[8] of this chamber is shown in Fig. 11.8. The two chambers were separated by an aluminum center piece. This piece was split so that foils could be placed within the center piece and irradiated in the same flux as the active parts of the counter. On each of the two faces of the center piece two nickel discs were mounted in depressions machined into the center piece. The outward face of each nickel disc, i.e., the face toward the chamber, was coated with uranium electrolytically deposited to a thickness of 0.1 mg/cm^2. One face was coated with depleted uranium, the other with the slightly enriched uranium, each having the same isotopic content as the foils used for the measurement. Through the electrolytic deposition technique, the quantity of uranium deposited on each disc was accurately known to within ± 3%.

The two foils, shown in the lower part of Fig. 11.8, were mounted inside the center piece of the chamber during the measurement. The total number of fissions in the depleted foil is proportional to the total count of the fission counter with the depleted deposit, while the total number of fissions in the slightly enriched foil is proportional to the total count of the chamber with the enriched deposit. Furthermore, the relative efficiencies of the chambers were determined by interchanging deposits. Thus the ratio of the fissions in the two foils is known.

To make the determination of P(t) the fission counter was irradiated in the reflector of the TRX critical facility. The length of irradiation was made equal to that used for a fast fission measurement. The total count of each chamber during the measurement was recorded. After the irradiation, the foils in the center piece of the counter were removed and the resultant fission product activity counted on a scintillation counter using the same bias as is used for a fast fission measurement.

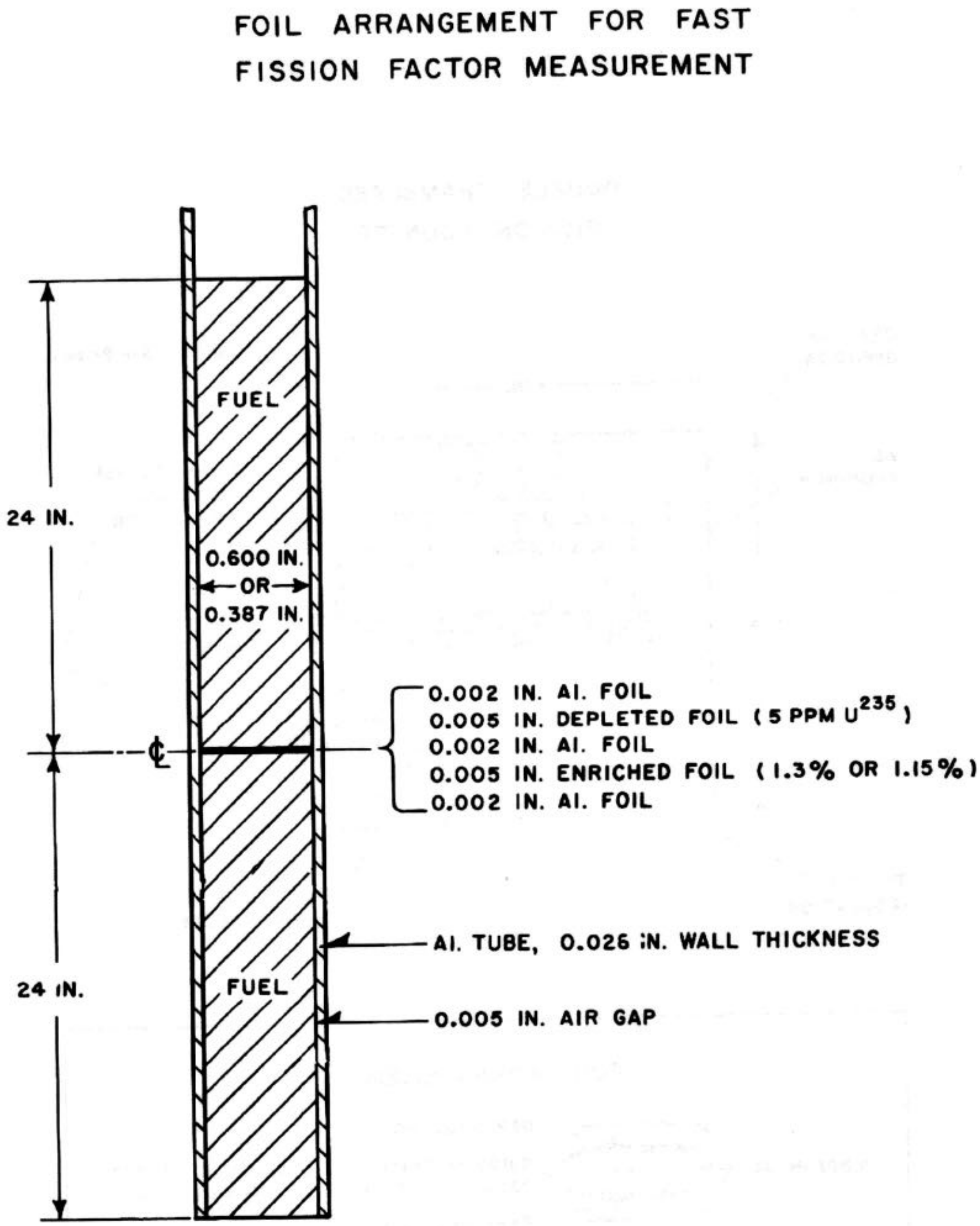

Fig. 11. 7 - Arrangement for Fast Fission Measurement.

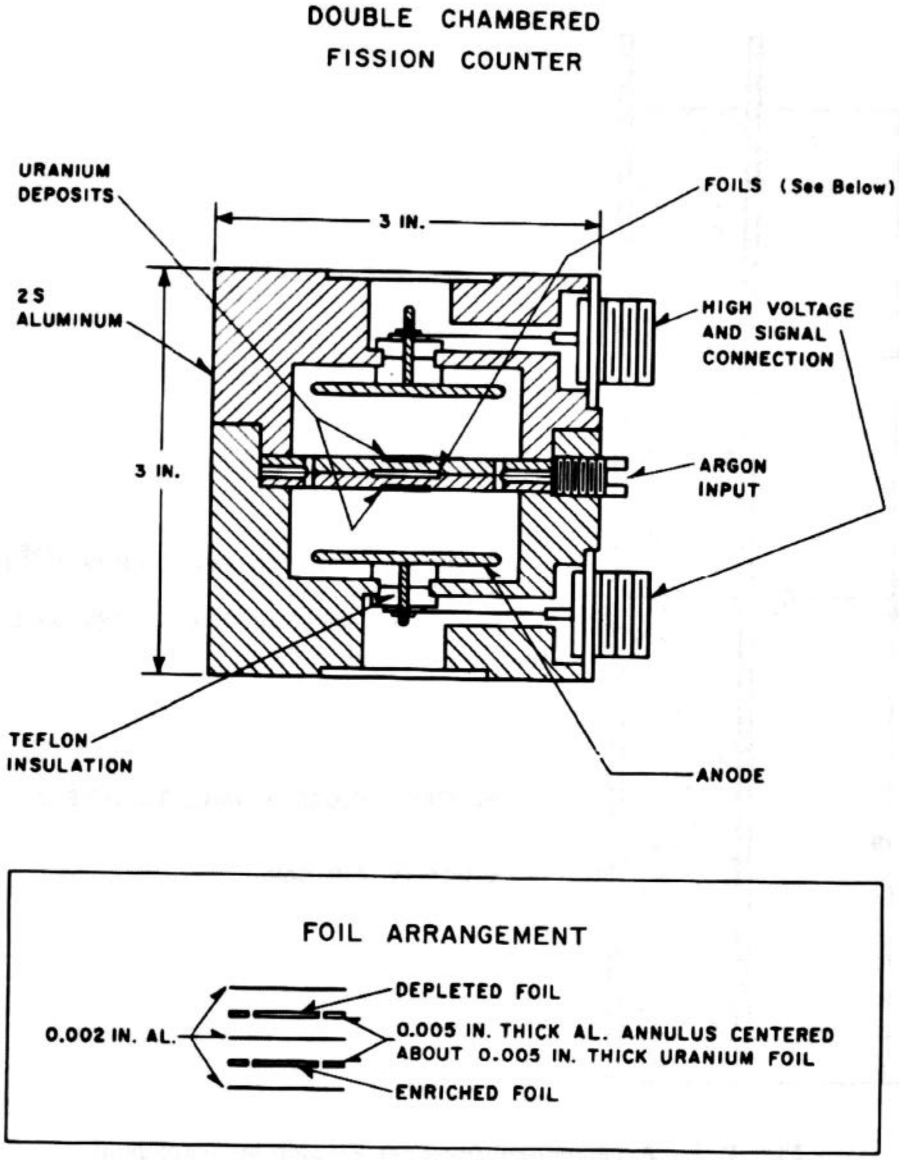

Fig. 11. 8 - Counter for Determination of P(t).

The data taken from such an irradiation experiment are reduced by the following analysis. The ratio of the fissions per uranium atom recorded from the deposits in the double-chambered counter can be written as

$$C = \frac{N_D^{28} \int_0^\infty \sigma_f^{28}(E)\ \phi(E)dE + N_D^{25} \int_0^\infty \sigma_f^{25}(E)\ \phi(E)dE}{N_E^{28} \int_0^\infty \sigma_f^{28}(E)\ \phi(E)dE + N_E^{25} \int_0^\infty \sigma_f^{25}(E)\ \phi(E)dE} \tag*{Eq. (11.28)}$$

As before, the ratio of the fission product activities from the foils normalized to equal weights, can be written

$$\gamma_c(t) = \frac{\mu^{28}(t)\ N_D^{28} \int_0^\infty \sigma_f^{28}(E)\ \phi(E)dE + \mu^{25}(t)\ N_D^{25} \int_0^\infty \sigma_f^{25}(E)\ \phi(E)dE}{\mu^{28}(t)\ N_E^{28} \int_0^\infty \sigma_f^{28}(E)\ \phi(E)dE + \mu^{25}(t)\ N_E^{25} \int_0^\infty \sigma_f^{25}(E)\ \phi(E)dE} \tag*{Eq. (11.29)}$$

Using the definitions given previously by Eq. (11.24) and eliminating the integrals between Eqs. (11.28) and (11.29), the equation for P(t) reduces to

$$P(t) = \frac{\mu^{25}(t)}{\mu^{28}(t)} = \left\{ \frac{\left(N_D^{28}/N_E^{28}\right) - \gamma_c(t)}{\gamma_c(t) - \left(N_D^{25}/N_E^{25}\right)} \right\} \left\{ \frac{C - \left(N_D^{25}/N_E^{25}\right)}{\left(N_D^{28}/N_E^{28}\right) - C} \right\} \tag*{Eq. (11.30)}$$

The value of P(t) given by Eq. (11.30) is then used in Eq. (11.26) with $\gamma(t)$ to obtain δ^{28}.

The double-chambered counter used in this experiment is a continuous flow type using argon gas. A typical characteristic curve of the counter's neutron response is shown in Fig. 11.9. In the operating range, from discriminator settings of 15 to 40 volts, the plateau has a slope of 2 per cent. Experiments with deposits interchanged have shown that the two chambers have characteristic curves and counting efficiencies that agree within 2 per cent.

A curve of P(t) is plotted in Fig. 11.10. This curve is dependent to some extent upon the time of irradiation and the efficiency and bias of the scintillation counter. It is, however, independent of the lattice in which it is measured. The slope of this curve is uncertain to 2 per cent, although the uncertainty in the magnitude of the curve is 5 per cent, due to the following uncertainties:

1. A 3 per cent uncertainty in the relative amounts of uranium in the enriched and depleted deposits of the fission counter;
2. A 2 per cent uncertainty in the relative efficiency of the two chambers in the fission counter;
3. A 2 per cent uncertainty in the background counting rate observed from the fission counter when it was irradiated without any fission element in it.

(c) Experimental Problems. One of the difficulties originally encountered in the fast fission measurement was an apparent variation of δ^{28} with the time after shutdown at which the activity ratios were measured. This was traced finally to the bremsstrahlung in the uranium foils from the 1.2 Mev β-ray emitted by U^{239}.[9] This is sufficiently energetic to produce pulses of energy greater than the originally used 393-kev counting bias. Figure 11.11 shows the value of δ^{28} obtained using a 393-kev bias and the 1.22 Mev bias as a function of time after the irradiation. The U^{239} decay has a 23.5 minute half-life which would make its effects

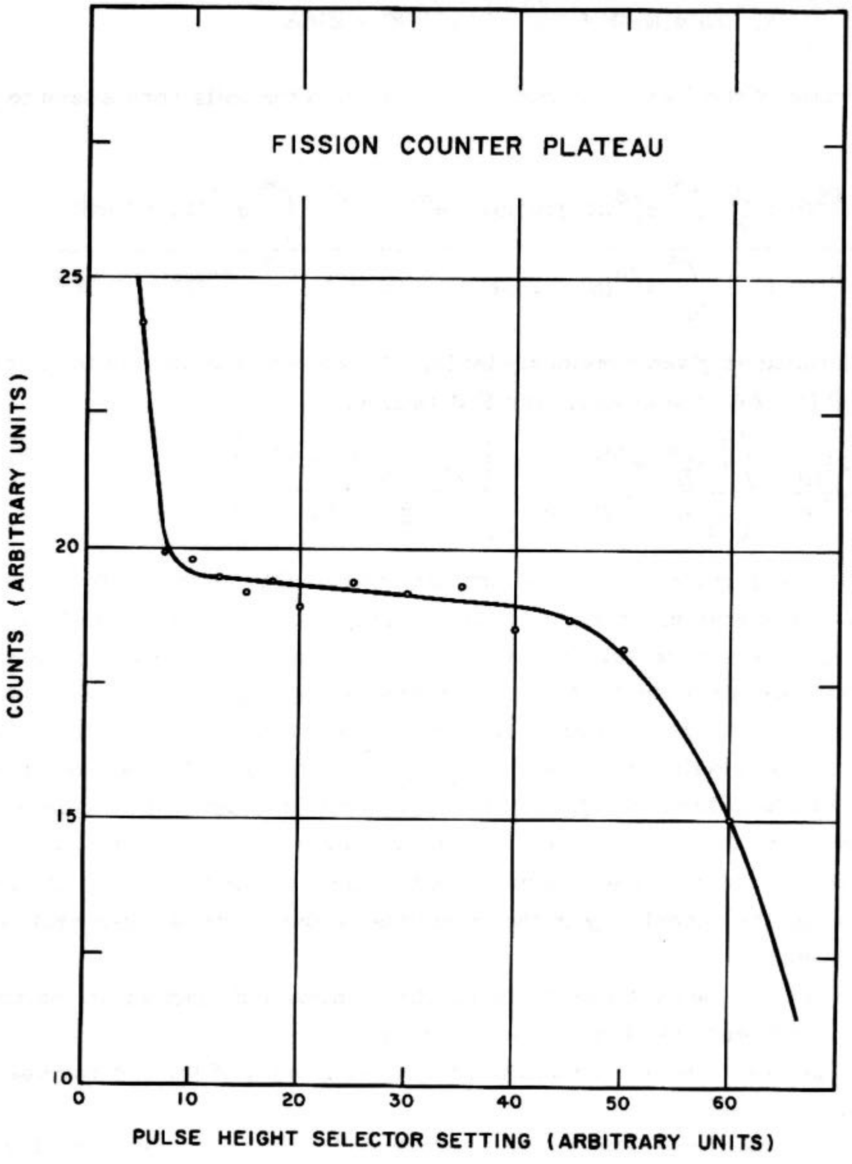

Fig. 11.9 - Fission Counter Operating Characteristics.

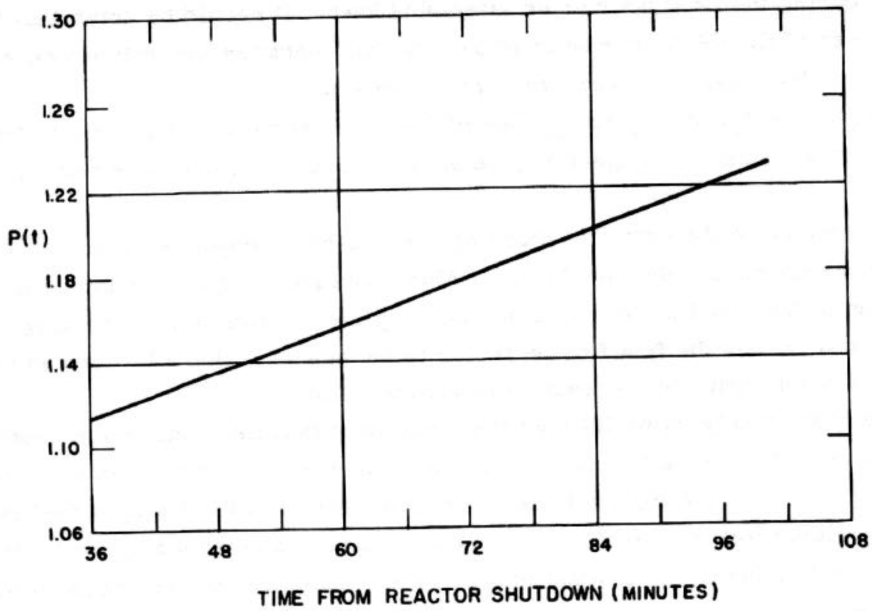

Fig. 11.10 - Correction Factor P(t) for Fast Fission Measurement.

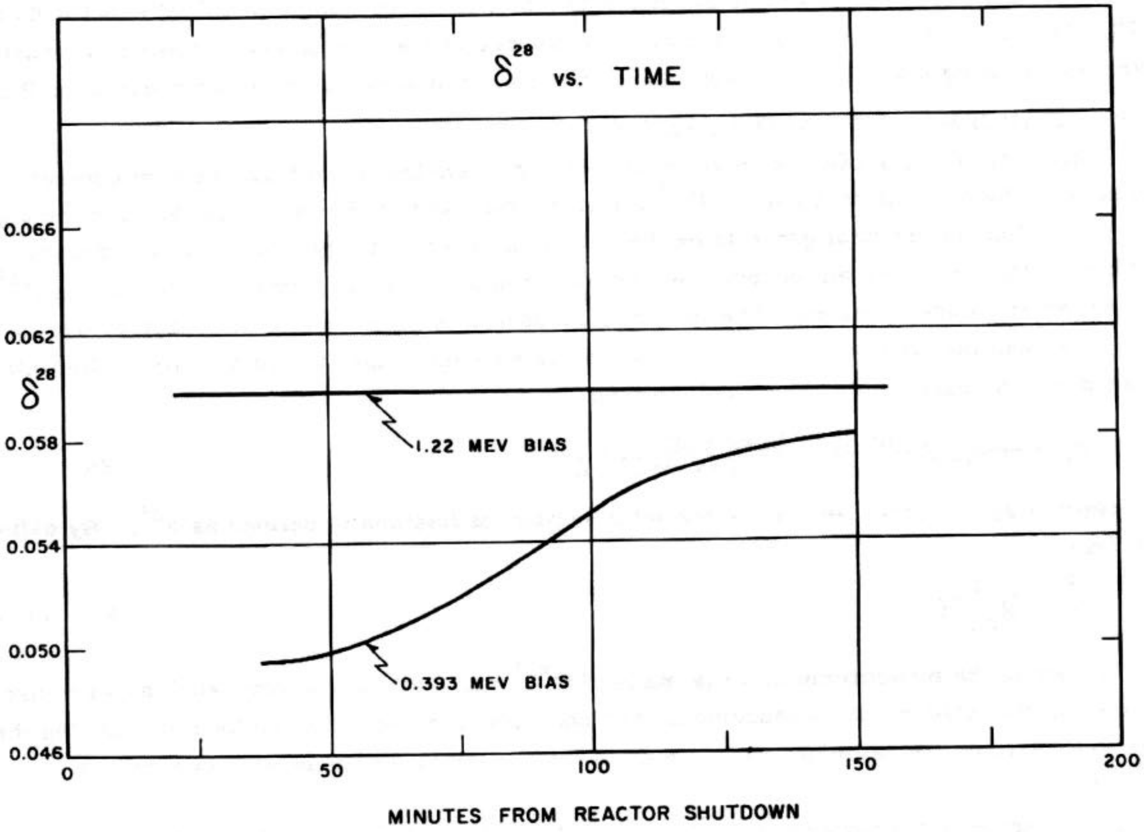

Fig. 11.11 - The Variation of δ^{28} with Time due to Bremsstrahlung.

most noticeable during the first hour or so after shutdown. It should be noted that the effect came about because of the difference in neutron spectrum between the lattice where the foils were irradiated and the reflector where P(t) was determined.

(d) Effect of Neighboring Rods. One of the interesting questions in fast fission effects in water lattices is the effect of neighboring rods compared to the neutrons born in the particular rod.

It has been noted from the data that there appears to be no dependence of the fast fission on rod size, fuel composition, or enrichment. Mean free path arguments indicate that a considerable fraction of the fast flux is due to neighboring rods. The strong coupling of rods in typical TRX lattices causes the fast fission factor to behave as if these lattices were homogeneous, i.e., to depend only on the water-to-uranium ratio.

In one of the high density oxide lattices the fraction of fast neutrons which cause a fission in U^{238} in the same rod in which they are born was measured. This was done by comparing the fission product activity of a highly depleted (5 ppm) uranium foil in a split fuel rod with that of a highly depleted foil in a rod in which the fuel had been replaced by lead. It was found that about 10 per cent of the U^{238} fissions in a rod are caused by neutrons born in that rod. The experiment supports the argument that the fast fission effect is mainly dependent on the water-to-uranium atom ratio for low enrichment lattices.

(e) Estimate of Errors. The over-all uncertainties in the most recent fast fission measurements are estimated to be about ± 0.003 to ± 0.004 in a value of δ^{28} of about 0.05 to 0.08. This uncertainty is a combination of the uncertainties in counting statistics in measuring γ and the counting statistics and other uncertainties listed above in the determination of P(t).

11.9 EPITHERMAL FISSION IN URANIUM-235

A quantity which is often of interest in both highly enriched and high uranium content reactors is the fraction of the total U^{235} fissions which are epithermal. By defining the upper energy limit of the thermal group to be the cadmium cut-off energy, for a given cadmium thickness, the measurement becomes extremely simple. Basically two foils containing U^{235} in a known ratio are required. The foils are exposed to a given flux in the reactor, one foil being bare and the other cadmium covered. After exposure, the fission activity in the foils is counted and the cadmium ratio R_c determined.

$$R_c = \frac{\text{Activity of Bare Foil}}{\text{Activity of Cadmium-Covered Foil}} \qquad \text{Eq. (11.31)}$$

The ratio of epicadmium fissions to the total number of fissions is defined as δ^{25}. By definition then

$$\delta^{25} = \frac{1}{R_c - 1} \qquad \text{Eq. (11.32)}$$

In making the measurement, foils made of U^{235} alloyed in aluminum, such as were used for the thermal utilization measurement, are convenient to use. The method of exposing the foils to determine the cadmium ratio either in the fuel or in the moderator is shown in Fig. 11.2.

Foils can be intercompared by using them alternately for the bare foil and the cadmium-covered foil. Care must be exercised in keeping the cadmium-covered foil some distance from the bare foil since the cadmium depresses the thermal flux locally. The separation shown in

Fig. 11.2 is satisfactory. Another precaution to be observed is to make certain that no water or other hydrogenous material gets inside the cadmium cover.

THE SPATIAL DISTRIBUTION OF RESONANCE NEUTRON CAPTURE IN URANIUM-238

by D. Klein, W. Baer, and G. G. Smith

The radial distribution of resonance neutron capture in a rod of uranium metal has been determined by two methods. One is called the foil method, the other, the spiral method. The measurements have been performed on a 1.3 per cent enriched rod of 0.387-inch diameter.

11.10 THE FOIL METHOD FOR DETERMINATION OF THE SPATIAL DISTRIBUTION OF RESONANCE CAPTURE

The detectors used for this measurement were U^{238} metal foils, 0.004-inch thick by 0.119 inch in diameter, depleted to 5 ppm of U^{235}. The foils are stacked in a 0.125-inch diameter hole drilled across the diameter of a 0.387-inch uranium metal fuel rod. The arrangement is shown in Fig. 11.12.

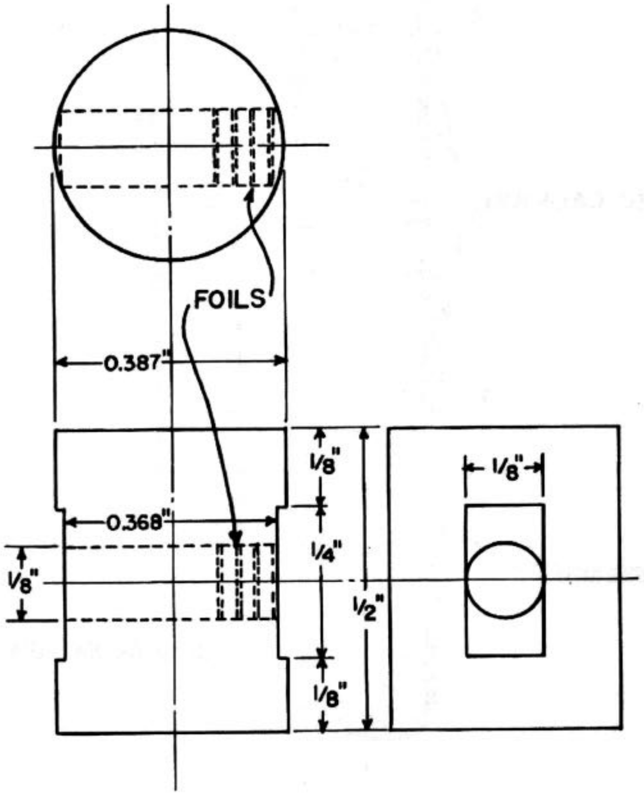

FOIL LOADING ASSEMBLY

Fig. 11.12 - Foil Arrangement Used to Determine Distribution of Resonance Capture.

At each end of the hole, the metal fuel rod is milled flat to a distance of 1/8 inch above and below the hole, so that the surface of the end foil will be coplanar with a flat surface. Foil positions within the rod are determined relative to this foil surface.

The method of loading the fuel rod section containing the foils is shown in the lower part of Fig. 11.13. This sketch also shows the cadmium cover arrangement which is used. After loading the foils in the fuel rod, it is irradiated at the center of the TRX lattice.

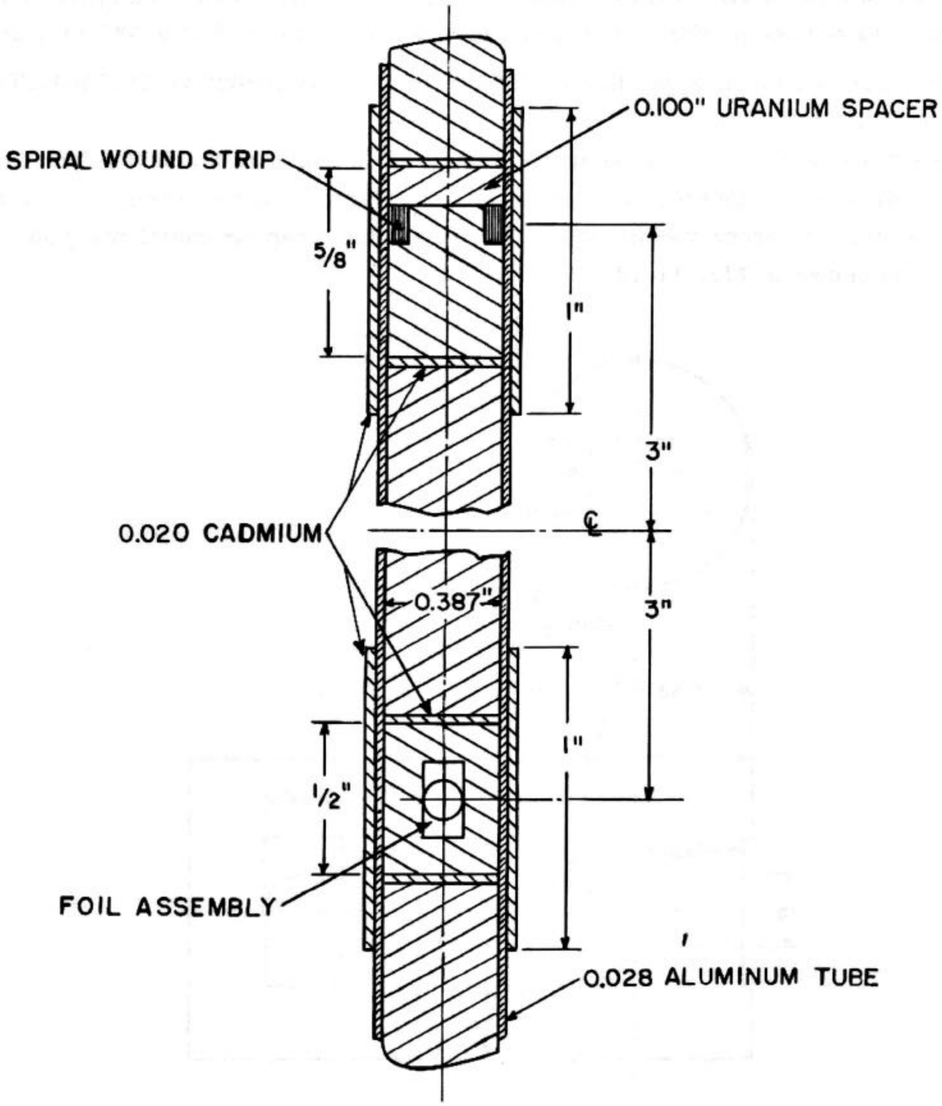

FOIL LOADING IN FUEL ROD

Fig. 11.13 - Location of Foils and Spiral in Fuel Rod.

The method of determining the U^{238} captures is identical to that described in Sec. 11.6 on the resonance escape probability. As described there, the 103 kev X-ray produced in the decay of Pu^{239} to the ground state is measured. Background corrections were checked and found to be less than 0.5 per cent of the total count at the lowest counting rate, and so were neglected.

It might be considered that the location of the foils relative to the surface of the rod is extremely important and must be carefully measured if this method is to be applied. On the inner foils, in addition, the various points on the foil are at somewhat different distances from the surface. These difficulties are minimized by the nature of the absorption. As will be seen later in results of the experiment, the spatial absorption curve drops very rapidly in the first few thousandths of an inch and then becomes relatively flat. For this reason the precise position of the inner foils is only of minor importance. The fourth foil, whose position is nominally 0.016 inch from the flat surface, does not vary in distance from the surface by more than 0.001 inch on the average. This variation can be neglected for this foil.

The problems associated with the location of the surface foils were also examined. Since it was not always possible to be sure that the surface of the end foil was coplanar with the rod surface to within less than 0.0005 inch, these end effects were also investigated. Experiments were performed with a foil taped to the flat surface of the fuel rod but above the hole. The activation of this foil agreed to within 2 per cent with the activation of a foil coplanar with the surface.

An experiment was also performed in which the first foil was replaced with a 0.004-inch foil of aluminum. The activation of the second foil was then compared with the activation of a foil coplanar with the surface. These activations agreed within the experimental errors. These checks indicate that the activation measured is due, almost entirely, to the normally incident flux on the surface of the foil and that end effects are unimportant.

11.11 THE SPIRAL METHOD FOR DETERMINATION OF THE SPATIAL DISTRIBUTION OF RESONANCE CAPTURE

The second method for measuring radial resonance capture in U^{238} uses a spiral of natural uranium metal foil. The arrangement of this foil on the slightly enriched metal fuel is shown in Fig. 11.14. The spiral, which is 1/8 inch wide, 30 inches long, and 0.002 inch thick, is wound onto an extension of the 0.387-inch fuel piece. This extension has been reduced in diameter to 1/4 inch, as shown on the figure. After wrapping the spiral on this extension, it is held in place by 0.001-inch thick Mylar tape. Measurements of the thickness of the spiral strip and the diameter of the finished assembly indicate that no more than 0.0005 inch of air is present in the winding.

The spiral assembly is mounted in the fuel rod as shown in the upper part of Fig. 11.13. A cadmium cover is provided as with the foil method. The assembly is irradiated at the center of the TRX lattice.

After irradiation, 0.2-inch long pieces are cut from each successive turn of the spiral. These pieces are cut from that section of the spiral which is 180 degrees from the point where the innermost turn of the spiral starts. Identification of this position is made by notching the spiral after it is wound onto the uranium metal. The determination of the resonance capture is made by the radiochemical separation technique described previously in Sec. 11-6 on resonance escape probability. Each of the foils is dissolved separately, neptunium tracer is

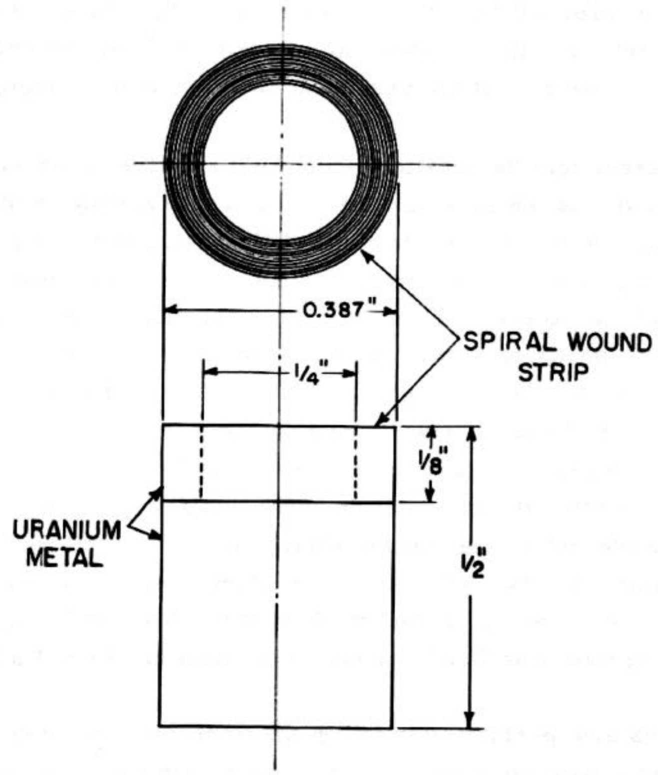

SPIRAL ASSEMBLY

Fig. 11.14 - Spiral Method for Determination of Distribution of Resonance Capture.

added and a neptunium separation carried out. Following this the solution is electroplated onto platinum foils and α- and β-counting is performed.

11.12 DATA TREATMENT - SPATIAL DISTRIBUTION OF RESONANCE NEUTRON CAPTURE

A composite curve made up of three foil runs and three spiral runs is plotted in Fig. 11.15, where foil activation is shown as a function of the distance from the rod surface. The runs were normalized together utilizing the points from 0.040 inch through the center of the rods. Points where the gradient of the curve varied rapidly were omitted from the normalization. This method of plotting was chosen, as compared to a histogram method, because all the foils were not of the same thickness. Since over 100 foils were used (different foils were used for each run), the normalization of runs would have been more difficult.

The positions of the foils were plotted at their mid-points. The position of the foil from the surface of the rod was determined by measuring the thickness of each foil. Since the surfaces of the detectors were not flat to better than 0.0004 inch due to oxidation and machining, the uncertainty in the position increases with depth. As discussed above, however, the effect of increasing foil mispositioning at large depths is not severe. The uncertainty in the position of the first foil is 0.0003 inch and the uncertainty in the position of the fifth foil is 0.001 inch.

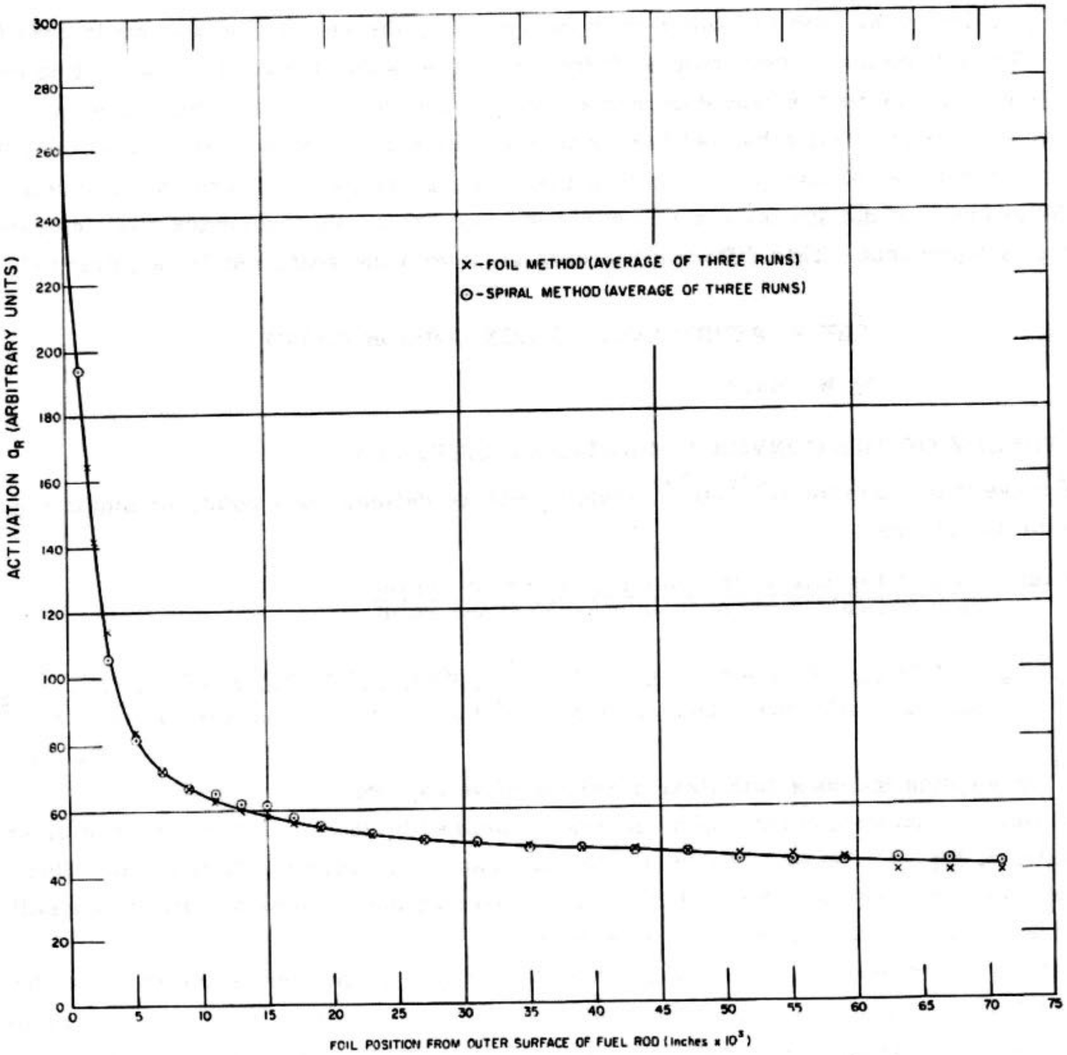

Fig. 11.15 - Spatial Distribution of Resonance Neutron Capture.

The position of the foil should also be corrected for the attenuation of the 103 kev activity and for the non-linearity of the spatial absorption through a foil. Only the latter effect need be considered for the spiral method. The position at which a point should be plotted is determined from the following expression:

$$\phi(x) = \frac{\int_d^{d+b} \phi(x)\, e^{-x/\lambda}\, dx}{\int_d^{d+b} e^{-x/\lambda}\, dx} \qquad \text{Eq. (11.33)}$$

where

$\phi(x)$ is the assumed spatial variation of the resonance flux. (Slab geometry can be assumed for the small distances considered.)

λ is the attenuation factor in uranium for the 103 kev X-ray (0.016 inch)

d is the depth of the foil measured from the surface

b is the thickness of the foil

Since the position of the first foil would vary the greatest, the calculation was made first for this foil. The attenuation effect would shift the position at which the first foil is plotted by 0.00014 inch. The correction would decrease for the other foils. Since other larger uncertainties exist, this correction has not been applied. The surface of the foil nearest the outer surface of the rod was always placed nearest the scintillation counter. For the first foil, where the gradient of the spatial absorption curve is greatest, the front-back counting rate difference is 4 per cent. This difference is consistent with the spatial shift calculated above.

THE MEASUREMENT OF CONVERSION RATIO

by W. Baer

11.13 THEORY OF THE CONVERSION RATIO MEASUREMENT

The conversion ratio for U^{235}-U^{238} systems will be defined for a point, or small region, of a reactor as follows:

$$\text{Conversion Ratio} = \frac{\text{Rate of Formation of Plutonium-239 at the Point}}{\text{Rate of Destruction of Uranium-235 at the Point}}$$

$$= \frac{\text{Rate of Epithermal Capture in } U^{238} + \text{Rate of Thermal Capture in } U^{238}}{\text{Rate of Epithermal Absorption in } U^{235} + \text{Rate of Thermal Absorption in } U^{235}} \qquad \text{Eq. (11.34)}$$

The U^{235} absorption includes both fission and radiative capture.

The over-all conversion ratio of a reactor is obtained by integrating the numerator and denominator of Eq. (11.34) over the volume of the reactor and forming their ratio. This section will be concerned with the technique for measuring the conversion ratio in a small region, i.e., a single fuel element, in a reactor.

Brief consideration should also be given to determining if the conversion ratio can be calculated from the measurements discussed previously. In connection with the resonance escape probability a quantity ρ was defined [Eq. (11.20)] which was the ratio of epithermal to thermal capture rates in U^{238}. This quantity was measured experimentally by a bare and cadmium-covered foil measurement. Another parameter which is required is the quantity R defined as the ratio of thermal capture rate in U^{238} to the sum of the thermal capture rate in U^{235} and U^{238} [Eq. (11.19)]. The parameter R is determined by integrating cross sections. Finally, the ratio of the epicadmium fission rate in U^{235} to the total fission rate was defined as δ^{25} [Eq. (11.31)]. This parameter is related to the cadmium ratio R_c of U^{235}.

From these quantities an expression can be deduced for the conversion ratio

$$\text{C. R.} = (\rho + 1)\left(\frac{R}{1 - R}\right)\left(\frac{R_c - 1}{R_c}\right) \qquad \text{Eq. (11.35)}$$

The only assumption necessary is that the ratio of epithermal absorption rate in U^{235} to the total absorption rate is the same as the ratio of the respective fission rates, i.e., the epithermal value of α^{25} for U^{235} is the same as the thermal value.

Since in general the epithermal-to-thermal flux ratio will vary from point to point in a complex reactor, it is necessary to measure ρ at the point in the lattice at which the conversion ratio is desired. Similarly, R_c will vary from point to point.

In developing a technique for measurement of the conversion ratio in the blanket lattice of the PWR reactor, a somewhat more direct approach was finally adopted. This method eliminated the necessity for exposing both bare and cadmium-covered foils in each fuel rod of the lattice. The method in essence is as follows: Exposing a high U^{238} content foil permits a measurement to be made which is proportional to the plutonium formed in the foil. This uses the measurement technique developed for the resonance escape probability measurement. Exposing a highly enriched foil permits a measurement to be made which is proportional to the U^{235} fissions which have occurred. This is the measurement technique developed for the thermal utilization measurement. The factors of proportionality corresponding to the absolute events in these two foils need not be obtained independently. Only the ratio of the proportionality factors is required. By exposing the foils in a highly thermal flux and measuring the counting rate ratios, the factors can be determined since the expected ratios of activation can be calculated from cross-section data. The equations for this will be developed to clarify the discussion.

Suppose that a foil having a high U^{238} content is irradiated and the decay of Pu^{239} to the ground state is measured as a function of time after shutdown by either of the methods described in connection with the resonance escape probability measurement. Let $P_b(t)$ be the counting rate of the foil as a function of time after shutdown. The total number of U^{238} captures in the foil during irradiation is related to $P_b(t)$ by a factor which is a function of time. Let $K_1(t)$ be this factor defined so that it gives the capture per U^{238} atom present in the foil.

$$\text{No. of } U^{238} \text{ absorptions per } U^{238} \text{ nucleus present} = K_1(t)\ P_b(t) \qquad \text{Eq. (11.36)}$$

Similarly, suppose that a foil containing enriched uranium is exposed. The gamma activity of this foil will be due mainly to fission products. This activity as measured will be denoted $F_b(t)$. As before, a factor $K_2(t)$ is defined which gives the number of fissions of U^{235} in the foil per U^{235} nucleus present.

$$\text{No. of } U^{235} \text{ fissions per } U^{235} \text{ nucleus present} = K_2(t)\ F_b(t) \qquad \text{Eq. (11.37)}$$

The number of U^{235} nuclei destroyed is determined by multiplying the number fissioned by $(1 + \alpha^{25})$ where

$$\alpha^{25} = \frac{\int_0^\infty \sigma_c^{25}(E)\ \phi(E)dE}{\int_0^\infty \sigma_f^{25}(E)\ \phi(E)dE} \qquad \text{Eq. (11.38)}$$

In this definition $\phi(E)$ is the neutron flux in the interval dE at E. The cross sections σ_c^{25} and σ_f^{25} are the U^{235} cross sections for capture and fission, respectively, as a function of energy. Thus:

$$\text{No. of } U^{235} \text{ nuclei destroyed per } U^{235} \text{ nucleus present} = K_2(t)\ F_b(t)\ (1 + \alpha^{25}) \qquad \text{Eq. (11.39)}$$

If Eq. (11.36) is multiplied by the number density N^{28} of U^{238} nuclei in the actual reactor fuel and Eq. (11.39) by N^{25}, the number density of U^{235} nuclei in the fuel, their quotient is the conversion ratio in the fuel.

$$\text{Conversion Ratio} = \frac{N^{28}K_1(t)\ P_b(t)}{N^{25}K_2(t)\ F_b(t)(1 + \alpha^{25})} \qquad \text{Eq. (11.40)}$$

It is now necessary to determine the functions $K_1(t)$ and $K_2(t)$ to obtain a value for the conversion ratio. Suppose a set of foils, one natural and one containing enriched uranium, are irradiated in a neutron flux with a large ratio of thermal to epithermal neutrons, so that the epicadmium activation of the foils may be neglected. In particular, a neutron spectrum similar to that found in a thermal column is desirable, since it is then possible to describe the neutron energy distribution quite precisely.

The activation per atom of the natural uranium foil due to U^{238} radiative captures in the thermal column may be written as

$$\left(\overline{\sigma_a^{28}\,\phi}\right)_{th} = K_1(t)\ P_{tc}(t) \qquad \text{Eq. (11.41)}$$

and the neutron absorption in the foil containing enriched uranium is

$$\left(\overline{\sigma_a^{25}\,\phi}\right)_{th} = K_2(t)\ F_{tc}(t)\ (1 + \alpha_{tc}^{25}) \qquad \text{Eq. (11.42)}$$

where the subscript (tc) indicates that the values of P (t), F (t) and α^{25} refer to the thermal column measurement. In Eqs. (11.41) and (11.42) ϕ is the thermal neutron flux at the irradiation position, and the cross sections $\overline{\sigma_a^{28}}$ and $\overline{\sigma_a^{25}}$ are the absorption cross sections of U^{235} and U^{238} averaged over the Maxwellian distribution of neutrons in the thermal column.

Solving Eqs. (11.41) and (11.42) for $K_1(t)$ and $K_2(t)$, respectively, and substituting in Eq. (11.40)

$$\text{Conversion Ratio} = \left(\frac{N_{28}}{N_{25}}\right) \frac{\left[\dfrac{P_b(t)}{P_{tc}(t)}\right]}{\left[\dfrac{F_b(t)}{F_{tc}(t)}\right]} \left(\frac{\overline{\sigma_a^{28}}}{\overline{\sigma_a^{25}}}\right)_{th} \left(\frac{1 + \alpha_{tc}^{25}}{1 + \alpha^{25}}\right) \qquad \text{Eq. (11.43)}$$

It is evident that the irradiations in the blanket and the thermal column must have the same duration in order to obtain meaningful values of $K_1(t)$ and $K_2(t)$. In addition, $P_b(t)$ and $P_{tc}(t)$ must be measured at the same time after the end of the irradiation. A similar requirement is made on the experimental values of $F_b(t)$ and $F_{tc}(t)$, but the quantities F(t) and P(t) need not be measured at the same time. In Eq. (11.43) the only quantity which is not readily obtained is the value of α^{25}. However, since the epithermal neutron flux magnitude is much lower than the thermal flux, the weighted value of α^{25} is not very much different that α_{tc}^{25}. For practical purposes, the ratio $(1+\alpha_{tc}^{25}/1+\alpha^{25})$ is set equal to unity. The conversion ratio may then be written

$$\text{Conversion Ratio} = \left(\frac{\Sigma_a^{28}}{\Sigma_a^{25}}\right)_{th} \frac{\left[\dfrac{P_b(t)}{P_{tc}(t)}\right]}{\left[\dfrac{F_b(t)}{F_{tc}(t)}\right]} \qquad \text{Eq. (11.44)}$$

In Eq. (11.44) Σ_a^{28} is the product $N_{28}\overline{\sigma_a^{28}}$ and similarly Σ_a^{25} is equal to $N_{25}\overline{\sigma_a^{25}}$. The number density applies to the fuel; the cross section is averaged over a Maxwellian spectrum in the thermal column.

11.14 CONVERSION RATIO MEASUREMENT - EXPERIMENTAL METHOD

As developed in the preceding section, a determination of the conversion ratio by this technique involves measurement of two relative quantities. The Pu^{239} production and U^{235} fission rates in the reactor are compared with the same quantities after irradiation of a similar set of foils in a thermal column. Knowledge of the neutron spectrum in the thermal column makes possible an absolute normalization to obtain a value of the reactor conversion ratio.

The experimental arrangement of the foils for critical assembly irradiations is shown in Fig. 11.16. The aluminum foil separators are used to insure that the foils do not contaminate each other. The foils are all 0.005 inch thick. Natural foils 1 and 4 are used to measure P(t). Natural foils 2 and 3 are used to buffer foils 1 and 4 from flux depression effects of the enriched foils. If a foil loading is made in the sequence natural No. 1, enriched No. 1, natural No. 2, enriched No. 2; then it is consistently observed that the ratio

$$\frac{P_1(t)}{P_2(t)} = 1.02 \pm 0.01,$$

which indicates some shielding of the natural foil surrounded by the enriched foils. For this reason, the scheme shown in Fig. 11.16 was adopted.

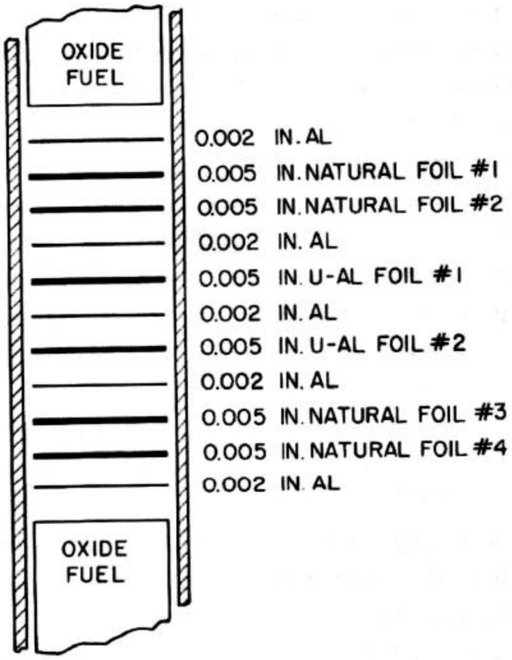

CONVERSION RATIO FOIL LOADING

Fig. 11.16 - Exploded View of Foil Arrangement in Fuel Rod.

The foils are sandwiched between two uranium oxide pellets and held together by 0.001-inch-thick Mylar tape. The foil package is then inserted into an aluminum fuel rod. An O-ring gasket seal and end cap are used to seal the open end of the fuel rod.

The chemical separation technique described in Sec. 11.6 is used to measure the Pu^{239} production. The foils are dissolved, Np^{237} tracer is added and a radiochemical separation of the neptunium performed. The separated material is electroplated on a platinum foil for the necessary α and β counting.

In practice, quantities proportional to Pu^{239} production in the reactor and thermal column are obtained at different times. The thermal column irradiations, assuming continued stability of electronic equipment, need only be done once and can be applied to all subsequent reactor irradiations. Thermal column irradiations were performed at the BNL thermal column, where the cadmium ratio for gold detectors is ~4000. Six irradiations of one hour duration were made. To ensure that each irradiation and subsequent chemical separation form a consistent set, two natural uranium foils were irradiated together. If subscripts (1) and (2) designate these foils, the ratios

$$\left(\frac{P_1}{P_2}\right)_{tc}$$

of normalized Np^{239} count rates should be unity at any time (t) after the end of each irradiation. The foils were irradiated in the center of the 8-inch square thermal column, and the four foils used (two natural and two enriched) were placed in an aluminum holder in a cloverleaf pattern with 1/2 inch between foil centers. Other investigators have shown the thermal column flux to be essentially flat across the span of the holder.

In the reactor irradiations, two natural uranium foils are also irradiated simultaneously for one hour as in the resonance escape probability measurement. After data reduction it is required that the normalized ratio P_{b_1}/P_{b_4} for a given position be 1.00 ± 0.02 to be acceptable. If the ratio is not within these limits, then neither value of P_b is used, since the technique usually does not permit identification of the incorrect chemical separation. Sometimes it is possible to confirm which separation is poor by examining the γ-ray spectrum from each neptunium deposit. It has been observed several times that Zr^{95} has passed through the separation process. Although a step of the chemical process is designed to remove zirconium, it appears that this particular technique is not always successful. The cause and remedy for this occasional failure is not known at this time.

A normalization similar to that described for the Pu^{239} production measurements is made to determine the number of U^{235} fissions. The foils used to detect the U^{235} fissions are 0.005 inch thick, 10 w/o enriched U^{235} in aluminum. These foils are used to ensure that there is no large flux depression caused by the foil when it is placed in the reactor. Calculations employing Bothe's expressions for flux depression indicate a flux depression of ~1.5 per cent with the 10 w/o uranium in aluminum foils in an isotropic thermal neutron flux. The fission product γ-rays are detected using a 1-3/4-inch-diameter by 2-inch-thick NaI(Tl) crystal and electronic counting equipment of the type discussed for the thermal utilization measurement by the integral method (cf. Sec. 11.3).

An estimate of the errors associated with this technique has been made by combining the uncertainties of the various procedures. The over-all uncertainty is estimated to be between ±0.02 and ±0.03 in a value of the conversion ratio of approximately one.

REFERENCES

1. J. R. Brown, B. H. Noordhoff, A. E. Profio, and W. O. Bateson, Reactor Properties of Water Moderated Slightly Enriched Uranium Lattices, Report WAPD-117, November 1954.
2. A. Z. Kranz, Measurements of Thermal Utilization, Resonance Escape Probability and Fast Fission Factor of Water Moderated Slightly Enriched Uranium Lattices, Report WAPD-134, September 1955.
3. A. Z. Kranz and G. G. Smith, A Second Report on Measurements of f, p, and ϵ of Water Moderated Slightly Enriched Uranium Lattices, Report WAPD-151, May 1956.
4. D. Klein, A. Z. Kranz, G. G. Smith, W. Baer, and J. DeJuren, Measurements of Thermal Utilization, Resonance Escape Probability, and Fast Effects in Water Moderated, Slightly Enriched Uranium and Uranium Oxide Lattices, Report WAPD-T-572, June 1957.
5. D. Klein, W. Baer, and G. G. Smith, Spatial Distribution of U-238 Resonance Neutron Capture in Uranium Metal Rods, Report WAPD-T-640, August 1957.
6. W. Baer, M. J. Galper, and N. Carbone, Measurements of the Conversion Ratio of the PWR Critical Facility Blanket, Report WAPD-T-528, July 1957.
7. H. Kouts, et al, Exponential Experiments with Slightly Enriched Uranium Rods in Ordinary Water, Session 21A, Volume 5, Paper P/600, International Conference on Peaceful Uses of Atomic Energy, Geneva, 1955.
8. G. Price, Fast Effect Measurements, Report BNL-1690, March 1956.
9. G. C. Hanna and P. R. Tunnecliffe, Report CRRP 623, January 1956.

Part IV

ANALYSIS OF SELECTED REACTOR EXPERIMENT DATA

Reactor experiments are performed to increase the confidence of the nuclear designer in his methods. Unavoidably, a single measured reactor parameter, for example the critical buckling, is the result of the interplay of many factors. The experiment is an integral result which does not indicate to the nuclear designer whether good agreement with experiment is coincidental or which of the many constituent factors is responsible for a serious disagreement. A single reactor experiment result, or even several, is frequently inconclusive and can only serve to indicate to the nuclear designer that he is in difficulty. It cannot generally assure him that there is no serious uncertainty.

To provide the necessary degree of confidence, an entire field of experimental results is required. Futhermore, it is well to provide redundant data so that the discrepancies can be isolated. This portion of the handbook reports on the results of reactor experiments intended to provide such a field of data both for high U^{238} content reactors and for highly enriched reactors.

The various complexities which enter into reactor experiments must be considered in terms of the model used to analyze the experiments. In the few-group diffusion theory model, which forms the basis for the design of pressurized water reactors discussed in this volume, the various factors which enter the model are as follows:

1. The nuclear cross section data
2. The group-averaged diffusion constants and macroscopic cross sections
3. The small scale heterogeneity - on the scale of the fuel elements
4. The large scale heterogeneity - on the scale of subassemblies and clusters
5. The over-all geometry
6. The control surfaces and localized absorbers

The program of experiments described in this section was planned to minimize the number of these factors entering the analysis. The experiments were, in fact, designed basically to limit the factors to the first three. Large scale heterogeneity effects, item 4, and localized absorbers, item 6, were introduced only under controlled conditions. In all cases the geometry was such as to permit one-dimensional analysis. These experiments are frequently referred to as "clean", critical experiments.

In this portion of the handbook the emphasis is primarily placed on the comparison of calculation with the experimental results. The facilities, techniques and procedures used to obtain the data are discussed in the preceding chapters which make up Part III.

Three chapters are included in this part. Chapter 12 deals with the high-uranium-content reactors. Chapter 13 treats the highly enriched reactors, with and without water channel heterogeneity present. Chapter 14 covers localized absorber and control surface experiments in highly enriched reactors.

Chapter 12

THE ANALYSIS OF HIGH U^{238} CONTENT REACTOR EXPERIMENTS

12.1 INTRODUCTION

This chapter deals with the results of reactor experiments and parameter measurements aimed primarily at understanding the problems associated with high U^{238} content reactors. For convenience in making the assemblies critical at a convenient size, the uranium used was slightly enriched. The principal aim, however, was to measure those properties associated with the high U^{238} content in the reactor. The experiments were conducted in simple lattices of fuel rods and moderating water with a minimum of structural material and fuel element cladding.

The bulk of the experimental measurements were performed with metallic uranium fuel in a joint Brookhaven-Bettis program. In 1952, prior to the establishment of the joint program, measurements had been undertaken at Brookhaven on water-uranium lattices using uranium metal rods about 0.75 inch in diameter and enriched to 1.0 per cent. These measurements were conducted in an exponential assembly using the Brookhaven reactor as the source.

The joint Brookhaven-Bettis program was started in 1953 and used three lots of slightly enriched uranium metal rods. The enrichments were nominally 1.0 per cent, 1.15 per cent, and 1.3 per cent. The rods were initially 0.600 inch in diameter and, as the program progressed, each lot was reduced in diameter to 0.387 inch and finally to 0.250 inch. The overall joint program with metal rods thus involved nine lots of material. Due to mechanical difficulties in fabricating the 0.250-inch-diameter rods, however, the dimensional and straightness tolerances could not be met. The results obtained with this group of rods are considered inferior to the remainder of the data and the program was terminated without complete measurements on this group.

The program consisted initially of buckling measurements as a function of water-to-uranium ratio. The measurements were conducted in an exponential facility at Brookhaven and in a critical facility (TRX) at Bettis. As techniques were developed, other measurements were made on the lattice. These included fast fission factor, thermal utilization, resonance escape probability, reflector savings, epithermal fission in U^{235}, temperature coefficient of reactivity, and differential water height measurements for migration area. The Brookhaven facilities were modified later to include critical experimentation. The joint program was completed in 1957.

Starting in 1955 and continuing through 1957, an additional program of measurements on uranium-oxide lattices was undertaken at Bettis. This was stimulated primarily by the interest in UO_2 fuel elements for the PWR. In this program, the same measurements were made as with the metal fuel. While only one enrichment was used, namely 1. 3 per cent, two oxide densities (69 and 96 per cent of theoretical density) and two fuel rod diameters (0. 600 inch and 0. 388 inch) were included in the program.

The material in this chapter is based on the results of these programs. While Bettis results are reported completely, Brookhaven data are also reported, where significant, as a basis for comparison or to extend the range of information. The description of the lattices used is given in Chap. 9, Secs. 9. 7 through 9. 11. The parameter measurement techniques are described in Chap. 11.

RESULTS OBTAINED WITH REACTOR EXPERIMENTS

by J.R. Brown

12. 2 LATTICE GEOMETRY

The fuel rod used in the experiments discussed in this portion of the chapter is shown in Fig. 9. 14 of Chap. 9. The cylindrical-rod fuel element, 48 inches long, is clad in an aluminum tube 0. 028-inch thick with a 0. 005-inch radial gap between the fuel and the aluminum cladding. The fuel rods are arranged in a hexagonal lattice as shown in the photograph of Fig. 9. 13. The basic unit of this lattice is an equilateral triangle; this is shown in Fig. 12. 1.

The equivalent cell radius, r_e, is also shown in Fig. 12. 1. This is the radius of a cylindrical cell whose volume is the same as two of the triangular cells of the lattice. The expression for r_e is given in Fig. 12. 1 in terms of the distance, x, between adjacent rod centers. The volume assigned to the over-all reactor is taken as the number of rods times the volume of the unit cell. In analysis of the reactor, this total volume is considered to be a right circular cylinder because of the good approximation of the periphery to such a cylinder.

In describing the lattice parameters the most frequently used variable is the water-to-uranium volume ratio, W/U. For the metal lattices this is simply the volume of moderator in a unit cell to the volume occupied by uranium fuel in a unit cell. For the oxide lattices the uranium volume is taken to be the volume of uranium metal corresponding to the weight of uranium in the uranium oxide fuel rod. Thus, for either the metal or oxide lattices, a given W/U ratio implies a specific hydrogen-to-uranium atomic ratio.

The geometries and nuclear densities of all of the lattices which were made critical at Bettis are given in Table 12. 1. In the oxide-fueled lattices, a slight hydrocarbon contamination, about 0. 5 per cent, as well as a slight admixture of UO_3, about 2. 5 per cent, have been taken into account in computing the number densities. The number densities given take into account the actual enrichments and volume ratios.

Table 12.1--LATTICE GEOMETRY AND NUCLEAR DENSITIES OF BETTIS CRITICAL LATTICES (at 20°C)

Lattice Designation	Nominal Ratio	Measured Enrichment	Dimensions		Volumetric Ratios			Homogenized Nuclear Densities ($cm^{-3} \times 10^{20}$)					
Fuel	W/U	Weight %	x(cm)	r_e(cm)	W/U	Al/U	W/UO_2	N_{U235}	N_{U238}	N_H	N_O	N_{Al}	N_C
U Metal 1.3%, 0.600 in.	1.5	1.294	2.404	1.263	1.515	0.198		2.276	171.8	368.2	184.1	43.43	
	2		2.616	1.374	2.017	0.198		1.929	145.3	414.5	207.2	36.80	
	3		2.990	1.570	3.011	0.198		1.477	111.3	473.8	236.9	28.18	
U Metal 1.15%, 0.600 in.	2	1.145	2.616	1.374	2.017	0.198		1.707	145.5	414.5	207.2	36.80	
	3		2.990	1.570	3.011	0.198		1.307	111.4	473.8	236.9	28.18	
U Metal 1.3%, 0.387 in.	2	1.296	1.725	0.906	2.024	0.318		1.843	138.8	397.4	198.7	56.41	
	3		1.961	1.030	3.018	0.318		1.426	107.4	458.3	229.1	43.64	
UO_2, 7.53 gm/cm^3 1.3%, 0.601 in.	3	1.311	2.205	1.158	3.048	0.198	1.071	0.9644	71.68	312.7	302.3	51.88	6.41
	4		2.359	1.239	4.000	0.198	1.405	0.8420	62.59	357.8	306.3	45.29	5.60
	5		2.512	1.319	5.000	0.198	1.756	0.7423	55.22	394.2	309.6	39.97	4.94
UO_2, 7.52 gm/cm^3 1.3%, 0.388 in.	4	1.311	1.558	0.818	3.953	0.317	1.386	0.8053	59.85	338.2	291.0	69.29	5.35
	5		1.652	0.868	4.947	0.317	1.734	0.7148	53.13	375.2	295.8	61.50	4.75
UO_2, 10.53 gm/cm^3 1.3%, 0.383 in.	3	1.311	1.558	0.818	2.904	0.324	1.426	1.102	81.92	338.4	334.9	69.14	0.19
	3.6		1.652	0.868	3.622	0.324	1.779	0.9797	72.82	375.0	334.8	61.46	0.17
	5		1.806	0.948	4.878	0.324	2.396	0.8203	60.97	422.6	334.7	51.46	0.15

x Distance between adjacent fuel rod centers (see Fig. 12.1)

r_e Radius of a circle of area equal to the unit cell area (see Fig. 12.1)

Al Aluminum

W Water

U Total uranium (density 18.9 gm/cm^3)

O Oxygen

C Carbon (from residue of hydrocarbon agglomerating agent)

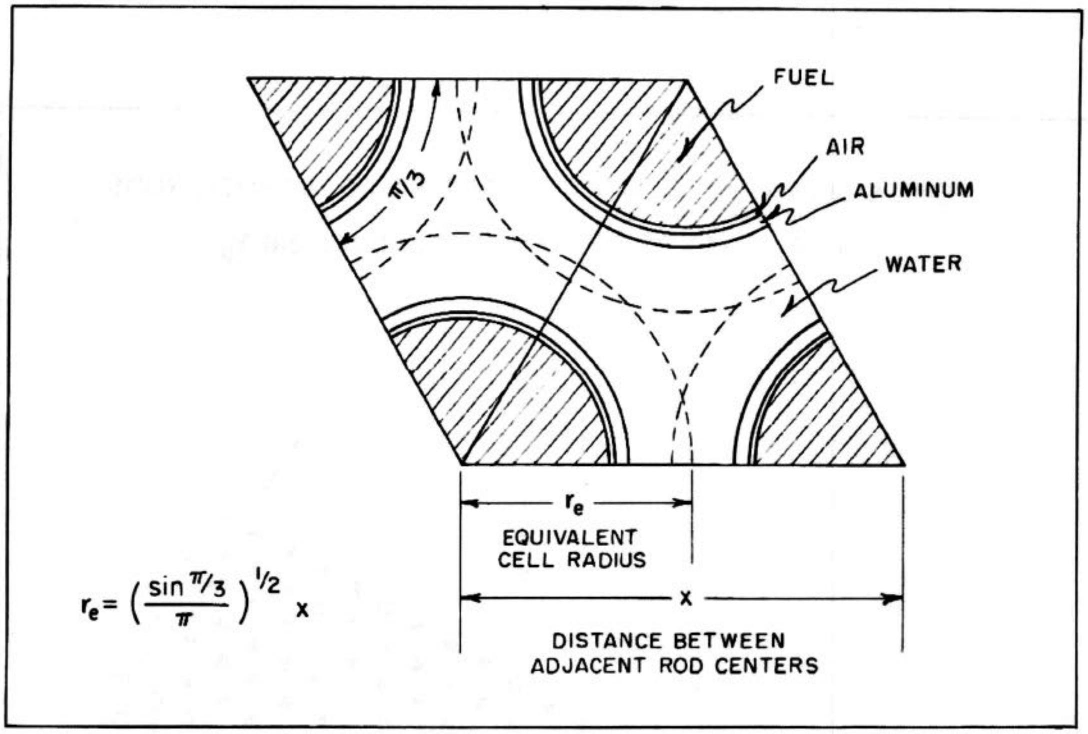

Fig. 12.1 - Cross Section of Unit Lattice Cell.

12.3 CRITICAL BUCKLING AND REFLECTOR SAVINGS

The dimensions of the equivalent bare reactor were obtained, in the Bettis procedure, from flux traverses. The assembly was made critical by adjustment of the total number of fuel rods, N, with no control rods in the reactor and with water completely covering the reactor. The periphery of the reactor was made as nearly cylindrical as possible. Figure 12.2 shows the loading pattern of a typical lattice. The solid circles are the fuel rod locations used; the open circles are the adjacent empty positions in the matrix plate.

The critical reactor was operated at a low power level sufficient to provide a measurable fission product activity in the fuel rods, after which radial and axial scans of the gamma activity of selected fuel rods were taken. The resulting distribution of activity was fitted by a least squares procedure to obtain the radial and axial bucklings.[1]

In the central region of a lattice whose dimensions are large compared with the characteristic neutron lengths, the neutron flux is separable into radial and axial functions independent of neutron energy. For a cylindrical reactor the flux, ϕ, in the asymptotic region may be written as

$$\phi = A J_o (B_r r) \cos (B_z z) \qquad \text{Eq. (12.1)}$$

where A is a constant. The radial buckling, B_r^2, and the axial buckling, B_z^2, are given as follows:

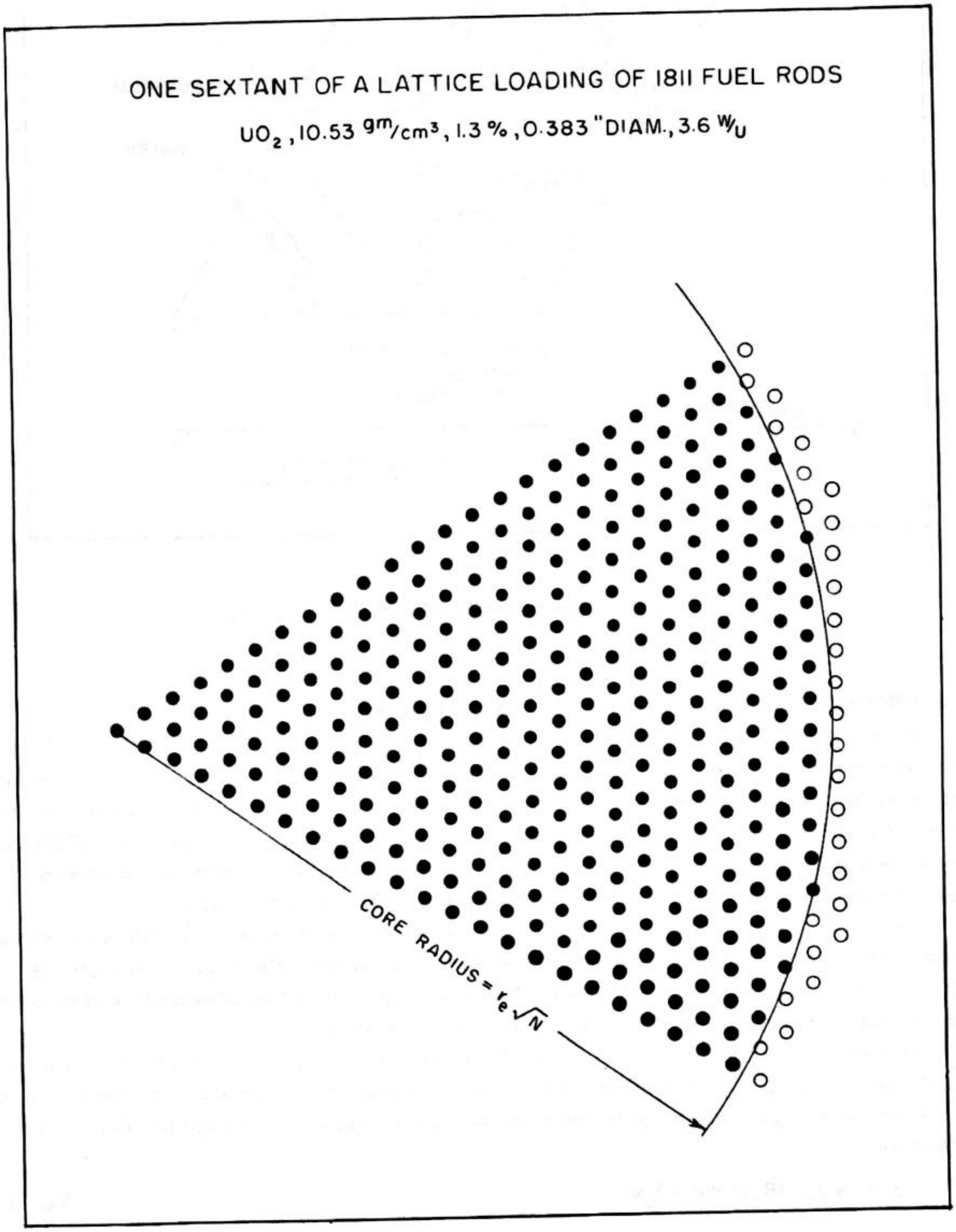

Fig. 12.2 - Critical Loading Pattern for an Oxide Rod Lattice.

$$B_r^2 = \left(\frac{2.405}{R_e}\right)^2 \qquad \text{Eq. (12.2a)}$$

$$B_z^2 = \left(\frac{\pi}{H_e}\right)^2 \qquad \text{Eq. (12.2b)}$$

where R_e and $H_e/2$ are the values of r and z, respectively, at which the radial and axial asymptotic fluxes extrapolate to zero.[2] If R and H are the physical dimensions of the reactor,

$$R_e = R + \lambda_r \qquad \text{Eq. (12.3a)}$$

$$H_e = H + \lambda_h \qquad \text{Eq. (12.3b)}$$

where λ_r is the radial reflector savings and λ_h is the total axial reflector savings. The total geometrical buckling is given by

$$B_g^2 = B_r^2 + B_z^2 \qquad \text{Eq. (12.4)}$$

A typical least squares fit of a radial distribution to obtain the radial buckling is shown in Fig. 12.3. The corresponding axial fit is shown in Fig. 12.4. The technique of point selection near the core boundary and the method of making the fit are discussed in Reference 1. From these fits, the values of R_e and H_e are obtained directly.

With R_e and H_e known, the radial and axial buckling B_r^2 and B_z^2 may be calculated using Eqs. (12.2a) and (12.2b); with B_r^2 and B_z^2 known, the total buckling B_g^2 may be calculated by Eq. (12.4). The reflector savings λ_r and λ_h are obtained by Eqs. (12.3a) and (12.3b). H is taken equal to the height of the fuel. The quantity R is determined from the effective cell radius, r_e, and the total number of fuel rods, N, by the equation

$$R = r_e \sqrt{N} \qquad \text{Eq. (12.5)}$$

which results from equating the total active radial area of the core to N times the cell area.

The results for the lattices measured at Bettis are given in Table 12.2. At the time of the measurements on some of the earlier metal lattices, the reflector savings measurements technique described above had not been developed. For these cases the Brookhaven values of the reflector savings are used. These were determined from a series of exponential experiments using successively larger core radii.[3]

In general, the Bettis and Brookhaven results for buckling agreed well as did the reflector savings results. Figure 12.5 shows a plot of some of the data on critical bucklings. For comparison, the Brookhaven data for the 1.3 per cent, 0.387-inch-diameter metal rods are also shown. Because the Brookhaven results were obtained from exponential experiments, a much wider range of lattices could be studied with the limited amount of material.

The results of Brookhaven buckling measurements on the 0.387-inch-diameter and 0.600-inch-diameter metal rods are presented graphically in Figs. 12.6 and 12.7. The Bettis results on metal fuel are shown for comparison. The terms BNL-I and BNL-II refer to an early and a later set of measurements, respectively.

The Brookhaven values for the radial reflector savings for the metal lattices are given in Fig. 12.8. Smooth curves have been drawn to give a reasonable fit to the experimental data. Within the precision of the experimental data there seems to be no dependence of the reflector

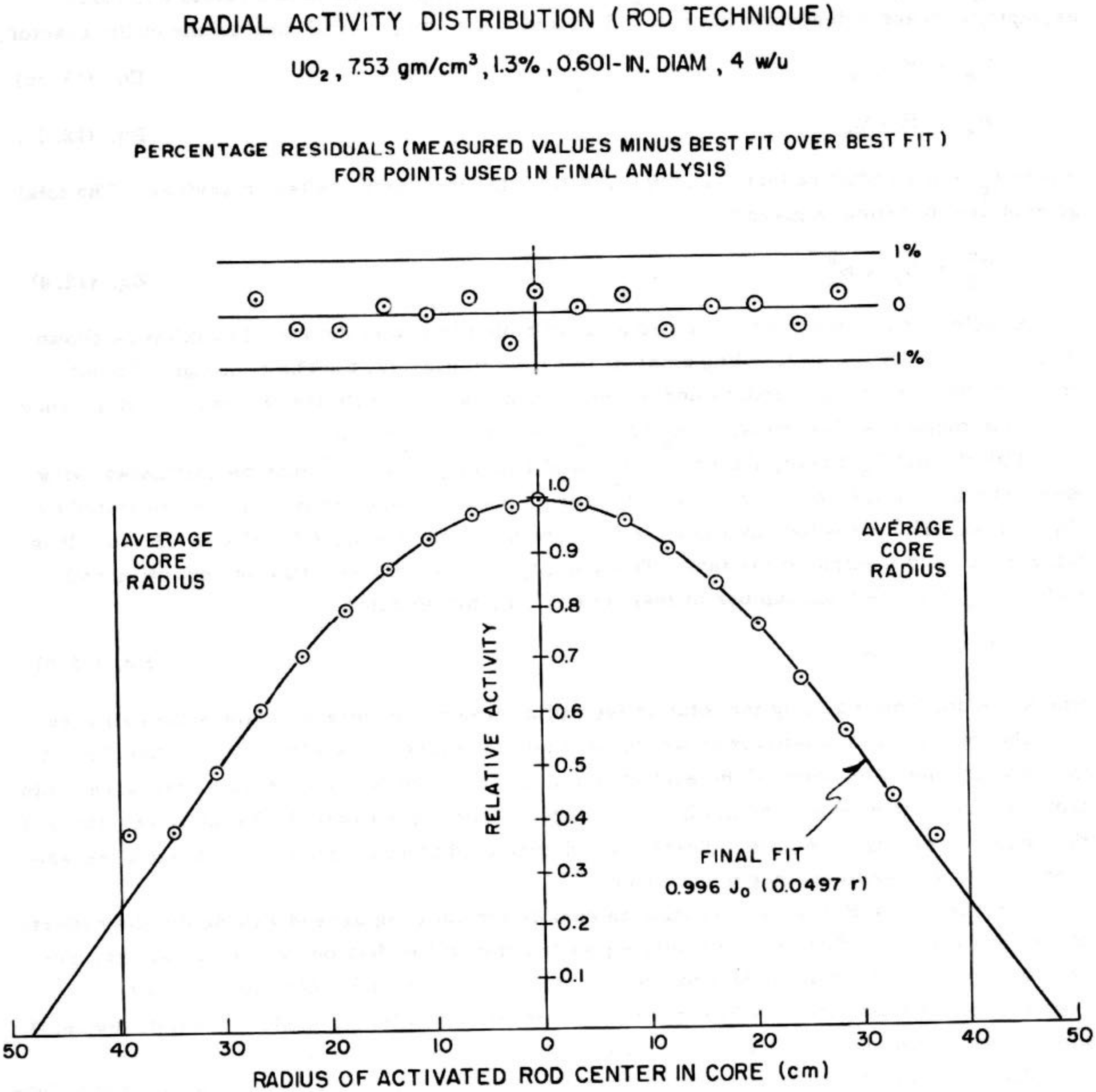

Fig. 12.3 - Least Squares Fit of Activity to Obtain Radial Buckling.

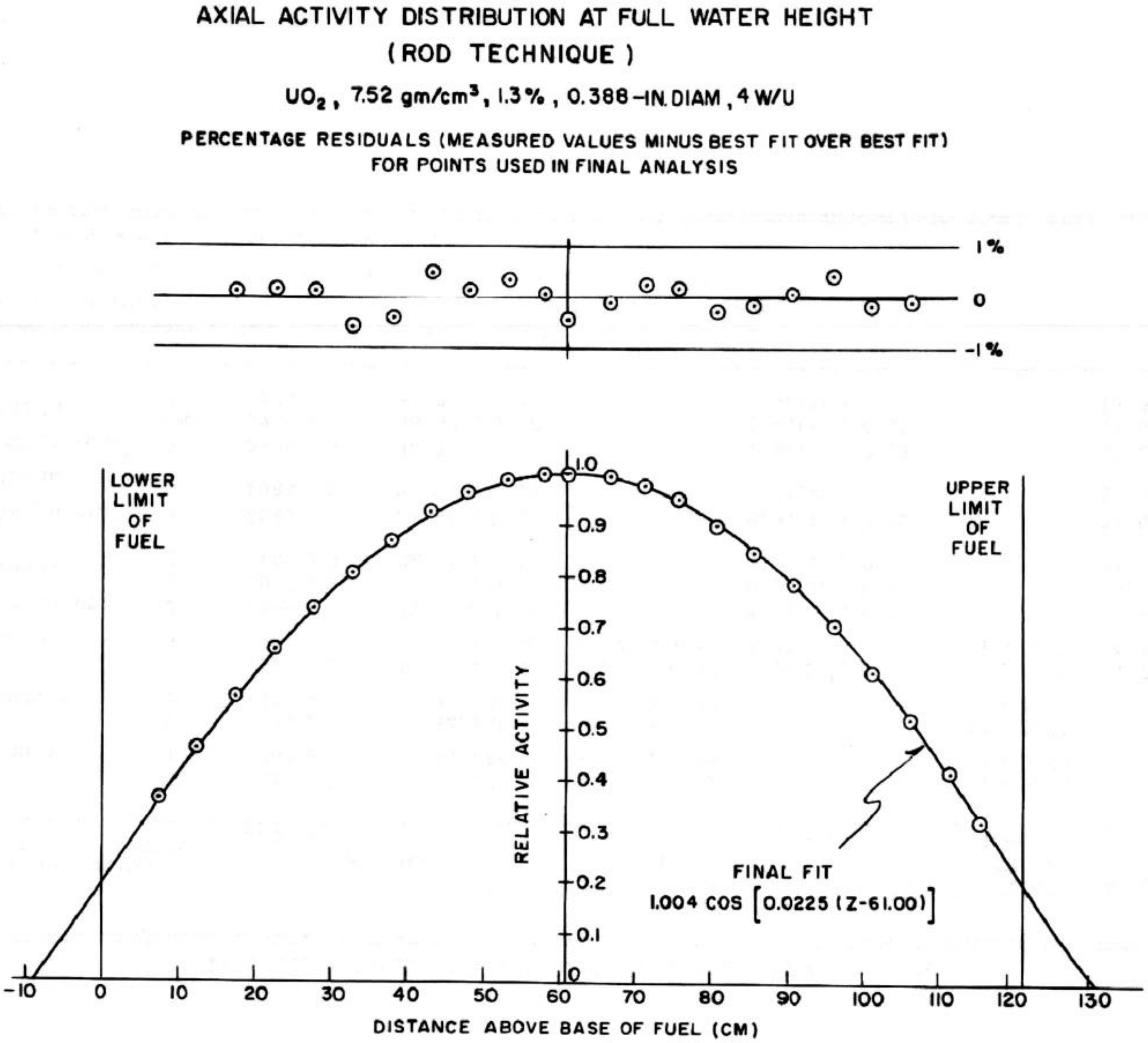

Fig. 12.4 - Least Squares Fit of Activity to Obtain Axial Buckling.

Table 12.2--BUCKLING AND REFLECTOR SAVINGS RESULTS

Lattice Designation		Critical No. of Fuel Rods at 20 °C	Critical Buckling (cm^{-2}) x 10^4		Radial Reflector Savings		Total Axial Reflector Savings (cm)
Fuel	W/U		Bettis (20 °C)	BNL‡	Bettis (cm)	BNL ‡ (cm)	
U Metal	2	335 ± 1	61.12*	61.08 ± 0.32		7.04 ± 0.06	
1.3%, 0.600 in.	3	264 ± 1	61.09*	60.99 ± 0.26		6.70 ± 0.05	
U Metal	2	464 ± 1	48.31*	48.22 ± 0.31		7.10 ± 0.25	
1.15%, 0.600 in.	3	377 ± 1	47.26*	47.12 ± 0.33		6.68 ± 0.10	
U Metal	2	904 ± 2	53.55 ± 0.48	52.56 ± 0.39	7.40(2)† ± 0.17	7.46 ± 0.09	14.07(1) ± 0.71
1.3%, 0.387 in.	3	630 ± 2	58.2 ± 1.00	59.25 ± 0.33	7.22(1) ± 0.31	6.94 ± 0.07	14.23(1) ± 0.82
UO_2, 7.53 gm/cm^3	3	1269 ± 3	28.37 ± 0.06		8.55(5) ± 0.06		17.82(5) ± 0.23
1.3%, 0.601 in.	4	1027 ± 3	30.17 ± 0.06		8.36(4) ± 0.06		16.72(4) ± 0.19
	5	987 ± 3	29.06 ± 0.07		7.92(4) ± 0.07		15.90(5) ± 0.22
UO_2, 7.52 gm/cm^3	4	3045 ± 3	25.28 ± 0.10		8.41(4) ± 0.12		17.06(6) ± 0.51
1.3%, 0.388 in.	5	2784 ± 3	25.21 ± 0.10		8.08(4) ± 0.12		15.37(3) ± 0.26
UO_2, 10.53 gm/cm^3	3	2173 ± 3	32.59 ± 0.15		7.86(6) ± 0.12		15.27(11) ± 0.41
1.3%, 0.383 in.	3.6	1755 ± 3	35.47 ± 0.18		7.41(5) ± 0.13		14.69(8) ± 0.43
	5	1575 ± 3	34.22 ± 0.13		7.10(7) ± 0.10		14.52(8) ± 0.17

* Calculated from number of fuel rods using BNL values of radial reflector savings and assuming the axial reflector savings is twice the radial value

‡ From Reference 3 and information received from R. Sher, July 1956

† Number of separate determinations indicated in parentheses

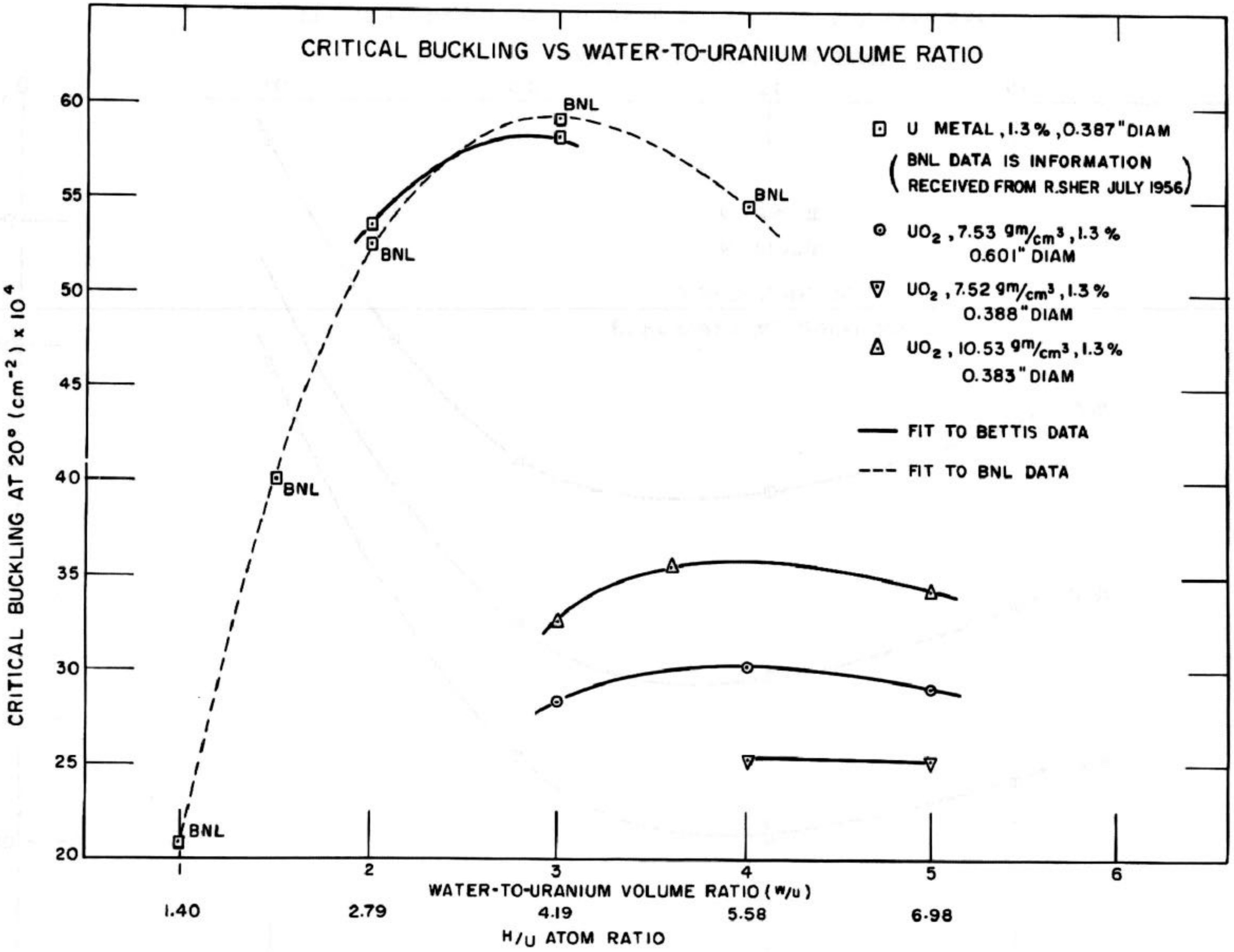

Fig. 12.5 - Critical Bucklings of Various Lattices.

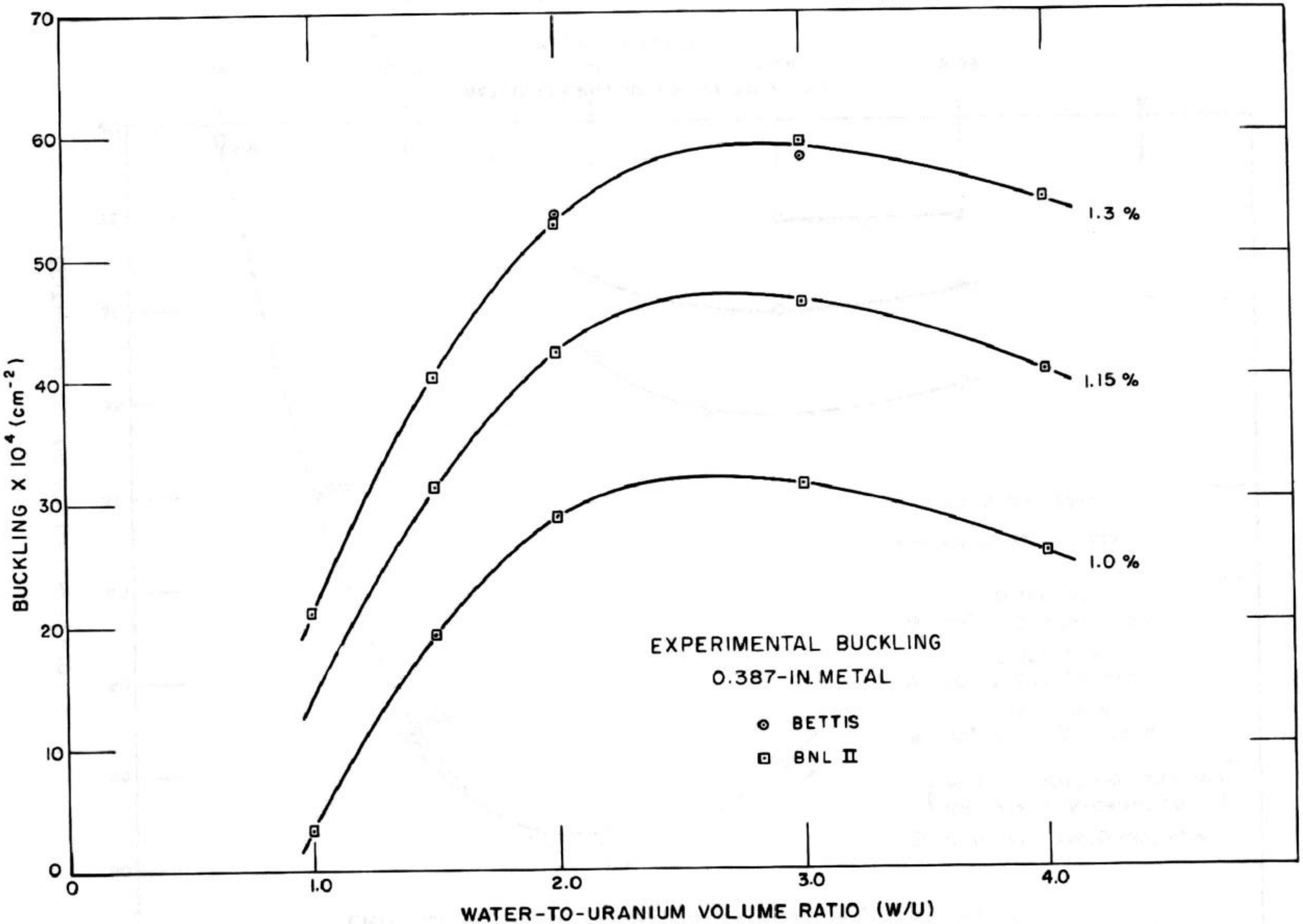

Fig. 12.6 - Experimental Buckling Data for 0.387-Inch Metal Rods.

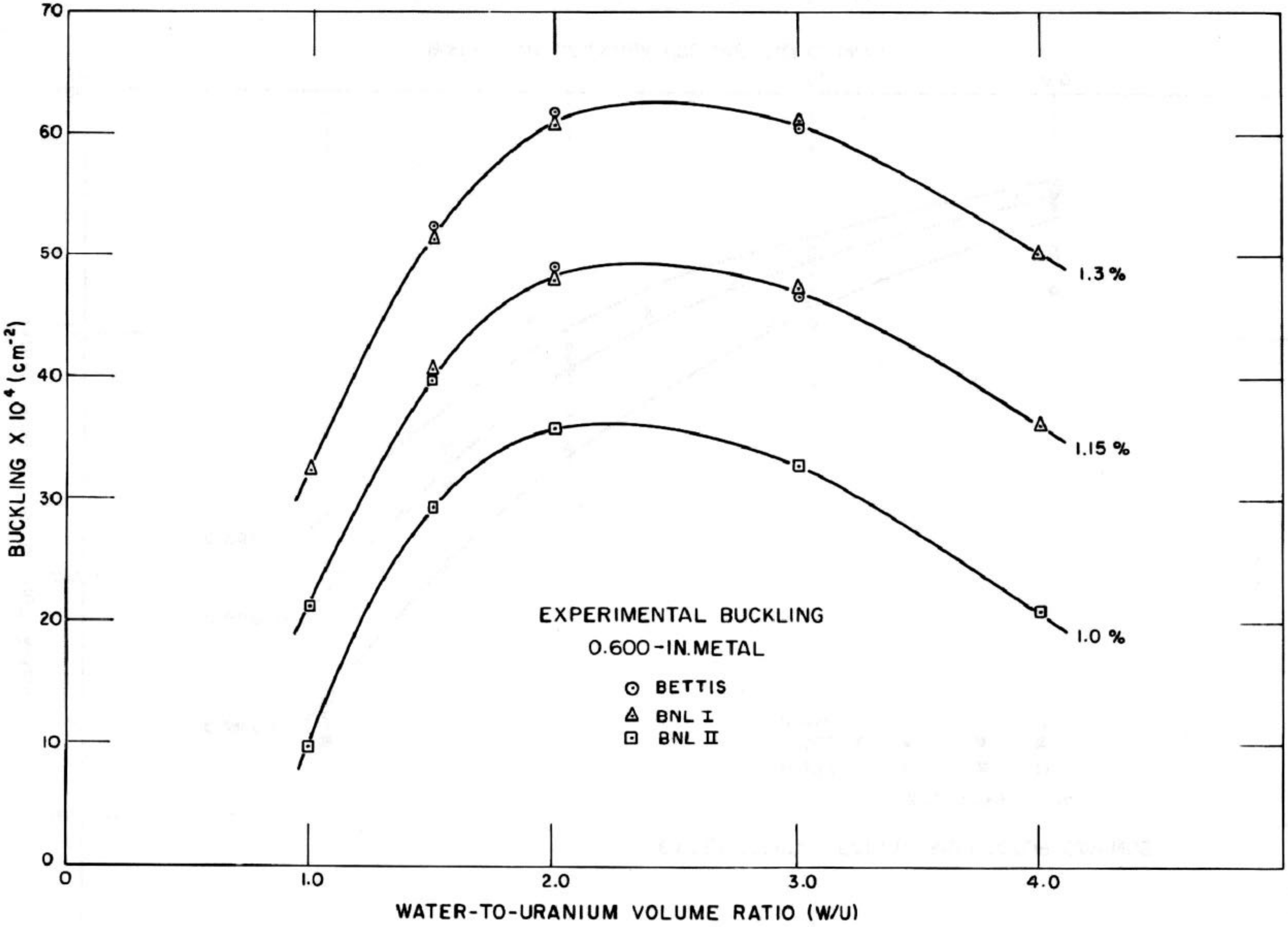

Fig. 12.7 - Experimental Buckling Data for 0.600-Inch M -tal Rods.

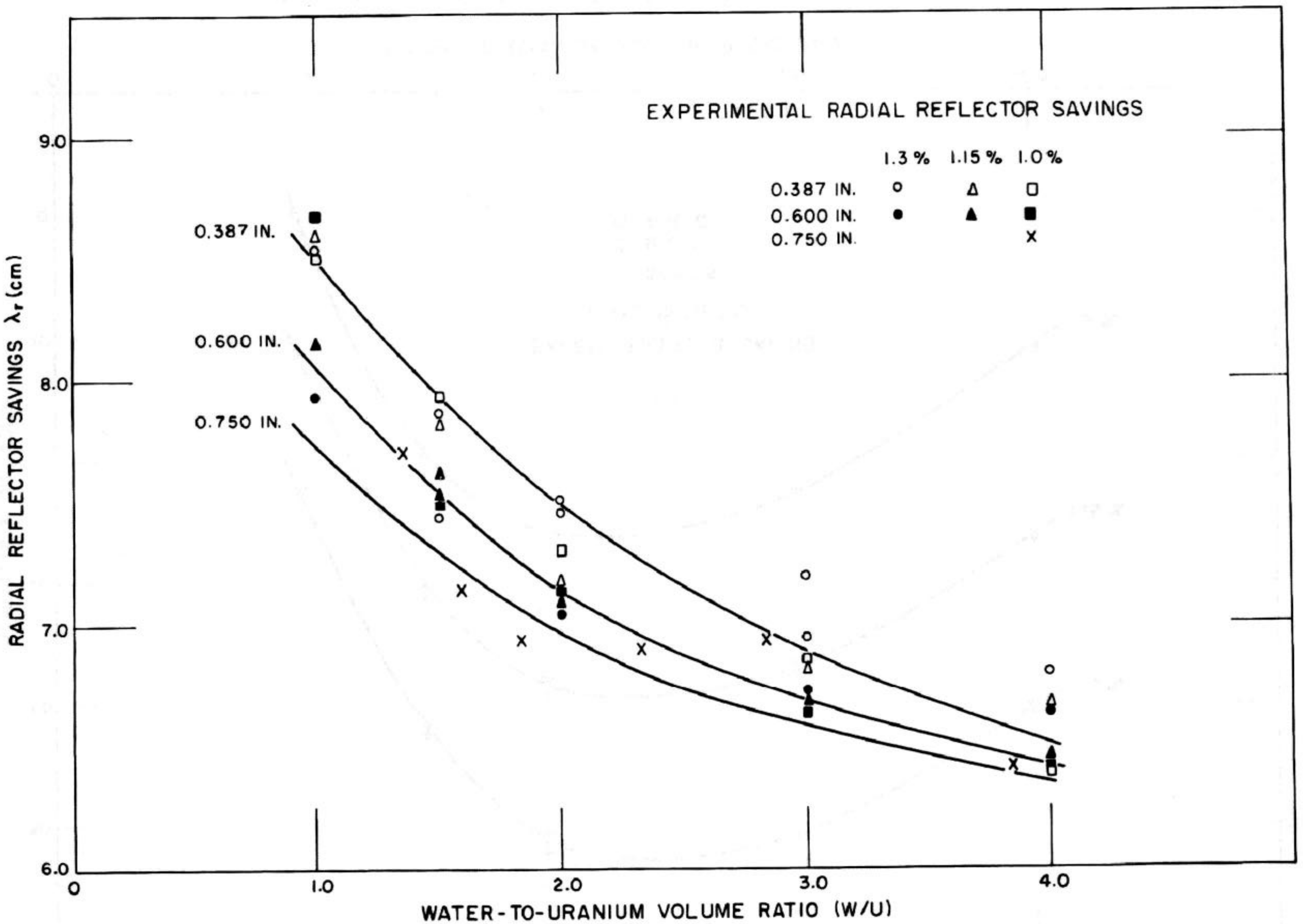

Fig. 12.8 - Reflector Savings for Metal Lattices (Brookhaven Data).

savings on enrichment. The principal parameter is the water-to-uranium ratio and, to some extent, the rod size.

12.4 TEMPERATURE COEFFICIENT OF REACTIVITY

The temperature coefficient of reactivity of all the TRX lattices was determined by measuring the reactivity change associated with a given temperature rise (from 20°C to about 50°C). The reactivity is measured by a period change associated with a given temperature change. In the results reported here, Keepin's data for delayed neutron periods and yields have been used[4] in the inhour equation to calculate reactivity from period measurements. Reference 1, Appendix B, gives the explicit form of the inhour equation used to calculate the reactivity.

From the experimental data a plot of temperature coefficient versus temperature is developed. An example is shown in Fig. 12.9. The data are fitted by least squares to a straight line with each point weighted inversely by the square of the estimated error at that point.

The data for all of the TRX lattices when treated in this way are tabulated in Table 12.3. The results of the fit are given in terms of the value of the coefficient at 20°C and 40°C. The quoted error is determined from the standard deviation of the residuals in the least squares procedure. The numbers in parentheses indicate the number of points used in the least squares fit.

In all but two cases the temperature coefficient is negative at 20°C. In every case the temperature coefficient is more negative at 40°C than at 20°C.

Table 12.3--TRX TEMPERATURE COEFFICIENT DATA

Lattice Designation		$\partial \rho/\partial \theta$ (°C^{-1}) x 10^4	
Fuel	W/U	20°C	40°C
U Metal	2	-0.36(2)* ± 0.02	-0.76 ± 0.02
1.3%, 0.600 in.	3	+0.10(6) ± 0.02	-0.19 ± 0.02
U Metal	2	-0.40(12) ± 0.02	-0.74 ± 0.02
1.15%, 0.600 in.	3	+0.11(4) ± 0.02	-0.14 ± 0.02
U Metal	2	-0.46(8) ± 0.04	-0.82 ± 0.04
1.3%, 0.387 in.	3	-0.47(6) ± 0.02	-0.78 ± 0.02
UO_2, 7.53 gm/cm^3	3	-0.71(10) ± 0.02	-0.93 ± 0.02
1.3%, 0.601 in.	4	-0.66(6) ± 0.02	-0.87 ± 0.02
	5	-0.55(6) ± 0.02	-0.83 ± 0.02
UO_2, 7.52 gm/cm^3	4	-0.85(5) ± 0.02	-1.02 ± 0.02
1.3%, 0.388 in.	5	-0.90(4) ± 0.03	-1.01 ± 0.03
UO_2, 10.53 gm/cm^3	3	-0.57(27) ± 0.07	-0.89 ± 0.07
1.3%, 0.383 in.	3.6	-0.69(38) ± 0.05	-0.87 ± 0.05
	5	-0.72(10) ± 0.02	-0.87 ± 0.02

* Number of points for making least squares fit

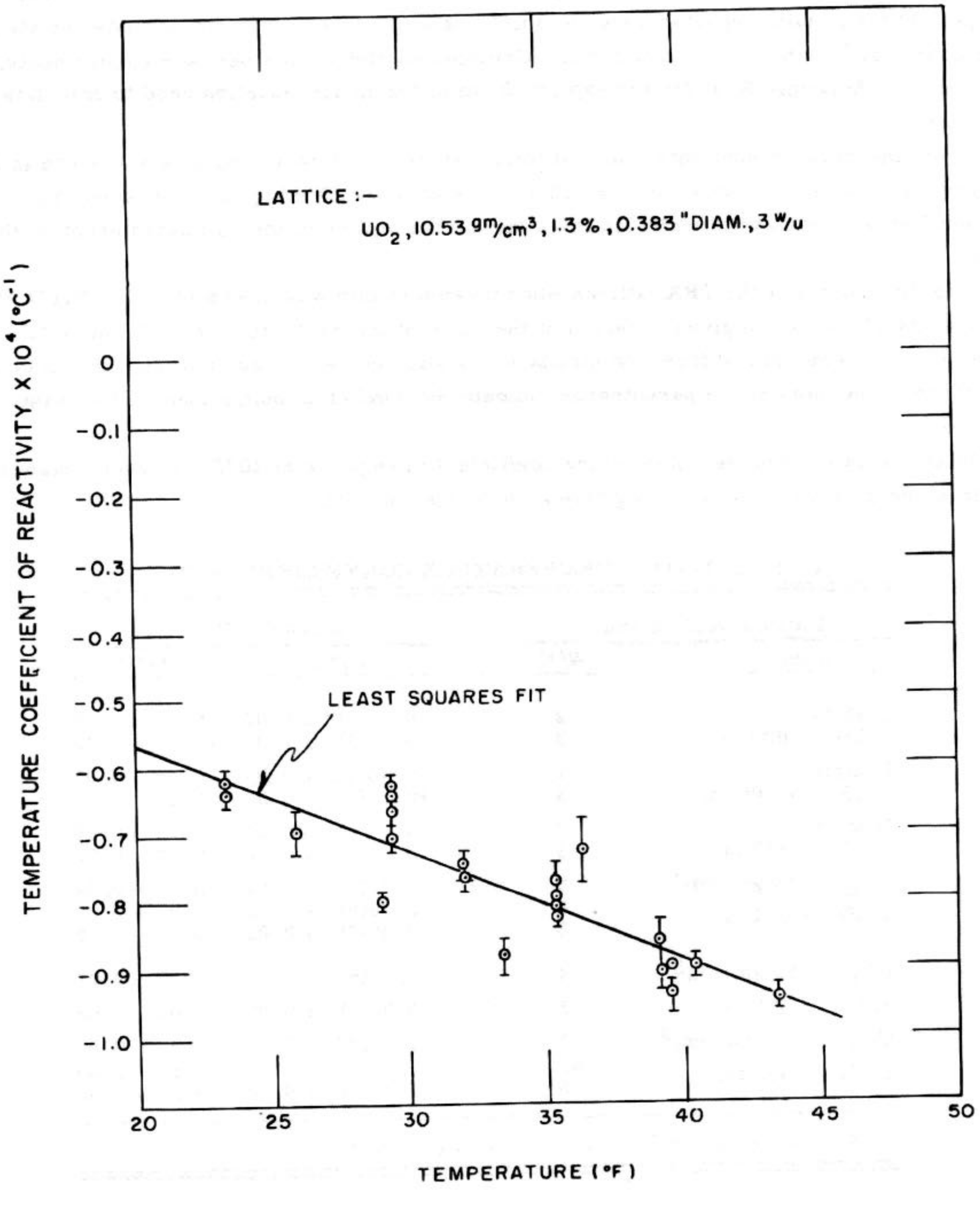

Fig. 12.9 - Temperature Coefficient of Reactivity as a Function of Temperature for an Oxide Lattice.

LATTICE CELL PARAMETER DATA

by D. Klein and G. G. Smith

12.5 INTRODUCTION

The techniques by which the lattice cell parameters, thermal utilization, resonance escape probability, and fast fission factor are measured have been discussed in detail in Chap. 11. The results obtained are compiled in this Section. Both Bettis and Brookhaven measurements are reported. In the reactor measurements the techniques used at the two laboratories were, in some cases, substantially different. In the cell measurements, however, very similar techniques were used. Because of the similarity of techniques and the frequent intercomparison of results, the reported results from the two laboratories for a parameter in a given lattice generally agree within the experimental uncertainty of the measurement.[3,5]

12.6 THERMAL UTILIZATION

The values obtained for the thermal utilization for all the Bettis measured lattices are given in Table 12.4. The uncertainties quoted in the table for the thermal utilization combine the following separate uncertainties:

1. A 2 per cent uncertainty in the measured flux ratios (water-to-fuel) including the uncertainty in the foil calibration
2. A 2 per cent uncertainty in the cross section values

The flux ratios for all the metal lattices measured are shown in Fig. 12.10. The values of thermal utilization calculated from these flux ratios are presented in Figs. 12.11 and 12.12.

12.7 RESONANCE ESCAPE PROBABILITY

The results obtained at Bettis for the resonance escape probability measurements are given in Table 12.5. As discussed in Chap. 11, such measurements are dependent upon a primary experimental quantity ρ , defined as follows:

$$\rho = \frac{\text{Radiative Capture in U}^{238}\text{ above the Cadmium Cutoff Energy}}{\text{Radiative Capture in U}^{238}\text{ below the Cadmium Cutoff Energy}}$$

The uncertainty indicated for p in Table 12.5 is the result of the following separate uncertainties:

1. A 3 per cent uncertainty in the value of ρ
2. A 2 per cent uncertainty in cross section data required to calculate p from ρ
3. An uncertainty of 0.5 per cent in f, the thermal utilization, which enters the calculation of p from ρ

Table 12.4--THERMAL UTILIZATION

Rod Diameter (in.)	Fuel	Enrichment (% U^{235})	Volume Ratio (W/U)	Volume Ratio (W/UO_2)	Flux Ratio ($\bar{\phi}_W$ / $\bar{\phi}_U$)	Thermal Utilization (f)
0.600	Metal	1.3	1.5	-	1.39 ± 0.04	0.918 ± 0.004
0.600	Metal	1.3	2.0	-	1.45 ± 0.04	0.890 ± 0.004
0.600	Metal	1.3	3.0	-	1.49 ± 0.04	0.843 ± 0.003
0.600	Metal	1.15	2.0	-	1.45 ± 0.04	0.881 ± 0.004
0.600	Metal	1.15	3.0	-	1.45 ± 0.04	0.835 ± 0.005
0.387	Metal	1.3	2.0	-	1.21 ± 0.04	0.904 ± 0.003
0.387	Metal	1.3	2.4	-	1.23 ± 0.01	0.890 ± 0.003
0.387	Metal	1.3	3.0	-	1.31 ± 0.04	0.857 ± 0.004
0.600	Oxide (7.53 gm/cm^3)	1.3	3.0	1.07	1.09 ± 0.03	0.873 ± 0.004
0.600	Oxide (7.53 gm/cm^3)	1.3	4.0	1.40	1.14 ± 0.03	0.837 ± 0.005
0.600	Oxide (7.53 gm/cm^3)	1.3	5.0	1.76	1.16 ± 0.03	0.805 ± 0.005
0.388	Oxide (7.53 gm/cm^3)	1.3	4.0	1.39	1.10 ± 0.01	0.836 ± 0.004
0.388	Oxide (7.53 gm/cm^3)	1.3	4.9	1.73	1.10 ± 0.01	0.807 ± 0.004
0.383	Oxide (10.53 gm/cm^3)	1.3	2.9	1.42	1.10 ± 0.01	0.874 ± 0.004
0.383	Oxide (10.53 gm/cm^3)	1.3	3.6	1.78	1.13 ± 0.01	0.848 ± 0.004
0.383	Oxide (10.53 gm/cm^3)	1.3	4.9	2.40	1.13 ± 0.01	0.809 ± 0.004

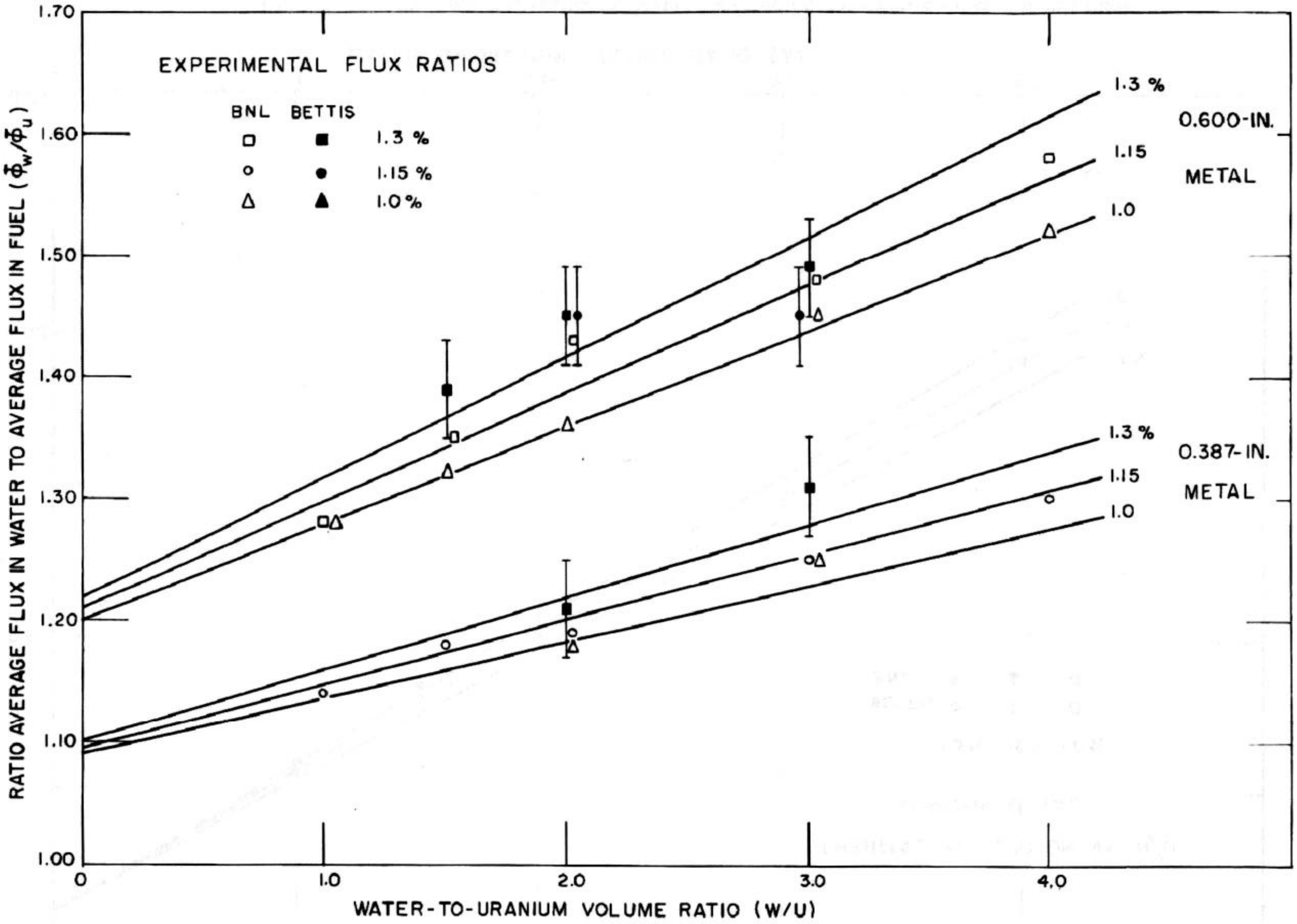

Fig. 12.10 - Measured Flux Ratios.

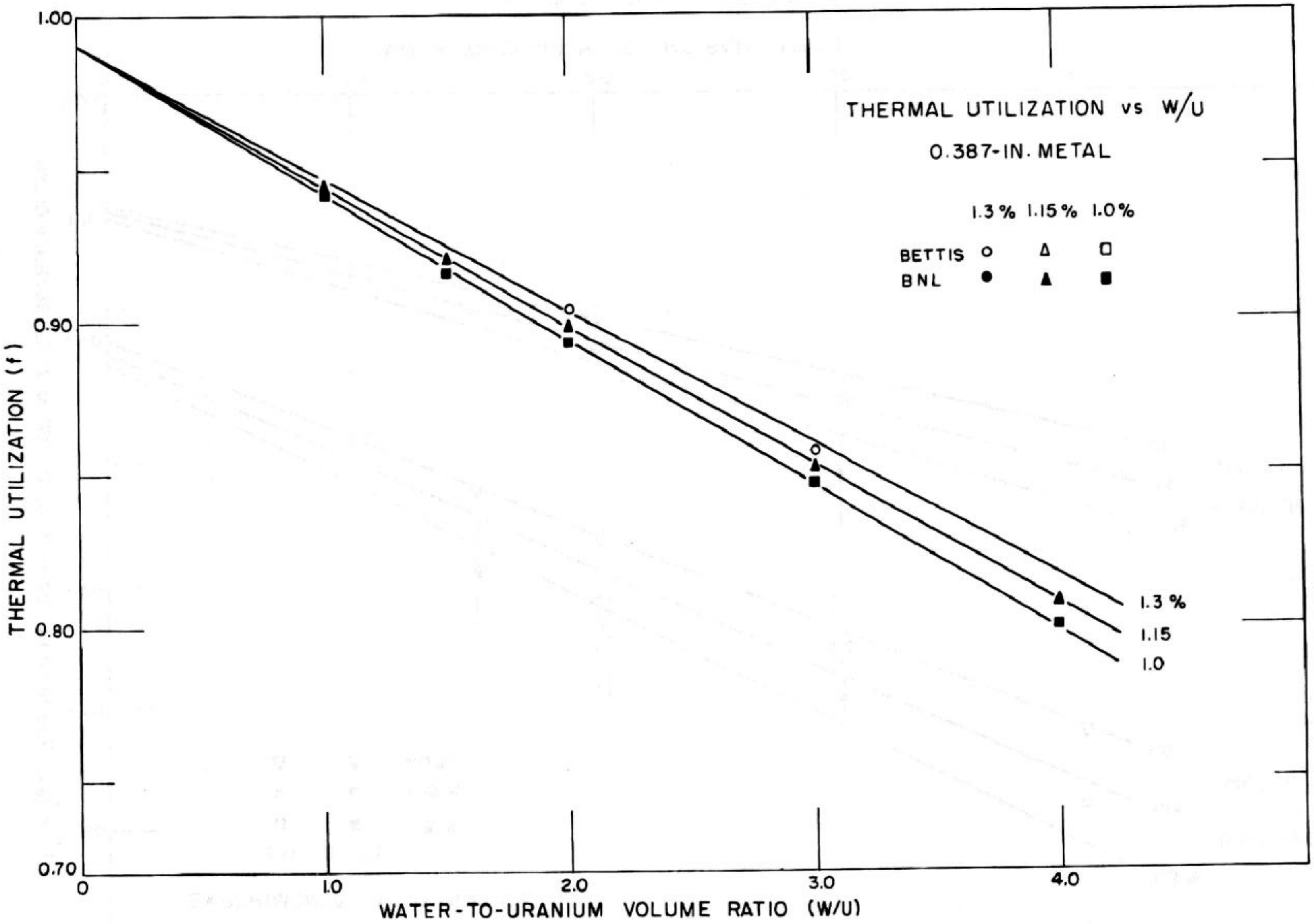

Fig. 12.11 - Thermal Utilization of Metal Lattices (0.387-inch-diameter metal fuel).

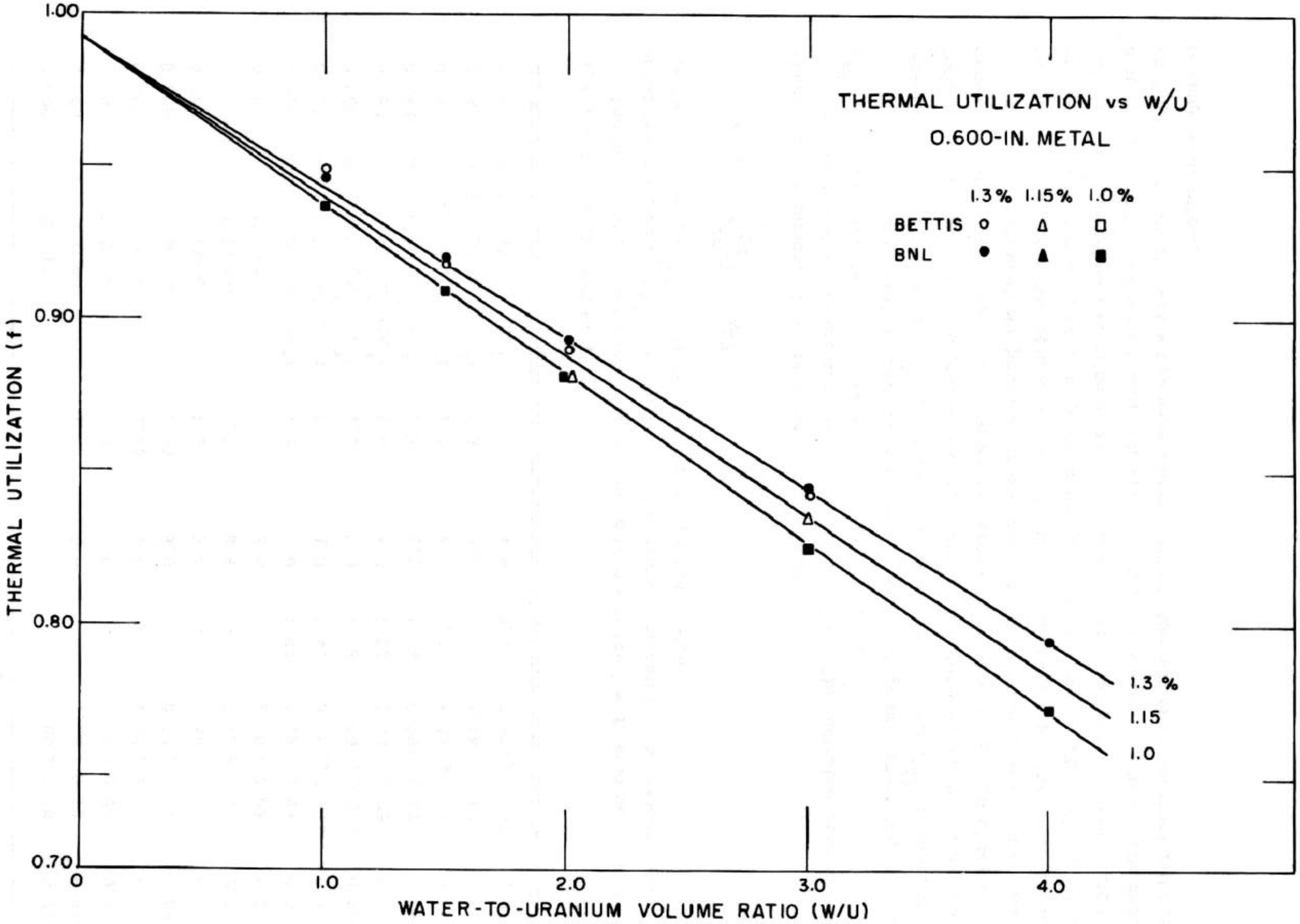

Fig. 12.12 - Thermal Utilization of Metal Lattices (0.600-inch-diameter metal fuel).

Table 12.5--MEASURED VALUES OF RESONANCE ESCAPE PROBABILITY

Rod Diameter (in.)	Fuel	Enrichment (% U^{235})	Volume Ratio (W/U)	Volume Ratio (W/UO_2)	Ratio Epithermal to Thermal Capture (ρ)	Resonance Escape Probability (p^{28})
0.600	U Metal	1.3	1.5	-	1.80 ± 0.18	0.720 ± 0.014
0.600	U Metal	1.3	2.0	-	1.24 ± 0.12	0.794 ± 0.016
0.600	U Metal	1.3	3.0	-	0.89 ± 0.09	0.850 ± 0.017
0.600	U Metal	1.15	2.0	-	1.20 ± 0.03	0.785 ± 0.005
0.600	U Metal	1.15	3.0	-	0.93 ± 0.04	0.833 ± 0.007
0.387	U Metal	1.3	2.0	-	1.59 ± 0.03	0.747 ± 0.005
0.387	U Metal	1.3	2.4	-	1.41 ± 0.06	0.772 ± 0.008
0.387	U Metal	1.3	3.0	-	1.18 ± 0.03	0.808 ± 0.005
0.600	UO_2(7.53 gm^2/cm^3)	1.3	3.0	1.07	1.19 ± 0.04	0.805 ± 0.006
0.600	UO_2(7.53 gm^2/cm^3)	1.3	4.0	1.40	0.994 ± 0.013	0.838 ± 0.003
0.600	UO_2(7.53 gm^2/cm^3)	1.3	5.0	1.76	0.807 ± 0.014	0.869 ± 0.003
0.388	UO_2(7.53 gm^2/cm^3)	1.3	4.0	1.39	1.04 ± 0.05	0.832 ± 0.007
0.388	UO_2(7.53 gm^2/cm^3)	1.3	4.9	1.73	0.901 ± 0.02	0.853 ± 0.004
0.383	UO_2(10.53 gm^2/cm^3)	1.3	2.9	1.42	1.43 ± 0.01	0.775 ± 0.004
0.383	UO_2(10.53 gm^2/cm^3)	1.3	3.6	1.78	1.15 ± 0.01	0.815 ± 0.004
0.383	UO_2(10.53 gm_2/cm^3)	1.3	4.9	2.40	0.934 ± 0.010	0.850 ± 0.004

12.8 FAST FISSION EFFECT

The fast fission effect can be described in terms of the fast fission factor ϵ or in terms of the related quantity δ^{28}. The quantity δ^{28} is simply the ratio of the fission rate in U^{238} to the fission rate in U^{235}. It is related to ϵ by the expression

$$\epsilon - 1 = \frac{\nu^{28} - 1}{\nu^{25}} \delta^{28} \qquad \text{Eq. (12.6)}$$

where ν is the number of neutrons emitted per fission.

The experimental results are compiled in Table 12.6. The indicated uncertainties in δ^{28} arise from uncertainties in the experimental procedure.[5]

In the lattices studied the fast fission effect arises in large part from neighboring rod effects, i.e., the fission in U^{238} in a given rod arises largely from U^{235} fissions in adjacent rods. Such a conclusion is supported by mean free path arguments and by direct experimental measurements. One of the lattices measured showed that only 10 per cent of the U^{238} fissions in a rod arise from neutrons produced in that rod. Thus, the fast fission factor should behave as if the lattices were homogeneous, i.e., it should depend only upon the water-to-uranium ratio and not on rod size, fuel composition or enrichment. Figure 12.13 shows the measured values of δ^{28} plotted as a function of water-to-uranium volume ratio. To correlate the results, a solid curve deduced from a multigroup calculation is shown on the figure. The results shown on Fig. 12.13 indicate that, within experimental error, the fast effect on these lattices is a homogeneous effect.

Table 12.6--FAST EFFECT DATA

Rod Diam. (in.)	Enrichment (% U^{235})	Fuel Composition	Fuel Density (gm/cm^3)	Volume Ratio (W/U)	Volume Ratio (W/UO_2)	U^{238} Fission per U^{235} Fission (δ^{28})	Fast Fission Factor (ϵ^{28})
0.600	1.15	Metal	-	2.0	-	0.104 ± 0.010	1.062 ± 0.006
0.600	1.15	Metal	-	3.0	-	0.081 ± 0.008	1.048 ± 0.004
0.387	1.3	Metal	-	2.0	-	0.099 ± 0.010	1.059 ± 0.005
0.387	1.3	Metal	-	3.0	-	0.078 ± 0.008	1.046 ± 0.004
0.600	1.3	UO_2	7.53	3.0	1.07	0.071 ± 0.007	1.042 ± 0.004
0.600	1.3	UO_2	7.53	4.0	1.40	0.059 ± 0.006	1.035 ± 0.003
0.600	1.3	UO_2	7.53	5.0	1.76	0.051 ± 0.004	1.030 ± 0.002
0.388	1.3	UO_2	7.53	4.0	1.39	0.063 ± 0.003	1.037 ± 0.002
0.388	1.3	UO_2	7.53	4.9	1.73	0.054 ± 0.003	1.032 ± 0.002
0.383	1.3	UO_2	10.53	2.9	1.42	0.078 ± 0.004	1.046 ± 0.002
0.383	1.3	UO_2	10.53	3.6	1.78	0.070 ± 0.004	1.042 ± 0.002
0.383	1.3	UO_2	10.53	4.9	2.40	0.057 ± 0.003	1.034 ± 0.002
0.387	1.3	Metal	-	2.4	-	0.099 ± 0.005	1.059 ± 0.003

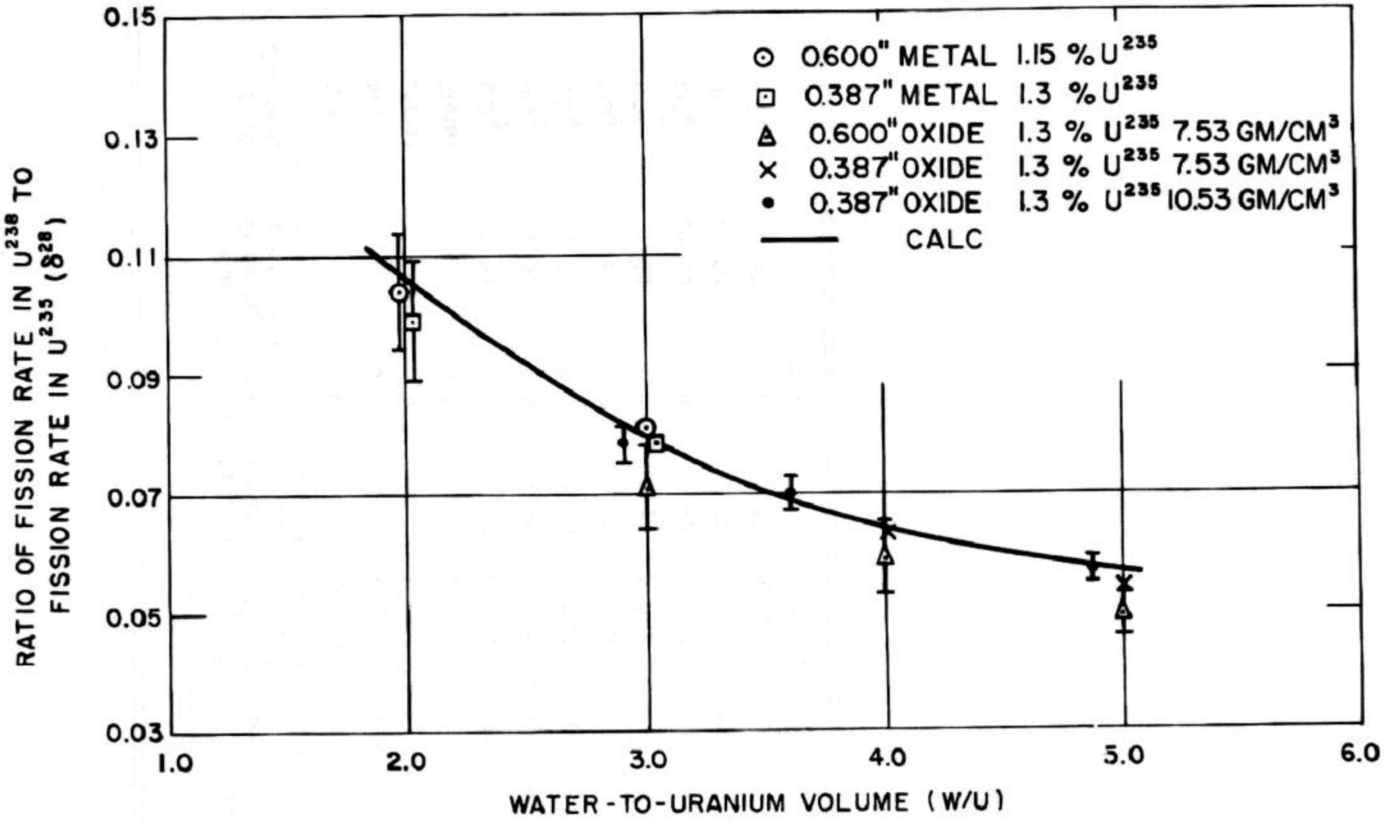

Fig. 12.13 - Ratio of U^{238} Fission Rate to U^{235} Fission Rate.

EXPERIMENTAL DETERMINATION OF THE MIGRATION AREA

by D.R. Harris and J.R. Brown

12.9 THEORETICAL BASIS OF MEASUREMENT

The relatively large size of the TRX lattices permits them to be analyzed as equivalent bare reactors. A bare reactor may be treated by the method of slowing down kernels and, if it is large, the leakage of neutrons may be represented by a term $(1 + B_g^2 M^2)$ where M^2 is the migration area and B_g^2 is the geometric buckling of the equivalent bare reactor. Thus,

$$k_{eff} = \frac{k_\infty}{1 + B_g^2 M^2} \qquad \text{Eq. (12.7)}$$

and the reactivity, ρ, is given by the expression

$$\rho = \frac{k_{eff} - 1}{k_{eff}} = 1 - \frac{1 + B_g^2 M^2}{k_\infty} \qquad \text{Eq. (12.8)}$$

If the derivative of ρ with respect to B_g^2 is formed from Eq. (12.8), then an expression for M^2 in terms of this derivative is

$$M^2 = \frac{-\partial\rho/\partial B_g^2}{1 + B_g^2 \;\partial\rho/\partial B_g^2} \qquad \text{Eq. (12.9)}$$

The fact that k_{eff} is unity at criticality is used in order to obtain this expression. Thus, the derivative $\partial\rho/\partial B_g^2$ is to be measured at criticality.

12.10 EXPERIMENTAL PROCEDURE

The required derivative can be obtained by measuring the period associated with a small change in the geometric buckling. The period is converted to a reactivity by use of the inhour relation. In determining the reactivity values in this experiment, Keepin's values for the delayed neutron yields and periods were used.[4]

The geometric buckling was changed experimentally by either modifying the radius at constant reactor height or changing the reactor height at constant radius. The latter experiment is the differential water height experiment discussed in Chap. 8. To change the effective radius, a few peripheral fuel rods were removed from the reactor by a remotely controlled mechanical system.[1] To calculate the change in buckling associated with these changes in the reactor, it is necessary to assume the reflector savings do not change significantly with the small change in size. This assumption seems well confirmed by the experimental data. Because of the small reactivity changes associated with the measurement, some care must be exercised to eliminate temperature effects and reactivity drifts.

12.11 ANISOTROPY OF THE MIGRATION AREA

Before the results of the measurements are presented, one further point must be developed. In analyzing the experimental data, it has been found that the results obtained from axial and radial buckling measurements could not be completly reconciled. Further study indicated that this was the result of a small but significant anisotropy of the migration area. The modification to Eq. (12.9) to treat this point required that the migration area be specified as either that in the axial or the radial direction. Davison has treated this topic with respect to thermal diffusion lengths.[6]

Let $M_\perp^2$ designate the migration area radially and $M_{/\!/}^2$ represent the axial migration area. The notation indicates that the direction is either parallel to the fuel rods or perpendicular to them. The expression for k_{eff} is now written

$$k_{eff} = \frac{k_\infty}{1 + M_\perp^2 B_r^2 + M_{/\!/}^2 B_z^2} \qquad \text{Eq. (12.10)}$$

Define the ratio of the two migration areas as A, i.e.,

$$A = \frac{M_{/\!/}^2}{M_\perp^2} \qquad \text{Eq. (12.11)}$$

This in effect permits either migration area to be used if the buckling is suitably modified. For example, Eq. (12.8) can be written with $M_\perp^2$ for M^2 provided

$$B_g^2 = B_r^2 + A\, B_z^2 \qquad \text{Eq. (12.12)}$$

If the derivation given for Eq. (12.9) is now reproduced, the following expressions are obtained:

$$M_\perp^2 = \frac{-\partial\rho / \partial B_r^2}{1 + B_g^2 \;\; \partial\rho/\partial B_r^2} \qquad \text{Eq. (12.13)}$$

and

$$M_\perp^2 = \frac{-\partial\rho / \partial B_z^2}{A + B_g^2 \;\; \partial\rho/\partial B_z^2} \qquad \text{Eq. (12.14)}$$

with B_g^2 given by Eq. (12.12).

The existence of lattice anisotropy can be demonstrated and the value of A calculated from a series of partial water height measurements on a given lattice. In the static partial water height experiments, the radius of the lattice is adjusted to give criticality at a given water height. From a pair of such experiments on a given lattice, the change in axial buckling, ΔB_z^2, required to compensate a given change in radial buckling, ΔB_r^2, gives the value of A.

$$A = \frac{\Delta B_r^2}{\Delta B_z^2} \qquad \text{Eq. (12.15)}$$

The results obtained in this way are summarized in Table 12.7. The errors quoted in the table are estimated from errors in the reflector savings only. Other uncertainties in the experiment, for example random reactivity shifts, will contribute significant errors but these have not been estimated. For three lattices, however, the dispersions of the individual values of A were too large to be accounted for by the errors in the reflector savings. The individual values of A were averaged for each lattice to give a composite. Within experimental error, the anisotropy appears to be the same for all lattices measured. A reasonable average anisotropy for all lattices is 1.05 ± 0.03.

12.12 MIGRATION AREA RESULTS

The values determined for the migration area of the lattices, taking anisotropy into account, are summarized in Table 12.8. The values tabulated are the perpendicular migration area. The total data available which are considered to be adequate in quality to permit inclusion in the table are limited. In particular, some of the axial derivatives have been excluded since it has been found recently that if the dry lattice above the water level is less than about 30 cm, the change in axial reflector savings contributes a significant error.[1] The error in the tabulated values is hard to assign because of the involved considerations; an estimate of this error is ± 4 per cent. It is gratifying to note that the agreement between axial and radial data is quite good where both have been properly measured.

Table 12.7--ANISOTROPY OF MIGRATION AREA

Lattice Designation		Pair of Water Heights Used In Determination	$A = \frac{B^2_{r_1} - B^2_{r_2}}{B^2_{z_2} - B^2_{z_1}}$	$\bar{A} = M_{\parallel}/M_{\perp}$ (Weighted Average)
Fuel	W/U			
U Metal 1.3%, 0.387 in.	2	Full, 100.2 cm	1.07 ± 0.05*	1.07 ± 0.05
UO_2, 7.53 gm/cm^3 1.3%, 0.601 in.	3	Full, 106.7 cm	0.99 ± 0.02	1.08 ± 0.05
		Full, 87.1 cm	1.09 ± 0.01	
		106.7 cm, 87.1 cm	1.15 ± 0.02	
	4	Full, 100.0 cm	1.02 ± 0.02	1.04 ± 0.01
		Full, 73.3 cm	1.04 ± 0.01	
		100.0 cm, 73.3 cm	1.05 ± 0.01	
	5	Full, 97.3 cm	1.00 ± 0.01	1.00 ± 0.03
UO_2, 7.52 gm/cm^3 1.3%, 0.388 in.	4	Full, 99.3 cm	1.04 ± 0.02	1.04 ± 0.03
	5	Full, 92.4 cm	1.06 ± 0.01	1.06 ± 0.03
UO_2, 10.53 gm/cm^3 1.3%, 0.383 in.	3	Full, 103.2 cm	1.01 ± 0.04	1.06 ± 0.03
		Full, 94.5 cm	1.01 ± 0.02	
		Full, 84.3 cm	1.06 ± 0.01	
		103.2 cm, 94.5 cm	1.00 ± 0.07	
		103.2 cm, 84.3 cm	1.09 ± 0.03	
		94.5 cm, 84.3 cm	1.16 ± 0.04	
	3.6	Full, 105.3 cm	0.97 ± 0.04	1.04 ± 0.03
		Full, 67.3 cm	1.04 ± 0.02	
		105.3 cm, 67.3 cm	1.05 ± 0.02	
	5	Full, 103.1 cm	1.05 ± 0.02	1.04 ± 0.01
		Full, 68.6 cm	1.04 ± 0.01	
		103.1 cm, 68.6 cm	1.04 ± 0.01	

* Errors calculated from errors of measured reflector savings only

Table 12.8 MIGRATION AREA (PERPENDICULAR TO FUEL)

Lattice Designation		$\partial\rho/\partial B^2_r$ (cm^2)	$(1/A)\ \partial\rho/\partial B^2_z$ (cm^2)	$M^2_{\perp}$ (cm^2)
Fuel	W/U			
U Metal 1.3%, 0.600 in.	2	- 28.2	--	34.1
U Metal 1.15%, 0.600 in.	2	- 26.9	--	30.9
U Metal 1.3%, 0.387 in.	2	- 29.0	--	34.2
	3	- 29.9	--	36.2
UO_2, 7.53 gm/cm^3 1.3%, 0.600 in.	3	- 46.1	- 46.6	53.4
	4	- 44.9	- 45.7	52.5
	5	- 41.1	--	46.7
UO_2, 7.52 gm/cm^3 1.3%, 0.388 in.	4	- 47.3	--	53.7
	5	- 48.2	--	54.9
UO_2, 10.53 gm/cm^3 1.3%, 0.383 in.	3	- 39.1	- 40.5	45.8
	3.6	- 38.6	- 37.9	44.3
	5	- 35.4	- 35.8	40.6

ANALYSIS OF URANIUM-WATER LATTICE DATA

by S. Stein and S. J. Lukasik

12.13 METHOD OF ANALYSIS

So far as the experimental data are concerned, they fall into two classes, namely, cell-parameters and over-all reactor measurements. From the theoretical point of view there is a somewhat different division. This is best discussed in terms of the calculational procedures.

The steps in the theoretical analysis are as follows:

1. Calculation of the cell parameters, thermal utilization and resonance escape probability. The fast fission factor is calculated on a homogeneous basis
2. Calculation of the neutron energy spectrum and appropriate group constants
3. Calculation of the over-all reactor properties by group diffusion theory

The cell parameters are determined from specific calculations for this purpose. The over-all reactor properties are calculated by treating the reactor as a homogeneous mixture, at least in each reactor region. The cell properties are introduced in this treatment through self-shielding factors. The group constants are calculated by first calculating the neutron spectrum. The neutron spectrum in the slowing-down energy region is calculated by the MUFT code (see Appendix E). This code computes the neutron spectrum from fission energy to thermal energy, taking neutron leakage into account through introduction of a single buckling, B_M^2. This buckling value is used to characterize a leakage corresponding to a fundamental mode. With this leakage, the spectrum is calculated by a transform method in P_1 approximation dividing the energy interval into 54 groups of approximately equal lethargy intervals. Microscopic cross section data and specified number densities are used in the spectrum calculation. From the calculated spectrum, the code proceeds to edit group constants for specified energy groups. The effect of finite fuel rod size is accounted for by introducing self-shielding factors which limit the resonance capture. The self-shielding factors are introduced in each calculation from prior knowledge of the resonance escape probability.

The thermal neutron energy spectrum is calculated by means of the SOFOCATE code (see Appendix D). This is a Wigner-Wilkins, free proton scattering calculation assuming the medium is homogeneous. Thermal-group constants are obtained through averaging of the nuclear cross sections over the calculated spectrum. The fine structure due to fuel rods is introduced by weighting the number densities of fuel and moderator according to a cell calculation of the thermal utilization.

Since the experimental data were taken in a number of different ways, it is possible to compare calculation and experiment in each of these categories. These are listed below:

1. Cell Parameters - Values of thermal utilization and resonance escape probability may be compared.

2. Spectrum Average Parameters - The fast fission factors in both U^{235} and U^{238} and the migration area may be compared.

3. The critical size, reflector savings and critical buckling may be compared.

Each of these is discussed in detail in the following sections.

12.14 RESONANCE ESCAPE PROBABILITY

The resonance capture in U^{238} in the fuel rods was calculated by means of a Monte Carlo code. There are at present three codes of this type in existence which calculate this quantity in the same manner. The first is the UNIVAC REP code by Richtmyer[7]; the second is the NORC WREP code created by Crane; the most recent is the 704-REP code created by Van Norton and Richtmyer at New York University.

While the successive codes have added refinements and new features, basically, all are designed to calculate the resonance capture in a unit cell of the TRX type lattice. The neutron is assumed to enter the resonance region at about 450 ev energy and its history is followed through to the lowest energy resonance in U^{238}. The explicit resonance properties of the first 18 resonances in U^{238} are used with Doppler broadening taken into account. Capture is considered only in the resonances.

It is necessary in computing the resonance capture to take into account two other mechanisms. The first is capture in the smooth 1/v background of the cross section. The second is the capture in the unresolved resonance structure above 450 ev. This latter is accounted for by calculation based on a simple nuclear model.[8] Both of the latter mechanisms of capture are introduced explicitly in the MUFT calculation by the use of energy dependent capture cross sections.

The Monte Carlo results are used to calculate self-shielding (L factors) for use in MUFT to reduce the effective resonance integral.[9] The actual numerical value of p due to all these sources of capture is edited by MUFT. The probable error in p due to statistics in the Monte Carlo calculation is estimated to be ± 0.002. This does not include uncertainties associated with the smooth capture cross section or that due to the unresolved resonances.

The theoretical and experimental data[10] are presented in Figs. 12.14 through 12.18. In these figures the subscript 0.45 assigned to p indicates that the smooth capture was cut off at a lower energy limit of 0.45 ev in order to correspond to the cadmium thickness used in the experiment.

While the comparison between calculation and experiment is generally quite good, both with respect to trend with water-to-uranium volume ratio and absolute value, there are a few deviations which are well outside the expected errors. This is especially true in the case of the high density oxide fuel of 0.387-inch diameter. In this case the measurements are the most recent and represent the highest accuracy achieved in a resonance capture measurement.

12.15 THERMAL UTILIZATION

The calculation of the thermal flux distribution in a lattice cell is probably the least satisfactory of all of the analytical procedures. There is not presently available a calculation of the thermal spectral distribution as a function of position in the cell. In the absence of such a calculation it is necessary to calculate the flux distribution in the cell as a monoenergetic case using some form of average cross sections. Even though the spatial calcula-

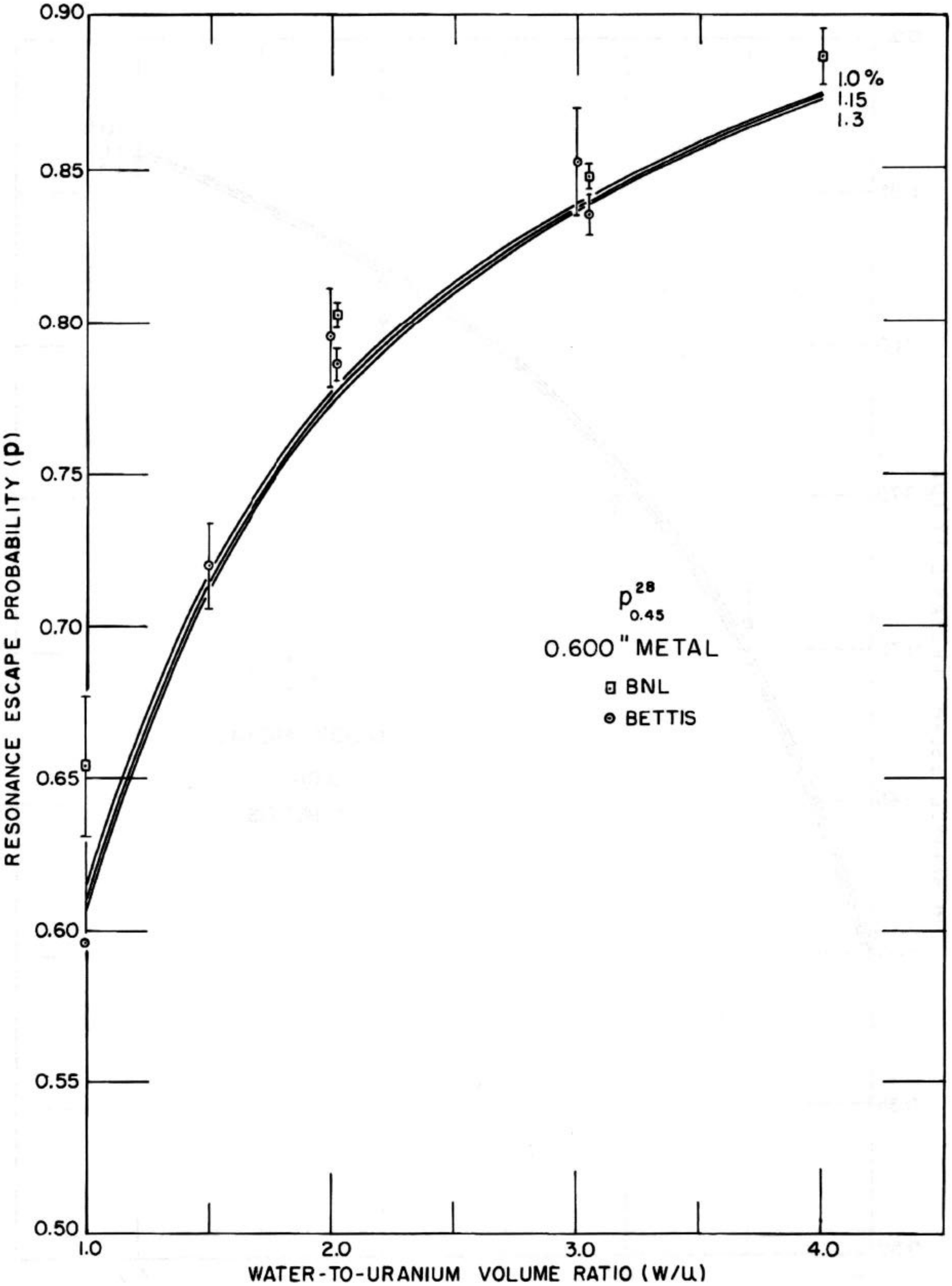

Fig. 12.14 - Resonance Escape Probability for 0.600-Inch-Diameter Metal Rod Lattices.

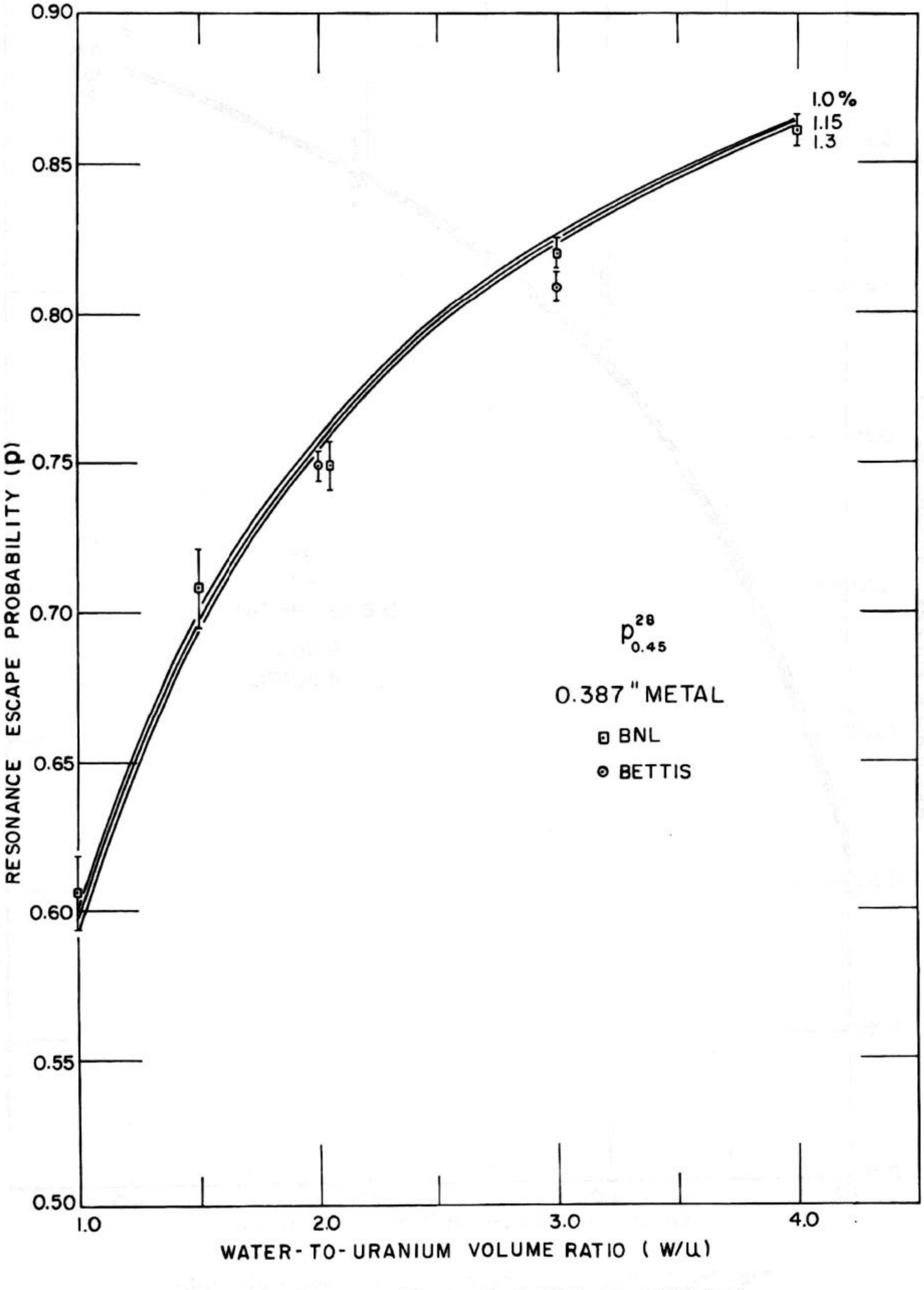

Fig. 12.15 - Resonance Escape Probability for 0.387-Inch-Diameter Metal Rod Lattices.

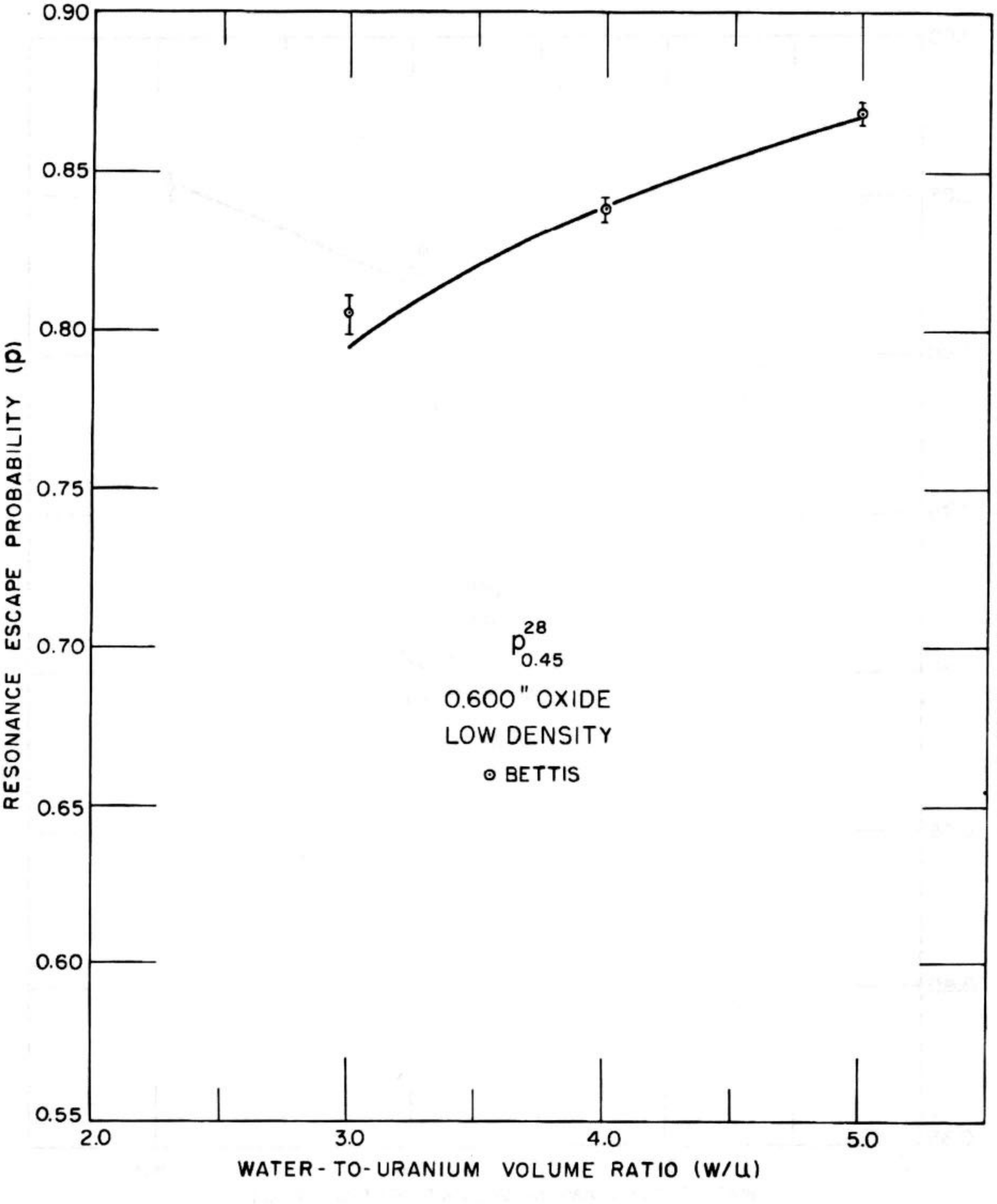

Fig. 12.16 - Resonance Escape Probability for 0.600-Inch-Diameter Oxide Rod Lattices.

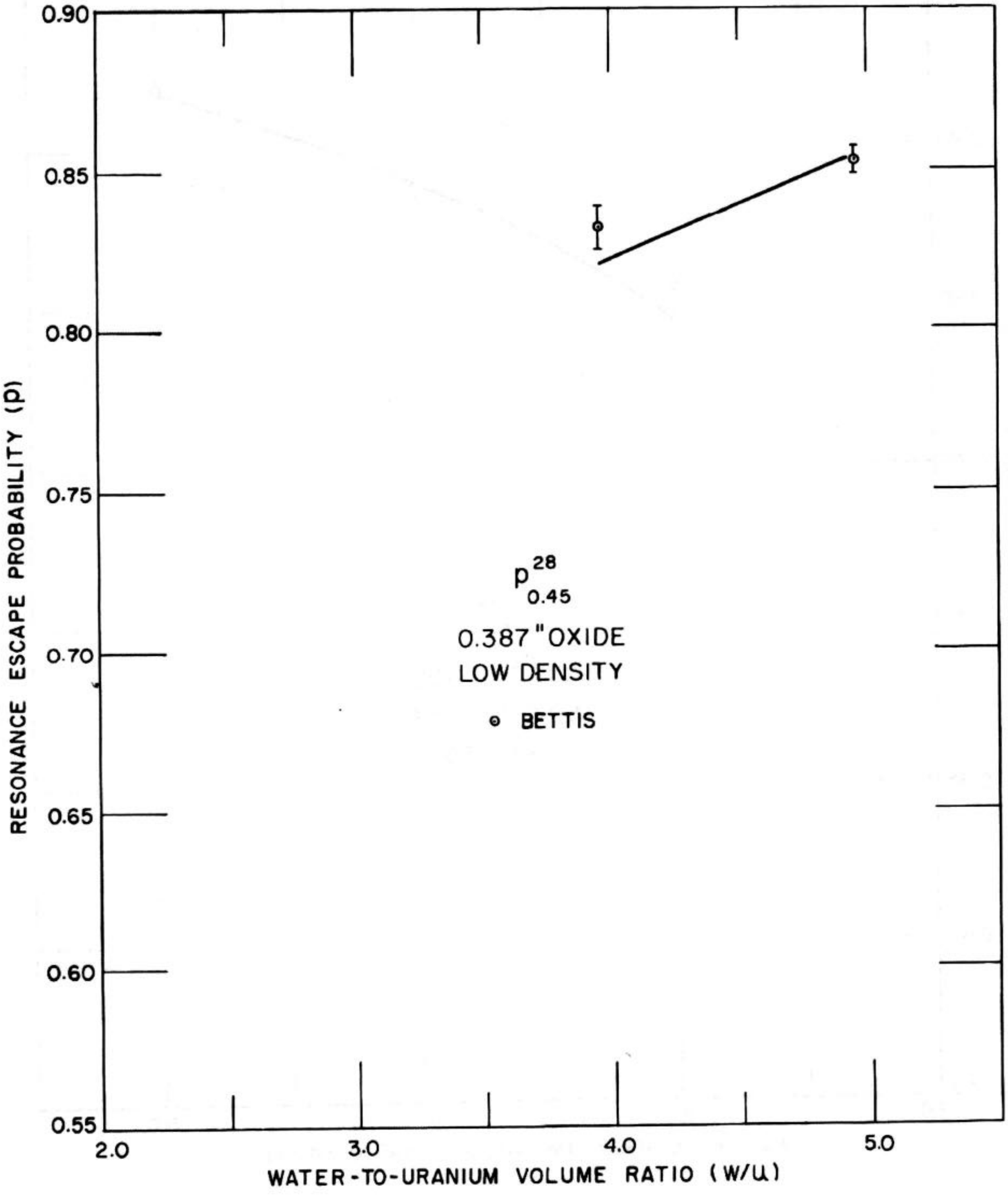

Fig. 12.17 - Resonance Escape Probability for 0.387-Inch-Diameter Oxide Rod Lattices.

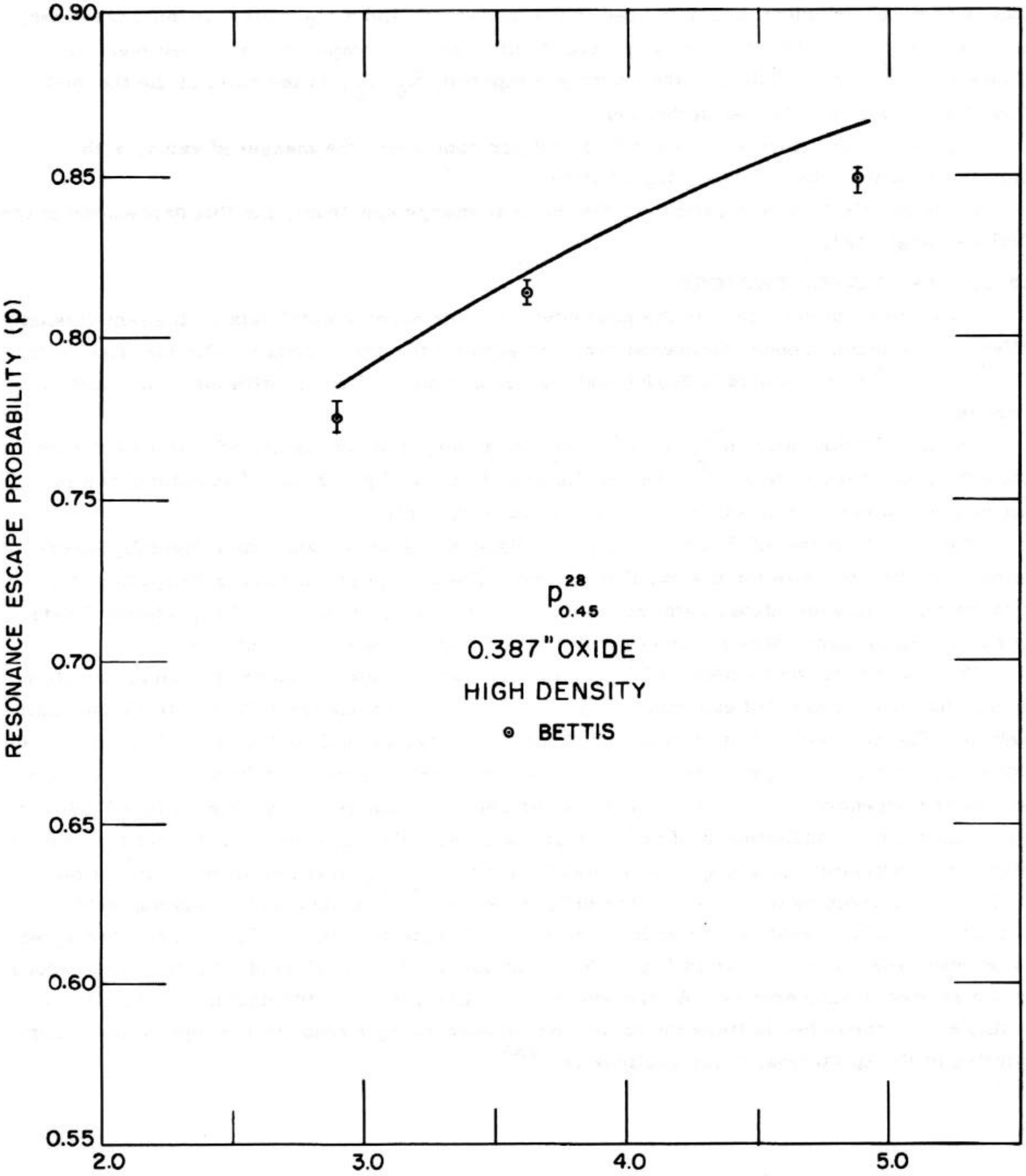

Fig. 12.18 - Resonance Escape Probability for 0.387-Inch-Diameter High Density Oxide Rod Lattices.

tion may be made relatively sophisticated in terms of transport theory approximation, the lack of a combined spatial-energy calculation represents a basic weakness.

The initial analysis of cell thermal flux distributions calculated by diffusion theory showed relatively poor agreement with experiment. An improved version is a one-group blackness theory in which diffusion theory is used in the moderator and a rigorous transport treatment is used in the fuel. The results calculated in this way are compared with experiment in Table 12.9.[10] For simplicity, the quantity compared, $\bar{\phi}_W/\bar{\phi}_U$, is the ratio of the thermal flux in the moderator to that in the fuel.

In general, the calculated result is 5 to 8 per cent below the measured value, with agreement best in the relatively tight lattices.

In the SOFOCATE calculations of the thermal energy spectrum, the flux depression in the fuel was neglected.

12.16 FAST FISSION FACTORS

It was noted in Sec. 12.8 in the presentation of the experimental data on the fast-fission effect that a homogeneous calculation gives essentially the entire effect. The fast fission in U^{238} and U^{235} is calculated in MUFT and may be compared directly with the experimental results.

The fast fission ratio, δ^{28}, for U^{238} has been computed and compared with experiment for a number of the lattices.[10] The results are shown in Fig. 12.13. The solid curve is the calculated value, a function only of metal-to-water ratio.

Figures 12.19 and 12.20 present a comparison of calculated and experimentally determined fast-fission ratio for the metal fuel rods. The data presented are principally from Brookhaven with some Bettis data included for comparison. Both sets of experimental data are in excellent agreement and in reasonably good agreement with calculation.

The fraction of the fissions in U^{235} which are due to neutrons above the cadmium cutoff energy has been measured experimentally. These can be compared with the MUFT calculated values. The calculation has been extended from 0.45 ev, the calculated cutoff for the cadmium thickness used in the experiment, to fission energy. For a given enrichment, the calculated values are dependent chiefly on metal-to-water ratio and can be represented within 3 per cent by a single curve, independent of rod size or material. The data for all of the lattices can be placed approximately on a single curve by plotting the data against hydrogen-to-U^{235} atom ratio. For a given ratio, however, the differences in U^{238} capture and in thermal self-shielding introduce weak trends with enrichment with opposing sign . The rather poor agreement with experiment, shown in Figs. 12.21 through 12.24, is believed largely due to errors in the earlier measurements. At present only the high density oxide data are believed to be reliable. On these few lattices the agreement is surprisingly good, in the light of the uncertainties in the epithermal cross sections of U^{235}.

Table 12.9--COMPARISON OF EXPERIMENTAL AND CALCULATED THERMAL FLUX RATIOS

Rod Diam (in.)	Fuel	Enrichment (% U^{235})	Volume Ratio (W/U)	$\bar{\phi}_W/\bar{\phi}_U$ Flux Ratio		
				Experimental		Flux Ratio Calculated
				Bettis	BNL	
0.600	Metal	1.3	1.0	----	1.29	1.26
0.600	Metal	1.3	1.5	1.39 ± 0.04	1.35	1.30
0.600	Metal	1.3	2.0	1.45 ± 0.04	1.44	1.34
0.600	Metal	1.3	3.0	1.49 ± 0.04	1.48	1.41
0.600	Metal	1.3	4.0	----	1.58	1.46
0.600	Metal	1.15	2.0	1.45 ± 0.04	----	1.31
0.600	Metal	1.15	3.0	1.45 ± 0.04	----	1.43
0.600	Metal	1.0	1.0	----	1.28	1.22
0.600	Metal	1.0	1.5	----	1.32	1.25
0.600	Metal	1.0	2.0	----	1.36	1.29
0.600	Metal	1.0	3.0	----	1.45	1.34
0.600	Metal	1.0	4.0	----	1.52	1.39
0.387	Metal	1.3	2.0	1.21 ± 0.04	----	1.16
0.387	Metal	1.3	3.0	1.31 ± 0.04	----	1.19
0.387	Metal	1.15	1.0	----	1.14	1.11
0.387	Metal	1.15	1.5	----	1.18	1.13
0.387	Metal	1.15	2.0	----	1.19	1.15
0.387	Metal	1.15	3.0	----	1.25	1.17
0.387	Metal	1.15	4.0	----	1.30	1.19
0.387	Metal	1.0	2.0	----	1.18	1.13
0.387	Metal	1.0	3.0	----	1.25	1.16
0.600	Low Density Oxide	1.3	3.0	1.09 ± 0.03	----	1.09
0.600	Low Density Oxide	1.3	4.0	1.14 ± 0.03	----	1.10
0.600	Low Density Oxide	1.3	5.0	1.16 ± 0.03	----	1.11
0.388	Low Density Oxide	1.3	4.0	1.10 ± 0.01	----	1.05
0.388	Low Density Oxide	1.3	5.0	1.10 ± 0.01	----	1.05
0.383	High Density Oxide	1.3	3.0	1.10 ± 0.01	----	1.07
0.383	High Density Oxide	1.3	3.5	1.13 ± 0.01	----	1.07
0.383	High Density Oxide	1.3	4.8	1.13 ± 0.01	----	1.08

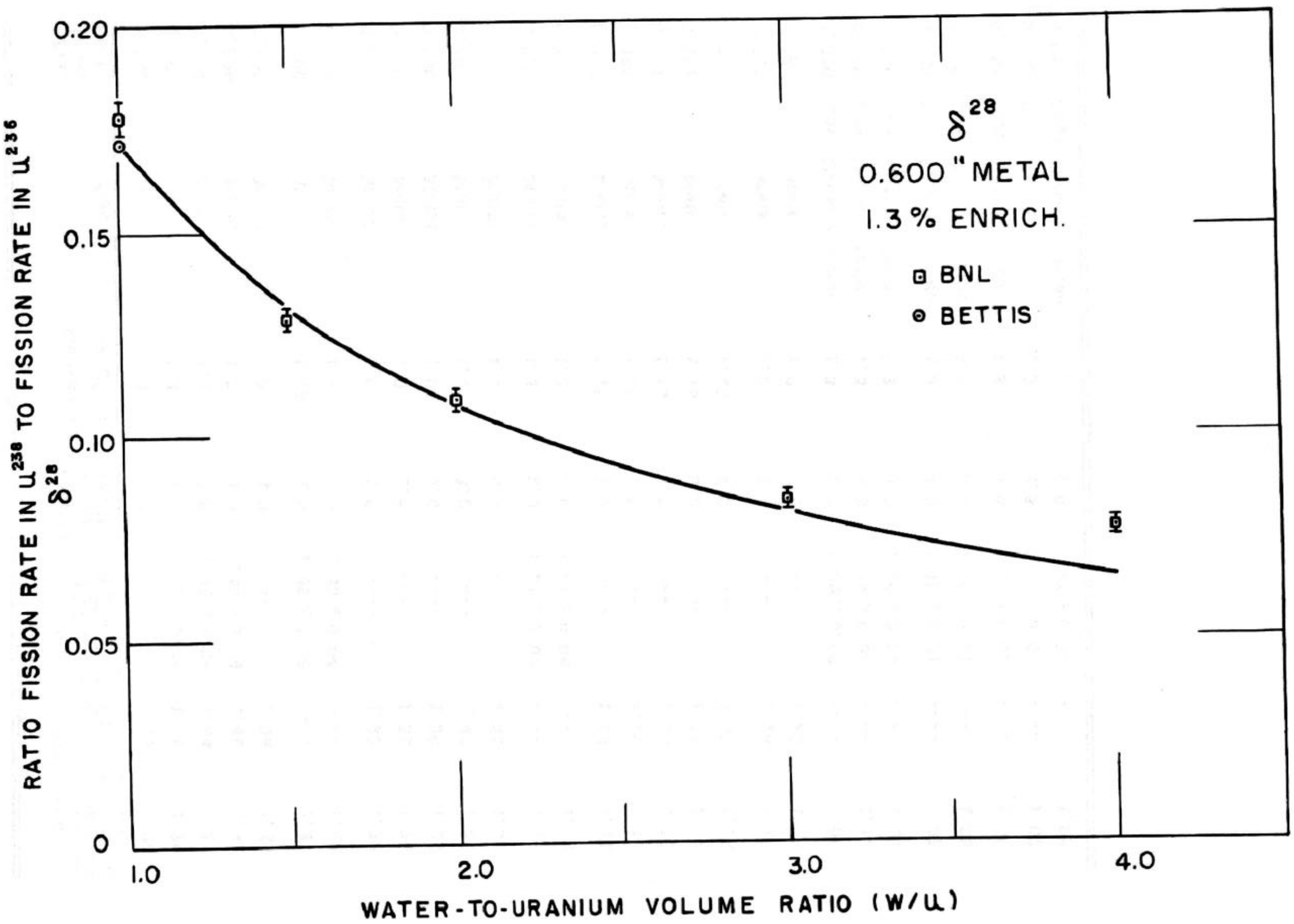

Fig. 12.19 - Fast Fission Ratio for 0.600-Inch-Diameter Metal Rod Lattices.

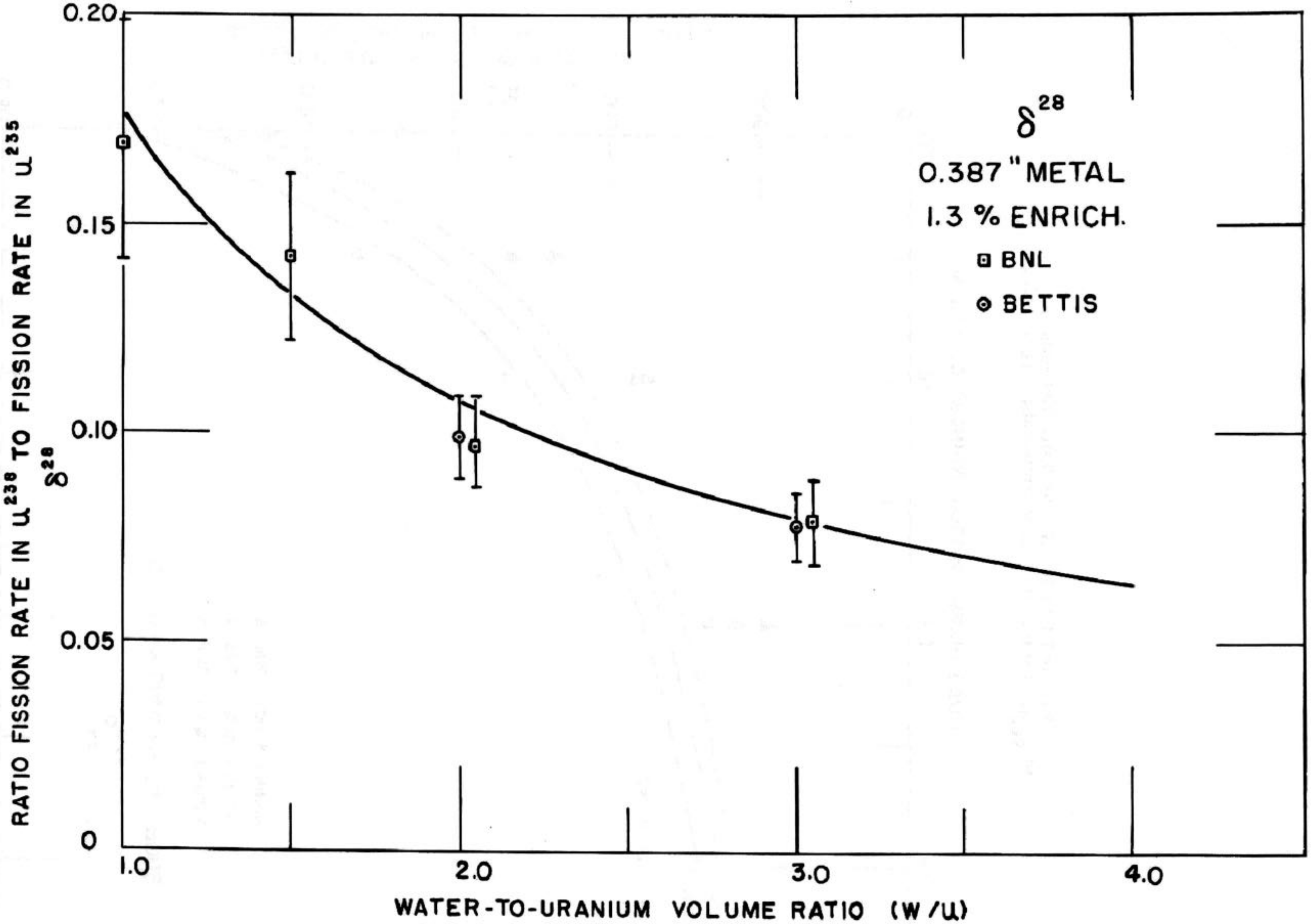

Fig. 12.20 - Fast Fission Ratio for 0.387-Inch-Diameter Metal Rod Lattices.

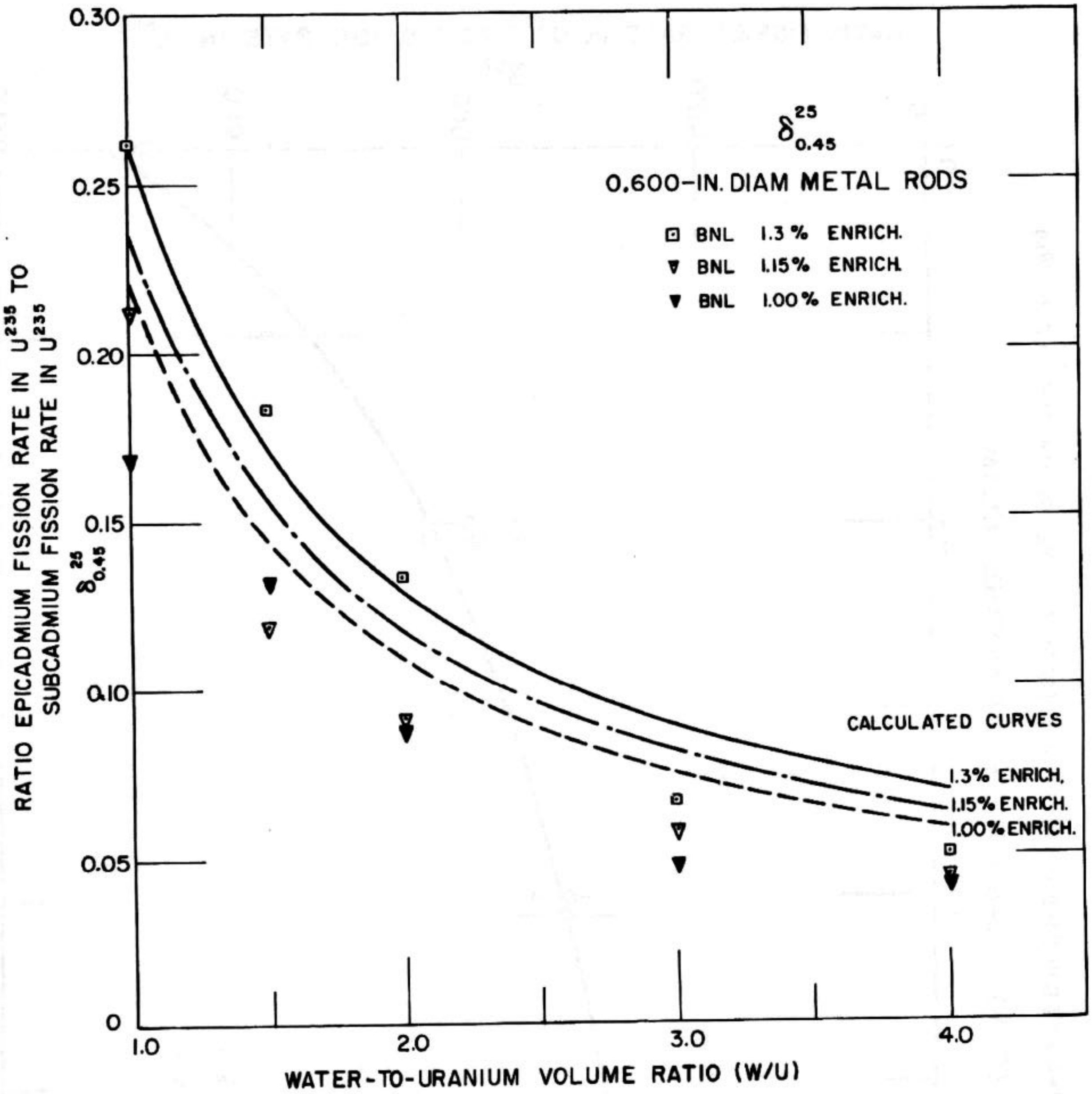

Fig. 12.21 - Epicadmium Fission Ratio in U^{235} in 0.600-Inch-Diameter Metal Rod Lattices.

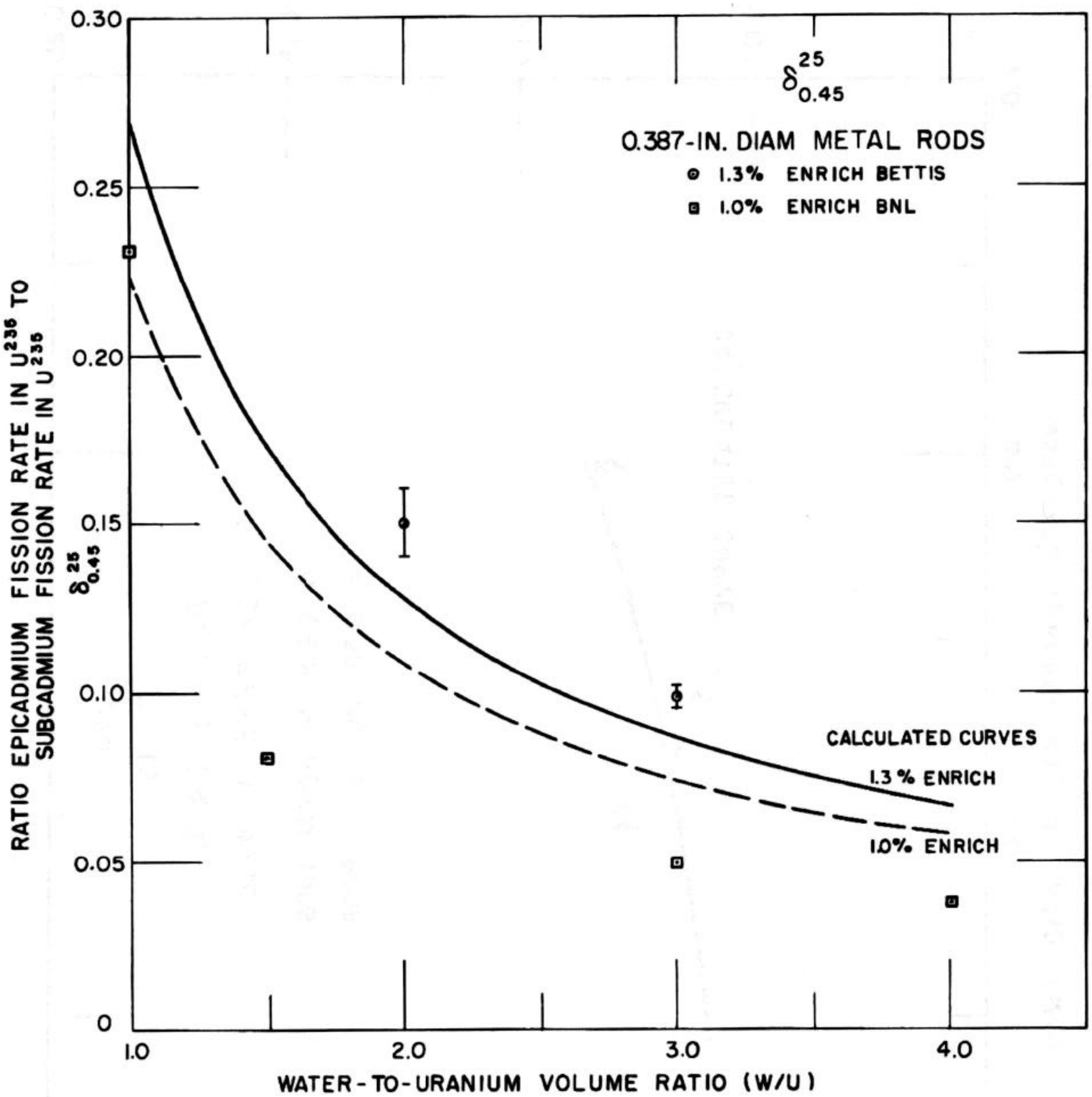

Fig. 12.22 - Epicadmium Fission Ratio in U^{235} in 0.387-Inch-Diameter Metal Rod Lattices.

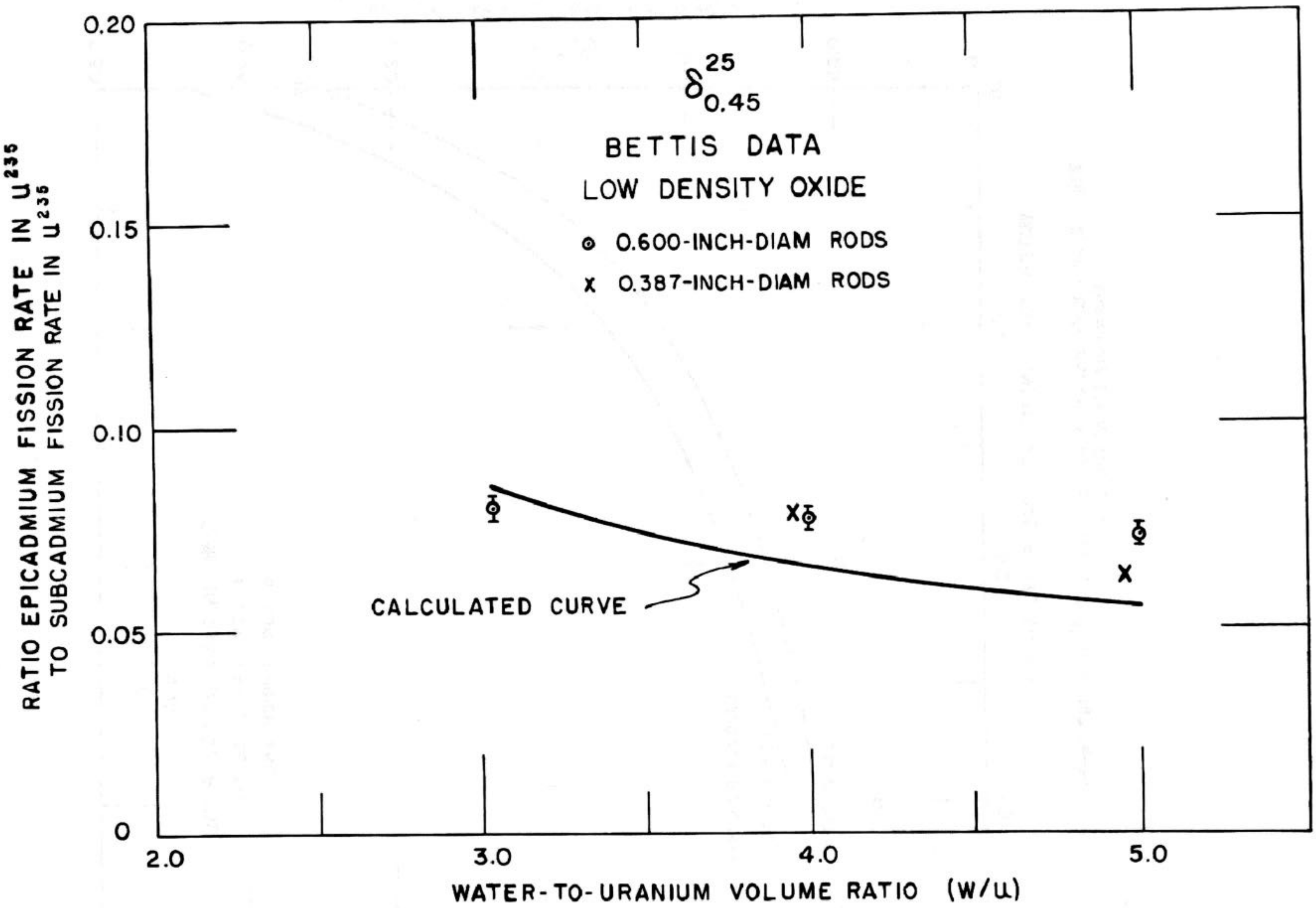

Fig. 12.23 - Epicadmium Fission Ratio in U^{235} in Low Density Oxide Rod Lattices.

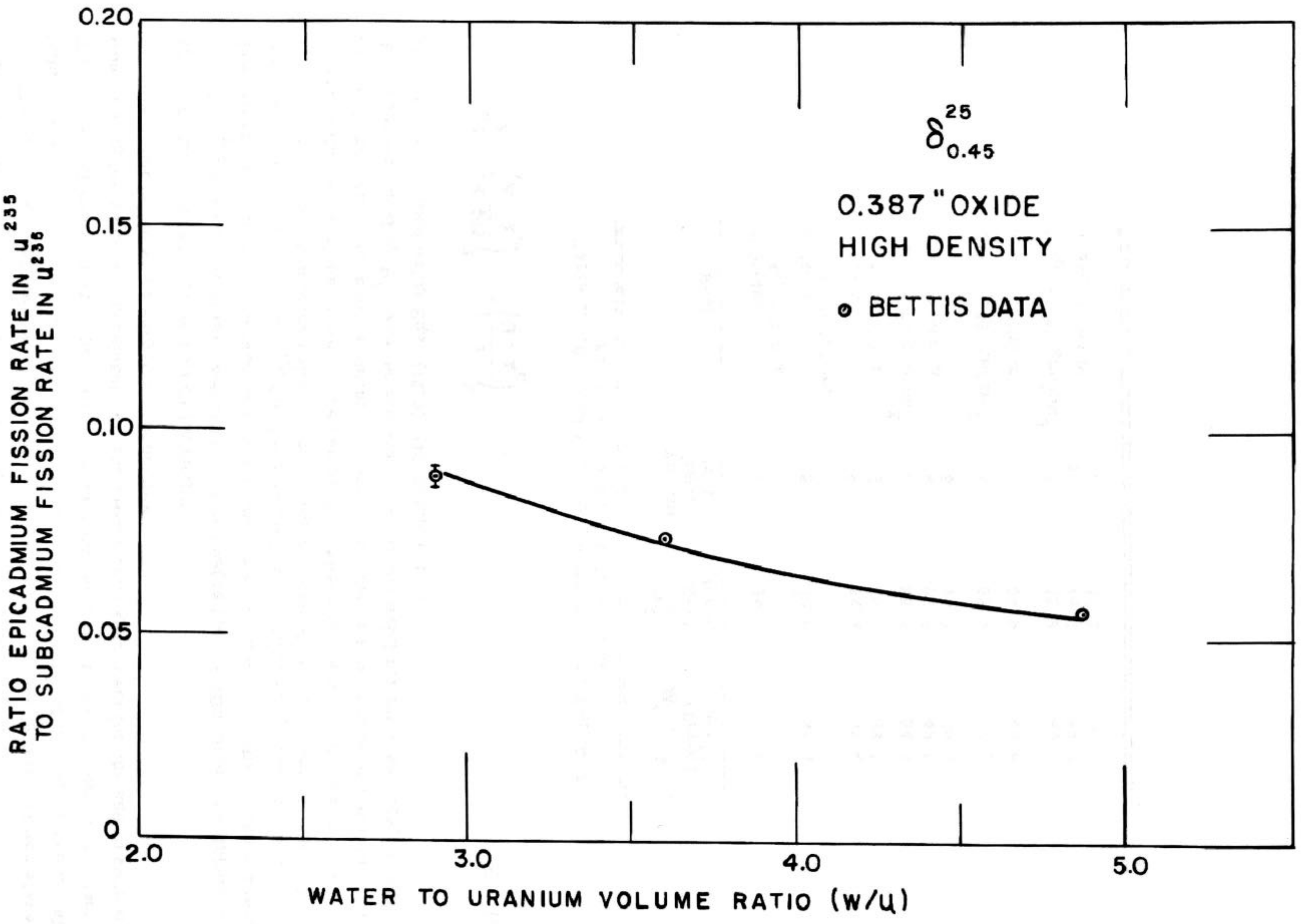

Fig. 12.24 - Epicadmium Fission Ratio in U^{235} in 0.387-Inch-Diameter High Density Oxide Rod Lattices.

12.17 MIGRATION AREA

The MUFT calculation provides a value of τ, while L^2 may be obtained from the thermal-group calculation of D_s and the macroscopic absorption cross section, Σ_a. Writing $M^2 = L^2 + \tau$, a set of values of the migration area may be calculated to be compared with the experimental results given in Table 12.8. The comparison is shown in Table 12.10.

The agreement between the calculated and experimental values is fair. Of the eleven values, seven agree within the estimated ± 4 per cent uncertainty of the experimental values. Two values differ by about 10 per cent, and the remaining two between 5 and 10 per cent. Considering the basic disagreement between theory and experiment for the age in pure water, the agreement is, in some respects, surprising.

12.18 OVER-ALL REACTOR CALCULATIONS

The k_{eff} was computed for each of the lattices using the WANDA code (see Appendix A). The two-group form was generally used since studies on a number of lattices showed that the two- and four-group values of k_{eff} for these large lattices differed by less than 0.1 per cent.

The calculation was made using the constants calculated by MUFT and SOFOCATE and the experimental value of the critical core radius, R. Where the lattice had not been made critical but had been measured in an exponential experiment, the critical radius was obtained from the measured buckling B^2, and the measured radial and axial reflector savings, λ_r and λ_h. Thus R is calculated using Eqs. (12.2), (12.3) and (12.4).

$$B_g^2 = \left(\frac{2.405}{R + \lambda_r}\right)^2 + \left(\frac{\pi}{H + \lambda_h}\right)^2 \qquad \text{Eq. (12.16)}$$

Table 12.10--COMPARISON OF EXPERIMENTAL AND CALCULATED MIGRATION AREAS

Fuel	Volume Ratio W/U	$M_\perp^2$ (Exp) (cm^2)	$M^2 = L^2 + \tau$ (Theor) (cm^2)
U Metal 1.3%, 0.600 in.	2	34.1	31.6
U Metal 1.15%, 0.600 in.	2	30.9	31.4
U Metal 1.3%, 0.387 in.	2	34.2	33.4
	3	36.2	32.1
UO_2, 7.53 gm/cm^3 1.3%, 0.600 in.	3	53.4	54.3
	4	52.5	49.5
	5	46.7	46.2
UO_2, 7.53 gm/cm^3 1.3%, 0.388 in.	4	53.7	53.6
	5	54.9	49.6
UO_2, 10.53 gm/cm^3 1.3%, 0.383 in.	3	45.8	44.7
	3.6	44.3	42.3
	5	40.6	--

In general, the calculated k_{eff} is different from unity. In all cases calculated, the k_{eff} was greater than one, i.e., the reactor is calculated to be supercritical. Table 12.11 gives the calculated results for the oxide lattices. In every case the calculated reactor is approximately 2 per cent supercritical. The results for the metal lattices are plotted in Figs. 12.25 and 12.26. Again, the calculated values of k_{eff} are high but somewhat less than those for the oxide lattices.

Table 12.11--CALCULATED VALUES OF k_{eff} FOR OXIDE CRITICAL LATTICES

Fuel	Volume Ratio W/U	k_{eff}
Low Density 1.3%, 0.600 in.	3	1.016
	4	1.022
	5	1.024
Low Density 1.3%, 0.388 in.	4	1.014
	5	1.021
High Density 1.3%, 0.383 in.	3	1.019
	3.6	1.019

The calculated reflector savings may be compared with the experimental values. The results are shown in Figs. 12.27 and 12.28 for the metal lattices. The calculated reflector savings are consistently about 0.5 cm less than the measured values. Because of the relatively large size of the reactor, this error in reflector savings has a relatively small effect on the criticality calculation.

Finally, the discrepancy in the calculated value of k_{eff} can be shown in another way. The WANDA code can provide a k_{eff} of unity by varying the buckling. This buckling may then be compared with the measured bucklings. The comparison is shown in Figs. 12.29 and 12.30 for the metal lattices. The notation "experimental flux ratios" refers to the use of $\bar{\phi}_W / \bar{\phi}_U$ as measured for computation of the thermal utilization rather than the theoretical value.

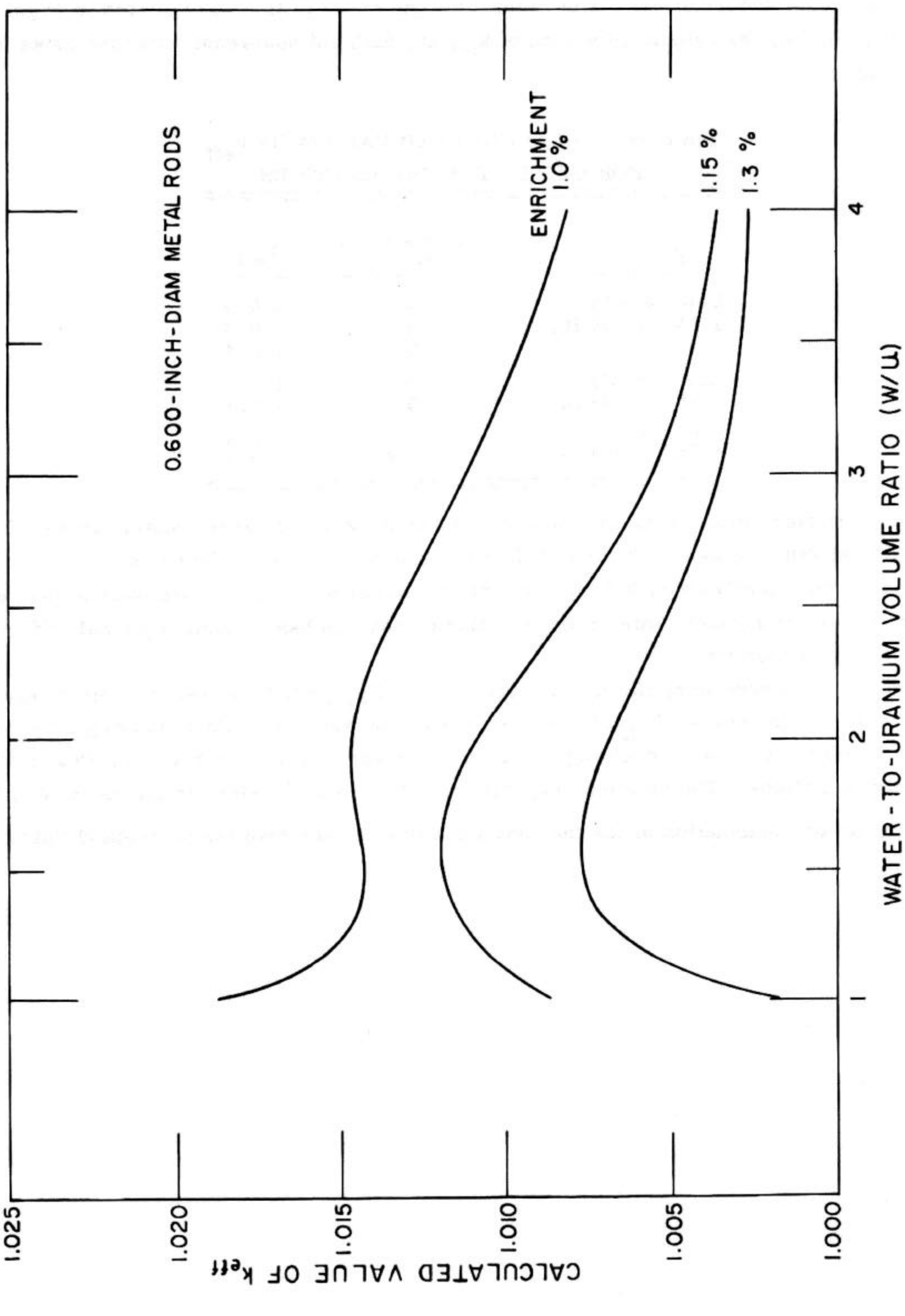

Fig. 12.25 - Calculated Value of k_{eff} for 0.600-Inch-Diameter Metal Lattices of Size Equal to Experimentally Determined Critical Size.

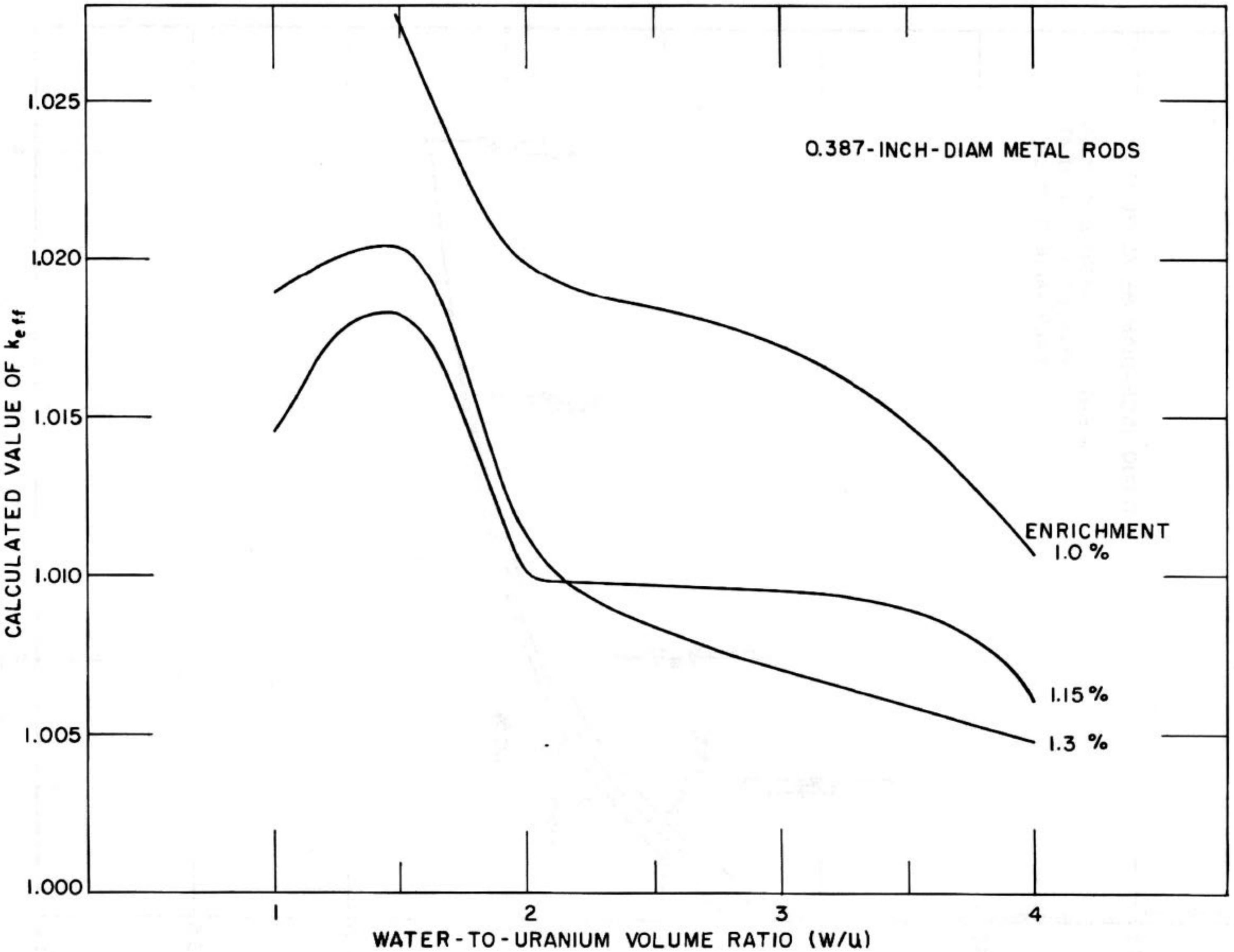

Fig. 12.26 - Calculated Value of k_{eff} for 0.387-Inch-Diameter Metal Lattices of Size Equal to Experimentally Determined Critical Size.

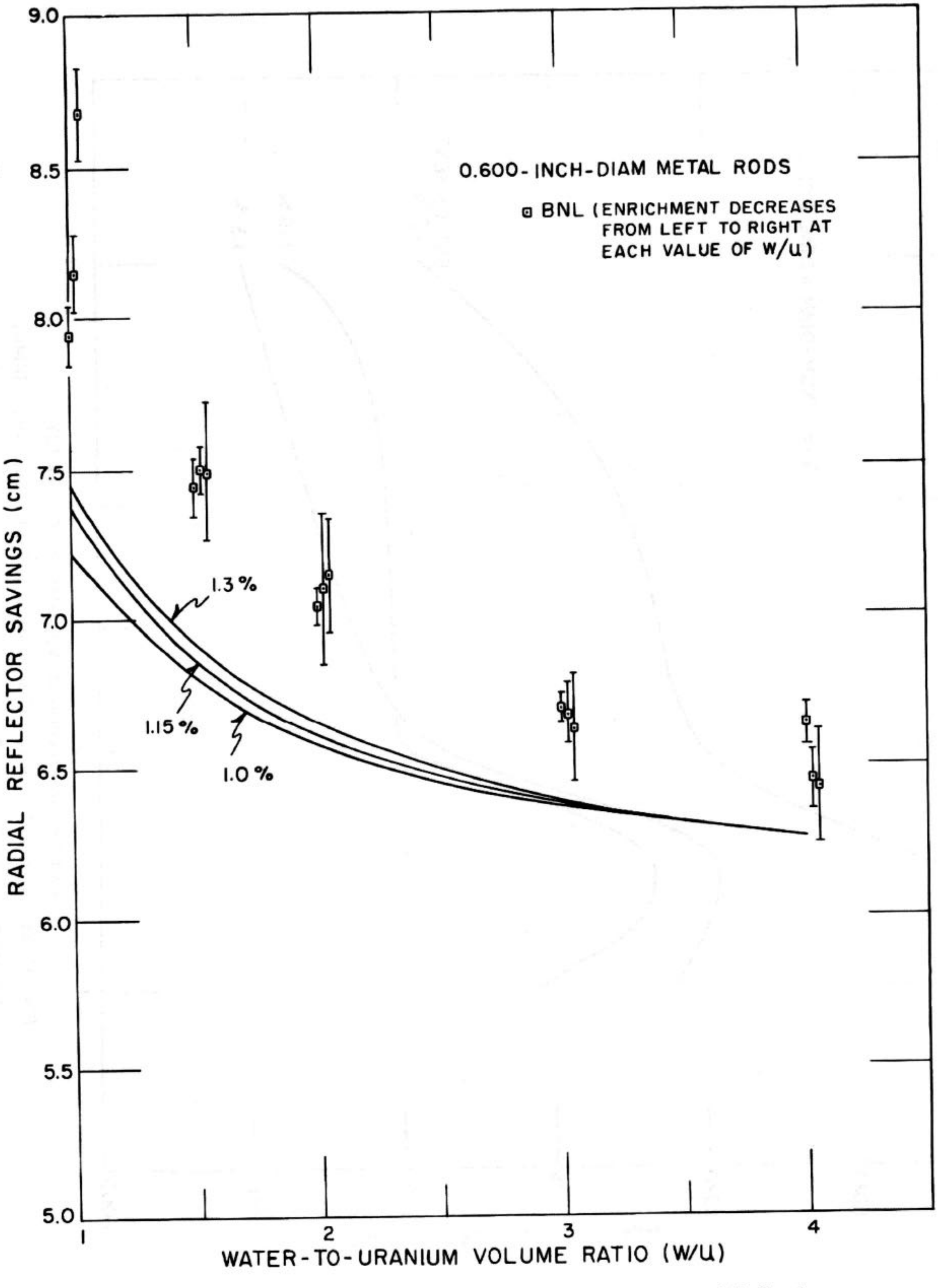

Fig. 12.27 - Comparison of Calculated and Experimental Reflector Savings for 0.600-Inch-Diameter Metal Rod Lattices.

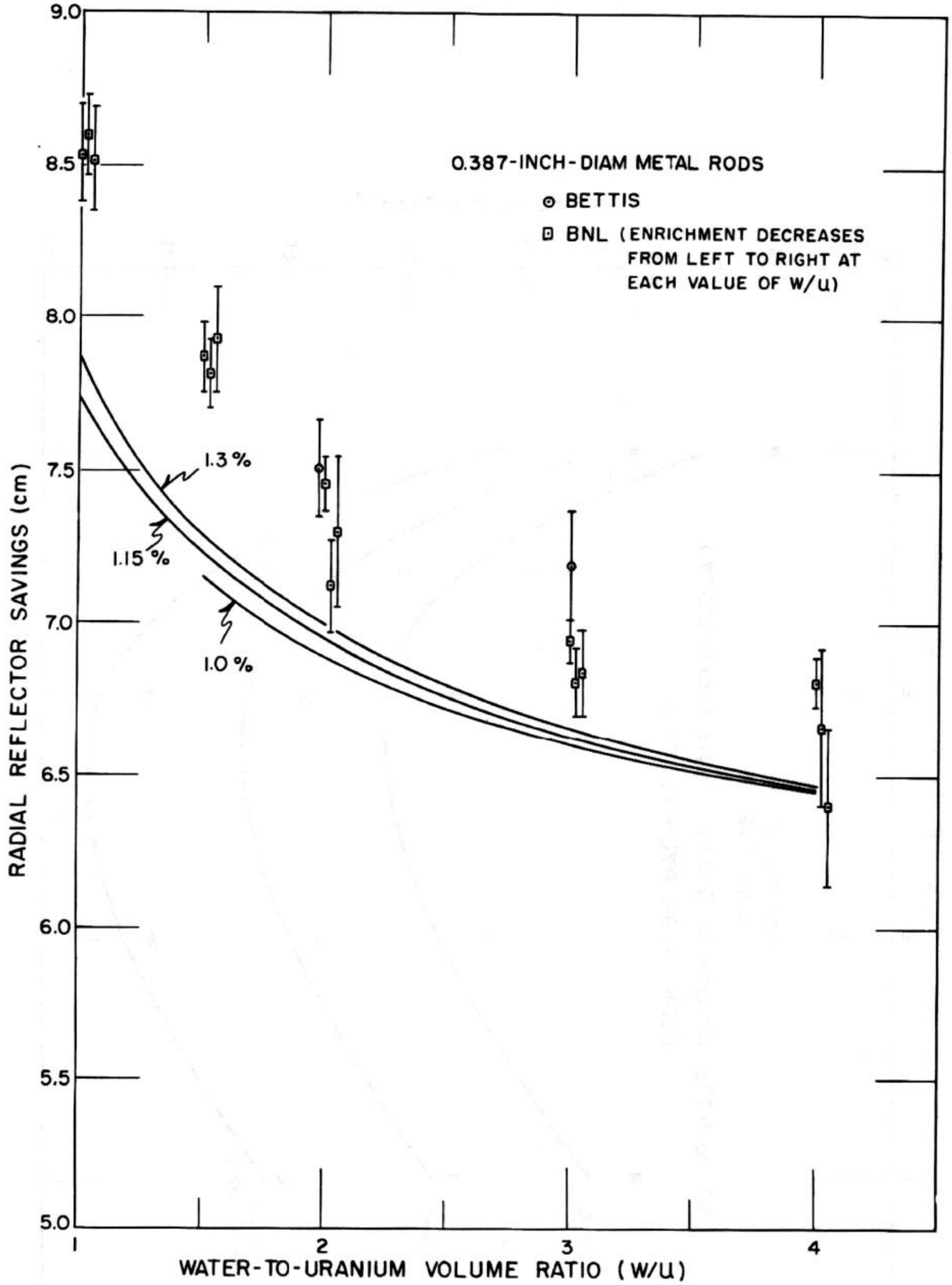

Fig. 12.28 - Comparison of Calculated and Experimental Reflector Savings for 0.387-Inch-Diameter Metal Rod Lattices.

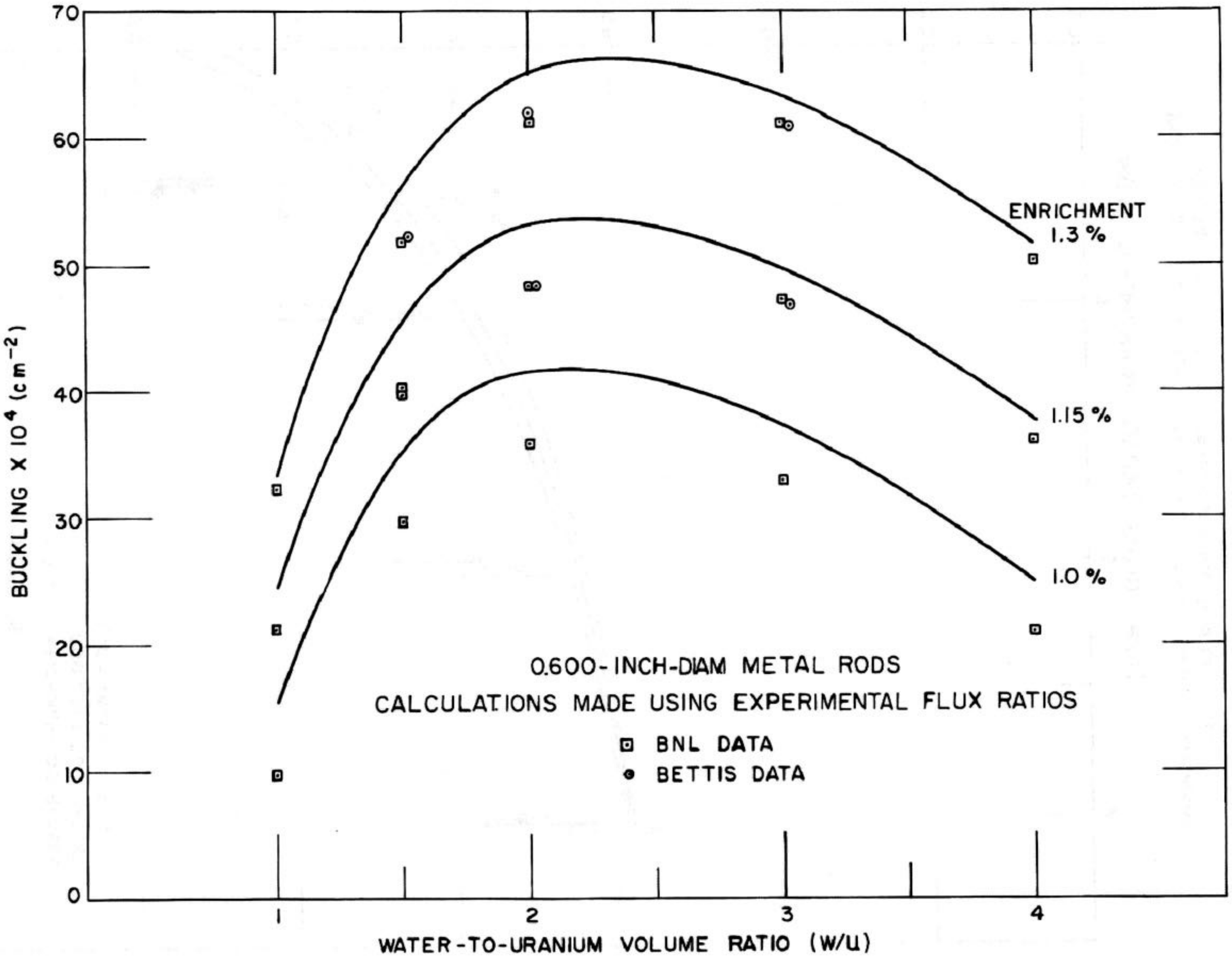

Fig. 12.29 - Comparison of Calculated and Experimental Bucklings for 0.600-Inch-Diameter Metal Rod Lattices.

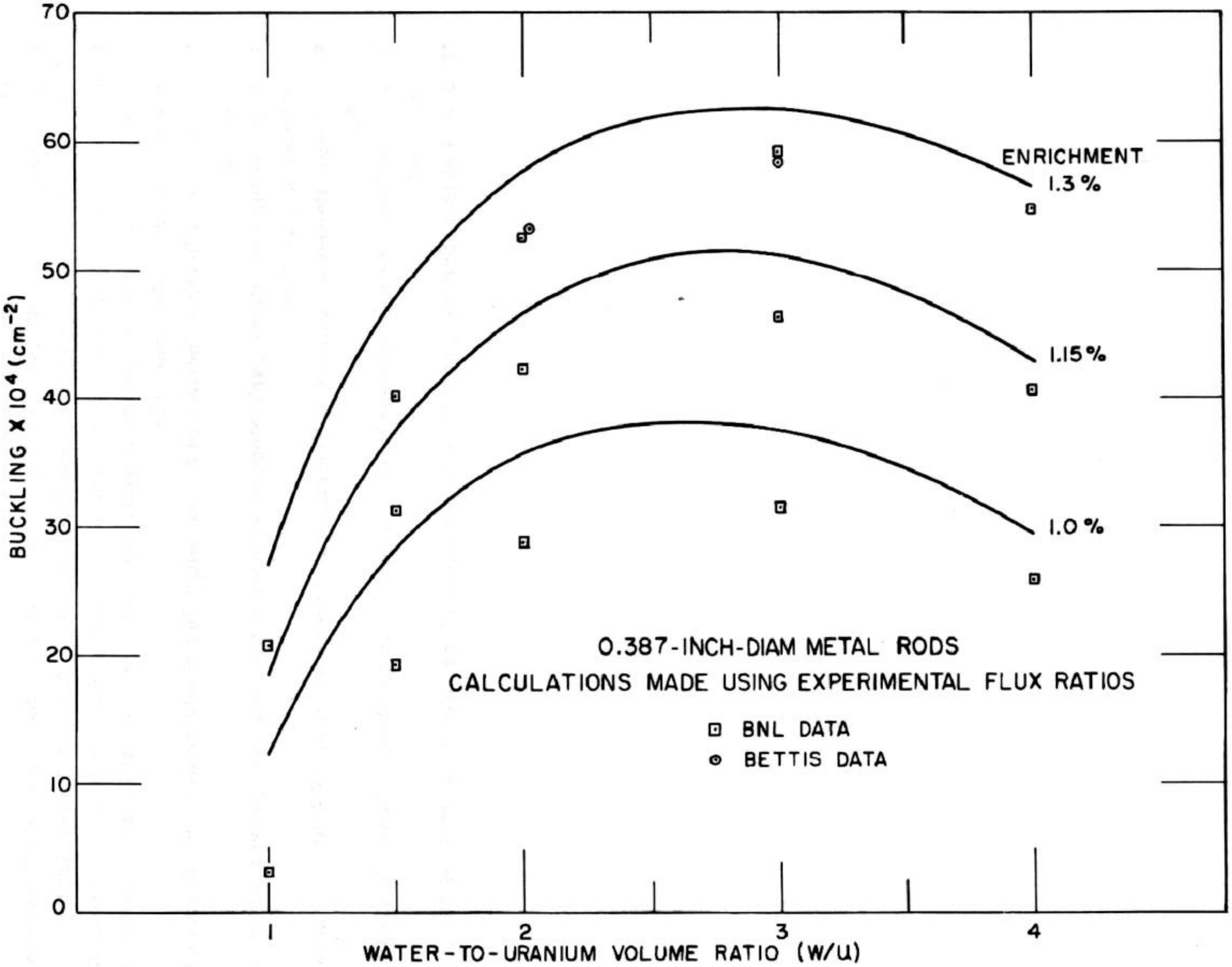

Fig. 12.30 - Comparison of Calculated and Experimental Bucklings for 0.387-Inch-Diameter Metal Rod Lattices.

REFERENCES

1. J.R. Brown et al, Kinetic and Buckling Measurements on Lattices of Slightly Enriched Uranium or UO_2 Rods in Light Water, Report WAPD-176, January 1958.
2. A.M. Weinberg, American Journal of Physics, 20:401 (1952).
3. H. Kouts et al, Exponential Experiments with Slightly Enriched Uranium Rods, Proceedings of the (1955) International Conference on the Peaceful Uses of Atomic Energy, 5:182 (1956).
4. G.R. Keepin, T.F. Wimett, and R.K. Zeigler, Delayed Neutrons from Fissionable Isotopes of Uranium, Plutonium, and Thorium, Phys. Rev., 107:1044 (1957).
5. D. Klein et al, Measurements of Thermal Utilization, Resonance Escape Probability, and Fast Effects in Water Moderated Slightly Enriched Uranium and Uranium Oxide Lattices, Report WAPD-T-572, June 1957.
6. B. Davison, Effective Thermal Diffusion Length in a Sandwich Reactor, Report CRT-715, July 1957.
7. R.D. Richtmyer, Monte Carlo Study of Resonance Escape in Hexagonal Reactor Lattices, NYO-6479, May 1955.
8. S. Stein, Resonance Capture in Heterogeneous Systems, Report WAPD-139, November 1955.
9. R.L. Hellens, Neutron Slowing Down in Group Diffusion Theory, Report WAPD-114, May 1956.
10. S.J. Lukasik, Summary of TRX Analysis Calculations, Report WAPD-TM-75, July 1957.

Chapter 13

THE ANALYSIS OF HIGHLY ENRICHED SLAB CRITICAL EXPERIMENTS

13.1 INTRODUCTION

This chapter presents the data obtained on an extensive series of highly enriched critical slab experiments and the analyses of these data by the standard methods used in the design of pressurized water reactors. These experiments and calculations are intended to provide a basis for assessing the validity of some of the methods used in the nuclear design of highly enriched reactors.

The slab experiment was carefully designed in two important respects in order to facilitate this assessment. First, the composition of the reactor was made homogeneous in a macroscopic sense; second, the geometry was made relatively simple. The intent of these design features was to test the analysis in as fundamental a manner as possible.

Two different pieces of information are obtained from each experiment, namely, the critical size and the flux distribution (thermal and epithermal). Since the comparison of the experiments and the calculations is made on an integral basis, agreement might be due to compensating errors. Therefore, a series of experiments was performed to broaden the base over which the validity of the calculations was examined. While the composition of the core itself was kept substantially unchanged throughout the series, varieties of reflectors and reflector compositions were used. In addition, water channels were introduced into the core itself in certain experiments.

The results of this work have shown good agreement between calculation and experiment with respect to criticality. In general, the calculated k_{eff} agreed with experiment within 1 per cent. In a few cases the deviation was as much as 2 per cent. On the other hand, systematic differences were found in thermal flux distributions, particularly in water reflectors and in thick water channels within the reactor.

DESCRIPTION OF THE EXPERIMENTS

by C.E. McFarland

13.2 DESCRIPTION OF THE REACTOR

The experiments were performed in the SFR critical facility which is described in some detail in Chap. 9. A few of the pertinent features of the reactor will be reviewed briefly here. The critical assemblies were constructed from close-packed, vertical fuel bundles. Figure 13.1 is a sketch of a fuel bundle.

Each of the bundles contained five zirconium metal plates; 45 inches long, 0.910 inch wide and 0.110 inch thick. The fuel (U_3O_8 enriched to over 90 per cent in U^{235}) was dispersed in polyethylene tapes. Four plastic-uranium fuel tapes, each 40.25 inches in length, were folded double in width and sandwiched between the five zirconium metal plates. A handling tab was attached to the top of the center (the third) zirconium plate while a tapered positioning pin was secured to the bottom of the same plate. The bundle, 45 inches in length with a cross-sectional area of 0.910 inch, was formed by fastening the zirconium metal plates and tapes together with aluminum rivets.

The slab cores were made up of an array of these fuel bundles. Each bundle within an array was positioned with its long axis vertical. The bundles were so arranged that the edges of the zirconium plates within any one bundle were perpendicular to the flat surface of the zirconium plates of the bundle immediately adjacent. The bottom of each bundle was secured in place by setting its tapered positioning pin into a tapered hole in an aluminum base plate. The base plate positioning holes were arranged in a square array with a 1-inch separation between holes. The bundles were supported laterally at the top by an egg-crate structure.

The entire core region was made up of these fuel bundles. When a metal-water reflector was provided for the slab, the reflector assembly was made up of metal strips arranged in bundles, as described above, but without fuel. The assembly, slab core and reflector, was mounted in a tank so that the assembly could be flooded with water. The slab was located in the tank in such a way that the water reflecting region between the tank walls and the assembly was a minimum of 20 inches. Figure 13.2 is a sketch of the slab arrangement.

Two control rods were used in each assembly. Each control rod was in the form of a long hollow cadmium tube with a square cross section equal in area to that of a group of four fuel bundles. Four fuel bundles, identical to those used to make up the reactor core, were attached to the bottom end of each of the control rods. Thus, as the control rods were withdrawn, the space previously occupied by the cadmium was filled by the four fuel bundles. This prevented the formation of a large, water-filled hole in the core and maintained the homogeneity of the

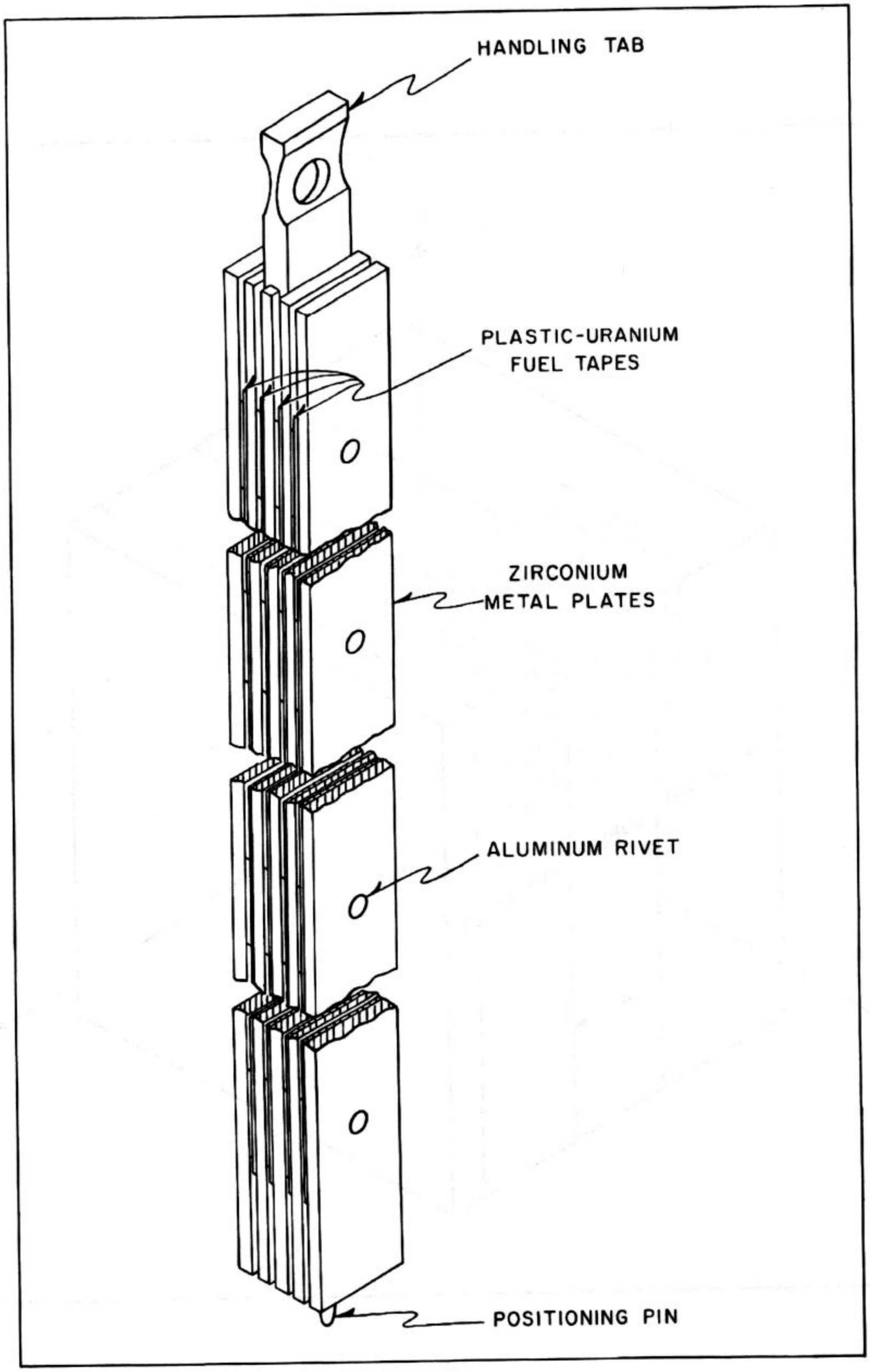

Fig. 13.1 - Fuel Bundle for Slab Critical Experiments.

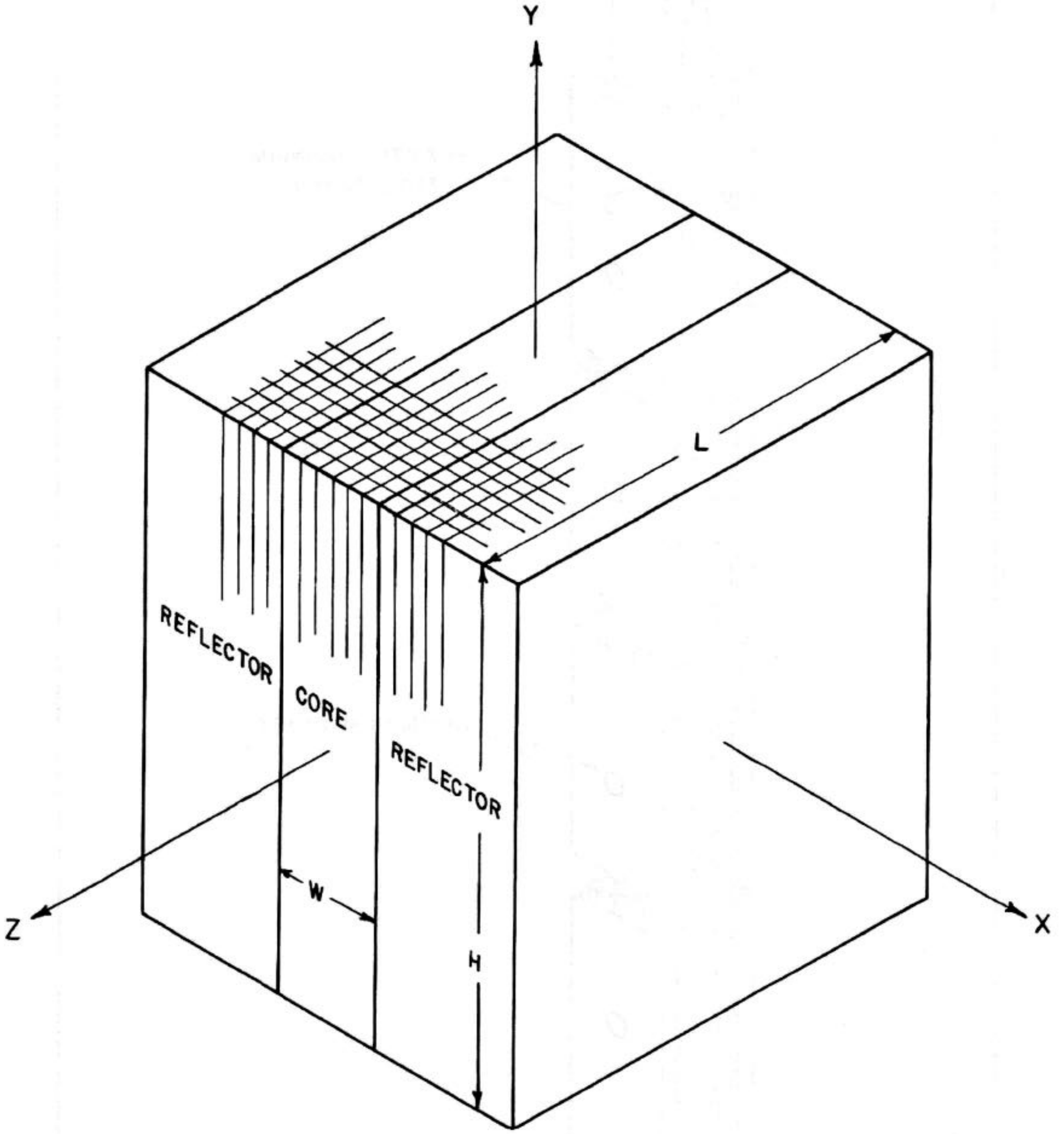

Fig. 13.2 - Sketch of Slab Assembly.

structure. The dimensions of each assembly were adjusted experimentally to make it critical with both control rods very nearly completely withdrawn. When the control rods were fully withdrawn, the tops of the movable fuel assemblies were at the same plane as the tops of the fixed bundles.

13.3 FLUX MAPPING TECHNIQUES

The flux traverses were taken, as described in Chap. 10, by activating bare and cadmium-covered manganese wires. Some details of the method will be reviewed briefly here.

The irradiated samples were in the form of small lengths of 14 per cent manganese-iron wire 1/2 inch long and 0.030 inch in diameter. The weights of the wires of any one given group were selected to be within ± 1/2 per cent of the group average to reduce errors due to non-uniform sample size. The wires were supported in place within the critical assemblies in Lucite or Plexiglas wands 1/16 inch thick and 1-1/2 inches wide. The wires were mounted in slots milled perpendicular to the long dimension of the wand, one wire to a slot. The wires were held in place within their respective slots by a strip of adhesive Mylar tape which covered the filled slots.

A previous investigation had shown that there was no significant disturbance of the flux shape due to interaction of the manganese wires when spaced 0.1 inch apart. It had also been determined that cadmium-covered wires spaced 0.5 inch apart did not interact seriously. These were the minimum spacings used in the traverse for the respective measurements. It had been found, however, that the presence of the cadmium-covered wires did affect the thermal flux locally. For this reason the cadmium-covered and bare wire traverses were taken with the wands separated but still located symmetrically about the axes of the core. The location of the traverses is shown on the diagrams of the various experiments.

The activity of the samples was measured by counting the beta decay. One-millimeter-thick anthracene crystals with photomultipliers were used for this purpose. Decay corrections were applied automatically using the techniques described in Chap. 10. The percentage of error in the measured activation at a given point on the flux traverse is estimated to be 5 per cent. This is due to the combination of uncertainties in counting, wire size, wire position, and non-uniform flux peaking in the vicinity of the wire samples.

13.4 METHOD OF PERFORMING EXPERIMENTS

The experiments were performed by adjusting the size of each lattice so that the control rods were essentially withdrawn completely with the core in a rectangular array. In general, one control rod had to be inserted slightly, of the order of 5 inches, to provide sufficient excess reactivity to reach a suitable power level. The control rod was calibrated to correct for this residual insertion.

Over the distance involved, the calibration of the control rod was essentially the same for all of the slabs. Figure 13.3 shows the calibration curve obtained for a control rod. This calibration was taken by the rod-bump period technique described in Chap. 8. For a rod insertion of the order of 5 inches, the reactivity involved is about 0.1 per cent. This residual reactivity, expressed fractionally, was added to unity for each of the critical slabs. Thus, the experimental values of k_{eff} given represent the neutron multiplication which would occur if the control rod were completely withdrawn.

At the higher flux levels used in taking flux traverses, some of the critical assemblies exhibited a reactivity drift. The reason for this drift is not known but is generally attributed

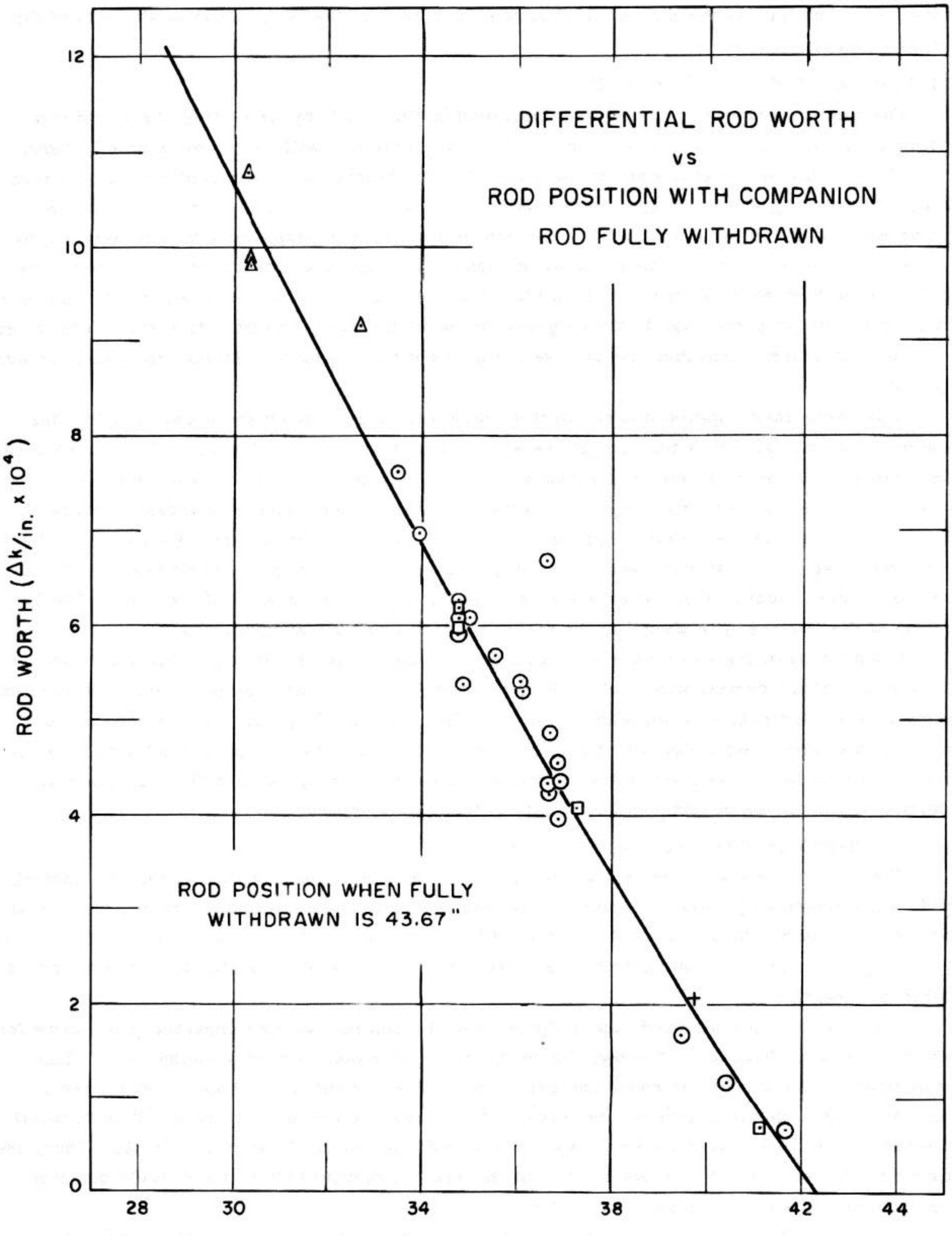

Fig. 13.3 - Control Rod Calibration Curve.

to gas bubbles on the reactor surfaces. Because of it, however, the experimental values of k_{eff} quoted are estimated to be uncertain to about 0.1 per cent.

13.5 SUMMARY OF EXPERIMENTS

A total of seven different assemblies were constructed using the same reactor core bundles. Table 13.1 gives the material inventory for each core bundle based on a loaded length of 40.25 inches. The calculated number densities for the core are also given in this table. If the density of hydrogen in polyethylene is taken as 1.2 times that in water, the metal-to-equivalent water volume ratio in the core is very close to unity.

Of the seven assemblies, three were bisected by water gaps. The others employed reflectors of varying composition. In three of the cases, different reflectors were used on the two sides of the slab. The experimental data obtained are presented in the subsequent sections of this chapter together with the calculated results.

Table 13.1--CORE COMPOSITION DATA

Material Inventory per Core Bundle	Nuclear Number Densities Used in Analysis in units of 10^{24} per cm^3
Effective volume of bundle = 40.25 in.^{3}	N^{235} = 0.0001717
Mass of U_3O_8 = 56.08 gm	N^{Zr} = 0.02132
Mass of polyethylene = 76.97 gm	N^{H} = 0.03368
Volume of zirconium = 20.11 ± 0.20 in.^{3}	N^{O} = 0.01233
Volume of water = 14.28 ± 0.53 in.^{3}	N^{C} = 0.00502
Volume of aluminum = 0.057 in.^{3}	N^{238} = 0.000012
Uranium was enriched to 93.37%	

ANALYSIS OF ZIRCONIUM CORE SLAB EXPERIMENTS

by A.D. Voorhis

13.6 GENERAL METHOD OF CALCULATION

Figure 13.2 shows a representative critical assembly. The core has a width W, which is comparatively small, and a length L and a height H which are comparatively large. The principal neutron leakage from the core occurs across the narrow dimension W. Therefore, the behavior of the assembly can be well described by a one-dimensional calculation along the X-axis (Fig. 13.2) treating the leakages along the Y and Z axes as corrections.

The criticality analysis was carried out as a one-dimensional diffusion type calculation along the X-axis assuming the core, reflectors, and surrounding water to be separate diffusing media. The diffusion calculation was made on an IBM-704 using the WANDA code (see Appendix A) for both two- and four-energy groups. The WANDA code has provision for incorporating a transverse buckling, B_T^2, to take account of neutron leakage along axes other than that being calculated, i.e., Y and Z axis leakage in this case. The method of determining B_T^2 will be discussed later.

The group constants used in the fast energy groups of the WANDA code were calculated by means of the MUFT-3 code (see Appendix E). The calculation was made in 54 energy groups. The MUFT codes have provision for insertion of a buckling, B^2, to describe the effect of leakage on the fast group constants. The buckling is chosen to simulate as closely as possible the average fast neutron leakage of the core.

The thermal group constants were calculated separately for each region. Because of the high thermal absorption in the core, it was decided to calculate the core constants by averaging over a hardened spectrum of the Wigner-Wilkins type. This calculation was made with the DONATE code (see Appendix D). The thermal hardening in regions other than the core was negligible due to the low absorption. The thermal constants for the reflector regions were calcultated by taking Maxwellian averages at 20°C.

13.7 DETAILS OF THE PROCEDURE FOR CALCULATION

The first step in the numerical procedure was to homogenize each of the regions and to calculate the mean nuclear number densities for each region at a temperature of 20°C. These number densities are listed in Table 13.1 for the reactor core. Taking the number densities for the core, the MUFT-3 code was used to calculate the fast group constants. Table 13.2 tabulates the results for both a four-group scheme and a two-group scheme. The energy range of each group is shown under the group designation for each scheme. The B^2 used in the MUFT-3 core calculation was 10^{-2} cm^{-2}. This corresponds to a multiplication constant of about 1.6

Table 13.2--CALCULATED GROUP DIFFUSION CONSTANTS FOR REACTOR CORE

		MUFT-3 Code ($B^2 = 10^{-2}$ cm^{-2})			DONATE Code ($B^2 = 0$ cm^{-2})
		Group 1 (10 Mev-821 kev)	Group 2 (821 kev-5.53 kev)	Group 3 (5.53 kev-0.625 ev)	(0.625 ev-0.0 ev)
4-Group Scheme	D (cm)	2.756	1.070	0.6586	0.3180
	Σ_r (cm^{-1})	0.05842	0.07442	0.07201	---
	Σ_a (cm^{-1})	0.000751	0.000460	0.006074	0.09231
	$\nu\Sigma_f$ (cm^{-1})	0.000630	0.000808	0.01063	0.1694
	χ	0.7517	0.2483	0.0000	0.0000
			Group 1 (10 Mev-0.625 ev)		Group 2 (0.625 ev-0.0 ev)
2-Group Scheme	D (cm)		1.526		0.3180
	Σ_r (cm^{-1})		0.02212		---
	Σ_a (cm^{-1})		0.002284		0.09231
	$\nu\Sigma_f$ (cm^{-1})		0.003764		0.1694
	χ		1.000		0.0000

Legend for Constants:

D - Group Diffusion Constant

Σ_r - Group Removal Cross Section (for transfer to next lower group)

Σ_a - Group Absorption Cross Section

Σ_f - Group Fission Cross Section for the core material and an age for the core material of around 60 cm^2.

The last column in Table 13.2 lists the thermal group constants as obtained from the DONATE code. In this case, the B^2 was taken to be zero since there was no thermal leakage out of the reactor (the effect of leakage on the thermal group constants is quite small in any event).

The constants shown in Table 13.2 will of course depend on the cross sections used for the individual nuclei. These cross sections are tabulated on a library of punched cards or a magnetic tape which forms an integral part of the scheme of calculations.[1, 2]

The constant X in Table 13.2 represents the fraction of fission energy neutrons which are assumed to originate within the particular energy group. The constant ν is the number of neutrons emitted in fission of U^{235}. This was taken as 2.46.

In the calculations of the constants no self-shielding was assumed for any of the nuclei.

In all cases, when averaging the thermal diffusion constant D over the thermal spectrum (either Wigner-Wilkins or Maxwellian), the binding of the hydrogen in the water molecule was accounted for by using the Radkowsky prescription for the effective mass.[3] In the case of the core region, it was assumed, for purposes of calculating D, that all of the hydrogen was bound to oxygen even though one-third of it was actually bound to carbon in polyethylene.

The transverse buckling (used in the WANDA calculation) which accounted for neutron leakage along the Y and Z axes (Fig. 13.2) was computed for each assembly using the relation

$$B_T^2 = \pi^2 \left[\frac{1}{(M + 2\delta)^2} + \frac{1}{(H + 2\delta)^2} \right] \qquad \text{Eq. (13.1)}$$

where M and H are the two long dimensions of the core shown in Fig. 13.2 and δ is an effective reflector savings at the core-water interface. The relation (Eq. (13.1)) implies that the neutron flux is almost a cosine in shape and is separable along the Y and Z axes of the assembly. In making this correction δ is taken to be constant as will be discussed in the next paragraph.

From typical epicadmium flux plots taken along the Z axis of the assembly it was apparent that this cosine-like behavior was approximated quite well by the fast neutrons which contribute over 90 per cent of the effective leakage from the critical assembly. Values of δ were obtained from the experimental plots of the epicadmium activation along the Z axis by fitting cosine curves to these plots and determining the distance beyond the core-water interface at which the cosine curves extrapolated to zero. In this way it was determined from a series of assemblies that

$$\delta = 3.2 \pm 0.2 \text{ inches.}$$

The value $\delta = 3.20$ inches was used in calculating B_T^2 for both the Y and Z axes. While the reflector savings along the Y axis is not precisely the same as that along the Z axis, a simple theoretical calculation shows that they differ by less than 5 per cent for the core sizes considered here. This error is less than the uncertainty with which δ is known.

In making the WANDA calculation it was necessary to set an outer boundary condition along the X axis. It was assumed that the neutron flux in all groups became zero at a large but finite distance from the central core. This point was 10 to 15 inches out in the outer water reflector.

The solution of the few-group diffusion equations by the WANDA code provides both a value of k_{eff} and the fluxes as a function of position in each energy group. The calculated assembly would be just critical if the calculated k_{eff} were unity. In the analyses of the experimental slabs, the calculated k_{eff} is compared directly with the corrected k_{eff} of the experimental assembly (with the rods fully withdrawn).

The number densities and calculated group constants for the various reflector compositions are given in Table 13.3 for pure water; in Table 13.4 for a zirconium-water reflector in a 1:1 metal-to-water volume ratio; in Table 13.5 for a zirconium-water reflector in a 7:3 metal-to-water volume ratio; in Table 13.6 for an aluminum-water reflector in a 1:1 metal-to-water volume ratio. These were calculated using the MUFT-3 code for the fast group constants and a Maxwellian average for the thermal group constants. The notation used is the same as that of Table 13.2.

13.8 EXPERIMENT NO. 1--WATER REFLECTED SLAB

This experiment employed a rectangular slab 6 inches by 31 inches by 40-1/4 inches. The slab was water reflected on all sides. The core dimensions are shown in the sketch of Fig. 13.4. The letters C and R in the plan view show the location of the two control rods. The letters A and B indicate the locations at which the transverse flux traverses (bare and cadmium-covered) were taken.

The criticality results are as follows:

Experimental k_{eff} (rod free)	1.001
Calculated k_{eff} (2-group)	1.026
Calculated k_{eff} (4-group)	1.005

These calculations were made using the constants tabulated in Table 13.2 for the core and the constants tabulated in Table 13.3 for the reflector.

The calculated thermal group flux and the epithermal flux (group-3) are plotted as the solid lines in Fig. 13.5. These fluxes are plotted to scale in their calculated ratios. The circles represent the measured thermal activation distribution and the triangular points, the epicadmium activation distribution. It should be noted that fluxes are being compared to activation data.

The measured activation curve was fitted to the calculated curves in a fairly arbitrary fashion. Generally, this was done by matching the points and the curves just outside the core boundary. The thermal and epithermal activations were normalized independently to the calculated curves.

The two-group results are shown in Fig. 13.6. Only the calculated thermal flux is plotted.

As normalized on the plot, the four-group calculation agrees with the measured thermal activation distribution within 10 per cent over most of the core and in the outer region of the reflector. If the normalization were adjusted to fit in the core, the calculated flux peak in the reflector would be too low and would be displaced too far out in the reflector. The experimental activation plot clearly shows the inhomogeneity of the core structure with a ripple of 1-inch wavelength.

The two-group eigenvalue is not only inferior to the four-group result but the thermal flux distribution represents a noticeably poorer fit to the activation data.

Table 13.3--DATA FOR PURE WATER REFLECTOR

Nuclear Number Densities Used In Analysis

$N^H = 0.06692 \times 10^{24} / cm^3$ $N^O = 0.03346 \times 10^{24}/cm^3$

Calculated Group Diffusion Constants

		MUFT-3 Code ($B^2 = 0.005\ cm^{-2}$)			Maxwellian (20°C) Average
		Group 1 (10 Mev-821 kev)	Group 2 (821 kev-5.53 kev)	Group 3 (5.53 kev-0.625 ev)	Group 4 (0.625 ev-0.0 ev)
4-Group Scheme	D (cm)	2.230	1.094	0.5899	0.1511
	Σ_r (cm^{-1})	0.1067	0.1499	0.1515	--
	Σ_a (cm^{-1})	0.001356	0.0000	0.0000	0.01915
			Group 1 (10 Mev-0.625 ev)		Group 2 (0.625 ev-0.0 ev)
2-Group Scheme	D (cm)		1.331		0.1511
	Σ_r (cm^{-1})		0.04846		--
	Σ_a (cm^{-1})		0.000475		0.1915

Table 13.4--DATA FOR ZIRCONIUM-WATER REFLECTOR (VOL. ZR/VOL. WATER = 1 : 1)

Nuclear Number Densities Used in Analysis

$N^{Zr} = 0.02113 \times 10^{24}/cm^3$	$N^H = 0.03346 \times 10^{24}/cm^3$	$N^O = 0.01673 \times 10^{24}/cm^3$

		Calculated Group Diffusion Constants MUFT-3 Code ($B^2 = 10^{-2}$ cm^2)			Maxwellian (20°C) Average
		Group 1 10 Mev-821 kev)	Group 2 (821 kev-5.53 kev)	Group 3 (5.53 kev-0.625 ev)	Group 4 (0.625 ev-0.0 ev)
4-Group Scheme	D (cm)	2.787	1.083	0.6778	0.2522
	Σ_r (cm^{-1})	0.05804	0.07384	0.07415	---
	Σ_a (cm^{-1})	0.000584	0.0000	0.000159	0.01317
			Group 1 (10 Mev-0.625 ev)		Group 2 (0.625 ev-0.0 ev)
2-Group Scheme	D (cm)		1.532		0.2522
	Σ_r (cm^{-1})		0.02338		---
	Σ_a (cm^{-1})		0.000248		0.01317

Table 13.5--DATA FOR ZIRCONIUM-WATER REFLECTOR (VOL. ZR/VOL. WATER = 7:3)

Nuclear Number Densities Used In Analysis

$N^{Zr} = 0.02980 \times 10^{24}/cm^3$ $N^{H} = 0.01994 \times 10^{24}/cm^3$ $N^{O} = 0.009970 \times 10^{24}/cm^3$

		Calculated Group Diffusion Constants MUFT-3 Code ($B^2 = 0.0025\ cm^2$)			Maxwellian (20°C) Average
		Group 1 (10 Mev-821 kev)	Group 2 (821 kev-5.53 kev)	Group 3 (5.53 kev-0.625 ev)	Group 4 (0.625 ev-0.0 ev)
4-Group Scheme	D (cm)	3.234	1.060	0.7256	0.3581
	Σ_r (cm^{-1})	0.03514	0.04537	0.04579	---
	Σ_a (cm^{-1})	0.000367	0.0000	0.0001	0.01062
			Group 1 (10 Mev-0.625 ev)		Group 2 (0.625 ev-0.0 ev)
2-Group Scheme	D (cm)		1.672		0.3581
	Σ_r (cm^{-1})		0.01492		---
	Σ_a (cm^{-1})		0.000144		0.01062

Table 13.6--DATA FOR ALUMINUM-WATER REFLECTOR (VOL. AL /VOL. WATER 1:1)

Nuclear Number Densities Used in Analysis

$N^{Al} = 0.03012 \times 10^{24}/cm^3$	$N^{H} = 0.03346 \times 10^{24}/cm^3$	$N^{O} = 0.01673 \times 10^{24}/cm^3$

		Calculated Group Diffusion Constants MUFT-3 Code ($B^2 = 0.0025$ cm^{-2})			Maxwellian (20°C) Average
		Group 1 (10 Mev-821 kev)	Group 2 (821 kev-5.53 kev)	Group 3 (5.53 kev-0.625 ev)	Group 4 (0.625 ev-0.0 ev)
4-Group Scheme	D (cm)	2.656	1.539	1.039	0.2785
	Σ_r (cm^{-1})	0.05630	0.0760	0.05553	---
	Σ_a (cm^{-1})	0.000865	0.0000	0.000363	0.01595
			Group 1 (10 Mev-0.625 ev)		Group 2 (0.625 ev-0.0 ev)
2-Group Scheme	D (cm)		1.620		0.2785
	Σ_r (cm^{-1})		0.02263		---
	Σ_a (cm^{-1})		0.000370		0.01595

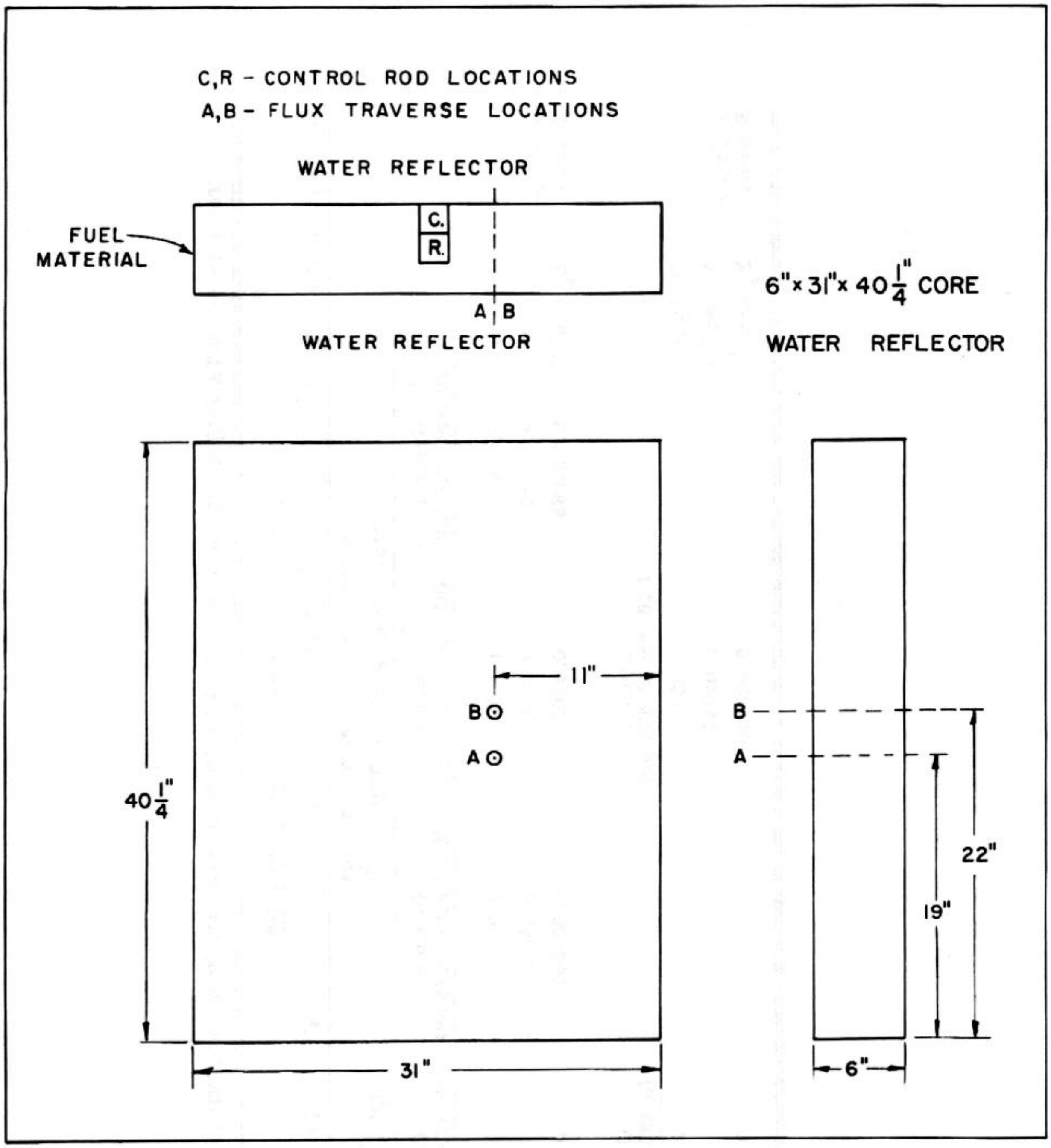

Fig. 13.4 - Sketch Showing Dimensions of Slab Experiment No. 1.

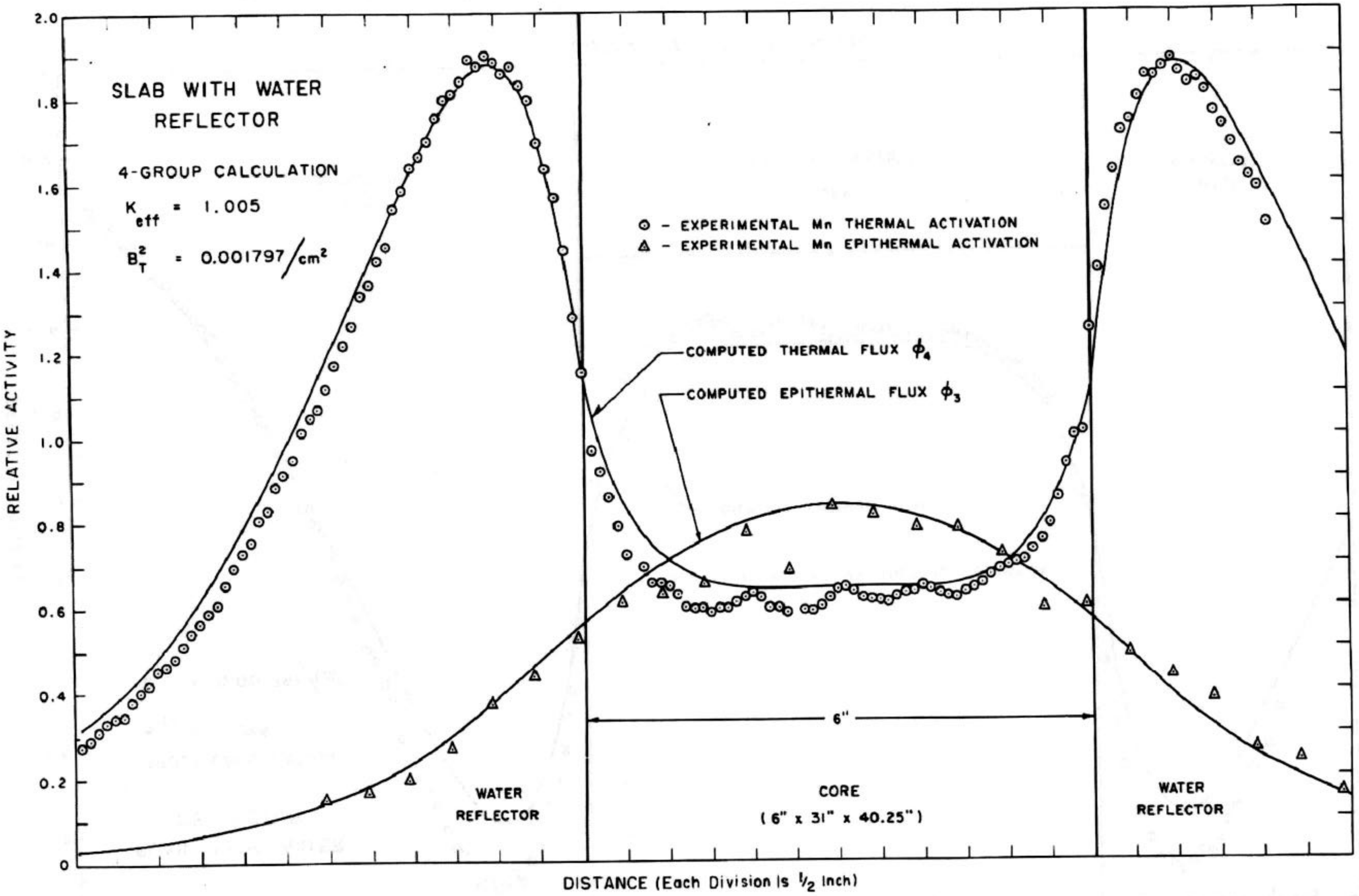

Fig. 13.5 - Flux Distributions for Experiment No. 1 - Four-Group Calculation.

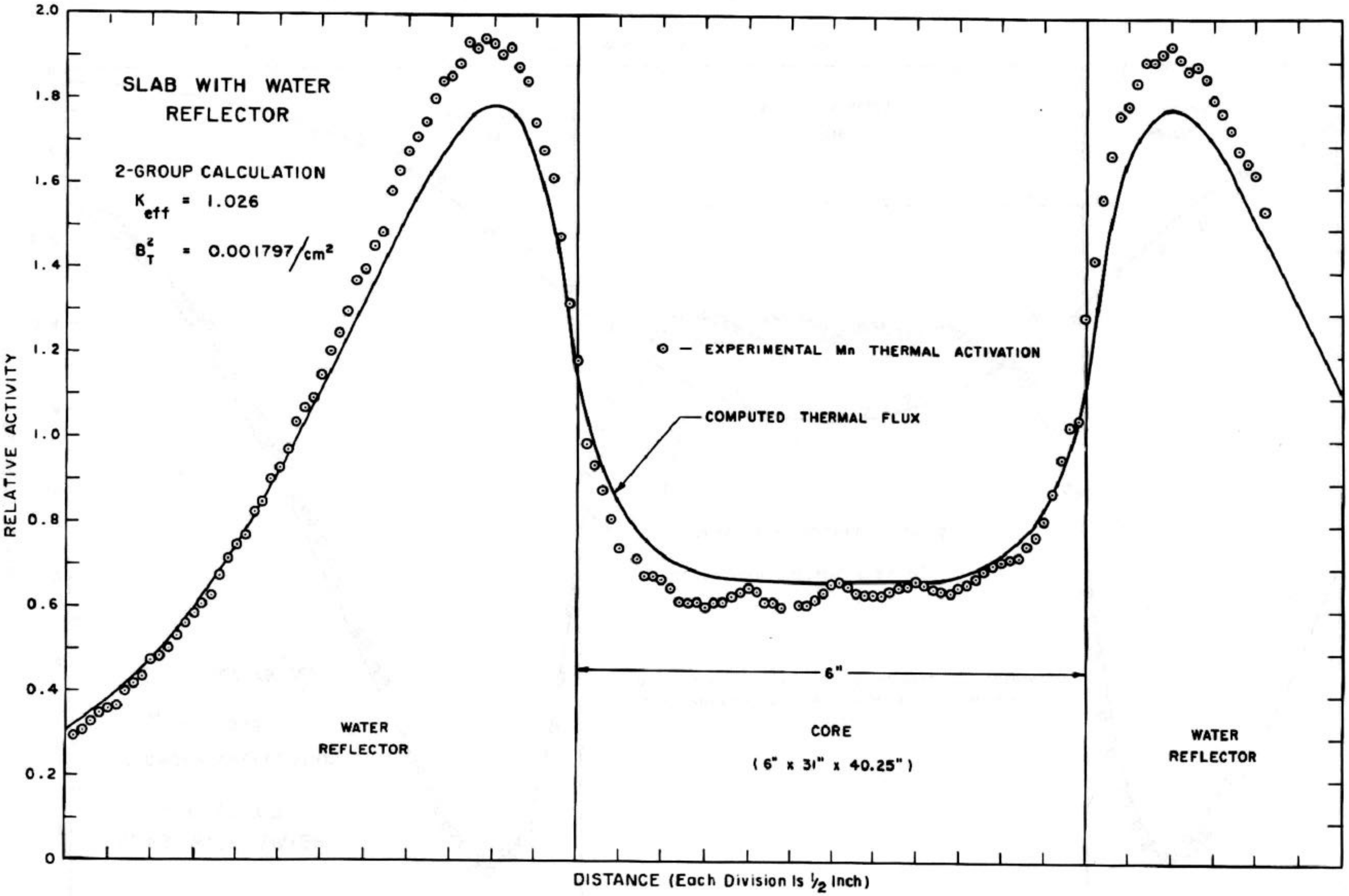

Fig. 13. 6 - Thermal Flux Distribution for Experiment No. 1 - Two-Group Calculation.

13.9 EXPERIMENT NO. 2--SLAB WITH 5/8-INCH WATER GAP AND THIN ASYMMETRIC ALUMINUM-WATER REFLECTOR

This experiment utilized a core 6-5/8 inches by 26 inches by 40-1/4 inches. Of the 6-5/8 inch core thickness, 6 inches was core material and 5/8 inch was an internal water gap which bisected the core. The core dimensions are shown on the sketch of Fig. 13.7. Because of experimental problems the geometry of this experiment was somewhat more complicated than that of the other experiment. An aluminum-water reflector was built up along one side of the core. This reflector was 1-5/8 inches thick over part of the slab length and 2-5/8 inches thick over the remainder. The core fuel material had a corresponding offset as is shown in Fig. 13.7. A water reflector surrounded the entire assembly.

The criticality results are as follows:

Experimental k_{eff} (rod free)	1.003
Calculated k_{eff} (4-group)	0.9987

These calculations were made using the constants tabulated in Table 13.2 for the core; the constants of Table 13.3 for the water reflector and control water gap; and the constants of Table 13.6 for the aluminum-water reflector region. Because of the two-dimensional nature of this problem, the PDQ code (see Appendix B) was used for the calculation. This code is the two-dimensional analogue of the one-dimensional WANDA code. By using the two-dimensional code, the offset in the core could be represented explicitly in the calculation.

The calculated thermal flux (group-4) and the epithermal flux (group-3) are plotted as the solid lines in Fig. 13.8. The calculated traverses are plotted for the same region of the core for which the experimental traverses were taken. The normalization to the experimental activation is again matched near the core-water reflector interface. The fit is generally poorer than in Experiment No. 1. If the calculated curve were dropped to fit the experimental data better in the fueled core region, the fit would be poorer in the water channel. The fit in the water reflector is quite poor with the calculated peak being too low and displaced too far out in the reflector. In the aluminum-water reflector region the fit is somewhat better than in the water reflector.

13.10 EXPERIMENT NO. 3--SLAB WITH 7/8-INCH WATER GAP AND WATER REFLECTOR

This experiment employed a core approximately 6-7/8 inches by 22 inches by 40-1/4 inches, completely water reflected. The core was bisected by a 7/8-inch water channel. The core dimensions are shown in the sketch of Fig. 13.9.

The criticality results are as follows:

Experimental k_{eff} (rod free)	1.000
Calculated k_{eff} (2-group)	1.030
Calculated k_{eff} (4-group)	1.014

These calculations were made using the constants in Table 13.2 for the core and the constants in Table 13.3 for the water reflector and the water gap.

Figure 13.10 shows the four-group thermal flux and resonance flux (group-3) calculations and the experimental activation results. The failure of the thermal flux to fit the activation distribution is quite marked. If the solid curve for the thermal flux were dropped to fit the minima in the core region, the flux peaks in the reflector and in the central water channel would be underestimated by the order of 10 per cent or possibly more. While it is not so conclusive, it again appears that the calculated thermal flux peak is shifted too far out in the reflector.

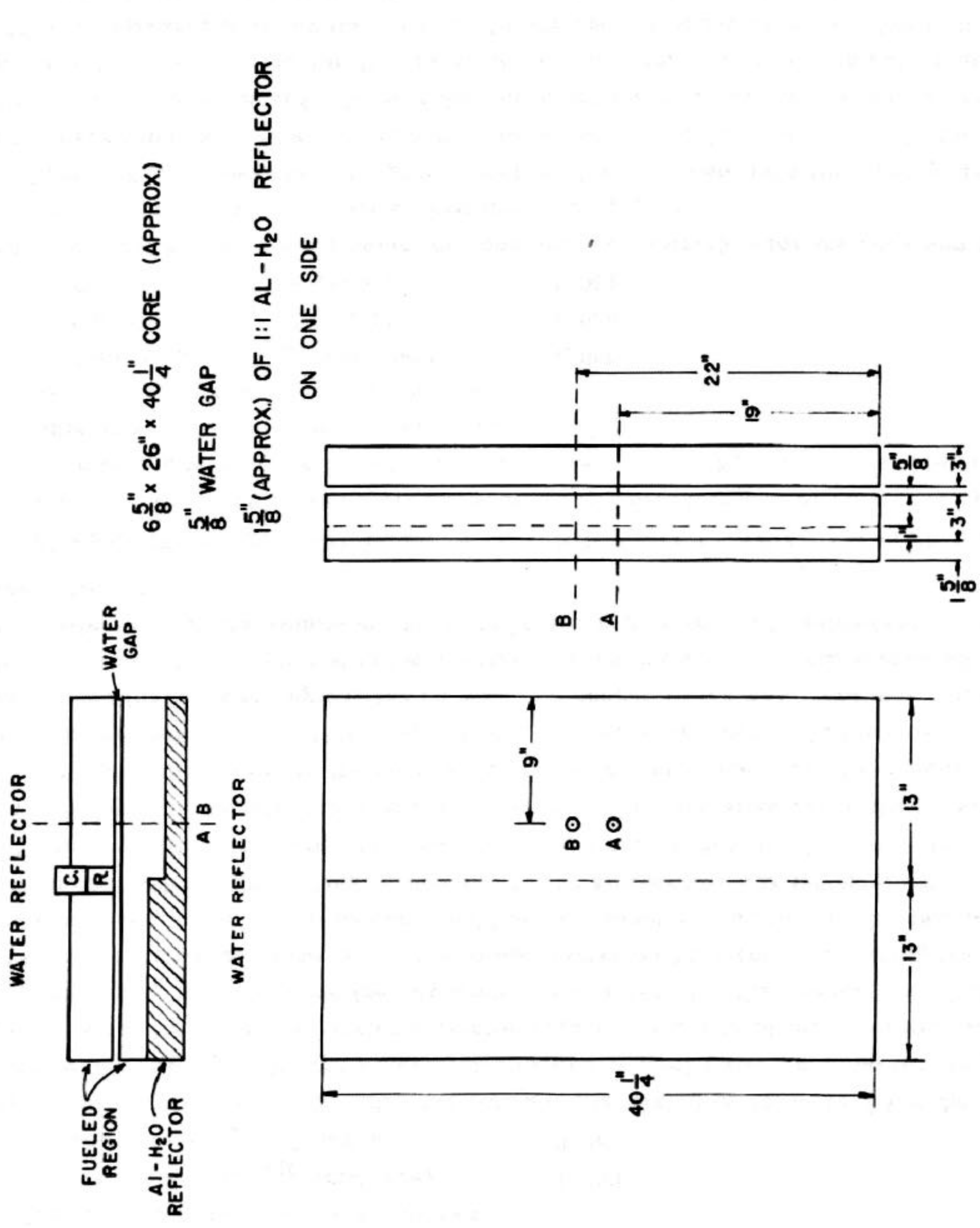

Fig. 13.7 - Sketch Showing Core Dimensions of Experiment No. 2.

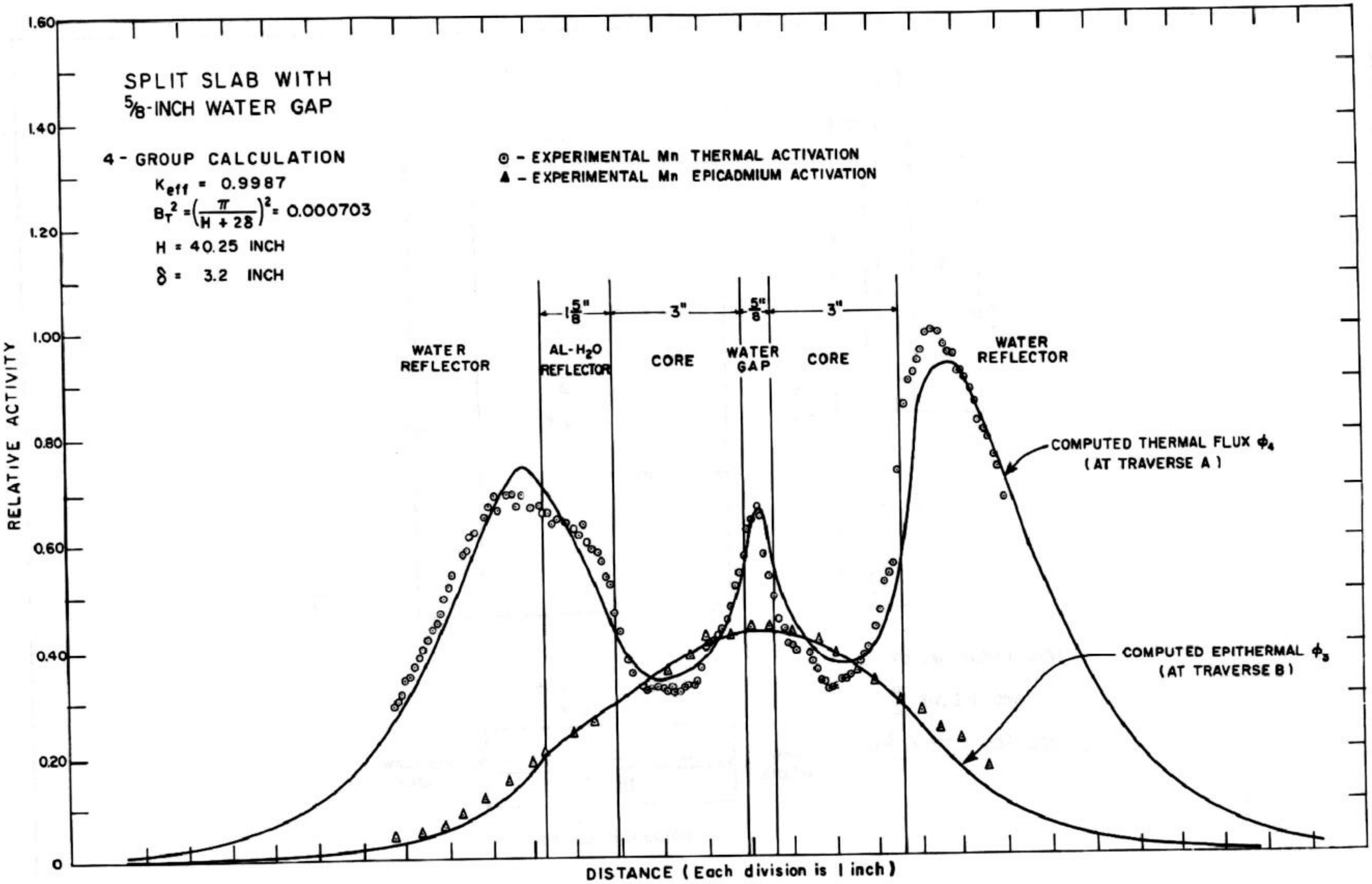

Fig. 13.8 - Flux Distributions for Experiment No. 2 - Four-Group Two-Dimensional Calculation.

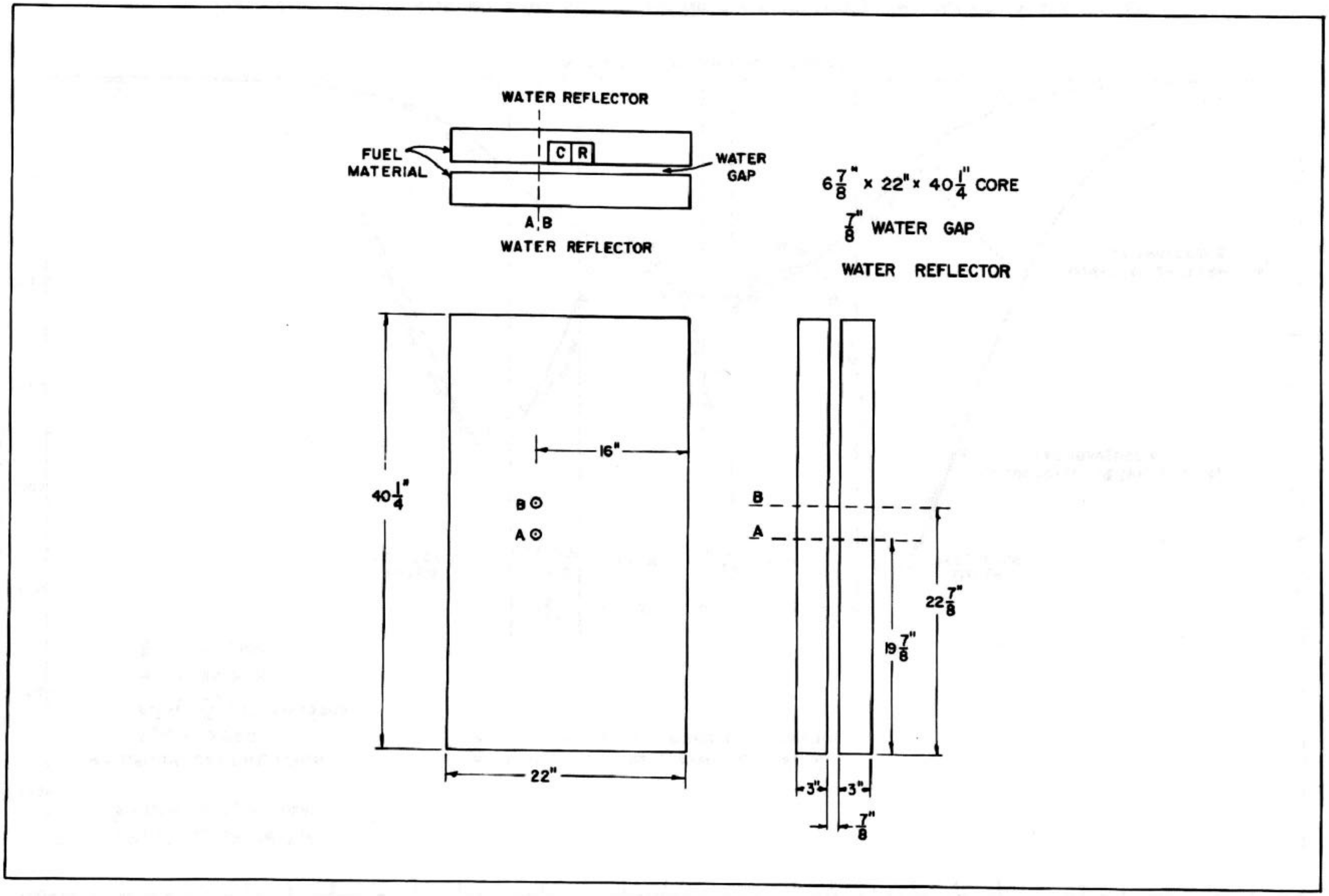

Fig. 13.9 - Sketch Showing Core Dimensions of Experiment No. 3.

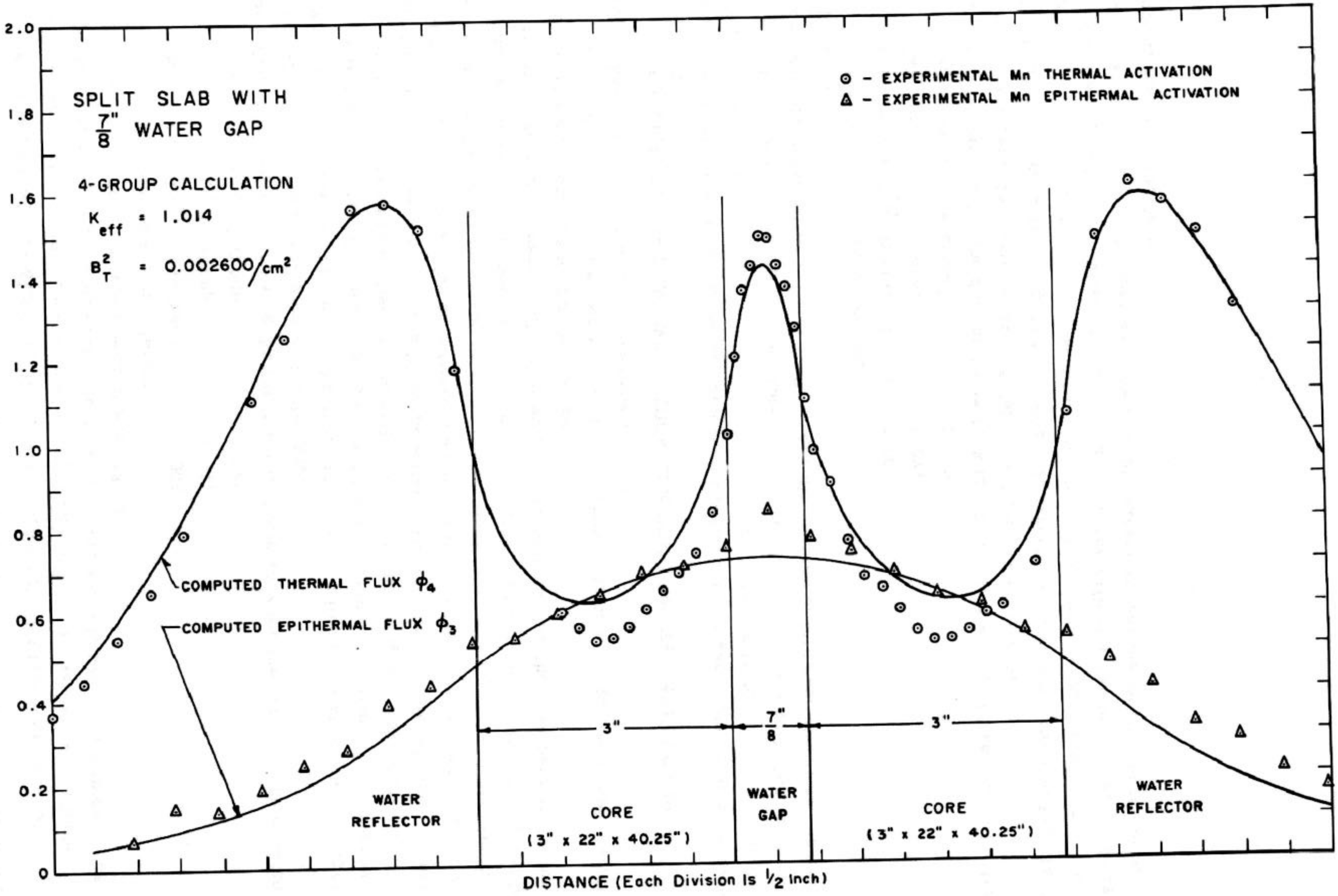

Fig. 13.10 - Flux Distributions for Experiment No. 3 - Four-Group Calculation.

Figure 13.11 shows the two-group thermal flux calculation compared with the activation distribution. The manner in which this distribution fails to meet the measured distribution is similar to the behavior of the four-group result but its failure is even more marked in the reflector. In the central water gap the two-group fit is about the same as the four-group fit.

13.11 EXPERIMENT NO. 4--SLAB WITH ONE-INCH GAP AND WATER REFLECTOR

This experiment utilized a core approximately 7 inches by 24 inches by 40-1/4 inches, completely water reflected. It was bisected by a water gap slightly over 1 inch thick. The core dimensions are shown on the sketch of Fig. 13.12.

The criticality results are as follows:

Experimental k_{eff} (rod free)	1.006
Calculated k_{eff} (2-group)	1.041
Calculated k_{eff} (4-group)	1.025

These calculations were made using the constants in Table 13.2 for the core and the constants in Table 13.3 for the water reflector and water gap.

Figure 13.13 shows the four-group thermal and resonance flux calculation and the experimental activation results. Curiously enough, the fit of the thermal flux from the four-group calculation to the experimental distribution within the core (including the water gap) seems better than in Experiment No. 3. The fit in the water reflector seems to be off about the usual amount including the tendency for an outward displacement. It is now also evident that the fit of the resonance flux to the measured distribution becomes markedly poorer with increasing water channel thickness. Not only is the distribution higher in the reflector than that given by the calculation, as was the case in all the previous experiments, but the peak near the water channel is not well described by the calculation.

The two-group calculation shown in Fig. 13.14, when compared to the four-group result, shows a behavior consistent with the previous results.

13.12 EXPERIMENT NO. 5--SLAB WITH THICK ZIRCONIUM-WATER REFLECTOR ON ONE SIDE

Experiment No. 5 reverted to the use of a core without a water gap. The core dimensions were 6 inches by 25 inches by 40-1/4 inches. A zirconium-water reflector with a 1:1 metal-to-water volume ratio was located on one side of the core. The reflector was 11 inches thick. The core was otherwise water reflected. The core dimensions of this experiment are shown on Fig. 13.15.

The criticality results are as follows:

Experimental k_{eff} (rod free)	1.005
Calculated k_{eff} (2-group)	1.027
Calculated k_{eff} (4-group)	1.009

These were calculated using the data of Table 13.2 for the core, the data of Table 13.4 for the zirconium-water reflector, and the data of Table 13.3 for the water reflector.

The four-group thermal (group-4) and epithermal (group-3) fluxes are shown on Fig. 13.16. The general fit of the thermal flux to the measured thermal activation seems about normal for the core and water reflector region. In the zirconium-water reflector region the lack of fit is similar to that with water reflectors with the possible exception that the location of the peak does not appear to be displaced.

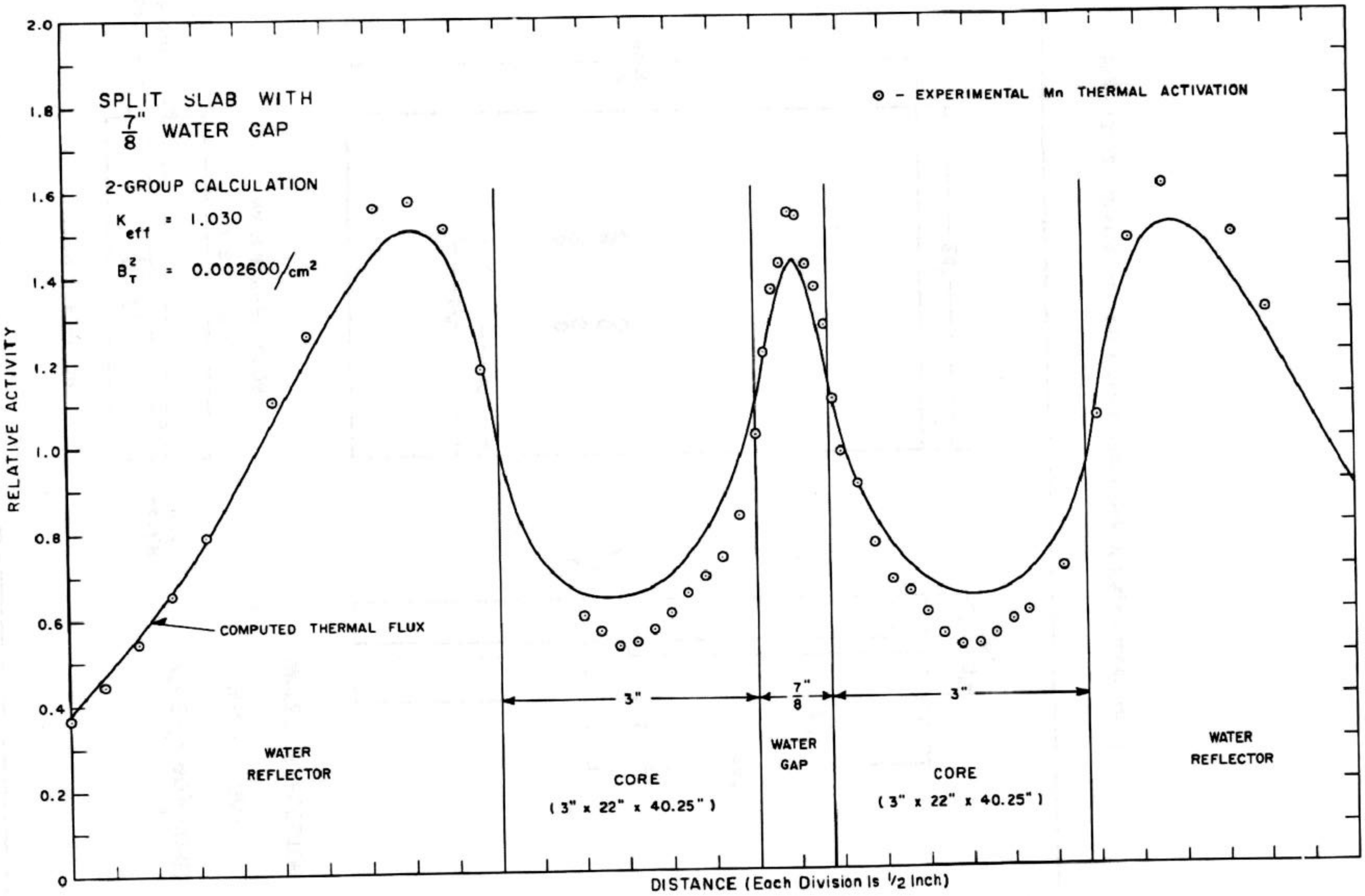

Fig. 13.11 - Flux Distributions for Experiment No. 3 - Two-Group Calculation.

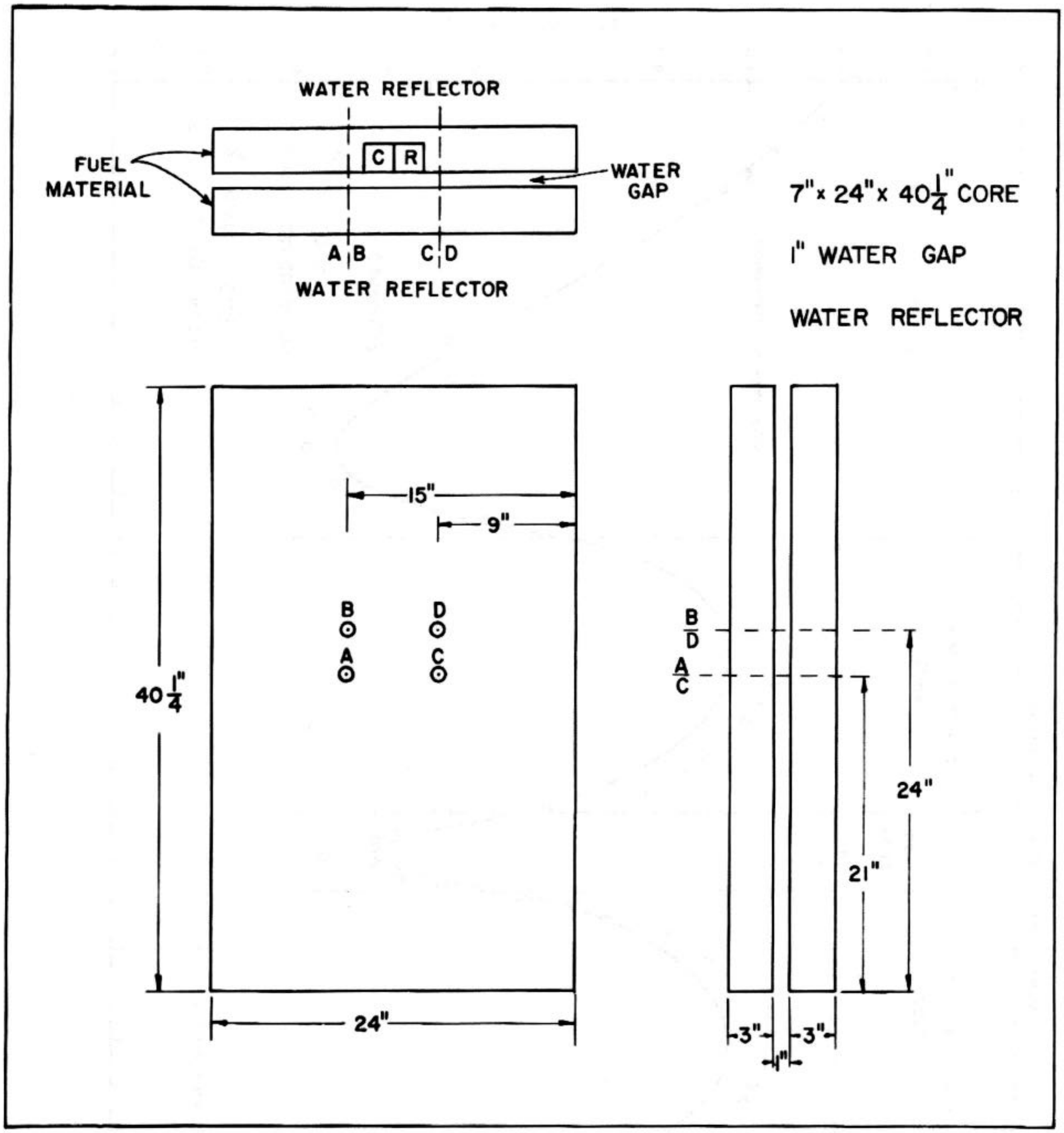

Fig. 13.12 - Sketch Showing Core Dimensions of Experiment No. 4.

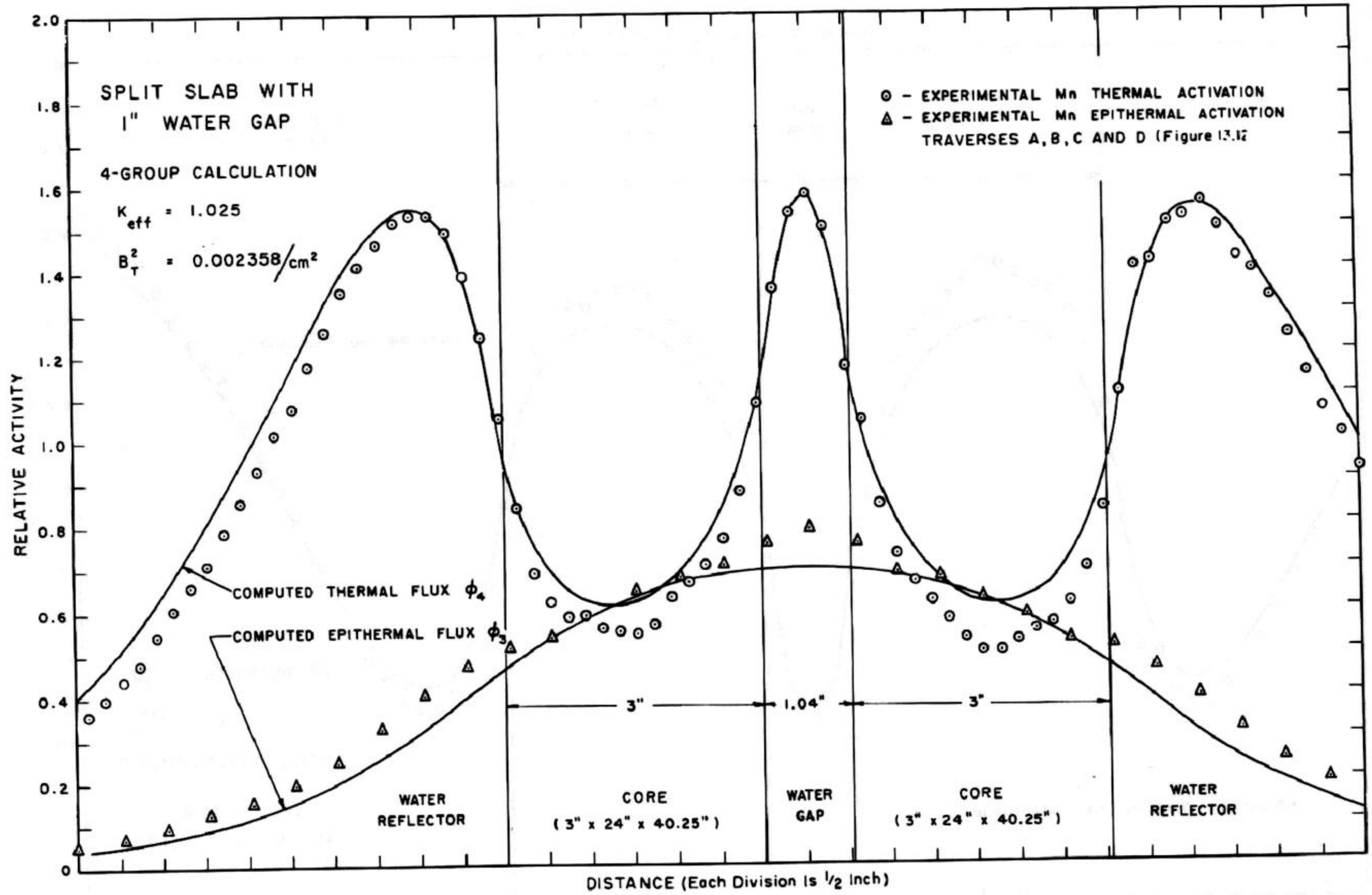

Fig. 13.13 - Flux Distributions for Experiment No. 4 - Four-Group Calculation.

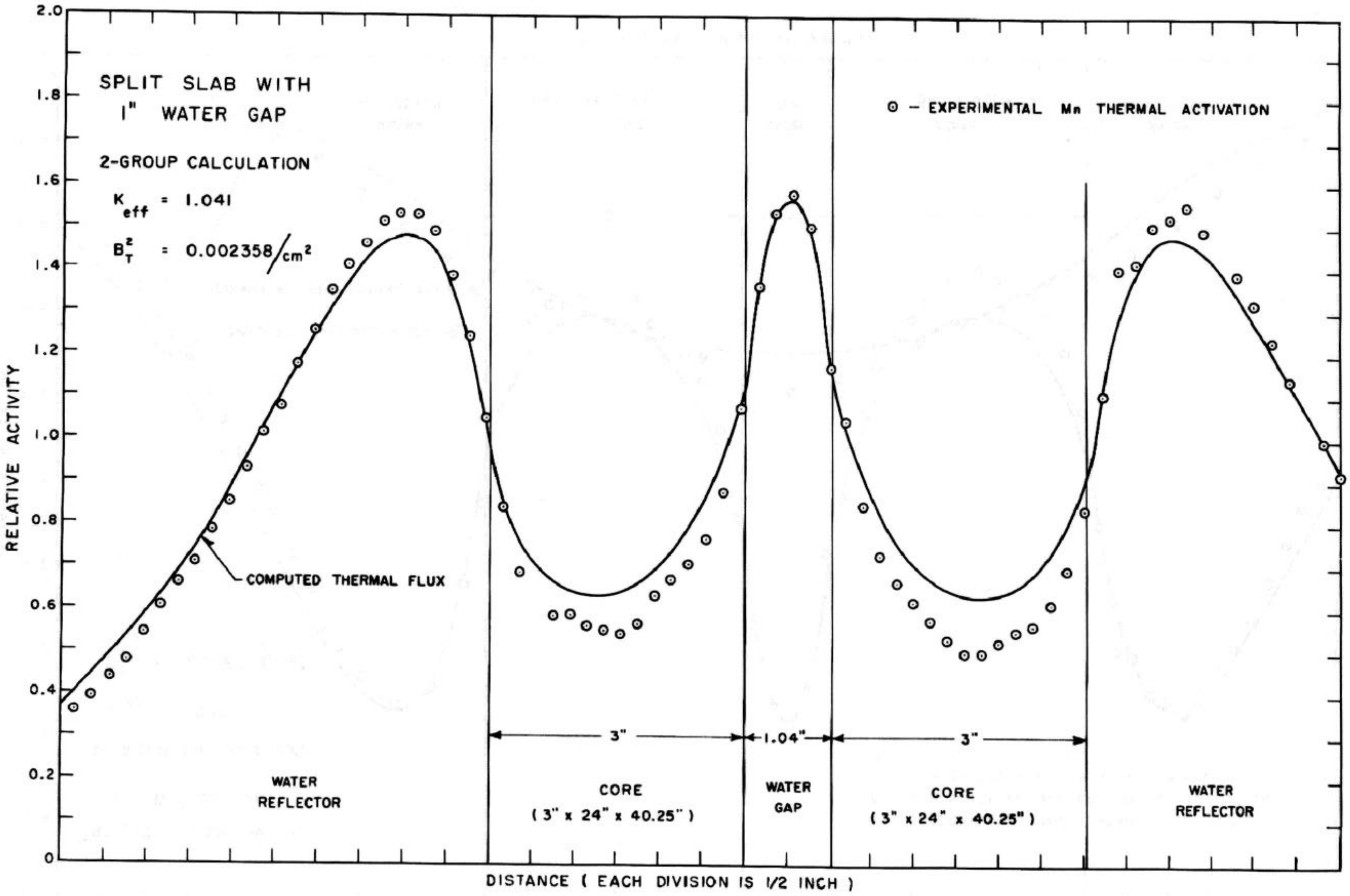

Fig. 13.14 - Flux Distributions for Experiment No. 4 – Two-Group Calculation.

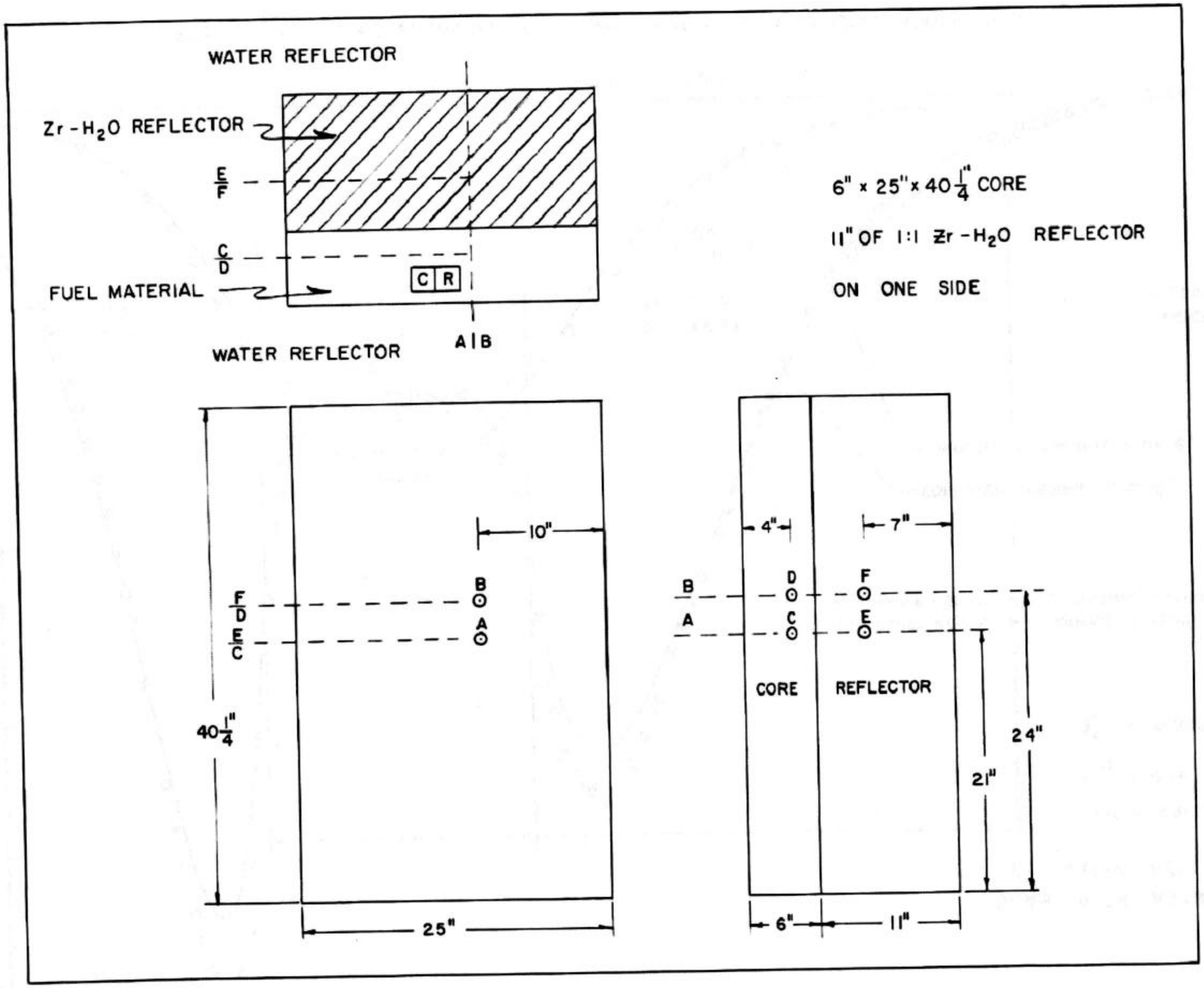

Fig. 13.15 - Sketch Showing Core Dimensions of Experiment No. 5.

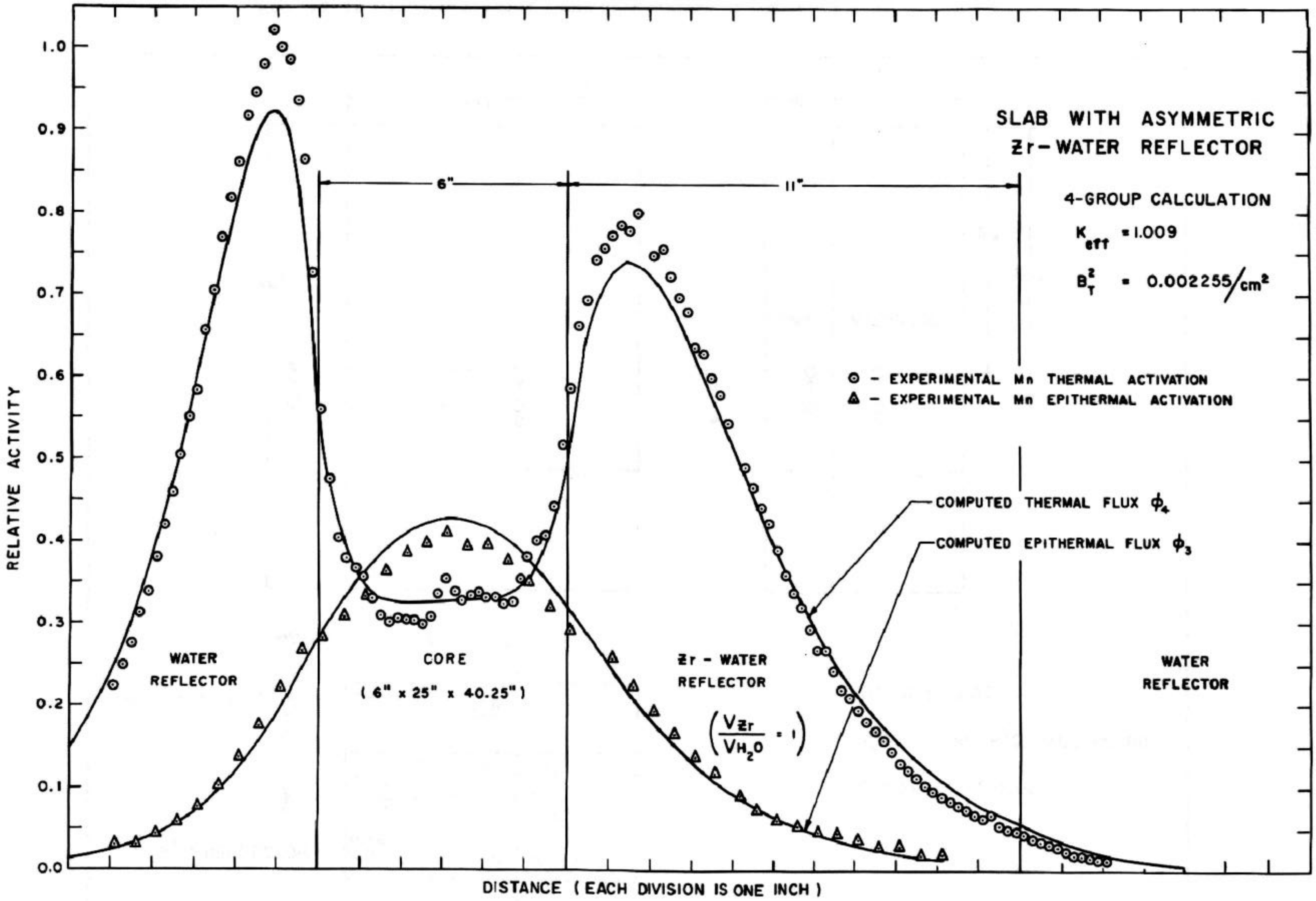

Fig. 13.16 - Flux Distributions for Experiment No. 5 - Four-Group Calculation.

13.13 EXPERIMENT NO. 6--SLAB WITH SYMMETRIC ZIRCONIUM-WATER REFLECTOR

This experiment used the same core width employed in Experiment No. 5, but the zirconium-water reflector was symmetric in this experiment. The core dimensions were 6 inches by 21 inches by 40-1/4 inches. The reflector was 1:1 in metal-to-water volume ratio and was 6 inches thick on each side of the core. Figure 13.17 shows the core dimensions of the experiment.

The criticality results were as follows:

Experimental k_{eff} (rod-free)	1.001
Calculated k_{eff} (2-group)	1.018
Calculated k_{eff} (4-group)	1.005

These were calculated using the data of Table 13.2 for the core, the data of Table 13.4 for the zirconium-water reflector, and the data of Table 13.3 for the water reflector.

The four-group thermal (group-4) and epithermal (group-3) flux distributions are given in Fig. 13.18 together with the activation distribution. The two-group calculation is shown in Fig. 13.19. The results obtained in both cases are very similar to those obtained with water reflectors. The calculated peak within the reflector is too low and too far out in the reflector. It is interesting to note that the four-group thermal flux seems to have the right shape at the interface between the water and zirconium-water reflector. The resonance flux, on the other hand, seems to be underestimated throughout the reflector. There seems to be a tendency for a slight reflector peak to show in the experimental data which the calculation fails to exhibit. This is similar to the peak that appeared in the central water channel in Experiments Nos. 3 and 4.

Figure 13.20 shows the results of a calculation along the length of the core and the corresponding activation distributions. These were taken along the traverses C and D of Fig. 13.17.

13.14 EXPERIMENT NO. 7--SLAB WITH ASYMMETRIC ZIRCONIUM-WATER REFLECTOR

This experiment is similar to Experiment No. 5 in that an asymmetric zirconium-water reflector was used. However, the zirconium-to-water volume ratio was considerably higher in this case, 7:3. The core dimensions were 6 inches by 23 inches by 40-1/4 inches. The zirconium-water reflector thickness was 10 inches. The remainder of the core was water reflected. Figure 13.21 shows the core dimensions of the experiment.

The criticality results are as follows:

Experimental k_{eff} (rod-free)	1.002
Calculated k_{eff} (2-group)	1.022
Calculated k_{eff} (4-group)	1.006

These were calculated using the data of Table 13.2 for the core, the data of Table 13.3 for the water, and the data of Table 13.5 for the zirconium-water reflector.

The calculated four-group thermal flux (group-4) distribution and resonance flux (group-3) distribution are shown on Fig. 13.22 together with the experimental activation results. The thermal flux distribution fits about as well as in the previous cases, to about 10 per cent. The reflector peak behavior is also about the same as in previous cases. The calculated resonance flux again fails to show the slight reflector peak observed in the experiment. In general, the ability of the calculation to show the difference in thermal flux between the two reflectors is quite good.

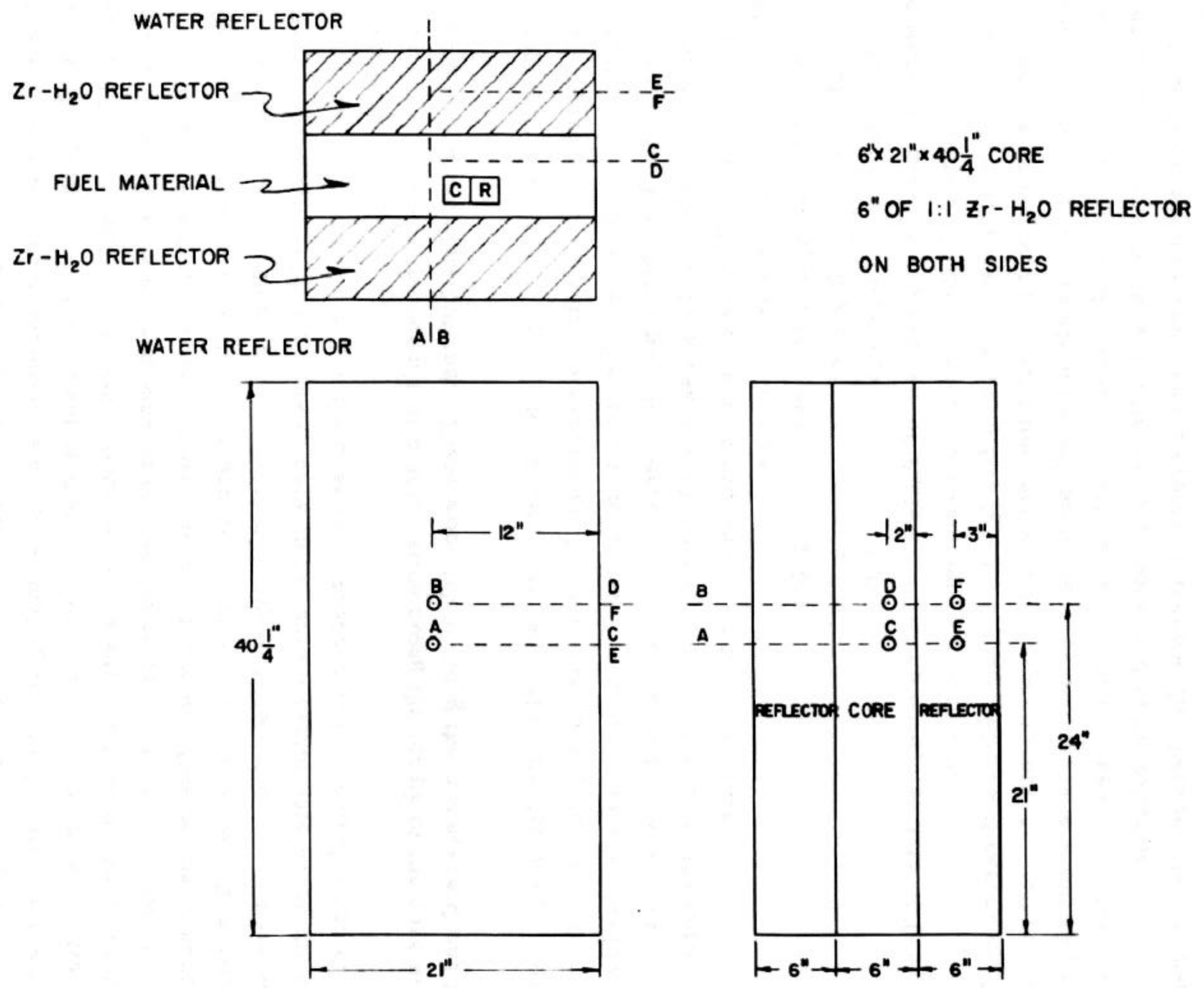

Fig. 13.17 - Sketch Showing Core Dimensions of Experiment No. 6.

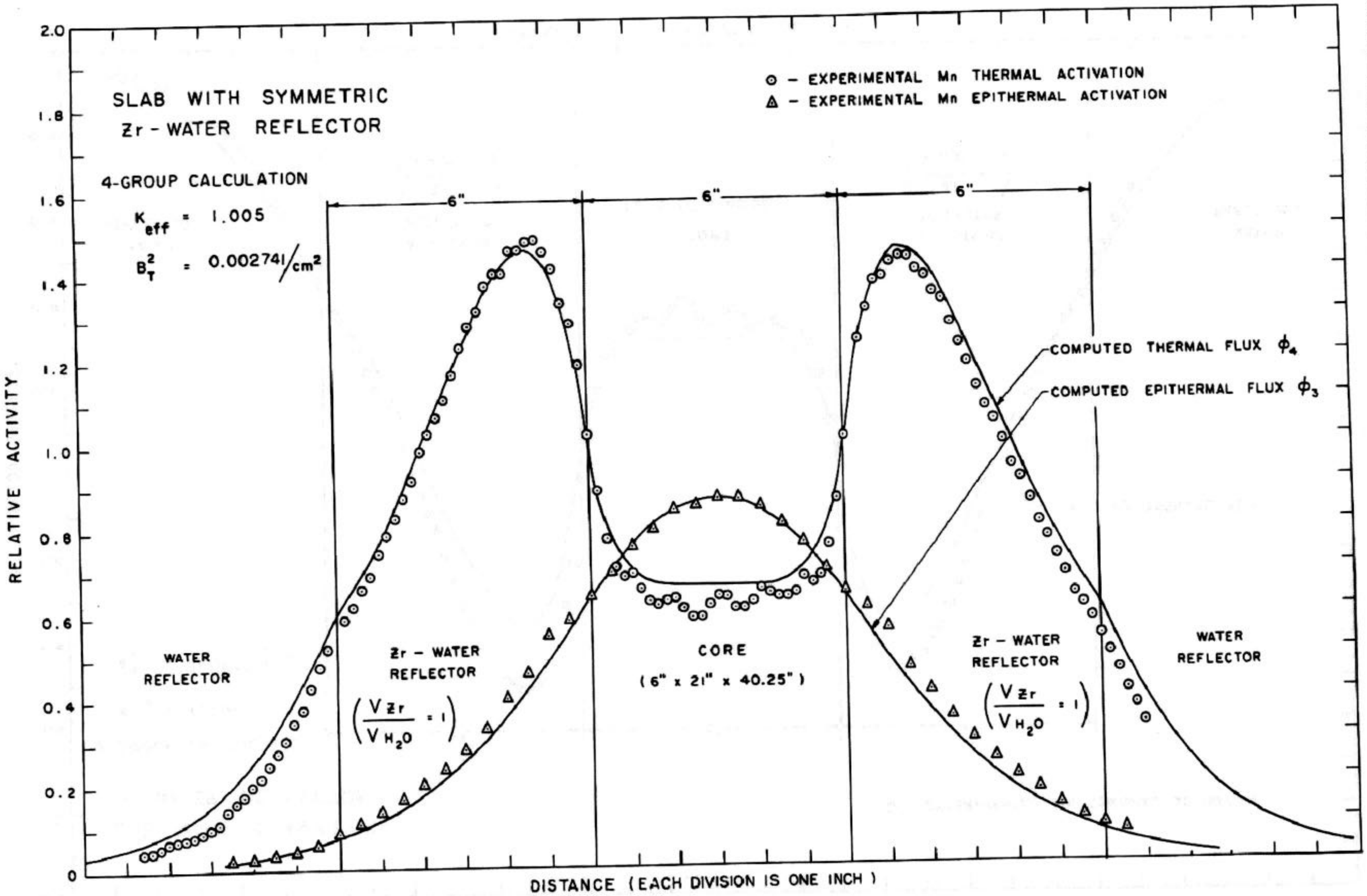

Fig. 13.18 - Flux Distributions for Experiment No. 6 - Four-Group Calculation.

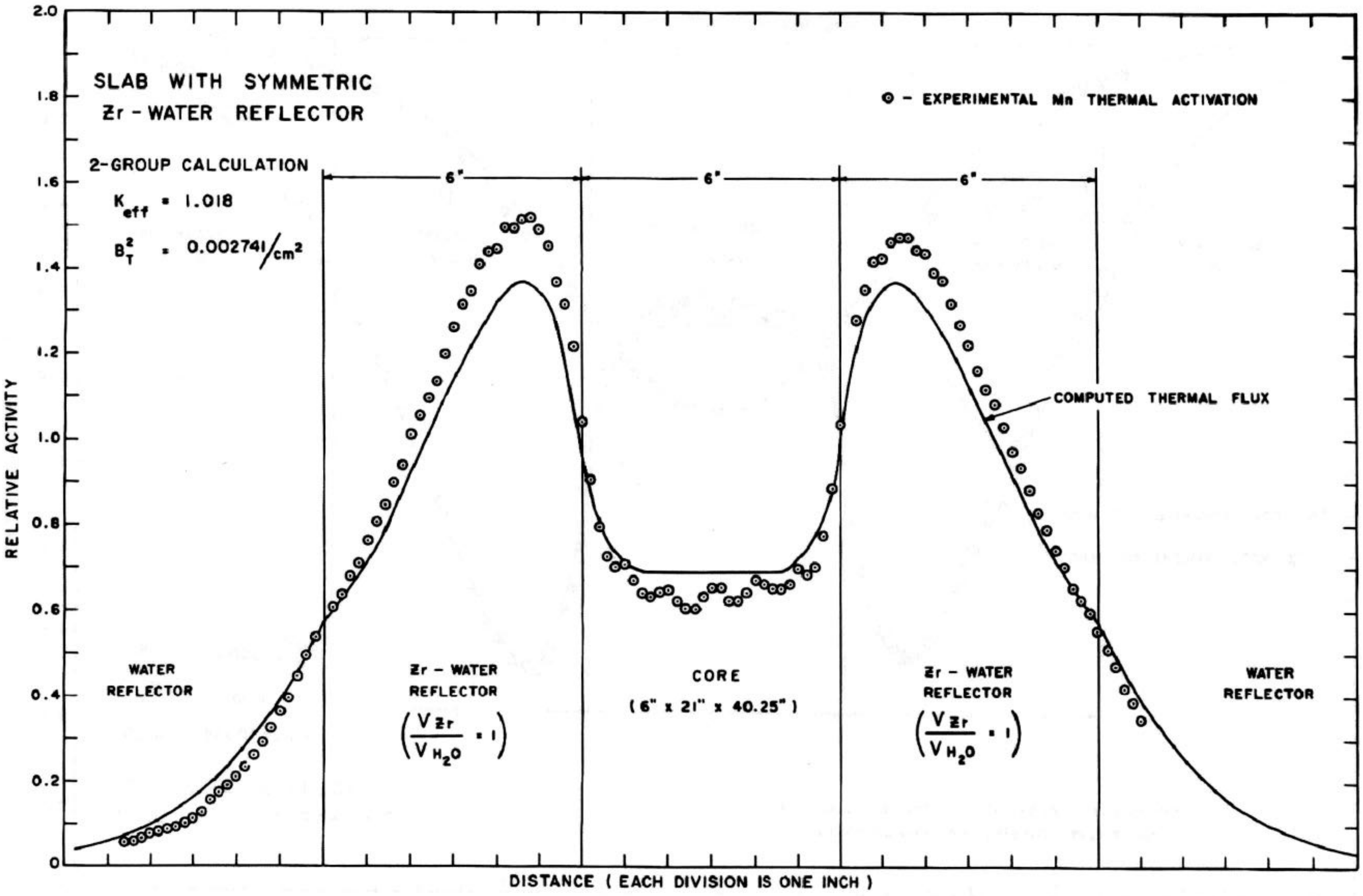

Fig. 13. 19 - Flux Distributions for Experiment No. 6 - Two-Group Calculation.

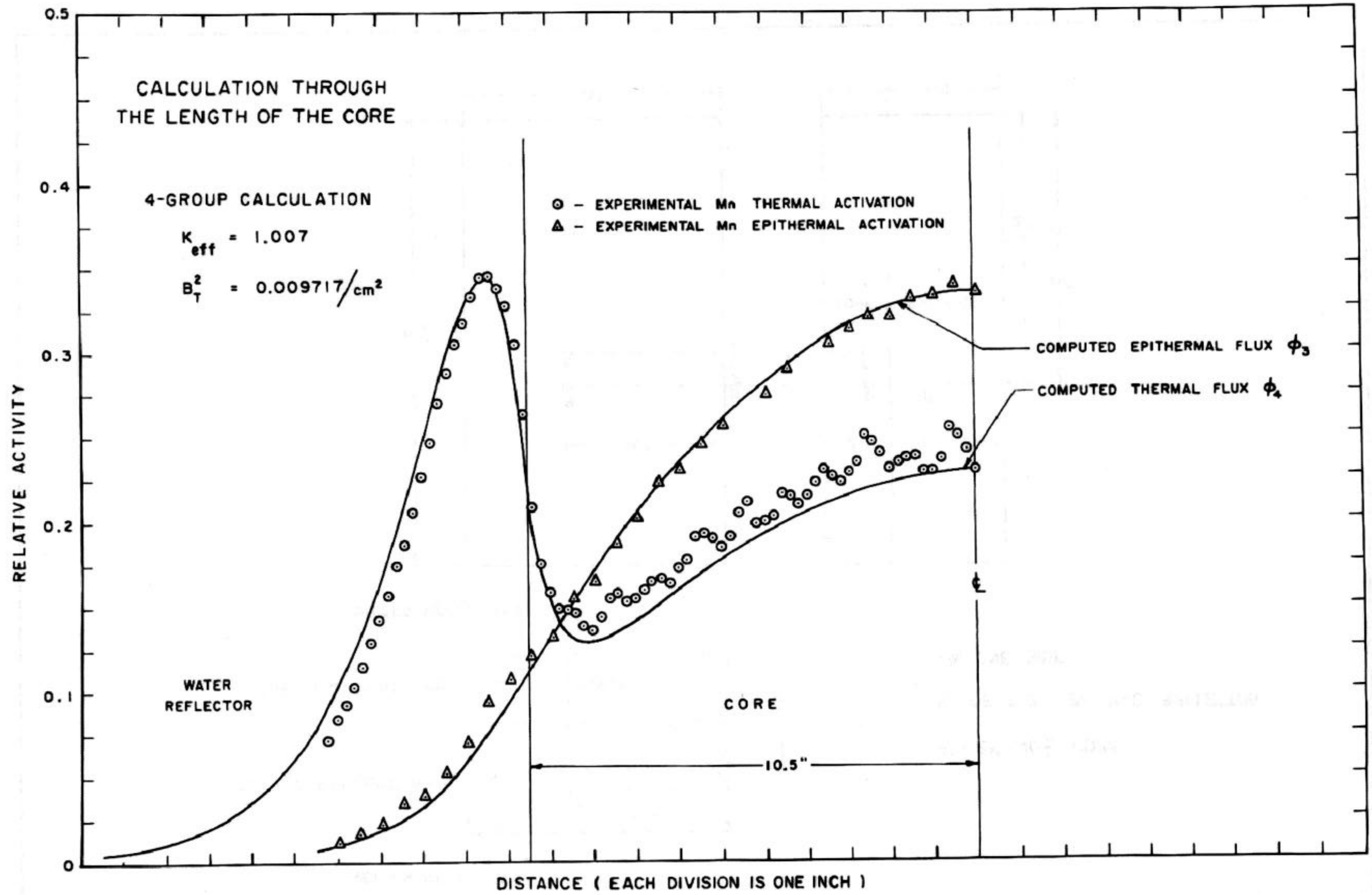

Fig. 13.20 - Longitudinal Flux Distributions for Experiment No. 6 - Four-Group Calculation.

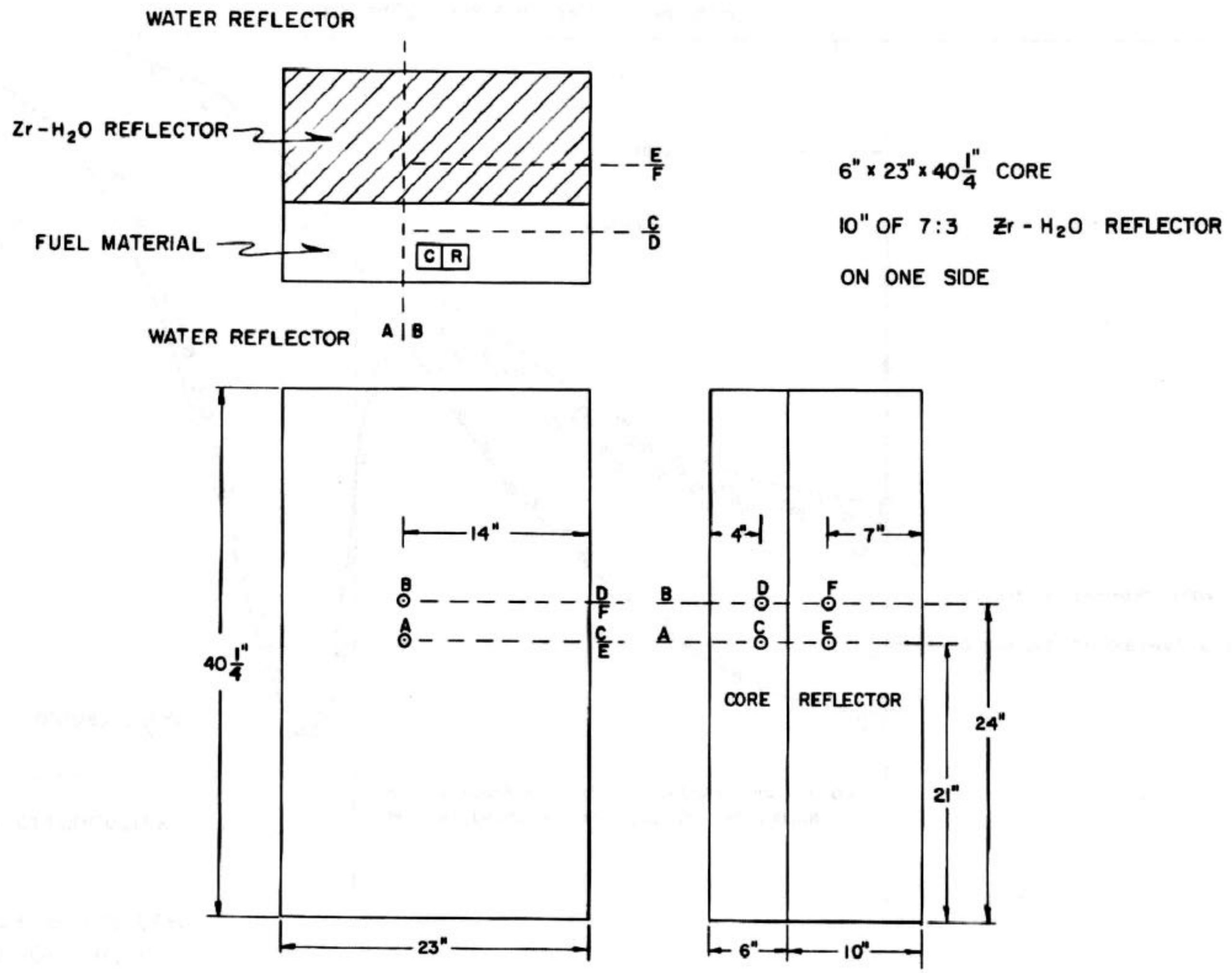

Fig. 13.21 - Sketch Showing Core Dimensions of Experiment No. 7.

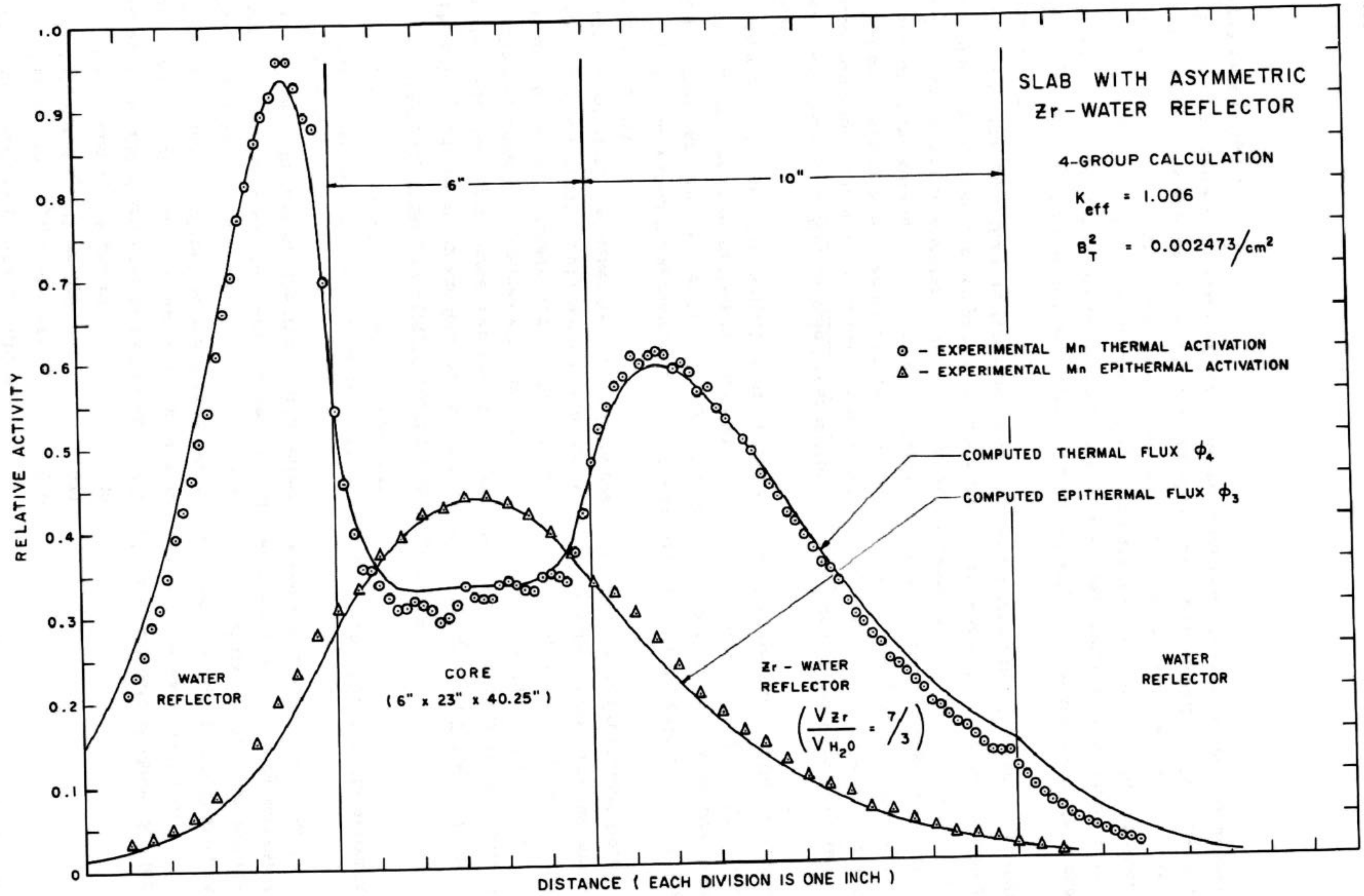

Fig. 13.22 - Flux Distributions for Experiment No. 7 - Four-Group Calculation.

13.15 EXPERIMENT NO. 8--SLAB WITH SYMMETRIC ALUMINUM-WATER REFLECTOR

In this experiment the core was provided with an aluminum-water reflector in a 1:1 volume ratio. The reflector on each side of the slab was 6 inches thick. The core dimensions of the experiment are shown in Fig. 13.23. The core size is 6 inches by 29 inches by 40-1/4 inches.

The criticality results are as follows:

Experimental k_{eff} (rod-free)	1.000
Calculated k_{eff} (2-group)	1.031
Calculated k_{eff} (4-group)	1.000

These were calculated using the data of Table 13.2 for the core, the data of Table 13.3 for the outer water region, and the data of Table 13.6 for the aluminum-water reflector.

The four-group calculated thermal flux (group-4) and resonance flux (group-3) are plotted on Fig. 13.24 along with the measured activation distributions. If the thermal flux were normalized in the reactor core, the reflector peak as calculated would be too low by somewhat over 10 per cent. In general, the fit with this reflector is somewhat poorer than with the other reflectors.

The two-group thermal flux calculation is shown on Fig. 13.25. The fit to the activation distribution is about equivalent to the four-group result.

13.16 SUMMARY OF RESULTS--CRITICALITY CALCULATIONS

The calculated two-group and four-group eigenvalues are compiled in Table 13.7 for comparison with the experimental results. If the cores with water channels are excluded, the four-group calculated values agree with the experimental values to within 0.005 in reactivity. The results with water channels are considerably poorer. The differences between calculation and experiment are 0.004, 0.014 and 0.019 in reactivity for the three cores. The two-group calculated eigenvalues are higher by about 0.02 in reactivity although in Experiment No. 8 the difference is 0.031.

To see to what extent the agreement is real, the uncertainties in the calculations will be examined. There are two sources of difficulty in the reactivity calculation; one relates to the input information, the other to the process by which the calculation is carried out. The first three items listed below refer to input uncertainties while the last two refer to the calculation procedure.

(a) Inaccuracy of the Microscopic Cross Section Used to Calculate the Group Constants. The uncertainty due to this factor is not known. It is believed, however, that the inaccuracies of the fast microscopic cross sections of the core nuclei will cause the greatest uncertainty since they affect the slowing down process and therefore the fast neutron leakage. The computed age to 0.625 ev for the core material used in these experiments is 62.5 cm^2. No direct experimental results are available to compare with this value. As to sensitivity, it should be noted that a 3 per cent change in the core fast neutron leakage would result in a 1.2 per cent change in the calculated k_{eff}.

(b) Uncertainties in the Reactor Geometry. This uncertainty includes the difficulty of specifying the exact position of the core-reflector boundary, i.e., the region over which the core material is homogenized for the calculation. It also includes the uncertainty in the reflector saving used for the Y and Z axes together with the possible errors which arise when a three-dimensional problem is assumed separable and calculated one-dimensionally. It has been estimated that an unfavorable combination of these uncertainties could lead to an error of as much as 1.5 per cent in k_{eff}.

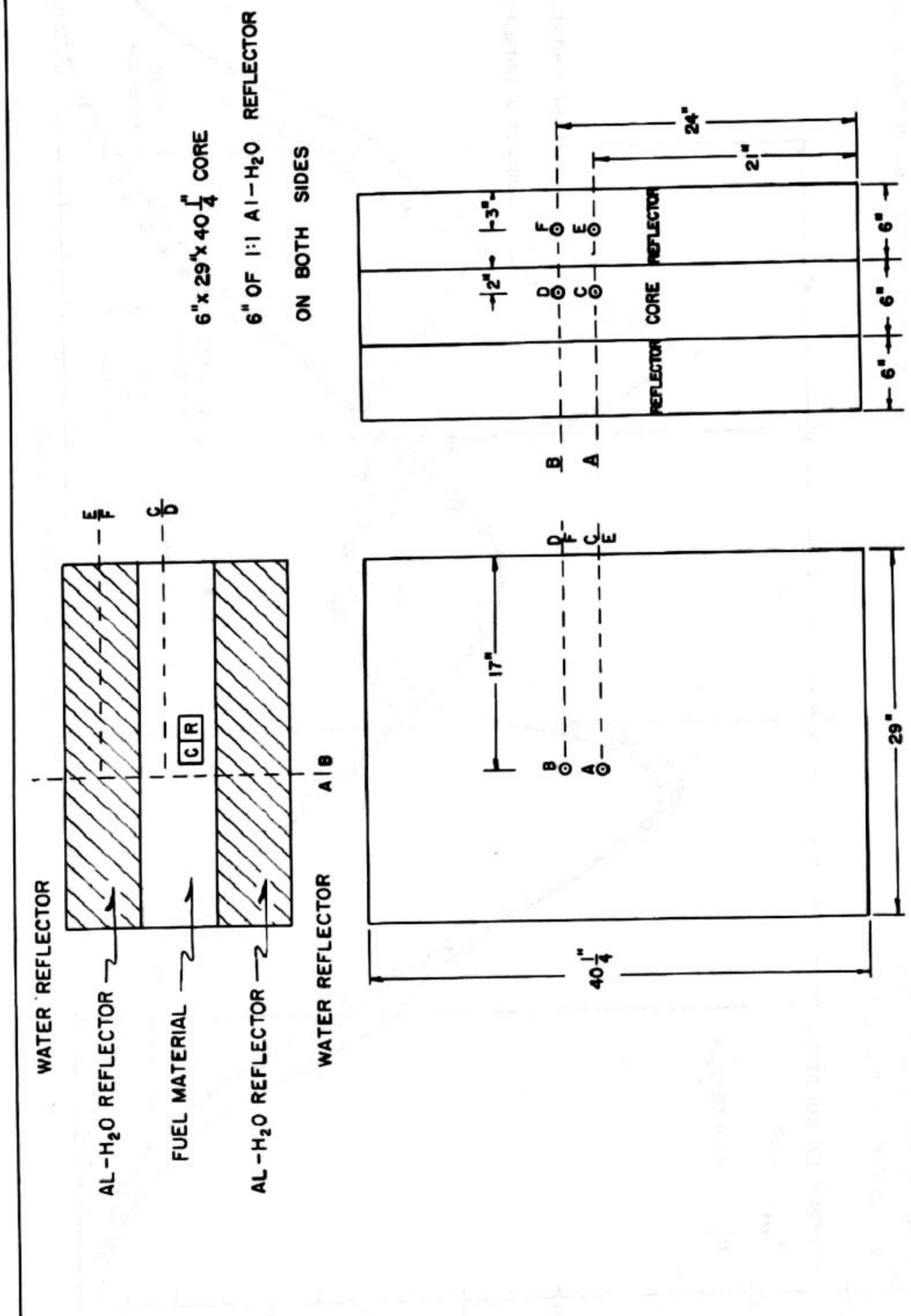

Fig. 13.23 - Sketch Showing Core Dimensions of Experiment No. 8.

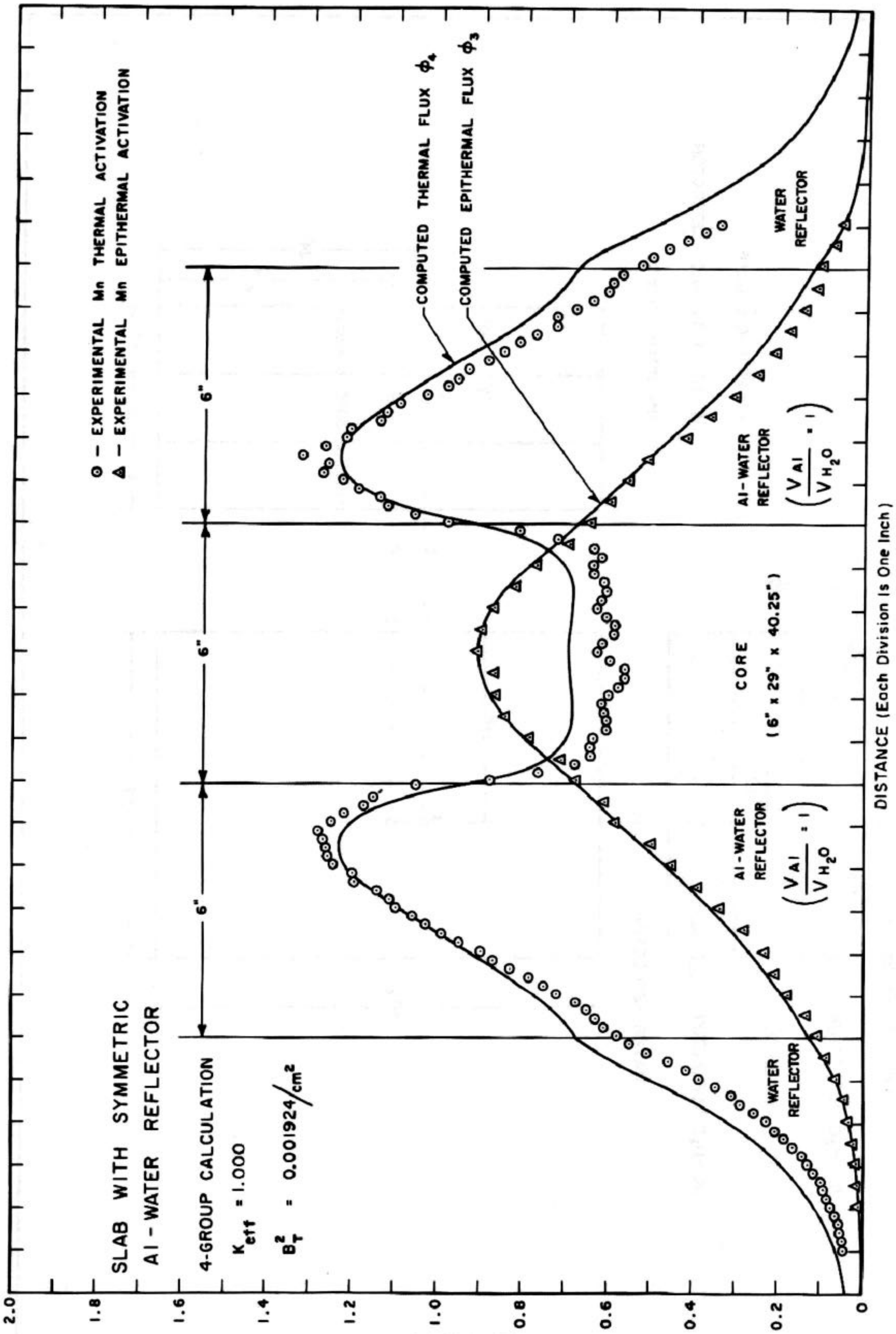

Fig. 13.24 - Flux Distributions for Experiment No. 8 - Four-Group Calculation.

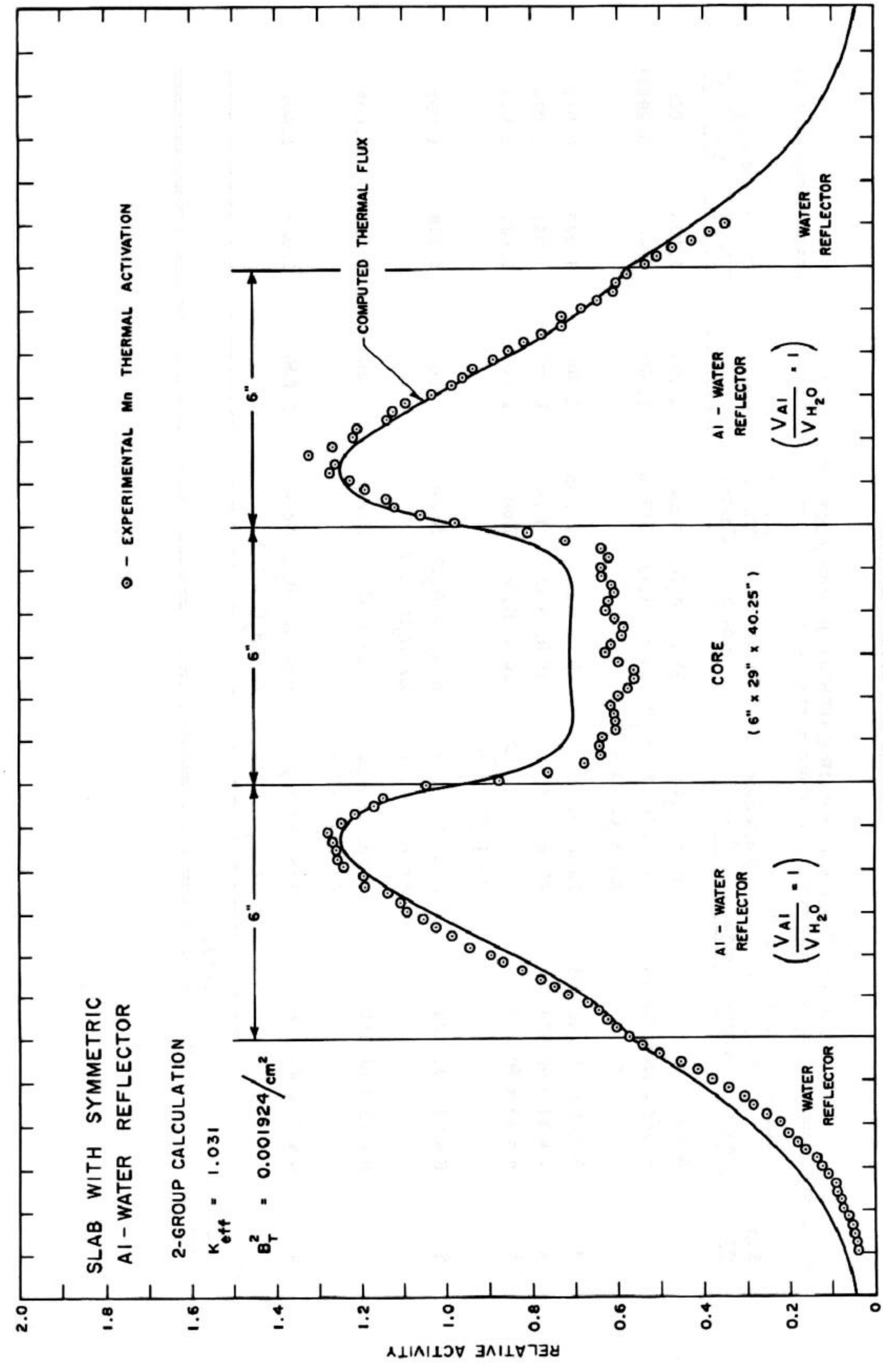

Fig. 13.25 - Flux Distributions for Experiment No. 8 - Two-Group Calculation.

Table 13.7--SUMMARY OF CRITICAL EXPERIMENT RESULTS

Exp No.	Critical Core Dimensions (in.) Width x Length x Height	Reflector Side 1	Reflector Side 2	Central Water Channel	Experimental Rod-Free k_{eff}	Calculated k_{eff}	
						2-Group	4-Group
1	6 x 31 x 40-1/4	20 in. H_2O	20 in. H_2O	None	1.001	1.026	1.005
2	6-5/8 x 26 x 40-1/4	1-5/8 in. Al-H_2O Al:H_2O = 1.0	20 in. H_2O	5/8 in.	1.003	---	0.9987*
3	6-7/8 x 22 x 40-1/4	20 in. H_2O	20 in. H_2O	7/8 in.	1.000	1.030	0.014
4	7 x 24 x 40-1/4	20 in. H_2O	20 in. H_2O	1 in.	1.006	1.041	1.025
5	6 x 25 x 40-1/4	11 in. Zr-H_2O Zr:H_2O = 1.0	20 in. H_2O	None	1.005	1.027	1.009
6	6 x 21 x 40-1/4	6 in. Zr-H_2O Zr:H_2O = 1.0	6 in. Zr-H_2O Zr:H_2O = 1.0	None	1.001	1.018	1.005
7	6 x 23 x 40-1/4	10 in. Zr-H_2O Zr:H_2O = 7/3	20 in. H_2O	None	1.002	1.022	1.006
8	6 x 29 x 40-1/4	6 in. Al-H_2O Al:H_2O = 1.0	6 in. Al-H_2O Al: H_2O = 1.0	None	1.000	1.031	1.000

* Two-Dimensional Calculation.

(c) Errors in the Material Inventory. The most important of these uncertainties is the hydrogen and uranium density in the core. The hydrogen density is uncertain because the water and tape volumes are uncertain. It is estimated that the water volume is uncertain to 4 per cent and the tape volume to 5 per cent. Because of the close match between the hydrogen densities in the tape and water, however, the two effects practically cancel, making the over-all uncertainty in the hydrogen density only about 1 per cent. The effect of this on the fast leakage results in an uncertainty in the computed k_{eff} of about 0.4 per cent. The uncertainty in the uranium density is estimated to be 1.5 per cent, but due to the high value of the thermal utilization the effect on k_{eff} is only about 0.1 per cent.

(d) Incorrect Calculation of the Core Spectrum. The difference in the values of k_{eff} between the two- and four-group schemes is believed due in large part to the fact that the fast diffusion constants of the core for one scheme are not consistent with those of the other. This inconsistency is due to the approximate manner in which the interaction with the reflector is taken into account by the MUFT-3 code in calculating the core fast neutron spectrum. As noted previously, the entire effect of the reflector in the MUFT system is described by assigning a fast buckling which is the same throughout the entire energy spectrum. A more detailed description of the interaction of the core and reflector as a function of energy is required to make it possible to compute consistent two- and four-group fast constants. This is particularly true of the thin, leaky cores treated here. It is estimated that use of the simple geometrical buckling approximation to calculate the core spectrum makes the k_{eff} of the two-group scheme uncertain to 2 per cent and that of the four-group scheme uncertain to 1 per cent. The higher values of k_{eff} obtained in the four-group scheme in experiments 3 and 4, where the core was bisected by a water channel, arise from this same sort of error. In this calculation no detailed description was used to determine the effect of the water gap on the fast neutron spectrum in the surrounding core.

Insofar as the thermal spectrum is concerned, the uncertainties in k_{eff} due to errors in calculating the thermal spectrum in the core appear to be small because of the high thermal utilization of the core around 0.9, and the small interaction with the reflector. Thus the value of ηf calculated for the thermal group was 1.835 when averaged over the hardened Wigner-Wilkins spectrum calculated from the DONATE code. A Maxwellian average at 20°C, had it been used, would give a value of ηf of 1.841. This represents an increase in k_{eff} of only about 0.3 per cent. Because of the larger uncertainties in k_{eff} due to other factors, it appears that the calculations of criticality for the cores used in this series are not sufficiently precise to cast any light on the details of the thermal spectrum hardening.

(e) Thermal Self-Shielding in the Core. No self-shielding was taken into account in computing the thermal and fission cross sections of the core. An estimate of the self-shielding within the fuel tape (0.021 inch thick) was made by using a simple one-dimensional transport calculation. The result showed that the rate of neutron absorption by the uranium on the tape was about 3 per cent less than the rate at infinite dilution. Because of the high thermal utilization, however, this would decrease the k_{eff} value by only about 0.3 per cent.

There is, in addition, further self-shielding due to the flux ripple through the structure of the fuel. This is due mainly to the small water gaps, of the order of 0.1 inch, between adjacent bundles. This effect can be observed on the thermal activation distributions. A cell calculation showed that this effect would decrease the k_{eff} by less than 0.1 per cent.

Taking all of these effects into consideration, it is perhaps remarkable that the agreement between experiment and the four-group calculation is as good as it appears to be. If the error and uncertainty estimates made here are reasonable, the agreement is in part due to offsetting of some of the errors and uncertainties.

13.17 SUMMARY OF RESULTS--FLUX DISTRIBUTIONS

As noted previously, the shape of the computedthermal flux (0-0.625 ev) fits the subcadmium manganese activation fairly well. It was noted that the fits were poorest at the reflector peaks and at the central water gap peaks. There seems to be little doubt that a correction for high leakage should be made in calculating the thermal spectrum in the vicinity of these peaks. This correction was not made in the calculations.

It will be noted in most of the cases that the ratio of the subcadmium activation at some point in the reflector to some point inside the core is generally greater than the computed thermal flux ratio for these same two points. This is the case because the thermal spectrum in the core is considerably harder than in the reflector. The measured subcadmium activation, because of the 1/v thermal absorption cross section of manganese, is proportional to the thermal neutron number density instead of the neutron flux. At a point in the core, the ratio of the thermal flux ϕ_c to the thermal activation A_c is given by

$$\frac{\phi_c}{A_c} = C_{Mn} \overline{V}_c \qquad \text{Eq. (13.2)}$$

where

$$\overline{V}_c = \frac{\int_o^{0.625} \phi_c(E)\, dE}{\int_o^{0.625} \phi_c(E)\, (1/v) dE} = \frac{\int_o^{0.625} v\, n_c(E) dE}{\int_o^{0.625} n_c(E) dE} \qquad \text{Eq. (13.3)}$$

and n_c is the number density of neutrons in the energy interval dE at E

$$n_c(E) = \frac{1}{v}\, \phi_c(E) \qquad \text{Eq. (13.4)}$$

The neutron velocity is v, a function of E. The constant C_{Mn} has a value characteristic of the manganese detecting wire. $\overline{V}_c$ is the average thermal neutron velocity in the core.

The integrals in Eq. (13.3)have an upper limit of 0.625 ev. For the subcadmium activation, however, the integration should extend only to about 0.4 ev. Such a distinction between the limits of integration is not important, however, because the manganese activation between 0.4 and 0.625 ev is only about 1 per cent of the total activation below 0.4 ev.

A set of equations similar to Eqs.(13.2) and(13.3)holds for the ratio of flux to activation at some point in the reflector. Thus,

$$\frac{\phi_r}{A_r} = C_{Mn} \overline{V}_r \qquad \text{Eq. (13.5)}$$

where $\overline{V}_r$ is the average neutron velocity in the reflector determined by averaging over the thermal spectrum of the reflector. Dividing Eq. (13.5) by Eq. (13.2) gives

$$\frac{A_r}{A_c} = \left(\frac{\overline{V}_c}{\overline{V}_r}\right) \frac{\phi_r}{\phi_c} \qquad \text{Eq. (13.6)}$$

The thermal spectrum in the reflector has practically a Maxwellian distribution at room temperature (20°C). Using such an assumption, the calculated value for $\overline{V}_r$ turns out to be 1.128 v_o, where v_o is the most probable velocity corresponding to kT of 0.025 ev. A hardened spectrum calculation in pure water gives a value for $\overline{V}_r$ of 1.161 v_o.

The DONATE code was used to calculate $\overline{V}_c$ in the core. It was found to be 1.409 v_o, where v_o is the same value as in the preceding paragraph. As a result the ratio of thermal activation at a point in the reflector to a point in the core would be estimated to be roughly 20 per cent higher than the ratio of the calculated thermal fluxes for the two points. This would be the ratio for points lying well within their respective regions since the thermal neutron spectrum is continuous across the core-reflector interface.

The 20 per cent estimate, while it probably represents an overcorrection, is in the right direction to account for the difference between the calculated fluxes and the measured activations.

The epicadmium manganese activation (0.4 ev-10 Mev) was compared in the graphs with the third-group calculated flux (0.625 ev-5.53 kev) from the four-group calculations. By assuming a 1/v manganese cross section and 1/E neutron spectrum, it is easy to show that about 80 per cent of the total epicadmium activation is due to neutrons with energies lying within the limits of the third-group flux. It was for this reason that the epicadmium activation was compared with the third-group flux. Little can be added to the discussion of the fit other than the general remark that it seems reasonably satisfactory. Reasons for the small but consistent departures are not known.

REFERENCES

1. R.L. Hellens and S. Lukasik, Multigroup Neutron Cross Sections : 54 Neutrons Groups, Report WAPD-TM-36, January 1957.
2. H. Amster, Cross Sections in the SOFACATE Code: Second Deck (of Cards), Report WAPD-TM-67, June 1957.
3. A. Radkowsky, Argonne Quarterly Report, Report ANL-4476, July 1950.
4. C.E. McFarland and A.D. Voorhis, Experimental and Theoretical Study of Critical Slabs--Effect of Different Reflector Arrangements and Compositions, Report WAPD-169, April 1957.

[redacted]

Chapter 14

THE ANALYSIS OF HIGHLY ENRICHED SLAB REACTOR CONTROL EXPERIMENTS

14.1 INTRODUCTION

In the preceding chapter the results of a series of carefully designed slab reactor experiments were analyzed by group diffusion theory techniques. The method of derivation of the group constants and their use in the calculations were, by intent, identical to the procedures used in the nuclear design of reactors. The comparison of the calculated with experimental results provided a measure of the reliability and accuracy of the design techniques.

This chapter describes an extension of this approach into the area of control rod worth studies. As before, the experiments were designed to involve a minimum of complication due to geometry and heterogeneity. While there is not, in the case of control rod worth, an established design procedure, the experiments were again analyzed within the framework of group diffusion theory. The intent was to examine the degree of confidence with which the nuclear design procedures could be extended to control rod worth calculations.

The results obtained so far are encouraging but not conclusive. It does appear in the cases examined that the control rod worth may be calculated reasonably well. The studies, however, are not sufficiently broad in scope to provide a thorough test. Further experimental data are required as well as an improvement in the precision of the analysis before a high degree of reliance can be placed on analytical methods of calculating control rod worths.

DESCRIPTION OF THE EXPERIMENTS

by T.M. Ryan

14.2 DESCRIPTION OF THE REACTOR

The critical assembly used for these experiments was the same highly enriched assembly used to conduct the experiments reported in Chap. 13. The core was again arranged in slab geometry with one dimension much smaller than the other two to permit a one-dimensional analysis. The reactor was completely water reflected for the control experiments with a water reflecting region about 20 inches thick.

The control experiments were conducted by locating a sheet of control material in the reactor core so that it bisected the narrow dimension of the slab. Figure 14.1 is a schematic diagram of the reactor. As indicated on this figure the reactor core had a narrow dimension W, a length L, and a height H. The absorbing membrane was made so as to extend at least 2 inches beyond the core dimensions into the water reflector.

The contruction and composition of the core material was the same as described in Chap. 13. As described there, the core was made up of an array of vertical bundles, 0.910-inch-square, and closely packed on a 1-inch-square base. A bundle was made up of five zirconium strips, each 0.110 inch by 0.910 inch by 45 inches in dimension, and eight polyethylene fuel tapes, each 0.021 inch by 0.850 inch by 40-1/4 inches in dimension. The material inventory of the core material is given in Table 13.1. This table also gives the nuclear number densities which apply to the core region. The metal-to-effective water volume ratio was close to unity in the core, based on the assumption that the hydrogen density in polyethylene is about 1.2 times that of water.

The reactor was again controlled with two cadmium control rods, each having a cross-sectional area of 2 square inches, with fuel bundles attached to the ends of the cadmium tube. As the rods were pulled out of the reactor, fuel bundles were pulled in. The letters C and R in Fig. 14.1 indicate the location of the control rods.

14.3 DESCRIPTION OF THE CONTROL MEMBRANES

The experiments were designed to illustrate the effect of a black thermal absorber, a gray thermal absorber with strong resonance absorption, and a 1/v absorber. Cadmium was used for the first type of absorber. Various thicknesses of gold were used for the second type of absorber. Boron was used for the third type of absorber.

In the cadmium experiment, commercially pure cadmium sheet material 0.020 inch thick was used. To obtain a control membrane of adequate size, two sheets were fastened side by side.

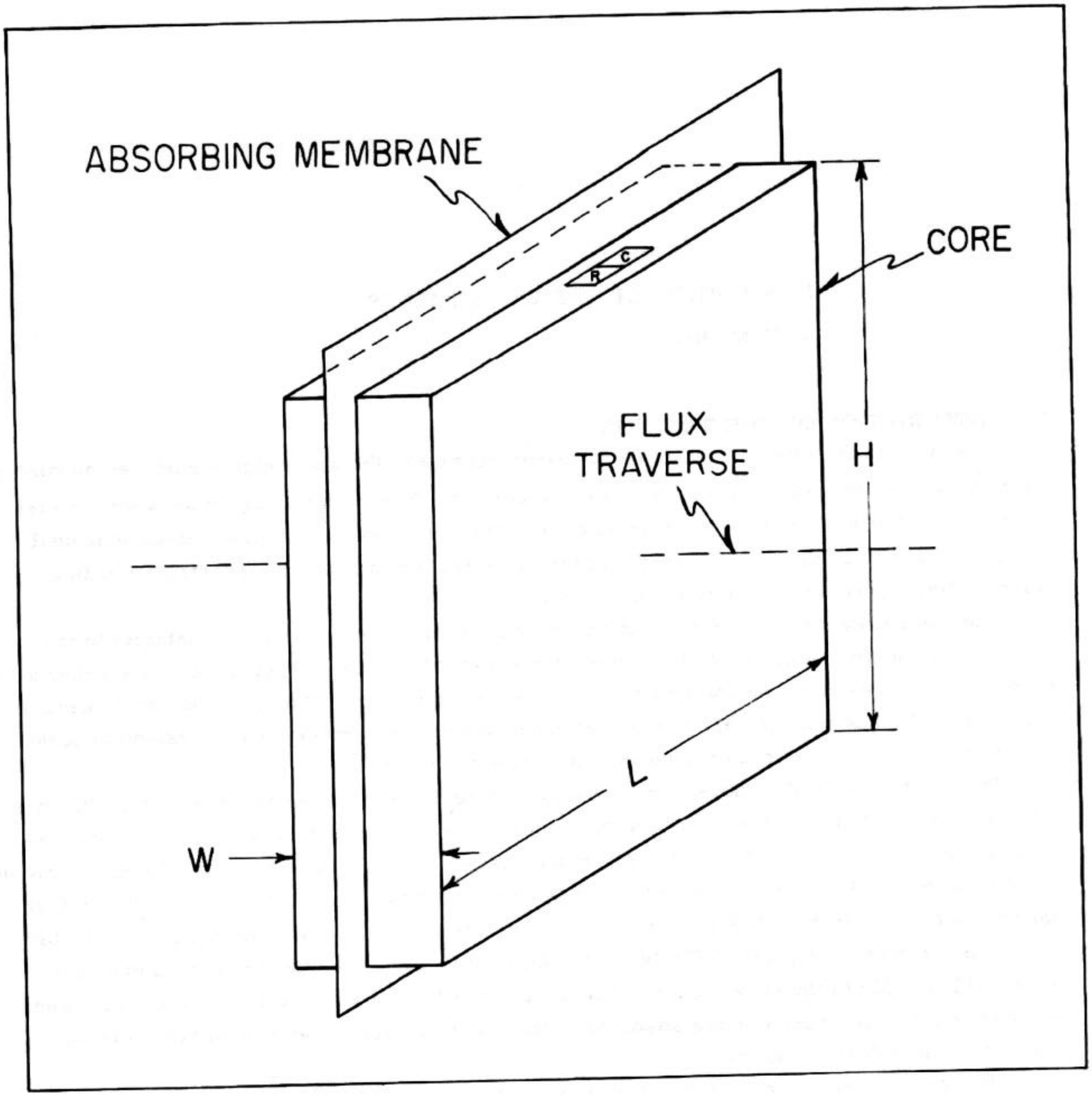

Fig. 14.1 - Sketch Showing the Geometry of the Control Sheet Experiments.

The gold experiment was performed using gold ribbons 4 inches wide and 36 inches long. The ribbons were fastened together, side by side, to obtain the necessary sheet width. The first gold experiment was performed using a single layer of gold sheet 0.010 inch thick. The second was performed using two gold sheets whose composite thickness was 0.030 inch (a gold sheet 0.020 inch thick was placed on a gold sheet 0.010 inch thick). The third experiment with gold used two sheets, each 0.020 inch thick, plus a sheet 0.010 inch thick to obtain a total thickness of 0.050 inch. The gold content of the sheets was analyzed to be 99.98 per cent gold with traces of silver present.

The boron sheet was constructed by sandwiching two layers of polyethylene tape, each having a thickness of 0.019 inch and containing a dispersion of natural boron, between two sheets of aluminum, each 0.025 inch thick. The average boron loading was 0.0012 gram/cm^2 of membrane surface. The average loading of polyethylene was 0.0878 gram/cm^2.

In placing the control sheet between the fuel bundles, the water gap was kept smaller than the 0.1-inch water gap normally present between adjacent fuel bundles. Thus there was no need to consider the water between the control sheet and the fuel zone explicitly.

14.4 ACTIVATION TRAVERSES

Neutron activation profiles were measured along various traverses through the critical core in each experiment. In general, the technique used was the same as that described in Chap. 13, except that other foil materials were included. Bare wire activation and epicadmium activation were measured with small wire detectors made of two materials, manganese and a highly enriched uranium alloy. Gold foils were also used. The wires were spaced 0.2 inch and 0.5 inch (for bare and cadmium-covered measurements, respectively) along 1/16-inch-thick Plexiglas wands which were inserted between the fuel bundles of the core. The gold foils were spaced 0.5 inch and 1.0 inch apart. The manganese detectors, 0.030-inch diameter by 0.5-inch length, were composed of 12 w/o manganese and 88 w/o iron. The gold foils, 0.001-inch thick by 3/16-inch diameter, were pure gold except for traces of silver as an impurity. The uranium detectors, 0.030-inch diameter by 0.5-inch length, were composed of approximately 6 w/o uranium and 94 w/o zirconium. The cadmium covers used to measure the epicadmium activation were 0.020 inch thick. Subcadmium activation profiles were obtained by subtraction of the epicadmium activation from the activation of the bare wires.

14.5 METHOD OF PERFORMING THE EXPERIMENT

In the performance of these experiments the membrane was installed in the reactor tank and the fuel bundles were loaded about the membrane until a critical slab configuration was reached. In the critical configuration the membrane either bisected the thin dimension of the slab or was displaced 1/2 inch from this position as the critical width and the size of the fuel bundles required. The control rods were usually inserted to a depth of 3 or 4 inches at criticality in order to attain a practical power level for activation measurements. As with the slab experiments described in Chap. 13, the residual reactivity due to the rod insertion was determined by calibration of the control rods. This reactivity was then added to unity in order to obtain the experimental rod-free k_{eff}.

The experimental data obtained are presented in the next section together with the analytical results.

THEORETICAL ANALYSIS OF CONTROL EXPERIMENTS

by M. Goldsmith

14.6 GENERAL ANALYTICAL PROCEDURE

The method used to analyze each critical assembly is the same, aside from the effect of the membrane, as that described in detail in Chap. 13. This procedure will be reviewed briefly. The highly enriched slab core has a small width W, large length L, and height H. The principal neutron leakage into the water from the core occurs along its narrow dimension W. As before, therefore, the neutron balance of the entire assembly was calculated by a one-dimensional diffusion calculation along the narrow dimension perpendicular to the absorbing membrane. The small neutron leakage along the other two axes of the core was accounted for by buckling corrections.

In this calculation, the core and water reflector regions are treated as separate homogeneous diffusion media. The average nuclear number densities of these two regions are given in Tables 13.1 and 13.3.

The one-dimensional diffusion problem is solved on a digital computer by using the WANDA code (see Appendix A). This is a one-dimensional, multiregion, few-group diffusion code. The calculation has been carried out using both two and four groups.

The fast group constants for the core and water regions were computed, as in Chap. 13, by using the MUFT-3 multigroup diffusion code (see Appendix E). The thermal group constants for the core were computed by using the DONATE code (see Appendix D) to take account of hardening in the thermal spectrum. The thermal group constants for the water reflector are Maxwellian averages. The constants for the core are given in Table 13.2 and for the water reflector in Table 13.3. Both the four-group and two-group constants are given in these tables. The details of the derivation of these constants are discussed in Chap. 13.

As before, the small neutron leakage along the two long axes of the core has been incorporated in the diffusion calculation by a transverse buckling B_T^2. This buckling is calculated in the usual manner, assuming cosine flux distributions along the two long axes of the core with a measured reflector savings of 3.2 inch at the core-water boundary.

The region occupied by the absorbing membrane is treated as a fictitious diffusion region whose net effect on the reactor is the same as the actual absorbing membrane. Thus, the absorption is treated within the framework of the WANDA diffusion calculation. The method of deriving the appropriate constants for this fictitious medium will be discussed in the following sections.

14.7 GENERAL TREATMENT OF ABSORBING MEMBRANE

The principal reason for replacing the actual absorbing region by a fictitious diffusion region is to fit it into the framework of the multiregion diffusion type codes. It is recognized that diffusion theory does not hold within the cadmium or gold sheet at those neutron energies where the material has an appreciable absorption effect. The aim is not to use diffusion theory for the actual region but to replace the actual region by a fictitious diffusion region whose net effect on the reactor, to a P_1 order of approximation in the neutron angular distribution at the surface of the absorber, is the same as the actual absorber. Once the group diffusion constants for this fictitious region are determined, it is a simple matter to make a one-dimensional calculation perpendicular to the absorbing membrane where core, water reflector, and the thin fictitious region are treated as separate diffusion media.

In the following discussion it is assumed that neither neutron fission nor neutron moderation is occurring inside the membrane, i.e., there is no internal source of neutrons in the membrane. The first restriction is completely valid for all the experimental membranes used. For the cadmium and gold membranes the second restriction is a good approximation because of the high scattering masses and thinness of the membranes. For the boron-polyethylene membrane, however, the second restriction is probably poor. This is discussed in a following section.

14.8 DETAILED TREATMENT OF ABSORBING MEMBRANE--DERIVATION OF BOUNDARY PARAMETERS

The first step in the analysis by which the absorbing membrane is replaced by a fictitious diffusion region is to obtain appropriate boundary conditions at the absorber face. In particular, the ratios of currents to fluxes are the significant quantities. Let $j^+(E)$ represent the net neutron current into one face of the absorber (e.g., the side in the positive x-direction) at an energy E. Let $\phi^+(E)$ represent the scalar flux at the same surface. Let $j^-(E)$ and $\phi^-(E)$ represent the current into the other face and the scalar flux value at the other face, respectively. Two quantities $\alpha(E)$ and $\beta(E)$ are defined as follows :

$$\alpha(E) \equiv \frac{j^+(E) + j^-(E)}{\phi^+(E) + \phi^-(E)} \qquad \text{Eq. (14.1)}$$

$$\beta(E) \equiv \frac{j^+(E) - j^-(E)}{\phi^+(E) - \phi^-(E)} \qquad \text{Eq. (14.2)}$$

It can be seen from these definitions that $\alpha(E)$ is a measure of the total current into the absorbing membrane while $\beta(E)$ is essentially a measure of the net current through the membrane.

Energy averages of $\alpha(E)$ and $\beta(E)$ will be taken to obtain appropriate group values. Before doing this, however, consideration will be given to how these quantities can be calculated.

The quantities $\alpha(E)$ and $\beta(E)$ are functions of the absorption and scattering within the membrane. If the scattering cross section is assumed to be zero, they can be computed approximately using simple optical penetration theory [1,2], which gives

$$\alpha(E) = \frac{F_o(E)}{2\left[2-F_1(E)\right]} \qquad \text{Eq. (14.3)}$$

$$\beta(E) = \frac{2-F_o(E)}{2F_1(E)} \qquad \text{Eq. (14.4)}$$

In these equations

$$F_o(E) = 1 - 2\int_o^1 d\mu\, \mu \exp\left[-\frac{2t\Sigma_a(E)}{\mu}\right] \qquad \text{Eq. (14.5)}$$

and

$$F_1(E) = 1 - 3\int_o^1 d\mu\, \mu^2 \exp\left[-\frac{2t\Sigma_a(E)}{\mu}\right] \qquad \text{Eq. (14.6)}$$

In the definitions of $F_o(E)$ and $F_1(E)$, 2t is the thickness of the membrane, and $\Sigma_a(E)$ is the macroscopic absorption cross section of the membrane at energy E.

Physically, the quantity F_o is the fraction of the isotropic component (P_o term) of the incident flux absorbed in the membrane, and F_1 is the fraction of the entering anisotropic component (P_1 term) which is absorbed. The integrals in Eqs. (14.5) and (14.6) are the well-known E-functions and are tabulated [3] as a function of the argument $2t\,\Sigma_a(E)$.

The values of α (E) and β(E) for two limiting cases of absorption in the membrane are important.

Case 1. Small absorption (transparent membrane) $t\Sigma_a(E) << 1$.

$$\alpha(E) = t\Sigma_a(E) << 1 \qquad \text{Eq. (14.7)}$$

$$\beta(E) = \frac{1}{3t\Sigma_a(E)} >> 1 \qquad \text{Eq. (14.8)}$$

Case 2. Large absorption (black membrane) $t\Sigma_a(E) >> 1$.

$$\alpha(E) = \beta(E) = \frac{1}{2} \qquad \text{Eq. (14.9)}$$

The computation of α(E) and β(E) is, in general, more difficult when scattering is present. The case where the membrane is situated in a symmetric flux $\phi^+(E) = \phi^-(E)$ is discussed in Reference 4 which also contains tables for finding F_o and F_1. Other methods for finding α and β when scattering is important are described in Reference 2.

The next step will be the definition of the appropriate group averages. First, ϕ*(E) is defined as the mean of the scalar fluxes on each side of the membrane, and j*(E) is defined as the net neutron current through the membrane.

$$\phi^*(E) \equiv \frac{1}{2}\left[\phi^+(E) + \phi^-(E)\right]$$

$$j^*(E) \equiv \left[j^+(E) - j^-(E)\right]$$

It is convenient at this point to introduce certain group averages. For the i^{th} energy group the group averages of α(E) and β(E) can be defined as follows:

$$<\alpha>_i \equiv \frac{\int_i \alpha(E)\, \phi^*(E)\, dE}{\int_i \phi^*(E)\, dE} \qquad \text{Eq. (14.10)}$$

$$<\beta>_i \equiv \frac{\int_i j^*\,(E)\, dE}{\int_i \frac{1}{\beta(E)}\, j^*(E)\, dE} \qquad \text{Eq. (14.11)}$$

If ϕ_i^+, ϕ_i^-, j_i^+, and j_i^- are defined as the total fluxes and currents over the i^{th} group ; for example

$$\phi_i^+ \equiv \int_i \phi^+(E)\, dE, \text{ etc.},$$

the following relations hold:

$$j_i^+ + j_i^- = <\alpha>_i (\phi_i^+ + \phi_i^-) \qquad \text{Eq. (14.12)}$$

$$j^+ - j^- = <\beta>_i (\phi_i^+ - \phi_i^-) \qquad \text{Eq. (14.13)}$$

or

$$j_i^+ = <\alpha>_i \frac{\phi_i^+ + \phi_i^-}{2} + <\beta>_i \frac{\phi_i^+ - \phi_i^-}{2}\,, \qquad \text{Eq. (14.14)}$$

$$j_i^- = <\alpha>_i \frac{\phi_i^+ + \phi_i^-}{2} - <\beta>_i \frac{\phi_i^+ - \phi_i^-}{2}\,. \qquad \text{Eq. (14.15)}$$

The parameters $<\alpha>_i$ and $<\beta>_i$ are related to logarithmic flux boundary conditions on each side of the membrane. If the membrane is located in a symmetrical flux (center of core), then $\phi_i^+ = \phi_i^-$ and $j_i^+ = j_i^-$ and the second term on the right of Eqs. (14.14) and (14.15) vanishes. In this case the logarithmic extrapolation distance for the flux(into the membrane) is the same on each side and is given by $D_i^c/<\alpha>_i$; where D_i^c is the core group diffusion constant. From Eq. (14.12) the total current into both sides of the membrane depends primarily on $<\alpha>_i$. From Eq. (14.13) the total current through the membrane depends primarily on $<\beta>_i$. In determining the reactivity effect of a membrane, it is usually more important to know $<\alpha>_i$ correctly than $<\beta>_i$ because the former determines the total rate of absorption in the membrane, whereas the latter determines only the current through the membrane due to a flux mismatch on either side. When the membrane is located in a symmetric flux, it is not necessary to know $<\beta>_i$. If, however, the membrane is located in a very strong flux gradient, it may be necessary to know $<\beta>_i$ as accurately as $<\alpha>_i$. The flux asymmetry about the membranes considered in this chapter was small, so that $<\alpha>_i$ was more important than $<\beta>_i$.

The averages defined by Eqs. (14.10) and (14.11) are to be taken over the neutron spectrum existing at the absorbing membrane surface. As a first approximation, these spectra,

$\phi^*(E)$ and $j^*(E)$, can be taken equal to the scalar flux spectrum $\phi_o(E)$ in the surrounding core away from the membrane. Higher order approximations, however, should take account of the local flux depression in the core at the membrane as a function of energy. This heterogeneous problem has not been solved for neutrons in the thermal range because of the mathematical difficulties presented by neutron up-scattering. An approximate solution to this problem, however, is known[1] for the fast neutron energy groups (down-scattering only) which can be used to calculate the flux depression at the membrane due to resonance absorption. With this effect taken into account, the group averages over the fast neutron spectrum can be expressed to the second order of approximation by

$$\langle\alpha\rangle_i = \frac{\displaystyle\int_i \frac{\alpha(E)\ \phi_o(E)}{1+\sqrt{3}\ \alpha(E)}\,dE}{\displaystyle\int_i \frac{\phi_o(E)}{1+\sqrt{3}\ \alpha(E)}\,dE} \qquad \text{Eq. (14.16)}$$

$$\langle\beta\rangle_i = \frac{\displaystyle\int_i \frac{\beta(E)\ \phi_o(E)}{1+\sqrt{3}\ \beta(E)}\,dE}{\displaystyle\int_i \frac{\phi_o(E)}{1+\sqrt{3}\ \beta(E)}} \qquad \text{Eq. (14.17)}$$

where $\phi_o(E)$ is the scalar fast flux spectrum in the surrounding core away from the membrane. These expressions are to be used for the fast neutron groups only, not for the thermal group. They are derived assuming a hydrogenous moderator with the fast scattering cross section of the moderator much larger than its fast absorption cross section.

14.9 DETAILED TREATMENT OF ABSORBING MEMBRANE--DERIVATION OF EQUIVALENT DIFFUSION THEORY CONSTANTS

Consider an infinite slab region of width 2t. In this region neutrons are being supplied through the sides, but there is no internal source. Let it first be assumed that diffusion theory does hold within the slab so that the scalar neutron flux ϕ and net current j obey the following equations in the slab,

$$D\,\frac{d^2\phi}{dx^2} - \Sigma_a\phi = 0 \qquad \text{Eq. (14.18)}$$

$$j = -D\,\frac{d\phi}{dx} \qquad \text{Eq. (14.19)}$$

In these equations, D is the diffusion constant and Σ_a is the macroscopic absorption cross section of the medium. The X-axis is taken perpendicular to the face of the slab.

The general solutions to Eqs. (14.18) and (14.19) may be written

$$\phi(x) = A\cosh\frac{x}{L} + B\sinh\frac{x}{L} \qquad \text{Eq. (14.20)}$$

$$j(x) = -\sqrt{D\Sigma_a}\left[A\sinh\frac{x}{L} + B\cosh\frac{x}{L}\right] \qquad \text{Eq. (14.21)}$$

where $L^2 \equiv D/\Sigma_a$, and A, B are arbitrary constants.

If ϕ^+ and ϕ^- are again used to designate the fluxes at the two surfaces of the slab (right and left, respectively) and j^+ and j^- are used to designate the currents into the two faces of the slab, the surface currents may be expressed in terms of the fluxes.

$$j^+ = \sqrt{D\Sigma_a}\left(\frac{\phi^+ + \phi^-}{2}\right)\tanh\frac{t}{L} + \sqrt{D\Sigma_a}\left(\frac{\phi^+ - \phi^-}{2}\right)\operatorname{ctnh}\frac{t}{L} \qquad \text{Eq. (14.22)}$$

$$j^- = \sqrt{D\Sigma_a}\left(\frac{\phi^+ + \phi^-}{2}\right)\tanh\frac{t}{L} - \sqrt{D\Sigma_a}\left(\frac{\phi^+ - \phi^-}{2}\right)\operatorname{ctnh}\frac{t}{L} \qquad \text{Eq. (14.23)}$$

By identifying Eqs. (14.22) and (14.23) with Eqs. (14.14) and (14.15) it is seen that

$$<\alpha> = \sqrt{D\Sigma_a}\tanh\frac{t}{L} \qquad \text{Eq. (14.24)}$$

$$<\beta> = \sqrt{D\Sigma_a}\operatorname{ctnh}\frac{t}{L} \qquad \text{Eq. (14.25)}$$

Thus the derivation leads to the following conclusion: If diffusion theory holds in the absorbing slab, the parameters $<\alpha>$ and $<\beta>$ may be calculated from the diffusion constants of the medium by using Eqs. (14.24) and (14.25).

Suppose, however, diffusion theory does not hold within the slab but the parameters $<\alpha>$ and $<\beta>$ are known from some other source of information. This slab medium then can be replaced by a fictitious diffusion medium having effective constants D and Σ_a which satisfy Eqs. (14.24) and (14.25). Such a fictitious diffusion medium would preserve the relation between fluxes and currents that existed at the surface of the original medium. The constants D and Σ_a can be solved in terms of $<\alpha>$ and $<\beta>$ as follows: Multiply and divide Eqs. (14.24) and (14.25) and apply the relation

$$2\tanh^{-1}x = \ln\left(\frac{1+x}{1-x}\right) \qquad \text{Eq. (14.26)}$$

The results are

$$\Sigma_a = \frac{\sqrt{<\alpha><\beta>}}{2t}\ln\left[\frac{1+\sqrt{\frac{<\alpha>}{<\beta>}}}{1-\sqrt{\frac{<\alpha>}{<\beta>}}}\right] \qquad \text{Eq. (14.27)}$$

$$D\Sigma_a = <\alpha><\beta> \qquad \text{Eq. (14.28)}$$

The procedure then is to calculate $<\alpha>_i <\beta>_i$ for each of the energy groups. From these the equivalent D_i and Σ_{ai} are calculated by Eqs. (14.27) and (14.28).

14.10 DETAILED TREATMENT OF ABSORBING MEMBRANES--CALCULATION OF NUMERICAL VALUES FOR BOUNDARY PARAMETERS

By assuming no scattering in the membrane, it can be shown from Eqs. (14.3) through (14.6) that, in general,

$$\frac{1}{4\alpha(E)} \leqq \beta(E) \leqq \frac{1}{3\alpha(E)} \qquad \text{Eq. (14.29)}$$

where the upper bound occurs in the limit of no absorptions, Eqs. (14.7) and (14.8), and the lower in the limit of infinite absorption, Eq. (14.9). From the definitions of the averages, Eqs. (14.10) and (14.11) or (14.16) and (14.17), a corresponding relation holds to a good approximation for the group averages; that is,

$$\frac{1}{4 < \alpha >_i} \leqq < \beta >_i \leqq \frac{1}{3 < \alpha >_i} \qquad \text{Eq. (14.30)}$$

Since an accurate calculation of $< \beta >_i$ is not important when the membrane is situated in an almost symmetric flux, $< \beta >_i$ can be estimated rapidly from $< \alpha >_i$ by using Eq. (14.30). The upper bound of this inequality can be used for $< \beta >_i$ if over an energy group most of the absorption in the membrane is small (resonance absorption) so that $< \alpha >_i << 1$. In that case, the effective group diffusion constants can be approximated from Eqs. (14.27) and (14.28) by

$$\Sigma_{ai} = \frac{< \alpha >_i}{t} \left[1 + < \alpha >_i^2 + \dots \right] \qquad \text{Eq. (14.31)}$$

$$D_i = \frac{t}{3 < \alpha >_i} \left[1 - < \alpha >_i^2 - \dots \right] \qquad \text{Eq. (14.32)}$$

when $< \alpha >_i << 1$ and $< \beta >_i = 1/3 < \alpha >_i$.

The lower bound of Eq. (14.30) must be used for $< \beta >_i$ if the membrane is black over most of the energy group so that $< \alpha >_i = 1/2$. In that case from Eqs. (14.27) and (14.28)

$$D_i \Sigma_{ai} = \frac{1}{4} \qquad \text{Eq. (14.33)}$$

for

$$t \sqrt{\frac{\Sigma_{ai}}{D_i}} >> 1 \qquad \text{Eq. (14.34)}$$

when $< \alpha >_i = 1/2$ and $< \beta >_i = 1/(4 < \alpha >_i) = 1/2$. It should be noted for this case that it does not matter what values are chosen for D_i and Σ_{ai} as long as they satisfy both conditions above. The mesh spacing in the membrane usually determines the choice.

Equations (14.3) and (14.4), which assume no scattering in the membrane. were used in computing $\alpha(E)$ and $\beta(E)$ for the cadmium and gold. The actual probability of scattering within these thin membranes is very low, and the probability of absorption far outweighs that of scattering at those energies where there is an appreciable absorption effect on the core. Table 14.1 gives the values of $< \alpha >_i$ and values of the effective D_i and Σ_{ai} computed for each membrane. Because the membranes were located in either a symmetric flux or one of slight asymmetry, only the $< \alpha >_i$ values were calculated accurately by averaging over the spectrum. The values of $< \beta >_i$ were estimated from the values of $< \alpha >_i$ by using Eq. (14.30).

Table 14.1--SUMMARY OF CALCULATIONS FOR CONSTANTS OF CADMIUM AND GOLD MEMBRANES

	Absorbing Membrane			
	20-mil Cd	10-mil Au	30-mil Au	50-mil Au
Four-Group Scheme				
1) Group One (10 Mev-821 kev)				
$<\alpha>$	0.0000	0.000064	0.000192	0.000320
Σ_a (cm^{-1})	0.0000	0.005018	0.005018	0.005018
D (cm)	2.765*	2.765*	2.765*	2.765*
2) Group Two (821 kev-5.53 kev)				
$<\alpha>$	0.0000	0.00050	0.00150	0.00250
Σ_a (cm^{-1})	0.0000	0.03934	0.03934	0.03934
D (cm)	1.070*	1.070*	1.070*	1.070*
3) Group Three (5.53 kev-0.625 ev)				
$<\alpha>$	0.003284	0.01676	0.03391	0.04537
Σ_a (cm^{-1})	0.1293	1.320	0.8911	0.7159
D (cm)	0.6586*	0.2525	0.3741	0.4656
4) Group Four (0.625 ev-0 ev)				
$<\alpha>$	0.5000	0.04428	0.1165	0.1776
Σ_a (cm^{-1})	82.49	3.494	3.100	2.885
D (cm)	0.003031	0.09540	0.1075	0.1155
Two-Group Scheme				
1) Group One (10 Mev-0.625 ev)				
$<\alpha>$	0.001008	0.005274	0.01044	0.01407
Σ_a (cm^{-1})	0.03972	0.4153	0.2740	0.2216
D (cm)	1.526*	0.8026	1.217	1.504
2) Group Two (0.625 ev-0 ev)				
$<\alpha>$	0.5000	0.04428	0.1165	0.1776
Σ_a (cm^{-1})	82.49	3.494	3.100	2.885
D (cm)	0.003031	0.09540	0.1075	0.1155

* The absorption was so small that the diffusion constant was arbitrarily made equal to that in the core (see discussion in text, Sec. 14.10).

The method of calculating the $<\alpha>_i$ was as follows. The macroscopic absorption cross section of each membrane as a function of energy was taken from cross-section tables.[5] From this and the thickness 2t, the capture probabilities F_o and F_1 were computed as functions of energy from Eqs. (14.5) and (14.6) by using the E-functions in Reference 3. The $\alpha(E)$ could then be calculated as a function of energy from Eqs. (14.3) and (14.4) and group averages $<\alpha>_i$ made over the energy intervals indicated in Table 14.1. For the thermal group, the average was made over the hardened thermal spectrum calculated by the DONATE code (see Appendix D) with no correction for flux depression at the membrane. The spectrum used for this average was that computed for the reactor core (see Chap. 13). For the fast groups the averages were made using Eqs. (14.16) and (14.17). This procedure corrects for the resonance dipping. The spectrum used in this calculation for ϕ (E) was that calculated by MUFT-3 for the reactor core (see Chap. 13, Sec. 13.6). This spectrum is essentially a 1/E spectrum with a broad peak in the Mev region due to the fission spectrum of U^{235}.

In calculating $<\alpha>_i$ for the fast neutrons at the gold membranes, the average of Eq. (14.16) over $\alpha(E)$ could be divided into two parts. At the lower energies near the large gold resonance at 4.9 ev the contribution to $\alpha(E)$ from the 1/v absorption could not be separated from that due to the resonance because the membrane was quite black in the region of this resonance. For these energies Eq. (14.16) had to be numerically integrated. At higher energies the absorption was small, and $\alpha(E) = t\Sigma_a(E)$. In this case the 1/v absorption could be separated from small resonances. The average over these small resonances was obtained from their Breit-Wigner parameters, as indicated in Reference 1.

Aside from $<\alpha>_{th}$ for the 20-mil cadmium membrane, all the resulting $<\alpha>_i$ were small enough so that the upper limit of inequality (Eq. (14.30)) could be used for calculating $<\beta>_i$ and Eqs. (14.31) and (14.32) could be used for calculating the effective diffusion constants. For the two fastest groups in the four-group scheme the absorption in all the membranes was so small that $<\alpha>_i$ practically vanished. As a result, the D_i from Eq. (14.32) became unrealistically large for these groups because no scattering in the membrane had been taken into account. For the purposes of the calculation, the D_i for these groups was arbitrarily given the same value as in the core. The 20-mil cadmium membrane was practically black over the entire thermal range. Consequently,

$$<\alpha>_{th} = 1/2 = <\beta>_{th}$$

for this membrane, and Eq. (14.33) was used to calculate the effective thermal diffusion constants.

The method described above is not applicable for analyzing the boron membrane because of the neutron moderation by the hydrogen in the boron-loaded polyethylene tapes. The total boron loading, however, was so small that diffusion theory could be used at all energies as an approximation for the neutron transport inside the membrane (that is, $\Sigma_{scat} >> \Sigma_{abs}$). Unfortunately, because of this small boron loading, the membrane had a relatively small effect on the reactivity of the core.

Group diffusion constants were calculated for the boron absorbing membrane as follows. The total membrane, including the aluminum sheets holding the tapes, was homogenized in the calculation. Group averages were made of the microscopic absorption cross sections of the nuclei present (boron, hydrogen, carbon, aluminum) over the flux spectrum of the surrounding core. Group macroscopic absorption cross sections Σ_{ai} for the membrane were calculated by linearly combining these averages according to the nuclear mixture. Group diffusion coefficients D_i and fast removal cross sections Σ_{ri} were calculated for the membrane by multiplying the corresponding constants calculated for the core (Tables 13. 1 and 13. 2) by the ratio of hydrogen density in the core to the hydrogen density in the membrane. The group diffusion constants calculated for this membrane appear in Table 14. 2.

Table 14. 2--SUMMARY OF GROUP CONSTANTS USED FOR BORON-POLYETHYLENE ABSORBING MEMBRANE

	Four-Group Scheme (See Table 14. 1 for energy ranges)			
	Group One	Group Two	Group Three	Group Four
D (cm)	2. 762	1. 069	0. 6578	0. 3176
Σ_a (cm^{-1})	0. 0000	0. 0000	0. 01009	0. 1770
$\Sigma_{removal}$ (cm^{-1})	0. 05849	0. 07451	0. 07210	---

	Two-Group Scheme (See Table 14. 1 for energy ranges)	
	Group One	Group Two
D (cm)	1. 524	0. 3176
Σ_a (cm^{-1})	0. 003160	0. 1770
$\Sigma_{removal}$ (cm^{-1})	0. 02215	---

14. 11 DETAILED TREATMENT OF ABSORBING MEMBRANES--CORRECTION TO FAST CORE CONSTANTS DUE TO ABSORBER

The group removal cross sections of the core given in Table 13. 2 were calculated with no account taken of the membrane. A small second order correction should be made to the cross section of the group lying just above thermal when there is a membrane in the core with appreciable fast (resonance) absorption. The reason for this correction is as follows. The fast resonance absorption in the membrane occurs at energies not too far above the thermal range. Consider now a two-group scheme with all fast neutrons in one group. The removal cross section of Table 13. 2 operates equally on all neutrons in this fast group. Actually, however, the neutrons slowing out of this group come predominantly from energies near the bottom of the group, and this is just where the fast resonances in the membrane are most effective in absorbing neutrons. The group removal cross section calculated without the membrane, Σ^o_{ri}, should be decreased, therefore, to give a corrected smaller cross section, Σ_{ri}. An approximate formula for calculating this correction has been developed.

For the gold membranes in the core considered here this correction can be calculated approximately from the relation

$$\frac{\Sigma_{ri}}{\Sigma^o_{ri}} - 1 = \frac{< z > - \int_{w_i}^{wg} z(u) \exp (u - ug)\, du}{\Sigma_{SH} w - < z >} \qquad \text{Eq (14. 35)}$$

where $$z = \frac{\alpha}{1 + \sqrt{3}},$$

$$< z > = \frac{< \alpha >}{1 + \sqrt{3} < \alpha >},$$

and the epithermal group, indicated by i, extends from lethargy u, to ug. The epithermal scattering cross-section of hydrogen is represented by Σ_{SH}. $< \alpha >_i$ is the average of $\alpha(E)$ of the membrane for this group, and 2w is the width of the core. The above correction was made to the group removal cross section of the core as given in Table 13.2 for each calculation with the gold membranes. The correction was negligible for the other membrane and was not made.

14.12 CADMIUM SHEET EXPERIMENT--DATA AND ANALYSIS

Figure 14.2 shows the dimensions of the critical slab with the cadmium sheet. The core dimensions are 9 inches by 26 inches by 40-1/4 inches. The cadmium sheet divided the core into two segments; one 4 inches thick, the other 5 inches thick. The letters A and B designate the location of the wands at which the activation traverses were taken.

The experimental rod-free k_{eff} of this core was 1.002. The calculated value of k_{eff} was 1.013 for the four-group calculation and 1.022 for the two-group calculation.

The k_{eff} of the core was also calculated with the absorbing membrane removed to obtain a measure of the effectiveness of the absorber. The value obtained was 1.157 with the four-group calculation. The decrease in k_{eff} due to the sheet, i.e., the difference in four-group k_{eff} with and without the sheet, is 0.144.

Figure 14.3 gives the calculated fluxes for the thermal group(group-4) and for the resonance group(group-3) obtained from the one-dimensional four-group calculation. The calculated fluxes are plotted to the same relative scale. The experimental subcadmium and epicadmium manganese activation traverses have each been normalized independently to the calculated flux plots. As in Chap.13, the fit was made to points just outside the core in the water reflector.

The fit of the activation data to the thermal flux is as good as that shown in Chap. 13 for simple slabs. Moreover, the nature of the deviation is very similar to that in the simpler cases. For this reason the calculated thermal flux distribution may be considered as quite satisfactory.

The epithermal activation data give a somewhat poorer fit to the calculated flux but by comparison with the simple slab results this fit may also be considered satisfactory.

Thus, it may be concluded that the calculation for the cadmium sheet is in quite good agreement with the experimental data both from the point of view of criticality and flux distribution.

14.13 GOLD SHEET EXPERIMENTS--DATA AND ANALYSIS

The gold experiments were intended to demonstrate the effect of substantial resonance capture. It is estimated that 25 per cent of the worth of the gold sheet is due to resonance capture. Three thicknesses of gold were used.

The 0.010-inch gold sheet experiment resulted in a reactor size of 7 inches by 32 inches by 39-5/8 inches (the plastic fuel tape shrank slightly over the several month period between the cadmium experiment and the gold experiment, but the net effect of this change was negligible). The gold sheet divided the slab into a three-inch and a four-inch segment.

The experimental rod-free k_{eff} was 1.000 for this experiment. The calculated four-group k_{eff} was 1.008 and the two-group k_{eff}, 1.024 with the membrane present. The calculated four-group k_{eff} with the membrane removed was 1.073. Thus, the four-group calculated loss in

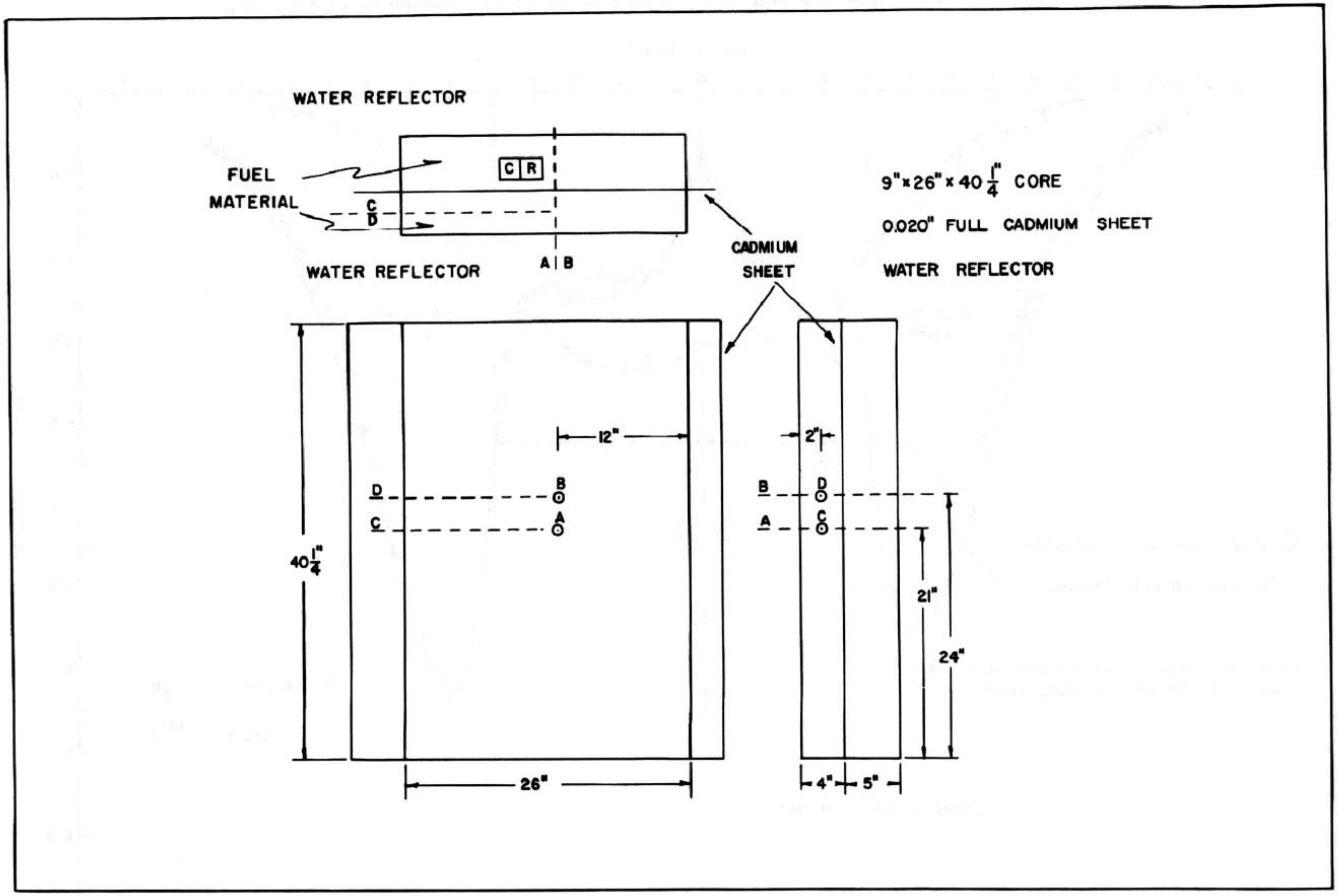

Fig. 14.2 - Sketch of Slab Experiment with Cadmium Sheet.

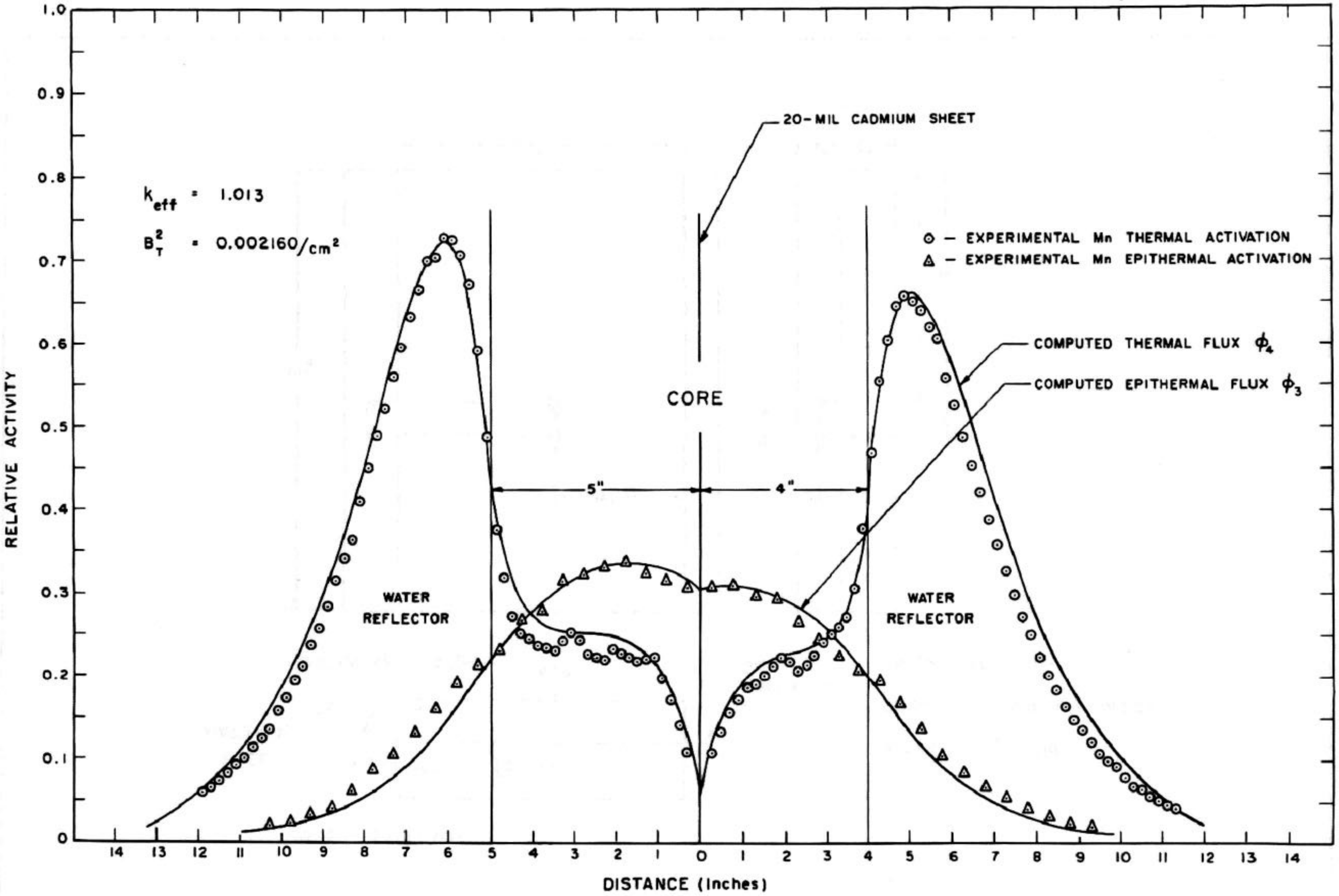

Fig. 14.3 - Comparison of Calculated Flux and Experimental Activations for Cadmium Sheet Experiment.

k_{eff} due to the membrane was 0.065.

Figure 14.4 shows the calculated resonance flux and thermal flux from the four-group calculation. The thermal and epithermal experimental activation data have been arbitrarily normalized to these plots, each independently. In this experiment both manganese and gold activations were taken. There appears to be relatively little difference in the two sets of experimental data. The fit of the calculated thermal flux to the activation data is somewhat poorer than with the cadmium experiment although it is fairly satisfactory. The experimental data show a peculiar asymmetry which is difficult to interpret.

The 0.030-inch gold sheet experiment resulted in a reactor size of 8 inches by 32-5/8 inches by 39-5/8 inches. Only five bundles were located on the end of the core instead of the eight necessary to complete the row. For this reason, the length of the core is taken as 32-5/8 inches. The gold sheet divided this core symmetrically.

The experimental rod-free k_{eff} was 1.001 for this core. The calculated four-group k_{eff} was 1.011 and the two-group k_{eff}, 1.023. The four-group calculated k_{eff} with the sheet removed was 1.132. Thus the four-group calculated drop in k_{eff} due to this membrane was 0.121.

Figure 14.5 shows the calculated resonance flux and the thermal flux from a four-group calculation. The experimental activation traverses have been arbitrarily normalized to these plots. In this case manganese was used to plot one-half of the slab and gold in the other half. The experimental activation data look quite similar for the two foil materials. The fit to the calculation is fairly satisfactory. It can be noted, in fact, that the general fit of the activation traverses to the calculated plots is within the limits of the fits obtained in the simpler slabs of Chap. 13.

The 0.050-inch gold sheet experiment resulted in a reactor size of 9 inches by 26-7/9 inches by 39-5/8 inches with the gold sheet dividing the reactor into a four-inch and a five-inch segment. As before, the 26-7/9-inch length indicates that seven of the nine holes on the end row of the slab were filled with core material.

The experimental rod-free k_{eff} was 1.000 for this core. The calculated four-group k_{eff} was 1.018 and the two-group k_{eff}, 1.025. The calculated k_{eff} with the membrane removed was 1.160. Thus, a four-group calculated value for the drop in k_{eff} due to the gold sheet was 0.142.

Figure 14.6 shows the calculated resonance flux and the thermal flux from a four-group calculation. Experimental activation traverses are also shown on this figure. The fit is quite good for this case.

14.14 BORON EXPERIMENTS--DATA AND ANALYSIS

The boron-polyethylene-aluminum sandwich resulted in a reactor whose critical dimensions were 7 inches by 23 inches by 39-5/8 inches. The absorbing sheet divided the reactor into a 4-inch and a 3-inch segment.

The experimental rod-free k_{eff} was 1.001. The four-group calculated k_{eff} was 1.016 and the two-group value was 1.031. With the absorbing sheet removed, the calculated four-group k_{eff} was 1.043. Thus, the four-group calculation gives the loss of k_{eff} of the reactor due to the absorber as 0.027.

The calculated thermal and resonance flux plots for this case are shown in Fig. 14.7 together with the arbitrarily normalized experimental activation traverses. The weak absorption of the boron results in a traverse having little or no dip at the sheet surface. The fit of the activation data to the calculated flux plots is fairly good.

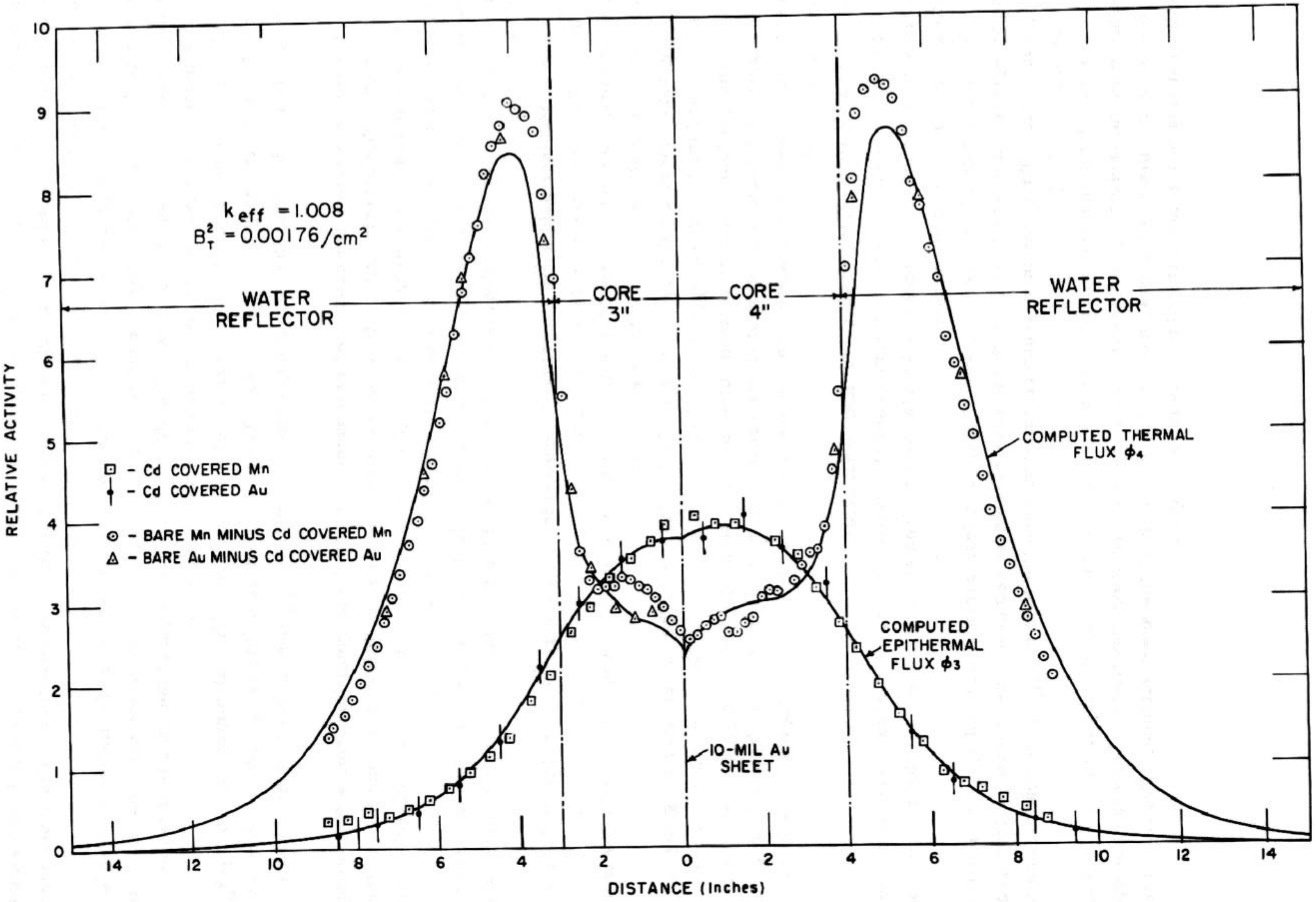

Fig. 14.4 - Comparison of Calculated Flux and Experimental Activation Data for 0.010-Inch Gold Sheet Experiment.

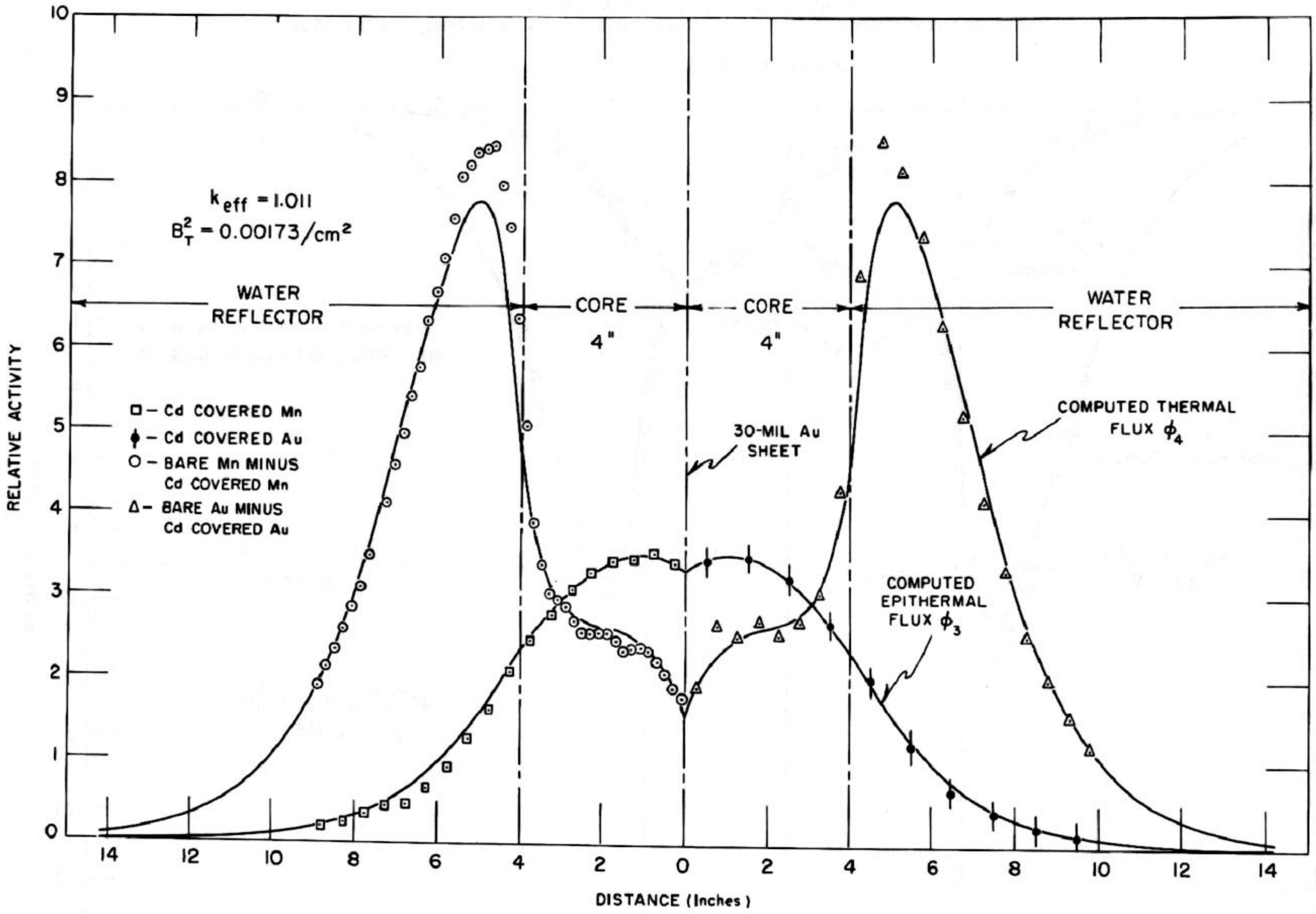

Fig. 14.5 - Comparison of Calculated Flux and Experimental Activation for 0.030-Inch Gold Sheet Experiment.

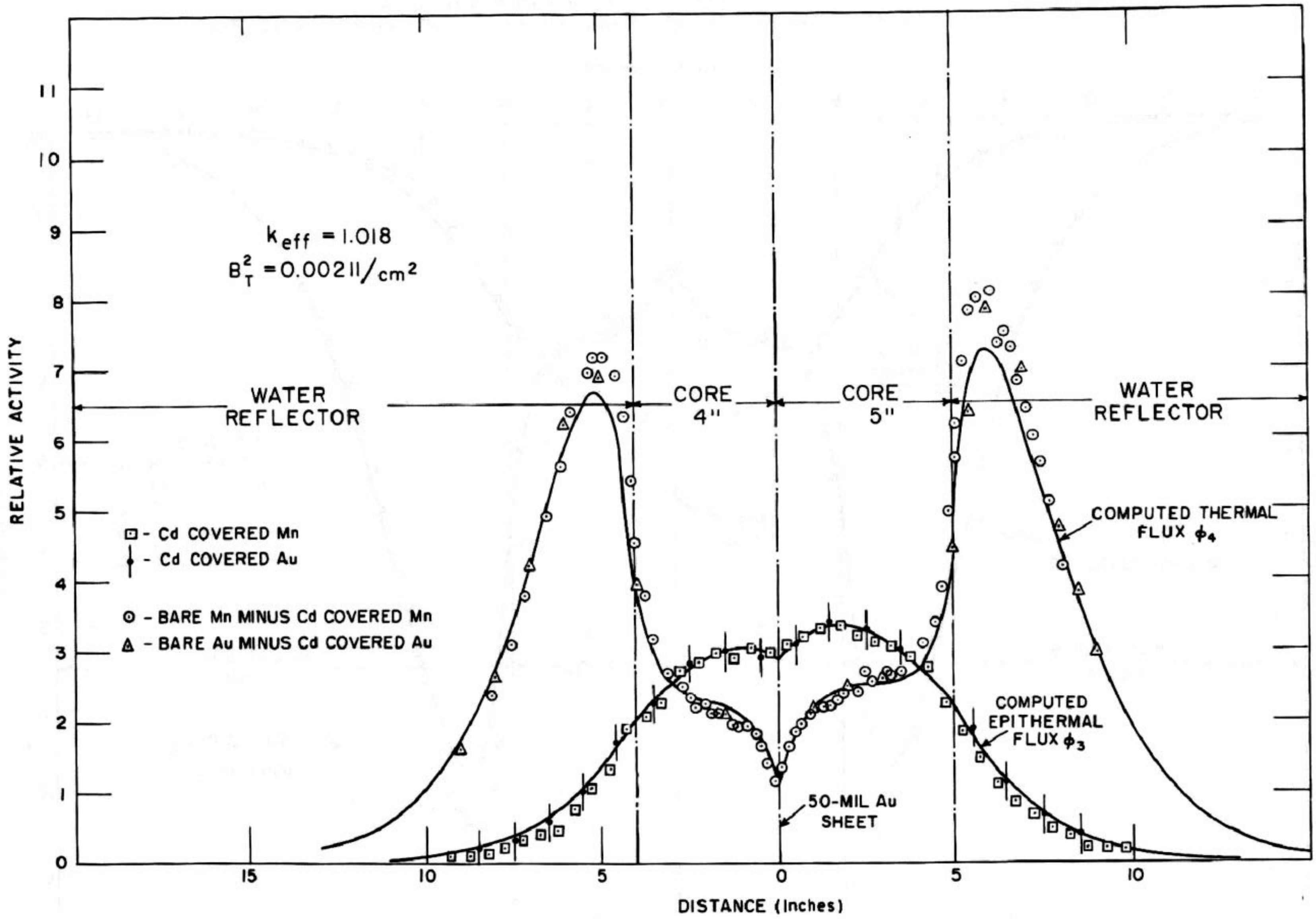

Fig. 14.6 - Comparison of Calculated Flux and Experimental Activation for 0.050-Inch Gold Sheet Experiment.

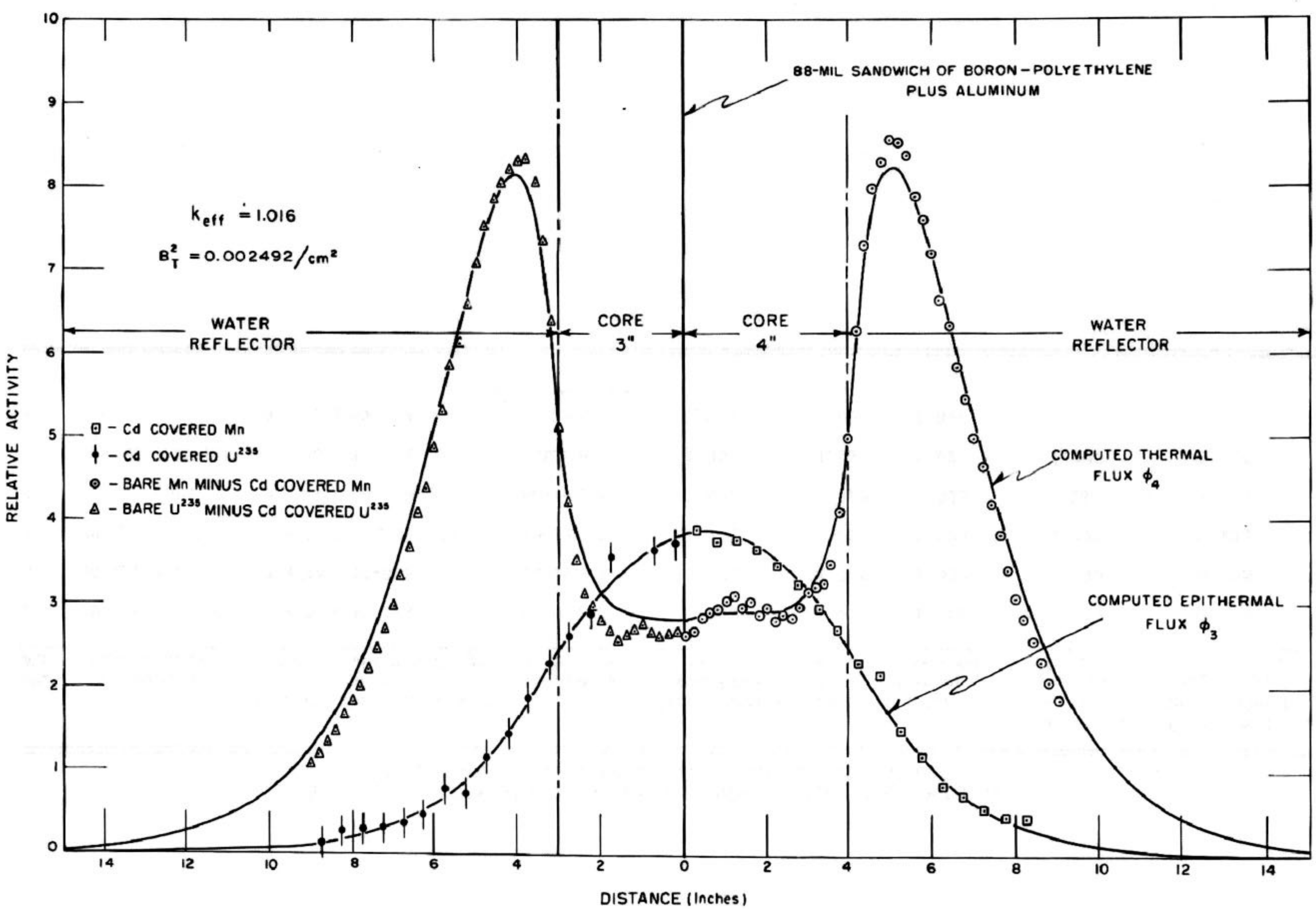

Fig. 14.7 - Comparison of Calculated Flux and Experimental Activation for Boron Sheet Experiment.

Table 14.3--COMPARISON OF EXPERIMENTAL AND THEORETICAL CRITICALITY DATA FOR CONTROL SHEET EXPERIMENTS

Exp No.	Membrane Composition	Critical Core Dimensions (in.) Width x Length x Height	Absorbing Membrane	Experimental Rod-Free k_{eff}	Calculated k_{eff} with Membrane 4-Group	Calculated k_{eff} with Membrane 2-Group	Calculated k_{eff} without Membrane (4-Group)	Calculated Loss in k_{eff} Due to Membrane (4-Group)
1	20-mil cadmium	9 x 26 x 40-1/4	20-mil Cd	1.002	1.013	1.022	1.157	0.144
2	10-mil gold	7 x 32 x 39-5/8	10-mil Au	1.000	1.008	1.024	1.073	0.065
3	30-mil gold	8 x 32-5/8 x 39-5/8	30-mil Au	1.001	1.011	1.023	1.132	0.121
4	50-mil gold	9 x 26-7/9 x 39-5/8	50-mil Au	1.000	1.018	1.025	1.160	0.142
5	Boron sandwich	7 x 23 x 39-5/8	Boron	1.001	1.016	1.031	1.043	0.027
6	None	6 x 31 x 40-1/4	None (Experiment 1 of Chap. 13)	1.001	1.005	1.026	---	---

14. 15 SUMMARY OF DATA

All of the criticality data, both experimental and calculated, are summarized in Table 14. 3. One of the cases of Chap. 13, a simple water reflected slab with no absorber, is included for comparison. In general, it appears that the diffusion calculation describes the absorption of the membranes fairly well although not as satisfactorily as might be desired. The deviation of the four-group calculated k_{eff} from the experimental value is consistently greater than the cases compared in Chap. 13. The cause of this difference must await further experimental and theoretical study of the problem.

REFERENCES

1. S. Stein, Resonance Capture in Heterogeneous Systems, Report WAPD-139, November 1955 (see also Volume 1 of this Handbook).
2. E. L. Wachspress, Thin Regions in Diffusion Theory Calculations, Report KAPL-M-ELW 6, January 17, 1957 (see also Proceedings of AEC Meeting on Control Rod Theory, Report TID-7532).
3. Case, Hoffmann, Placzek, Introduction to the Theory of Neutron Diffusion, Vol. I , Superintendent of Documents, U. S. Government Printing Office, June 1953.
4. D. Schiff, S. Stein, Escape Probability and Capture Fraction for Gray Slabs, Report WAPD-149, June 1956.
5. D. J. Hughes et al, Neutron Cross Sections, Report BNL-325, Jan. 1957.
6. A. D. Voorhis, T. M. Ryan, M. Goldsmith, and R. T. Jones, Experimental and Theoretical Study of Critical Slabs - Effect of Absorbing Membranes of Cadmium, Gold, and Boron, Report WAPD-170, April 1957.

Part V

REACTOR AND PLANT KINETICS

In this section the problems of reactor plant stability are examined and methods for analyzing these problems are presented. A pressurized water reactor is inherently coupled to the remainder of the plant through its temperature coefficient of reactivity and its pressure coefficient of reactivity. Thus any change in the plant condition, for example a change in load, will cause a reactivity change in the reactor which will affect the manner in which the over-all plant responds to the load change. In the language of the systems engineer, this coupling represents feedback; futhermore, the presence of feedback can, under certain circumstances, result in instability of the system.

There are a number of feedback effects in a pressurized water reactor plant in addition to the two mentioned above. The recirculation of the primary coolant introduces feedback which affects the plant dynamics. Xenon poisoning is another feedback effect of importance. Finally, the external control system which is imposed on the system represents one or more feedback loops.

There are basically two methods for analyzing the stability of feedback systems. One of these is the frequency response method in which the system is presumed to be oscillating with small amplitude at an arbitrary frequency. This oscillation is induced by imposing an oscillating component on one of the parameters of the system, for example, the reactivity; the aim of this method is to analyze the response of the system to the oscillation. In particular, if the effect of feedback enhances the amplitude of oscillation of the chosen parameter, the system is unstable. Conditions can be formulated in mathematical terms which represent stability criteria. These are given in standard texts on feedback theory.[1]

The other method of stability analysis which may be used is the transient response method. In this scheme of analysis, the response of the system to a sudden change in a parameter is calculated. The chief advantage of this method of analysis is that the actual change in plant parameters during the transient is determined.

In the study of reactor plant dynamics both methods are used. The frequency response analysis is used to define the regions of questionable stability. The transient analysis is used to study the actual plant response in those regions.

Reactor plant kinetic equations are not only complicated but the equations are non-linear as well. The frequency response analysis can only be carried through by linearizing the equations . The general procedure is to study the problems analytically by the frequency response method and to test the stability analysis by transient response computation. While the transient response is invariably calculated by making use of analog computing equipment, the steady-state analysis may be calculated directly or, if the equations are not linearized, calculated by analog computers.

The material in this section of the handbook will be limited to derivation of the reactor plant equations and consideration of the frequency response analysis of these equations. A discussion of analog computation techniques is beyond the scope of this handbook. For such techniques, the reader is referred to standard texts on the subject.[2] To illustrate certain problems, the results obtained by analog computation of transient conditions are given in the text.

In the steady state analysis of systems the terms degenerative and regenerative feedback are important concepts. In a feedback loop, if a small change or displacement of a parameter (such as reactivity) is fed back in such fashion as to reduce the magnitude of the change, the loop is called degenerative. A loop may be stable in a time-independent condition, i.e., at zero frequency, but unstable under oscillation at a particular frequency. This can occur if there is a time delay associated with the feedback effect. With such a time delay, the possibility arises that at some frequency the time delay may represent a half period of the oscillation and thus be fed back in a regenerative fashion.

The quantitative study of feedback systems is carried out by calculation of the loop gain. In the case of reactivity, for example, the loop gain is the complex ratio of the feedback reactivity to the input reactivity (assumed sinusoidal and of arbitrary frequency). A stability criterion which is satisfactory for the reactor plant problems considered in this section is that the magnitude of the loop gain must be less than unity at all frequencies where the argument (phase shift) is an integral multiple of 2π.

The material of this section is divided into two chapters. The first deals with the stability analysis of certain feedback loops in pressurized water reactor plants. The second chapter deals with the analysis of the over-all plant, in particular the external control system.

References are given at the end of Chap. 15.

Chapter 15

ANALYSIS OF THE INHERENT STABILITY OF PRESSURIZED WATER REACTOR PLANTS

by J. N. Grace and N. J. Curlee

15.1 INTRODUCTION

(a) The Transfer Function. A basic technique used in the frequency response method of reactor analysis is linearization of equations by means of the small signal assumption. This assumption will be used in the development of the concept of a transfer function.

Let P and Q represent two parameters of an assumed physical system and assume that P and Q are functionally related within the system. The frequency response method of analysis is carried out by assuming that one of the parameters, for example P, is subjected to a sinusoidal variation of small, arbitrary amplitude $|\delta P|$ and of frequency ω. Thus, if P_o is the steady-state value of P,

$$P = P_o + \delta P = P_o + |\delta P| \, \epsilon^{j\omega t} \qquad \text{Eq. (15.1)}$$

where it is understood that only the real part of P is interpreted to have physical significance.

Now since Q is functionally related to P by the physical system, the assumed small oscillation of P will result in a small oscillation in Q, of the same frequency ω, and of amplitude $|\delta Q|$. Thus, if Q_o is the steady-state value of Q,

$$Q = Q_o + \delta Q = Q_o + |\delta Q| \, \epsilon^{j(\omega t + \alpha)} \qquad \text{Eq. (15.2)}$$

where α is a phase shift which, in general, is a function of ω.

The quantity δP is called the input ; it is the independent variable or the so-called driving function. The quantity δQ is the output and is the dependent variable. The ratio of output to input, as a function of frequency, is called the transfer function. Generally speaking, a transfer function is defined for a component of a system or for a coupled system of components.

In terms of this definition the transfer function, F_{QP}, is defined by the equation

$$\delta Q \equiv F_{QP} \, \delta P \qquad \text{Eq. (15.3)}$$

It is important to note that the transfer function gives the output δQ resulting from an arbitrary input δP. The transfer function is frequently designated by the notation

$$F_{QP} \equiv \left(\frac{\delta Q}{\delta P}\right)$$

Clearly, F_{QP} is a complex function of ω. Thus,

$$F_{QP} = \frac{|\delta Q|}{|\delta P|}\ \epsilon^{j\alpha}$$

In general, F_{QP} is also a function of P_o and Q_o.

The transfer function F_{QP} can only be determined from the equations of the physical system. In solving these equations to obtain F_{QP}, the assumption is made that $|\delta P| << P_o$ and $|\delta Q| << Q_o$ and that only the first order terms in the differentials δP and δQ need be retained. This linearization process is referred to as the small-signal approximation.

The definition of transfer functions may be continued and other functions defined relating the input δP to other system output parameters. If R is another such parameter, a transfer function may be written relating R and P just as was done with P and Q. If δQ represents an input to δR, it is also possible to write a transfer function relating R and Q. Thus,

$$\delta R \equiv F_{RQ}\ \delta Q \equiv F_{RQ}\ F_{QP}\ \delta P$$

and

$$F_{RP} \equiv F_{RQ}\ F_{QP}$$

Thus, the over-all transfer function for an in-line coupled system of components is the product of the transfer functions of the individual components.

(b) Feedback and Stability. In the frequency response analysis of a system with feedback it is important to define the transfer functions carefully. Since the system with feedback forms a closed loop, it is not simple to make a clear distinction between the input and output variables. A frequently used technique is to open the loop at some appropriate point in order to define the transfer functions. In a reactor plant the reactor itself provides a natural point for opening the loop.

Consider a reactor coupled to a plant and assume the reactor has a negative temperature coefficient of reactivity. Assume further that the reactor is provided with means for varying the reactivity in an oscillatory way, for example through control rod motion.

The two principal variables to be considered, so far as the reactor is concerned, are the reactivity, ρ, and the power level of the reactor. The power level of the reactor is proportional to the average neutron flux in the reactor ϕ, and this parameter will be used as representative of the reactor power level. Because of the form of the equations, however, a more convenient parameter is

$$y = \log_e \phi$$

Then the oscillatory differential δy is

$$\delta y = \frac{1}{\phi_o}\delta\phi$$

where ϕ_o is the steady-state value of ϕ. Since the steady-state value of the reactor, ρ, is zero, the symbol ρ itself will be used to represent the oscillatory differential of reactivity.

Making use of the loop-opening technique, the reactor is first considered independent of the plant. It is assumed that an oscillatory differential reactivity is induced in the reactor, by a small amplitude oscillation of the control rods. The differential reactivity ρ is the input or driving variable. The first transfer function defined is G, the reactor transfer function. This transfer function is defined to give the reactor oscillatory power response for an arbitrary oscillatory reactivity input.

$$\frac{\delta\phi}{\phi_o} \equiv G\rho \qquad \text{Eq. (15.4)}$$

As defined, G is a function dependent only on the kinetic properties of the reactor. It may be calculated using only the reactor kinetics equations.

Next the feedback will be considered. If the reactor power level has an oscillatory component $\delta\phi/\phi_o$, all of the temperatures throughout the reactor plant will have an oscillatory component of this frequency. Since the reactor temperature itself will have an oscillatory component, there will be a reactivity fed back into the reactor as a consequence of the changing reactor temperature. Let F represent the reactivity transfer function which gives the reactivity feedback into the reactor as a consequence of the reactor power level variation.

$$\rho \equiv F\,\frac{\delta\phi}{\phi_o} \qquad \text{Eq. (15.5)}$$

As defined, F depends on the plant parameters, namely, specific heats, flowrates, plant temperatures, etc. It is calculated by assuming the reactor power level has an oscillating component of the reactor mean temperature. Note that Eq. (15.5) gives the reactivity as a function of reactor power while Eq. (15.4) gives reactor power as a function of reactivity.

The next step is to close the feedback loop. This is accomplished by adding the reactivities at the reactor. Let ρ_{IMP} represent the arbitrary impressed reactivity on the reactor due to the oscillating control rod motion. In the absence of feedback, Eq. (15.4) gives the resulting reactor response.

$$\frac{\delta\phi}{\phi_o} = G\,\rho_{IMP} \qquad \text{Eq. (15.4a)}$$

Due to the reactor response in power level a reactivity feedback will occur given by Eq. (15.5). Designate the reactivity feedback as ρ_{FB}.

$$\rho_{FB} = F\,\frac{\delta\phi}{\phi_o} \qquad \text{Eq. (15.5a)}$$

The net reactivity available to the reactor, ρ_{NET}, is the sum of the reactivities

$$\rho_{NET} = \rho_{IMP} + \rho_{FB} \qquad \text{Eq. (15.6)}$$

and the resulting reactor response will correspond to the net reactivity

$$\left(\frac{\delta\phi}{\phi_o}\right) = G\,\rho_{NET} = G\,(\rho_{IMP} + \rho_{FB})$$

Substitution of Eq. (15.5a) for ρ_{FB} gives

$$\frac{\delta\phi}{\phi_o} = \left(\frac{G}{1-FG}\right)\rho_{IMP} \qquad \text{Eq. (15.7)}$$

Comparison of Eq. (15. 7) with Eq. (15. 4a) shows that as a consequence of feedback the reactor response is increased by the factor

$$\left(\frac{1}{1\text{-}FG}\right)$$

The factor FG is frequently called the loop gain. If the loop gain is unity with a phase angle of 360 degrees, the reactor response is infinite for an arbitrarily small amplitude of excitation. The stability criterion, namely the system is stable if

$$|FG| < 1$$

for phase angles which are a multiple of 360 degrees, is derived from the form of Eq. (15. 7).

If the loop gain is less than unity, but in a given frequency range approaches unity and has a phase shift which is a multiple of 360 degrees, the factor

$$\left(\frac{1}{1\text{-}FG}\right)$$

becomes large in this frequency range. The system is then said to have a resonance at the frequency ω_R where the phase shift is a multiple of 360 degrees.

(c) Multiple Feedback Loops. There are, in general, a number of feedback loops in a reactor plant. The temperature feedback has been discussed. There is also a feedback effect associated with primary loop pressure. Another feedback effect is associated with xenon poisoning of the reactor. A transfer function F can be defined for each of these parameters just as Eq. (15. 5) defined the transfer function for reactor temperature. In this way a series of transfer functions F_1, F_2, F_3, etc., may be defined. The reactivity feedback from these is a set of values ρ_1, ρ_2, ρ_3, etc. The net reactivity is the sum of the impressed reactivity and these feedback reactivities.

$$\rho_{NET} = \rho_{IMP} + \rho_1 + \rho_2 + \rho_3 \qquad \text{Eq. (15. 8)}$$

This leads to the reactor response equation

$$\frac{\delta\phi}{\phi_o} = \frac{G}{[1 - G(F_1 + F_2 + F_3)]}\ \rho_{IMP} \qquad \text{Eq. (15. 9)}$$

The total loop gain is now the sum of the individual feedback loop gains.

$$\text{Total Loop Gain} = F_1G + F_2G + F_3G$$

A useful result for the application of transfer function methods can be derived by assuming for the moment that only two feedback loops are present. From Eq. (15. 9) the reactor response is given by

$$\frac{\delta\phi}{\phi_o} = \frac{G}{[1 - G(F_1 + F_2)]}\ \rho_{IMP} \qquad \text{Eq. (15. 9a)}$$

By simple algebraic manipulation this can be put in the form

$$\frac{\delta\phi}{\phi_o} = \frac{\left(\frac{G}{1 - F_1G}\right)}{\left[1 - \left(\frac{G}{1 - F_1G}\right)F_2\right]}\ \rho_{IMP} \qquad \text{Eq. (15. 9b)}$$

Thus, if the over-all reactor response has been calculated for one feedback loop, the effect of an additional feedback loop can be readily determined. The reactor response with feedback is considered to be the reactor transfer function for addition of the second loop. In this formulation the loop gain is

$$\left(\frac{G}{1 - F_1 G}\right) F_2$$

Clearly, this can be extended to a series of feedback loops by calculating the response for addition of one feedback loop at a time.

(d) Reactivity Coefficients. It is frequently convenient to calculate transfer functions for a plant for parameters other than the reactivity. By so doing it is sometimes possible to generalize results by calculating dimensionless quantities or variables which might apply to a range of conditions. For example, instead of calculating the reactivity feedback due to temperature, it may be more general to calculate the reactor temperature change. If T_R is the reactor mean temperature,

$$\delta T_R \equiv F_T \frac{\delta\phi}{\phi_o} \qquad \text{Eq. (15.10)}$$

defines the transfer function F_T. The reactivity feedback ρ_T is obtained by introducing the temperature coefficient of reactivity α_T.

$$\rho_T = \alpha_T \, \delta T_R = \alpha_T F_T \frac{\delta\phi}{\phi_o} \qquad \text{Eq. (15.11)}$$

The advantage of calculating F_T is that, once obtained, the response of the plant for a range of values of α_T may be readily computed. Similar remarks may be made concerning other variables.

(e) Effects of Characteristic Times on the Analysis of Reactor Plant Stability. A straightforward method of computing the stability characteristics of the over-all reactor plant would be the application of Eq. (15.9). This would require the computation of the individual transfer functions F_1, F_2, F_3, etc., for each feedback loop in the system and the combining of these to obtain the total loop gain. This latter step is an involved procedure algebraically and is generally unnecessary because of the properties of the reactor plant feedback loops.

The stability analysis of reactor plants is made easier by the wide spread in characteristic frequencies associated with the various feedback loops. These characteristic frequencies differ by orders of magnitude so that it is possible, in any given frequency range, to limit consideration to a few feedback loops.

The lowest frequency is that associated with fuel depletion. The characteristic time for this effect is of the order of hundreds of hours. The next higher frequency of importance is associated with xenon poisoning. The characteristic time is of the order of ten hours. Between this frequency range and the next higher characteristic frequencies, there is a large gap. The next higher characteristic frequencies above xenon are of the order of tenths of a cycle per second and are associated with primary loop circulation times and the principal delayed neutron effects. Above this, the next higher frequencies are of the order of one cycle per second. These are associated with transit time of the coolant through the reactor, transit time of the coolant through the boiler and the pressurizer surge line cutoff frequency. Still higher frequencies of the order of ten cycles per second are associated with the heat transfer properties from the reactor fuel elements to the coolant. The highest frequency range, of the order of 100 to 1000 cycles per second, is associated with the lifetime of the neutrons in the reactor.

In the treatment of the reactor plant stability, in a particular frequency range those effects which are of lower characteristic frequency by several orders of magnitude are considered to be stationary. Those effects which are of higher characteristic frequency are considered to take place instantaneously. The range between the characteristic times of the xenon effects, of the order of ten hours, and the loop circulation and delayed neutron characteristic times, of the order of tens of seconds, is very large. In this range the analysis of the plant stability may be carried out on a quasi-stationary basis. This represents a considerable simplification.

(f) Material Presented in This Chapter. In the following section the reactor transfer function will be derived from the reactor kinetic equations. In the subsequent sections the next topic treated will be the xenon transfer function.

Derivation of the other transfer functions requires the plant equations. These are presented, and using these the temperature coefficient feedback is treated for slow variations. The next topic treats the combination of xenon and temperature coefficient feedback for slow variations. The pressurizer dynamic equations are derived next and the remainder of the chapter treats the pressurizer and temperature coefficient feedback, first on a slow basis and finally for high frequencies.

The presentation in this chapter is intended to illustrate the method of analysis used for various types of problems and typical results.

15.2 THE REACTOR TRANSFER FUNCTION

The reactor transfer function, G, is defined by Eq. (15.4) and depends only on the kinetic properties of the reactor. The reactor kinetics equations are written assuming separability of the spatial and time variables. The equations are derived on the basis of a one-group bare reactor model.[3] If (n) represents the neutron density in the reactor, C_i the concentration of delayed neutron emitters, ρ the reactivity, and λ_i the decay constant of the delayed neutron emitters, then

$$\frac{dn}{dt} = \frac{\rho}{\Lambda} n - \sum_i \frac{dC_i}{dt} \qquad \text{Eq. (15.12)}$$

$$\frac{dC_i}{dt} = \frac{\beta_i n}{\Lambda} - \sum_i \lambda_i C_i \qquad \text{Eq. (15.13)}$$

In Eqs. (15.12) and (15.13),

$\Lambda = \frac{\Lambda_o}{k_{eff}}$ where Λ_o is the effective lifetime for neutrons in the reactor

β_i = the yield of the i^{th} group of delayed neutrons in fission

β = the total yield of delayed neutrons in fission and is equal to $\sum_i \beta_i$

In these equations, (n) can be considered to be the spatial average concentration of neutrons in the reactor or proportional to the total number ; C_i must be taken in the same sense. If (n) is considered to be the average density of neutrons in the reactor and $\bar{v}$ the average velocity of the neutrons, the neutron flux ϕ is equal to $n\bar{v}$. Thus Eqs. (15.12) and (15.13) could be written in terms of the neutron flux.

While Eqs. (15.12) and (15.13) represent an extremely simple model of a reactor, they may be extended to more complicated models. For example, the concept of an effective value for β can be used to take into account the fact that the delayed neutrons are emitted at lower energy than the mean energy of fission neutrons. Furthermore, the effect of a reflector can be introduced.[4] For purposes of this discussion, however, the simple equations are adequate.

The reactor transfer function is derived by writing the neutron density as the sum of a constant n_o plus the sinusoidal component of amplitude δn. That is,

$$n(t) = n_o + \delta n \; \epsilon^{j\omega t}$$

The delayed neutron emitter concentration is similarly written

$$C_i(t) = C_{io} + \delta C_i \; \epsilon^{j\omega t}$$

The expressions for $n(t)$ and $C_i(t)$ are substituted into the kinetic equations. To linearize the equations it is necessary to neglect the second order product $\rho\delta n$. The result, substituting $\delta\phi/\phi_o$ for its equal $\delta n/n_o$, is

$$\frac{\delta\phi/\phi_o}{\rho} = \frac{1}{j\omega\left[\Lambda + \beta \sum_i \frac{1}{j\omega + \lambda_i}\right]} \qquad \text{Eq. (15.14)}$$

Figure 15.1 shows the magnitude of the reactor transfer function while Fig. 15.2 shows the phase of the reactor transfer function as a function of frequency with the neutron lifetime, Λ, as a parameter. The effect of the neutron lifetime on the magnitude of the transfer function is negligible for frequencies below one-half cycle per second. On the other hand, some phase shift dispersion with neutron lifetime is observed at frequencies as low as 0.05 cycle per second. Maximum phase shift occurs for frequencies around one cycle per second. At very low frequencies the reactor transfer function increases as $1/\omega$ and has a fixed phase shift of 90 degrees.

15.3 THE XENON TRANSFER FUNCTION

The fission product poisons which are explicitly taken into account in reactor kinetics problems are xenon and samarium. The well know equations for these fission products may be found in standard texts.[3]

$$\frac{dX}{dt} = \gamma_x \Sigma_f \phi + \lambda_i I - \sigma_x \phi X - \lambda_x X \qquad \text{Eq. (15.15)}$$

$$\frac{dI}{dt} = \gamma_i \Sigma_f \phi - \lambda_i I \qquad \text{Eq. (15.16)}$$

In these equations

Σ_f is the macroscopic cross section for fission (cm^{-1})
X is the density of xenon-135 nuclei (number / cm^3)
I is the density of iodine-135 nuclei (number / cm^3)
γ_x is the direct fractional yield of xenon-135 in fission
γ_i is the fractional yield of iodine-135 in fission
λ_i is the decay constant of iodine-135

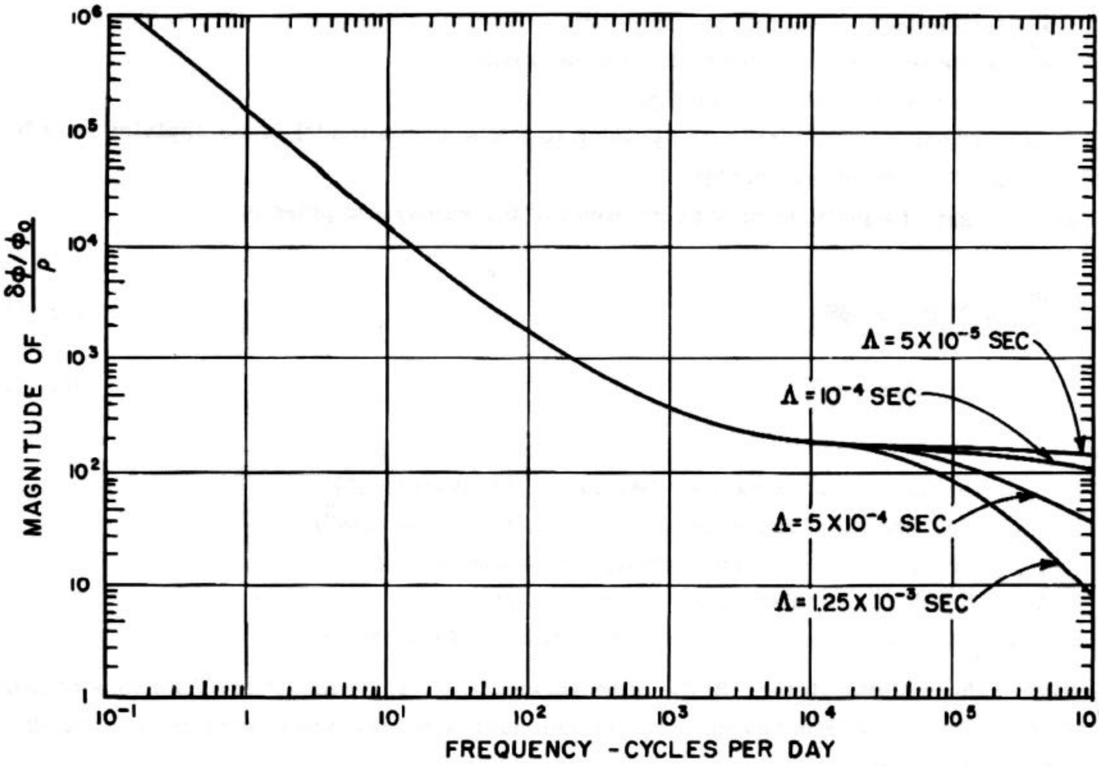

Fig. 15.1 - Magnitude of the Reactor Transfer Function.

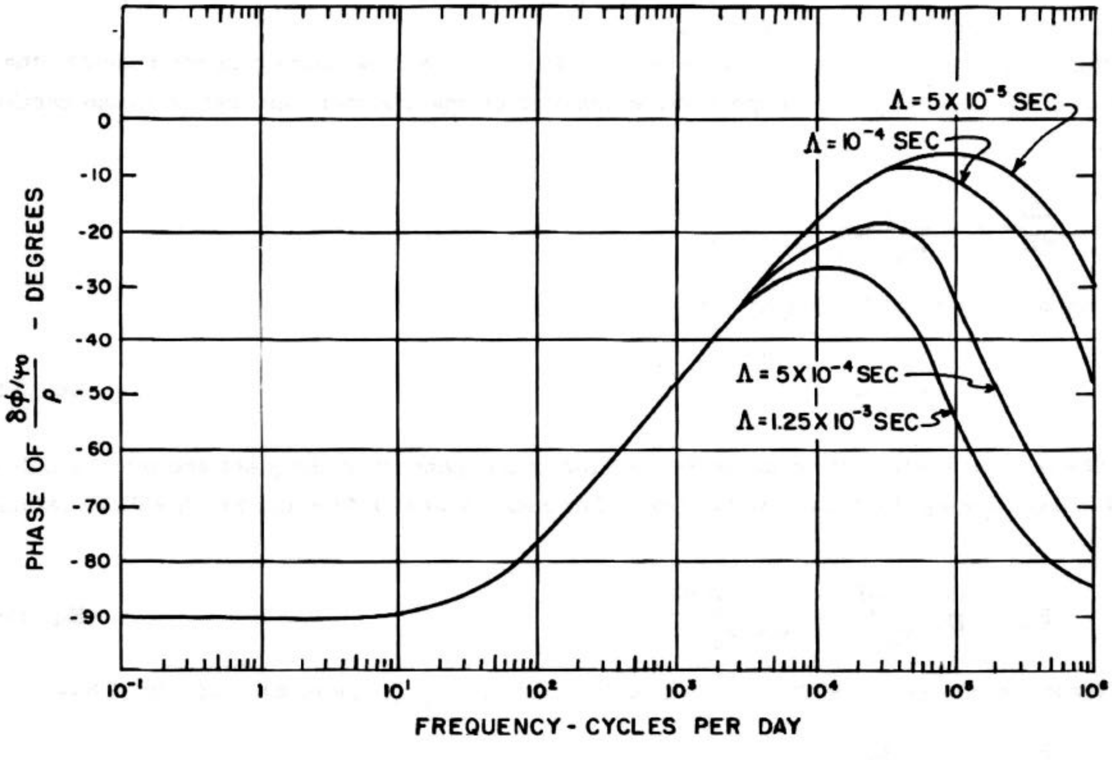

Fig. 15.2 - Phase of the Reactor Transfer Function.

λ_x is the decay constant of xenon-135
σ_x is the microscopic cross section for xenon
and ϕ is the neutron flux density.

These equations can be considered as applying to a one-group model or as applying only to the thermal group of a multigroup model.

A similar set of equations may be written for the samarium poisons.

$$\frac{dS}{dt} = \lambda_p P - \sigma_s \phi S \qquad \text{Eq. (15.17)}$$

$$\frac{dP}{dt} = \gamma_p \Sigma_f \phi - \lambda_p P \qquad \text{Eq. (15.18)}$$

where

S is the density of samarium-147 nuclei (number/cm^3)
P is the density of promethium-147 nuclei (number/cm^3)
σ_s is the microscopic cross section of samarium-147
λ_p is the decay constant of promethium-147
and γ_p is the fractional yield of promethium-147 in fission.

In Eqs. (15.15) through (15.18) the concentrations X, I, S, and P are functions of time; X (t) and S (t) may be considered to be, in circuit language, the output variables. The driving function is the flux ϕ (t).

The reactor model considered in this discussion is the so-called point model in which spatial variations are not taken into account. The flux ϕ (t) will be considered to be an appropriate average which would yield the same reactivity changes with xenon poisoning as does the actual distribution of flux in the reactor.

For small reactivity changes around criticality in a thermal homogeneous reactor, the derivative of reactivity with respect to the non-fission macroscopic absorption cross section, Σ_a, is

$$\frac{d\rho}{d\Sigma_a} = -\frac{1}{\Sigma_a + \Sigma_f}$$

Thus for an increment Σ_x $(= \sigma_x X)$

$$d\rho = -\frac{\Sigma_x}{\Sigma_a + \Sigma_f} \qquad \text{Eq. (15.19)}$$

The feedback effect of xenon on the reactor is independent of the plant and may be calculated without taking the plant into account. The xenon transfer function which will be calculated is

$$F_x \equiv \frac{(\delta\Sigma_x/\Sigma_f)}{(\delta\phi/\phi_o)} \equiv \frac{(\sigma_x/\Sigma_f)\,\delta X}{(\delta\phi/\phi_o)} \qquad \text{Eq. (15.20)}$$

The xenon reactivity transfer function is obtained from F_x by use of Eq. (15.19). Thus,

$$\frac{\rho_x}{(\delta\phi/\phi_o)} = \frac{\Sigma_f}{\Sigma_a + \Sigma_f}\, \epsilon^{j\pi}\, F_x \equiv \alpha_x F_x \qquad \text{Eq. (15.21)}$$

where α_x is the xenon reactivity coefficient. This definition of F_x provides greater generality in the sense discussed in Sec. 15.1 (d).

The xenon transfer function can be calculated using Eqs. (15.15) and (15.16). The xenon number density is expressed as

$$X(t) = X_o + \delta X \epsilon^{j\omega t}$$

with a similar expression for the iodine number density. It is assumed that the steady state components, i.e., n_o, X_o, I_o, etc., satisfy Eqs. (15.15) and (15.16) as do the time-dependent components. Furthermore, it is again necessary to neglect second order terms such as $\delta X \delta n$. The result of the calculation is

$$F_x = \frac{\dfrac{\sigma_x \delta X}{\Sigma_f}}{\dfrac{\delta \phi}{\phi_o}} = \frac{\left[\dfrac{\lambda_x}{\sigma_x \phi_o}(\gamma_i + \gamma_x) + \dfrac{j\omega}{\lambda_i}\left(\dfrac{\gamma_x \lambda_x}{\sigma_x \phi_o} - \gamma_i\right)\right]}{\left[\left(1 + \dfrac{\lambda_x}{\sigma_x \phi_o}\right)\left(1 + \dfrac{j\omega}{\lambda_i}\right)\left(1 + \dfrac{\lambda_x}{\sigma_x \phi_o} + \dfrac{j\omega}{\sigma_x \phi_o}\right)\right]} \qquad \text{Eq. (15.22)}$$

The stationary values of the xenon number density and the flux density are connected by the equation

$$X_o = \Sigma_f \phi_o \left(\frac{\gamma_i + \gamma_x}{\lambda_x + \sigma_x \phi_o}\right) \qquad \text{Eq. (15.23)}$$

By substitution of Eq. (15.23) in Eq. (15.22) and the use of Eq. (15.21) an expression for the xenon reactivity transfer function is obtained.

$$\frac{\rho}{\left(\dfrac{\delta \phi}{\phi_o}\right)} = \left(\frac{\Sigma_f}{\Sigma_a + \Sigma_f}\right) \epsilon^{j\pi} \left\{ \frac{\left[\dfrac{\lambda_x}{\sigma_x \phi_o}(\gamma_i + \gamma_x) + \dfrac{j\omega}{\lambda_i}\left(\dfrac{\gamma_x \lambda_x}{\sigma_x \phi_o} - \gamma_i\right)\right]}{\left[\left(1 + \dfrac{\lambda_x}{\sigma_x \phi_o}\right)\left(1 + \dfrac{j\omega}{\lambda_i}\right)\left(1 + \dfrac{\lambda_x}{\sigma_x \phi_o} + \dfrac{j\omega}{\sigma_x \phi_o}\right)\right]} \right\} \qquad \text{Eq. (15.24)}$$

The expression in braces is the xenon transfer function, F_x, while the coefficient is α_x, the reactivity coefficient.

Figures 15.3 and 15.4 show the magnitude and phase shift of the xenon transfer function respectively. Since ϕ_o is involved in the expression for the xenon transfer function, it is shown on the figures as a parameter.

Equation (15.24) shows that there is a phase shift of 180 degrees in the xenon reactivity coefficient. Thus, where the phase of the xenon transfer function is 180 degrees, the xenon reactivity oscillation is in phase with the disturbance causing it and the possibility of instability is present. The phase shift necessary for instability occurs at a frequency of about one cycle per day. The question of instability due to xenon will be discussed after considering the effect of reactor temperature on reactivity.

One further point of interest deals with the samarium poisoning. It can be shown by use of Eqs. (15.17) and (15.18), with substitution of appropriate constants, that samarium has a negligible effect on the reactor stability compared with xenon. For this reason the effect of samarium will not be treated explicitly.

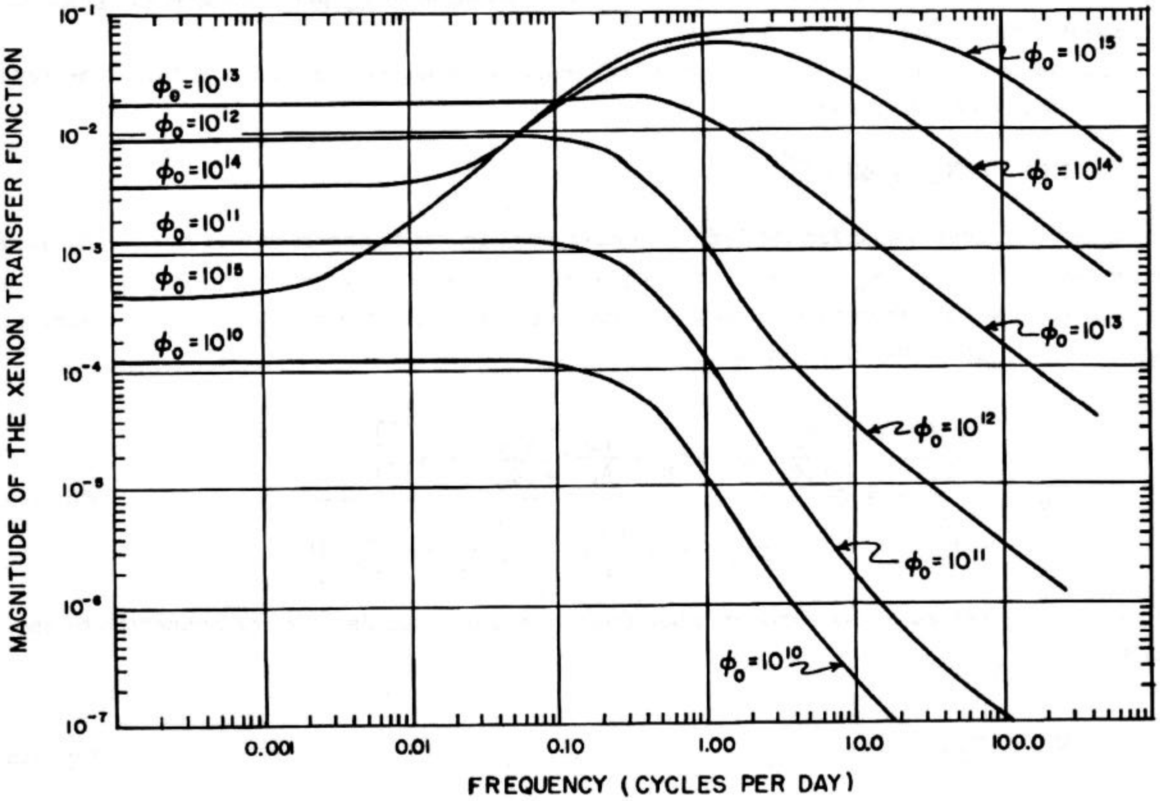

Fig. 15.3 - Magnitude of the Xenon Transfer Function.

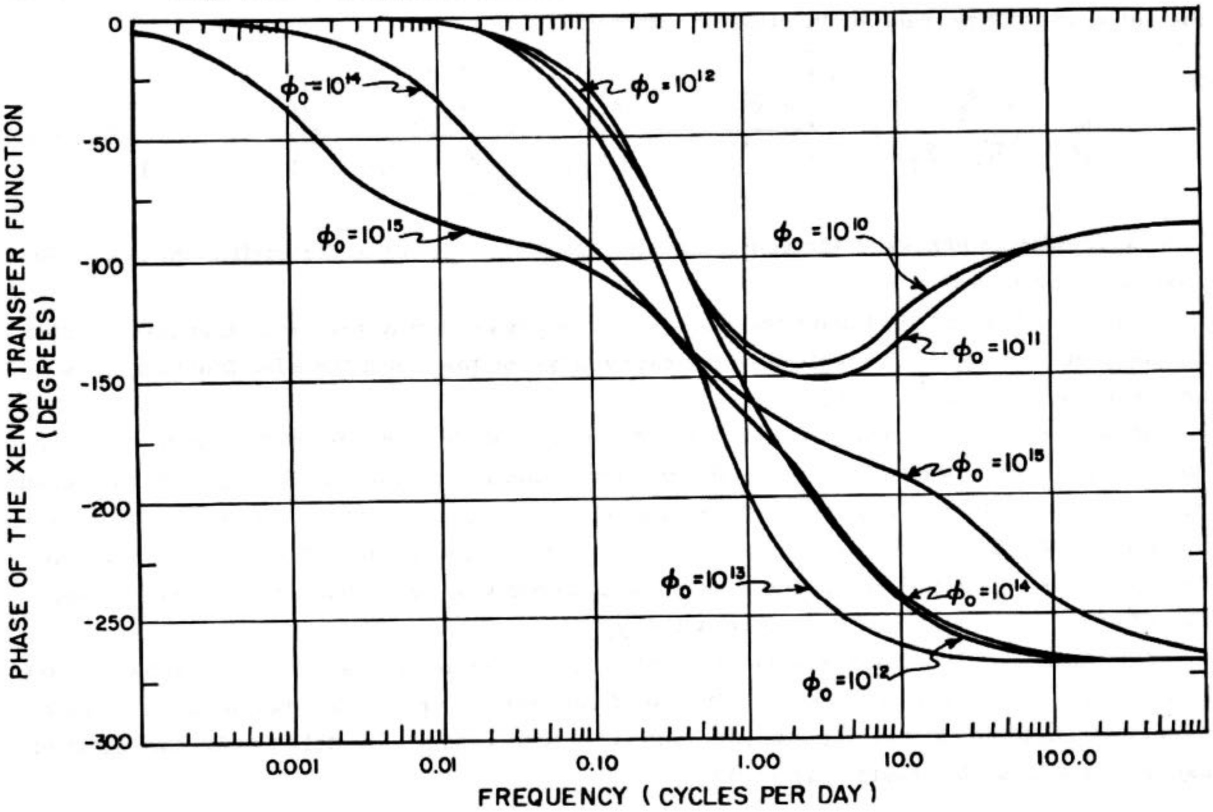

Fig. 15.4 - Phase of the Xenon Transfer Function.

15.4 THE REACTOR PLANT EQUATIONS

In order to derive the transfer functions for the temperature coefficient of reactivity and the pressure coefficient of reactivity, the plant equations must be used. These are presented and discussed briefly in this section to illustrate the considerations which are taken into account.

A simplified model of the reactor plant is shown in Fig. 15.5.

(a) Reactor Heat Transfer Equations. The simplest description of heat transfer in a reactor is based on a one-section model. The use of the simple model leads to a set of ordinary differential equations which are sufficiently accurate for the majority of problems in reactor stability and transient analysis. There is a limitation, however, on the maximum speed of reactor transients which this model can handle. Modification of the equations for application to the analysis of fast transients is a straightforward extension of the method presented here.

In the one-section model, heat transfer in the reactor is assumed to occur at a single point; thereby spatial variations are neglected. Two points of energy storage are included, the reactor metal and the coolant in the core. Two ordinary differential equations are obtained.

$$Q = C_{rm} \frac{dT_m}{dt} + h_r (T_{rm} - T_{rw}) \qquad \text{Eq. (15.25)}$$

and

$$h_r (T_{rm} - T_{rw}) = C_{rw} \frac{dT_{rw}}{dt} + F_w c (T_{r_o} - T_{r_i}) \qquad \text{Eq. (15.26)}$$

where

$$T_{rw} = \frac{1}{2} (T_{r_i} + T_{r_o}) \qquad \text{Eq. (15.27)}$$

These equations are derived directly from considerations of heat balance. In these equations

[redacted]

C_{rm} = total thermal capacity of reactor metal (Btu/°F)
$T_{rm}(t)$ = average reactor metal temperature (°F)
$h_r(F_w)$ = total heat transfer coefficient (Btu/sec°F)

[redacted]

C_{rw} = total thermal capacity of reactor water (Btu/°F)
$F_w(t)$ = total coolant flow rate (lb/sec)
c = specific thermal capacity of coolant (Btu/lb°F)
$T_{r_o}(t)$ = reactor outlet average coolant temperature (°F)
$T_{r_i}(t)$ = reactor inlet average coolant temperature (°F)

These equations are used to derive $T_{r_o}(t)$ and $T_{rw}(t)$ for given variations of Q(t), $T_{r_i}(t)$ and F_w. The variable $T_{r_o}(t)$ feeds into the primary loop, and $T_{rw}(t)$ affects reactivity feedback, which in turn affects Q.

(b) Primary Piping Equations. In circulating through the primary loop the coolant undergoes mixing and transport delay effects. For example, a transient in coolant temperature at the core outlet does not appear at the vessel outlet until some time later, and, furthermore,

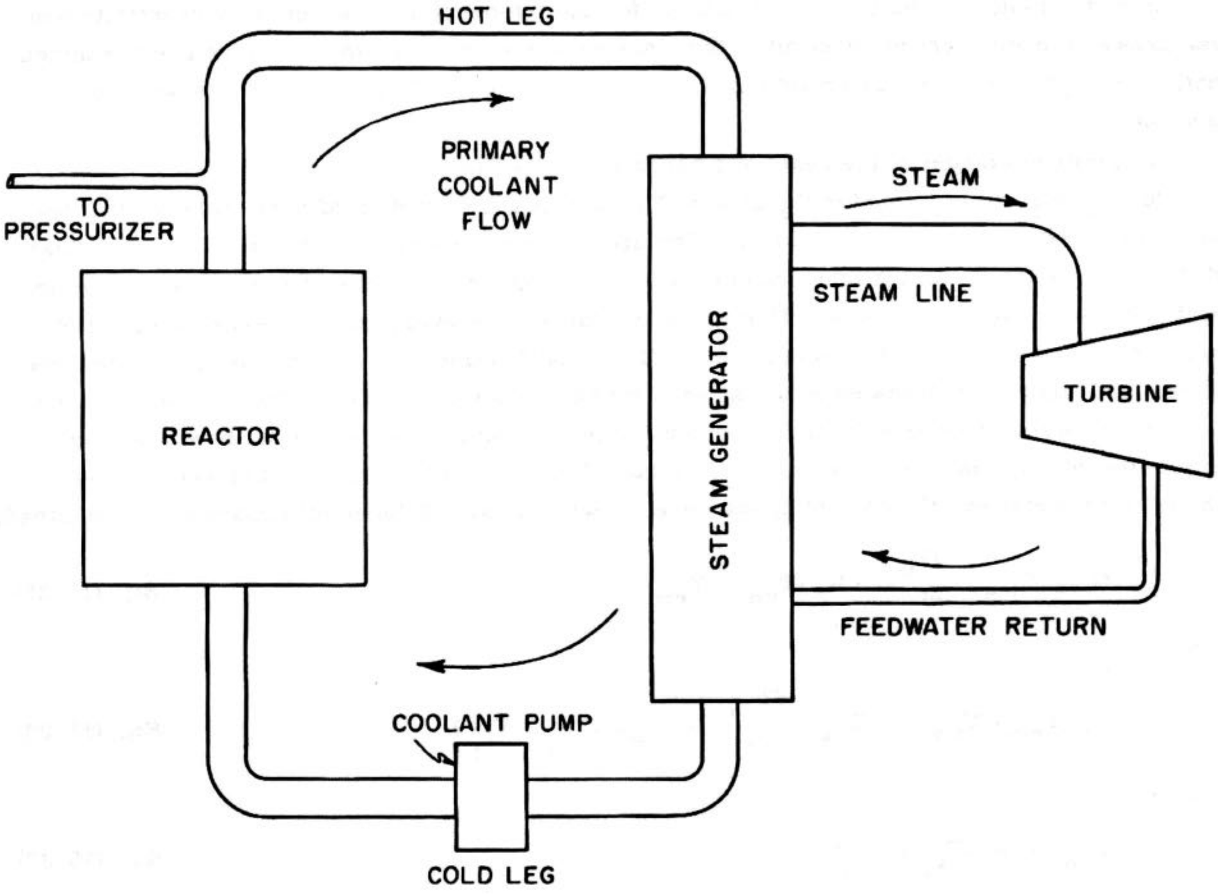

Fig. 15. 5 - Simplified Schematic Diagram of the Reactor Plant.

its shape (temperature at a point vs time) is changed. It is necessary to describe these effects by means of equations so that the filtering of temperature transients can be included in the representation of the primary loop. It is possible to describe these filtering effects by combinations of two types of time delays: A pure transport delay and a simple mixing delay.

A pure transport delay is that which delays a transient by a fixed amount of time without altering its shape. The outlet coolant temperature T_o of a component of the primary loop causing such a delay is simply equal to the inlet temperature displaced in time by an amount τ_t, the transport delay, expressed as

$$T_o(t + \tau_t) = T_i(t) \qquad \text{Eq. (15.28)}$$

A mixing delay is derived by assuming complete mixing in the volume concerned. Then the outlet temperature T_o is equal to the average temperature in the volume concerned. A power balance for a particular section or component requires that the net power flowing into the volume be equal to the rate of increase in stored energy.

Consider a section into which water is flowing at the rate F_w at a temperature $T_i(t)$. The water leaves the section at the rate F_w and at a temperature $T_o(t)$. $T_o(t)$ is equal to the mixed or average temperature T_{av} in the volume. If M_{ws} is the mass of water in the section, an energy balance over the time Δt yields the equation

$$\Delta t \ c \ F_w \left[T_i(t) - T_o(t)\right] = c\, M_{ws} \frac{dT_{av}}{dt} \Delta t = c\, M_{ws} \frac{dT_o}{dt} \Delta t \qquad \text{Eq. (15.29)}$$

where c is the specific heat.
The resulting equation is

$$\left(\frac{M_{ws}}{F_w} \frac{dT_o}{dt} + T_o\right) = \tau_m \frac{dT_o}{dt} + T_o = T_i \qquad \text{Eq. (15.30)}$$

where $\tau_m \equiv M_{ws}/F_w$ and is called the mixing delay.

In general, the filtering effect on coolant temperature of a section of the primary loop is described by a combination of mixing and transport delays:

$$\tau_m \frac{dT_o(t)}{dt} + T_o(t) = T_i\,(t - \tau_t) \qquad \text{Eq. (15.31)}$$

where τ_m is now modified and is given by the equation

$$\tau_m + \tau_t = M_{ws}/F_w \qquad \text{Eq. (15.32)}$$

The decision as to how to divide the total time delay between mixing and transport is based on the geometry of the particular section of the coolant loop and the expected flow pattern. For example, a straight pipe will cause primarily a transport delay with relatively little mixing delay. A more complicated geometry may cause both. Because greater filtering effects occur in the heat transfer section of the heat exchanger, the division between transport and mixing does not have to be accurately predicted. However, it is important that the sum of the two delays accurately represent the effect of the total volume in which water is transported and mixed; otherwise, the thermal capacity is not properly represented, and an error is introduced in the calculation of changes in coolant volume and pressurizer surges.

With the exclusion of the heat transfer sections of the reactor and heat exchanger, mixing and transport effects are encountered in the primary loop as follows. In the piping between the reactor vessel outlet and the heat exchanger inlet and between the heat exchanger outlet and the reactor vessel inlet, pure transport delays may be assumed. Combined mixing and transport effects are encountered in the reactor vessel between the vessel inlet and the core inlet and between the core outlet and the vessel outlet. [redacted] In the inlet and outlet plenums of the heat exchanger, combined mixing and transport delays may be assumed.

The thermal capacity of the coolant contained in the core is included in the reactor heat transfer equations given in (a) above. Thus, the delay in the core itself is implicitly contained in these equations and should not be included again as a transport or mixing delay. Similarly, the heat transfer equations of the heat exchanger include the thermal capacity of primary water; consequently, no additional delay should be included.

(c) Heat Exchanger Equations. The derivation of a set of differential equations for the heat exchanger and the secondary loop is based on the assumptions that the state of the steam produced is always dry and saturated and that the water on the secondary side is always at the saturation temperature for the existing pressure. Thus, it becomes possible to use the saturation temperature in the heat transfer equations as the temperature existing on the steam side of the heat exchanger.

As in the derivation of reactor heat transfer equations, a one-section model is used for the heat exchanger. Two points of energy storage are assumed; the primary coolant water and the water on the secondary side. The thermal capacity of the boiler metal may be included with the secondary water, since the thermal resistance on the primary side of the heat exchanger predominates. Based on this model, the following equations are readily derived:

$$F_w\, c\, (T_{b_i} - T_{b_o}) = C_{bw} \frac{dT_{bw}}{dt} + h_b\, (T_{bw} - T_s) \qquad \text{Eq (15.33)}$$

$$h_b\, (T_{bw} - T_s) = C_{bs} \frac{dT_s}{dt} + P_L \qquad \text{Eq. (15.34)}$$

$$T_{bw} = \frac{1}{2}\, (T_{b_i} + T_{b_o}) \qquad \text{Eq. (15.35)}$$

where

T_{b_i} (t) = inlet primary water temperature (°F)
T_{b_o} (t) = outlet primary water temperature (°F)
T_{bw} (t) = average primary water temperature (°F)
T_s(p) = saturation temperature at secondary pressure (°F)
$h_b(F_w)$ = total effective heat transfer coefficient (Btu/sec°F)
C_{bw} = total thermal capacity of primary water in heat exchanger tubes (Btu/°F)
C_{bs} = total thermal capacity of water on secondary side and boiler metal (Btu/°F)
P_L = net power delivered by the steam generator (Btu/sec)

Equation (15.35), which gives the average coolant temperature T_{bw}, is valid when the primary coolant temperature drop from inlet to outlet is small compared with the mean temperature drop from the primary to the secondary side of the heat exchanger. In instances where this requirement is not satisfied, the equation may still be used if the heat transfer coefficient h_b is properly modified.

(d) Pressurizer Equations. The determination of coolant surge rate is obtained by integrating the net power transferred to the coolant. The difference between the heat transfer rates at the reactor and the heat exchanger is the rate of storage of energy in the coolant. The surge rate caused by volume expansion, which must be accomodated by the pressurizer, is directly proportional to this power difference:

$$\text{Surge rate} = \frac{dV}{dt} = M_{wp} \left.\frac{\partial v}{\partial T}\right|_p \frac{dT}{dt} = \frac{1}{c} \left.\frac{\partial v}{\partial T}\right|_p \Delta P \qquad \text{Eq. (15.36)}$$

where

V = volume of primary coolant
M_{wp} = mass of primary coolant
$\left.\frac{\partial v}{\partial T}\right|_p$ = temperature coefficient of expansion
ΔP = rate of energy storage in coolant

Surge rates accompanying power transients are determined by simultaneous solution of the reactor and plant equations, including Eq. (15.36), under the given transients. The pressurizer equations are treated in greater detail later in this chapter.

(e) Thermal Shield Equations. [redacted] The effect often may be neglected. However, the equations are given below for completeness.

$$C_{sm} \frac{dT_{sm}}{dt} = h_s (T_{sw} - T_{sm}) \qquad \text{Eq (15.37)}$$

and

$$C_{sw} \frac{dT_{sw}}{dt} = F_w c (T_{is} - T_{os}) - h_s (T_{sw} - T_{sm}) \qquad \text{Eq. (15.38)}$$

where

C_{sm} = thermal capacity of shield metal (Btu/°F)
C_{sw} = thermal capacity of shield water (Btu/°F)
T_{sm} = average temperature of shield metal (°F)
T_{sw} = average temperature of shield water (°F)
h_s = total heat transfer coefficient (Btu/sec°F)
T_{is} = shield inlet water temperature (°F)
T_{os} = shield outlet water temperature (°F)
and F_w is, as before, the coolant flow rate

(f) Secondary Loop Equations. The derivation of equations for the secondary loop is based on the assumption that the steam at the outlet of the steam generator is dry and saturated. This assumption is justified because (1) steam separators and recirculation are employed to obtain high quality steam and (2) superheating is not used in pressurized water reactors because of the small temperature differences available.

The power delivered by the steam generator is proportional to the product of steam flow rate and the difference of enthalpy between the steam and the feedwater.

$$h_b (T_{bw} - T_s) = F_s (H_s - H_{fw}) + C_{bs} \frac{dT_s}{dt} \qquad \text{Eq. (15.39)}$$

where

F_s = steam flow rate (lb/hr)
H_s = steam enthalpy
H_{fw} = feedwater enthalpy

and the symbols T_{bw}, T_s and h_b have the same significance as in (c) above.

The enthalpy of saturated steam is nearly constant^5 over a wide range of pressure [redacted] Thus the enthalpy difference may be regarded as a constant, and the power delivered is directly proportional to the steam flow rate.

The impedance to steam flow caused by the turbine is nearly independent of turbine speed. By assuming constant back pressure, the steam flow rate is proportional to the throttle pressure at a given throttle opening.

$$F_s \equiv p_s A \qquad \text{Eq. (15.40)}$$

where

p_s = saturation pressure

A = proportionality factor which is a function of the throttle opening.

(g) Limitations of the One-Section Approximation. The lumping of the distributed parameter heat transfer problem in the reactor and in the heat exchanger imposes limitations on the speed of transients and the frequency of oscillations which may be accurately analyzed by using the equations derived. The formulation of a rigorous set of criteria for universal application appears to be impractical because of the non-linear nature of the equations and the wide variety of problems in transients and frequency response which must be considered. However, it is possible to obtain analytically some approximations for the limitations by frequency response methods and by analog simulation of transients. The frequency response approach leads to a criterion which requires that the angular frequency of periodic variations should not exceed $1/\tau$ for a one-section model where τ is the coolant transport time through the heat transfer section. The maximum permissible frequency is directly proportional to the number of sections used in the model; a one-section model is adequate for the majority of transients encountered in practice.

15.5 EFFECT OF REACTOR TEMPERATURE COEFFICIENT AT LOW FREQUENCIES

In this section the effect of the reactor temperature coefficient will be treated as a quasi-stationary problem. As noted in Sec. 15.1 (e), there is a large frequency range in which such a treatment is valid. [redacted] The recirculation time of the primary coolant is of the order of seconds and the equilibration times for temperature changes in primary loop components are of the order of tens of seconds. The reactor kinetic response to a small reactivity change will have reached a steady-state condition in a matter of minutes. If the highest frequency to be discussed in this section is limited to the order of cycles per hour, it is clear that a quasi-stationary condition will prevail.

If α_T is the temperature coefficient of reactivity of the reactor at operating temperature and T_{rw} is the average water temperature of the reactor, the reactor is in equilibrium when

$$\rho + \alpha_T \, \delta T_{rw} = 0 \qquad \text{Eq. (15.41)}$$

where δT_{rw} is the departure of the average reactor water temperature from its steady-state value. If α_T is negative, a positive reactivity increment will be counteracted by a rise in the average water temperature in the reactor.

In general, a change in reactivity will lead to a change in average loop temperature as well as a change in the reactor inlet temperature and the outlet water temperature. Let δT_{r_o} and δT_{r_i} represent the changes in the reactor outlet water temperature T_{r_o} and the reactor inlet temperature T_{r_i}, respectively. As noted in Eq. (15.27)

$$T_{rw} = \frac{T_{r_o} + T_{r_i}}{2} = \frac{T_{r_o} - T_{r_i}}{2} + T_{r_i} \qquad \text{Eq. (15.27)}$$

and by definition

$$\delta T_{rw} = \frac{\delta T_{r_o} + \delta T_{r_i}}{2} = \frac{\delta T_{r_o} - \delta T_{r_i}}{2} + \delta T_{r_i} \qquad \text{Eq. (15.42)}$$

For constant flow of coolant, the reactor output power is proportional to the temperature rise of the coolant in passing through the reactor. Thus

$$\frac{\delta\phi}{\phi_o} = \frac{\delta T_{r_o} - \delta T_{r_i}}{T_{r_o} - T_{r_i}} = \frac{\delta T_{rw} - \delta T_{r_i}}{T_{rw} - T_{r_i}} \qquad \text{Eq. (15.43)}$$

Substitution of Eq. (15.41) into Eq. (15.43) gives

$$\frac{\rho}{\alpha_T} = \delta T_{r_i} + \frac{\delta\phi}{\phi_o}\,(T_{rw} - T_{r_i}) \qquad \text{Eq. (15.44)}$$

If, for the moment, the situation without recirculation is considered, there is no change in the inlet water temperature. Thus,

$$\frac{\rho}{\frac{\delta\phi}{\phi_o}} = \alpha_T\,(T_{rw} - T_{r_i}) \qquad \text{Eq. (15.45)}$$

The rise in reactor power required to compensate for an impressed reactivity change ρ is given by Eq. (15.45). If recirculation is present, the rise in net reactor power required to compensate the impressed reactivity increment is less than that given by Eq. (15.45). With recirculation the first stage following an impressed reactivity increment is a power rise such as is given by Eq. (15.45). When the higher temperature water has cycled through the loop, however, the reactor inlet temperature has increased. Therefore, it is not necessary that the coolant temperature rise in the reactor compensate entirely for the reactivity increment. In fact, after the initial power rise, which raises the mean temperature of the primary loop and its components, the power level drops back toward its original value. It remains only slightly higher because the higher primary loop temperature produces a higher steam pressure in the secondary system, and, for a fixed turbine throttle opening, a higher steam flow to the turbine.

The increase in reactor inlet temperature can be calculated directly. Equation (15.34) for the boiler is

$$h_b\,(T_{bw} - T_s) = C_{bs}\,\frac{dT_s}{dt} + P_L \qquad \text{Eq. (15.34)}$$

For a steady-state condition the derivative term is zero. Thus,

$$h_b(T_{bw} - T_s) = P_L \qquad \text{Eq. (15.46)}$$

where P_L, the load power, is proportional to the reactor power. Thus,

$$\frac{\delta\phi}{\phi_o} = \frac{\delta T_{bw} - \delta T_s}{T_{bw} - T_s}$$

which, when transposed, gives

$$\delta T_{bw} = \delta T_s + \frac{\delta\phi}{\phi_o}(T_{bw} - T_s) \qquad \text{Eq. (15.47)}$$

The value of δT_s can be obtained from Eq. (15.40) for the steam flow rate.

$$F_s \equiv p_s A \qquad \text{Eq. (15.40)}$$

If it is assumed that the steam remains dry and saturated, the change in power is directly proportional to the change in flow rate.

$$\frac{\delta\phi}{\phi_o} = \frac{\delta p_s}{p_s} \qquad \text{Eq. (15.48)}$$

Now the temperature change accompanying the pressure change at saturation is given by

$$\delta T_s = \left(\frac{\partial T}{\partial p}\right)_{sat} \delta p_s = \left(\frac{\partial T}{\partial p}\right)_{sat} p_s \frac{\delta\phi}{\phi_o} \qquad \text{Eq. (15.49)}$$

The increase in reactor inlet water temperature is taken as being equal to the increase in boiler primary water temperature since transport delays are neglected in this quasi-stationary treatment.

$$\delta T_{r_i} = \delta T_{bw} = \frac{\delta\phi}{\phi_o}\left[(T_{bw} - T_s) + \left(\frac{\partial T}{\partial p}\right)_{sat} p_s\right] \qquad \text{Eq. (15.50)}$$

Substitution of Eq. (15.50) in Eq. (15.44), noting that $T_{bw} = T_{rw}$, yields

$$\frac{\rho}{\frac{\delta\phi}{\phi_o}} = \alpha_T \left[(T_{rw} - T_{r_i}) + (T_{rw} - T_s) + \left(\frac{\partial T}{\partial p}\right)_{sat} p_s\right] \qquad \text{Eq. (15.51)}$$

If the quantity in brackets is denoted as F_{Ts}, the transfer coefficient for the quasi-stationary case, Eq. (15.51) becomes

$$\frac{\rho}{\frac{\delta\phi}{\phi_o}} = \alpha_T F_{Ts} \qquad \text{Eq. (15.51a)}$$

The result may be illustrated by a numerical example. The plant being considered as an example has the following characteristics:

[redacted]

[redacted]

15.6 XENON LOOP STABILITY

The plots of the phase of the xenon transfer function shown in Fig. 15.4 indicate that for sufficiently large values of the flux, the phase shift can equal or exceed 180 degrees. Since the xenon reactivity coefficient α_x contains a phase shift of 180 degrees, the xenon poisoning can lead to a reactivity feedback with a total phase shift of 360 degrees. Thus, in the absence of stabilizing influences, a reactor could oscillate in power level due to xenon poisoning at a frequency of one to two cycles per day. This xenon instability is generally not considered troublesome since it occurs at such a low frequency that simple external control can overcome the instability. This discussion will treat the stabilizing effect of the negative temperature coefficient of reactivity on the xenon instability. Since the xenon instability is of very low frequency, the quasi-stationary analysis given in the preceding section for the temperature feedback effect may be used.

The temperature coefficient reactivity feedback phase is 180 degrees for all frequencies which are sufficiently low. The xenon reactivity feedback phase is 360 degrees for the critical frequency, i.e., that frequency which may be the frequency of instability. If consideration is limited to this frequency, the reactivity feedbacks may be added directly. If ρ_{FB} is the net reactivity feedback

$$\rho_{FB} = \rho_T + \rho_x$$

If ρ_T exceeds ρ_x in magnitude, the feedback will be degenerative since ρ_T is negative and ρ_x is positive. Thus, at the critical frequency the system is stable if

$$|\rho_T| > \rho_x$$

or

$$\frac{\rho_x}{|\rho_T|} < 1$$

From Eqs. (15.21) and (15.51), the system is stable if

$$\frac{\rho_x}{|\rho_T|} = \frac{\alpha_x F_x}{|\alpha_T F_{Ts}|} = \frac{\alpha_x \; F_x}{\left|\alpha_T \left[(T_{rw} - T_{r_i}) + (T_{rw} - T_s) + \left(\frac{\partial T}{\partial p}\right)_{sat} p_s\right]\right|} < 1 \qquad \text{Eq. (15.52)}$$

To examine this equation numerically the critical frequencies, i.e., those frequencies for the various flux levels at which the xenon transfer function has a phase shift of 180 degrees, were selected from Fig. 15.4. The corresponding values of the magnitude of the xenon transfer function were selected from Fig. 15.3 and plotted as Fig. 15.6. This plot shows that there is a negligible possibility of instability due to xenon at flux levels below about 4×10^{11} neutrons/cm^2/second. The tendency toward instability increases monotonically with flux level. Since the temperature coefficient of reactivity enters the stability criterion directly, any instability could, in principle, be overcome by a negative temperature coefficient of reactivity sufficiently large in magnitude.

Fig. 15.6 - Magnitude of the Xenon Transfer Function at the Critical Frequency.

[redacted]

15.7 PRESSURIZER SYSTEM DYNAMICS

The remainder of this chapter will deal with the combined effects of pressure and temperature on plant stability. In this section, the pressurizer system dynamic equations will be derived. In the sections following, the stability problems will be discussed.

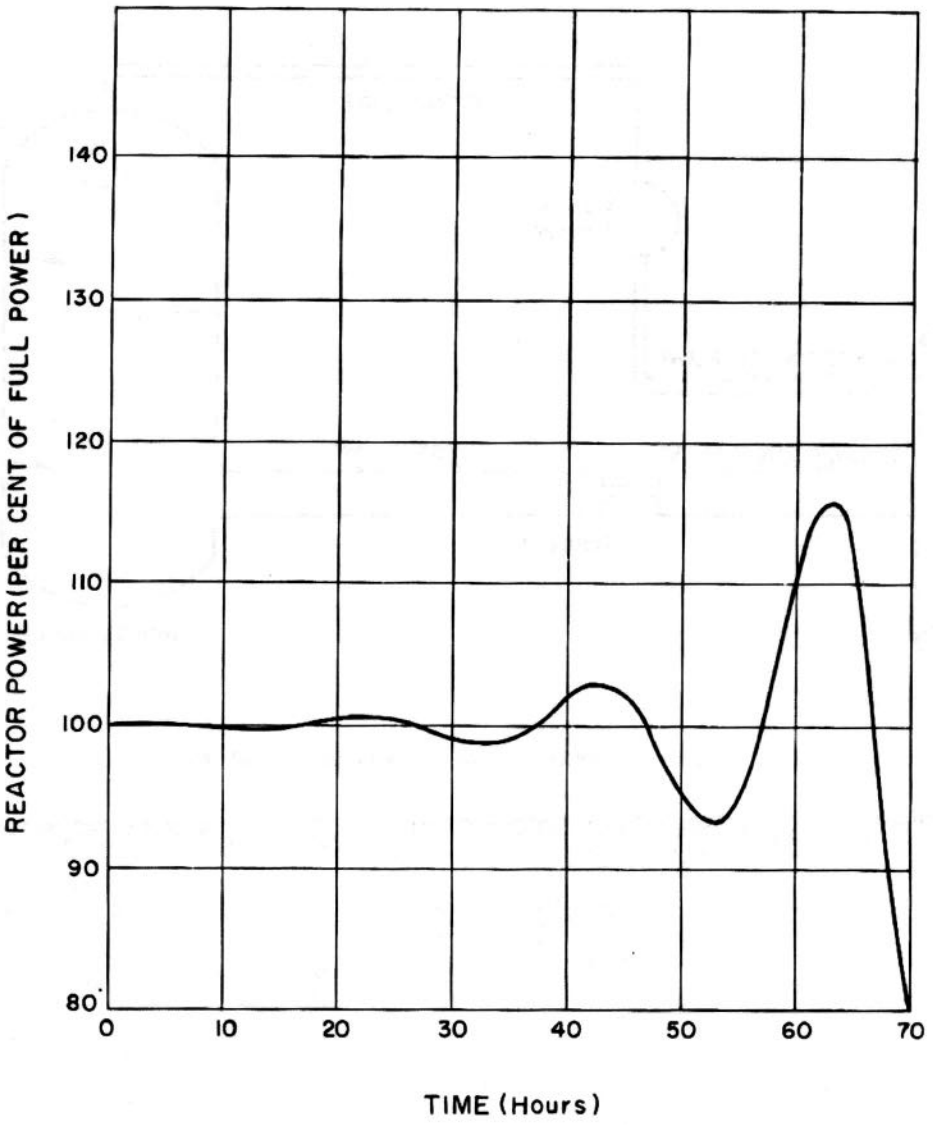

Fig. 15.7 - Reactor Power Level as a Function of Time with an Unstable Xenon Reactivity Feedback.

The pressurizer is connected to the primary loop through a surge line; the pressurizer itself is a vessel partially filled with water with the remainder of the vessel filled with steam. The water in the pressurizer is heated by electrical heaters to maintain the appropriate steady-state pressure in the system. The pressurizer is generally equipped with a spray which serves two purposes. The first is reduction of pressure maxima caused by heating of the primary loop. The second is degassification of the primary water. In this discussion it will be assumed that there is a steady-state flow through the spray for degassification. The surge line may consist of sections having different flow areas. These may be heat exchangers in the line or reduced diameter sections which provide damping. A diagram of the pressurizer system is shown in Fig. 15.8.

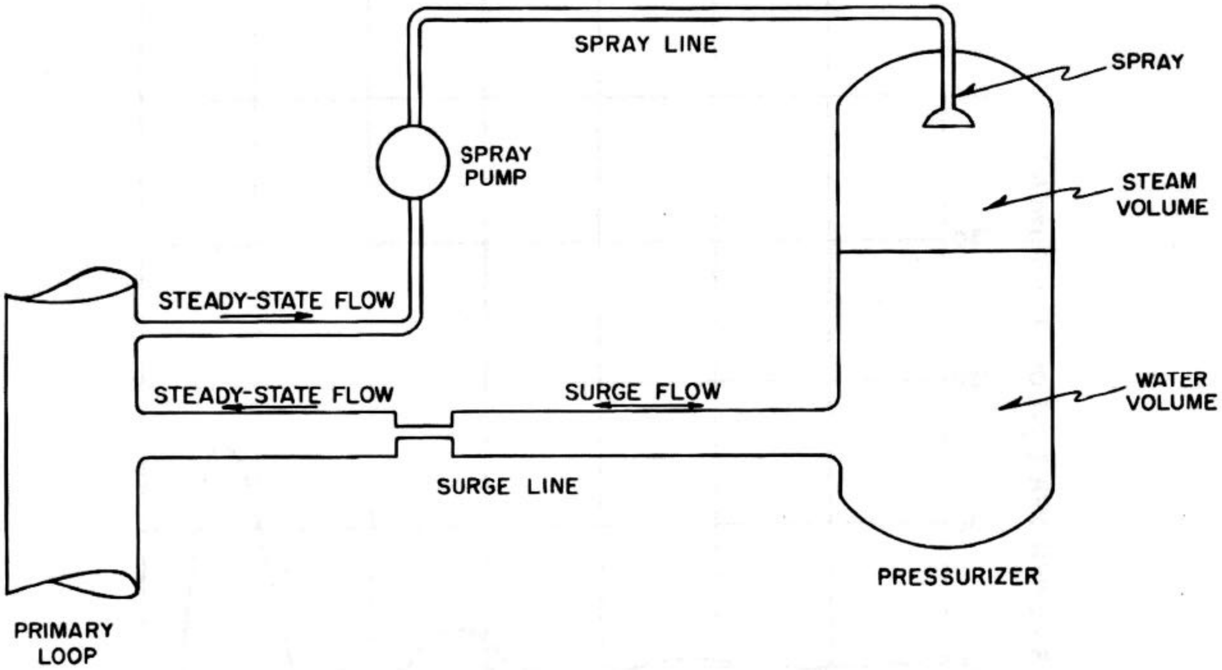

Fig. 15.8 - Diagram of the Pressurizer System.

[redacted]

In addition, there is a possibility of instability arising from the pressurizer system. A rise in pressure in the reactor will cause a mass flow of water toward the pressurizer. The water flow will compress the steam volume and increase the pressurizer pressure. The kinetic energy of the moving water could lead to an excess flow into the pressurizer and a transient drop in reactor pressure. This would be compensated for by a return flow of water from the pressurizer to the reactor. In the absence of adequate damping, the possibility of a sustained oscillation exists. This possibility will be examined following the derivation of the equations.

The first equation to be derived will deal with the flow of water into the pressurizer under dynamic conditions; a time dependent differential equation for the water density in the reactor will be derived.

The reactor pressure will be designated by p, the pressurizer pressure by p_p. The steady-state pressure difference between the pressurizer and reactor due to the degassifier flow will be designated Δp_{ss}. Thus, for the steady-state

$$p_{po} - p_o = \Delta p_{ss} \qquad \text{Eq. (15.53)}$$

Where the subscript o designates the steady-state value. For a transient condition

$$p_p - p = \Delta p_{ss} + dp_p - dp \qquad \text{Eq. (15.54)}$$

where dp_p represents the change in p_p from its steady-state value and dp represents the change in p from its steady-state value.

The thermodynamic state of the water in the primary loop is governed by an equation of state relating the pressure p, the temperature T, and the density θ. The pressure can be written as an explicit function of the other two variables, i. e., p (T, θ). The incremental pressure dp can be written

$$dp = \left(\frac{\partial p}{\partial T}\right)_\theta dT + \left(\frac{\partial p}{\partial \theta}\right)_T d\theta \qquad \text{Eq. (15.55)}$$

The incremental change in the pressurizer pressure can be written

$$dp_p = \frac{dp_p}{dV_p} dV_p$$

where V_p is the pressurizer steam volume and dp_p/dV_p is a constant of the pressurizer. The change in pressurizer steam volume is just equal to the increase in volume of the coolant in the primary system. The fractional increase in primary loop density $\frac{d\theta}{\theta}$ times the primary loop volume V_o is the decrease in volume of coolant in the primary system. Thus

$$dp_p = -\frac{dp_p}{dV_p} \frac{d\theta}{\theta} V_o \qquad \text{Eq. (15.56)}$$

Equation (15.54) can then be written

$$p_p - p = \Delta p_{ss} - \left(\frac{\partial p}{\partial T}\right)_\theta dT - \left[\left(\frac{\partial p}{\partial \theta}\right)_T \theta + V_o \frac{dp_p}{dV_p}\right] \frac{d\theta}{\theta} \qquad \text{Eq. (15.57)}$$

The pressure difference across the surge pipe is responsible for the flow of water in the surge line. Suppose the surge line has two sections in series. Section 1 has a flow area A_1, a total mass of water M_1, and an average water velocity v_1. Section 2 has characteristic values A_2, M_2, and v_2. Density changes in the surge line are neglected (this was assumed implicitly above when the increase in primary loop coolant volume was set equal to the decrease in pressurizer steam volume). The flow equation for the surge line is

$$p_p - p = \frac{M_1}{A_1} \frac{dv_1}{dt} + \frac{M_2}{A_2} \frac{dv_2}{dt} + f_1 (v_1) + f_2(v_2) \qquad \text{Eq. (15.58)}$$

where $f_1(v_1)$ and $f_2(v_2)$ are the friction pressure drops in the pipe sections 1 and 2, respectively. The form of the friction pressure drop is assumed to be a proportionality factor times the velocity squared with the proportionality factor varying as $v^{-0.2}$. Thus

$$f_1(v_1) = a_1 \left|v_1\right|^{1.8} \qquad \text{Eq. (15.59a)}$$

$$f_2(v_2) = a_2 \left|v_2\right|^{1.8} \qquad \text{Eq. (15.59b)}$$

where a_1 and a_2 are constants.

Because of the steady flow into the spray system, v_1 and v_2 have steady-state values plus a time dependent portion.

$$v_1 = v_{1_o} + v_1(t) \qquad \text{Eq. (15.60a)}$$

$$v_2 = v_{2_o} + v_2(t) \qquad \text{Eq. (15.60b)}$$

The mass flow through pipe section 1 is equal to the mass flow in pipe section 2, since they are in series. Thus,

$$\theta v_1 A_1 = \theta v_2 A_2 \qquad \text{Eq. (15.61)}$$

Since the time-dependent portion of the mass flow is equal to the increase in the mass of water in the primary loop,

$$\theta v_1(t) A_1 = \theta v_2(t) A_2 = V_o \frac{d\theta}{dt} \qquad \text{Eq. (15.62)}$$

Differentiating Eq. (15.62) with respect to time yields

$$\theta \frac{dv_1}{dt} A_1 = \theta \frac{dv_2}{dt} A_2 = V_o \frac{d^2\theta}{dt^2} \qquad \text{Eq. (15.63)}$$

(The change in density in the surge line is neglected as noted above.) Equation (15.63) may be substituted in Eq. (15.58). Before this is done, however, the friction functions will be calculated.

The total friction pressure drop is the sum of f_1 and f_2. If the steady-state flow volume is designated as F_o, adding Eqs. (15.59a) and (15.59b) and substituting from Eqs. (15.53), (15.60) and (15.62) gives the result

$$f_1(v_1) + f_2(v_2) = \left[1 + \frac{V_o}{\theta F_o} \frac{d\theta}{dt}\right]^{1.8} \Delta p_{ss} \qquad \text{Eq. (15.64)}$$

Substitution of Eqs. (15.63) and (15.64) in Eq. (15.58) yields

$$p_p - p = \left[\frac{M_1}{A_1^{\,2}} + \frac{M_2}{A_2^{\,2}}\right] \frac{V_o}{\theta} \frac{d^2\theta}{dt^2} + \left[1 + \frac{V_o}{\theta F_o} \frac{d\theta}{dt}\right]^{1.8} \Delta p_{ss} \qquad \text{Eq. (15.65)}$$

To obtain Eq. (15.66), Eq. (15.65) is combined with Eq. (15.57).

$$\left(\frac{\partial p}{\partial T}\right)_\theta dT = -\left[\left(\frac{\partial p}{\partial \theta}\right)_T \theta + V_o \frac{dp_p}{dV_p}\right] \frac{d\theta}{\theta} - \left[\frac{M_1}{A_1^{\,2}} + \frac{M_2}{A_2^{\,2}}\right] \frac{V_o}{\theta} \frac{d^2\theta}{dt^2}$$

$$- \left\{ \left[1 + \frac{V_o}{\theta F_o} \frac{d\theta}{dt}\right]^{1.8} - 1 \right\} \Delta p_{ss} \qquad \text{Eq. (15.66)}$$

Equation (15. 66) provides a relationship between the thermodynamic variables p, T and θ. Through this relationship an explicit value can be obtained for the total derivative of the pressure with respect to the temperature. To make Eq. (15. 66) more tractable the friction term is linearized by expanding it and taking the first term.

Next, the time dependent variables are assumed representable by a steady-state value plus an oscillatory component of frequency ω.

$$\theta = \theta_o + \delta\theta\, \epsilon^{j\omega t}$$

$$p = p_o + \delta p\, \epsilon^{j\omega t}$$

$$T = T_o + \delta T \epsilon^{j\omega t}$$

Substituting these, Eq. (15. 66) can be solved for $\frac{\delta\theta}{\delta T}$.

$$\frac{\delta\theta}{\delta T} = - \frac{\theta \left(\frac{\partial p}{\partial T}\right)_\theta}{\left\{ \left[\left(\frac{\partial p}{\partial \theta}\right)_T \theta + V_o \frac{dp_p}{dV_p}\right] - \omega^2 V_o \left[\frac{M_1}{A_1^2} + \frac{M_2}{A_2^2}\right] + j\omega\ 1.8 \frac{V_o}{F_o} \Delta p_{ss} \right\}} \qquad \text{Eq. (15. 67)}$$

Equation (15. 55) may be rewritten for the oscillatory condition

$$\frac{\delta p}{\delta T} = \left(\frac{\partial p}{\partial T}\right)_\theta + \left(\frac{\partial p}{\partial \theta}\right)_T \frac{\delta\theta}{\delta T}$$

Using Eq. (15. 67) and the modified form of Eq. (15. 55), the following expression for $\frac{\delta p}{\delta T}$ is obtained

$$\frac{\delta p}{\delta T} = \left(\frac{\partial p}{\partial T}\right)_\theta \left(1 - \frac{\theta \left(\frac{\partial p}{\partial \theta}\right)_T}{\left\{ \left[\left(\frac{\partial p}{\partial \theta}\right)_T \theta + V_o \frac{dp_p}{dV_p}\right] - \omega^2 V_o \left[\frac{M_1}{A_1^2} + \frac{M_2}{A_2^2}\right] + j\omega\ 1.8 \frac{V_o}{F_o} \Delta p_{ss} \right\}} \right)$$

Eq. (15. 68)

This is the required relation to carry out the stability analysis.

A numerical example has been calculated using the following values for the parameters in the equations.

[redacted]

[redacted]

15.8 COMBINED REACTIVITY EFFECT OF PRESSURE COEFFICIENT AND TEMPERATURE COEFFICIENT--SLOW VARIATIONS

In this section the plant stability will be considered taking both pressure and temperature effects into account. The treatment will be limited to the quasi-stationary case in this section.

The reactor temperature coefficient of reactivity applies to the mean reactor water temperature, T_{rw}. This temperature may differ substantially from the mean primary loop temperature T of Eq. (15.68). The pressure of the primary system is determined by T rather than by T_{rw}. In the primary system the pressure p is uniform for the frequencies being considered. Thus the combined reactivity effect of temperature and pressure is given by Eq. (15.69).

$$\rho = \left(\frac{\partial \rho}{\partial T_{rw}}\right)_p \delta T_{rw} + \left(\frac{\partial \rho}{\partial p_{rw}}\right)_{T_{rw}} \frac{\delta p}{\delta T} \; \delta T \qquad \text{Eq. (15.69)}$$

This may be written

$$\rho = \alpha_T \, \delta T_{rw} + \alpha_p \frac{\delta p}{\delta T} \, \delta T \qquad \text{Eq. (15.69a)}$$

since by definition

$$\alpha_T \equiv \left(\frac{\partial \rho}{\partial T_{rw}}\right)_p$$

and

$$\alpha_p \equiv \left(\frac{\partial \rho}{\partial p_{rw}}\right)_{T_{rw}}$$

In general, δT_{rw} and δT differ in both magnitude and phase. However, for sufficiently slow oscillations, of the order of a few cycles per hour, they are essentially equal. Under these conditions

$$\rho = (\alpha_T + \alpha_p \frac{\delta p}{\delta T}) \; \delta T \qquad \text{Eq. (15.70)}$$

This is the relation which holds for the quasi-stationary case. For these slow oscillations,

[redacted]

Eq. (15.68) may be simplified. The mass of the water in the surge line will not affect the pressure. The pressure will be determined primarily by the pressurizer characteristics. Dropping the terms in ω and ω^2 in Eq. (15.68) and noting further that for practical designs

$$\theta\left(\frac{\partial p}{\partial \theta}\right)_T \theta >> V_o \frac{dp_p}{dV_p}$$

then

$$\frac{\delta p}{\delta T} \cong \frac{1}{\theta} \frac{\left(\frac{\partial p}{\partial T}\right)_\theta}{\left(\frac{\partial p}{\partial \theta}\right)_T} V_o \frac{dp_p}{dV_p} \qquad \text{Eq. (15.71)}$$

To complete the treatment of the quasi-stationary case it is necessary to derive an expression for δT, the amplitude of the average primary loop temperature variation. The results obtained in Sec. 15.5 for slow temperature variation can be applied. Equation (15.50) of that section gives for δT_{ri}, the amplitude of the reactor inlet water temperature,

$$\delta T_{ri} = \frac{\delta \phi}{\phi_o}\left[(T_{bw} - T_s) + \left(\frac{\partial T}{\partial p}\right)_{sat} p_s\right] \qquad \text{Eq. (15.50)}$$

Then, since the flow is constant, the reactor outlet temperature amplitude can be obtained from Eq. (15.43).

$$\frac{\delta\phi}{\phi_o} = \frac{\delta T_{ro} - \delta T_{ri}}{T_{ro} - T_{ri}} \qquad \text{Eq. (15.43)}$$

Next, consider the fractions of the total primary coolant which are at hot leg temperature, cold leg temperature, reactor temperature, and boiler water temperature (see Fig. 15.5). Denote these masses of coolant as M_H, M_c, M_{rw}, and M_{bw}, respectively. The reactor water temperature and the boiler water temperature are equal for the quasi-stationary case and are the mean of the hot leg and cold leg temperatures. The computation is carried out in a straightforward manner with the result

$$\delta T = \frac{\delta\phi}{\phi_o}\left\{\left[(T_{bw} - T_s) + \left(\frac{\partial T}{\partial p}\right)_{sat} p_s\right] + \left[\frac{M_H + \dfrac{M_{bw} + M_{rw}}{2}}{M_H + M_c + M_{rw} + M_{bw}}\right]\left[T_{ro} - T_{ri}\right]\right\} \qquad \text{Eq. (15.72)}$$

[redacted]

15.9 REACTIVITY EFFECTS OF PRESSURE AND TEMPERATURE--RAPID VARIATIONS

The analysis of the plant response to combined temperature and pressure variations becomes considerably more complicated when the frequencies considered are sufficiently high to introduce phase differences in the response of various units. Because of the complicated algebraic expressions which are involved in a quantitative discussion, only a qualitative discussion will be presented. Typical results will be used to illustrate the discussion.

The first transfer function to be considered is that of the reactor water temperature without recirculation of the primary loop water. With no recirculation of the primary coolant taken into account, there is no coupling of the plant load to the reactor. The reactor inlet temperature, T_{ri}, is therefore constant. The mean reactor temperature, T_{rw}, is calculated using the reactor equations of Sec. 15.4(a). The oscillatory component of the reactor power results in an oscillatory component of the reactor metal and reactor coolant temperatures.

The feedback condition without primary water recirculation is of only limited interest, however. To derive the equivalent transfer function with recirculation, all of the reactor plant equations given in Sec. 15.4 must be introduced.

Figure 15.10 shows the transfer function for mean reactor water temperature with recirculation. The oscillatory nature of this transfer function at frequencies greater than 0.1 cycle per second is very pronounced. These resonances are due to coolant recirculation. At lower frequencies the time delays are unimportant. At very high frequencies the oscillatory nature of the transfer function persists but the response is limited.

The reactivity feedback associated with the reactor water temperature

$$\rho_T = \alpha_T \left(\frac{\delta T_{rw}}{\delta\phi/\phi_o}\right) \frac{\delta\phi}{\phi_o} \equiv F \frac{\delta\phi}{\phi_o}$$

where α_T is the temperature coefficient of reactivity and F is the transfer function for reactivity. The over-all response of the reactor with feedback is given by Eq. (15. 7).

$$\frac{\delta\phi}{\phi_o} = \left(\frac{G}{1 - FG}\right) \rho_{IMP} \qquad \text{Eq. (15. 7)}$$

where G is the reactor transfer function. The magnitude and phase of G are given in Figs. 15. 1 and 15. 2, respectively. If the transfer function G is multiplied by α_T times the transfer function for reactor water temperature, the over-all loop gain FG for temperature feedback may be obtained. Introducing this into Eq. (15. 7), the over-all reactor response with temperature feedback with recirculation may be calculated. [redacted]

[redacted]

Fig. 15.10 - Magnitude and Phase of the Transfer Function for Reactor Water Temperature with Primary Water Recirculation.

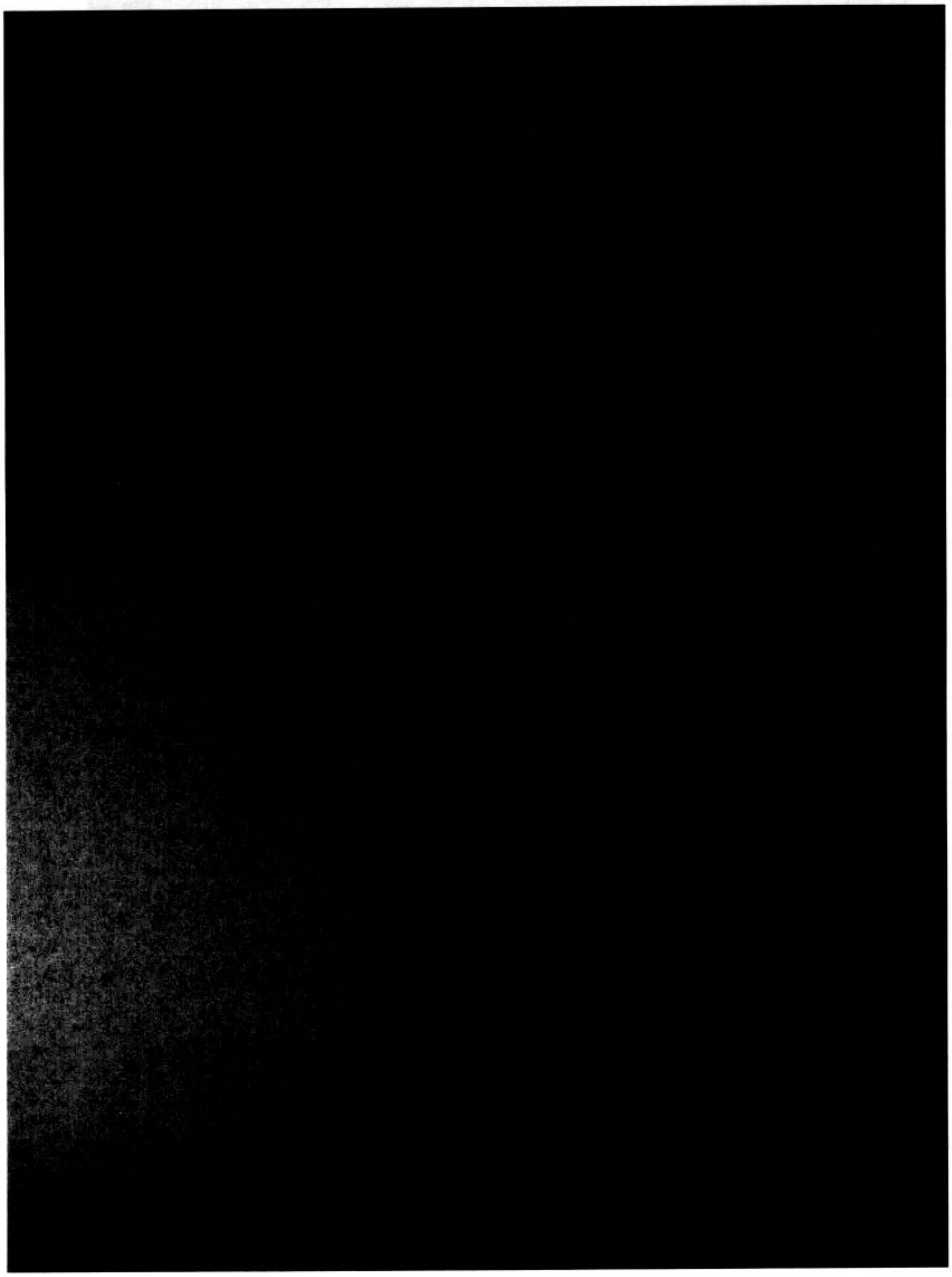

Fig. 15.11 - Magnitude and Phase of the Over-all Reactor Transfer Function with Temperature Feedback and Recirculation.

[redacted]

Fig. 15.12 - Magnitude and Phase of the Transfer Function for Average Primary Loop Water Temperature.

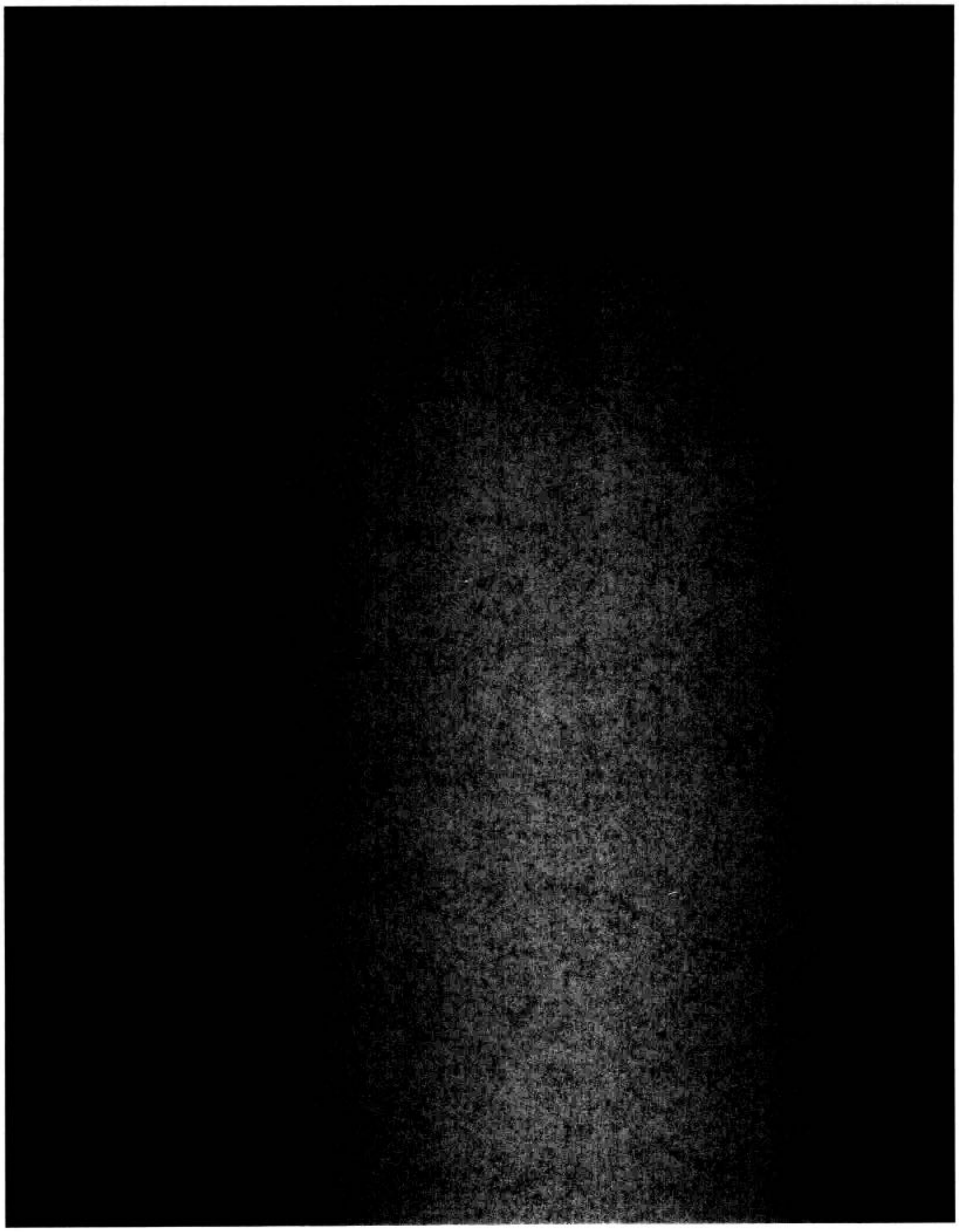

Fig. 15.13 - Over-all Loop Gain with Both Pressure Feedback and Temperature Feedback with Recirculation.

REFERENCES

1. Chestnut and Mayer, Servomechanisms and Regulating System Design, John Wiley and Sons, New York, 1951.
2. Korn and Korn, Electronic Analog Computers, McGraw-Hill Book Co., New York, 1952.
3. S. Glasstone and M. C. Edlund, The Elements of Nuclear Reactor Theory, D. Van Nostrand Co., Inc., New York, 1952.
4. A. F. Henry, Computation of Parameters Appearing in the Reactor Kinetics Equations, Report WAPD-142, December 1955.
5. Joseph H. Keenan and Frederick G. Keyes, Table 4, Thermodynamic Properties of Steam, John Wiley and Sons, New York, 1936.

BIBLIOGRAPHY

1. M. A. Schultz, Control of Nuclear Reactor and Power Plants, McGraw-Hill Book Co., Inc., New York, 1955.
2. M. F. Gardner and J. L. Barnes, Transients in Linear Systems, John Wiley and Sons, New York.
3. J. N. Grace, M. A. Schultz, and T. E. Fairey, Inherent Reactor Stability, Proceedings of the 1955 Conference on Nuclear Engineering UCLA, Berkeley Calif., California Book Co., Ltd., 1955.

Chapter 16

THE SYNTHESIS OF REACTOR CONTROL SYSTEMS

by J.N. Grace and N.J. Curlee

16.1 INTRODUCTION--OUTLINE OF CONTROL SYSTEM REQUIREMENTS

In this chapter the design of a reactor control system will be considered in the light of the reactor-to-plant coupling discussed in the previous chapter. Because of this coupling, the reactor and plant control must be considered as a unit.

There are a number of requirements that a reactor plant control system must satisfy:

1. It must adjust the reactor power level to meet the steady-state load demand.
2. It must be stable to changes in load demand over the control range.
3. It must maintain the plant components within prescribed temperature ranges during steady-state or transient conditions.
4. It must limit the rates of change of temperature to prescribed limits during transient conditions.
5. It must protect the plant during emergency conditions.

It is beyond the scope of this treatment to consider the reasons for the establishment of limits on temperature or rates of change of temperature. Likewise, the considerations governing the plant protective system will not be treated here. This discussion will be limited to the properties of systems which adjust the reactor power level to demand within set limits of temperature and rates of change of temperature. While the steady-state properties will be considered in setting the system requirements, the chief emphasis will be on the transient response of the system.

The method of analysis will be the frequency response method used in the preceding chapter. This method permits an analysis of selected system properties. Analog computer studies may then be used to verify the properties of selected systems under simulated transient conditions.

Two general classes of control systems will be examined. The first is one which does not depend upon inherent stability properties of the plant for its design. The second class of systems treated makes use of assumed plant stability properties.

There is no unique control system for a reactor plant which meets the design requirements. In general, many systems of control and many variations within a given system can be found which are satisfactory. For this reason, the selection of a system must be guided by the experience and background of the designer. In synthesizing the systems to be analyzed, attention will be given to the motivation for various selections.

16.2 ELEMENTARY POWER DEMAND COMPARATOR CONTROL SYSTEM--STEADY-STATE

(a) General Nature of System. A power demand comparator control system is one which makes no assumptions concerning the inherent stability of the plant. In principle, it operates as follows: Let P denote the fraction of total rated power being delivered by the reactor. Let P_L represent the steady-state thermal load demand. The control system compares P with P_L and takes the action necessary to reduce the difference between P and P_L to less than some acceptable error. The system basically comprises (1) a unit which determines P_L, (2) a unit which determines P, (3) a comparator which examines the difference between P and P_L and determines whether corrective action need be taken, and (4) a means of adjusting the power level of the reactor and plant conditions to correct the difference between P and P_L.

(b) Thermal Load Demand Signal. The thermal load demand P_L may be obtained directly or by inference. For example, the thermal load demand might be inferred from the position of the turbine throttle valve control dial. A somewhat better demand indication might be obtained by continuous measurement of the actual opening of the turbine throttle valve. For pressurized water plants an even simpler and more direct scheme can be used. The thermal load power is the product of the steam flow-rate and the enthalpy drop in the secondary loop. [redacted] Thus, the thermal load is proportional to the steam flow-rate. Therefore, a measurement of the steam flow-rate can be used as a thermal load demand signal. In this chapter, F_S will designate the steam flow-rate as a fraction of full load flow-rate.

(c) Reactor Output Power Measurement. The reactor output power may be measured by a calorimetric method or a nuclear method. In the calorimetric method the coolant inlet and outlet temperatures and the rate of flow of coolant are measured. The rate of flow to primary coolant multiplied by the temperature rise in the reactor and the specific heat of the coolant gives the reactor output power in absolute terms. This direct method is attractive but has several difficulties. The coolant temperatures are measured most reliably in the coolant lines outside the pressure vessel. Even with constant inlet temperature this results in an appreciable delay in the power measurement since the coolant must pass through the exit plenum of the reactor vessel into the pipes leading to the boiler before its temperature can be measured. A second difficulty is the response time of the thermometers themselves which can introduce an appreciable delay. There are, moreover, other minor difficulties.

For these reasons, in control systems of this type it has been customary to make a relative measurement of reactor power through neutron detection instruments. [redacted] A suitable system is one which calibrates the neutron instruments continuously by measuring the power level calorimetrically and adjusting the neutron detector signal delivered to the comparator. [redacted] The calorimetric measurement may be made in the primary or secondary circuit.

(d) Function of Comparator. The function of the comparator is to determine the difference between P and P_L. The magnitude of the difference is compared with an allowable error and a determination made as to the need for corrective action and the sign of the correction. The output of the comparator is a signal for appropriate corrective action.

At this point it is clear that the control system being formulated by this discussion has a most serious weakness. Although the system corrects the error in power level, the integral of the power error with time leads to a shift in average loop temperature. Stated another way, the control system as formulated has no capability for maintaining the plant within prescribed operating temperature limits. To consider this problem it is necessary to discuss briefly the plant operating program.

(e) Plant Operating Program. The control system under discussion in this chapter is a power range control system. [redacted] The plant designer has established a suitable program of plant conditions over the power control range. For each output power in the control range there is a set of appropriate plant conditions including flow-rate of the primary coolant, temperature rise of the coolant in the reactor, reactor coolant inlet temperature, reactor coolant outlet temperature, reactor mean temperature, secondary steam pressure and steam flow-rate. Not all of these variables are independent. For example, the flow-rate of the primary coolant, one reactor temperature (either inlet, outlet, or mean) and the steam flow-rate determine all the other variables.

The plant designer has selected in advance a program of plant conditions which are compatible with his design. The size of the pressurizer, the size of the surge line, the maximum boiler pressure in the secondary loop have all been selected on the basis of this program. The programs chosen usually fall into two classes; these are constant temperature programs and constant steam pressure programs.

The temperature difference between the primary coolant and the steam in the boiler secondary depends upon the plant load and increases with increasing load. Thus at constant primary loop temperature, the secondary steam pressure falls with increasing load. A constant steam pressure program would require a wide variation in primary loop mean temperature with load. This is difficult to accomplish. For this reason pressurized water reactors are designed with constant temperature programs rather than with constant pressure programs. The temperature which is maintained constant may be the reactor inlet temperature, the reactor outlet temperature, the mean temperature, or some arbitrary combination of these. The point of importance is that a temperature is available as a reference which the control system is required to maintain.

(f) Additional Function of the Comparator. The comparator, therefore, has an additional function. It must not only provide for the difference in power between the thermal load demand and the actual reactor power, it must, in addition, maintain the specified reference temperature within a prescribed error limit. The reference temperature is designated as T_R

The actual measured temperature to be compared with T_R will be designated as T_M.

[redacted]

(g) Control Rod System. [redacted]

(h) Synthesis of Elementary Control System. The discussion of the steady-state requirements of the control system given in this section leads to a system for generation of the reactor power demand signal in which the total demand, as a fraction of full power, is made up of two components. One portion of the demand is the thermal load requirement P_L, the other portion is the power necessary to restore the reference temperature to its design condition. If the total power demand is designated by P_D and the power demand necessary for temperature correction by P_T, then the total power demand

$$P_D = P_L + P_T \qquad \text{Eq. (16.1)}$$

The control system operates to adjust the reactor power to match P_D. In the proposed system

$$P_L = K_1 F_S \qquad \text{Eq. (16.2)}$$

$$P_T = K_2 (T_R - T_M) \qquad \text{Eq. (16.3)}$$

$$P_D = K_1 F_S + K_2 (T_R - T_M) \qquad \text{Eq. (16.4)}$$

In the above equations, K_1 is a dimensionless constant (measured in per cent of total power per per cent of full load steam flow) and K_2 is a constant measured in units of fraction of full load power per degree temperature difference.

The control scheme given by Eq. (16.4) will have no temperature error in the steady state if $K_1 = 1$. If K_2 is made as large as possible, the temperature error during a transient will be a minimum. The dynamic properties of this simple control proposal will now be considered.

16.3 ELEMENTARY POWER DEMAND COMPARATOR CONTROL SYSTEM--STABILITY ANALYSIS

The stability analysis is carried out by the techniques discussed in Chap. 15. The control loop consists of the reactor and plant with F_S and T_M as the output variables which are fed back into the reactor. The transfer functions $\frac{\delta F_S}{\delta\phi/\phi_o}$ and $\frac{\delta T_M}{\delta\phi/\phi_o}$ must be studied in order to determine the system stability. These will be fed back into the reactor via Eq. (16.4) as a reactivity increment. The reactor response (transfer function G) of Chap. 15 completes the loop.

It is convenient to study the properties of the loop by consideration of the transfer functions for F_S and T_M. Since K_1 and K_2 are as yet undetermined, the feedback is not fixed. It is, in fact, the purpose of the analysis to arrive at suitable values for these constants. For convenience in analysis the feedback into the reactor will be assumed to be carried out by means of a fast regulating rod system. With such a system the reactor transfer function, $\delta P/\delta P_D$, will have a gain of unity and essentially no phase shift for the frequency range of interest, 0.001 to 0.1 cycle per second. Thus the stability analysis can be limited to consideration of the transfer function

$$\frac{\delta P_D}{\delta\phi/\phi_o} = K_1 \frac{\delta F_S}{\delta\phi/\phi_o} - K_2 \frac{\delta T_M}{\delta\phi/\phi_o} \qquad \text{Eq. (16.5)}$$

Equation (16.5) follows from Eq. (16.4) and the fact that the entire loop gain is

$$\frac{\delta P}{\delta P_D} \quad \frac{\delta P_D}{\delta\phi/\phi_o}$$

since it has been assumed that the reactor transfer function, $\delta P/\delta P_D$, is unity in the frequency range of interest.

Application of the customary stability criterion would indicate that the system will oscillate if the transfer function given by Eq. (16.5) has a gain of one and a corresponding phase shift which is an integral multiple of 360 degrees. Stated more precisely, the system will be unstable if the locus of the transfer function encloses the point $(1, 0^o)$ on the complex plane.

In the design of an operating system, the application of a stability requirement no more rigid than this would probably be unsatisfactory. First, there are errors in the analysis, particularly in the models chosen to represent the behavior of the plant components. Second, there could be errors in the plant adjustment, for example, in feedback settings. Furthermore, a system which is barely stable exhibits erratic transient behavior with large overshoots. For these reasons, a more rigid stability requirement must be imposed.

The required safety factor for design and operating purposes can be obtained by requiring either a gain margin or a phase margin. Gain margin is the factor by which the loop gain is less than unity when the phase shift is a multiple of 360 degrees. Phase margin is the amount by which the phase shift is less than 360 degrees when the gain is unity. For purposes of this chapter, selection of a gain margin is more useful than a phase margin. A gain margin of four will be arbitrarily required in this analysis.

With the establishment of the stability criterion to be used, the analysis can proceed. The transfer functions for both F_S and T_M are functions of the plant operating power level. For this reason they must be calculated at several power levels. It is generally satisfactory to compute three levels: Minimum plant power, half power, and full power.

An example of a specific reactor plant will be given in order to illustrate the method. The same example will be used in the next several sections of this chapter to illustrate the synthesis of a satisfactory demand-type control system. Transfer functions for F_S and T_M have been calculated for this reactor plant at the power levels suggested. The equations used in calculating the transfer functions are of the general type given in Chap. 15. One feature which has been added is a thermometer delay for T_M. [redacted]

[redacted]

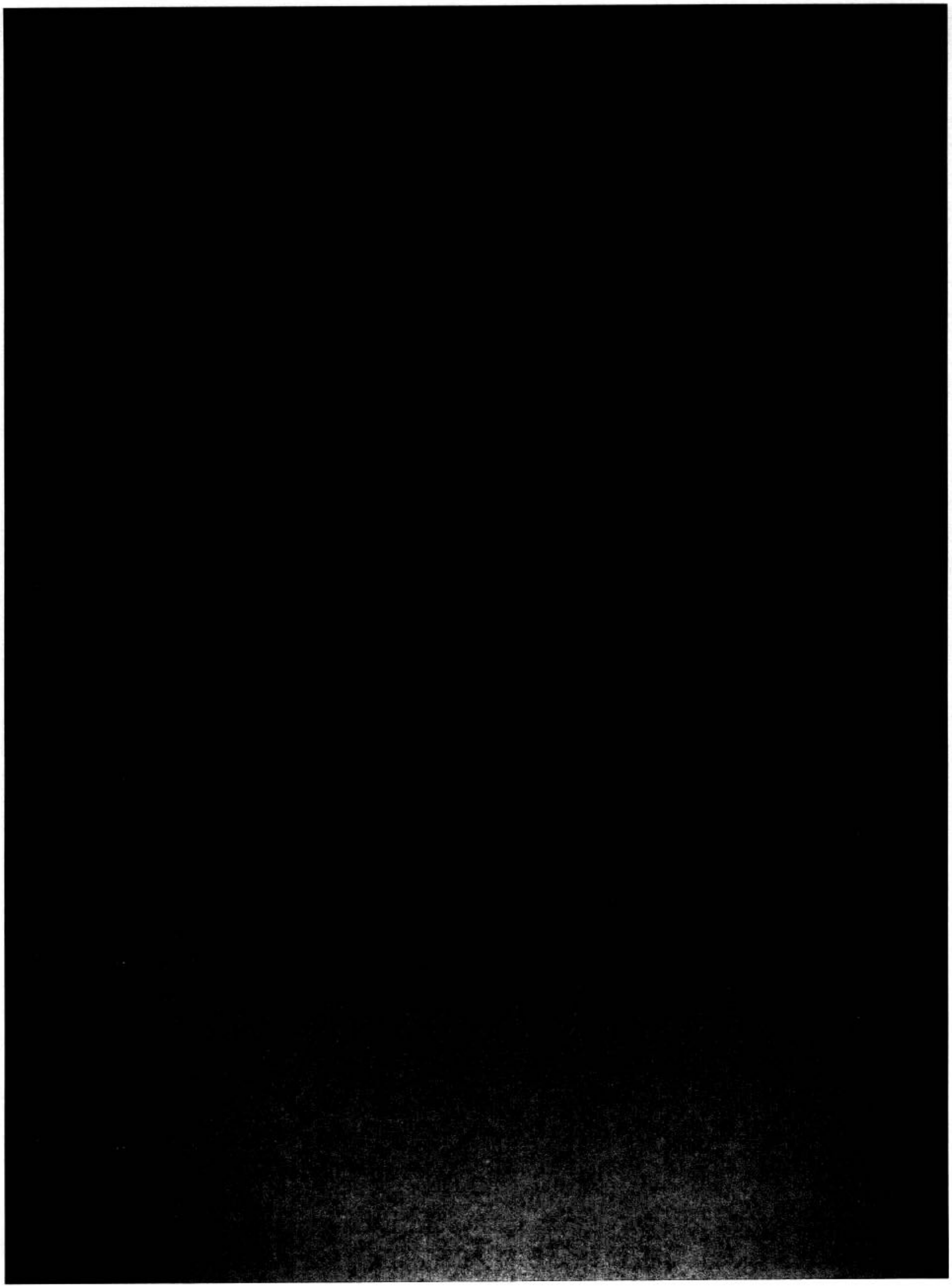

[redacted]

16.4 POWER DEMAND COMPARATOR CONTROL SYSTEM--ADDITION OF ERROR SIGNAL INTEGRATION

In the design of control systems, if the maximum permitted gain (as governed by stability considerations) does not provide a sufficiently small steady-state error, integration of the error signal is added. To rectify the difficulty of the preceding section, the power demand signal is modified to include integration of the T_R error. The modified function is

$$P_D = K_1 F_S + K_2 \left[(T_R - T_M) + \frac{1}{\tau} \int (T_R - T_M)\, dt \right] \qquad \text{Eq. (16.7)}$$

In this equation τ is a characteristic time whose magnitude is to be determined.

Equation (16.7) is clearly satisfactory in the steady-state, for so long as T_R and T_M differ, the integral term provides a demand signal. Thus, with K_1 less than unity, the deficiency is made up not by a steady-state error in T_M, but by accumulation of the error signal in T_M. However, the integrated error signal is only effective compared with the error signal itself when its duration is of the order of τ or greater. Thus, τ has the significance of a time interval during which the error signal must be present in order that the integral term be significant. Therefore, in order to limit the duration of transients, it is desirable to have τ relatively small.

The stability analysis, including the addition of an error integration term has been carried out for the same reactor plant considered in the preceding section. As before, the stability analysis was carried out through the evaluation of the transfer function, $\dfrac{\delta P_D}{\delta\phi/\varphi_o}$.

[redacted]

[redacted]

16.5 POWER DEMAND COMPARATOR CONTROL SYSTEM--ADDITION OF DERIVATIVE SIGNAL

The large temperature error which must exist for times longer than τ in the reactor plant reduces the usefulness of the demand signal given by Eq. (16.8). The changes needed to produce a more satisfactory signal can be found only by making a detailed study of the transfer function for the demand signal and the limitations which the stability criterion places upon it. Through such a study one finds that the transient situation can be improved either by speeding up the integration time or by increasing K_1. Of the two, an increase in K_1 seems to be the preferable approach. Two methods can be found which permit a real improvement in the transient response of the plant to be made. One method involves the addition of a derivative term to the demand signal. This method is discussed in this section. The other method is discussed in the following section.

[redacted]

[redacted]

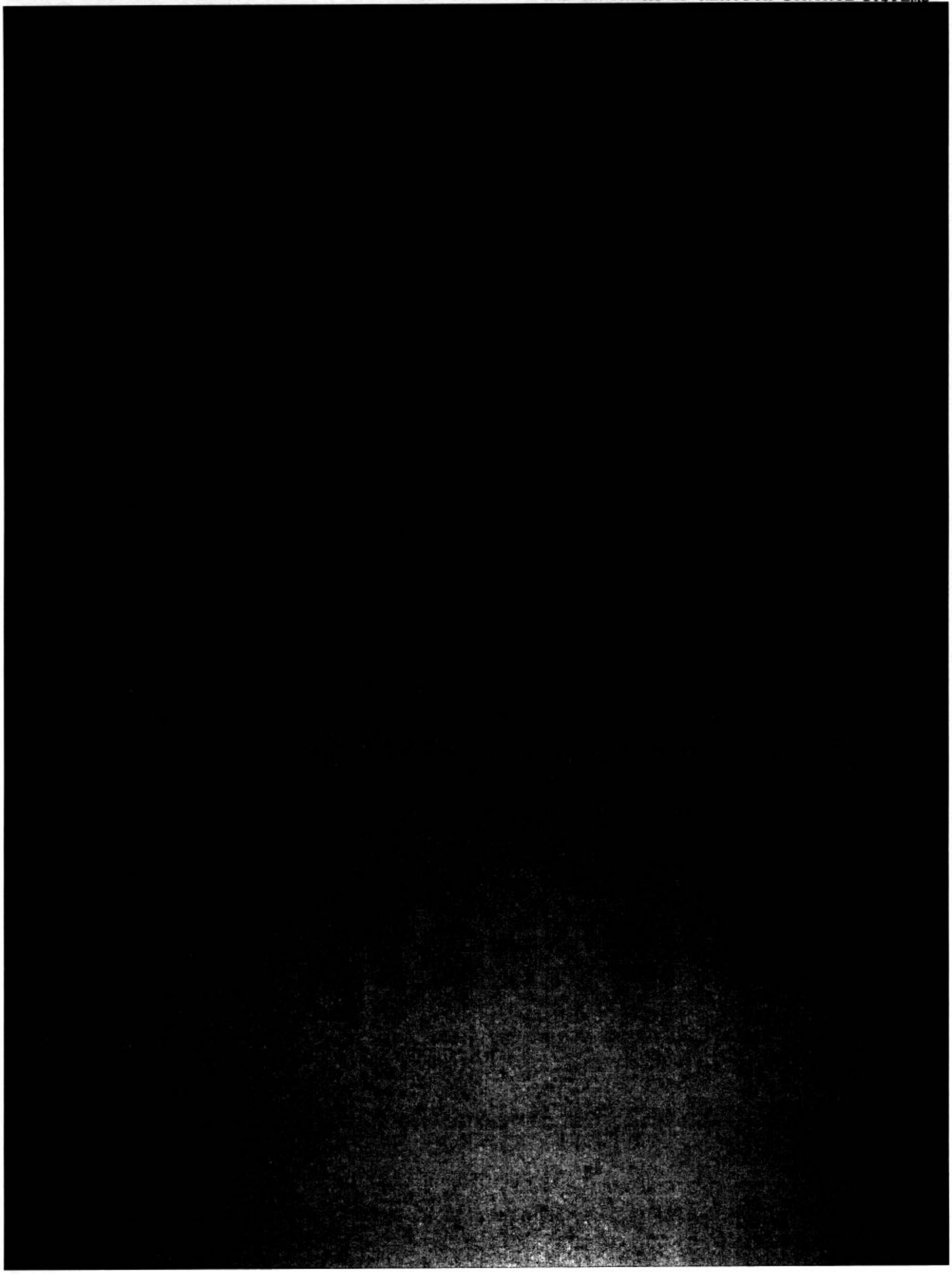

[redacted]

16.6 POWER DEMAND COMPARATOR CONTROL SYSTEM--ADDITION OF TEMPERATURE RESPONSE DELAY

A markedly different solution to the difficulty discovered in Sec. 16.4 may be found. Instead of the addition of a temperature derivative signal, in this case the response time of the temperature sensing device may be increased with beneficial effects. [redacted]

[redacted]

[redacted]

16.7 POWER DEMAND COMPARATOR CONTROL SYSTEM--TRANSIENT RESPONSE STUDIES

The final design test of the operability of a control system is made by transient studies employing a plant simulator. [redacted]

16.8 CONTROL SYSTEM WITH INHERENT REACTOR STABILITY

(a) General Outline of Self-Stabilizing System. The power demand comparator type of control system described in the preceding sections does not make use of any inherent stability properties of the reactor. In pressurized water reactor plants the reactor can be designed to have a substantial negative temperature coefficient of reactivity at operating temperatures. This can be used to regulate the reactor response to changes in power demand. The rod system becomes a slow follow-up system for readjusting plant conditions to design values.

The system operates as follows: With the reactor at a power level P, assume the throttle is opened, demanding greater power. The increased steam flow cools the boiler which in turn reduces the temperature of the reactor inlet water. This drops the mean reactor temperature, and the reactor power rises until the original mean reactor temperature is attained. The reactor now supplies the increased load at the original mean reactor temperature with no rod motion.

A system of this type is simplest if the plant is designed with a program using constant mean reactor temperature. [redacted]

[redacted]

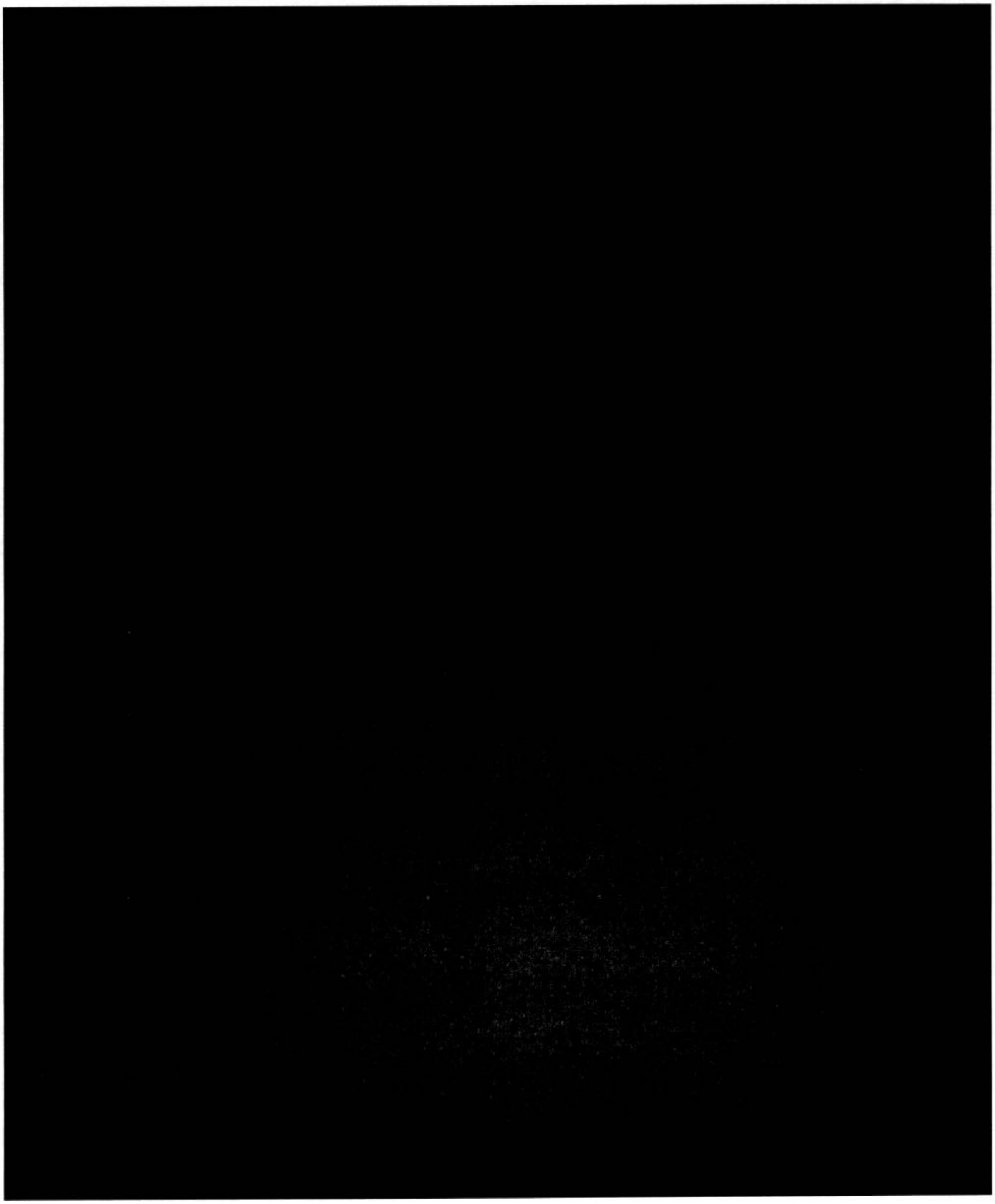

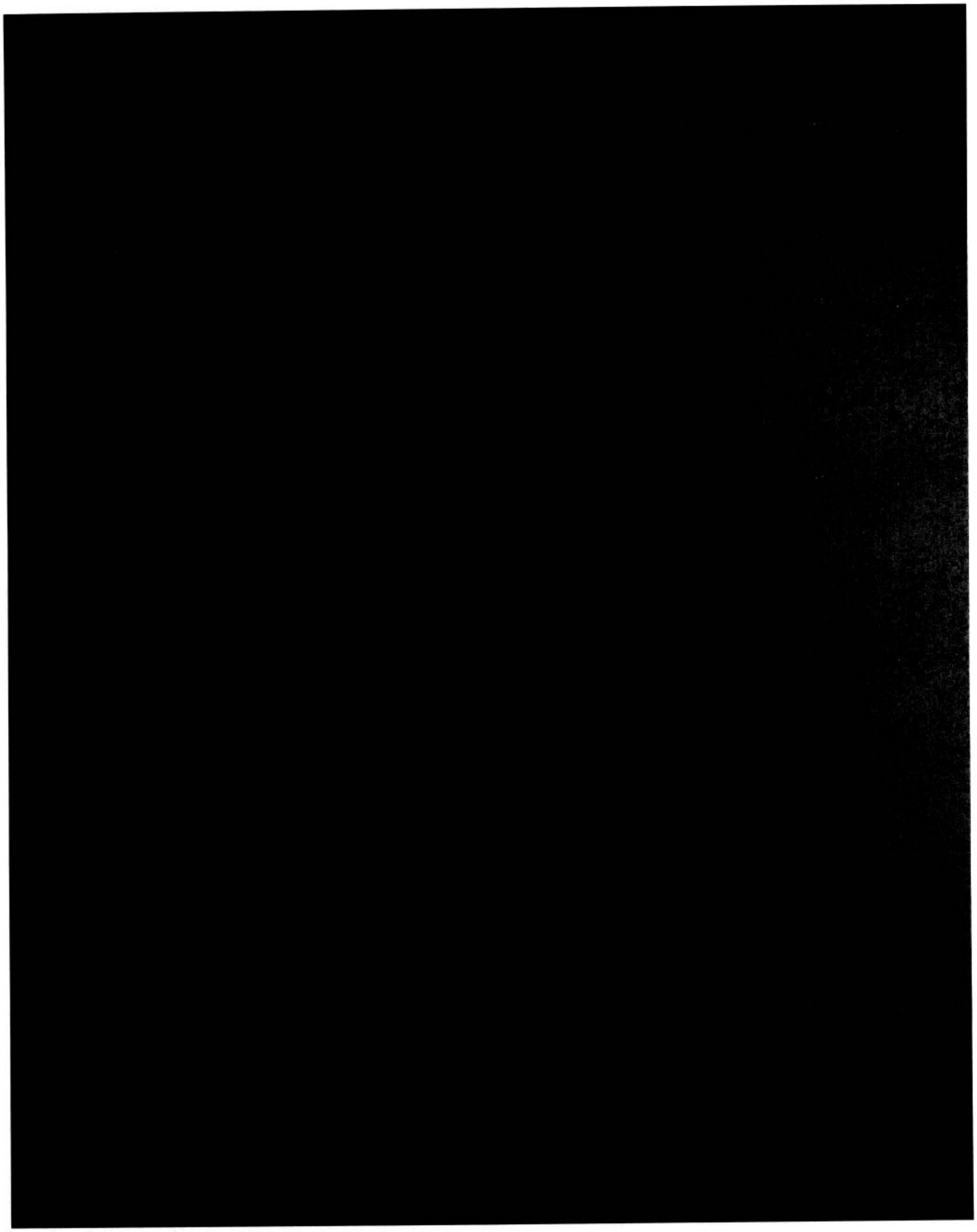

In a control system utilizing the inherent stability of the reactor the rapid load adjustments come about through the self-stability of the plant. [redacted]

The reference condition to which the plant is readjusted may be a temperature, as indicated above, or a steam pressure. With temperature reference control, the only plant measurement required for control is the reference temperature. [redacted]

In a pressure reference system, the basic measurement is the secondary steam pressure p_S. With a constant pressure plant program, this is the only measurement required for control purposes. With a constant temperature program for the plant, the references pressure must be readjusted with load. This is accomplished by measurement of the steam flow fraction F_S. The reference pressure p_R is then

$$p_R = p_{RO} + a_1 F_S$$

where p_{RO} is the base reference pressure and a_1 is a constant (negative) which maintains the appropriate temperature program. This error signal is

$$p_S - p_R = p_S - \left(p_{RO} + a_1 F_S\right)$$

While this system appears somewhat more complex than the temperature reference system, it has two advantages which may be important: (1) Measurements are made only on the secondary side, and (2) the required measurements are relatively simple.

So far as a stability analysis is concerned, both systems are essentially equivalent. Only the temperature reference system will be discussed.

(b) Advantages of Self-Stabilizing System over Demand System. The control system making use of the inherent reactor stability has a number of important advantages over the demand system discussed previously. These advantages are almost all associated with greater simplicity and, because of the greater simplicity, greater reliability.

In the self-stabilizing system only a single temperature measurement is required for control. No nuclear instrument measurement is required, eliminating any need for a nuclear instrument calibration system. Thus, the comparator becomes extremely simple. Accurate adjustment of instruments to provide precise signals, circuits and instruments for integration and differentiation can all be eliminated. The elimination of components and simplification of circuits not only increases reliability but permits the use of a smaller gain margin in stability analysis. This may be done since provision need not be made for instrument and circuit error. The gain margin may also be reduced because the slow system response is less apt to cause transient overshoot.

(c) Description of Self-Stabilizing System. Figure 16.9 is a functional diagram of the control system. There are now three basic parts to the control system:

1. The device sensing the plant temperature.

2. The comparator which compares the plant temperature with a reference value. The comparator provides an output signal which calls for reactivity addition, reactivity subtraction,

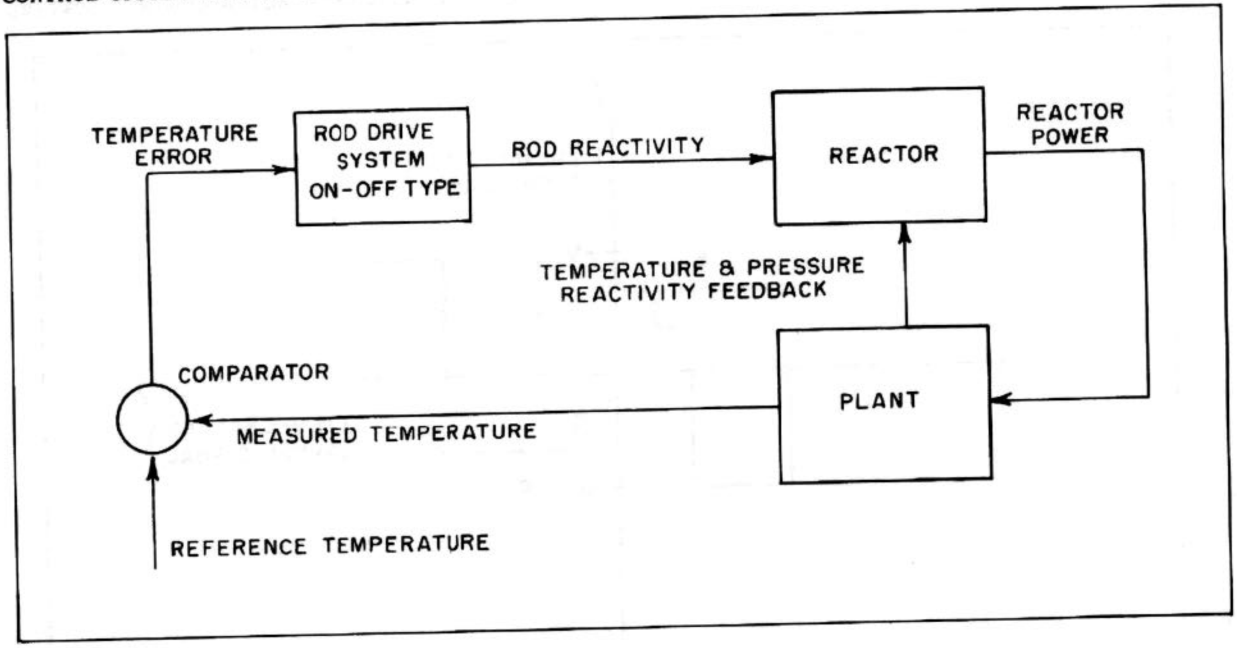

Fig. 16.9 - Functional Diagram of Self-Stabilizing Control System Using a Temperature Reference.

or no reactivity change.

3. The shim rod bank which executes the reactivity instruction from the comparator

Two error limits must be provided to assure stability of the on-off type rod control system, a start limit and a stop limit. If the error limits were equal, the system could hunt continuously. The start error limit, designated by (b), exceeds the stop error limit, designated by (a). When the magnitude of the error signal (x) exceeds (b), the rod motion starts. Rod motion continues until the error is less than the stop limit (a). While in motion, the rod reactivity rate is uniform, although the rate will vary with the position of the rod bank in the reactor. The start-to-stop ratio (b/a) is a significant system parameter. The shim rod reactivity rate V (measured in reactivity per second) is even more important, however. Figure 16.10 illustrates the system diagrammatically.

The slow reactivity additions required in the reactor due to depletion or xenon buildup are sensed by the temperature drop which this reactivity loss brings about. Likewise, with xenon burnout the reactivity subtraction required is sensed through the temperature rise which takes place.

(d) Stability Analysis. The stability of the control scheme will again be analyzed by means of the frequency response technique. There are, however, some additional complications. These result from the non-linearity of the system. One non-linearity has been encounted in the previous analyses, the dependence of the transfer function on the system power level. This non-linearity was handled previously by use of the small signal approximation and analyzing the system at three levels of power; namely, minimum control range power, half power, and full power.

The new non-linearity is associated with the on-off, constant reactivity rate rod control system. This is illustrated by Fig. 16.11 which shows the response of the rod drive system to a sinusoidal error signal. The complex transfer function describing this response depends

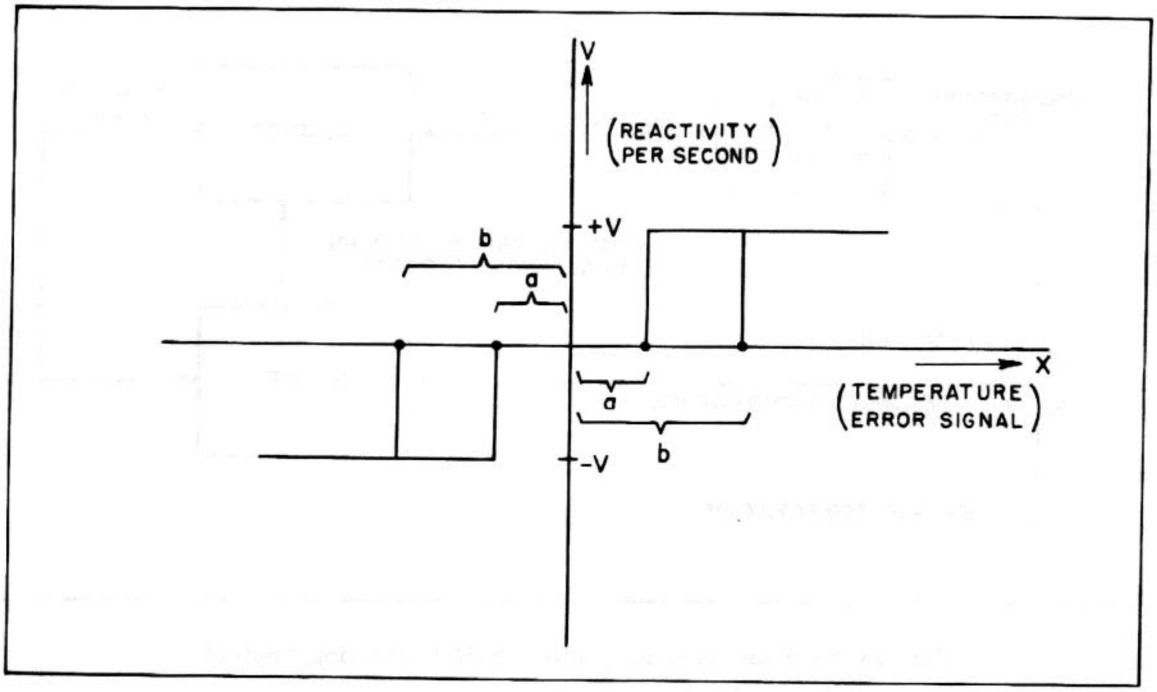

Fig. 16. 10 - Schematic Diagram Showing the Reactivity Rate as a Function of the Error Signal.

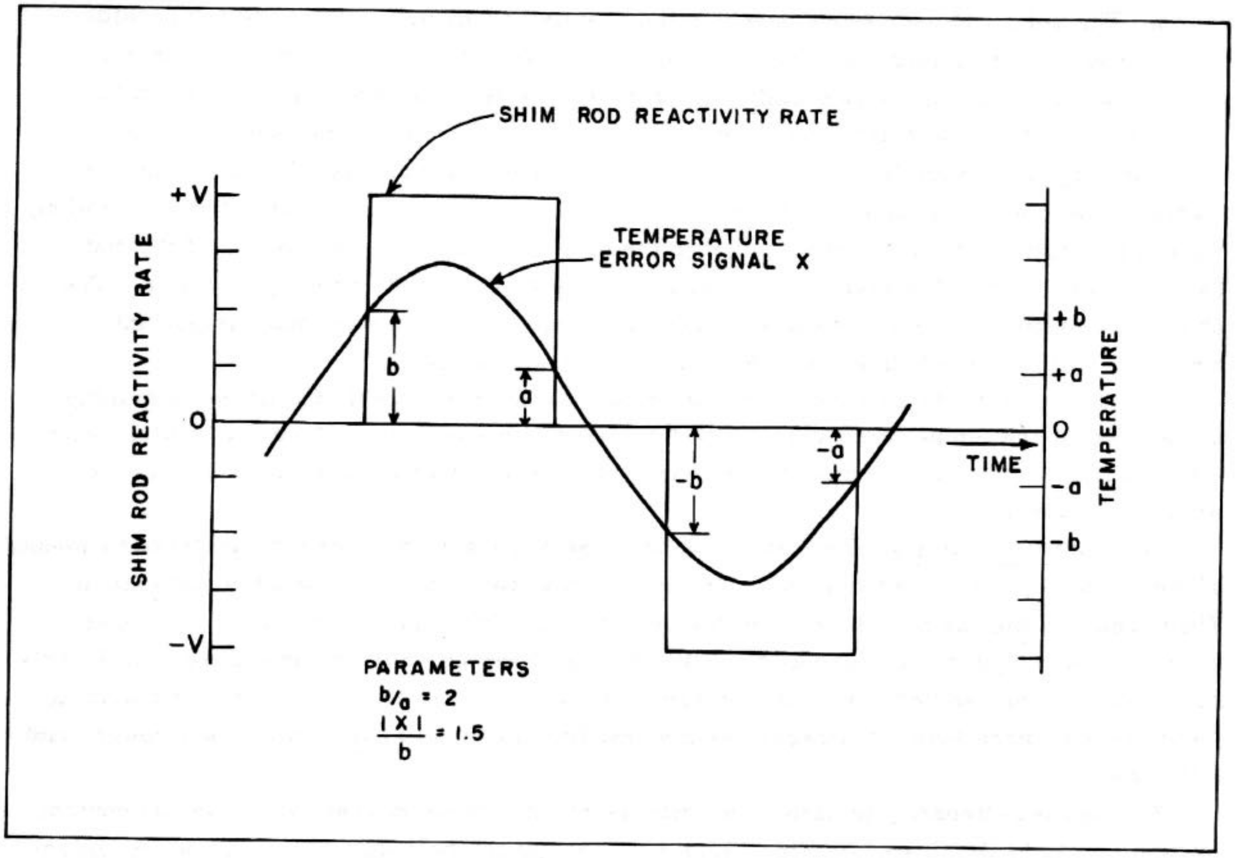

Fig. 16. 11 - Response of the Control Rod Bank to a Sinusoidal Error Signal.

upon the amplitude of the error signal. Consequently, the transfer function of the complete control loop depends on amplitude as well as frequency. The method to be used for analysis involves separation of the frequency dependent components of the loop gain, which are linear, from the non-linear amplitude dependent components.

16.9 STABILITY ANALYSIS OF SYSTEM WITH INHERENT REACTOR STABILITY

Before undertaking the study of this system with its non-linear aspects, it is useful to consider briefly the procedure applied to linear systems. The first step in the analysis was the determination of the transfer function of the control variable for small oscillations of the reactor power. If the control variable is temperature, then the transfer function F_T is, by definition

$$F_T \equiv \frac{\delta T_M}{\delta\phi/\phi_o}$$

The reactivity resulting from the response of the control variable is given by a reactivity coefficient α times the change in the control variable.

$$\rho = \alpha\,\delta T_M = \alpha F_T \frac{\delta\phi}{\phi_o}$$

The resulting power oscillation is determined by the reactor transfer function G,

$$\frac{\delta\phi}{\phi_o} = G\rho = G\alpha F_T \frac{\delta\phi}{\phi_o}$$

The stability analysis is carried out by study of the over-all loop gain, $G\alpha F_T$. If this gain is unity with a phase shift which is a multiple of 360 degrees, the system is unstable.

The important parameters may be identified by referring to Fig. 16.11. First, if the error signal amplitude $|\delta T_M|$ is less than the start signal (b), the loop gain is zero since there is no rod motion. When $|\delta T_M|$ exceeds (b), there is some rod motion at constant velocity over part of the positive and part of the negative portions of the error cycle. If (b/a) is unity, the rod reactivity rate is symmetrical with respect to the error wave. Whenever $b/a > 1$, the rod reactivity rate is retarded in phase with respect to the error signal. As the error signal amplitude increases, the fraction of the cycle over which rod motion takes place increases. As the error signal increases, the dependence of the rod velocity on (b/a) is reduced and its phase shift with respect to the error wave is reduced. Thus, the ratio (b/a) becomes unimportant for relatively large values of $\delta T_M/b$.

The analysis on the feedback loop will be treated by resolving the rod reactivity rate wave into a Fourier series and considering only the fundamental term. In this way the gain of the loop can be examined at each frequency. If the presence of harmonics in the system were to result in an instability, this will then be determined when values of the fundamental frequency corresponding to this harmonic are treated. Stated another way, if a rectangular wave of frequency ω can excite an instability of frequency $n\omega$ in the system (where n is an integer) because the rectangular wave contains components of frequency $n\omega$, this instability will be detected when the fundamental frequency is $n\omega$. The only possible source of difficulty is the added gain that the system might have at the frequency $n\omega$. If this were the case, and the rods were driven with a rectangular wave of frequency ω, the system would have an amplified harmonic component circulating in the loop. This would not constitute a stable oscillation of the harmonic frequency and it would disappear when the driving signal was removed. This possibility can be avoided by providing a reasonable gain margin at all frequencies.

Figure 16. 12 illustrates the situation. The temperature error signal, a sinusoidal wave of frequency ω, excites a rectangular wave of rod reactivity rate of frequency ω. The fundamental of the rod reactivity rate wave is the sinusoidal wave shown which lags the error signal. The total added reactivity is the trapezoidal-shaped wave which lies either wholly above or wholly below the axis depending upon whether the initial rod motion was inward or outward. The fundamental component of the total added reactivity is displaced by the average reactivity addition due to the rod motion.

It is convenient for this problem to write the loop gain in terms of the fundamental component of the rod reactivity rate rather than the reactivity itself. The rod reactivity rate as a complex function of time will be denoted as v_1. Now define a reactor transfer function Γ which relates the power amplitude to the reactivity rate

$$\Gamma = \frac{\delta\phi/\phi_o}{v_1}$$

(Since v_1 is simply $j\omega\rho$, the function Γ is very similar to the function G previously used.) If a function is now defined which converts the error signal δT_M to a fundamental component rod reactivity rate, an equation for the loop gain may be written.

$$\text{Loop Gain} = \Gamma\left(\frac{v_1}{\delta T_M}\right) F_T \qquad \text{Eq. (16. 12)}$$

where $\left(\frac{v_1}{\delta T_M}\right)$ indicates the desired conversion function.

To analyze this problem it will be necessary to determine the conversion function $\left(\frac{v_1}{\delta T_M}\right)$ for a variety of values of V, b and a. Some generality can be achieved by noting that the fundamental component rod reactivity rate v_1 is directly proportional to the actual rod reactivity rate V. Thus the conversion function should be defined to yield the dimensionless ratio v_1/V. Furthermore, the fundamental component of the rod reactivity rate must be the same for all waves for which $\delta T_M/b$ and b/a are the same. Thus, the form of the conversion function desired is one which will convert the dimensionless ratio $\delta T_M/b$ to the dimensionless ratio v_1/V. Let the conversion function in this special form be designated as A. Then the equation

$$v_1/V = A\,\frac{\delta T_M}{b} \qquad \text{Eq. (16. 13)}$$

serves to define the conversion function A. A is a function of $\delta T_M/b$ and (b/a). Because the conversion function has been defined in this dimensionless way, the loop gain must contain a factor V/b to adjust the units appropriately. That is, in terms of the conversion function $\left(\frac{v_1}{\delta T_M}\right)$ defined by Eq. (16. 12), $\left(\frac{v_1}{\delta T_M}\right) = \frac{V}{b}\,A$, and

$$\text{Loop Gain} = \Gamma\,\frac{V}{b}\,A\,F_T \qquad \text{Eq. (16. 14)}$$

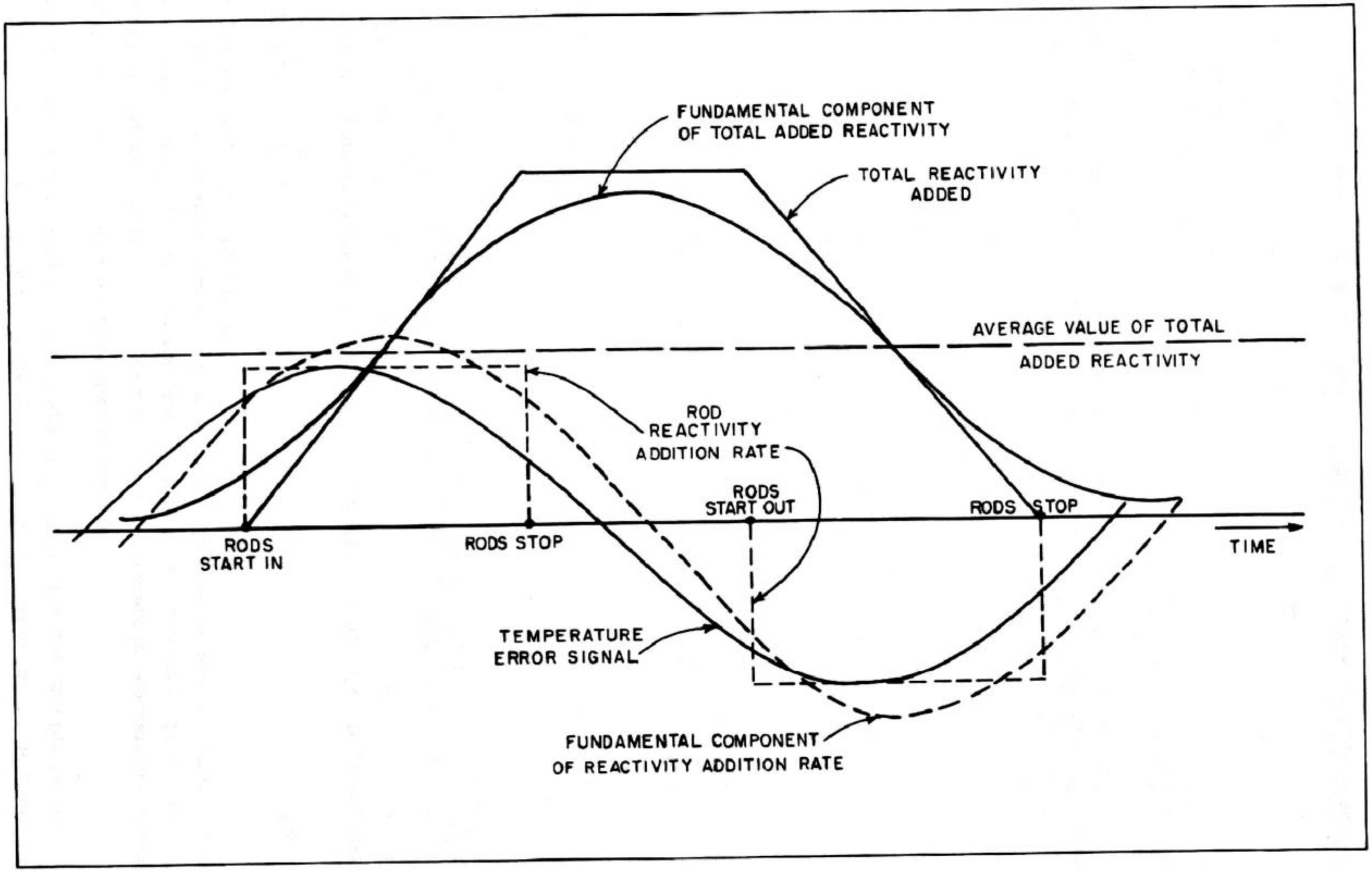

Fig. 16.12 - Diagram Showing Relationship Between Temperature Error Signal, Rod Reactivity Addition Rate and Total Added Reactivity.

The function A can be calculated numerically for assumed parameter values. Figure 16.13 is a plot of the function A for values of $\frac{|\delta T_M|}{b}$ ranging from 1 to 6 and with (b/a) as a parameter. Figure 16.14 is a polar plot of the function A. The cutoff indicated on Fig. 16.14 occurs for a value of $\frac{|\delta T_M|}{b}$ equal to one. The subscript appearing on the A in Fig. 16.14 indicates the value of (b/a). Thus A_2 is the value of A for a (b/a) of two. The numbers in the neighborhood of the plotted points are the values of $\frac{|\delta T_M|}{b}$ for these points indicating functional dependence on amplitude rather than frequency.

In examining the control system for stability, it is convenient to separate the amplitude dependent portion of the loop gain from the other factors in the loop gain. In Eq. (16.14) the function A constitutes the amplitude dependent portion. Now the system is unstable if the loop gain is one or from Eq. (16.14), if

$$(\Gamma F_T)^{-1} = \frac{V}{b} A \qquad \text{Eq. (16.15)}$$

Thus, if the linear portion of the loop gain $(\Gamma F_T)^{-1}$ is plotted on the polar diagram, and if a plot of the non-linear function $\frac{V}{b}A$ is made on the same diagram, the system is stable if the two plots do not intersect.

[redacted]

16.10 SIMULATOR STUDIES OF SYSTEM WITH INHERENT REACTOR STABILITY

The final test of the validity of the design analysis for this system, as with all systems, must be carried out by making transient response studies. [redacted]

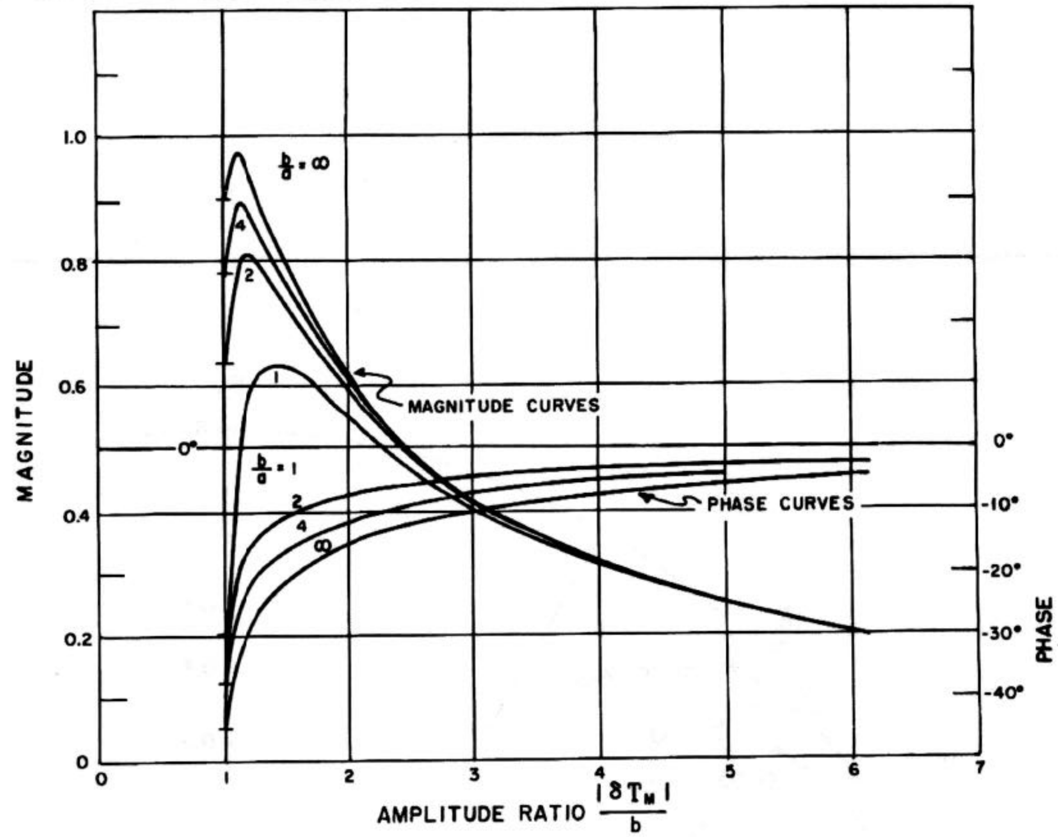

Fig. 16.13 - Magnitude and Phase of the Non-Linear Transfer Function A.

[redacted]

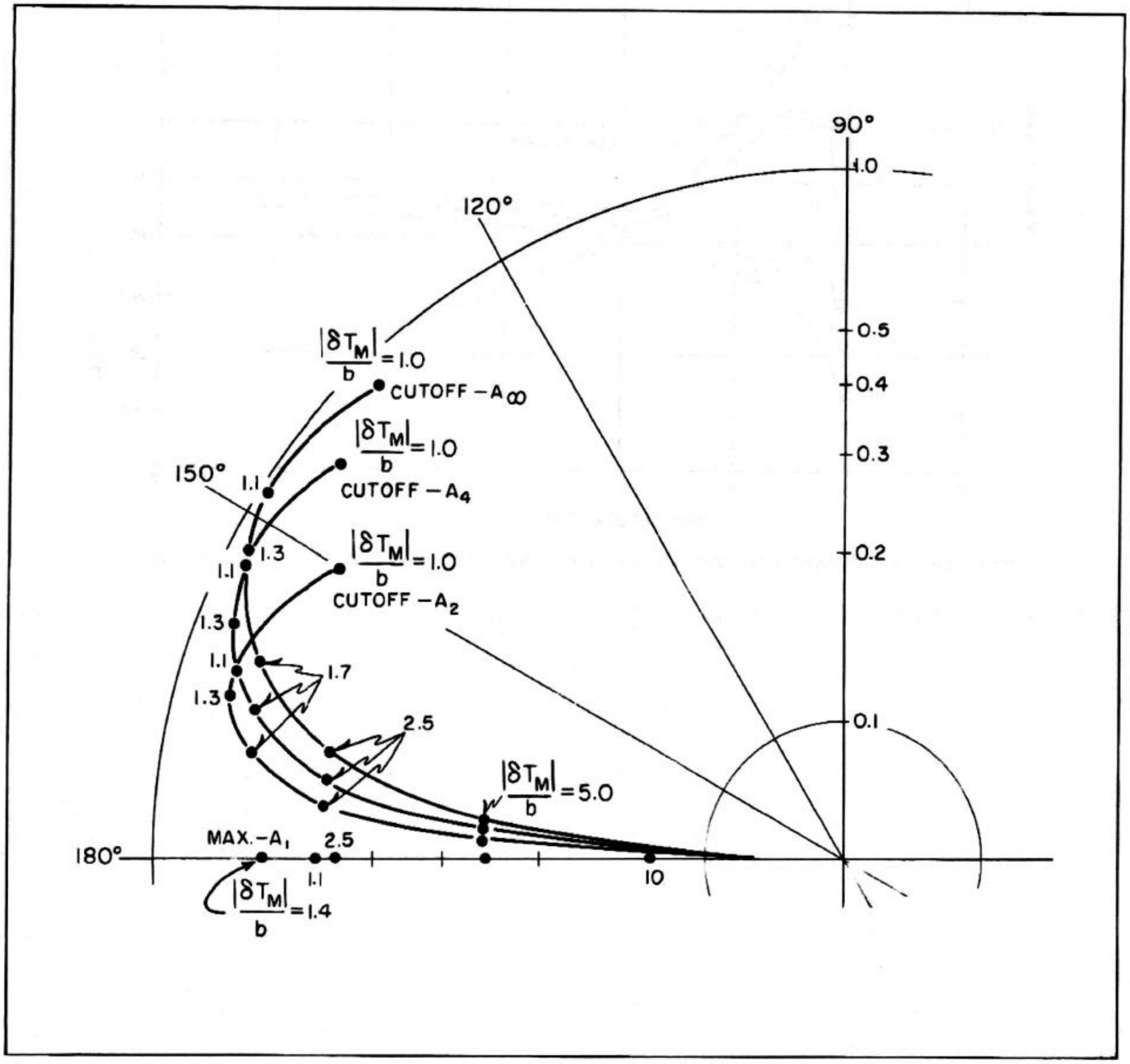

Fig. 16. 14 - Polar Diagram of the Non-Linear Transfer Function A.

[redacted]

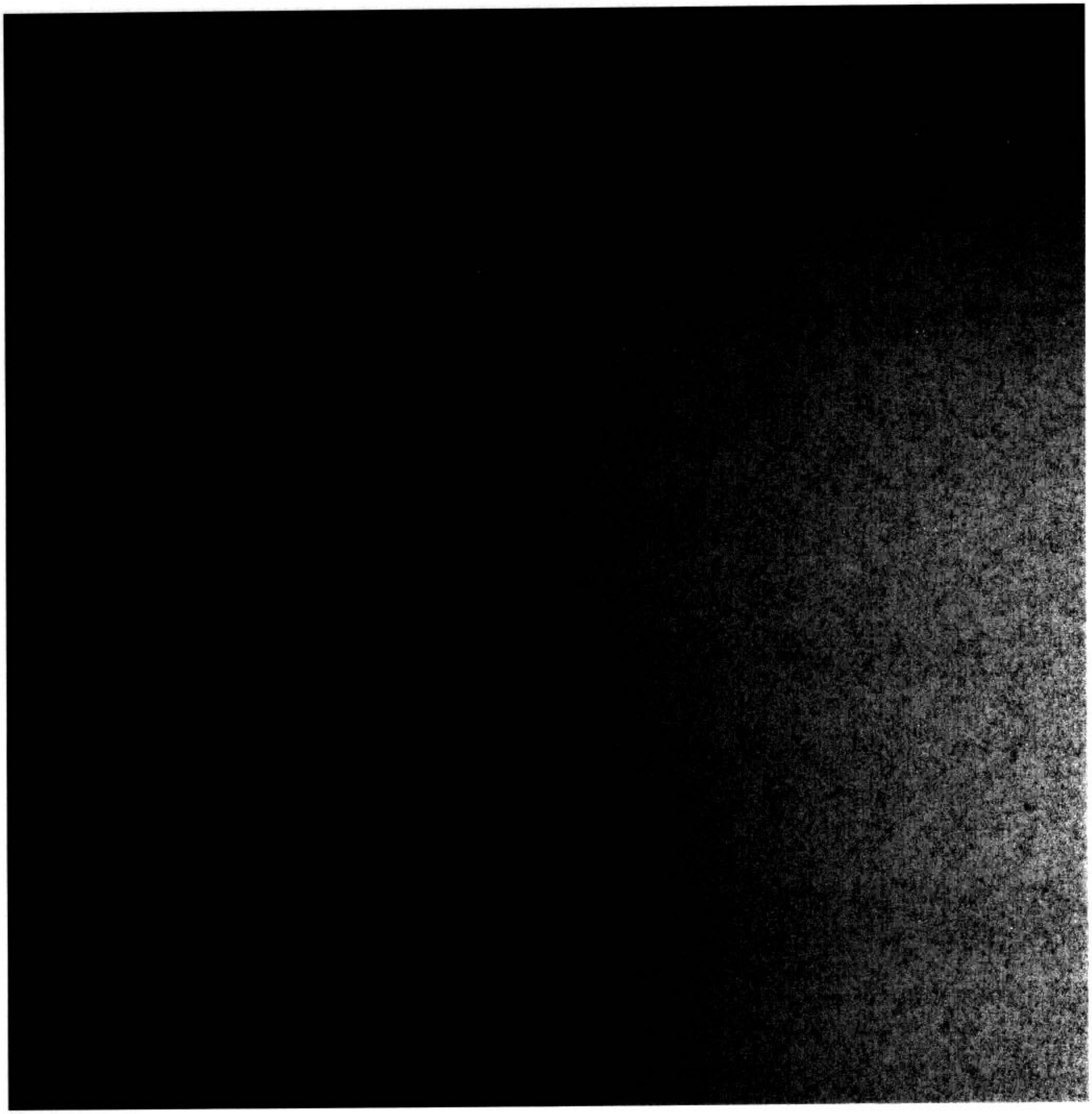

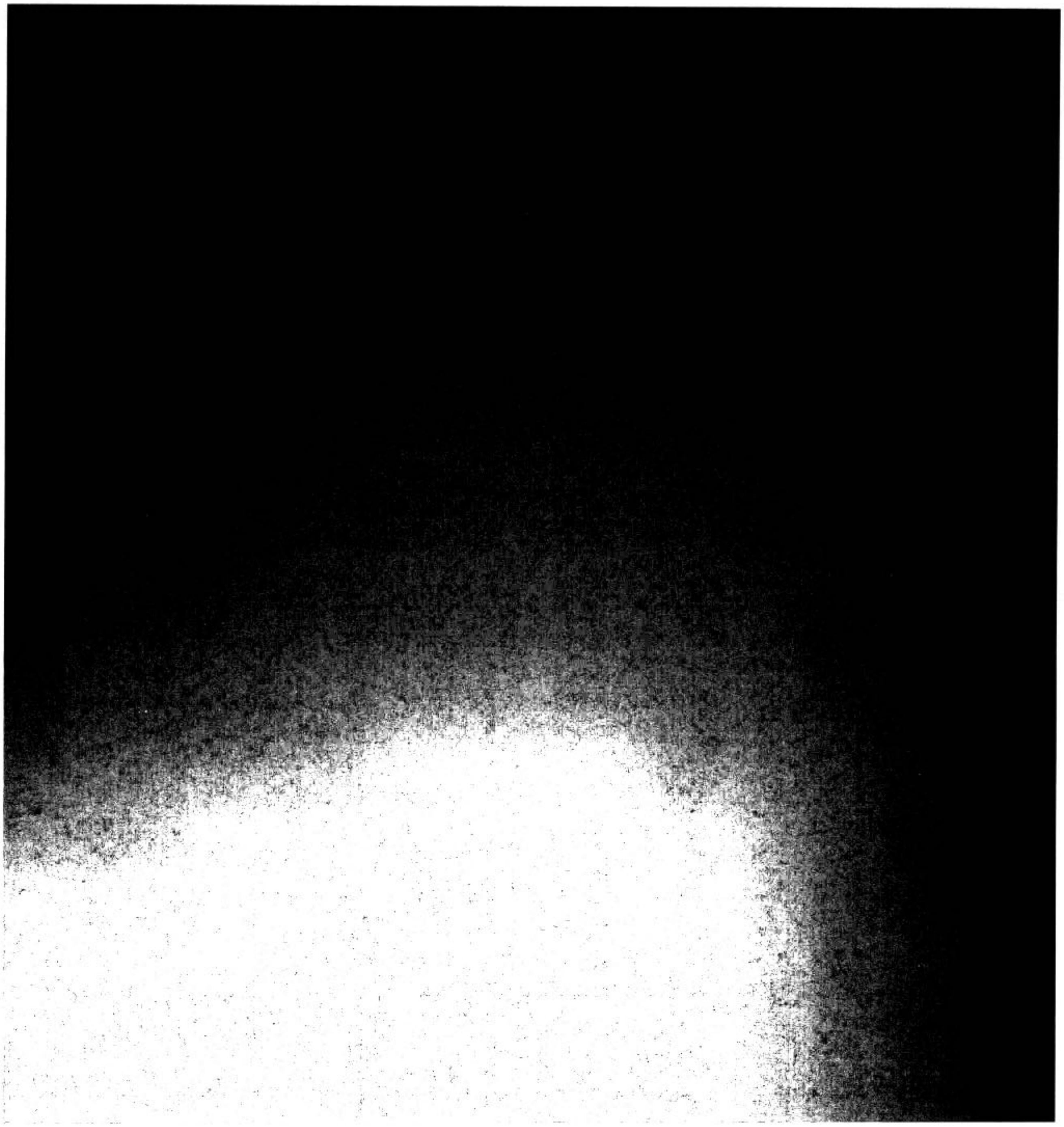

[redacted]

GENERAL REFERENCES

1. J. N. Grace, Synthesis of Control Systems for Nuclear Power Plants, Institute of Radio Engineers Convention Record, March 1954.
2. R. J. Kochenburger, A Frequency Response Method for Analyzing and Synthesizing Contactor Servomechanism, American Institute of Electrical Engineers Transactions, Vol. 69, 1950.
3. H. M. James, N. B. Nichols, and R. S. Phillips, Theory of Servomechanisms, McGraw-Hill Book Co., New York, 1947.
4. M. A. Schultz, Control of Nuclear Reactors and Power Plants, McGraw-Hill Book Co., New York, 1955.

Part VI

SPECIAL TOPICS IN THE NUCLEAR DESIGN OF PRESSURIZED WATER REACTORS

This part of the handbook treats two special problems in the nuclear design of pressurized water reactors. These are, first, reactor control, particularly the calculation of control rod worth and, second, synthesis methods. Both are important in the design of reactors and, for this reason, the design descriptions given in Parts I and II have referred to methods of treating these problems. There is a tendency, however, in the earlier chapters to concentrate on the results of design studies. For this reason, it seemed advisable to discuss the design techniques themselves in a separate part of the handbook.

The methods of calculating control rod worths are perhaps the most unsatisfactory aspect of the technology of nuclear design. While the problem of calculating control rod worth is a formidable one if the requisite precision is to be achieved, an even more serious difficulty is the absence of an adequate body of experimental information with which to test the theory. This information does not yet exist in sufficient range and variety to be considered satisfactory. For that reason, the control-rod worth calculations are not yet established as reliable design techniques.

There are basically two problems in the analysis of control rod worth. One is the calculation of the neutron absorption of a single rod. The other is the calculation of the effect of interaction of control rods upon each other. This latter problem is handled in three ways. In the first method, the effect of rods is calculated by representing the rods explicitly in the over-all reactor. While there are certain analytical techniques for carrying this out,[1] they are limited to rods which are circular cylinders and which are arranged in concentric circles. For pressurized water reactors, the most satisfactory explicit technique has been numerical computation using digital computers.

The second method of calculating control rod interaction is sometimes called a cell meth-of. In this technique the control rod is associated with an appropriate volume of the reactor and its neutron absorption, both fast and slow, is represented as a distributed poison within the cell of reactor material. The over-all reactor is then treated as an assembly of cells which may or may not be poisoned. This latter treatment simplifies the over-all reactor calculation. There remains, however, the problem of calculation of the single control rod in its cell of reactor material.

The third method of calculating control rod interaction is a combination of these techniques. Through a cell calculation an equivalence is established between the rod shape used in the reactor design and another shape which may be handled more readily. Most frequently the rods have been transformed into equivalent circular cylindrical rods. The interaction problem is then treated by calculating the reactor with the array of equivalent rods.

The treatment of the single control rod within a cell of material poses a number of difficulties. First, the choice of the appropriate cell volume is not always clear. Second, there is the question of treating the complex rod geometry. Third, the problem arises as to what boundary conditions should be applied at the rod surface for the thermal neutron group. Fourth, there is the matter of appropriate group constants, or some alternate treatment, for the epithermal absorption which usually involves resonances. The latter two problems have been treated to some extent in Chap. 14 where the worth of a sheet of control material is calculated free of geometrical complications. This treatment, as is the case with other parts of control theory, is not yet fully developed or tested.

The chapter on control-rod worth calculation is, therefore, fragmentary in nature. Various methods of treating parts of the problem are developed but no complete and unified treatment is available.

Chapter 18 deals with synthesis techniques for making psudeo three-dimensional calculations of reactors by combining one- and two-dimensional calculations. Originally, these methods were developed out of necessity since no multi-dimensional reactor calculational technique was available. While this is no longer true, it appears that synthesis methods will continue to be important. Primarily, this comes about because they are faster and, therefore, less costly than full three-dimensional calculations. Their field of application will be in survey studies, where precision is not extremely important, and in determination of the approximate criticality conditions prior to running full scale three-dimensional calculations. In Chap. 18 two basically different synthesis schemes are presented. These are the flux-weighted average synthesis method and the axial-line synthesis method. Both have been widely used for reactor design purposes.

REFERENCES

1. H. L. Garabedian, Control Rod Theory for a Cylindrical Reactor, Report WAPD-18, August, 1950.

Chapter 17

THE TREATMENT OF REACTOR CONTROL

17.1 INTRODUCTION

This chapter deals with the problem of assessing the control design of a reactor. By its fragmentary character this chapter reflects the incomplete state of development of this subject. [redacted]

The first topic treated in the chapter is the application of diffusion theory to calculate the neutron capture in a control rod. This method is widely used for calculation of the thermal neutron capture in the rods because control rod materials are black in the thermal neutron range and the resulting boundary conditions for the calculation are relatively easy to apply. The use of digital computation has made it relatively simple to use this method for computing neutron capture in control rods. Explicit rod representation is discussed, followed by a treatment of the cell-type of calculation.

The next topic treated is the area absorption method of calculating control rod worth. This method, also a diffusion type treatment, was developed primarily to enable equivalence to be established between control rods of different shapes. Thus, the actual control rods used in a reactor may be replaced by rods of a different shape whose worth may be more readily calculated. Following the theoretical discussion, experimental results are presented.

The next topic treated is the empirical determination of the equivalent cross section of control rod materials for capture of epithermal neutrons. Because of the complicated resonance structure of common control rod materials in the epithermal range, the calculation of equivalent capture cross sections is difficult. Two treatments of the empirical determinations are presented, based on independent experimental information.

Next, some experimental data are presented on the relative worth of coupons of various control rod materials. Such data are of importance in screening possible control materials.

[redacted]

DIFFUSION THEORY CALCULATION OF CONTROL RODS

by A. F. Henry

17.2 OVER-ALL EFFECT OF RODS IN THE REACTOR

There are two classes of problems associated with control rods. These are as follows:

1. The number, size, and location of control rods in a reactor required to maintain the reactor subcritical by a fixed amount when the rods are inserted in the reactor. An important sub-case is the calculation of the reactor with individual rods removed.

2. The power distribution in the reactor which results from a given configuration of control rods in the critical reactor.

This distinction is convenient since a solution of the shutdown problem requires only a two-dimensional calculation (the rods being fully inserted), whereas a comparably accurate computation of power distribution is generally a problem in three dimensions.

Since the largest part of nuclear design is carried out by the use of diffusion theory, it is natural to consider the application of a diffusion theory treatment to the calculation of control rod problems. This, in fact, has been the approach adopted for the calculation of control rod worths from the earliest development of reactor theory. The existence of diffusion-type digital computer codes such as those described in Appendices A and B makes it convenient to apply this method for pressurized water reactors.

The over-all properties of the reactor with control rods present are calculated by treating the control rods as boundaries in the diffusing media or as separate media having certain equivalent diffusion properties. [redacted]

There are difficulties, however. First, the approximate boundary conditions or equivalent diffusion constants must be known. Second, the capacity of the digital computer may limit the explicit representation of the entire complement of control rods.

Considering the latter point first, an IBM-704 computer with the largest internal memory unit available, 32,000 words, permits a total of 6500 mesh points on the PDQ two-dimensional code. [redacted] Some advantage can be taken of non-uniform point distribution but it is questionable whether a full complement of inserted control rods could be adequately represented on such a mesh. Additional mesh points can be obtained by use of the Cuthill two-dimensional code for the NORC which permits a mesh approximately 100 x 200 by the use of external tapes for memory.

For small cores, an explicit representation of all control rods inserted may be feasible on a two-dimensional diffusion code. In many cases such representation is not feasible so that recourse must be had to cell methods. These will be discussed in the following section.

In the application of diffusion theory to control rod worth problems both the use of boundary conditions on the rod and equivalent diffusion constants within the rod media have been used. It is customary to use the boundary condition for the thermal neutron group. The rods are treated as black in the thermal group with the logarithmic derivative of the thermal group flux taken as $1/0.71\lambda_{tr}$ at the rod surface. For the fast group of a two-group theory, or the resonance group of a four-group theory, the rod is treated as a diffusion medium having a diffusion constant and effective absorption cross section. The method of obtaining the constants analytically is discussed in Chap. 14. Empirical techniques for establishing effective values of these parameters are discussed later in this chapter.

It is assumed in this treatment that the boundary conditions or effective diffusion properties of the control rod material are, for practical purposes, independent of the control rod geometrical shape or of the size of the reactor, and depend only upon the control rod material, the control rod thickness and the reactor material in which the control rod is located. With this assumption, the values of the appropriate boundary conditions and effective diffusion constants may be computed or measured using the most convenient geometric configuration and then applied to a wide range of configurations.

In summary, explicit calculations of reactor shutdown can be made with diffusion theory using appropriate boundary conditions and effective diffusion constants for the control rod surface. Such calculations are limited by the capability of the computer code to accept sufficient mesh points to permit adequate representation of the rod number, size, thickness, and location. Explicit representation of control rods is possible in certain reactors, but not for others. For the others, cell methods are used.

17.3 CELL METHOD OF CALCULATING THE EFFECT OF CONTROL RODS

In the cell method the control problem is calculated in two steps. First, the control rod is associated with a given fraction of the core volume, the cell. Then, using a diffusion theory calculation, the fraction of the neutrons slowing down in the cell which are captured in the rod is calculated. Next, equivalent macroscopic poison cross sections, both thermal and epithermal, are calculated whose magnitudes are such that when distributed homogeneously throughout the cell, the same fraction of neutrons is captured in the distributed poison as is captured by the actual rod. In the final step, the reactor is represented as a group of cells, with or without rods as the case may be, and a calculation of its over-all properties carried out.

The cell procedure has several advantages for survey studies in terms of flexibility and versatility. The worths of rods in a range of reactor material may be determined in terms of homogeneous poison and a large range of reactor problems studied without repeating the rod worth calculation. For many purposes, in fact, the specific rod geometry need not be considered until the desired rod worth in terms of distributed poison has been established. The chief advantage of the cell method, however, is its applicability to problems in which explicit rod representation is not possible.

The cell method does have some weaknesses. First, the effect of the control rod on the leakage from the reactor may not be correctly represented by the homogeneous cell poison. Second, the interaction between control rods may not be correctly represented.

The choice of cell volume is somewhat arbitrary and is generally made intuitively. For cross-shaped control rods distributed uniformly throughout a uniformly loaded cylindrical core, one choice is to associate with each control rod a volume equal to the total core volume divided by the total number of rods. Another choice is to associate each control rod with its fuel cluster. [redacted]

Once the volume associated with a control rod is determined, the corresponding homogeneous poison is found from cell theory. That is, the rod plus that volume of core material associated with it are treated as a composite region from which there is no net leakage of neutrons. For a cell, if the rate at which neutrons of a given energy group appear per unit volume is q, the fraction of neutrons absorbed in the rod is the net leakage rate across the surface of the rod $\left(\int_S D\nabla\phi\cdot d\underline{S}\right)$ divided by the net production rate in the cell $\left(\int_V q\,dV\right)$. Then, if Σ is the average macroscopic cross section for neutron removal by absorption (or energy degradation plus absorption if the group is not thermal), the homogeneous poison cross section Σ_p equivalent to the control rod is determined by the relationship

$$\frac{\Sigma_p}{\Sigma_p + \Sigma} = \frac{\int_S D\nabla\phi\cdot d\underline{S}}{\int_V q\,dV} \qquad \text{Eq. (17.1)}$$

The flux, ϕ, is determined by solving the diffusion equation

$$D\nabla^2\phi - \Sigma\phi + q = 0 \qquad \text{Eq. (17.2)}$$

subject to the cell boundary condition $\nabla\phi\cdot\underline{n}_1 = 0$, $\underline{n}_1$ being a unit vector in the direction of the surface of the cell. The other boundary condition involving the current across the rod surface depends on the nature of the rod material and the energy group involved.

The source term, q, may be represented in several ways depending on the specific problem at hand and the amount of numerical complexity acceptable. The simplest procedure is to make q a constant everywhere outside of the control rod. The next degree of complexity is applicable to situations wherein various regions of the cell have moderator fractions differing from one another. In such cases the source term may be taken everywhere proportional to the moderator volume fraction. Finally, if epithermal absorption and the attendant flux dip near the rod are important, q may be taken as the spatially dependent neutron transfer rate from higher energy groups. In this case equations similar to Eq. (17.2) are written for each energy group, the source term for the i^{th} group being given in terms of the removal cross section and flux of the (i-1)st group. Thus,

$$q_i(\underline{r}) = \Sigma_r^{(i-1)}(\underline{r})\,\phi^{(i-1)}(\underline{r}) \qquad \text{Eq. (17.3)}$$

where $\underline{r}$ denotes spatial position and Σ_r is the macroscopic removal cross section from the (i-1)st group. In this latter procedure, if three or four energy groups are used, the source term for the highest energy group may be taken as spatially constant.

It is quite unlikely that the equivalent poison cross section given by Eq. (17.1) correctly specifies the fraction of neutrons absorbed by the rod in the actual core since the cell boundary conditions are not fulfilled in the reactor. Further, as noted above, even if Σ_p does give the fractional absorption correctly, there is no reason to suppose its use will yield the correct shutdown since in general its effect on over-all leakage of neutrons from the core will differ from that of the actual rods.

17.4 EXAMINATION OF VALIDITY OF CELL METHOD

As a first step in examining the validity of computing shutdown by cell theory, a series of simple slab calculations were performed.[1] Four uniformly loaded bare slab cores were assumed to be controlled by thin, evenly spaced sheets of control rod material with one, two, three, and four sheets as shown in Fig. 17.1. Loadings were computed by two-group diffusion theory so that the cores were very nearly critical with the control slabs present. These solutions were obtained by digital computer methods.

Next, the cell theory was applied to these cases. The cell sizes shown in Fig. 17.1 were used. Shutdown was calculated from the two-group bare core formula using a homogeneous Σ_p determined from Eq. (17.1). The results are compared to the explicit solution results in Table 17.1. This table presents the effective k of the uncontrolled reactor, the k_{eff} of the reactor with explicit representation of control rods, and the k_{eff} with control as calculated by cell theory. The k_{eff} fractional error in the last column is defined as

$$\frac{k_{eff}(\text{exact}) - k_{eff}(\text{cell})}{k_{eff}(\text{uncontrolled}) - 1}$$

This is a measure of how well the entire control worth is calculated.

Table 17.1--COMPARISON OF CELL METHOD COMPUTATIONS OF SHUTDOWN WITH EXACT SOLUTIONS FOR THERMALLY BLACK SHEETS OF CONTROL MATERIAL IN BARE SLAB CORES

No. of Control Slabs	k_{eff} of Uncontrolled Core	k_{eff} with Control Present		k_{eff} Fractional Error
		Explicit Rod Solution	Cell Solution	
1	1.132	0.999	1.057	- 0.44
2	1.152	1.025	1.017	0.053
3	1.218	1.033	1.024	0.041
4	1.259	1.011	1.011	0.000

In the results shown in Table 17.1, only thermal absorption was taken into account. Similar results have been found with epithermal absorption.

The cell method can apparently give good results if the cell dimensions are not too large. The results are quite poor, however, if as in the first case, the cell is taken to be the entire reactor. In the case of the single control sheet, it is necessary to choose the size of the cell associated with the control sheet to be smaller than the entire core size and thus to distribute its poison equivalent over a region smaller than the entire core.

The cell method has also been examined for a seed-blanket core consisting of a central highly enriched slab blanketed by slabs of equal thicknesses of core material containing natural uranium. A single central control sheet was used in the reactor. Three different seed thicknesses were calculated. The loading of the seed was chosen in each case so that the core was approximately critical with the control sheet present. A cell equal in size to the entire seed was then chosen and the Σ_p corresponding to the control sheet was computed. With the resultant value of Σ_p present in the seed only, shutdown was again calculated. Results for thermally black control material appear in Table 17.2.

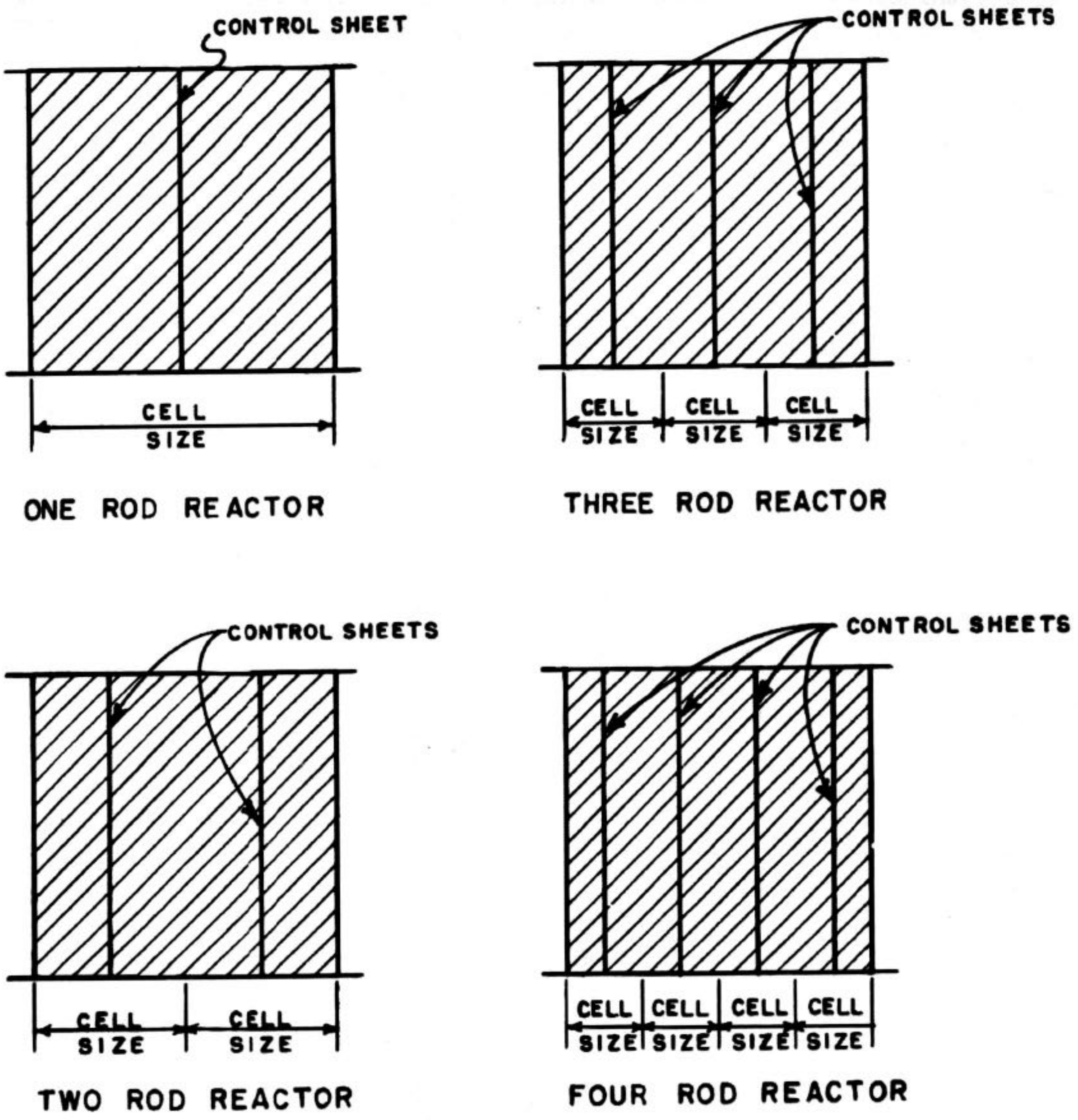

Fig. 17.1 - Slab Reactors Used to Study Validity of the Cell Method.

Table 17.2--COMPARISON OF CELL METHOD COMPUTATIONS OF SHUTDOWN WITH EXACT SOLUTIONS FOR THERMALLY BLACK CONTROL SLABS IN SLAB SEED CORES

Thickness of Seed (inches)	k_{eff} of Uncontrolled Core	k_{eff} with Control Present		k_{eff} Fractional Error
		Explicit Rod Solution	Cell Solution	
4.0	1.259	0.983	0.996	- 0.050
6.0	1.180	0.991	1.008	- 0.094
8.0	1.133	0.989	1.007	- 0.135

The results for control slabs which absorbed fast as well as thermal neutrons were similar to those tabulated.

The fact that these one-dimensional studies give reasonably satisfactory results when the boundaries of the cell are not too far from the surface of the rod is encouraging. [redacted]

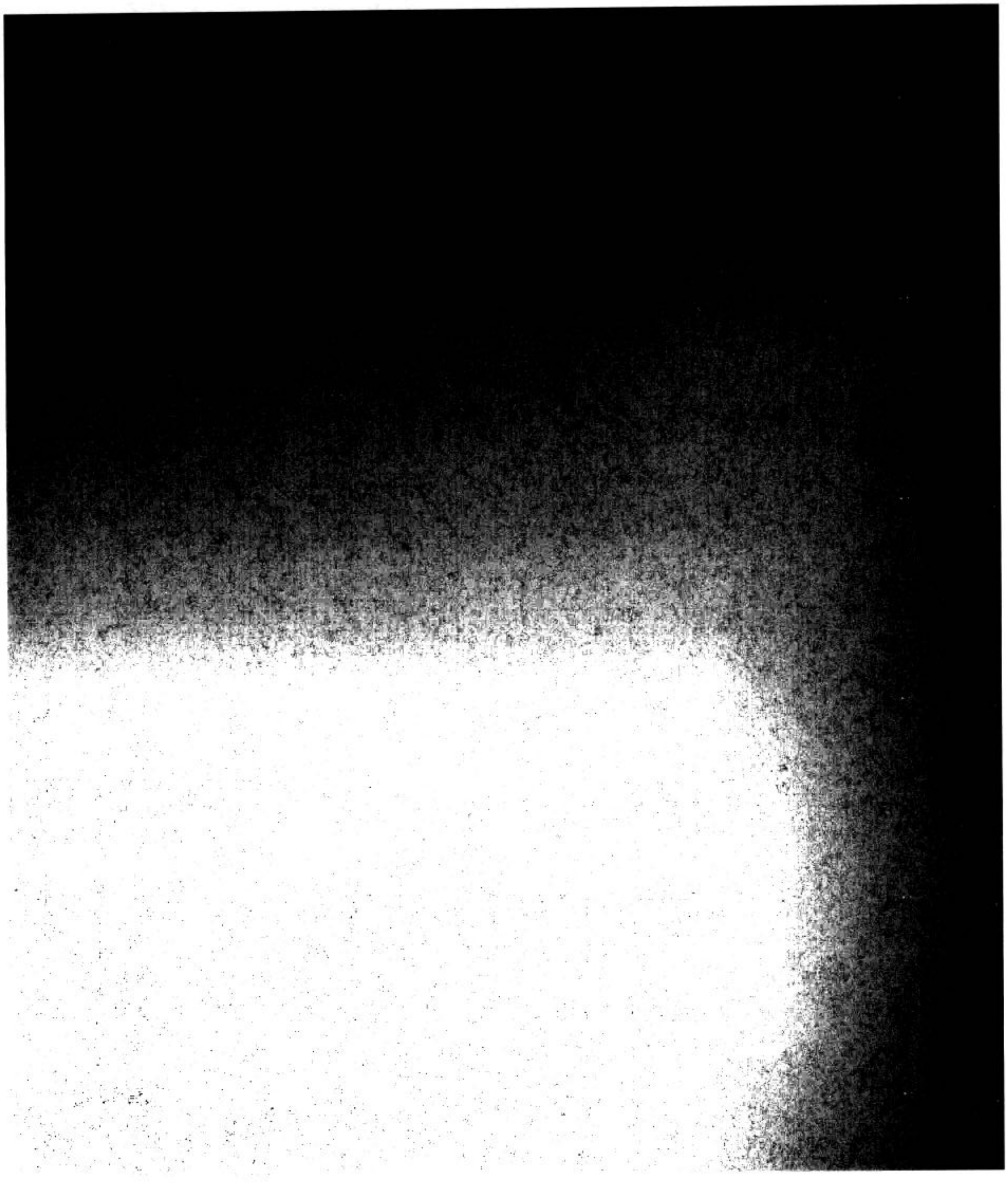

[redacted]

THE AREA ABSORPTION TECHNIQUE FOR CALCULATING ROD WORTH

by H. E. Stevens

17.6 INTRODUCTION

The area absorption technique is an analytical method of calculating the worth of control rods of various shapes. It is similar to the preceding treatment in that it is based essentially on diffusion theory with transport theory corrections introduced for boundary conditions. It is a particularly convenient technique for calculating the equivalence between rods of various geometric shapes. Several topical reports describing the theory and technique are available.[3, 4, 5]

In the area absorption method, it is assumed that in the cell of reactor material the slowing-down density is independent of position in the neighborhood of the rod. One-velocity diffusion theory is used to calculate the absorption of the control rod in the thermal group.

The results of the calculation are expressed in terms of an absorption area C. This area is defined as the ratio of the number of neutrons absorbed by the rod per unit length per unit time to the number of neutrons thermalized per unit time per unit volume outside the rod. No thermalization is assumed to occur in the rod itself. The absorption area C is related to the distributed homogeneous cross section Σ_p of the preceding treatment (see Sec. 17.3) by the equation

$$\frac{C}{A} = \frac{\Sigma_p}{\Sigma_p + \Sigma} \qquad \text{Eq. (17.7)}$$

where A is the cross-sectional area of the cell excluding the area of the rod itself.

17.7 ANALYTICAL RESULTS FOR SPECIAL SHAPES

Only a brief summary of the analytical results will be given here. A detailed exposition of the analysis is presented in the original paper (see Reference 3).

The absorption area of certain simple geometric shapes may be calculated analytically by solving Eq. (17.2) with a spatially uniform source subject to the condition that the flux vanishes at the surface of the rod, i.e., assuming the rod to be thermally black. For a circularly cylindrical, thermally black rod of radius R in an infinite medium, the diffusion approximation yields

$$C = 2\pi RL \frac{K_1(R/L)}{K_o(R/L)} \qquad \text{Eq. (17.8)}$$

where $K_j(\nu)$ is the modified Bessel function which vanishes at infinity, and L is the diffusion length. For small values of R/L, Eq. (17.8) becomes

$$C = \frac{2\pi L^2}{\log_e \frac{2L}{\gamma R}} \qquad \text{Eq. (17.9)}$$

with $\gamma = 1.781$; for large values of R/L, the equation becomes

$$C \cong (2\pi R + \pi L)\, L \qquad \text{Eq. (17.10)}$$

(a) Limit of Large Diffusion Length. The values of absorption area for simple rod geometries in the large L limit may be obtained by standard methods of conformal mapping. These are given in Tables 17.4 and 17.5 in terms of r_{eff}, the radius of the equivalent circular cylindrical rod. Values of C, the absorption area, may be obtained by substituting the values of r_{eff} for R in Eq. (17.8). The geometry of the simple rod shapes calculated is shown in Fig. 17.3. This figure shows the geometry of the rod section. All rods are cylinders.

Table 17.4--VALUES OF r_{eff} FOR CERTAIN SIMPLE ROD SHAPES (LARGE L LIMIT)

Rod	r_{eff}
Ribbon	$\ell/2$
Cross	$\ell/\sqrt{2}$
Ellipse	$a + \ell/2$

Table 17.5--VALUES OF r_{eff} FOR RECTANGULAR ROD

a/ℓ	r_{eff}/ℓ
0.0	0.50
0.0864	0.5464
0.4438	0.7878
0.7936	0.8076
1.0170	0.8802
1.2836	0.9640
1.606	1.0628
2.000	1.1804

(b) Limit of Small Diffusion Length. In the limit of small diffusion length L, the rod surface may be considered to be a plane in the first approximation so that the absorption area is equal to the perimeter times L.

$$C = L \cdot (\text{perimeter}) \qquad \text{Eq. (17.11)}$$

For rods of arbitrary cross section, it is possible to obtain a correction to Eq. (17.11) of the order of L^2. In the expansion of the absorption area in powers of L, the term L^2 may be considered as arising from a correction of order L to the rod perimeter. This is developed below.

If L is sufficiently small, the control rod cross section may be regarded as a polygon,

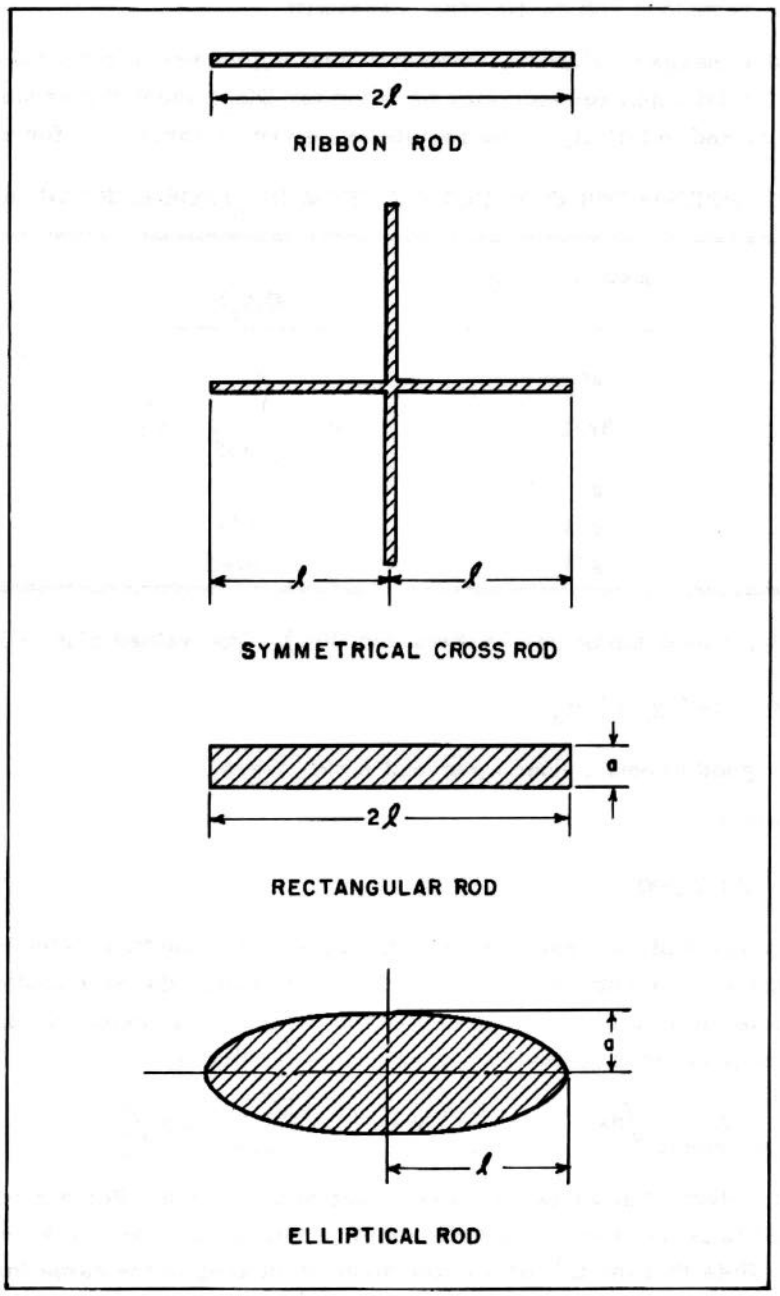

Fig. 17.3 - Sketches of Simple Rod Shapes.

each of whose sides is large compared with L. For this condition to be possible, the radius of curvature of the curved portions of the control rod surface must be everywhere large compared with L. If the diffusion length is small compared with the distances between corners of the equivalent polygon, the interaction between corners may be neglected so that each corner makes its own separate contribution to the change in effective perimeter. Thus for small L, the absorption area C is given by

$$C = L\left[\text{perimeter} + L \sum_{\text{corners}} D(\alpha_o)\right] + \text{Terms of Order } L^3 \qquad \text{Eq. (17.12)}$$

where L $D(\alpha_o)$ is the change in effective perimeter due to a corner of external angle α_o.

A solution to the diffusion equation may be found for $D(\alpha_o)$ under the assumption that the sides of the angle extend to infinity. The results are given in Table 17.6 for specific angles.

Table 17.6--PERIMETER CORRECTION TERM $D(\alpha_o)$ FOR CERTAIN ANGLES

Exterior Angle α_o	$D(\alpha_o)$
2π	1
$3\pi/2$	$4/3\pi\left[\frac{4\pi}{3\sqrt{3}} - 1\right]$
π	0
$\pi/2$	$-4/\pi$
$\pi/3$	$-4/\sqrt{3}$

Certain limiting expressions may be given for $D(\alpha_o)$. For values of $\alpha_o \to 0$

$$D(\alpha_o) \cong -(4 \log_e 2)/\alpha_o \qquad \text{Eq. (17.13a)}$$

This expression is good to better than 5 per cent for $\alpha_o \leqq \pi/5$.

When α_o is near π,

$$D(\alpha_o) \cong 1/2\,(\alpha_o - \pi) \qquad \text{Eq. (17.13b)}$$

This expression means that, for any section of the control rod surface which has a radius of curvature everywhere large compared with the diffusion length, the contribution to the change in effective perimeter is equal to L times half of the net change in external angle. Thus, for a control rod whose perimeter is made up of segments of curves,

$$C \cong L\left[\sum_{\text{segments}} \int ds \left(1 + \frac{L}{2\rho}\right) + L \sum_{\text{corners}} D(\alpha_o)\right] \qquad \text{Eq. (17.14)}$$

where ds is the arc element and ρ is the local radius of curvature. For a circular rod, the effective perimeter is larger than the actual perimeter by L times $2\pi \times 1/2$, in agreement with Eq. (17.10). Note that the L^2 term in the absorption area is the same for all rods without sharp corners.

(c) Intermediate Diffusion Length. For cases in which neither the large nor the small diffusion length approximations are valid, it is often possible to obtain accurate numerical values of the absorption area by means of variational expressions. Variational expressions of two types are used. One provides an upper bound and the other a lower bound to the absorption area. Solutions have been found for the ribbon rod and for the symmetrical cross rod.

The results for the ribbon rod are given in Table 17.7. The first column, labeled Large Diffusion Length Limit, lists the result obtained when $R = r_{eff} = \ell/2$ is substituted in Eq. (17.8) to obtain C. The second column, labeled Small Diffusion Length Limit, is obtained using Eq. (17.12) with $\Sigma D(\alpha_o) = 2$. The other two columns list variational results. Results are given as the ratio $C/4\ell L$.

Table 17.7--ABSORPTION AREA FOR THERMALLY BLACK RIBBON

$L/2\ell$	$C/4\ell L$			
	Large Diffusion Length Limit	Small Diffusion Length Limit	Variational (Lower Bound)	Variational (Upper Bound)
0.2	1.061	1.200	1.175	1.200
0.5	1.407	1.500	1.468	1.496
1.0	1.909	2.000	1.934	1.965
2.0	2.786	3.000	2.782	2.819
5.0	5.021	6.000	4.984	5.054
10.0	8.244	11.000	8.15	8.367

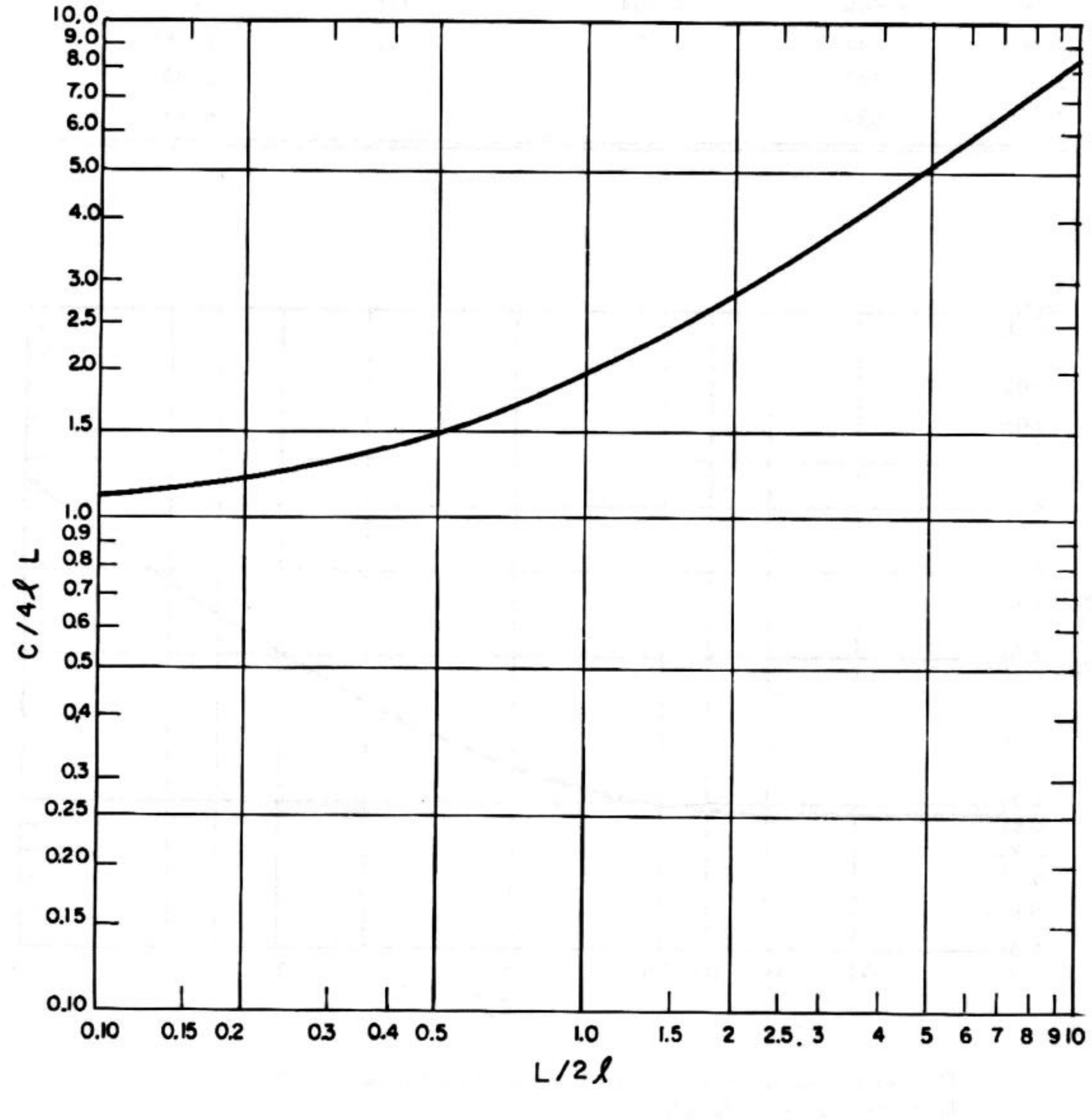

C is absorption area; ℓ is half width of ribbon;
L is the diffusion length.

Fig. 17.4 - Absorption Area for Thermally Black Ribbon (best estimate).

A best estimate result, intermediate between the variational bounds, is plotted in Fig. 17.4.

The equivalent results for the symmetrical cross-shaped rod are given in Table 17.8 and Fig. 17.5. For the Large Diffusion Length Limit, Eq. (17.8) was used with $R = r_{eff} = \ell/\sqrt{2}$. For the Small Diffusion Length Limit, Eq. (17.12) was used with $\Sigma D(\alpha_0) = -1.09$.

Table 17.8--ABSORPTION AREAS FOR THERMALLY BLACK CROSS-SHAPED ROD

	C/8ℓL			
L/2ℓ	Large Diffusion Length Limit	Small Diffusion Length Limit	Variational (Upper Bound)	Variational (Lower Bound)
0.1	0.630	0.973	0.973	--
0.2	0.697	0.945	0.960	--
0.5	0.880	0.864	1.025	--
1.0	1.148	0.727	1.232	1.185
2.5	1.833	--	--	1.821
10.0	4.529	--	--	4.44

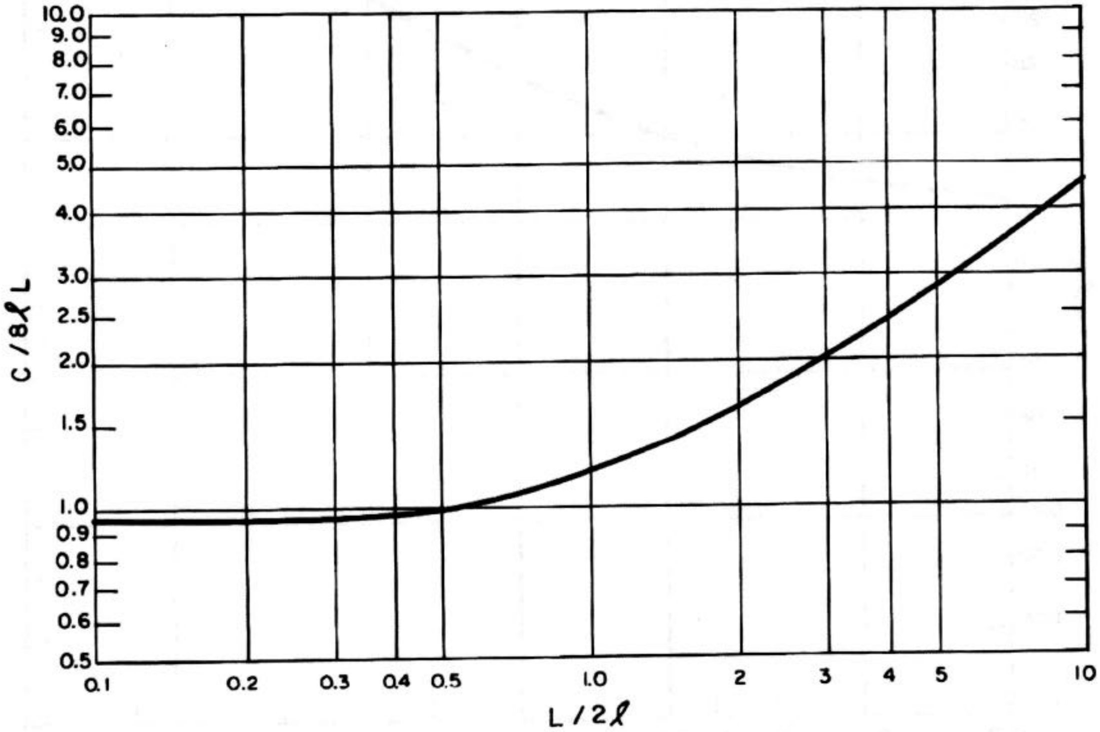

C is absorption area; ℓ is half-span of rod (Fig. 17.3);
L is the diffusion length.

Fig. 17.5 - Absorption Area for a Thermally Black Cross (Best Estimate).

(d) Boundary Condition Correction. The preceding results have been calculated by diffusion theory on the basis that the flux vanishes at the surface of the control rod. A transport theory correction to this calculation can be made by using diffusion theory, as before, in the medium outside the rod but applying a logarithmic boundary condition at the surface of the absorbing rod (see Eq. (17.5)). If the reciprocal of the logarithmic derivative is denoted as δ,

$$\frac{1}{\phi}\frac{\partial\phi}{\partial n} = \frac{1}{\delta} \qquad \text{Eq. (17.15)}$$

The value of the absorption area for a circularly cylindrical rod of radius r_o is given by an expression similar to Eq. (17.8), but slightly modified.

$$C = \frac{2\pi r_o L}{\dfrac{K_o\left(\frac{r_o}{L}\right)}{K_1\left(\frac{r_o}{L}\right)} + \dfrac{\delta}{L}} \qquad \text{Eq. (17.16)}$$

Values of δ/λ_{tr} for cylindrical surfaces range from 0.71 for large r_o/λ_{tr} to 1.33 for small values of r_o/λ.[3,6] These may be used when L is large compared to both r_o and λ_{tr}. If L is large compared to λ_{tr} but r_o and L are comparable, the rod surface may be treated as a plane surface in computing δ. For the limit r_o/L and L/λ_{tr} both large compared to unity, the absorption area is equal to the perimeter times $(L - 0.71\lambda_{tr})$.

17.8 AREA ABSORPTION THEORY FOR GRAY CONTROL RODS

The preceding section discussed the area absorption theory for control rods which are black to thermal neutrons. Similar results can be obtained for gray control rods under the assumption that the diffusion length L is small compared to the rod dimensions. The development is carried out using diffusion theory and the concept of self-shielding factors.[7]

For a nonblack absorber slab, the current of neutrons j^- which emerges from the opposite side of a slab into which a neutron current j^+ is directed is

$$j^- = j^+ (1 - 2f\,\Sigma t) \qquad \text{Eq. (17.17)}$$

where Σ is the macroscopic absorption cross section of the absorber,

t is the thickness of the absorber,

f is the self-shielding factor for slabs corresponding to the value of Σt.

If this nonblack absorber slab is in a symmetrical neutron flux (that is, the same currents are entering on each side), then simple diffusion theory provides the relations

$$j^- = \frac{\phi}{4} - \frac{\lambda}{6}\,\nabla\phi \qquad \text{Eq. (17.18a)}$$

$$j^+ = \frac{\phi}{4} + \frac{\lambda}{6}\,\nabla\phi \qquad \text{Eq. (17.18b)}$$

Substituting the expressions for j^+ and j^- into Eq. (17.17) leads directly to the value of δ, the extrapolation length

$$\delta = \frac{\phi}{\nabla\phi} = \frac{2}{3}\lambda\,\frac{1 - f\Sigma t}{f\Sigma t} \qquad \text{Eq. (17.19)}$$

Using this boundary condition, the absorption area of the slab is calculated as

$$C = \frac{L}{1+\frac{\delta}{L}} = \frac{L}{1+\frac{2}{3}\frac{\lambda}{L}\left[\frac{1}{f\Sigma t} - 1\right]} \qquad \text{Eq. (17.20)}$$

The values of f for a slab are given in Fig. XIV of Reference 7. For increasing absorption, Σt approaches infinity and $f\Sigma t$ approaches 0.5. In the limit of a black slab, δ is $2/3\ \lambda$ and

$$C = \frac{L}{1+\frac{2}{3}\frac{\lambda}{L}} \qquad \text{Eq. (17.21)}$$

Using the values of f from Reference 7, the value of C/L as given by Eq. (17.20) was calculated for a range of values of Σt and L/λ. The results are plotted in Fig. 17.6.

17.9 CORRECTION TO AREA ABSORPTION CALCULATIONS

The results of the preceding section, particularly the curves in Fig. 17.6, show that the area absorption of the slab absorber, when the extrapolation distance is taken into account, depends upon the ratio λ/L. When this ratio is very small, C/L approaches unity as the slab blackness is increased. On the other hand, when λ/L is the order of unity, C/L approaches the limit 0.6 as the slab blackness increases.

In pressurized water reactors, L tends to be small and thus λ becomes comparable with L. It is therefore necessary to correct for this in estimating rod worths by the area absorption method. In certain heavily loaded pressurized water reactors, the control rod worth is reduced by as much as 25 per cent by this correction.

For the case of small L, Eq. (17.12) gives C/L in terms of the rod perimeter plus corrections associated with angles. To a first approximation the correction due to the extrapolation can be taken into account by multiplying the perimeter by the factor C/L from Fig. 17.6. Thus the absorption area C of a rod in the small diffusion length limit would be

$$C = \left\{L\left[\text{Perimeter} + L \sum_{\text{corners}} D(\alpha_o)\right]\right\}\left\{\text{Value of C/L from Fig. 17.6}\right\} \qquad \text{Eq.(17.22)}$$

The factor by which the actual rod perimeter should be multiplied to obtain the effective perimeter is tabulated in Table 17.9. By multiplication of the true perimeter by this factor and the appropriate factor from Fig. 17.6, the area absorption of a rod may be determined for the small diffusion length limit.

17.10 APPLICATION TO SEVERAL ENERGY GROUPS

The method outlined in Sec. 17.8 for calculating the absorption area for absorbing slabs has been extended to take epithermal absorption into account. A constant source q is assumed to enter the epithermal group by degradation of neutrons from a higher energy group. The diffusion equations are as follows:

$$-D_2\nabla^2\phi_2 + (\Sigma_{r2} + \Sigma_{a2})\,\phi_2 = q \qquad \text{Eq.(17.23a)}$$

$$-D_3\nabla^2\phi_3 + \Sigma_{a3}\phi_3 = \Sigma_{r2}\phi_2 \qquad \text{Eq. (17.23b)}$$

In these equations, the subscript 2 refers to the epithermal group and the subscript 3 to the thermal group, D is the diffusion constant, Σ_a is the macroscopic absorption cross section, and Σ_r is the group removal cross section.

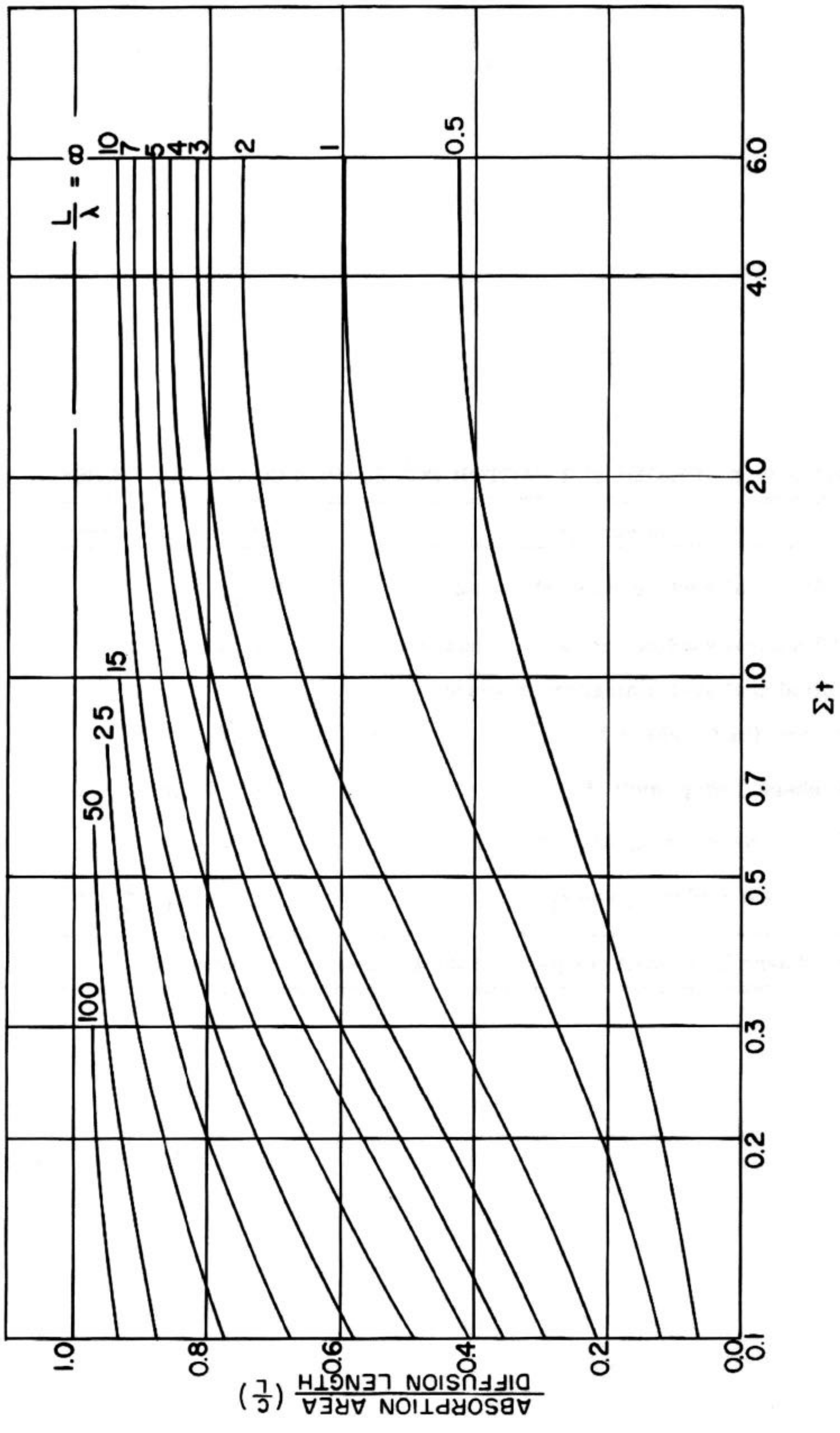

Fig. 17.6 – Absorption Area for an Infinite Plane Absorber.

Table 17. 9--PERIMETER FACTOR FOR SIMPLE CONFIGURATIONS*

Configuration	Perimeter Factor
Cylindrical surface external to source	$1 - \frac{L}{2R}$
Cylindrical surface with source external	$1 + \frac{L}{2R}$
Cylindrical shell immersed in source	1
Ribbon (half width ℓ)	$1 + \frac{L}{2\ell}$
Y shape (wing width ℓ)	$1 + 0.28 \frac{L}{2\ell}$
Cross shape (wing width ℓ)	$1 - 0.27 \frac{L}{2\ell}$
Rectangle (sides ℓ_1 and ℓ_2)	$1 + 2.41 \frac{L}{2(\ell_1 + \ell_2)}$

* Where L is small compared to the geometrical dimensions.

The solutions of these equations give for the currents into the slab

$$D_2 \nabla \phi_2 = q \frac{L_2}{\left[1 + \frac{2D_2}{L_2}\left(\frac{1}{f_2 \Sigma_2 t} - 1\right)\right]} \qquad \text{Eq. (17.24a)}$$

$$D_3 \nabla \phi_3 = q \left\{ \frac{L_3}{\left[1 + \frac{\Sigma_{a2}}{\Sigma_{r2}}\right]\left[1 + \frac{2\,D_3}{L_3}\left(\frac{1}{f_3 \Sigma_3 t} - 1\right)\right]} \right\} \cdot \left\{ 1 - \frac{1}{\left[1 + \frac{L_3}{L_2}\right]\left[1 + \frac{2\,D_2}{L_2}\left(\frac{1}{f_2 \Sigma_2 t} - 1\right)\right]} \right\} \qquad \text{Eq. (17.24b)}$$

In these equations

$$L_2{}^2 = \frac{D_2}{\Sigma_{a2} + \Sigma_{r2}}$$

$$L_3{}^2 = \frac{D_3}{\Sigma_{a3}}$$

Σ_2 and Σ_3 are the macroscopic cross sections of the absorber, and f_2 and f_3 are the self-shielding factors.

In the application of this result, the current into the slab ($D \nabla \phi$) divided by q is the absorption area for the slab in the group under consideration. In applying this to other rod shapes the rod perimeter and the perimeter correction factor are multiplied by $\frac{D \nabla \phi}{q}$ to obtain the total absorption area of the rod as in Sec. 17.9.

For use in multi-group calculations, the area absorption may be introduced in two ways. The first is that suggested in Sec. 17.6 by Eq. (17.7). Another method is to reduce the slowing-down density into a particular group by the factor (1 - C/A). The two approaches are essentially identical. For the distributed poison method, Eq. (17.7) becomes

$$\frac{C_2}{A} = \frac{\Sigma_{p2}}{\Sigma_{p2} + \Sigma_{r2} + \Sigma_{a2}} \qquad \text{Eq. (17.25a)}$$

$$\frac{C_3}{A} = \frac{\Sigma_{p3}}{\Sigma_{p3} + \Sigma_{a3}} \qquad \text{Eq. (17.25b)}$$

17.11 INTERACTING BLACK CONTROL RODS

The absorption areas presented in the preceding sections were calculated for a single, isolated rod in an infinite medium. In this section the effect of finite cell size will be considered. The results presented are for thermally black control rods for which the flux is assumed to vanish at the rod surface. The absorption area for a finite cell size will be designated C_f to distinguish it from the value C_i for an isolated rod in an infinite medium. The cell boundary condition applied is that the net neutron current at the cell boundary vanishes. For cell sizes in which the cell boundary is several diffusion lengths from the absorbing rod, C_i and C_f are approximately equal.

(a) Cylindrical Rod in a Cylindrical Cell. Let the radius of the rod be R and the cell radius be designated as T. The absorption area is given by the expression

$$C_f = 2\pi RL \left[\frac{I_1\,(T/L)\,K_1\,(R/L) - K_1\,(T/L)\,I_1\,(R/L)}{I_1\,(T/L)\,K_o\,(R/L) + K_1\,(T/L)\,I_o\,(R/L)} \right] \qquad \text{Eq. (17.26)}$$

As T/L approaches infinity, C_f approaches

$$2\pi RL\,\frac{K_1\,(R/L)}{K_o\,(R/L)}$$

the value of C for an infinite medium as given by Eq. (17.8)

(b) Slab Absorber in a Slab Cell. This is the geometry shown in Fig. 17.2. The absorbing slab has a total width 2a and the cell a total width 2m. The absorption area for this case is

$$C_f = 2\,L\,\tanh\left(\frac{m-a}{L}\right) \qquad \text{Eq. (17.27)}$$

As m/L approaches infinity, C_f approaches the value 2L.

(c) Periodic Array of Cruciform Rods. The geometry of the array is shown in Fig. 17.7. The absorption area, in terms of the cell area A, is given by the expression

$$\frac{C_f}{A} = 1 - \frac{64}{\pi^6}\left(\frac{M}{L}\right)^2 \sum_{\substack{j,p \geqq 1 \\ \text{odd}}} \frac{1}{j^2p^2}\,\frac{1}{j^2 + p^2 + \left(\frac{M}{\pi L}\right)^2} \qquad \text{Eq. (17.28)}$$

This expression is derived for the condition in which the rod tips touch. They are shown slightly separated in Fig. 17.7 for clarity.

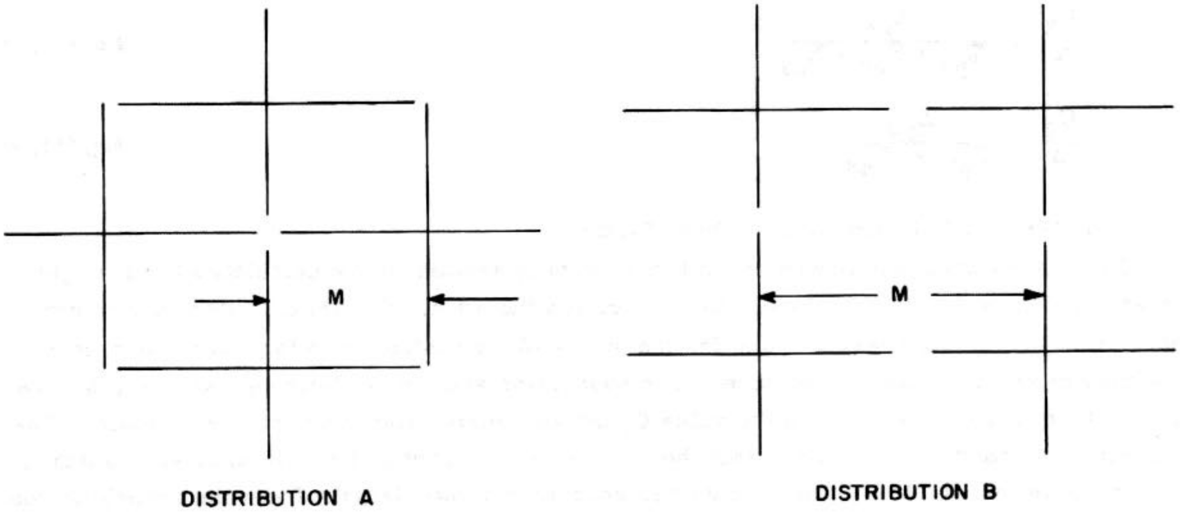

Fig. 17.7 - Periodic Array of Cruciform Rods.

For limiting values of $\left(\frac{M}{\pi L}\right)$ the sum may be approximated as follows:

$$\frac{M}{\pi L}\text{ large; } \quad \sum \cong \frac{\pi^6}{64}\left(\frac{L}{M}\right)^2\left(1-\frac{4L}{M}+\frac{16\pi L^2}{3M^2}\right)+O\left(\epsilon^{-\frac{M}{L}}\right)$$

$$\frac{M}{\pi L}\text{ small} \quad \sum \cong \frac{1}{2+\left(\frac{M}{\pi L}\right)^2}+0.0282-0.0024\left(\frac{M}{\pi L}\right)^2+0.0002\left(\frac{M}{\pi L}\right)^4+O\left[\left(\frac{M}{\pi L}\right)^6\right]$$

For $\left(\frac{M}{\pi L}\right)$ in the range 1.4 to 2.0, the two approximations agree to better than 1 per cent.

(d) Comparison of Cell Values with Infinite Media Values. The values of the absorption area for various rod shapes when calculated for cells as compared with the value when calculated for an infinite medium are shown in Fig. 17.8. Here the value $(1 - C_f/A)$ is plotted against the abscissa C_i/A. The departure of the curves from the straight line $(1 - C_i/A)$ indicates the reduction in effectiveness of the rod due to the finite cell size. The quantity $(1 - C_f/A)$ is the ratio of the cell multiplication with the rod present to the multiplication with the rod absent. Note the fairly wide range of multiplication over which the interaction produces very little effect.

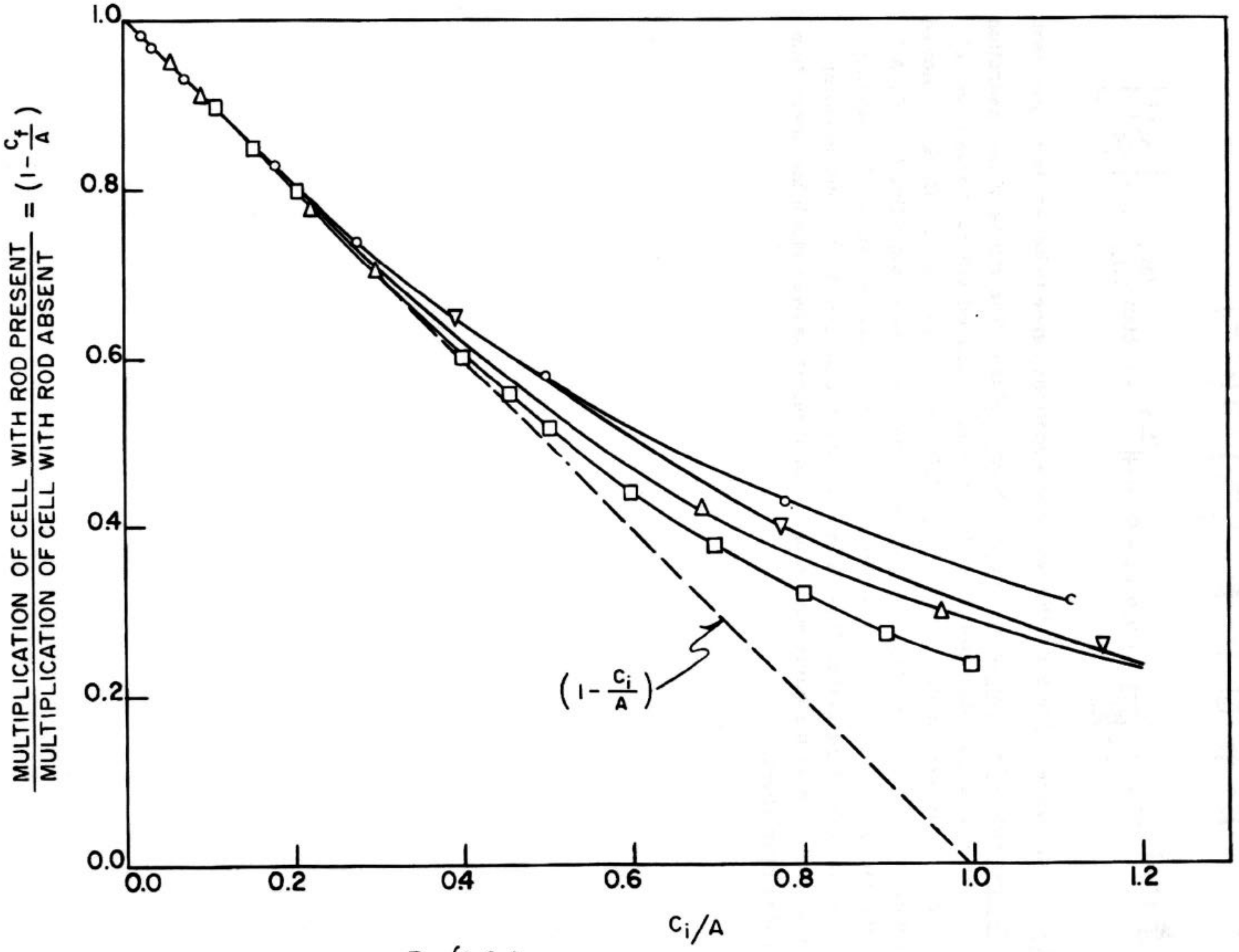

Rods $\frac{R}{L}$ $\begin{cases} 1.2 & \triangle \\ 0.2 & \text{o} \end{cases}$; Slab (any thickness) □ ; Crosses ▽

Fig. 17.8 - Effect of Cell Size on Rod Absorption Area.

THE EFFECTS OF ROD SHAPE ON CONTROL ROD WORTH

by D. R. Bach and S. W. Kitchen

17.12 INTRODUCTION

The effectiveness of single control rods has been measured in a reactor for rods of different sizes, materials, and varying thermal neutron absorption. The results obtained in these measurements have been interpreted in terms of the absorption area theory discussed in the preceding sections of this chapter in order to examine the applicability of this theory. While no attempt has been made to make an absolute comparison of rod worth with theory, measurements have been made of the relative worth of slab absorbers as compared with cruciform-shaped absorbers.

[redacted]

Pages 811 - 840 have been redacted in their entirety.

[redacted]

REFERENCES

1. A. F. Henry, Review of Methods Used in Control Rod Anaylsis for Reactor Design at Bettis, Report of Reactor Control Meeting, Report TID-7532 (Pt. 1), U.S. AEC, March, 1957.
2. Erich Erlbach, Peter A. M. Gram, Ralph C. Minehart, Cell Calculations for Cross-Shaped Control Rods, Report WAPD-TM-23, November, 1956.
3. H. Hurwitz, Jr., and G. M. Roe, Absorption of Neutrons by Black Control Rods, Jour. Nuclear Energy, Vol. 2, pp. 85-100, (1955).
4. J. H. Smith and J. C. Stewart, One-Group Criticality Conditions for a Black Eccentric Control Rod, Report KAPL-1414, October 5, 1955.
5. J. C. Stewart and J. H. Smith, Interaction of Black Control Rods, Report KAPL-1471, January 8, 1956.
6. B. Davidson, Influence of a Black Sphere and of a Black Cylinder upon the Neutron Density in an Infinite Non-Capturing Medium, Phys. Soc. of London Proc., Vol. 64, pp. 881-902, (1951).
7. M. L. Storm, H. Hurwitz, Jr., and G. M. Roe, Gamma-Ray Absorption Distributions for Plane, Spherical, and Cylindrical Geometries, Report KAPL-783, July 24, 1952. See also Chap. 22, Vol. III of this handbook.
8. J. A. Wheeler, Principles of Nuclear Power, Report N-2292, p. 66B, 1944.
9. A. Radkowsky, Theory and Application of Burnable Poisons, Proceedings of the Second International Conference on the Peaceful Uses of Atomic Energy, Paper 1900, 1958.

Chapter 18

REACTOR SYNTHESIS TECHNIQUES

18.1 INTRODUCTION

The power distribution in a pressurized water reactor cannot be described properly by simple, separable solutions. In a plane normal to the cylindrical axis of the reactor, the distribution is strongly affected by the geometric design details; water channels, control rod cross sections, subassembly structure, etc. The axial distribution is determined principally by the presence of partially inserted control rods. At the beginning of life these two factors, geometric design detail and partially inserted control rods, are the principal reasons that the power distribution cannot be described simply. Taking reactor lifetime into account, additional factors enter; namely, nonuniform fuel depletion and poison buildup.

The very limited margins that are available to the reactor designer make it essential that the three-dimensional nature of the problem be considered in the design. The difficulty is that no computational technique is, at the time of writing, available for doing this directly. The largest digital computers available today do not have sufficient speed to handle the problem. Therefore, various schemes for approximating the three-dimensional case by combining one- and two-dimensional solutions have been developed. A number of such schemes have been used. In this chapter two will be described in detail.

It is worth noting that synthesis schemes will be used in the future even though computers capable of solving the three-dimensional problem directly will come into use. The reason for this is associated with the relatively high cost of a three-dimensional solution compared with a synthesis solution. Synthesis solutions will be used in two ways: First, for initial studies and survey work and, second, for fixing approximate control rod withdrawal locations to be used in detailed three-dimensional studies. It seems probable that true three-dimensional lifetime analyses of a reactor will not be carried out until most of the design details of the reactor have been established.

The advent of computers in the next year or two capable of solving three-dimensional problems will enhance the value of synthesis methods. One of the difficulties with synthesis methods at present is that there is little basis for estimating their accuracy. It is difficult to obtain data experimentally with sufficient accuracy and detail to make a good test. By comparing synthesis solutions with three-dimensional solutions in a series of typical cases, however, the accuracy to be expected with the synthesis method can be established.

The synthesis schemes which have been developed have been influenced by the fact that most of the reactor geometric design detail is associated with the plane normal to the axis while the effect of partial insertion of control rods is associated with the axial distribution. It is natural, therefore, to solve the problem in the plane normal to the axis as a two-dimensional problem taking the geometric detail into account. Various two-dimensional solutions are then combined with an axial one-dimensional analysis to complete the solution. Clearly such a procedure must assume the solution is a product of the axial solution and the solution in the plane. This assumption is basic to any synthesis method.

[redacted]

In lifetime studies the general procedure is, first, to divide the core along the axis into a number of sections, ten or more. Next, the relative power produced in each slice or section at a given time in life is determined by calculating an axial distribution. From this normalized power, the depletion in each section over a lifetime step is calculated. This leads to new values for the constants in each section. The sections are then combined again by an axial solution with appropriate adjustment of control rod positions for criticality. Following this a new time step is taken. This procedure will be clarified in the detailed discussion of the synthesis schemes.

The various synthesis schemes differ principally in the manner in which the constants in each slice are developed and the way in which the axial problem is handled.

THE FLUX-WEIGHTED SYNTHESIS TECHNIQUE

by J. E. Meyer and N. Baron

18.2 FLUX-WEIGHTING TECHNIQUE - GENERAL OUTLINE OF METHOD

When a flux-weighting technique is used, the reactor power distribution is assumed separable into two multiplicative components, an axial distribution, and a distribution in the plane normal to the axis. The distribution in the plane is commonly referred to as a radial distribution although it is calculated in an x, y coordinate system. The slices or sections normal to the cylinder axis into which the reactor is divided are referred to as radial sections.

The axial distribution is calculated using the average properties of each radial section. The axial flux distribution is normalized so that the axial flux multiplied by the average fission cross sections in the appropriate radial slices is equal to the desired total fission rate for the reactor.

The axial distribution is continuous in such a synthesis scheme. However, the three-dimensional power distribution along a given axial line is generally discontinuous at each interface between radial slices since the radial distributions are, in general, different in each section.

The equations for the synthesis method will be developed for a two-group scheme (the extension to four energy groups is straightforward). Let $\phi_1(x, y, z)$ and $\phi_2(x, y, z)$ represent the neutron flux in the fast and slow energy group, respectively. These are each written in separable form as $R(x, y)$ and $Z(z)$. Thus

$$\begin{aligned} \phi_1(x, y, z) &= R_1(x, y)\, Z_1(z) \\ \phi_2(x, y, z) &= R_2(x, y)\, Z_2(z) \end{aligned} \qquad \text{Eq. (18.1)}$$

Now $\phi(x, y, z)$ must be normalized to give the fission rate corresponding to the assumed power level. In the product form either function may be adjusted. We choose, arbitrarily, the following scheme of normalization. We define

$$\frac{1}{A} \int_{x, y} R(x, y)\, dx\, dy = 1 \qquad \text{Eq. (18.2)}$$

for either R_1 or R_2. The area of the radial section of the reactor which is fueled is given by

$$A = \int_{x, y} dx\, dy\ .$$

It follows then that

$$Z(z) = \frac{1}{A} \int_{x, y} \phi(x, y, z)\, dx\, dy \qquad \text{Eq. (18.3)}$$

for either Z_1 or Z_2. Thus $Z(z)$ is the average flux in the plane at the axial position z.

One point should be mentioned concerning the normalization of $R(x, y)$. Equation (18.2) normalizes $R_1(x, y)$ and $R_2(x, y)$ to the same average value, independent of the group diffusion equations. The group equations will, however, establish a ratio of fast-to-slow flux. It will be necessary, therefore, to have a factor in the radial equations to provide the necessary flexibility to permit solution of the equations. This point will be discussed later in the treatment.

18.3 FLUX-WEIGHTING TECHNIQUE - AXIAL SOLUTION OF THE EQUATION

The two group diffusion equations given below are to be solved.

$$D_1 \nabla^2 \phi_1 - (\Sigma_{r1} + \Sigma_{a1})\, \phi_1 + \frac{\nu\Sigma_{f1}\phi_1 + \nu\Sigma_{f2}\phi_2}{\lambda} = 0 \qquad \text{Eq. (18.4)}$$

$$D_2 \nabla^2 \phi_2 - \Sigma_{a2}\phi_2 + \Sigma_{r1}\phi_1 = 0 \qquad \text{Eq. (18.5)}$$

In these equations subscript 1 refers to the fast group, subscript 2 to the thermal group. ϕ is the neutron flux, D is the diffusion constant, ν is the number of neutrons emitted per fission, Σ_f is the fission cross section, Σ_a is the group absorption cross section, Σ_{r1} is the removal or transfer cross section for neutrons slowing down from the fast group to the thermal group, and λ is the eigenvalue of the equations. In this formulation D_1 and D_2 are assumed independent of position. If this is not the case, the first term of the equation is $\nabla D \nabla \phi$.

Substitution of ϕ [Eq. (18.1)] in Eqs. (18.4) and (18.5) leads to

$$Z_1D_1\nabla^2_{x,y}R_1 + R_1D_1\nabla^2_zZ_1 - (\Sigma_{r1} + \Sigma_{a1})\, R_1Z_1 + \frac{\nu\Sigma_{f1}R_1Z_1 + \nu\Sigma_{f2}R_2Z_2}{\lambda} = 0\,, \qquad \text{Eq. (18.6)}$$

and

$$Z_2D_2\nabla^2_{x,y}R_2 + R_2D_2\nabla^2_zZ_2 - \Sigma_{a2}R_2Z_2 + \Sigma_{r1}R_1Z_1 = 0\,. \qquad \text{Eq. (18.7)}$$

When Eqs. (18.6) and (18.7) are multiplied by 1/A and then integrated over the fueled region in the radial plane, the following equations are obtained.

$$\bar{D}_1\nabla^2_zZ_1 - (\bar{\Sigma}_{r1} + \bar{\Sigma}_{a1} + B^2_{r1}\bar{D}_1)\, Z_1 + \frac{\nu\bar{\Sigma}_{f1}Z_1 + \nu\bar{\Sigma}_{f2}Z_2}{\lambda} = 0 \qquad \text{Eq. (18.8)}$$

$$\bar{D}_2\nabla^2_zZ_2 - (\bar{\Sigma}_{a2} + B^2_{r2}\bar{D}_2)\, Z_2 + \bar{\Sigma}_{r1}Z_1 = 0 \qquad \text{Eq. (18.9)}$$

By definition:

$$\bar{D}_1 \equiv \frac{1}{A} \int_{x,y} D_1R_1(x,y)\, dxdy \qquad \text{Eq. (18.10a)}$$

$$\bar{D}_2 \equiv \frac{1}{A} \int_{x,y} D_2R_2(x,y)\, dxdy \qquad \text{Eq. (18.10b)}$$

$$\bar{\Sigma}_{r1} \equiv \frac{1}{A} \int_{x,y} \Sigma_{ri}R_1(x,y)\, dxdy \qquad \text{Eq. (18.10c)}$$

$$\bar{\Sigma}_{a1} \equiv \frac{1}{A} \int_{x,y} \Sigma_{a1}R_1(x,y)\, dxdy \qquad \text{Eq. (18.10d)}$$

$$\bar{\Sigma}_{a2} \equiv \frac{1}{A} \int_{x,y} \Sigma_{a2}R_2(x,y)\, dxdy \qquad \text{Eq. (18.10e)}$$

$$\bar{\Sigma}_{f1} \equiv \frac{1}{A} \int_{x,y} \Sigma_{f1}R_1(x,y)\, dxdy \qquad \text{Eq. (18.10f)}$$

$$\bar{\Sigma}_{f2} \equiv \frac{1}{A} \int_{x,y} \Sigma_{f2}R_2(x,y)\, dxdy \qquad \text{Eq. (18.10g)}$$

$$B^2_{r1} \equiv -\frac{1}{A}\,\frac{1}{\bar{D}_1} \int_{x,y} D_1\nabla^2_{x,y}R_1(x,y)\, dxdy \qquad \text{Eq. (18.10h)}$$

$$B^2_{r2} \equiv -\frac{1}{A}\,\frac{1}{\bar{D}_2} \int_{x,y} D_2\nabla_{x,y}R^2_2(x,y)\, dxdy \qquad \text{Eq. (18.10j)}$$

The term flux-weighting is derived from the definitions for the average axial parameters given in Eqs. (18.10a) through (18.10j). It should also be noted that each of the parameters defined in Eqs. (18.10a) through (18.10j) is a function of z.

Equations (18.8) and (18.9) are two-group diffusion equations for a one-dimensional axial problem in which the parameters and radial leakage terms are functions of z. Any of the techniques for solution of such equations, in particular such digital computer codes as WANDA (see Appendix A), may be used to solve this problem. It is clear, however, that the radial functions, R, must be known in order to define the parameters of the axial problem. The method for obtaining R will be discussed in the next section. It should be noted that even with a limited number of sections a large number of points may be used in the axial mesh in order to obtain the flux variations in satisfactory detail.

The axial normalization of the flux is carried out as follows: If C_1 and C_2 are the energy releases per fission for fission by fast and slow group neutrons, respectively, the fission power density at a point in the reactor is

$$p = C_1\Sigma_{f1}\phi_1 + C_2\Sigma_{f2}\phi_2 \qquad \text{Eq. (18.11)}$$

The total fission power release in the reactor, P, is the integral of the power density over the fueled volume of the reactor

$$P = \int_V p\,dV = \int_V [C_1\Sigma_{f1}\phi_1 + C_2\Sigma_{f2}\phi_2]\,dV \qquad \text{Eq. (18.12)}$$

Substituting the functions R(x, y) and Z(z) from Eq. (18.1) into Eq. (18.12) and integrating over the radial section leads to the equation

$$P = V\left\{\frac{1}{L}\int_0^L [C_1\overline{\Sigma}_{f1}Z_1(z) + C_2\overline{\Sigma}_{f2}Z_2(z)]\,dz\right\} \qquad \text{Eq. (18.13)}$$

where V is the fueled volume of the reactor and L is the axial length of the fueled volume. The quantity in braces is the average fission power density in the core.

The solutions of Eqs. (18.8) and (18.9) are normalized to the desired reactor output power by Eq. (18.13).

18.4 FLUX-WEIGHTING TECHNIQUE - RADIAL SOLUTION OF THE EQUATIONS

The separated two-group equations, Eqs. (18.6) and (18.7), form the starting point in the development of the radial equations. Note that the functions R_1 and R_2 are arbitrarily normalized. As pointed out previously, it will be necessary to permit the slow-to-fast flux ratio to be adjusted to a value appropriate to the equations. This is readily carried out by making use of Z_1 and Z_2, which are the average fast and slow flux, respectively, in the plane. The average fast-to-slow flux ratio in the plane as, F_r, is defined by

$$F_r \equiv \frac{Z_1}{Z_2} \qquad \text{Eq. (18.14)}$$

Within the plane B^2_{z1} and B^2_{z2} are defined by the equations

$$\begin{aligned} \nabla^2_z Z_1 &\equiv - B^2_{z1} Z_1 \\ \nabla^2_z Z_2 &\equiv - B^2_{z2} Z_2 . \end{aligned} \qquad \text{Eq. (18.15)}$$

Substituting the equation for B^2_{z1} in Eq. (18.6) and the equation for B^2_{z2} in Eq. (18.7) yields the following two-group equations in the radial plane:

$$D_1\nabla^2_{x,y}R_1 - (\Sigma_{r1} + \Sigma_{a1} + B^2_{z1}D_1)\,R_1 + \frac{\nu\Sigma_{f1}R_1 + \nu\Sigma_{f2}R_2/F_r}{\lambda} = 0 \qquad \text{Eq. (18.16)}$$

$$D_2\nabla^2_{x,y}R_2 - (\Sigma_{a2} + B^2_{z2}D_2)\,R_2 + \Sigma_{r1}R_1F_r = 0 \qquad \text{Eq. (18.17)}$$

The introduction of B^2_{z1} and B^2_{z2} has not impaired the generality of the equations. A constant times Z has been substituted for the definite values of $\partial^2Z_1/\partial z^2$ and $\partial^2Z_2/\partial z^2$ in each radial section. If the section under consideration is thick and extends, for example, from $z = a$ to $z = b$, Eqs. (18.6) and (18.7) may be integrated with respect to z. Thus for terms involving Z_1 or Z_2,

$$\int_a^b Z(z)\, dz = (b - a)\, \overline{Z} \qquad \text{Eq. (18.18)}$$

where $\overline{Z}$ is the average value. For the derivative term

$$\int_a^b \nabla_z^2\, Z(z)\, dx = \frac{dZ}{dz}\bigg|_a^b \qquad \text{Eq. (18.19)}$$

Thus an average value of B_z^2 is given by:

$$B_z^2 = -\frac{\dfrac{dZ}{dz}\bigg|_a^b}{(b - a)\, \overline{Z}} \qquad \text{Eq. (18.20)}$$

for a thick section.

Equations (18.16) and (18.17) may be solved, to an arbitrary multiplicative factor, for the quantities $F_rR_1(x, y)$ and $R_2(x, y)$ by any of the standard methods. In particular a digital computer solution may be obtained using the PDQ code (see Appendix B). The ratio F_r may be obtained directly from the solutions, even with the arbitrary multiplicative factor, since F_r is simply the ratio of the average fast flux to the average slow flux. The factor obviously will cancel in taking this ratio. The appropriate normalization for R_1 and R_2 may be obtained by applying Eq. (18.2).

One point may be noted here regarding the radial solutions. The calculation of B_{r1}^2 and B_{r2}^2 is most readily and accurately performed by alternate forms of Eqs. (18.10h) and (18.10j). These are derived by substitution using Eqs. (18.16) and (18.17).

$$B_{r1}^2 = -\left(\overline{\Sigma}_{r1}/\overline{D}_1 + \bar{\bar{\Sigma}}_{a1}/\overline{D}_1 + B_{z1}^2\right) + \frac{(\nu\overline{\Sigma}_{f1}/\overline{D}_1) + (\nu\overline{\Sigma}_{f2}/F_r\overline{D}_1)}{\lambda_r} \qquad \text{Eq. (18.10k)}$$

$$B_{r2}^2 = -\left(\bar{\bar{\Sigma}}_{a2}/\overline{D}_2 + B_{z2}^2\right) + \left(\bar{\bar{\Sigma}}_{R1}F_r/\overline{D}_2\right) \qquad \text{Eq. (18.10l)}$$

18.5 FLUX-WEIGHTING TECHNIQUE - METHOD OF APPLICATION

Solutions of the two-group diffusion equations by the synthesis method is basically an iterative process between radial and axial solutions. In Eqs. (18.16) and (18.17) the entire influence of the axial problem on the radial solution in the section is represented by the numbers B_{z1}^2 and B_{z2}^2. If these numbers are estimated, solutions may be obtained for Eqs. (18.16) and (18.17) since all the other parameters are known. Using these solutions the normalized functions R_1 and R_2 may be obtained. Substituting R_1 and R_2 in Eqs. (18.10a) through (18.10l) permits the constants for the axial problem (in that particular axial section) to be determined. The axial parameters necessary to obtain solutions to the axial problem [Eqs. (18.8) and (18.9)] are all determined once the solutions for all the sections are available. Once the axial solution is found the assumed values of B_{z1}^2 and B_{z2}^2 for the radial problem may then be corrected and new radial solutions obtained. The new radial solutions permit a new axial solution to be obtained, etc. The convergence of this process depends basically on the fact that the term B_z^2D is smaller by a factor of two or three than the Σ's with which it is associated. Thus an initial error in the estimate of B_z^2 does not have a serious effect on the solution and the iterative process will converge rapidly. For many purposes, in fact, the solution is satisfactory without iteration.

Consider Eqs. (18.16) and (18.17). Use of other than converged iterated values for B_{z1}^2 and B_{z2}^2 will result in three effects. First, the functional shapes $R_1(x, y)$ and $R_2(x, y)$ will be wrong. Second, the ratio of fast-to-slow flux will be wrong. Third, the eigenvalue λ will be different from unity. Of the three, the first is more important and will appear chiefly in the value of B_{r1}^2 and B_{r2}^2. If a problem for an axial region of the core with few axial discontinuities is being considered, then B_{z1}^2 would be expected to be equal to B_{z2}^2. The shape functions would then be in error only to the extent that $(\Sigma_{r1} + \Sigma_{a1})$ and Σ_{a2} change significantly from region to region in the radial section. If the reactor design is such that these quantities do change, then the effect which the leakage terms B_z^2D have will be different in the different regions and this will result in an incorrect flux amplitude ratio from one region to another. On the other hand if B_z^2D is numerically small compared with the Σ's, even a substantial error in B_z^2 will have little effect on the flux shapes.

If, however, a problem near the bottom reflector is being considered, the axial leakage will be quite different in the two groups. The sign of B_{z1}^2 will be positive, that of B_{z2}^2 negative, and both may have an absolute value considerably higher than the group independent B_z^2. In this case errors in axial bucklings will have a larger effect on the flux shapes. In reactors in which the region adjacent to the bottom reflector is important in terms of reactivity, care must be exercised in applying the radial bucklings obtained from non-iterated synthesized solutions to the sections near the bottom reflector. The importance of the errors in flux shapes can only be assessed by comparing the solutions using different values of B_z^2.

The other effects of the errors in axial bucklings are an incorrect fast-to-slow ratio and an incorrect eigenvalue. If the functions R_1 and R_2 are correct in shape, an error in F_r is relatively unimportant. The reason is that the parameters entering the axial problem are evaluated with normalized functions R_1 and R_2. The only other use of either F_r or λ is the entry of F_r into the power normalization of Eq. (18.13). The entry is limited to the power produced by fast neutron fission. Since this is generally less than 20% of the total fission power, a substantial error in F_r will not be serious. While it might be supposed that use of the axial equation solutions would eliminate this error, the structure of the existing depletion codes is such that the radial section must be depleted according to the solutions obtained for the radial problem.

Thus the general procedure for applying the synthesis scheme is as follows:

(a) The reactor is first divided into a number of radial sections, the number depending on the type of rod programming and the detail with which the lifetime depletion is to be studied.

(b) At the beginning of life all parameters in Eqs. (18.16) and (18.17) are known for each radial section except B_{z1}^2 and B_{z2}^2. As a start these are taken equal and adjusted in magnitude until an eigenvalue near unity is obtained for the solution of Eqs. (18.16) and (18.17). An eigenvalue lying between 0.95 and 1.05 is generally satisfactory for this step.

(c) The solutions for the radial sections are normalized according to Eq. (18.2).

(d) For each radial section the average parameters for the axial equations are obtained using Eqs. (18.10a) through (18.10l).

(e) The axial equations, Eqs. (18.8) and (18.9), are solved using these parameters. The necessary control rod withdrawal or insertion is made to obtain an eigenvalue of unity.

(f) The values B_{z1}^2 and B_{z2}^2 are computed from the axial solution for each radial section. With these corrected values the radial equations are again solved in each section. Steps (c) to (e) are now repeated. This iterative process is continued until satisfactory convergence is obtained.

(g) Using Eq. (18.13), the average flux level in each radial section is obtained for the assumed reactor output power.

(h) Each radial section is depleted at this flux level for a given operating time interval and a new set of parameters obtained for each radial section. With these parameters and an assumed B_z^2, the iterative process steps (b) through (f) are repeated.

(i) The entire process is repeated for another time step.

The synthesis procedure gives the power distribution in the reactor at various stages of reactor lifetime and the control rod positions for criticality during lifetime. [redacted]

It is clear that if the radial to axial iteration procedure at any given stage of lifetime is carried over a number of cycles, the appropriate axial leakages to be used in the radial equations will be obtained and the eigenvalue of the axial and radial problems can both be converged to unity. Under these conditions the fast-to-slow flux ratio in a given section will be the same whether the radial or axial solutions are used. There is some question, however, in view of the approximation represented by the product form of the solution, whether such a detailed iterative procedure is warranted. Without a comparison of synthesis solutions with true three-dimensional lifetime depletion studies, it is a matter of judgment whether iteration is or is not warranted.

18.6 FLUX-WEIGHTING TECHNIQUE - EXAMPLE OF SYNTHESIS

To provide some guidance as to the applicability of the synthesized solution, a synthesis of two one-dimensional solutions has been compared to the exact solution of the group diffusion equations for a two-dimensional case. The synthesized solution is made up of two one-dimensional solutions and it is compared with the two-dimensional solution of the problem.

Figure 18.1 shows the reactor geometry. The reactor has a rectangular cross section and its depth (the dimension normal to the plane of the figure) is assumed infinite. Five channels are shown in the reactor section. The two outer channels are water channels, the inner pair contain partially withdrawn control sheets, and the center channel is a fully inserted control sheet. The outer periphery of the reactor is assumed to be surrounded by a water reflector.

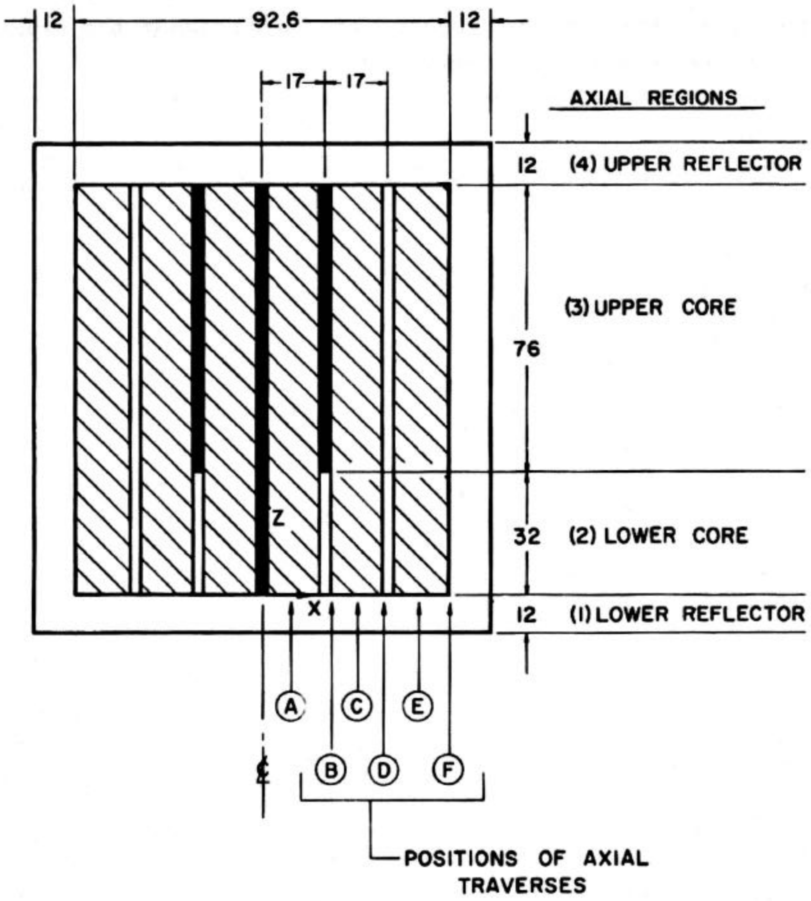

Fig. 18.1 - Geometry of the Calculated Reactor.

NOTES:

1. All dimensions in cm.
2. All control sheets and water channels 1.6 cm thick.
3. Reactor is uniform and infinitely long in direction normal to plane of figure.

The reactor composition is assumed uniform throughout. Since a lifetime calculation is not made, only four regions are required to represent the reactor. These are as follows:

(a) Lower reflector,
(b) Lower core,
(c) Upper core,
(d) Upper reflector.

The boundary between the upper and lower core regions is at the tips of the partially inserted control sheets.

The composition of the reactor is given in Table 18.1. Since the reactor geometry and composition were assumed, the eigenvalue will not necessarily be unity.

Table 18.1 - MATERIAL PROPERTIES OF REACTOR USED FOR THE EXAMPLE

Material	Σ_{r1} (cm^{-1})	Σ_{a1} (cm^{-1})	Σ_{f1} (cm^{-1})	D_1 (cm)	Σ_{a2} (cm^{-1})	$\nu\Sigma_{f2}$ (cm^{-1})	D_2 (cm)
Fuel Region	0.0160	-0.0008*	0*	1.70	0.0550	0.0832	0.420
Water	0.0410	0.0	0	1.60	0.0120	0.0	0.230
Control Sheets	0.0	0.10	0	0.50	1.50	0.0	0.10

* The effect of fast fissioning was approximated by assuming Σ_{a1} to be negative.

The two-dimensional solution was synthesized using two one-dimensional solutions for the lower and upper core region and combining them with an axial one-dimensional solution. Figure 18.2 gives the one-dimensional solution in the lower core region. Figure 18.3 shows the solution in the upper core region. The average axial fluxes for the synthesis procedure are shown in Fig. 18.4.

The fluxes along axial lines at locations A, B, C, D, E, and F of Fig. 18.1 were calculated by using average axial fluxes. Plots of the slow fluxes are shown in Figs. 18.5 through 18.10. The calculated two-dimensional traces are shown on the same figures for comparison.

In obtaining the synthesized solutions three radial iterations were carried out. In the first radial solution B_{z1}^2 and B_{z2}^2 were assumed to be equal and were adjusted to give the radial solution with an eigenvalue of unity for each region of the core. Successive iterations were carried out using the bucklings obtained in the previous solutions. For the reflector regions the buckling was taken equal to the buckling of the fast group in the adjacent fueled region. Table 18.2 shows the results obtained with the successive iterations.

The two-dimensional solution of the problem gave an eigenvalue of 1.023. The iterated synthesis procedure gives an eigenvalue of 1.033 which is about 1 per cent in error. Both the eigenvalue and the flux ratios have converged satisfactorily after two iterations. The third iteration is clearly unnecessary. The zero order of iterations is not quite satisfactory chiefly because the radial problem was initially adjusted to give an eigenvalue of one.

Comparison of the synthesized flux distributions with the two-dimensional results shows reasonably good agreement except for the transition zone in the neighborhood of the partially inserted rod tips. The synthesized solutions show much more abrupt changes in flux level than does the two-dimensional solution.

THE AXIAL LINE SYNTHESIS TECHNIQUE

by T. E. Fairey

18.7 AXIAL LINE TECHNIQUE - INTRODUCTION

The axial line synthesis technique is a simpler method than the flux-weighting technique covered in the preceding sections. Because of this simplicity, considerably less computation is required to apply the method. While there are variants of the line synthesis technique, the

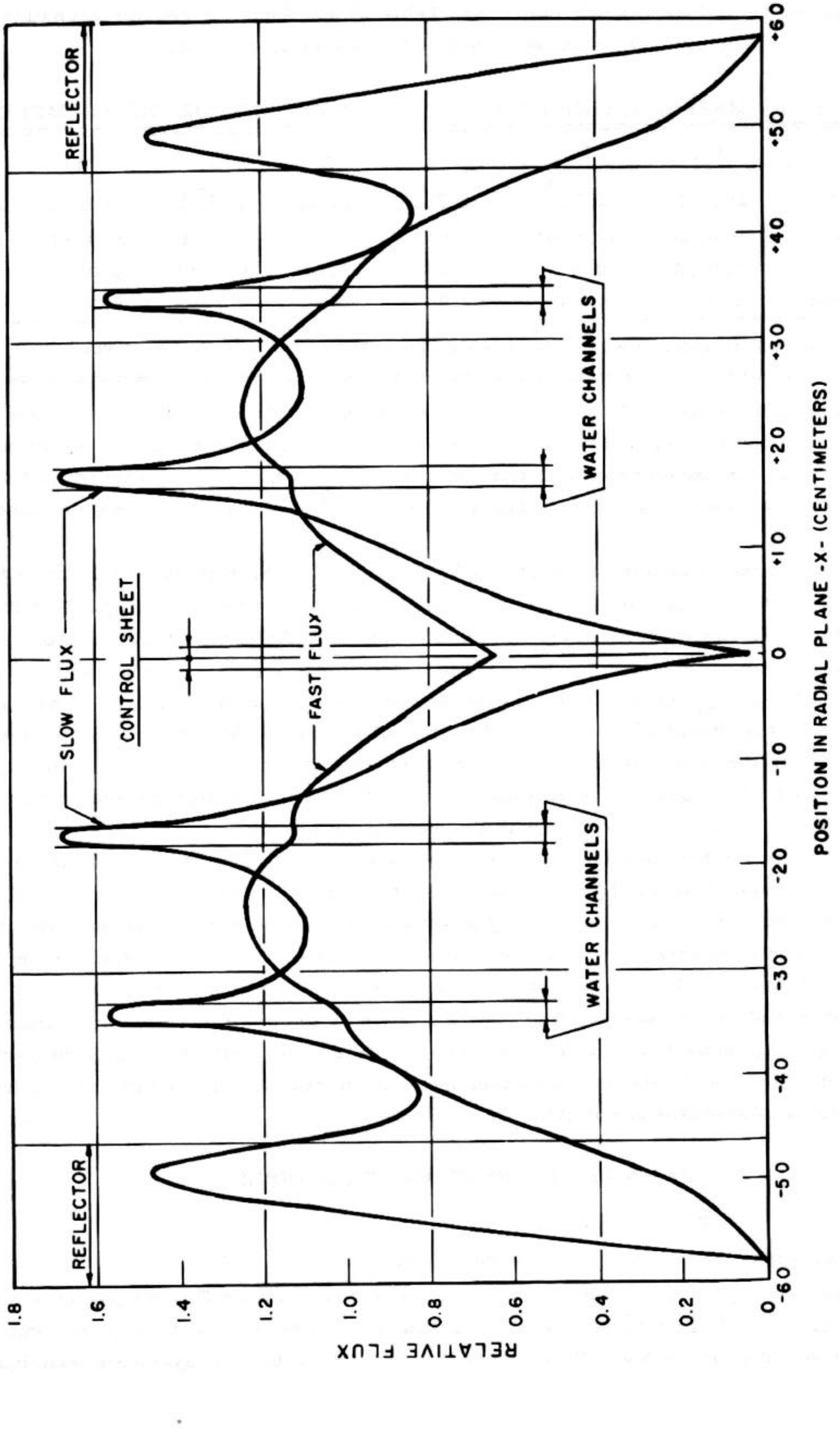

Fig. 18.2 - One-Dimensional Solution - Lower Core Region.

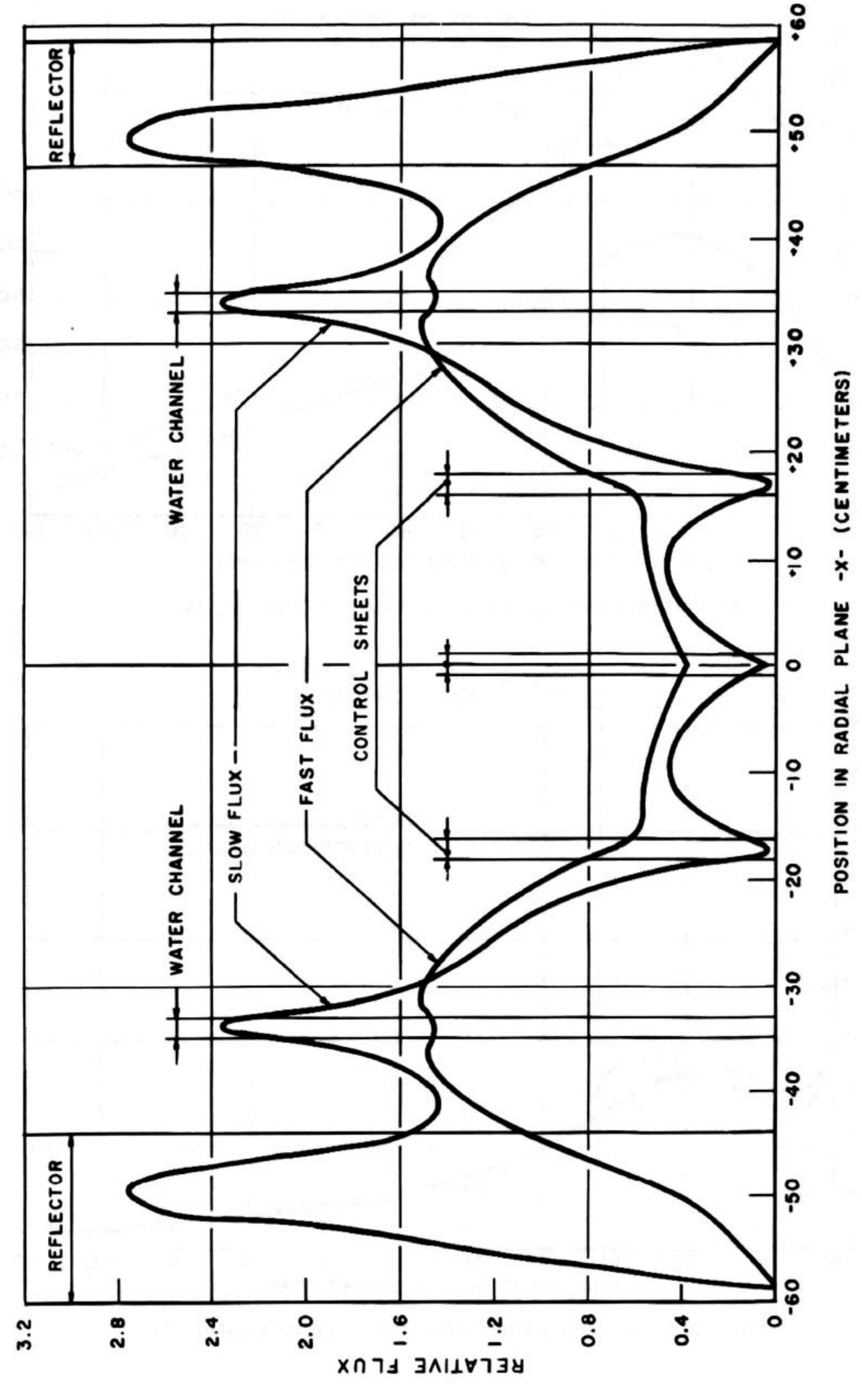

Fig. 18.3 - One-Dimensional Solution - Upper Core Region.

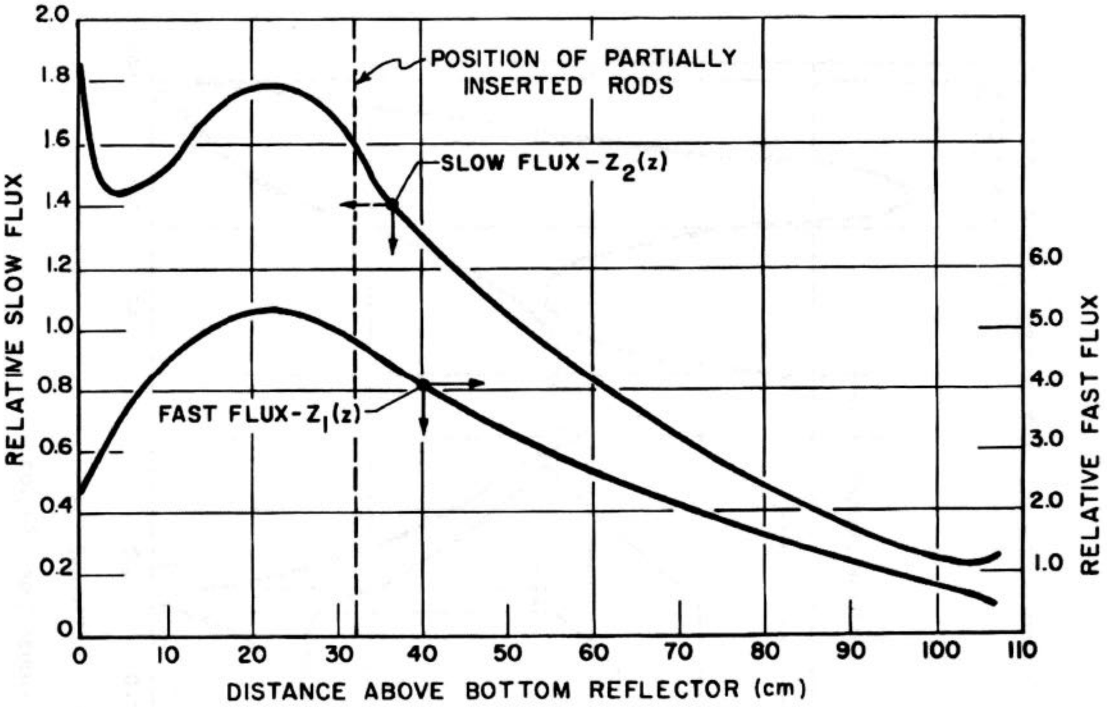

Fig. 18.4 - Average Axial Synthesized Flux Shapes.

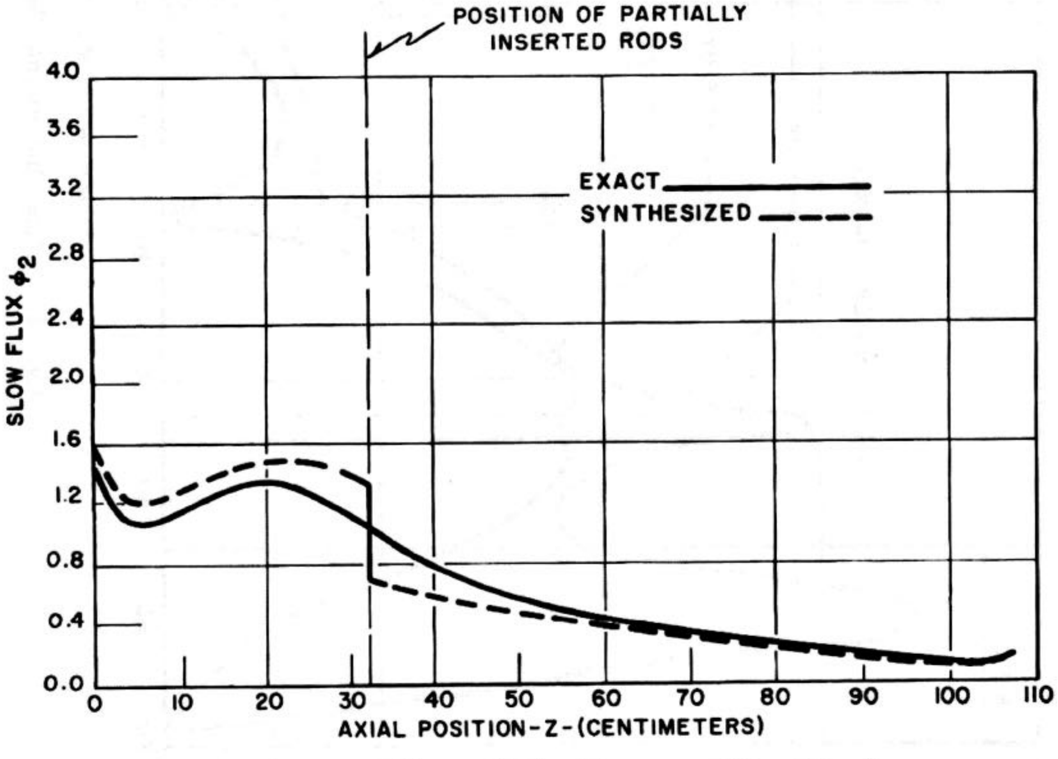

Fig. 18.5 - Axial Thermal Flux Traverse at Location A.

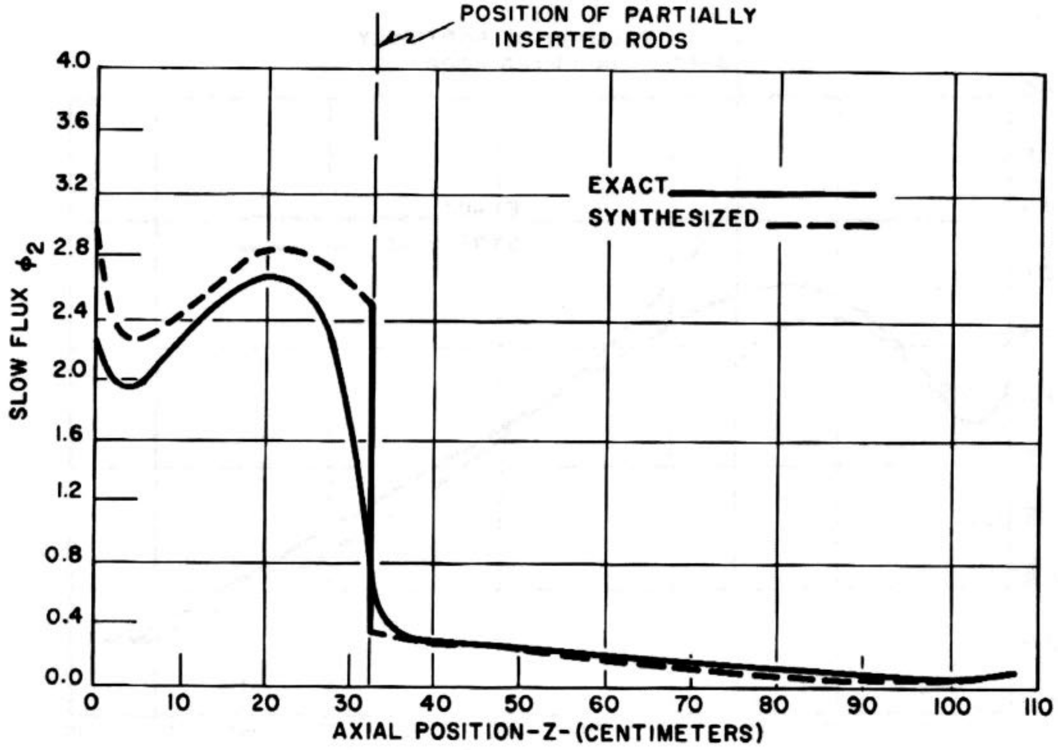

Fig. 18.6 - Axial Thermal Flux Traverse at Location B.

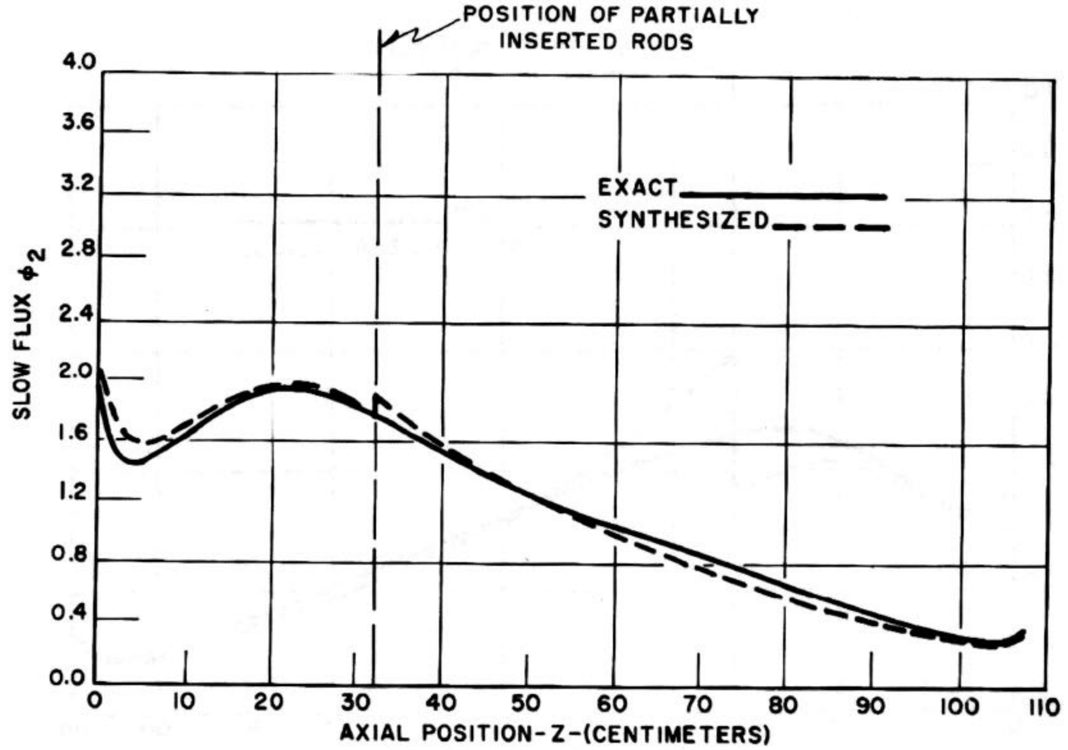

Fig. 18.7 - Axial Thermal Flux Traverse at Location C.

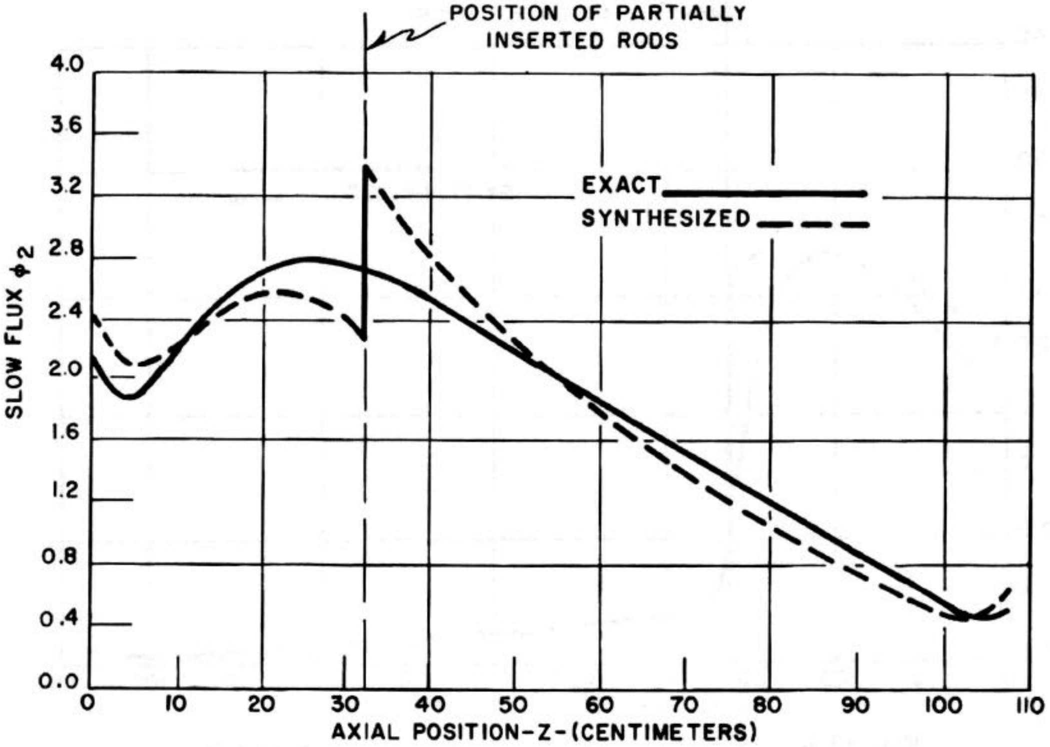

Fig. 18.8 - Axial Thermal Flux Traverse at Location D.

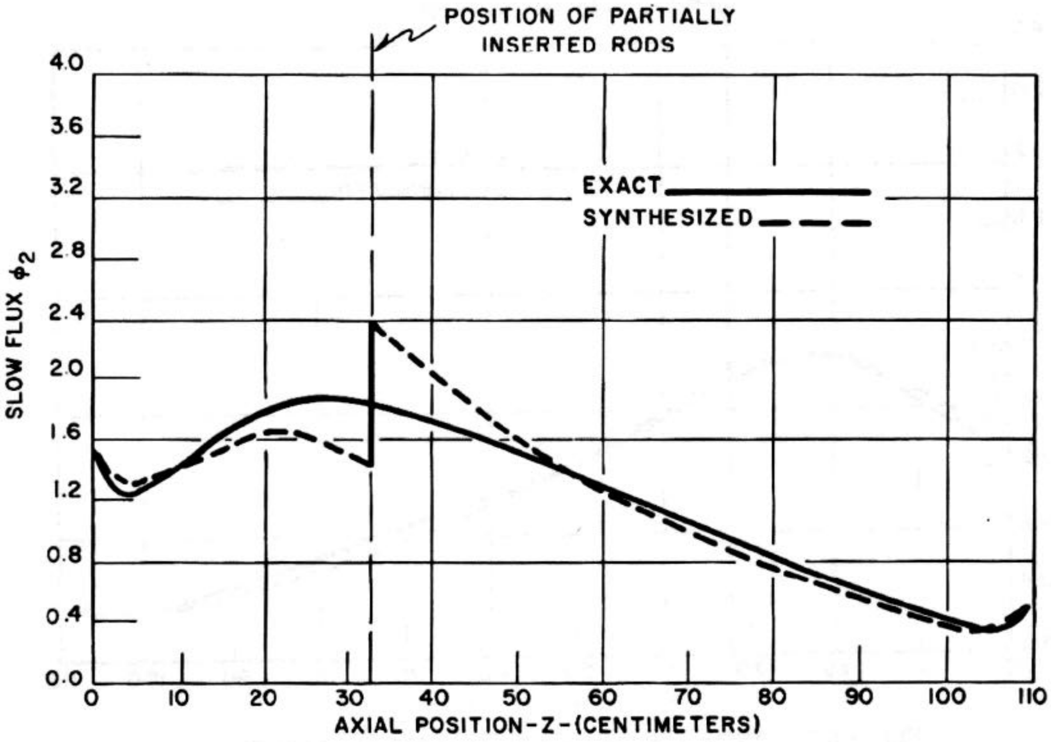

Fig. 18.9 - Axial Thermal Flux Traverse at Location E.

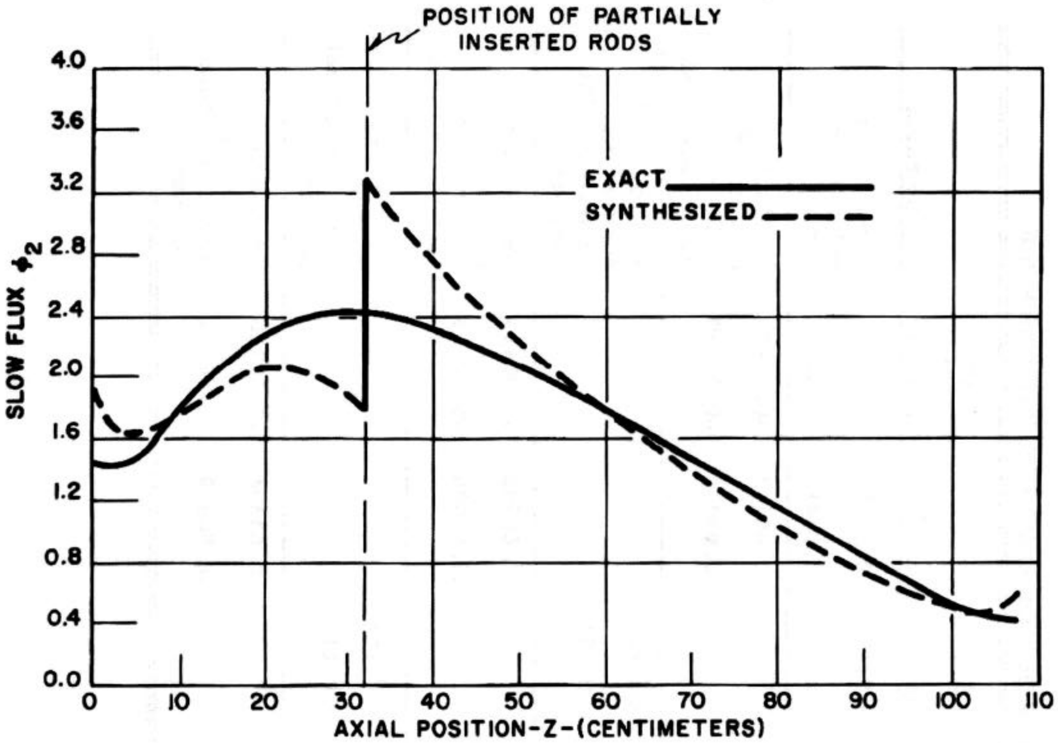

Fig. 18.10 - Axial Thermal Flux Traverse at Location F.

one described here is the original and the simplest. Basically, it makes use of one-dimensional radial solutions and one-dimensional axial solutions of the two-group diffusion equations. The procedure is not, however, limited to one-dimensional radial solutions but may be used with two-dimensional solutions as well.

[redacted]

In the one-dimensional axial line synthesis technique there is no attempt to take the details of the reactor heterogeneity into account. [redacted] For thermal design purposes the effects of heterogeneities in the radial section are treated by the use of flux peaking factors. Figure 18.11 shows a diagram of a homogenized reactor to which the line synthesis technique could be applied. Three radial zones are shown. [redacted] There are two axial zones; the rod-free and the rodded regions. [redacted]

Table 18. 2 - RESULTS OF SUCCESSIVE ITERATIONS ON REACTOR USED FOR THE EXAMPLE

Order of Iteration	Region	F_r	F_z	λ_r	λ_z	B^2_{r1} (cm^{-2})	B^2_{r2} (cm^{-2})	B^2_{z1} (cm^{-2})	B^2_{z2} (cm^{-2})	Remarks
0	Lower Core	2.986	--	1.000	--	0.00477	-0.01986	0.00267	0.00267	First radial solution; B^2_z assumed.
	Upper Core	3.146	--	1.000	--	0.00645	-0.01127	0.00017	0.00017	
0	Lower Core	--	2.786	--	1.043			0.00313	-0.00496	First axial solution; B^2_r from first radial case used.
	Upper Core	--	3.094	--				-0.00022	-0.00180	
1	Lower Core	2.804	--	1.032	--	0.00484	-0.01917			Second radial solution; B^2_z from first axial case used.
	Upper Core	3.101	--	1.044	--	0.00640	-0.01104			
1	Lower Core	--	2.822	--	1.032			0.00302	-0.00426	Second axial solution; B^2_r from second radial case used.
	Upper Core	--	3.108	--				-0.00008	-0.00153	
2	Lower Core	2.821	--	1.034		0.00482	-0.01922			Third radial Solution; B^2_z from second axial case used.
	Upper Core	3.106	--	1.032		0.00642	-0.01112			
2	Lower Core	--	2.820	--	1.033			0.00304	-0.00426	Third axial solution; B^2_r from third radial case used.
	Upper Core	--	3.105	--				-0.00010	-0.00154	

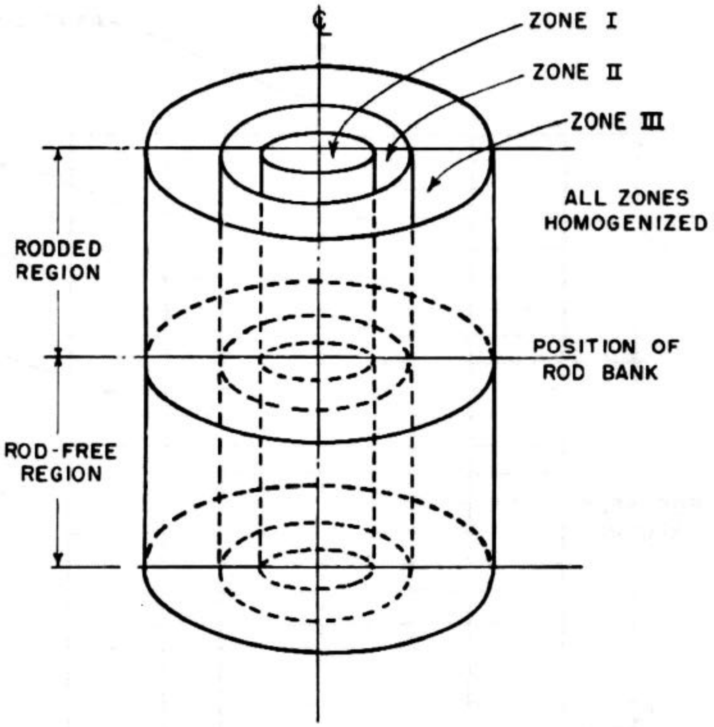

Fig. 18.11 - Reactor Model for Application of Line Synthesis

18.8 AXIAL LINE TECHNIQUE - OUTLINE OF METHOD

The basic idea in the line synthesis method is to calculate the actual flux distribution along one axial line in the reactor, the centerline. The flux calculation is made, of course, for the homogenized model of the reactor. The line synthesis method will be outlined broadly in this section and discussed in detail in the next section.

In principle the calculation is carried out as follows: The reactor is divided into an arbitrary number of radial sections as shown in Fig. 18.12. In each radial section the flux distribution is calculated by two-group diffusion theory. The radial calculations are made with the material constants of the radial section under consideration. Axial leakage is taken into account by an axial buckling which is adjusted to make the radial calculation critical.

With the radial calculation solved in each section, an axial calculation is performed along an axial line of the reactor. In this calculation the actual material constants along the line in each radial section are used. Radial leakage at each point of the axial calculation is accounted for by the use of the radial buckling from the radial section calculations. Criticality of the axial calculation is obtained by adjusting the position of the rod bank. In a simple reactor calculated one-dimensionally in the radial section, the axial line chosen is generally the centerline. This is not necessary, however, and in more complicated reactors, other axial lines may be more convenient. This is particularly true if the reactor is calculated two-dimensionally in the radial section.

The problem can be iterated by returning to the radial calculation with modified values of the axial buckling. If desired, the axial and radial problems can be converged by cycling between the two calculations.

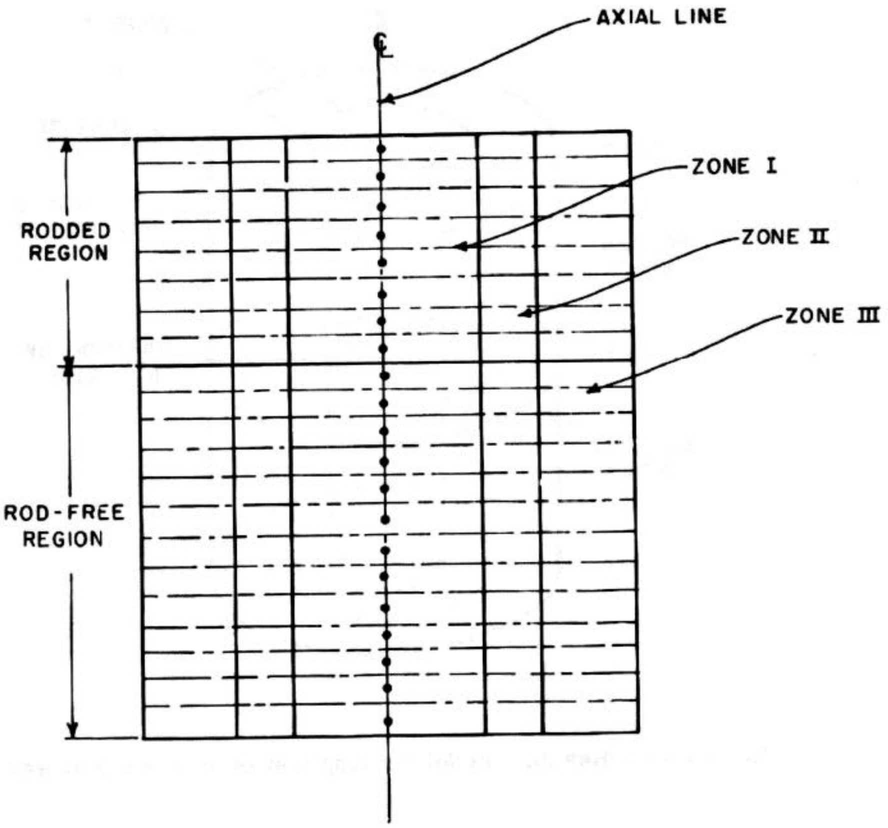

Fig. 18.12 - Sketch Showing Division of Reactor into Radial Sections

The number of axial points chosen should be sufficient to describe the axial flux distribution adequately. The number of radial sections used may be any number from two up to the number of axial points. At the beginning of life there are only two radial sections, the rodded and rod-free sections. With depletion the number will increase depending on the extent to which it is desired to consider differences in depletion. As applied in practice it is not burdensome to make the number of radial sections equal to the number of axial points.

The normalization is made along the axial line; for a simple reactor this will be assumed to be the centerline. In each radial section the flux at the center ($r = 0$) is set equal to the flux obtained at the corresponding axial position in the axial calculation. Thus the array of radial fluxes for the position $r = 0$ will represent the axial flux distribution. This is illustrated in Fig. 18.13.

To obtain an absolute normalization the fission rate per unit volume is summed over the reactor using the relative normalization described above. By equating the total fission rate to that necessary to produce the desired thermal power, an absolute flux normalization may be obtained.

With absolute flux normalization reactor lifetime depletion studies may be made. This is done by depleting each radial section for a specified operating time. At the end of this time step new material constants for the radial section are determined. These are used to perform new radial calculations, following which a new axial calculation is performed. The axial

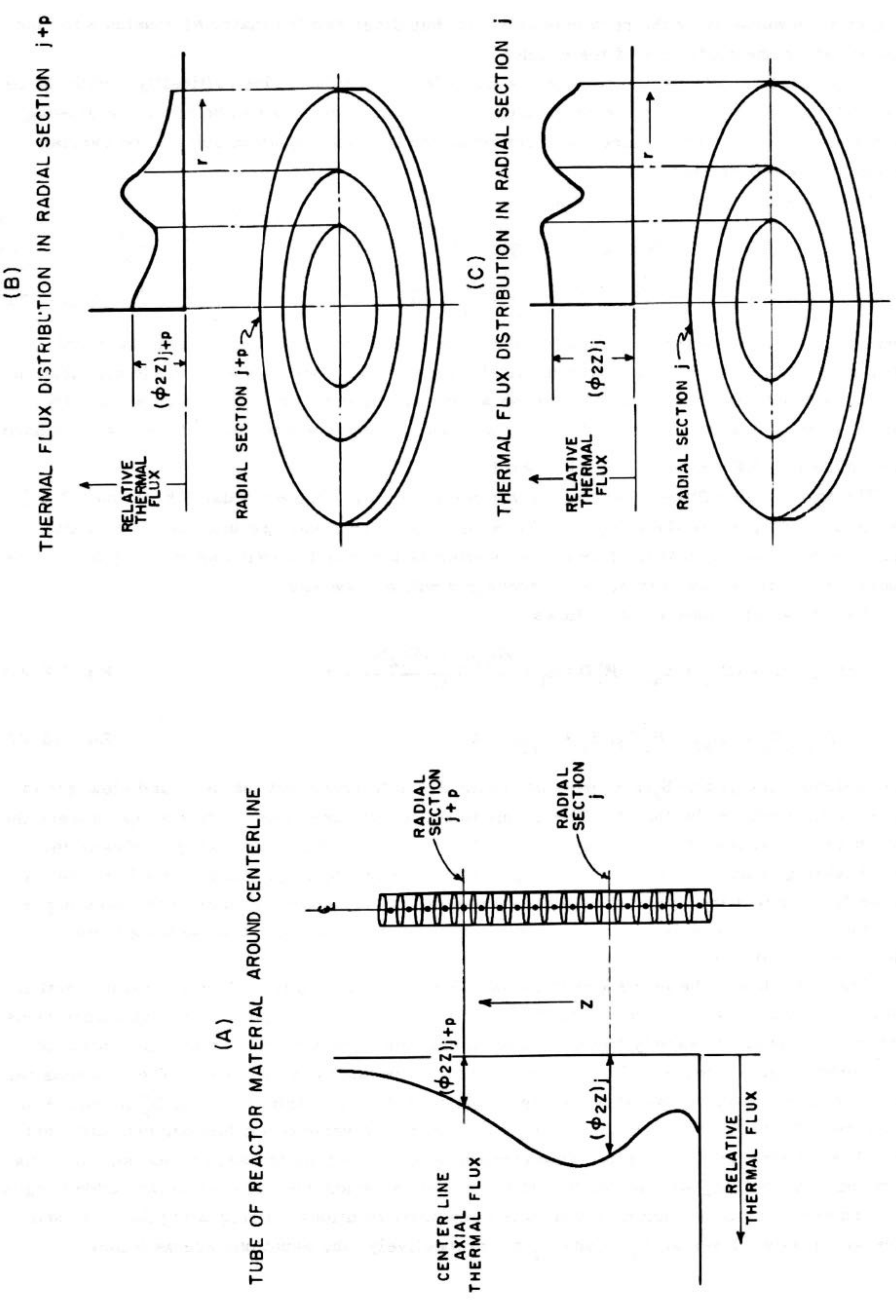

Fig. 18.13 - Application of Line Synthesis Method to Reactor Model

calculation is made using the recalculated radial bucklings and the material constants for the material along the centerline of the reactor.

In the axial calculation the rod bank position is readjusted to give criticality. With the new axial and radial distributions a new absolute normalization for flux can be made. Following this a new time step can be calculated permitting the lifetime depletion study to be carried through another time step.

The procedure outlined above allows calculation of the power distribution and rod bank positions for criticality over the duration of the reactor lifetime. [redacted]

In outline, this is the axial line synthesis technique. It differs from the flux-weighting technique in several respects, some of which can already be identified. First, the axial calculation of flux represents a specific axial distribution rather than an average distribution. Second, the material constants along the axial line are used for the axial calculation rather than average constants. Other differences will become evident when the details are considered.

18.9 AXIAL LINE TECHNIQUE - DETAILS OF APPLICATION

The two-group diffusion equations given earlier in this chapter [Eqs. (18.4) and (18.5)] are the starting point of the analysis. As before, they are separated into radial and axial equations by assuming that the flux can be written as a product function as in Eq. (18.1). The separated equations have certain differences and will be rewritten.

The radial equations are as follows:

$$D_1\nabla^2_{x,y}S_1 - (\Sigma_{r1} + \Sigma_{a1} + B_z^2 D_1)\, S_1 + \frac{\nu\Sigma_{f1}S_1 + \nu\Sigma_{f2}S_2}{\lambda_r} = 0 \qquad \text{Eq. (18.21)}$$

$$D_2\nabla^2_{x,y}S_2 - (\Sigma_{a2} + B_z^2 D_2)\, S_2 + \Sigma_{r1}S_1 = 0 \qquad \text{Eq. (18.22)}$$

The symbols $S_1(x, y)$ and $S_2(x, y)$ have been introduced to represent the fast- and slow-group radial components of the fluxes. These functions are not normalized at this stage as were the corresponding R_1 and R_2 functions in Eqs. (18.16) and (18.17). Only a single value of the axial buckling is used instead of the group-dependent bucklings B_{z1}^2 and B_{z2}^2 used previously. (In the first step of the iteration with the flux-weighting technique, a single axial buckling is also used.) The eigenvalue λ is shown with a subscript r to identify it as arising from Eqs. (18.21) and (18.22).

The first step in the procedure is to solve Eqs. (18.21) and (18.22) in the radial section using the appropriate material constants at each point of the homogenized multiple-zone radial section. As noted previously two-dimensional solutions could be used in the application of this method; here, however, S_1 and S_2 will be taken as functions of r only. The solutions can be obtained by use of the WANDA code (see Appendix A). The axial buckling B_z^2 is varied to bring the solution to criticality, i.e., $\lambda_r = 1$; however, a value of λ a few per cent different from 1 is considered acceptable. This procedure is carried out for each radial section. As might be expected, B_z^2 will be positive in the rod-free region and negative in the rodded region.

The next step in the solution is to obtain the axial solutions. Designating the fast- and slow-group axial fluxes as $T_1(z)$ and $T_2(z)$, respectively, the equations are as follows:

$$D_1\nabla_z^2T_1 - (\Sigma_{r1} + \Sigma_{a1} + B_r^2D_1)\ T_1 + \frac{\nu\Sigma_{f1}T_1 + \nu\Sigma_{f2}T_2}{\lambda_z} = 0 \qquad \text{Eq. (18.23)}$$

$$D_2\nabla_z^2T_2 - (\Sigma_{a2} + B_r^2D_2)\ T_2 + \Sigma_{r1}T_1 = 0 \qquad \text{Eq. (18.24)}$$

The material constants in the axial equations are taken to be those along the axial line where the calculation is being made. The radial buckling in these equations is a function of z and is determined from the equation

$$B_z^2(z_j) + B_r^2(z_j) = B_m^2(z_j) \qquad \text{Eq. (18.25)}$$

where B_m^2 is the material buckling of the reactor material at the axial point under consideration and B_z^2 is the axial buckling used in Eqs. (18.21) and (18.22) to give criticality of the radial section. The symbol z_j indicates that the calculation is made for the j^{th} axial point.

The material buckling, B_m^2, to be used in Eq. (18.25) is given below.

$$B_m^2 \equiv -\frac{1}{2}\left(\frac{1}{L^2}+\frac{1}{\tau}\right)+\frac{1}{2}\left[\left(\frac{1}{L^2}+\frac{1}{\tau}\right)^2+\frac{4(k_\infty - 1)}{L^2\tau}\right]^{1/2} \qquad \text{Eq. (18.26)}$$

where

$$L^2 \equiv \frac{D_2}{\Sigma_{a2}} \qquad \text{Eq. (18.26a)}$$

$$\tau \equiv \frac{D_1}{\Sigma_{r1} + \Sigma_{a1} - \frac{\nu\Sigma_{f1}}{\lambda_r}} \qquad \text{Eq. (18.26b)}$$

$$k_\infty \equiv (\eta f)_2\ (\epsilon p) \qquad \text{Eq. (18.26c)}$$

$$(\eta f)_2 \equiv \frac{\nu\ \Sigma_{f2}}{\lambda_r\Sigma_{a2}} \qquad \text{Eq. (18.26d)}$$

$$\epsilon p \equiv \frac{\Sigma_{r1}}{\Sigma_{r1} + \Sigma_{a1} - \frac{\nu\Sigma_{f1}}{\lambda_r}} \qquad \text{Eq. (18.26e)}$$

B_m^2 is evaluated for each radial section at r = 0, using the eigenvalue λ_r obtained in the solution of the radial section equations.

Equations (18.23) and (18.24) may be solved by a one-dimensional digital computer code such as WANDA (see Appendix A). In the solution, the axial position of the control rod bank is adjusted to give criticality, i.e., $\lambda_z = 1$.

At this point it would be possible to iterate the solutions; in fact, group-dependent bucklings from the solution to Eqs. (18.23) and (18.24) could be introduced into Eqs. (18.21) and (18.22). In depletion studies this is not done, however, because it would destroy the essential simplicity of the calculation. At the beginning of life, however, an iteration study may be useful for another purpose. It can serve to demonstrate the sensitivity of the solutions to the bucklings used and to determine how close to unity the eigenvalue should be adjusted.

There are two slightly different normalization procedures which may be used. In the preceding section a flux normalization was described such that the radial section thermal flux of the j^{th} section S_{2j} at the position of the axial line was made equal to the axial thermal flux at that section. In terms of the radial and axial functions

$$S_{2j}(0,0) = T_2(z_j) \,. \qquad \text{Eq. (18.27)}$$

In general the fast fluxes will not be equal.

$$S_{1j}(0,0) \neq T_1(z_j)$$

The reason for this is twofold. First, without iteration there will be a small discrepancy in the fast-to-slow flux ratio between the axial and radial solutions. Second, if group-dependent bucklings corresponding to each axial point are not introduced into the radial equations, some residual discrepancy will exist because the fast-to-slow flux ratio in a transition region, i.e., near the rod bank boundary, will not be the same as that given by the radial solution. These errors are small, however, principally because most of the fissioning occurs in the thermal group.

A power normalization, however, would appear to be more consistent than a flux normalization and is preferred. This is carried out as follows:

$$T_1(z_j)\,\Sigma_{f1}(z_j) + T_2(z_j)\,\Sigma_{f2}(z_j) = S_{1j}(0,0)\,\Sigma_{f1}(0,0) + S_{2j}(0,0)\,\Sigma_{f2}(0,0) \qquad \text{Eq. (18.28)}$$

Since the ratio S_{2j}/S_{1j} is established by the radial section solution and the ratio T_1/T_2 by the axial solution, this equation normalizes the radial solutions to the axial solution.

In carrying out the absolute normalization it is convenient to introduce some additional notation. Again using C_1 and C_2 to represent the energy release per fission for fast and slow fission, respectively, the average power density $\bar{p}_j$ in the j^{th} radial section is

$$\bar{p}_j = \frac{\int \left[C_1\Sigma_{f1}(x,y)\,S_{1j}(x,y) + C_2\Sigma_{f2}(x,y)\,S_{2j}(x,y)\right] dxdy}{\int dxdy} \qquad \text{Eq. (18.29)}$$

where the integrations are carried out over the entire fueled region of the radial section. The ratio of the average power density in the radial section to that at the center of the section will be designated as q_j.

$$q_j = \frac{\bar{p}_j}{p_j(0,0)} = \frac{\bar{p}_j}{C_1\Sigma_{f1}(0,0)\,S_{1j}(0,0) + C_2\Sigma_{f2}(0,0)\,S_{2j}(0,0)} \qquad \text{Eq. (18.30)}$$

The total output power from the reactor is

$$P = \sum_j q_j \Delta z_j \left[T_1(z_j)\,\Sigma_{f1}(z_j) + T_2(z_j)\,\Sigma_{f2}(z_j)\right] \qquad \text{Eq. (18.31)}$$

where Δz_j is the axial thickness of the j^{th} radial section.

In Eq. (18.31) the q_j's may be obtained from the radial solutions without normalization, the Σ's are known and the ratio of T_1/T_2 is known. Thus, setting a value for P normalizes the T's and thus normalizes the S's by Eq. (18.28).

To carry out a lifetime depletion study, a series of time steps are taken. The reactor is recalculated at each time step.

At the start of life, or at any given point in life at which the reactor material constants are known, the radial and axial equations are solved as outlined above. The fluxes are normalized by Eqs. (18.31) and (18.28). It is assumed that the reactor fluxes and material properties remain at these values over a fixed time interval. At the end of this interval the material composition is recalculated at each point on the assumption that the fission rate remained constant during the interval. Thus, new material constants can be obtained for each point in the reactor and the reactor recalculated.

The application of the line synthesis technique can be made relatively simple for lifetime studies by preparing in advance certain data in graphical form. First, certain typical radial sections are carried through a series of arbitrary lifetime depletion steps. At the end of each time step the section is recalculated for criticality by varying B_z^2. This calculation can be made conveniently with a digital computer code such as CANDLE (see Appendix C). From the series of perhaps ten or more such steps, the pertinent information needed for the axial calculation and power normalization is abstracted and plotted in terms of a suitable independent variable. This variable might be energy or flux time. Flux time at the center of the radial section is a convenient variable. The following quantities are obtained from the radial section calculations and plotted as functions of flux time at the center of the reactor.

(a) The macroscopic fission cross section (Σ_{f1} and Σ_{f2}) at the center of the radial section.
(b) The other pertinent material constants (D_1, D_2, Σ_{a1}, Σ_{a2}) at the center of the radial section.
(c) The radial buckling at the center of the radial section. [Eq. (18.25)].
(d) The ratio of average power density in the radial section to that at the center of the section (q_j).

With these variables plotted and a normalized axial flux distribution available, a given time interval will represent a specific flux time at each axial point. From the curves the new values at each point can be obtained immediately. Following the axial recalculation with the new constants, a new normalization can be made. In this way a series of axial calculations representing a lifetime depletion study can be made with appropriate adjustment of the constants at each axial point.

There is little that can be said in a general way about the validity of the line synthesis technique. The scheme is a highly intuitive one although certain of the weaknesses in the arguments are apparent. In those cases when it is applicable it would seem probable that it would give reasonably good results for the beginning of life but that the results would be very questionable at high depletions. The reason for this lack of confidence with high depletion is the use of principal mode solutions to describe transverse leakage. With high depletion it is unlikely that the fast-to-slow flux ratios anywhere in the core will have values characteristic of the principal modes. In summary, the scheme has real advantages as a rapid method for analysis of a reactor over its lifetime but lacking detailed comparisons with multi-dimension depletion studies, there is little that can be said by way of evaluation.

REFERENCES

1. J. E. Meyer, Synthesis of Three-Dimensional Power Shapes--Flux-Weighting Technique, Bettis Technical Review, Vol. 1, No. 4, October 1957.
2. R. R. Schiff, Synthesis of Three-Dimensional Power Distributions for a Nonuniformly Depleted Core, Bettis Technical Review, Vol. 1, No. 4, October 1957.
3. R. S. Halgas and M. Bender, Half-Height Cadmium Slab, Bettis Technical Review, Vol. 1, No. 4, October 1957.
4. R. S. Wick and J. D. Butler, The Use of the Equivalent Bare Core Model for Calculating the Criticality of Slab-Type Reactors and a Comparison to Experiment, Bettis Technical Review, Vol. 1, No. 4, October 1957.

APPENDICES

INTRODUCTION

The material for these Appendices was assembled and written by Dr. B. H. Mount from reports and material at Bettis, KAPL, and the David Taylor Model Basin Applied Mathematics Laboratory. Dr. R. Ehrlich provided much of the KAPL material and Dr. E. Cuthill the material from the DTMB Applied Mathematics Laboratory.

Appendix A

FEW-GROUP, ONE-DIMENSIONAL DIFFUSION THEORY CODES

CONTENTS

A.1 AML-17

The AML-17 code solves on the UNIVAC-I the time-independent two-group neutron-diffusion equations

$$-D_f \nabla^2 \phi_f + (\Sigma_f^a + D_f B_r^2)\, \phi_f = \eta \Sigma_a^s\, \phi_s$$

$$-D_s \nabla^2 \phi_s + (\Sigma_s^1 + \Sigma_s^2 + D_s B_r^2)\, \phi_s = \Sigma_f^s\, \phi_f$$

in one dimension in rectangular, cylindrical, or spherical geometry.

The code permits a mesh of up to 30 points with variable spacing between points. It permits pointwise variation of the two diffusion parameters and the five macroscopic cross-section parameters in the above equations.

The code computes the eigenvalue and the fast- and slow-group fluxes. The calculations are done in the floating-decimal mode. The typical computing time per problem is approximately twenty minutes.

A.2 LIL ABNER

The LIL ABNER code solves on the IBM-650 the few-group diffusion equations

$$\left\{- \nabla\cdot D_i\, \nabla\phi_i + \Sigma_i\, \phi_i = \frac{\chi_i \psi}{\lambda} + \Sigma_{i-1}^R \phi_{i-1}\right\}_{i=1}^{k}, \quad 1 \leq k \leq 8$$

in one dimension in rectangular, cylindrical, or spherical geometry. Here

$$\Sigma_i = \Sigma_i^a + \Sigma_i^R + B^2 D_i$$

and

$$\psi = \sum_{i=1}^{k} (\nu\Sigma^f)_i \phi_i$$

LIL ABNER allows at most ten regions and one hundred mesh points. The mesh spacing as well as all of the physical parameters must be constant within a region; in fact, this restriction can be taken to define a region. Each region must contain an even number of mesh intervals. Boundary conditions of zero flux or zero current can be specified at each outer boundary.

LIL ABNER computes the fluxes, ϕ_i; the fission source, ψ, at every point; and the eigenvalue, λ, by successive iterations. The problem is complete when the difference between successive eigenvalues or the difference between a maximum and a minimum eigenvalue satisfy an input criterion.

The calculations are made in floating decimal using the IBM floating-point interpretive system. Input to the code includes the geometric and physical parameters, the convergence criterion, and the initial source guess. Output cards contain eigenvalues, fluxes, and source.

An estimate of the running time may be obtained by using the formula $T = P \cdot G/200$ where P is the number of points, G is the number of groups and T is the machine time in hours. The solution time will, of course, vary with the convergence criterion and the initial source guess.

A specially wired control panel is needed to run all problems. The computer must have a 2000-word drum.

A.3 ENSIGN

The ENSIGN code for the IBM-650 is the fixed-point version of the LIL ABNER code. It solves the same problems by the same techniques. The running time per problem is approximately one-third of the LIL ABNER running time.

A.4 WANDA

The WANDA code solves on the IBM-704 the few-group neutron-diffusion equations

$$\left\{ -\nabla \cdot D_i \nabla\phi_i + \Sigma_i\phi_i = \frac{\chi_i\psi}{\lambda} + \Sigma_{i-1}^R \phi_{i-1} \right\}_{i=1}^{k}, \quad k \leqq 4$$

in one dimension in rectangular, cylindrical, or spherical geometry. Here

$$\Sigma_i = \Sigma_i^a + \Sigma_i^R + B^2 D_i + t_i \Sigma_k^p$$

and

$$\psi = \sum_{i=1}^{k} \nu_i \Sigma_i^f \phi_i$$

By successive source iterations, WANDA obtains the pointwise values of fluxes and source and the eigenvalue, λ. It is possible to cause WANDA to do one of three criticality searches: (1) by varying the buckling in a set of regions or throughout the reactor, (2) by varying the amount of homogeneous poison in a set of regions, and (3) by moving a poison boundary in a multiplying region.

WANDA allows a maximum of 250 mesh intervals in at most 25 regions, an even number of intervals being required in each region. It requires an IBM-704 with at least 8,192 words of core storage, one unit of four logical drums and one tape unit. Problem running time will vary from one to fifteen minutes depending on the initial source guess, the number of points, and the type of search. Three minutes is a typical running time.

Certain of the input data may be specified, either pointwise or as regionwise constants. The basic items of input are the geometric and physical parameters, initial estimate of the source, and initial estimate of the parameters which are varied in the criticality searches.

The output includes eigenvalues, fluxes and source pointwise, source averaged over each region, regional volumes, flux integrated over each region and for the whole reactor, and region checks which are proportional to the leakage from each region for each group.

A. 5 PROD II

PROD II obtains on the IBM-650 the approximate solution of the multigroup age-diffusion equation in one space dimension in slab, cylindrical, or spherical geometry. The program allows for the option of including or excluding inelastic scattering and the Selengut-Goertzel term for hydrogen scattering. Neutron balance calculations are performed to check the conservation of neutrons in each region.

The boundary conditions at the origin are either zero flux or zero gradient. At the outer boundary, the generalized gradient condition may be applied.

Operationally, PROD II consists of two parts, each of which accepts input data on punched cards and creates output data on punched cards. The output cards of either part are acceptable as input to the other part.

Part I: The Multigroup Calculation solves the three-point formula for flux at each point, punching these fluxes on output cards.

Part II: The Power Calculation computes the pointwise values of the power and then the eigenvalue, punching the normalized power on output cards. The maximum size problem may be determined as follows: Let G be the number of groups, R the number of regions, C the number of regions in the core, and P the number of mesh points. Then $G \leqq 50$, $C < 50$, $CG \leqq 1000$, and $P + R \leqq 98$.

Problem solution time (in minutes) may be estimated by the formula $T = PG/40$. If inelastic scattering is omitted, the computing time is cut approximately in half. An additional saving in solution time occurs when the Selengut-Goertzel term is omitted.

REFERENCES

1. AML-17 Code - further information is available from the Applied Mathematics Laboratory of the David Taylor Model Basin.
2. H. Bohl, Jr., E. M. Gelbard, and R. Suarez, A Few Group One-Dimensional Code for the IBM-650, Report WAPD-TM-3, July 1956.
3. B. L. Anderson, H. Bohl, Jr., E. M. Gelbard, E. H. Stoves, ENSIGN Code, Report WAPD-TM-33, January 1957.
4. O. J. Marlowe, C. P. Saalbach, L. M. Culpepper, D. S. McCarty, WANDA -- A One-Dimensional Few-Group Diffusion Equation Code for the IBM-704, Report WAPD-TM-28, November 1956.
5. G. J. Habetler, One-Space-Dimensional Multigroup for the IBM-650, Part I. Equations, Report KAPL-1415, December 1, 1955.
6. V. A. Walbran, One-Space-Dimensional Multigroup for the IBM-650, Part II. Machine Program, Report KAPL-1531, April 10, 1956.

The LIL ABNER, ENSIGN, and WANDA Codes are available from Mr. Donald Cashman, Applied Programming Publications, Applied Science Division, IBM Corp., 590 Madison Ave., New York 22, New York.

Appendix B

FEW-GROUP, TWO-DIMENSIONAL DIFFUSION THEORY CODES

CONTENTS

B.1 CUTHILL

The CUTHILL code solves on the UNIVAC-I the two-group time-independent neutron-diffusion equations in (x, y) geometry. The equations

$$D^1 \nabla^2 \phi^1 - (\Sigma_a^1 + \Sigma_r^1 + B_z^2 D^1) \phi^1 + \eta \Sigma_f^2 \phi^2 = 0$$

and

$$D^2 \nabla^2 \phi^2 - (\Sigma_a^2 + B_z^2 D^2) \phi^2 + \Sigma_r^1 \phi^1 = 0$$

are solved at the node points of a rectangular mesh superimposed on the reactor section.

The interior regions are either diffusion regions or control rod regions. At interfaces which involve control rod regions, a logarithmic derivative condition is imposed on the thermal flux. Otherwise, at all interfaces the fluxes and currents are assumed to be continuous. Within each region D^1, D^2, Σ_a^1 and Σ_r^1 are constant, while Σ_a^2 and Σ_f^2 may be regionwise constants or may vary pointwise.

The code allows as many as 59 x 118 points with constant mesh spacing and as many as nine different material compositions. It prints out a "picture" of the arrangement of compositions over the reactor section. Information indicating the progress of the calculations is printed on-line. Pointwise values of the fluxes and their regionwise integrals are written on magnetic tape for off-line printing.

A rough estimate of the computing time may be obtained by assuming that it requires about one hour for each one hundred points in the mesh.

B.2 ACE OR NORC-CUTHILL

The ACE code solves on the NORC the same problem that is solved by the CUTHILL code on UNIVAC-I. It allows as many as 18,720 points (96 x 195), variable mesh spacing in both coordinate directions and as many as 18 compositions.

The running time may be estimated by assuming a speed of 500 mesh points per hour.

B.3 QED-2

The QED-2 code solves the two-group, steady-state, neutron-diffusion equations

$$-\nabla\cdot D_f \nabla\phi_f + (\Sigma_f^a + D_f B_z^2)\, \phi_f = \eta\Sigma_{25}\phi_s$$

$$-\nabla\cdot D_s \nabla\phi_s + (\Sigma_s + D_s B_z^2)\, \phi_s = \Sigma_f^s\, \phi_f$$

on the IBM-704 computer. The solution is obtained over a rectangular region of the x-y plane. A mesh of horizontal and vertical lines is imposed on this rectangular region of solution. with a maximum of 50 mesh lines in each coordinate direction. The code obtains the values of ϕ_f and ϕ_s at each of the resulting mesh points together with a single value of η.

The rectangular region is composed of at most nine different subregions, with the values of D_f, Σ_f^a, Σ_{25}, D_s, Σ_s, and Σ_f^s constant within each subregion. The mesh spacing must be chosen in such a way that the external boundaries and the interfaces between subregions fall exactly on mesh lines.

Either a zero flux or a zero current condition may be applied at each external boundary. The same condition must be applied in each lethargy group. In addition, a logarithmic derivative condition may be applied at internal interfaces. This condition is used to represent control rods and assigns a value to the current/flux ratio at the rod interface.

One core storage unit of 4096 words, one drum unit of 8192 words, and three or four tape units, depending upon the on-line/off-line output option, are required. The code imposes slight restrictions on geometric complexity and number of mesh interval changes in order to fit a 2500-point problem into the internal storage of the computer.

Input to the QED-2 code consists of the value of the buckling, an eigenvalue approximation and a convergence parameter, values of the group-dependent parameters and a flux approximation for each subregion, the mesh intervals in each coordinate direction, the four boundary conditions, and the arrangement of subregions in the mesh. At the beginning of a problem, the code prints on-line an edit of the input and a "picture" of the mesh which indicates the arrangement of the subregions and the location of interfaces. At the end of the problem, the region averages and pointwise flux values may be printed on-line or written on tape for off-line printing.

A QED-2 problem is iterated until

$$\frac{\bar{\eta}^{(m)} - \underline{\eta}^{(m)}}{2\eta^{(m)}} \leqq \epsilon^2$$

where ϵ is an input parameter and the superscript (m) indicates the quantities calculated at the end of iteration (m). If $\epsilon = 0.05$, the running time of a typical 2500-point problem is one hour.

B.4 PDQ-2

The PDQ-2 code solves on the IBM-704 the few-group time-independent neutron-diffusion equations

$$\left\{ -\nabla \cdot D_i \nabla \phi_i + \Sigma_i \phi_i = \frac{\chi_i \psi}{\lambda} + \Sigma^R_{i-1} \phi_{i-1} \right\}^k_{i=1}, \quad k \leqq 4$$

over a rectangle in either rectangular or cylindrical geometry. Here

$$\Sigma_i = \Sigma^a_i + \Sigma^R_i + B^2 D_i$$

and

$$\psi = \sum_{i=1}^{k} \nu_i \Sigma^f_i \phi_i$$

Each of the four sides of the bounding rectangle may have either of two boundary conditions applied in all groups, either zero flux on the boundary or zero current across the boundary. Control rods may be represented by assigning a value to the ratio of current to flux at the bounding surface of the rods.

The parameters D_i, Σ^a_i, Σ^R_i and $\nu_i \Sigma^f_i$ are constant over each of the regions. A maximum of 35 regions are allowed. The χ_i are functions only of the lethargy group. A mesh of horizontal and vertical lines is imposed on the rectangular region. The spacings between these lines are chosen such that all boundaries, internal and external, lie on mesh lines. PDQ-2 computes the fission source, ψ, and the group fluxes, ϕ_i, at each point of the mesh. The maximum number of points allowed depends on the size of the core memory and whether or not one unit of four logical drums is on the IBM-704. This variation is shown in the following table:

Core Size	4K	8K	16K	32K
With 4 drums	1250	2500	3750	6500
With no drums		1000	2500	5250

In addition to the core and drum storage indicated above, PDQ-2 requires six tape units.

Input required by PDQ-2 includes the number of groups, number of material compositions, number of points in each direction, four boundary conditions, the mesh spacings, buckling, estimated eigenvalue, λ, convergence criterion, χ_1, χ_2, and χ_3 ($\chi_4 = 0$) and the arrangement of materials within the rectangular boundary. For each material all of the group-dependent parameters and a flux estimate must be specified.

Before starting the solution of the problem, PDQ-2 prints on the attached printer all of the numerical input as well as a picture of the specified arrangement of materials. During the solution of the problem, certain information is printed to indicate progress. The most significant number printed is the eigenvalue, λ, after each source iteration. At the conclusion of the problem certain region integrals and averages are printed on-line, and pointwise values of fluxes and sources are written on magnetic tape for off-line printing.

The iterations of a PDQ-2 problem are continued until

$$\frac{\bar{\lambda}^{(m)} - \underline{\lambda}^{(m)}}{2\lambda^{(m)}} \leqq \epsilon^2$$

where ϵ is the input convergence parameter and (m) is the iteration index.

If $\epsilon = 0.05$, a reasonable estimate of running time may be obtained by using the formula $T = P \cdot G/100$ where P is the number of points, G is the number of groups, and T is expected running time in minutes. If a problem possesses symmetry about a diagonal, the running time can be halved.

B.5 MUG II

The MUG II code obtains on the UNIVAC-I the approximate solution to the multi-group age diffusion equation in two space dimensions in cartesian or cylindrical geometry, with or without the Selengut-Goertzel term for hydrogen scattering. The coordinate referred to as $(x^{(1)}, x^{(2)})$ may be either (x,y), (r,z), or (r, θ).

The code allows at most ten different material compositions in at most 64 regions. It allows at most nine interfaces (including boundaries) normal to each coordinate direction. Mesh spacing in each direction is required to be constant, all interfaces being required to lie on mesh lines. The maximum number of the points in the $x^{(1)}$ direction is 100 and 59 in the $x^{(2)}$ direction. The maximum number of energy groups allowed is 100.

The boundary conditions may be zero flux in all groups on any boundary, the logarithmic derivative of flux on any boundary equal to a given function of lethargy, or a periodic flux or gradient condition on the $x^{(2)}$ boundaries.

B.6 TOSPY

The TOSPY code solves the two-dimensional multi-group diffusion equation on UNIVAC-I in either cartesian or cylindrical geometry. It allows at most 19 groups, 100 rows and 59 columns of mesh points. It allows zero flux, zero current, or generalized gradient conditions on the outer boundaries of the region.

The code requires the specially-defined orders "lnm", "2nm", "30m", and "40m" which are on the computer at New York University and the two machines at the David Taylor Model Basin. TOSPY has been superseded by the CURE code on the IBM-704.

B.7 CURE

The CURE code solves on the IBM-704 the multi-group or the few-group neutron diffusion equation in two dimensions in (x,y), (r,z), or (r, θ) geometry. Inelastic scattering and the Selengut-Goertzel treatment of hydrogen slowing-down are included in the multi-group version of the code.

The following boundary conditions are treated:

1. Zero flux on the boundary
2. Given non-zero flux
3. Zero current across boundary
4. Given ratio of current to flux at boundary
5. Periodic behavior of flux and current azimuthally

The CURE code includes a library of microscopic data from which macroscopic data may be computed. Optionally, in the few-group version the macroscopic data may be supplied as input.

The code requires seven tape units. No drum unit is required.

The basic mesh is a rectangular array of I x J points. From this basic mesh, one deletes the points outside the boundaries of the specified region. Further deletions of points within the boundaries are permitted. Fluxes and power are computed at those points of the I x J mesh which remain after deletions. Upper limits on I, J, the product (I+1)(J+1), and the number of flux points are determined by the size of the core storage of the computer. These limits are given in the following table.

Core Store	Max I,J	(I+1)(J+1)	Flux Points
8,192	50	1400	644
16,384	120	2600	1516
32,768	200	7475	3275

CURE has three xenon options: (1) no xenon, (2) steady-state xenon, and (3) peak xenon.

A rough estimate of the machine time required by a problem can be obtained by the formula $T = P \cdot G/60$ where T is the machine time in minutes, P is the number of flux points, and G is the number of groups

REFERENCES

1. CUTHILL Code - additional information may be obtained from the Applied Mathematics Laboratory of the David Taylor Model Basin.
2. ACE or NORC-CUTHILL Code - additional information may be obtained from the Applied Mathematics Laboratory of the David Taylor Model Basin.
3. G. G. Bilodeau, W. R. Cadwell, J. P. Dorsey, J. G. Fairey, R. S. Varga, PDQ -- An IBM-704 Code to Solve the Two-Dimensional Few-Group Neutron-Diffusion Equations, Report WAPD-TM-70, August 1957.
4. R. H. Stark, Preparation of Input Data for Two-Space-Dimension Multigroup, Report KAPL-1068, October 26, 1954.
5. E. L. Wachspress, A Generalized Two-Space-Dimension Multigroup Coding for the IBM-704, Report KAPL-1724, April 30, 1957.

The PDQ-2 and CURE Codes are available from Mr. Donald Cashman, Applied Programming Publications, Applied Science Division, IBM Corp., 590 Madison Ave., New York 22, New York.

Appendix C

FEW-GROUP, ONE- AND TWO-DIMENSIONAL DEPLETION CODES

CONTENTS

C.1 AML-67A

The AML-67A code solves on the UNIVAC-I the time-dependent two-group neutron-diffusion equation in one dimension in rectangular or cylindrical geometry. The AML-17 code is incorporated in AML-67A to solve the spatial equations at each time step for eigenvalue and fluxes.

The code allows up to 16 time steps, each of arbitrary length, during which the pointwise fluxes are assumed constant. Radial problems require that $d\phi/dr = 0$ at the origin and allow either $\phi = 0$ or $d\phi/dr \neq 0$ at the outer boundary to simulate a reflector. For slab problems either boundary can have zero flux or a specified flux gradient. The flux gradient is put into the code by fictitious nuclear constants at the end points. Compositions may vary pointwise with at most 15 sequential changes in composition.

At each time-step the flux shapes are normalized by specifying the fission rate per unit area in slab geometry or per unit height in cylindrical geometry. Then the depletion and build-up of isotopes of uranium and plutonium are computed at each mesh point. The pointwise concentrations of xenon, samarium, iodine, and promethium and the long-lived fission product poisons also are computed.

Two types of fueled regions are allowed: Type-A regions which contain U^{235}, and type-B regions which contain both U^{235} and U^{238}.

Criticality is achieved, if desired, at each time-step by varying parameter, α, which contributes to the total cross section term in the equation for the thermal group flux.

The typical running time is approximately one-half hour per time-step.

C.2 CANDLE

CANDLE is an IBM-704 code which takes into account both the space- and time-dependence of the diffusion coefficient D, the removal cross section Σ^R, the absorption cross section Σ^a, and the fission rate per unit flux $\nu\Sigma^f$, in the solution of the few-group neutron diffusion equation

$$\left\{ -\nabla\cdot D_i(r)\,\nabla\phi_i(r) + \Sigma_i^T(r)\phi_i(r) = \frac{\chi_i\psi(r)}{\lambda} + \Sigma_{i-1}^R(r)\,\phi_{i-1}(r) \right\}_{i=1}^{k}$$

in one space dimension. Here i indicates the lethargy group, k the thermal group (k = 2 or 4),

$$\psi_i(r) = \sum_{i=1}^{k} \left[\nu\Sigma^f(r)\right]_i \phi_i(r)$$

and

$$\Sigma_i^T(r) = B_i^2(r)D_i(r) + \Sigma_i^R(r) + \Sigma_i^a(r) + t_i\,\Sigma_k^p(r)$$

The buckling $B_i^2(r)$, is a group-and region-dependent input quantity. $\Sigma_k^p(r)$ is a region-dependent poison and t_i is the fraction applied in the i^{th} group, $t_k \equiv 1$.

The few-group parameters D, Σ^R, Σ^a, and $\nu\Sigma^f$ are calculated at each mesh point utilizing a library of effective microscopic cross sections for the fast groups and input values of the thermal microscopic cross sections, thermal self-shielding factor, and the resonance escape probability for U^{238}. Two-group parameters are calculated from the four-group constants by taking weighted averages.

After having calculated the parameters for the diffusion equation, CANDLE solves for the resulting flux distribution, iterating until the convergence criterion on the eigenvalue and source is satisfied.

As options, the CANDLE code provides three means by which the quantity λ may be forced to approach 1.0:

1. Adjusting a group-independent buckling in a set of regions.
2. Adjusting the homogeneous poison Σ_k^p in a set of regions.
3. Adjusting the position of a boundary separating the poisoned and unpoisoned sections of a multiplying region.

At the conclusion of the spatial portion of the code, the fluxes are normalized to a specified power level. These power-normalized fluxes are assumed constant over the time interval represented in the approximate solution to the depletion equations.

Results of each time step are recorded on magnetic tape. At any time after the calculation is completed, a selective edit may be performed to obtain pointwise values of the flux, source, power, macroscopic cross sections, isotopic number densities, and combinations of these values. The supervisory output, which is printed on-line during the calculation, includes the eigenvalues and control parameters, if used.

In order to change parameters in a problem, the user may elect to use the isotopic number densities from any time step of a previously run problem. This is called the continuation option.

CANDLE permits a maximum of 250 mesh intervals distributed over at most 25 regions to be used to describe a problem. No more than 25 time steps may be requested and at most

30 elements may be specified. The code requires an IBM-704 with at least 8,192 words of core storage, 4 logical drums, and 4 tape units. The running time per time step for a 181-point problem may vary from 3 minutes for a non-search case to 15 minutes for a boundary-search problem.

C.3 DRIFT

The DRIFT code for the NORC computer obtains the solution of the time-dependent two-group neutron-diffusion equation in two dimensions. For each time-step the ACE code is used to determine the spatial distribution of fast and slow fluxes. These fluxes are normalized to constant reactor power.

At each point the fuel fraction, π_T, at the end of the time-step is obtained by multiplying π_{T-1} by $(1 - \sigma_a^{25}\, \Phi^{(2)}\, \Delta t)$. If the computed value becomes negative, it is set to zero. A table-look-up procedure is used to obtain $\Sigma_f^{(2)}$ and $\Sigma_a^{(2)}$ as functions of the fuel fraction at each point.

The new values of $\Sigma_f^{(2)}$ and $\Sigma_a^{(2)}$ are used as input data for the next time-step. Likewise, the flux for time-step T may be used as the initial guess for the flux of time-step (T+1). For each new time-step the buckling, B_z^2, may be changed and the material composition of any non-fuel region may be respecified.

C.4 TURBO

The TURBO code is a two-dimensional few-group depletion code for the IBM-704. The PDQ code is used to compute neutron flux values from the two- or four-group diffusion equations. The parameters required in these equations are derived from effective one-velocity microscopic cross sections for the elements comprising the media. These elements are described by their isotopic densities and thermal self-shielding factors. Assuming flux and power to be constant for a specified period of time (a time-step), the time-dependent isotopic densities can be recomputed for the beginning of the next time-step.

The calculation can be done for either x-y or r-z geometry. By using a suitable synthesis scheme, it is possible to piece together two-dimensional (i.e., x-y) calculations to simulate a three-dimensional calculation (see Chap 18).

The PDQ description in Appendix B gives the equations solved and method of solution. The few-group parameters required are calculated from equations of the type $\Sigma_i(x) = \sum_M N^M(x)\, \sigma_i^M$, for the fast groups or $\Sigma_k(x) = \sum N^M(x)\, g^M \sigma_k^M$ in the thermal group where M ranges over 30 possible isotopes. [redacted] In the third group a correction is made for U^{238} resonance. Two-group constants are obtained by taking weighted averages of the four-group constants.

The neutron flux values obtained from the PDQ calculation are normalized to a specified power output for the section of the reactor considered and used in the depletion equations which have the general form

$$\frac{dN^M}{dt} = -\left(\lambda^M + \sum_i \sigma_a^{M,i}\, \phi_n^i + g^M \sigma_a^{M,k}\, \phi_i^k\right) N_n^M(t)$$

$$+ \lambda^{M-1}\, N_{(t)}^{M-1} + \left(\sum_i \sigma_c^{M',i}\, \phi_n^i + g^{M'} \sigma_c^{M',k}\, \phi_n^k\right) N_n^{M'}(t)$$

Here N_n^M, N_n^{M-1}, and $N_n^{M'}$ denote densities of different isotopes at a mesh point n, λ is a decay constant, $\sigma_a = \sigma_c + \sigma_f$ is a microscopic absorption cross section, and g^k is a thermal self-shielding factor.

A maximum xenon calculation is also provided in which the flux at a particular time-step is reduced by a specified amount and used to deplete the isotopic densities over a specified time interval which may allow maximum xenon build-up. A routine is also available to allow the study of refueling or interchange of subassemblies.

The output from the code consists of the on-line printout provided by PDQ plus the ratio of the power produced in each region to the total power and the fraction of the power within each region produced by each fissionable isotope. A binary output tape is also generated which can be selectively processed at any time to provide printing of:

1. Average power at each mesh point
2. Isotopic density for any isotope at each point
3. Values of any of the macroscopic cross sections used in the spatial calculation at each point for any group
4. Values of the neutron flux for any group at each point
5. Values of the source calculated in the spatial integration at each point
6. The average isotopic densities for each region and the total area
7. The flux-weighted averages of the macroscopic cross sections for use in a synthesis calculation

In addition, the isotopic densities can be obtained for the beginning and/or the end of the time-step. To allow special edits to be done using the WOLONTIS system (Bell Laboratory Interpretive System) on the IBM-650, certain of the above quantities can be punched onto cards in a convenient form.

The calculation is done automatically for one time-step at a time. The data deck is read for each subsequent calculation to allow the changing of thermal cross sections, thermal self-shielding factors, fixed isotopic densities, and the like. A typical computing time for a 2500 mesh-point problem is 1.5 hours per time-step. If the running time for a similar PDQ problem is known, then the TURBO time-step will require about one-third more time.

The code requires at least 8,192 words of core storage, one drum unit, ten tape units, and an off-line printer. Larger core capacity is utilized as in PDQ to minimize computing time and restricts the maximum number of mesh points as follows:

Words in core	8K	16K	32K
Mesh points	2500	3750	6500

REFERENCES

1. O. J. Marlowe, P. A. Ombrellaro, CANDLE -- A One-Dimensional Few-Group Depletion Code for the IBM-704, Report WAPD-TM-53, May 1957.
2. O. J. Marlowe, P. A. Ombrellaro, CANDLE -- A One-Dimensional Few-Group Depletion Code for the IBM-704, ADDENDUM 1 -- CANDLE 2, Report WAPD-TM-53, ADDENDUM 1, October 1957.
3. L. M. Culpepper, CANDLE -- A One-Dimensional Few-Group Depletion Code for the IBM-704, ADDENDUM 2 -- CANDLE 3, Report WAPD-TM-53, ADDENDUM 2, October 1957.
4. DRIFT Code - additional information may be obtained from the Applied Mathematics Laboratory of the David Taylor Model Basin.
5. J. B. Callaghan et al, TURBO -- A Two-Dimensional Few-Group Depletion Code for the IBM-704, Report WAPD-TM-95, November 1957.
6. G. G. Bilodeau et al, PDQ -- An IBM-704 Code to Solve the Two-Dimensional Few-Group Neutron-Diffusion Equations, Report WAPD-TM-70, August 1957.
7. P. A. Ombrellaro, Effective Fast-Group Cross Sections in Four-Group Theory, Report WAPD-TM-63, May 1957.
8. J. G. Fairey et al, PROP and JET -- A Program for the Synthesis and Survey of Three-Dimensional Power Shapes on the IBM-704, Report WAPD-TM-116, May 1958.
9. G. W. Hoffman, One-Dimensional Few-Group Burnout Code -- Isotopic Density Equations, Report WAPD-TM-2, April 1956.

The CANDLE and TURBO Codes are available from Mr. Donald Cashman, Applied Programming Publications, Applied Science Division, IBM Corp., 590 Madison Ave., New York 22, New York.

Appendix D

THERMAL NEUTRON ENERGY DISTRIBUTION CODES

CONTENTS

D.1 SOFOCATE

The SOFOCATE code solves on the IBM-704 the Wigner-Wilkins differential equation for the distribution of thermal neutrons in equilibrium with a hydrogen-moderated homogeneous mixture where the absorption cross sections of the constituents may vary arbitrarily with energy.

The SOFOCATE code computes the neutron flux, the macroscopic absorption cross section, $\nu\Sigma_f$, the flux averaged diffusion constant and the microscopic fission cross sections. In addition, any desired function may be averaged over the resultant flux.

The code requires a core size of 4,096 words, 4 magnetic drums, and 4 magnetic tapes. One additional tape is required if tape output is desired.

Temperature, buckling, energy limit (< 2.0 ev), moderator, number densities of isotopes in the mixture, and the identification number of those functions whose flux-averaged values are desired are supplied as inputs to the code.

A typical problem running time is 30 seconds.

D.2 DONATE

The DONATE code solves on the IBM-650 essentially the same problem solved on the IBM-704 by SOFOCATE.

A typical running time is about 2 hours.

REFERENCES

1. H. Amster and R. Suarez, The Calculation of Thermal Constants Averaged over a Wigner-Wilkins Flux Spectrum: Description of the SOFOCATE Code, Report WAPD-TM-39, January 1957.
2. H. Amster and R. Suarez, Distribution of Neutrons at Thermal Energies -- Description of DONATE Code, Report WAPD-PM-45, May 1956.

The SOFOCATE and DONATE Codes are available from Mr. Donald Cashman, Applied Programming Publications, Applied Science Division, IBM Corp.,590 Madison Ave., New York 22, New York.

Appendix E

FAST CONSTANT PREPARATION CODES FOR FEW-GROUP METHODS

CONTENTS

E. 1 MUFT-3

The MUFT-3 code computes on the IBM-650 the Fourier transform of the slowing-down distribution from a point source in space. The equations which are solved are those which determine the first two Legendre coefficients of the flux. By suitable choice of coefficients in these equations, one can arrive at either (1) the P-1 approximation, (2) the B-1 approximation,(3) the P-1, SG approximation, or (4) the B-1, SG approximation. In a single run of the MUFT-3 code, results may be obtained according to any or all of these approximations.

The code accepts as input the isotopic number densities of the constituents of a mixture and the microscopic data for each of these isotopes. The number of groups in the input must be less than 200. In addition, the multi-group source spectrum is supplied as input.

The output of MUFT-3 is a set of few-group constants for each of five different group structures: Seven-group, five-group, three-group, two-group, and one-group.

The typical running time is five minutes per approximation per problem.

E. 2 MUFT-4

MUFT-4 is an IBM-704 code which computes the Fourier transform of the flux and slowing down density due to a plane source in an infinite medium of prescribed composition and determines the fast flux spectrum in a one-dimensional reactor of given buckling. The age in the composition is determined from the output by interpreting the output as a Fourier transform. By interpreting the output as a flux spectrum, fast-group macroscopic parameters are edited by the code.

Input data to the code as specified by the requestor are number densities, buckling, and self-shielding factors which are used in treatment of resonances. A preassembled library (using three associated library tape preparation programs, LTP1, LTP2, and LTP3) which contains microscopic cross sections, resonance parameters, and inelastic scattering matrices for the isotopes in the composition must also be available as input. Source spectra corresponding to various types of sources are also included on the library tape. The problem requestor has the choice of one of the following four approximation schemes:

1. P-1
2. Selengut (B-1 in the code notation)
3. P-1, Selengut-Goertzel
4. B-1, Selengut-Goertzel

If hydrogen is not present in the composition, a nonhydrogenous moderator is specified to be used in computation of the resonance integrals.

In addition to the few-group cross sections and the material age, the code will compute the flux and current spectra, the isotropic slowing down densities for hydrogen and the heavy isotopes and the anisotropic slowing down densities.

For a few selected isotopes of the composition in the problem, the code will edit the absorption and fission cross sections, separating the smooth and resonant contributions.

The code is limited to 100 lethargy groups with 3 fast few-group schemes; one-group, two-group, and three-group. Information for as many as 45 isotopes may be stored on a library tape; however, at most, 15 of these may be used in any one problem.

Average running time of a normal problem is eleven seconds; if additional edits are requested, the running time may approach one minute and forty-five seconds.

The machine requirements are as follows:

Core size	≧ 8k
Drums	Not used
Tapes	2 (or 3)*
Off-line printer	
STZ instruction	

---

*See Appendix C, WAPD-TM-72, p. 32.

REFERENCES

1. R. L. Hellens, R. W. Long, B. H. Mount, Multigroup Fourier Transform Calculation -- Description of MUFT-III Code, Report WAPD-TM-4, July 1956.
2. H. Bohl, Jr., E. M. Gelbard, and G. H. Ryan, MUFT-4 -- Fast Neutron Spectrum Code for the IBM-704, Report WAPD-TM-72, July 1957.
3. R. L. Hellens, Neutron Slowing Down in Group Diffusion Theory, Report WAPD-114, May 1956.

The MUFT-3 and MUFT-4 Codes are available from Mr. Donald Cashman, Applied Programming Publications, Applied Science Division, IBM Corp., 590 Madison Ave., New York 22, New York.

Appendix F

LEAST SQUARES CURVE FITTING CODES

CONTENTS

F.1 COFIT

The COFIT code computes on the IBM-704 the parameters A, B, and C in the expression $y = A \cos B(x - C)$ by the least squares technique based on 4 to 500 points of observed data. It also computes and prints the standard deviations of the estimates of A, B, and C.

A 4,096-word IBM-704 without tapes or drums is sufficient for this code. The running time per problem varies from 2 to about 8 minutes.

F.2 EXFIT

The EXFIT code is analogous to COFIT, except that it solves for the parameters A and B in the expression $y = Ae^{Bx}$.

F.3 F0030

The F0030 code is analogous to COFIT, except that it finds A, B, C in the expression $y = Ae^{Bx} + C$.

REFERENCES

1. B. L. Anderson and T. J. Lawton, COFIT -- A Least Squares Cosine Fitting Program for the IBM-704, Report WAPD-TM-26, October 1956.

The COFIT, EXFIT, and F0030 Codes are available from Mr. Donald Cashman, Applied Programming Publications, Applied Science Division, IBM Corp., 590 Madison Ave., New York 22, New York.

Appendix G

FEW-GROUP, THREE-DIMENSIONAL DIFFUSION THEORY CODES

CONTENTS

G.1 TRIXY

TRIXY is a code for the IBM-704 which solves the multi-group time-independent neutron-diffusion equations over a rectangular parallelepiped in the cartesian coordinate system. The equations solved by TRIXY are

$$\left\{ -\nabla\cdot D_i\,\nabla\phi_i + (\Sigma_i^a + \Sigma_i^R)\,\phi_i = \frac{\chi_i S}{f} + \Sigma_{i-1}^R\,\phi_{i-1} \right\}_{i=1}^{k}$$

where

$$S = \sum_{i=1}^{k} \Sigma_i^f\,\phi_i$$

Each of the six faces of the bounding rectangular parallelepiped may be specified independently either as having zero flux or by giving the ratio of outward current to the flux.

A mesh of horizontal and vertical planes is imposed on the rectangular parallelepiped with the mesh points determined by the intersections of the mesh planes. The composition of each mesh rectangular parallelpiped must be homogeneous. The χ_i are functions only of the lethargy group. The power distribution, S, and the group fluxes, ϕ_i, are computed at each mesh point. The maximum number of mesh planes and the number of different material compositions permitted within the mesh is dependent upon the size of the core memory and is as follows:

Memory	Number of Different Compositions	Maximum Number of Mesh Planes
8,192	200	72 perpendicular to x axis 36 perpendicular to y axis 36 perpendicular to z axis No more than 1,000 points in the yz plane
16,384	475	72 perpendicular to each axis No more than 2,000 points in the yz plane
32,768	975	72 perpendicular to each axis No more than 4,000 points in the yz plane

The product of the number of mesh points and the number of energy groups, k, is limited to about 150,000.

TRIXY requires six tape units. The input to TRIXY consists of:

1. Configuration information
2. Composition constants (D, Σ^a, Σ^R, Σ^f) for each material and each group
3. The value of χ for each group
4. The six boundary conditions
5. Mesh spacings
6. Rough power guess for a coarse mesh
7. Convergence criterion for the flux
8. Convergence criterion for the power distribution.

After each source iteration, certain information is printed. One of the numbers printed refers to criticality. At the conclusion of the problem, various items of information may be written on magnetic tape for off-line printing. The items available for off-line printing include fluxes, average fluxes, flux integrals, power densities, power integrals, and the number of fissions per source neutron.

Most TRIXY problems will run more than several hours. A three-group problem with 6,000 mesh points will normally take about eight hours.

G.2 TKO-1

TKO-1 is an IBM-704 code which finds a discrete numerical approximation over a rectangular parallelepiped for the few-group, time-independent, neutron-diffusion equations

$$\left\{ -\nabla\cdot D_i \nabla\phi_i + (\Sigma_i^a + \Sigma_i^R)\,\phi_i = \frac{\chi_i\psi}{\lambda} + \Sigma_{i-1}^R\phi_{i-1} \right\}_{i=1}^{k}, \quad k \leq 4$$

A mesh of horizontal and vertical planes is imposed on the rectangular parallelpiped, with a maximum of 28 planes in each coordinate direction. The code is restricted to the treatment of problems which are symmetric with respect to the plane x=y. Hence the flux and source values, ϕ_i and ψ, are obtained only at the mesh points on and to one side of this symmetry axis. Designating the boundary planes in the x and y coordinate directions by ss and the boundary plane in the z coordinate direction by uu, the total number of solution points (boundary points excluded) is

$$\frac{(ss-1)(ss)(uu-1)}{2}$$

This number is restricted to 2700 and 4750 on 16,384-word and 32,768-word computers, respectively. The code requires one drum unit and six tape units in addition to this core storage.

The rectangular parallelepiped is composed of at most 511 different regions, and the values of D_i, Σ_i^a, and Σ_i^R are regionwise constant. Variable mesh spacing is permitted, and the mesh must be chosen in such a way that all region interfaces lie on mesh planes.

Either a zero flux or a zero current condition may be applied at each boundary plane, the same condition being applied in each lethargy group. A logarithmic derivative condition may also be used at internal interfaces for control rod representation. This condition sets the current to flux ratio at the rod boundary.

Input to TKO-1 includes the number of groups and regions, the outer boundaries and boundary conditions, an eigenvalue approximation and a convergence parameter, the mesh intervals and orientation of regions in the mesh, and the group-dependent parameters, including a flux approximation, for each region. The only on-line output is an indication of the degree of convergence attained at the end of each iteration. The off-line printout consists of a complete edit of the input, a "picture" of each different x-y plane with all regions and interfaces indicated, the region volumes, the region integrated and averaged flux and source, and the pointwise flux and source values.

TKO-1 problems are iterated until

$$\frac{\bar{\lambda}^{(m)} - \underline{\lambda}^{(m)}}{2\lambda^{(m)}} \leqq \epsilon^2$$

where ϵ is the input convergence parameter and (m) is the iteration index. For $\epsilon = 0.05$, the running time of a 2700-point problem varies from 1.0 to 2.5 hours, depending upon the number of groups and the physical dimensions of the problem.

REFERENCES

1. Paul Greebler, TRIXY -- A Computer Program for Multi-group Nuclear Reactor Calculations in Three-Space Dimensions, Report KAPL-1549, August 1, 1956.
2. Ouida A. Clendinning, TRIXY -- A Three-Dimensional Multi-group Code: Input Preparation, Report KAPL-M-OAC-1, January 29, 1958.
3. W. R. Cadwell, TKO -- A Three-Dimensional Neutron-Diffusion Code for the IBM-704, Report WAPD-TM-143, July 1958.

Appendix H

FEW-GROUP, THREE-DIMENSIONAL DEPLETION CODES

CONTENTS

H.1 DRACO

DRACO 1, a three-dimensional few-group depletion code for the IBM-704, provides a means of studying the flux and power levels and the depletion and build-up of materials within a reactor for specified intervals of time during which the flux and power are assumed to be constant.

With a library of fast cross sections, various input quantities, and information from the previous time-step calculation, the group constants D, Σ^r, Σ^a, and $\nu\Sigma^f$ are calculated for each mesh rectangular parallelepiped of the region under consideration. A modified version of TKO-1 uses these quantities in solving the neutron-diffusion equations

$$\left\{ - \nabla\cdot D_i \nabla\phi_i + \Sigma_i^T \phi_i = \frac{\chi_i \sum_{i=1}^{k} \nu\Sigma_i^f \phi_i}{\lambda} + \Sigma_{i-1}^r \phi_{i-1} \right\}_{i=1}^{k}$$

where

$k = 2$ or 4

$\Sigma_j^T = \Sigma_i^a + \Sigma_i^r$

The pointwise fluxes resulting from this calculation are averaged over each mesh rectangular parallelepiped and are normalized to a specified power output. [redacted]

DRACO 1 requires 16,384 or 32,768 words of core storage, at least one drum unit, and nine tape units. DRACO 2, the maximum-xenon calculation requires 10 tape units. DRACO will handle two- or four-group problems and allows a maximum of 50 initial material compositions. Assuming a mesh imposed on some rectangular parallelepiped by intersecting horizontal and vertical planes spaced along the X, Y, and Z coordinate axes, the following conditions must be met where ss, tt, and uu are the last planes in the X, Y, and Z coordinate directions, respectively:

1. ss = tt
2. ss $\leq$ 28 and uu $\leq$ 28
3. $1/2\ (ss-1)(ss)(uu-1) \leqq 2685$ or $\leqq 4750$ for 16,384 and 32,786 core storage, respectively.

The plane X=Y must be a symmetry plane. Zero flux or zero current may be imposed at any of the outer boundaries.

The following quantities are required as input for each time-step: Information pertaining to the geometry of the problem; option control information; the length of the time-step; net power per time-step; initial eigenvalue guess; convergence criterion; percentage of homogeneous poison per group; integral of the fission spectrum for epithermal groups; the iodine yield for U^{235}, U^{238}, Pu^{239}, and Pu^{241}; mesh descriptions; composition description; thermal cross sections to be applied in specified compositions; flux guess; MUFT buckling for two-group problems; resonance escape probability of U^{238}; homogeneous poison (optional); isotopic densities; thermal self-shielding (optional); and logarithmic derivatives (optional). The geometry, the mesh spacing, and the time-dependent isotopic densities may not be changed between time-steps. To facilities the moving of rods, composition numbering may be altered.

The most important information printed on-line during a time-step calculation pertains to the progress of the iteration. Off-line edits make the following information available for each time-step: point flux, point power, power per mesh rectangular parallelepiped, beginning isotopic densities, final isotopic densities, macroscopic data, and power integrals.

Running time for a two-group, quarter-core problem with 3000 interior points is approximately two hours per time-step.

REFERENCES

1. D. McCarty, C. King, H. Henderson, J. Mandel, DRACO -- A Three-Dimensional Few-Group Depletion Code for the IBM-704, Report WAPD-TM-137.
2. G. W. Hoffman, One-Dimensional Few-Group Burnout Code -- Isotopic Density Equations, Report WAPD-TM-2, April 1956.
3. P. A. Ombrellaro, Effective Fast-Group Cross Sections in Four-Group Theory, Report WAPD-TM-63, May 1957.